NAZARBAYEV UNIVERSITY

REAL-TIME SEISMIC WAVE VELOCITY DETERMINATION FOR ACCURATE EVENT SOURCE LOCATIONS IN UNDERGROUND MINES

by

Zarina Mukhamedyarova

Submitted in partial fulfillment of the requirements

for the degree of

Doctor of Philosophy in Mining Engineering

June, 2024

REAL-TIME SEISMIC WAVE VELOCITY DETERMINATION FOR ACCURATE EVENT SOURCE LOCATIONS IN UNDERGROUND MINES

by

Zarina Mukhamedyarov

Submitted in partial fulfillment of the requirements for the degree of

Doctor of Philosophy in Mining Engineering

School of Mining and Geosciences

Nazarbayev University

November, 2024

Supervised by Fidelis Suorineni

DECLARATION

I declare that the research contained in this thesis, unless otherwise formally indicated within the text, is the original work of the author's original work. The thesis has not been previously submitted to this or any other university for a degree and does not incorporate any material already submitted for a degree.

Signature:

Date:

Abstract

This study addresses the considerable impact of human-induced seismic activity in underground mining on safety, productivity, and operational costs. Accurate prediction of microseismic and rockburst source locations is crucial for mitigating unforeseen events such as rockbursts. Current limitations in predicting the timing of these events necessitate a focus on probable locations. The research aims to overcome this limitation by developing a methodology that tracks and adapts to changes in ground conditions, providing a real-time solution for selecting appropriate velocity models in seismic monitoring systems. By considering the constantly changing velocity model in underground mining environments, the approach seeks to improve the reliability of source location calculations, ultimately enhancing worker safety and mining productivity. The study recognizes the evolving characteristics of rock masses and voids during mining, highlighting the inadequacy of a constant velocity model in source location algorithms. Laboratory experiments, simulating underground mine conditions with continuous changes, generated data for this study. Analysis reveals that, due to the heterogeneity and continuous changes in the mining environment, seismic wave velocity cannot be treated as a constant in source location algorithms. Predicting real-time seismic wave velocities significantly enhances the accuracy of seismic event source location. Dynamic numerical modeling in FLAC3D, using laboratory data, was employed to understand wave propagation and the physics of the problem. Machine-learning methodologies, including Linear Regression models trained on laboratory data and Deep Artificial Neural Networks for heightened precision, were harnessed to predict seismic wave velocities under varying conditions.

Acknowledgements

I wish to extend my heartfelt gratitude to Professor Fidelis Suorineni, my supervisor during my PhD study. Professor Suorineni's boundless energy and commitment to our shared goals have been a tremendous source of inspiration and motivation for me. His valuable feedback and constructive comments have played a pivotal role in keeping my work on the right track, ensuring its quality. I acknowledge Nazarbayev University for support through the Collaborative Research Program Grant 091019CRP2102.

I also want to express my deep appreciation to my family and friends. Their constant motivation and unwavering emotional support have been my pillars of strength throughout this journey.

Table of Contents

List of Figures

List of Tables

Acronyms and definitions

AE	Acoustic emission
ANN	Artificial neural networks
ASTM	American Society for Testing and Materials
CNN	Convolutional neural networks
DL	Deep learning
DT	Decision tree
FLAC	Fast Lagrangian Analysis of Continua
GAN	Generative adversarial networks
HDT	Hit definition time
HLT	Hit lockout time
MAE	Mean absolute error
ML	Machine learning
MS	Microseismicity
PDT	Peak definition time
ReLU	Rectified linear unit
RMR	Rock mass rating
RQD	Rock quality designation
SCA	Static cracking agent
UCS	Uniaxial compressive strength

1. INTRODUCTION

1.1. Background

Seismicity is the phenomenon that occurs naturally by earthquake activity or unnaturally by induced earth vibrations from man–made activity. This study focuses on seismicity in underground mining caused by human activity. The sudden release of energy from the rock mass or crust resulting in a set of seismic waves going through the rock mass or crust is known as a seismic event. In the case of mining, a seismic activity that causes the damage of an excavation, machinery and or personnel injury, is defined as rockburst. Phenomena such as rockburst and seismicity may dramatically impact the operation of mines in terms of safety, productivity, and operating costs. However, despite technological progress, predicting the time of occurrence of the rockburst is still controversial and debatable in the mining industry and rock engineering. According to the research of Trifu and Suorineni (2009), the time of occurrence of rockburst is hard to predict, and the only way to deal with this problem is to identify possible rockburst areas using numerical modeling and experience.

With current technological advances, microseismic monitoring systems have become very popular, and are widely used in the mining industry, especially in deep underground mining projects. The microseismic monitoring system helps to monitor mining-induced seismicity for the estimation of potential seismic hazard sources. Also, this tool is essential to control the seismic risk in terms of exposure of facilities and workforce to its consequences. The microseismic monitoring system plays an integral part in the understanding of the rockburst mechanism due to its capability to detect and recognize mine seismic zones. However, the accuracy and prediction of the microseismic monitoring system event source locations depend on the input velocity. Periodically updating input velocity models in seismic monitoring systems are time consuming and can result in erratic source locations in between the updating periods.

Current technologies cannot precisely identify the location or forecast the time of occurrence of a rockburst. Because underground mine seismicity significantly affects personnel safety and mine productivity, finding possible solutions for accurate seismic event source locations is vital for mitigating rockburst effects. The underground mine environment is challenging to control, while the laboratory is a perfect controlled environment to simulate and study seismicity. In this context discrete physical modeling is adopted in this study. Rather than relying on a singular block subject to modifications to reflect the dynamic ground conditions in mining environments (a labor-intensive approach) we used individual blocks. Each of the blocks represented a different stage in the mining process in time, structure, and geometry. This chapter presents the necessity for improving current velocity models in seismic monitoring systems, defines the research problem, establishes the research objectives, significance of the outcome to industry and science and provides the structure of the thesis.

1.2. Problem definition

Recent research has identified that wave velocities in rock masses in underground mining are not constant as previously often assumed in seismic monitoring systems source location algorithms. Rock masses in mining environments are continuously degraded because of mining. Blasting and excavation induced stresses result in fracturing of the rock mass. The presence of water accelerates weathering and erosion. Hence, the use of 3D velocity models based on 3D ray tracing in heterogeneous media that can consider the presence of voids from mining activities are being actively researched (Trifu & Shumila, 2010). This approach showed some improvements in the accuracy of seismic event source locations. However, seismic wave velocity changes are not only due to the introduction of voids but also several other sources of rock mass degradation including stress-induced fracturing and the state of the voids created including their constantly changing size, shapes and content (i.e. type of backfilling used or empty). In the current practice in accounting for voids in seismic wave velocities, the velocity in the seismic monitoring systems is periodically updated using development blasts or weight drops. However, because the rock mass condition is constantly changing in mining, real-time velocity changes must be predicted and used in the seismic monitoring systems source location calculation algorithm. This is because the event sources located in constantly changing ground conditions between the velocity updates will not be reliable. Moreover, even though frequent velocity updates may improve the situation, it is both challenging and costly to implement.

1.3. Research objectives

The primary purpose of the research is to create innovative methods for monitoring changes in velocity within continuously degrading ground conditions due to mining activities in underground mining environments. The goal is to predict the most suitable velocity model in real-time for use in seismic source location calculations in seismic monitoring systems.

The detailed research objectives are to:

1) Imitate changing rock mass conditions in mining environments using rock samples with different parameters, including holes, open voids, and variations in backfill and fracture conditions.
2) Simulate mining-induced fracturing effects by intentionally fracturing rock blocks with voids, both filled and unfilled, to understand the impact fractures and rock mass quality have on seismic wave velocity.

3) Understand the sensitivity of seismic wave velocity to various factors in the underground mining environment. Conduct dynamic 3D numerical modeling on FLAC3D to simulate and analyze the velocity changes within the rock mass under varying conditions.
4) Use machine learning (ML) for seismic wave velocity for various underground mine conditions in real-time seismic event source locations determination.

1.4. Scope of the research

The research is aimed at investigating underground mining conditions in a controlled laboratory environment backed with numerical modelling to understand the effect of continuously changing mining environment on seismic wave velocity and its impact on the accuracy of seismic source locations. Since the rockburst is site-specific, it depends on the strength of the rock mass, in situ stress state, mining method, the shape of the opening, and geology. This fact complicates the creation of a general solution for the purpose of accurate estimation of rockburst source location. Therefore, the outcome of the study should be considered as a procedure for accurate seismic event source location in any type of underground mine. It can be achieved by correlating rock mass quality and velocity as in Barton and Grimstad (1993). To understand a rather complex problem, dynamic numerical modelling of seismic events, together with laboratory tests, gave a strong basis for the development of the 3D velocity model to improve the accuracy of seismic source location. Input parameters for the modelling were provided through laboratory tests that mimicked the continuously changing mining environment. The study did not account confining stresses. This aspect is planned for future study.

1.5. Significance of the research

Rockburst in deep underground mines requires great attention and, currently, it is one of the great challenges in rock engineering and mining science (Wagner 2019). Major decisions related to seismicity are made based on the monitoring of seismic activities.

The significance of the research outcome to the mining industry and science is in the following:

- Accurate seismic source locations
- Significant boost to mine safety
- Reduction in downtimes due to rockburst
    - Increased mine productivity
- Accurate cave propagation monitoring in block caving mining and accurate monitoring of fracture growth and propagation in hydraulic fracturing
- Stress change prediction from rock mass response will expand knowledge in rock science.

Accurate location of zones with high seismic risks is the critical task of effective seismic monitoring systems. It will allow prevention of fatalities and production delays through safe evacuation of equipment and workers before rockburst occurs and safe re-entry after seismic activity.

1.6. Approach

To achieve the research goal the following tasks need to be completed:

1. Mimicking the mine environment in the laboratory
    a. mimic the changing mining environment rock mass conditions:
        - Preparation of homogeneous cubic rock/concrete samples from granite and concrete with different sizes and hole diameters representing

increasing mine maturity with time, where increasing sample size stands for increasing mine and increasing hole diameter represents increasing extraction ratio with time.

- Filling holes in the rock/concrete samples with different contents: empty, 0% cement (100% dry sand), 0% cement (water-saturated sand), 5% cement, 10% cement and 15% cement, 20% cement cured for 8hours-28days.

- The fracturing of the blocks to capture stress-induced damage from mining.

    - Static cracking agent is used in holes to fracture the blocks to see the fracturing and hole, fracturing and backfill effect on seismic wave velocity.
    - The fractures will be mapped to related degrees of fracturing on rock blocks quality (rock mass quality).

b. Determination of wave velocity through rock blocks at the different conditions described above using the SAEU3H AE system. Wave velocities will be determined for each rock condition stated in item 1a above.

c. Determination of numerical modeling input parameters and validation of concrete block qualities.

    - mechanical properties of granite and concrete blocks
    - mechanical backfill properties with time (uncemented and cemented sand fill)

2. 3D dynamic numerical modeling using FLAC3D to understand the physics of the event source locations problem and to collaborate the laboratory testing results.
3. Application of Machine Learning techniques for the prediction of seismic wave velocity in real-time for given ground conditions to be used as input in the seismic monitoring systems algorithm for source location determination.

1.7. Thesis Outline

This thesis is organized into seven chapters. First, mining induced seismicity is discussed, and then, each chapter addresses a specific objective of this research as follows:

- Chapter 1 – Introduction:

This chapter provides background to the problem, highlights the significance of improving the accuracy of mining-induced rockburst prediction methods, and presents the significance, objectives, approach, and scope of the research.

- Chapter 2 – Literature Review:

This chapter reviews the current state-of-the-art in rockburst prediction and mitigation. It covers microseismic monitoring systems and their limitations, as well as the impact of the input velocity model on seismic event source locations.

- Chapter 3 – Methodology:

This chapter details the methods employed to achieve the primary aim of accurately identifying the seismic source location. These methods encompass laboratory experiments, numerical modeling, and machine learning.

- Chapter 4 – Laboratory experiments on discrete physical models mimicking mine environment:

This chapter describes the laboratory setup, including materials and equipment used to simulate continuous rock mass degradation in underground mines and presents the results of laboratory tests using Acoustic Emission (AE) equipment. It outlines the procedure for velocity calculation, discusses the impact of continuous rock mass degradation on seismic wave velocity, explains the Rock Mass Rating (RMR) calculation procedure, and details the final database used as a basis for numerical modeling and machine learning.

- Chapter 5 – Dynamic Numerical Modeling:

This chapter describes the numerical modeling procedure, starting with model construction and ending with the presentation of sensitivity and parametric analysis results.

- Chapter 6 - Machine Learning:

This chapter includes a description of machine learning techniques applied to velocity prediction and event source location.

- Chapter 7 – Conclusions and Recommendations:

This chapter summarizes the findings and provides recommendations based on the research conducted.

2. LITERATURE REVIEW

2.1. Mining-induced Seismicity

With increasing production and depletion of mineral resources, underground mines are going deeper worldwide (Feng et al., 2019). Moreover, there are geotechnical engineering projects such as tunnels and underground laboratories located in very deep formations with complicated geology and ground conditions (Jiang et al., 2010; C. Zhang et al., 2012). High in situ stresses coupled with complex geology result in a series of hazards such as rockbursts, rock mass caving and excavation deformations (Fall et al., 2010; Palei & Das, 2009; Ranjith et al., 2017; Shi et al., 2020; Xie et al., 2015).

Rockburst is defined as a sudden and violent seismic event induced by excavation that causes damage to an excavation (Kaiser et al., 1996). Due to its high intensity and abruptness, rockburst is classified as one of the most hazardous dynamicl events in underground mining. It causes damage to excavations, machinery and injury to personnel. Rockburst can be categorized in three groups based on source mechanism: strainburst, pillar burst and fault-slip burst (Cai, 2013; Hedley, 1992; Kaiser & Cai, 2012). The most common type of rockburst in underground mines is strainburst (Cai, 2013; Zhang et al., 2012). Strainburst is caused by the tangential stress induced by excavation and results in violent and unstable rock failure (Kaiser & Cai, 2012). Pillar burst is a sudden and violent collapse of a pillar, or a portion of it, at times resulting in the breaking and expulsion of rock fragments from the pillar (Hauquin et al., 2018). It occurs when the accumulated elastic strain energy comes to the critical level where the released energy surpasses dissipated energy. A massive amount of failed rocks are released and the magnitude is usually larger than that of a strainburst (Kaiser et al., 1996).

The majority of rockburst studies are focused on the causes, risk assessment, time of occurrence, prediction, prevention and mitigation. Rockburst study methodologies can be classified into five types: empirical, analytical, experimental, data-based, and numerical. According to (Manouchehrian & Cai, 2018) there is not yet an efficient way to control rockbursts due to its complexity and influence of many factors including geological conditions, in situ stresses, induced stresses and mining operations acting as triggering conditions (Gao et al., 2019). Nevertheless, the problem of rockburst can be managed in two ways. First, by controlling the damage caused by seismic activity, and second by controlling the location and magnitude of the seismic event. In the case of numerous exhibitions and high magnitude seismic events, ground support systems could not prevent the damage of mines. If potential harm is high and cannot be managed by a support system alone, then monitoring of the location, time of occurrence and magnitude of the event is required since predicting time of rockburst occurrence remains elusive. Monitoring of the location, time of occurrence and magnitude of rockbursts as a means of rockburst effects mitigation is called the strategic approach to rockburst management. It is observed that some rockburst types are caused by mining sequence, excavation shape, or a combination of these factors with geological structures. The strategic approach relies on changing mining sequence, stoping sequence, and in some cases the original mine design (Kaiser et al., 1996). However, recently a combined approach that includes all proactive measures as tele-remote mining, elevated ground support, updated enhanced support systems, and minimization of worker and equipment exposure by using seismic monitoring systems has been found more advantageous than the separate application of any particular element (Trifu & Suorineni, 2009).

The probability of rockburst occurrence is evaluated based on the seismic history of the particular mine and analogous mines. Hazards from mining-induced seismicity are divided into two types: rockburst hazard and seismic hazard. The former is the probability of a seismic event resulting in damage, while the latter is the probability of occurrence of a seismic event. It means that not all seismic activities result in damage.

From a geomechanical perspective the main seismic hazards can be classified as follows:

1. Microseismic Density: Microseismic activity is a sign of rockmass degradation that may cause ground fall. Damage caused by microseismic density is classified as a permanent hazard since the damage is irreversible.
2. Seismically Active Planes: The presence and quantity of active planes state the hazard level. Seismically active planes relate to a short or medium-term hazard.

    a. Major seismic events can be caused by an active plane.

    b. Two or more active planes increase the fall of ground hazard.

    c. Local rockburst is caused by gravity and seismic energy release and has a potential risk to personnel safety, mining openings, and equipment.

3. Dynamic Stress Loading: large seismic events as rockbursts result in serious excavation damage by inducing dynamic stress loading. The relating hazard is classified as a short-term hazard (Malek et al., 2008).

The examination of rockburst case studies unveils that the detrimental effects of rockbursts are frequently concentrated and lack uniformity. To elucidate further, the magnitude of damage incurred in an excavation due to a rockburst exhibits variability across different locations. The localized nature of rockburst damage emanates from intricate mechanisms underlying rockburst phenomena and the combined influence of various factors contributing to their occurrence. While numerous factors affecting rockburst damages have been recognized, the precise conditions triggering rockburst incidents within a complex subterranean environment remain unknown (Manouchehrian & Cai, 2017).

2.2. Rockburst mitigation methods

To address the issue of seismic activity in mining operations, researchers globally have dedicated substantial efforts towards comprehending rockburst mechanisms, prediction techniques, and prevention methods (Zhou et al., 2018). A fundamental aspect of mitigating rockburst disasters is the implementation of accurate monitoring and early warning systems.

Presently, monitoring and early warning methods for rockbursts mitigation can be categorized into two primary groups: conventional rock mechanics methods (such as the drill cuttings method and rock mass deformation measurement method) and geophysical methods (including microseismic monitoring (MS) (Qin et al., 2019).

2.2.1. Microseismic monitoring systems

2.2.1.1. Predictive methods

Geophysical techniques, particularly the microseismic monitoring system, have gained widespread usage in underground mines owing to their non-contact nature, continuous data acquisition, and automatic monitoring capabilities. The microseismic monitoring system has proven to be an effective tool for assessing the occurrence of rockburst hazards by analyzing vibration wave signals resulting from roof breakage or rock mass fractures. By monitoring and providing warnings regarding potential rockburst hazards, the microseismic monitoring system aids in determining the displacement and the fracture state of the rock mass. The system identifies zones of stress-induced fracturing in terms of mining activity. The microseismic monitoring system is essential to provide a quick response to abnormal activity such as events with high magnitude. Providing a quick and reliable location of seismic events is one of the critical tasks of mine seismicity monitoring. The seismic event source location is made of two steps: the first is the calculation of propagation time, and the second is the inverse procedure. In mining sites, various derived indices such as energy level, frequency of occurrence, main frequency of vibration waves, and fractal dimension are commonly utilized to evaluate the present hazard status.

Zhang et al. (2021) conducted an investigation into the functional relationship between MS energy and rock damage using classical Benioff strain theory. As a result, they proposed a novel parameter for predicting rockburst incidents based on the time of occurance. Liang et al. (2020) employed the wavelet packet transform method to analyze the intricate waveforms of MS events. Their findings demonstrated a downward shift phenomenon in the energy distribution of frequency bands, which can serve as an early warning indicator for rockburst occurrences. Yu et al. (2022) highlighted the abnormal changes in source parameters of MS tremors, such as MS event density, seismic energy density, cumulative volume, energy index, and b-values, as valuable warning signs for identifying potential rockburst incidents. Mondal and Roy (2019) analyzed MS events preceding or occurring during roof falls and surface blasting, utilizing Fractal Dimension and b-value. Their results indicated that these two parameters contributed to the identification of precursor signatures for spatial-temporal forecasting of rockburst events. Xue et al. (2020) proposed several statistical parameters, including cumulative apparent volume, energy index, and cumulative released energy, and investigated their relationship with rockburst events. Their analysis provided a valuable reference for rockburst prediction. Feng et al. (2016) introduced a fractal calculation method to examine the self-similarity of energy distribution in MS events during immediate rockburst development. They observed that the daily energy fractal dimension of MS events increased as immediate rockburst approached, serving as a guide to mitigate the risk of immediate rockburst during the excavation of deep, and hard-rock tunnels. Moreover, the application of the MS system in rockburst monitoring has a long history, resulting in a substantial accumulation of monitoring data over the years. This data has laid the groundwork for the application of artificial intelligence (AI) algorithms in rockburst hazard prediction in terms of location. In recent years, numerous scholars have successfully applied decision trees, Bayesian networks, logistic regression, neural networks, and other techniques to predict rockburst incidents, with practical applications in mine sites (Xue et al., 2023). Nonetheless, the warning indicators discussed above may yield different outcomes for the same event due to their distinct principles in reflecting the progression of rockburst precursors. This disparity can potentially impede the accurate assessment of hazard states by mine personnel. Moreover, the prediction of rockbursts presents a prominent class imbalance issue, limiting the practical effectiveness of machine learning algorithms and often leading to overfitting phenomena. Consequently, achieving precise prevention and control of rockbursts in the field solely through the analysis of MS warning indicators from a time series perspective is challenging.

2.2.1.2. Velocity models for microseismic monitoring systems

The ability to monitor a 3D volume with 3D sensors distribution is a perfect configuration that will provide the most accurate source location and parameters. Nevertheless, 1D (linear) and 2D (planar) sensors distribution also can produce reliable results and can be used as a microseismic array in tunnels where height is not important. Installation of triaxial sensors is vital in the case of linear or planar sensors distribution to avoid non-uniqueness.

The velocity model accepted for the rock mass is the key factor affecting the accuracy of seismic event locations. A single velocity model is based on the assumption that the whole volume has the same elastic properties and is considered isotropic and homogeneous with known location sources as blast holes or zones of high impact and doesnot change with time. Nevertheless, most mines still use a single velocity model for microseismic monitoring. 2D models use several parallel layers that could be with or without anisotropy. The most structured velocity model is a 3D model with six horizontal layers and the 3D shape of the voids and caves. The mining environment is very complicated because of geological structures, natural cavities, and excavation activities. Therefore, the 3D velocity model is a practical approach that can integrate layers, voids, and blocks. The homogeneous velocity model is inappropriate for seismic monitoring in the mining environment due to continuously changing conditions. The general 3D velocity model can be constructed. Construction of the 3D velocity model is possible through ray-tracing or wave front reconstruction (Trifu & Shumila, 2010). However, ray-tracing faces limitations during implementation; one of them is a sharp increase in velocity within the medium. Therefore, ray tracing is applicable only for a restricted group of velocity models and is better to handle through numerical modeling. Trifu and Shumila (2010) proposed an updated Fast Marching Method (FMM) algorithm for wave front reconstruction. The algorithm considers travel time and velocity, and the 3D model derived based on available geological and structural information—the method calculates variable velocity models through wavefront reconstruction. The algorithm is adapted for low-velocity volumes, which stands for caves or mined-out stopes. The ordinary FMM provides both speed and accuracy to get practical results; however, the method requires simulation of the first arrived wave front.

3D distribution of sensors is an optimal arrangement and commonly will lead to higher precision in source locations. Isolines alter while passing the horizontal layers and cave zones, which results in lower velocity. Analysis of the seismic mechanism is commonly conducted by moment tensor calculation with no assumptions mentioned above. Conducting an assumption-free analysis provides the framework for potential failures.

Seismic moment tensor inversion is the method developed to apply a 3D velocity model. It requires the direction of seismic energy towards the sensor and distance correction to the amplitude. A combination of the moment tensor inversion method with a 3D velocity model will result in more accurate input data. Source mechanism analysis is performed for a better understanding of the failure mechanics related to the location of rock fractures (Collins et al., 2014).

2.2.2. Spatial-temporal prediction method

In recent years researchers have proposed rockburst warning methods that adopt a "spatial-temporal integration" approach (Cai et al., 2015). Cai et al. (2014) proposed the utilization of active and passive seismic tomography to depict geological discontinuities in linear images, enabling the assessment of stress redistribution and the identification of high-seismicity zones for rockburst hazard evaluation. Li et al. (2021) identified sharp-rise-sharp-drop variations in total daily energy, event count, energy deviation (≥20), and event count deviation (≥1) as temporal precursors for high-energy tremors. By combining these temporal indicators with the spatial evolution patterns of high-energy density index of MS (EDIM), velocity, and velocity anomaly regions, they developed a spatial-temporal integrated early warning method for rockbursts. Cai et al. (2014) developed a spatial-temporal prediction method for rockbursts by utilizing multidimensional information from MS monitoring and constructing contour maps for each indicator. Wang et al. (2018) employed temporal and spatial distribution graphs of tremors along with energy density cloud images to identify high-stress regions.

Despite notable progress in rockburst early warning methods, most approaches rely on qualitative descriptions such as continuous indicator increase or assessments of whether indicators exceed critical values. These methods either depend on human judgment based on indicator trends or are limited by dynamically changing critical values due to the complex conditions in mining operations, hindering their large-scale application. Furthermore, when predicting rockbursts from a spatial perspective, the majority of images are generated through complex modeling and calculations, making it challenging to meet the timely and accurate warning requirements of mine sites.

Extensive laboratory research and field observations have demonstrated that rockbursts follow a nonlinear developmental process (Li et al., 2021). Due to the incomplete understanding of the underlying mechanisms causing rockburst, it is challenging to identify a single measurement indicator that fully captures the entire evolution process of rockbursts. Nevertheless, rockbursts result from the stress-induced damage to rock formations, characterized by the internal initiation, propagation, convergence, and connection of fractures, ultimately forming large fissures. The energy released during this process propagates outward as vibration waves, electromagnetic signals, and other forms. Consequently, indicators that quantify the characteristics of energy release signals from various dimensions (such as MS energy, frequency, etc.) also exhibit changes. A comprehensive analysis of these changing patterns is crucial for detecting anomalous trends prior to extensive coal-rock damage, serving as a key factor in rockburst warning systems. Furthermore, accurately identifying and quantifying the spatial variations in warning indicators at specific local locations are essential for the precise prevention and control of rockbursts.

2.2.3. Ground Support and Backfill

Enhanced ground support is a system to control the damage caused by seismic activity. Together with the type of support system, it is essential to select the right timing and location of support installation. Enhanced support is a type of integrated support consisting of cone bolts, mesh, shotcrete arches or zero-gauge straps. The combination of these two support systems has demonstrated its efficiency in burst-prone conditions and in zones close to seismically active geological structures. Enhanced support is more effective when established at the early development stage since delayed installation leads to additional challenges over time caused by high in-situ stresses (Malek et al., 2008).

Seismic energy release is a dynamic process, which is not consistent or constant. Most of the mine area will not be affected; therefore, support installation for all mine areas is not relevant as it is extremely expensive. A seismic hazard map is the means for strategic determination of places for enhanced support installation to ensure ground stability. Moreover, it assists in further planning of mine development by constructing infrastructure away from the risky areas or by setting a stronger support system. However, enhanced support systems are costly and cannot be installed all over the whole mine development (Malek et al., 2008). Assessment of the possibility of rockburst damage in a particular part of the mine is necessary to forecast the support system's timing and placement.

Backfill is another type of ground support, and different kinds of backfill have considerable effect on rock mass response to mining activities. However, backfill is regional, and the replacement of the backfill system with another is an expensive and slow process. Backfill could reduce rockburst damage only in the case of relatively thin, tabular orebodies, while in massive and more extensive orebodies, the effect of backfilling is negligible. The main reason for that is material porosity because for orebodies with large thickness, it is not possible to place backfill with enough density to resist convergence (Kaiser et al., 1996). The potential energy in the orebody walls is the result of walls converging after mining activities. The energy source that causes rockburst is the potential energy in the walls. Part of the energy released in the form of seismicity is reported as rockburst or seismic activity if it causes damage. Backfill can be applied to reduce the amount of released energy by absorbing a part of potential energy in the orebody walls. As a result, the severity of the rockburst will decrease due to the changed energy balance. Part of the released energy after the mining activities continues to be stored in the pillars and walls, another part is absorbed by backfill, and the rest is released. The released energy is consumed by rock mass fracturing in the form of seismic energy. Several factors govern the energy of the wall rocks and the released energy. The most crucial factors are depth, stress level, the stope span, and wall rock modulus. The energy amount is proportional to the square of the depth (stress). It means that with increasing stress, wall rock stiffness has to be raised, and stope span decreased (Kaiser et al., 1996).

2.2.4. Simulation and prediction of rockburst stress conditions

Despite significant advances in research, conventional testing methods fall short in accurately simulating the stress conditions that lead to rockbursts. Rockbursts typically occur near excavated boundaries where the stress state transitions from a triaxial equilibrium state to a newly redistributed state after excavation. In this redistributed state, tangential stress progressively increases and can eventually reach the rock’s ultimate strength, leading to a rockburst.

Recently, He et al. (2010) introduced a modified true-triaxial testing system designed to address these limitations. This system can unload pressure on one surface of the rock sample to replicate stress concentrations around a free face and measure the kinetic energy released during a rockburst. The apparatus includes key components such as a hydraulic loading and unloading system, a data acquisition system for monitoring force and displacement changes, high-speed cameras to measure the kinetic energy of ejected rock fragments, an acoustic emission system to observe damage progression, and an infrared monitoring system to assess surface temperature and internal damage.

In the true-triaxial testing setup, loads are applied simultaneously along three principal stress directions to simulate a predefined in-situ stress state. The specimen is then subjected to constant loads until a uniform stress distribution is achieved. Subsequently, one surface of the sample, subjected to radial stress, is abruptly unloaded while the axial stress is maintained and incrementally increased until the specimen fails. The enhanced capabilities of this true-triaxial system have led researchers to explore various factors affecting rockburst hazards, including moisture content, temperature, tunnel axis stress, sample aspect ratio, and unloading rate.

During rockburst tests, rocks fail severely at a specific stress level known as rockburst maximum stress. Accurate prediction of this stress level for different rock types, considering critical rock mechanical characteristics, can aid engineers in identifying rockburst hazards under various in-situ stress conditions, thereby improving the stability of underground structures and supporting numerical studies. Furthermore, predictive models developed by He et al. using multiple linear regression, artificial neural networks, and support vector machines offer valuable tools for estimating rockburst stress when testing facilities are unavailable.

Shirani Faradonbeh et al. (2020) formulated two crucial rockburst parameters in their study — maximum rockburst stress and rockburst risk index - using data from true-triaxial unloading tests and robust data-driven methodologies.

Parametric analyses of the generalized evolutionary programming models for rockburst stress and rockburst risk index revealed that the stress level at which rockburst occurs increases monotonically with unconfined compressive strength and vertical stress. Conversely, the rockburst risk index decreases non-linearly with parameters such as rock modulus, elastic modulus, Poisson’s ratio and rockburst stress. Additionally, strong correlations between rockburst parameters and their input variables suggest that these inputs are effective indicators for assessing and predicting rockburst phenomena in deep underground environments.

2.3. Simplex Method

The simplex method, initially proposed by Nelder and Mead (1965) as an optimization algorithm for function minimization, has garnered widespread acceptance across various scientific and engineering disciplines. Mohsin et al. (2021) contribute to the discourse on optimization methods, accentuating the efficacy and adaptability of the simplex method. Its proficiency in handling intricate, non-linear problems positions it as a promising choice for applications such as seismic event source location. The Simplex method is based on the idea that, for a set of sensor arrival times, the error for any given point can be calculated by comparing the observed and predicted arrival times. This creates an error space where each point is associated with an error value, and the point with the smallest error corresponds to the event location.

The method of finding this point of minimal error using the Simplex method is unique. It starts by creating a Simplex figure, which is then moved through the error space according to rules based on the errors at its vertices. The solution is found when the Simplex figure reaches a low-error area in the error space. A Simplex is a geometric shape with one more vertex than the dimension of the space it is in; for example, a triangle in two dimensions or a tetrahedron in three dimensions. In comparison to other source location algorithms, the Simplex method has two major advantages. First, it has a strong tendency to converge, with little risk of divergence. Second, it is highly adaptable, able to accommodate a variety of conditions and requirements. It can use P- and S-wave velocities at the same time, work with different velocity models, and employ either least squares or absolute value optimization methods. The author suggests that the Simplex method should be considered a primary method for source location due to its unique combination of essential features that ensure reliable, accurate, and robust source location (Blake & Leighton, 1970).

The computational efficiency of the simplex method assumes paramount importance in seismic event source location, where real-time processing is imperative. Aster et al. (2018) extend the conversation to the application of optimization methods, including the simplex method, in solving inverse problems within the domain of seismic monitoring. The inherent complexities of these inverse problems, stemming from uncertainties in velocity predictions and sensor measurements, underscore the necessity for robust optimization techniques.

Spall (2003) introduces a stochastic search and optimization perspective, addressing challenges posed by uncertainties in seismic monitoring. This stochastic approach enhances the applicability of the simplex method, particularly in scenarios where uncertainties in velocity predictions and sensor measurements prevail.

Expanding the perspective, Song et al. (2023) delve into the broader applications of optimization methods, encompassing the simplex method, in control theory. While not directly centered on seismic monitoring, this literature provides insightful perspectives into potential synergies with the field, presenting a holistic view of optimization applications.

In conclusion, the simplex method emerges as a potent and versatile optimization tool in seismic event source location. Its adaptability to varying geological conditions, ability to handle uncertainties, and computational efficiency position it as an asset in the progression of seismic monitoring systems. Ongoing research endeavors are crucial for further refining and extending the application of the simplex method, addressing the multifaceted challenges.

2.4. Numerical Modelling

A mathematical description of a physical (or other) behavior based on pertinent hypotheses and simplifying assumptions is known as numerical modeling (Sirois & Grilli, 2015). (Jing, 2003; Jing & Hudson, 2002) stated that numerical modeling methods in rock mechanics can be divided into continuum, discontinuum and hybrid methods.

Significant progress has been made using numerical modeling to understand physical processes in rock mechanics and rock engineering at various scales over the last 50 years due to the rapid advancements in computer technology and software. The numerical modeling method provides the benefits of low cost, safety, time savings, and flexibility compared to other methods like physical modelling and field tests. It may also offer more information.

According to Salamon and Kazár (1993), numerical modeling might be helpful for a variety of aspects of the rockburst problem, including the relationship between mining activities and the associated seismicity, the source mechanism, and the consequences of seismic waves on mining excavations. Numerical simulation techniques have been extensively used up to this point to examine the causes underlying rock mass failure as well as the mechanical response of complex rock masses. The simulation results, such as seismic locations, magnitudes, and mechanisms obtained from the numerical model compared with seismic data in the field, give further confidence that the model can behave in a realistic manner, even though the model is obviously a significant simplification of reality. Accurate prediction of rockburst occurrence time is very complicated due to the randomness and complexity of rockbursts mechanism (Qian, 2014; Zhou et al., 2018). However, the occurrence of rockbursts is primarily determined by changes in ground stress caused by excavation. Geological survey technology, ground stress detection technology, rock mechanics theories and methods, and long-term numerical simulation development have enabled qualitative and quantitative prediction of the location and intensity of rockbursts (Qian, 2014). According to researchers, the era of quantitative rockburst prediction has arrived, and this quantitative advancement requires a combination of numerical simulation and on-site observation (Cai, 2016).

Numerical modeling is the best way to evaluate the response of rock mass to different mining systems and mining sequences. Moreover, issues related to the sequencing and mining systems are very complex and hard to adjust. Numerical modeling is the proper approach to assessing mining strategies to reduce the rate at which energy is released from the system.

Numerical models can provide measurements of stress strain changes caused by large-scale mining, when geotechnical monitoring is not available (Wang et al., 2021). Designed numerical models could suggest the best locations for access and proper stope sequencing. However, the process of rock mass response to mining that causes seismic energy release and potential damage to the excavations is complex and still not thoroughly understood. Therefore, laboratory experiments in a controlled environment are an appropriate solution for seismicity study.

Factors controlling the seismic activity in the mine are not equivalent to those controlling the volume of the damage caused by seismicity. High stress is not the only factor causing seismicity; therefore, not all highly stressed areas provoke rockbursts. There is a strong correlation between areas with a considerable decline in the volume of stored energy and seismically active regions. A threefold analysis is needed for the assessment of potential energy release that responds to mining works. Major components of the analysis are:

- Analysis of stress
- Analysis of energy
- Analysis of the loading system.

Several conditions need to be satisfied with seismic energy release from the rock mass:

a) applied stresses have to surpass the strength of the rock mass

b) a considerable volume of energy needs to be stored and released

c) energy release must be in a short period to initiate the dynamic, non-linear response of the rock mass.

Therefore, simulation of mining activity by considering threefold analysis is critical for assessing potential damage caused by seismicity (Kaiser et al., 1996).

2.5. Summary

Rockburst events have a significant impact on both personnel safety and mine production. Preventing such incidents is recognized as superior to dealing with their consequences. Recent research indicates that microseismic monitoring systems have become indispensable tools in deep underground mines, enabling the characterization of mining-induced seismicity to comprehensively evaluate seismic hazards. These monitoring systems play a vital role in minimizing personnel and equipment exposure to potential seismic hazards, thereby mitigating seismic risks.

The effectiveness of seismic monitoring systems heavily relies on their ability to identify, locate, and quantify mine seismic events, leading to a better understanding of rockbursting mechanisms. This understanding is instrumental in managing and mitigating seismic hazards, resulting in enhanced worker safety and improved mining productivity. However, the accuracy of these systems in reliably locating event sources is closely linked to the input velocity used in the event source calculation algorithm.

Using a single static input velocity or assuming a layered model with a homogeneous rock mass in an underground mining environment is unrealistic and often results in significant source location errors. Underground mining operations lead to continuous changes in rock mass qualities and void conditions. Mining-induced stress alterations can cause fracturing of the rock mass, deteriorating its quality and inducing fault movements. Furthermore, voids created during ore extraction may be backfilled with materials of varying types and strengths, while some voids remain unfilled. Consequently, the conditions surrounding underground excavations and the state of the created voids continuously evolve during mining operations. Consequently, the use of a single static input velocity or a layered model with a homogeneous rock mass in seismic monitoring systems for source location calculations is inappropriate.

After reviewing the literature, it becomes evident that a significant source of uncertainty affecting source location accuracy lies in the velocity model utilized in the location algorithm. Establishing a reliable velocity model in mining is challenging due to encountering multiple rock types and the constant changes in rock mass conditions resulting from the creation of voids and stress alterations. This complexity necessitates a continuously changing velocity model, which contrasts with the current assumptions of using single (homogeneous rock mass assumption) or variable static constant velocity models (layered rocks assumption) in seismic monitoring systems for seismic source location calculations.

3. METHODOLOGY

To achieve the thesis objectives, three main tasks need to be completed. The first one involves the application of discrete physical models in a laboratory environment to mimic rock mass degradation in underground mining. The laboratory, serving as a controlled environment, offers an intelligent avenue to understand seismic wave velocity variations attributed to ground condition degradation. Conducting experiments in controlled environments allows researchers the flexibility to adjust essential variables, closely examining their effects both individually and in combination on the outcomes. Homogeneous cubic granite and concrete samples of different sizes and hole diameters represent increasing mine maturity over time, where an increase in sample size signifies increasing mine size and an increase in hole diameter represents an increasing extraction ratio over time. The voids were filled with different types of materials (various mix ratios of sand, cement, and water) representing different backfill types at various stages of curing. To simulate mining-induced stress fracturing, the rock blocks were fractured using a static cracking agent. After mimicking rock mass degradation in underground mining, the wave velocity was determined through rock blocks under the conditions described above using the Acoustic Emission (AE) system. The data from the experiments were then gathered into a database for use in subsequent tasks.

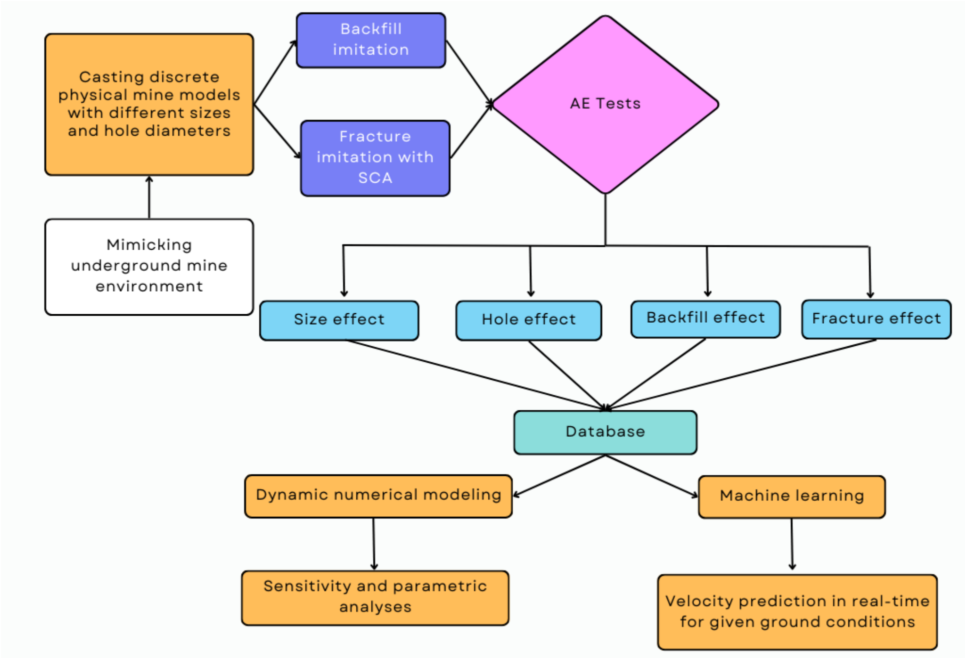

Figure 1. Schematic representation of methodology

The second task entails the use of numerical modeling to understand the sensitivity of seismic wave velocity to various factors in the underground mining environment, given that seismic wave velocity strongly correlates with physical rock properties. For this purpose, dynamic numerical modeling in FLAC3D was conducted. The choice of program was based on the type of material being modeled and the spatial dimensions of the problem. FLAC3D, which uses continuum mechanics, is suitable for materials considered as continuous solids, in contrast to UDEC and 3DEC, which are based on the discrete element method and are ideal for distinctly separated or fractured materials. The study focuses on investigating how void presence and the elastic characteristics of rock influence the velocity of seismic waves within rock samples under transient conditions. To achieve this, results from laboratory experiments with granite and concrete cubes are simulated using dynamic numerical modeling in FLAC3D.

The main goal of this task is to perform sensitivity and parametric analyses using a numerical simulation of granite and concrete cubes, considering their dynamic behavior. The data used for creating the simulation comes from experiments involving AE described in the first task. Fully understanding how different factors impact this analysis is crucial, especially regarding how fast waves move through the rock and how seismic waves propagate. This in-depth exploration is essential because having an accurate understanding of wave speed can help predict rockburst incidents more reliably.

The third task involves using machine learning to predict seismic wave velocity for various underground mine conditions in real-time, to be used as input in the seismic monitoring systems algorithm for source location determination. This approach is a novel, three-pronged method involving the application of machine learning techniques for velocity prediction and seismic event source location, using the simplex method. The database generated with AE equipment was used to train the models. The first phase focuses on predicting the velocity of seismic waves under various conditions using machine learning algorithms, including Linear Regression, Artificial Neural Networks (ANN), and Decision Trees (inclusive of ensemble methods such as Random Forest and Gradient Boosted Trees), to identify the best-performing model. The second phase involves applying the simplex method for the preliminary location of seismic event sources. The simplex method optimizes an objective function representing the seismic wave travel time (dependent on the predicted velocities) and the potential seismic event locations. To address the errors observed in the second phase, both the original and an augmented dataset were used to train a machine learning model to predict the seismic event location directly. This phase aims to offer a refined and more accurate prediction of seismic event locations.

In summary, the comprehensive methodology integrates AE testing within controlled laboratory conditions, dynamic numerical modeling in FLAC3D, and the application of machine learning. This holistic approach serves as the foundation for subsequent chapters, enhancing the strength of the study and facilitating further analysis and exploration.

4. LABORATORY EXPERIMENTS ON DISCRETE PHYSICAL MODELS MIMICKING MINE ENVIRONMENT

4.1. Materials and methods

To understand changes in seismic wave velocity in constantly degrading rock mass conditions, laboratory tests that mimic the underground mine conditions in a controlled laboratory environment are conducted. Blocks of concrete and granite were used to mimic various stages and conditions in underground mining. The blocks used were in the form of cubes. Sample material choice was based on material homogeneity. The cube sizes varied between150 mm and 450mm (Figure 2) considering the effect of boundary conditions based on theory of elasticity. Each cube size was with and without hole to represent increasing mine extraction with time. The concrete cubes were cast in accordance with ASTM C-109 standard. The cubes were tested after curing for 28 days, when they would gain 99% of their strength (Memon et al., 2018). The holes were in the center of the cubes and through the blocks. The hole diameters varied between 50 mm in the 150 mm cube to 150 mm in the 450 mm cube in increments of 25 mm, while the cube sizes increased by 75 mm from the 150 mm cube to the 450 mm cube (Table 1) to represent a mine with an increasing extraction ratio with time.

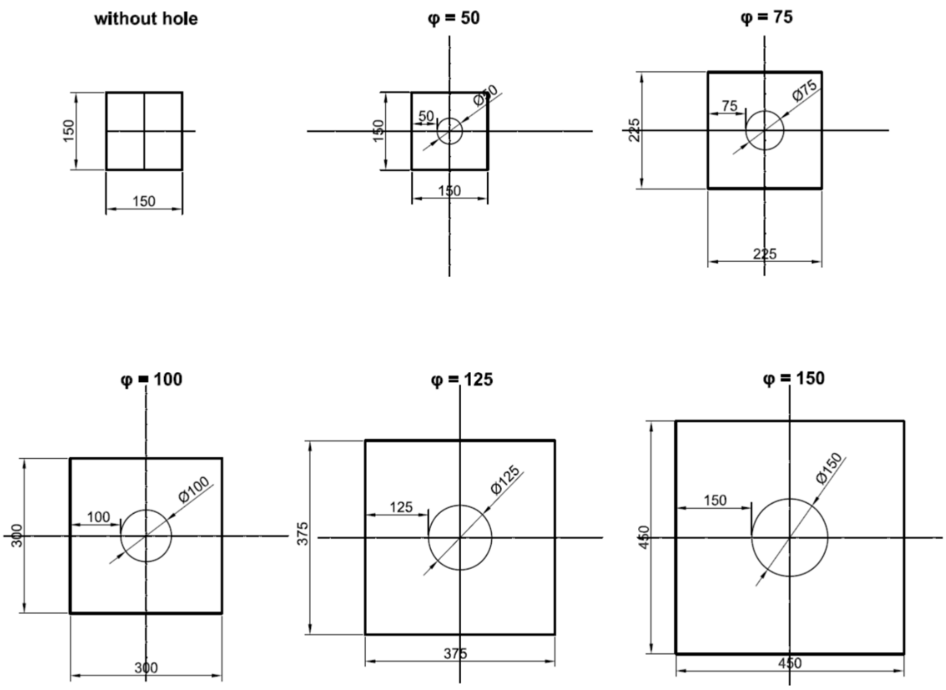

Figure 2. Sample sizes

Table 1. Geometry of rock samples

Cube size (mm)	Material type	Hole diameter (mm)
150	concrete	0 (No hole)
150	concrete	50
225	concrete	0 (No. hole)
225	concrete	75
300	granite	0 (No hole)
300	granite	100
375	concrete	0 (No. hole)
375	concrete	125
450	concrete	0 (No. hole)
450	concrete	150

The mimicked mine voids in the cubes were filled with various mixtures of sand, cement, and water at various mix ratios to represent different backfilling at different extraction stages and times. Backfill ratio of 0% cement (100% dry sand), 0% cement (water-saturated sand), 5%

cement, 10% cement, 15% cement and 20% cement contents were used. Each backfill type was tested at various stages of curing (8 hours, 1 day, 7 days, 14 days, and 28 days) to see the backfill cement ratio and time effect on seismic wave velocity.

Induced stress and blasting effects were simulated using a static cracking agent (SCA), which is a highly expansive powdered cementitious material for rock and concrete breakage (Xu et al., 2022). The damage extent in the rock and concrete cubes was determined using a modified Rock Mass Rating (RMR) system (Bieniawski, 1973) 1989 version (Bieniawski, 1989) modified for laboratory scale application. Fractures in the rock and concrete cubes mimic joints in real mines. AE tests were conducted to determine wave velocity going through each cube condition tested including backfilling and fracturing states. Eight sensors were placed on the cubes at known locations with one acting as pulser to generate the wave across the hole and the other seven sensors were receivers. Data derived from the AE tests included the arrival time of the wave at each sensor. Sensor 1 (pulser) was placed at the middle of the front view of the cube to enable the wave generated pass across the hole in the center of the block (Figure 3).

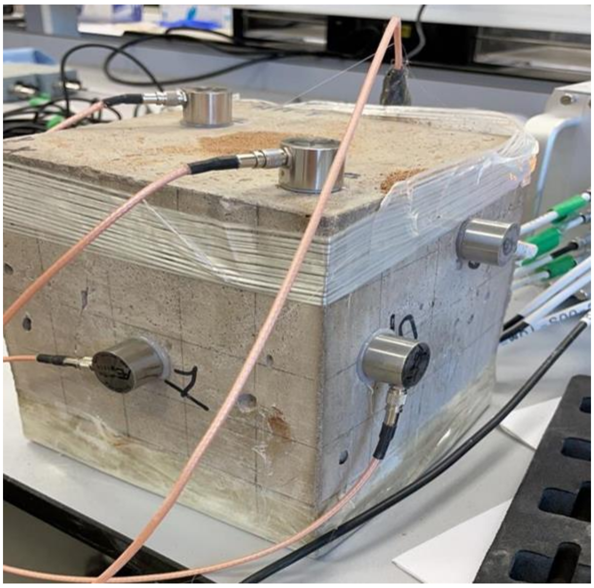

Figure 3. AE sensors attached to the rock sample

In mining practice, voids such as stopes are usually filled with backfill of various types. To mimic backfilling, the holes in the blocks were subsequently filled with backfill (Figure 4) with different cement to sand ratios of 0%, 5%, 10%, 15%, and 20%. The 0% cement content backfill was tested dry and wet. Each of the backfill types was cured for 8 hours, 1 day, 7 days, 14 days, and 28 days and tested to account for curing time impact on seismic wave velocity.

Figure 4. Granite rock samples with the cube size 300 mm with and without holes (hole diameter is 100 mm)

Initially, samples with holes were tested empty to represent a mine without a backfill. In the following tests the holes were filled with different cement to sand ratio backfills cured for 8 hours, 1 day, 7 days, 14 days, and 28 days to represent a mine with different backfill types and ages.

4.1.1. Granite cubes

The study used laboratory experiments with homogeneous rock samples of granite. Sample homogeneity was the critical factor for the choice of rock type. The surfaces of the cubes must be polished to a tolerance of 1 mm, with each opposite face parallel to each other. The homogeneity and isotropy of the rock allowed for the results to be comparable. It was a challenge to prepare granite cubes in-house to meet these specifications. Hence, a professional stone vendor was used.

Ideally, it was planned to use only granite cubes for the project. However, the cost of the granite cubes and the challenge of obtaining samples that were consistent in composition resulted in the use of synthetic rock in the form of concrete cubes.

4.1.2. Concrete cubes

The concrete cubes were molded in the laboratory with a mixture of sand and cement to represent rock. Sieve analysis was performed using vibratory sieve shaker AS 200 basic to remove clay particles, organic materials and oversize fragments from the sand. Particles larger than 4mm were removed as oversize fragments and particles less than 0.002 mm were removed as clay. A suitable cement to sand ratio was established through ASTM C-109 C standard (C109/109M-16a, 2016). The cubes were used after curing for 28 days. Material proportions for standard mortars according to ASTM C-109 C standard were used as follows:

- sand to cement ratio of 2.75 and
- water to cement ratio of 0.485.

After filling the mould with the mixture of it was vibrated for 4 minutes for compaction and the release of excess air. Samples of 37mm diameter and 74mm height were prepared from the same mixture for the UCS test as a control measure to ensure all blocks were similar in strength.

4.1.3. Backfill Characteristics and Curing

Core samples with a cement content of 5%, 10%, 15%, 20% were molded in wooden molds (Figure 5 a,b). The cement, sand and water mixture preparation consisted of two stages: blending dry components (cement and sand) and wet components (mixture of cement, sand, and water). Each procedure was carried out for 3 minutes. According to the ASTM standard recommended length to diameter ratio of core specimen for UCS tests is of 2-2.5. The prepared backfill core samples have diameters of 37 mm and heights of 80 mm. All backfill samples were polished and checked for the smoothness of the end surfaces by an absolute digimatic indicator shown in Figure 5 c and d. According to the ASTM standard difference of sample, the surface has not exceeded 1 mm.

 

a) b)

 

c) d)

Figure 5. Preparation of core samples for UCS testing at various ages: molding (a); core samples (b); polishing (c); smoothness check (d).

The backfill strength was determined using the UCS tests. The UCS tests were performed at each curing ages of 1 day, 7 days, 14 days, and 28 days. UCS tests on core samples cured for 8 hours were not considered because the samples were too weak and wet for the testing procedure. Five tests were conducted at each sample age for each backfill type, Figure 6 shows the average value of each UCS test.

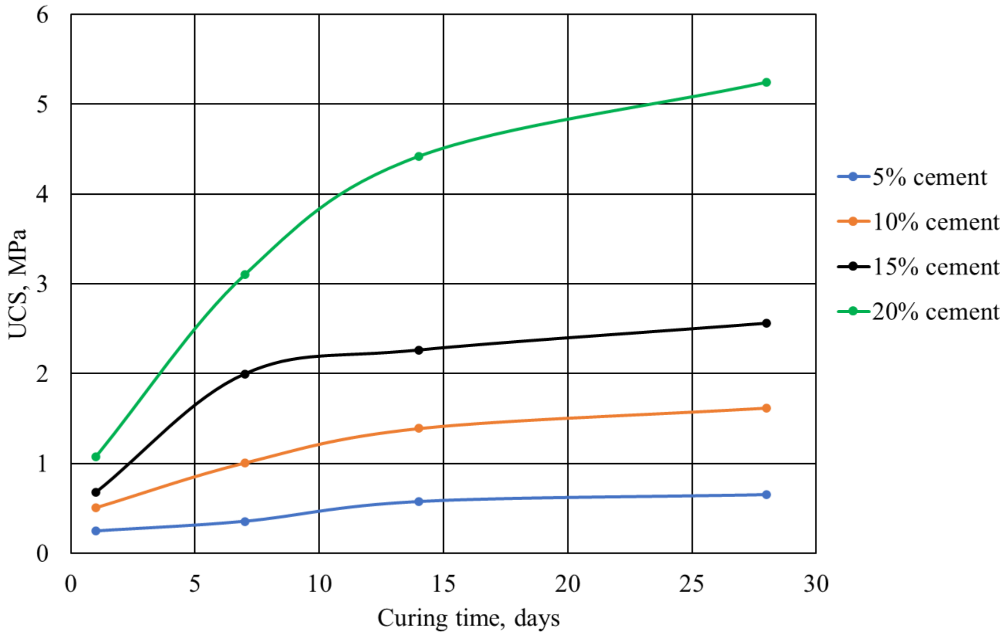

Figure 6. Backfill strength and curing time relationship.

The uniaxial compressive strength increases with curing time and cement content. UCS tests on core samples representing a backfill with cement content of 5%, 10%, 15%, 20% cured for 28 days showed higher magnitude than 1 day cured samples with the same cement content. Strength increased 2.65 times for samples with 5% cement, 3.1 times for samples with 10% cement, 3.75 times for samples with 15% cement and 4.9 times for samples with 20% cement.

4.1.4. Fracturing of cubes to mimic blast and stress induced fractures in underground mining

A static cracking agent (SCA) was used to induce fractures in the cubes instead of blasting. SCA is a highly expansive powdered cementitious material for the fragmentation of rocks and concrete (Xu et al., 2022). The SCA composition is provided in Table 2. After mixing with water and pouring into a hole the SCA expands and creates a pressure on the hole walls to fracture the rock or concrete. SCA is environmentally friendly and safe since it does not release any toxic fumes and harmful substances. Moreover, no noise and flying materials are experienced in the expansion and demolishing processes of the fragmented materials.

The SCA powder was mixed with clean water at SCA to water ratio of 20%. The mixture was poured into the holes of block within 5 minutes after preparation at a room temperature of 25 ℃ and water temperature of 20 ℃. Fracturing of the blocks occurred after 2-3 hours of filling (Figure 7).

Table 2. Chemical Characterization of SCA (KSGidro, 2022)

SiO2	MgO	Fe2O3	CaO	AI2O3
5.10%	2.20%	1.40%	87.10%	2.40%

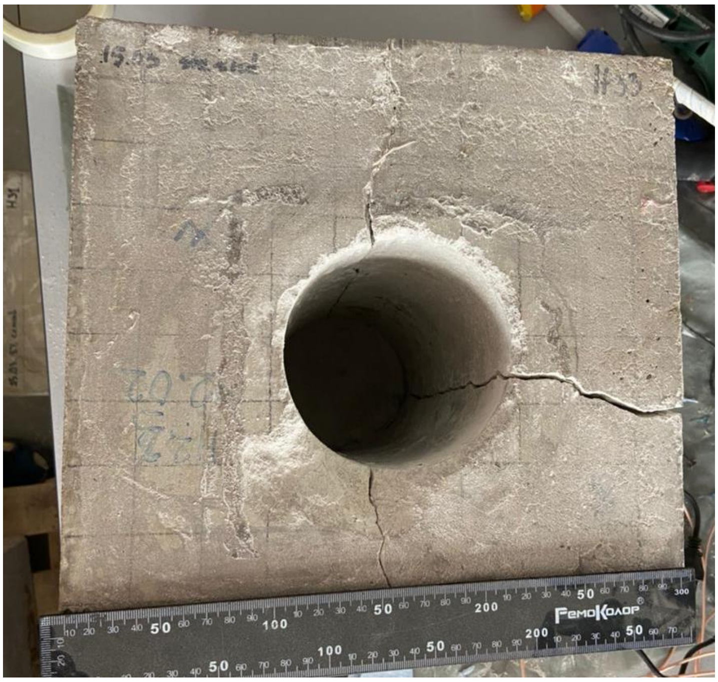

Figure 7. Fractured cube with 3 joints

4.2. Acoustic Emission Testing

4.2.1. Equipment

Acoustic Emission Testing (AET) is a technique used for the non-destructive testing of materials. AET can track the changes in material behavior. This technique offers one the ability to observe crack propagations appearing deep inside a material. Different terms are used to define instabilities or "events" caused by rock fracturing at different scales as shown in Figure 8.

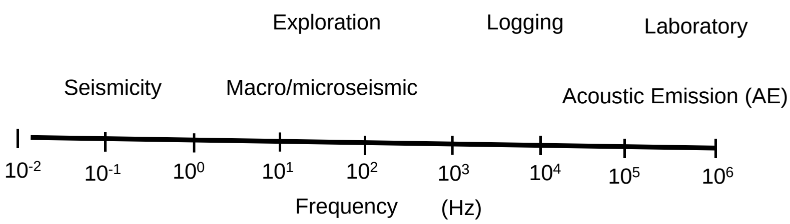

Figure 8. Monitoring frequency ranges of earthquakes, macro/microseismic activity, acoustic emission, and associated fields of study/domains of research (CAMIRO, 1996)

CAMIRO (CAMIRO, 1996) notes that in mine seismology, large events in the seismic range are often called mine tremors or mine-induced seismic events. Smaller events often located close to active mine stopes are usually defined as "microseismic events" due to their much smaller magnitudes. At the lowest end of the magnitude spectrum, "acoustic emission" is often used to indicate high-frequency emissions or "rock noise" monitored in rock samples under loading in laboratory or observed in localized failure areas within a mine. It is known that the boundaries between these different categories are not very well defined and many authors such as Dong et al. (Dong et al., 2017) use the term "acoustic emission microseismic" or simply "AE/MS" to refer to the latter two categories in a general manner. Therefore, microseismicity during the failure process while loading a material is very similar to acoustic emission (AE). Acoustic emissions are characterized as the energy released in stressed materials. The release of localized strain energy can be due to fracturing and can be recorded on the material's surface by sensors. Therefore, AET is compared with seismological techniques since they have similar concepts but different scales.

AET has been used to track rock mass defects at the very early stage prior to complete failure. The main difference from other non-destructive tests is the type of data received and the application mechanism. For instance, in the ultrasound method, artificially created signal and source-receiver are used to determine the geometric shape of a defect in a sample. In contrast, AET can determine elastic waves going through fractures in a sample (Grosse et al., 2022). Compared to other non-destructive methods, AET requires only a few sensors under certain conditions that can have signals passing a trigger level threshold. AET does not need access to all sides of the sample, as is required for all other methods of through-transmission (Grosse et al., 2022).

Figure 9 illustrates a standard AE detection system. AE sensors transform dynamic motions into electric signals and detect AE waves at a material's surface. A preamplifier and main amplifier are used to increase weak AE signals and could provide more than 1000 times gain. Elastic waves generated by the source propagate in the material and are detected by AE sensors (Grosse et al., 2022).

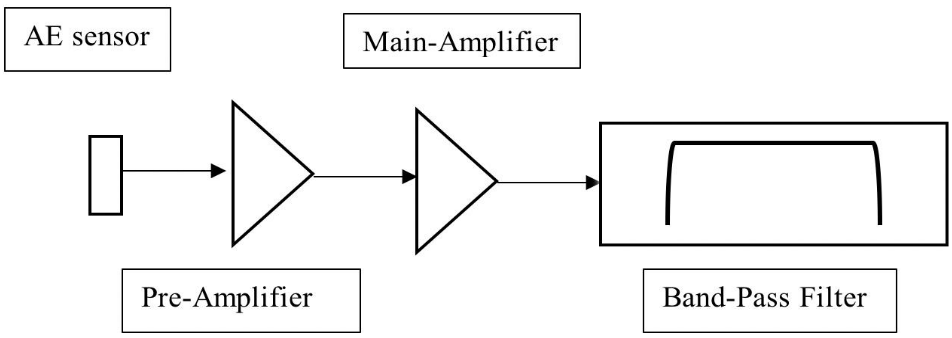

Figure 9. AE detection system (Grosse et al., 2022)

The AE method has been used to study mine seismicity by Dong and Li (2013), Kennet et al. (2000). The AE system and accessories are shown in Figure 9. In this study the SAEU3H AE system was used. The SAEU3H AE system is a multi-channel system that consists of AE data acquisition modules, chassis with front and rear panels, an optional network communication module, a laptop, eight sensors, preamplifiers, and cables (Figure 10).

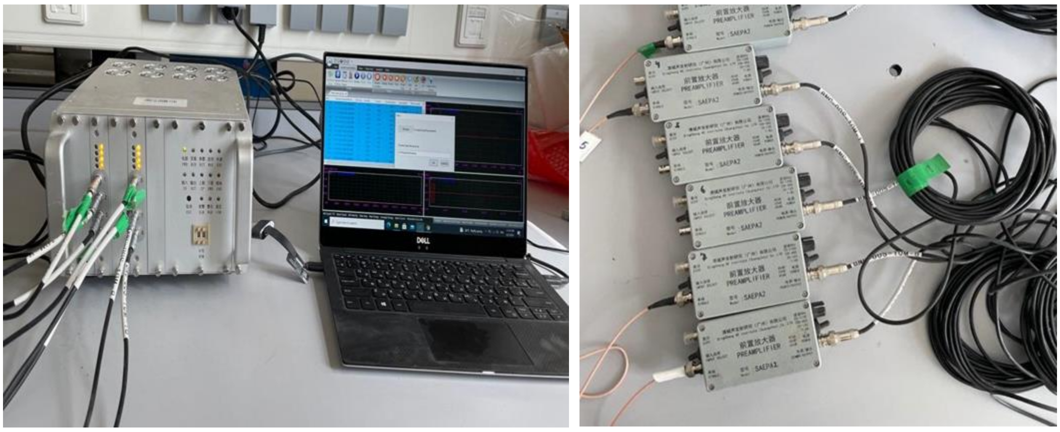

(a) AE data acquisition modules, chassis with front and rear panels, optional network communication module, laptop

(b) Preamplifiers and cables

Figure 10. AE system and accessories

In the laboratory tests in this research, AE sensors were attached to the surface of the cubes using hot glue, as shown in Figure 11. Eight sensors were attached to each cube with one sensor used as source that generated a pulse and the other seven sensors served as receivers that received the pulse wave. The wave was generated as a pulse from sensor number 1 placed in the middle of the front view of the cube to enable waves to go across the hole.

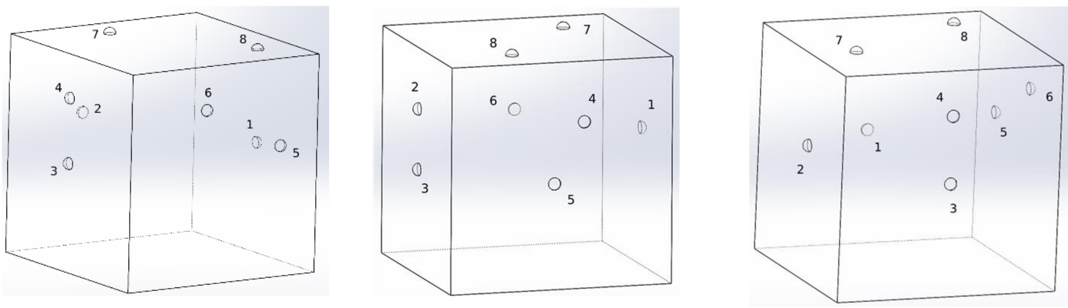

(a) 150 mm cube (b) 225 mm cube (c) 300 mm cube

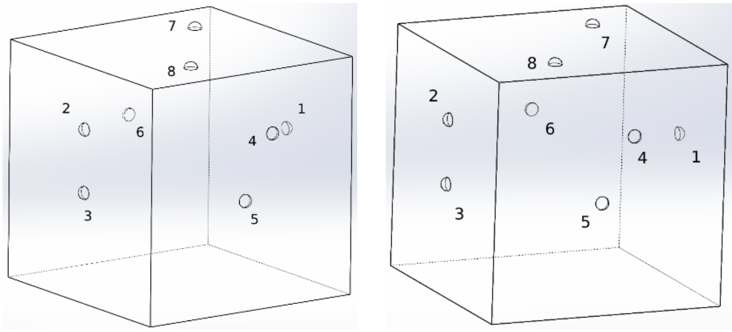

(d) 375 mm cube (e) 450 mm cube

Figure 11. Sensor positions on the various cube sizes without hole

The sensor type used in the experiments for 150 mm, 225 mm, and 300 mm cube sizes is the SR150M High-frequency broadband AE sensor. The frequency range of the sensor is 60-400 kHz; peak sensitivity is > 75 dB. SRI150 sensor type was used for larger cubes of 375 mm and 450 mm. This sensor has a built-in preamplifier with a frequency range of 60 kHz – 400 kHz and a sensitivity of 40 dB. This change in sensor type was necessitated by the fact that with the SR150M sensors wave arrival times could not be detected at the receiving sensors due to seismic wave attenuation in inelastic materials such as rocks and concrete materials used in the study. Seismic waves attenuate with time and distance in inelastic materials due to various inelastic energy loss mechanisms such as porosity, fractures and microscopic movements along mineral dislocations or shear heating at grain boundaries (Ammon et al., 2021). According to (Ammon et al., 2021) seismic wave attenuation (∈) is often quantified using a quantity called the quality factor (Q) (Equation 1).

$$\in = \frac{\gamma}{m\omega_o} = \frac{1}{2Q} \qquad (1)$$

Where γ=coefficient of friction, m=mass and ω_o=resonant frequency

A low attenuation (high quality factor Q) may be indicative of a tightly bound rock mass, or one that can propagate a displacement pulse with little or no energy loss, thus reaching the free surface with nearly full strength, and vice versa. Hence, with the larger cubes and SR150M sensors energy loss stopped the wave propagation before they reached the receiving sensors, therefore requiring a change to the SRI150 sensors. (CAMIRO, 1996) notes that the properties of the rock mass affect the way seismic waves propagate through the medium and that this influence is not restricted to the velocity of the waves, but also includes the relative amplitude and frequency content of the signals referred to as signal degradation or attenuation. In a mining environment, seismic waves propagating through a host medium are affected by the rock type, backfill, voids, state of stress, and the type of structures (faults, shears, joints) and their distribution.

4.2.2. Measurement setup

The selection of the appropriate AE sensors was based on both the operating frequency range of the AE transducer and the properties of the wave propagation medium. In particular, the former needs to be compatible with the frequencies at which the corrosion is expected to generate AE (Di Benedetti et al., 2014). The material through which the waves propagate is concrete, a low-frequency propagation material. In addition, (Yuyama et al., 2007) pointed out that for concrete monitoring, even though the sensitivity of the AE sensors increases as the resonant frequency decreases, transducers with low resonant frequency (30 kHz) are prone to extensive noise detection. In light of these considerations, AE sensors with the frequency range of 60-400 kHz and peak sensitivity > 75 dB were used.

The peak definition time (PDT), the hit definition time (HDT), and the hit lockout time (HLT) are important parameters for AE data acquisition. The Pulse Detection Time (PDT) refers to the elapsed time, as recorded by a counter that is reset to zero upon detection of a new maximum signal, prior to the determination of the true peak of the AE waveform as depicted in Figure 12. The HDT represents the amount of time, recorded by a counter reset to zero upon detection of a threshold crossing, required for the system to conclude the end of a hit, finalize the measurement process, and preserve the attributes of the recorded signal as illustrated in Figure 13. Finally, the HLT is the period of time following the conclusion of a hit during which the system does not respond to any threshold crossings and is utilized to prevent the measurement of reflections and late arriving signals (Di Benedetti et al., 2014).

To avoid an increase in the duration of the AE activity resulting from the reflections interfering with one another, PDT, HDT, and HLT were selected equal to 200, 400, and 3000 μs, respectively.

Table 3. Summary of AE software settings

Parameter	**Unit**	**Value**
Threshold	dB	30
Parameters of timing		
PDT	μs	200
HDT	μs	400
HLT	μs	3000
Waveform setup		
Sampling rate	MSPS	10000
Sampling frequency	Points	10000
Digital filter		
Lower	kHz	60
Upper	kHz	400

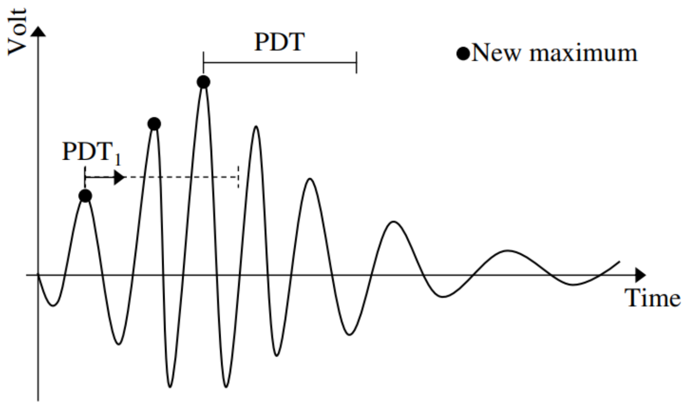

Figure 12. Peak definition time

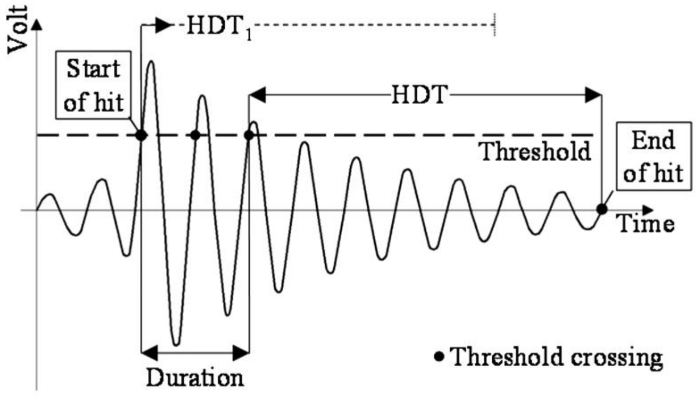

Figure 13. Hit definition time

4.2.3. Procedure of velocity calculation with AE equipment

Hedley (1992) stated that seismic monitoring systems basically measure the arrival times of the seismic waves and that knowing the coordinates of the sensors and assuming a uniform velocity at which the seismic signals travel through the rock, an estimate of the source location can be determined. There are two general methods of source location determination based on the arrival times of the P-waves alone, or the arrival times of both the P- and S-waves (Hedley, 1992). In this research we used the direct method of source locations by (Blake et al., 1974) and discussed in (Hedley, 1992).

Data derived from the AE tests provided the arrival time of the wave at each sensor. Knowing each sensor's arrival times and location coordinates, the distances from the pulse source to the receiving sensor locations were calculated. Knowing the distance from the source to each sensor and the wave arrival time at the sensor, the corresponding seismic wave velocities were calculated from Equation (2).

$$d_i = \sqrt{(x_i - x_1)^2 + (y_i - y_1)^2 + (z_i - z_1)^2} \tag{2}$$

Where $i = 2, 3, 4, 5, 6, 7, 8$ and x, y, z – sensor coordinates.

For each wave arrival time, the test was repeated five times and the average arrival time at each sensor used in calculating the wave velocity to the corresponding sensor.

Wave velocity was calculated by the following equation, using the subtraction of wave arrival time and wave generated time:

$$v = \frac{d_i}{\Delta t} \tag{3}$$

Where d_i is the distance of each sensor 2,3,4,5,6,7 8 from the source at x_1, y_1, z_1, and Δt is the wave arrival time from the source.

The procedure described for the distance calculations assumes the material is homogeneous and without voids or fractures to affect the wave path (i.e., the procedure assumes the so-called straight ray path concept) (Morkel et al., 2022; Peng et al., 2020). Appendix 1 provides the complete database obtained in the study for subsequent application in numerical modelling and machine learning.

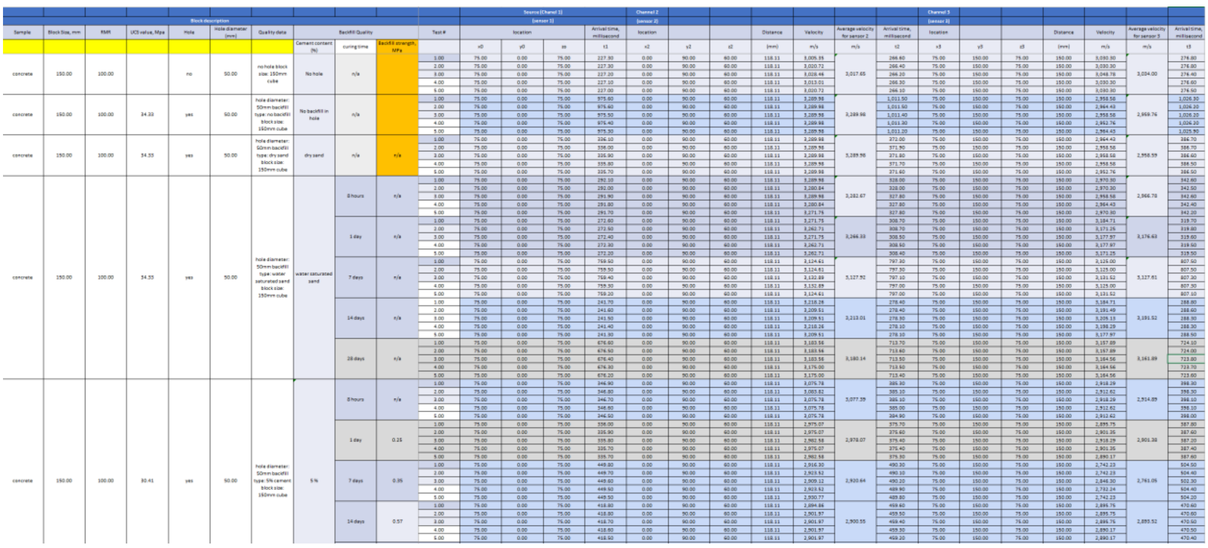

Figure 14. Snapshot of AE results database

As shown in Figure 14 and in Appendix 1, the collected data include the following:

- Type of material (rock or concrete)
- Backfill type, quality, and curing time
- Location of each source
- Arrival time of the wave to each sensor
- The calculated velocity of the wave at each sensor.

4.3. Analysis of results from AE tests

4.3.1. Size effect on seismic wave velocity

One of the primary objectives of the research was to see the effect of size, voids, and different backfill contents and age on seismic wave velocity. Figure 15 shows seismic wave velocities for cubes of all sizes without holes. Based on test results shown in Figure 15, except at sensor 7, there is no significant difference in seismic wave velocities with increasing cube size. The range of wave velocities of between 3,000 to 3500 m/s is within the values of 3160 to 3818m/s with a small variation in the velocities for all five cubes could be from the concrete mix quality variations and possible errors in the determination of the wave arrival times.

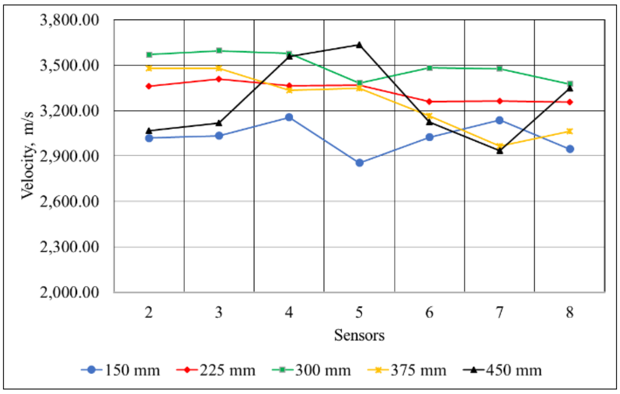

Figure 15. Seismic wave velocities on concrete cubes without holes

4.3.2. Hole effect on seismic wave velocity

Figure 16 shows the results of AE tests on concrete cubes with empty holes. According to the test results in Figure 16, the velocities in the 150-, 225-, 300- and 375-mm cubes with holes of 50-, 75-, 100- and 125-mm diameters are not significantly affected compared with their equivalent cubes without holes. For these cubes the velocities at the sensors range between 3033 to 3577 m/s. The cube size of 450 mm with a hole diameter of 150 mm shows a significant change in the seismic wave velocity at sensors 2, 3, 6 and 7. Sensors 4 and 5 show relatively higher velocities of 3558 and 3635 m/s respectively, implying that they are not affected by the void. Sensors 6 and 7 show the most significant drop in velocities of almost 1500 m/s from the peak value in the 450 mm cube with a hole diameter of 150 mm. The significant drop in velocities is caused by the sensors' location across the hole from the source sensor. Wave energy attenuation is high due to the empty 150 mm diameter hole and effect of ray path tracing that is ignored in the distance calculation, resulting in longer arrival time and therefore lower velocities. The results show that ray paths being assumed straight in this case were not significantly affected by the holes in the smaller cubes but were impacted by the hole diameter of 150 mm in the 450 mm cube with the severity depending on the sensor location relative to the source and hole.

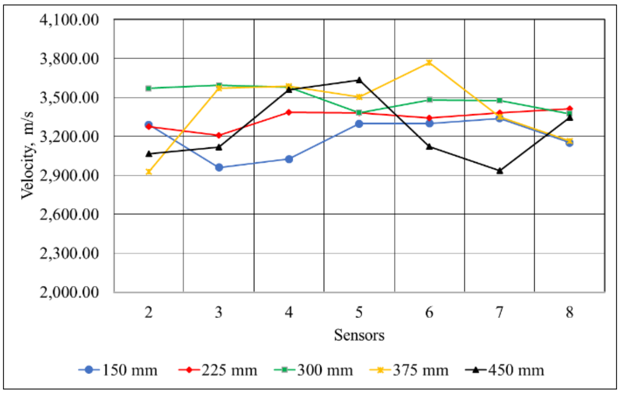

Figure 16. Seismic wave velocities in blocks with holes of different diameters at sensor locations

4.3.3. Backfill effect on seismic wave velocity

Figure 17 shows seismic wave velocity results for each backfill type at cured age for wet sand (0% cement), 5% and 20% cement respectively for the cube size of 150 mm with a hole diameter of 50 mm. Based on the positions of sensors 2, 3 4 and 5 in Figure 16a for wet sand the ray paths of these sensors are not impacted by the backfill in the void, while the ray paths from the source to sensors 7 are significantly impacted by the void and its contents in days 14 and 28 when the wet sand would have been dry. For the higher cement content backfill (15% and 20% cement), there is less impact on the wave velocity at 28 days curing time as can be seen in Figure 17c. In Figure 17b, there is a general decrease in velocities for all curing times at sensors 5 to 8 that is attributed to the void and its content and the locations of these sensors relative to the source. Figure 17c with a backfill cement content of 20% shows significant impact of the void and its content on the pulse wave velocities at sensors 5, 6 and 8 because of their relative locations to the void and source. It is reasonable to say that, even though straight ray paths were assumed in the pulse wave velocity calculations the impact of the void and its contents is visible without ray tracing but could be better with ray tracing.

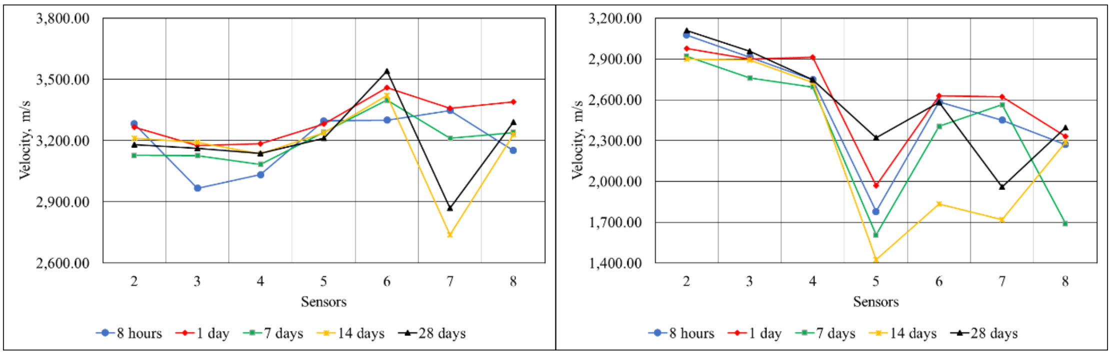

(a) Wet sand (0% cement) (b) 5% cement

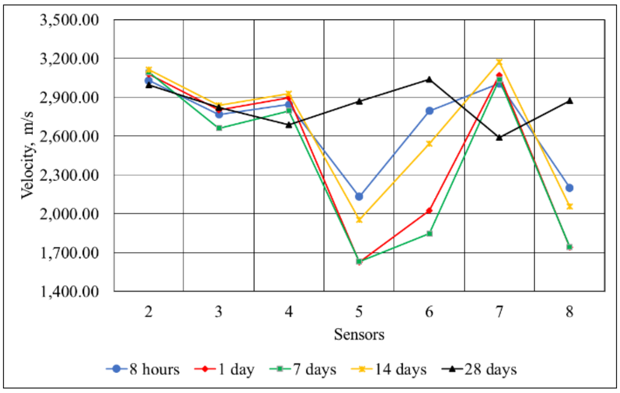

(c) 20% Cement

Figure 17. Backfill effect on seismic wave velocity for 150 mm cube with 50 mm diameter hole (a) Wet sand - 0% cement (b) 5% cement (c) 20% cement backfill.

Figure 18 shows the impact of the void and backfill effect on wave velocities at the receiving sensors on the 225 mm cube with 5% and 15% cement content backfill in the void. In Figure 18a for 5% cement content backfill, the wave velocities for all the cured times fall within the range of 2879 to 3200 m/s like what happens in concrete cube without hole. The pulse wave velocity is significantly affected from the source to the receiving sensors 2 and 4 in Figure 18b because of the void and backfill.

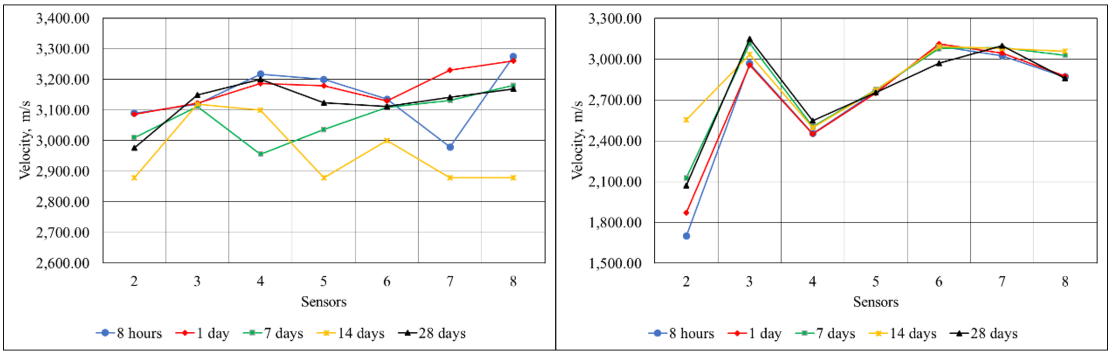

(a) 5% cement (b) 15% cement

Figure 18. Backfill effect on seismic wave velocity for 225 mm concrete cube with 75 mm diameter hole (a) 5% cement (b) 15% cement

Figure 19 shows the AE test results for the 300 mm granite cube with different cement content backfills at different ages. Figure 19 a-d shows drops in velocities at sensors 3, 4 and 7 which reflects their relative locations to the source and void.

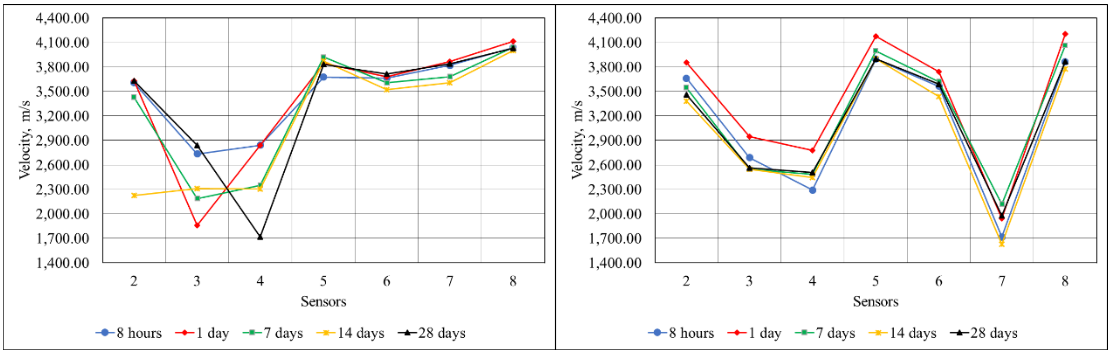

(a) 5% cement (b) 10% cement

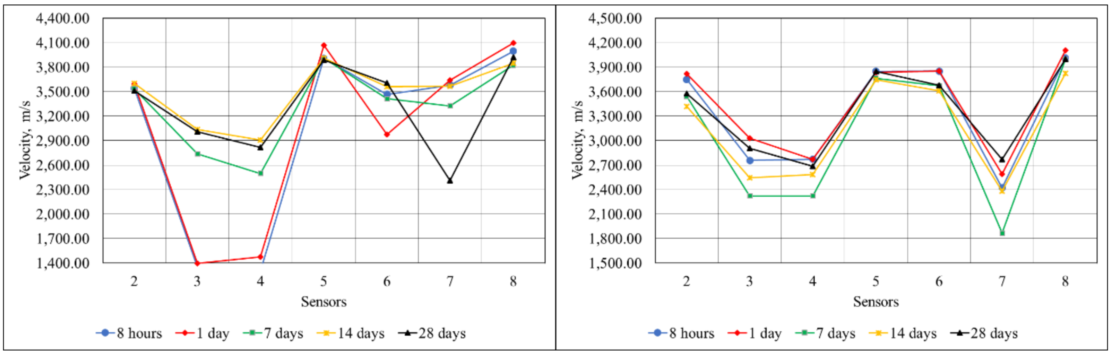

(c) 15% cement (d) 20% cement

Figure 19. Backfill effect on seismic wave velocity for 300 mm granite cube with 100 mm diameter hole (a) 5% cement (b) 10% cement (c) 15% cement (d) 20% cement

The velocities to the other sensors are not impacted and implies their ray paths were not affected by the void. Velocities at sensors 2, 5, 6 and 8 are not impacted and fall in the range of 3600 m/s to 4,100 m/s.

According to Figure 20 sensors numbers 7 and 8 are significantly affected by the void of 125 mm diameter and changes in backfill properties with time in the 375 mm cube. The two sensors are located at the top of the cube near the void and wave paths to these sensors are impacted by the void and its contents to different degrees.

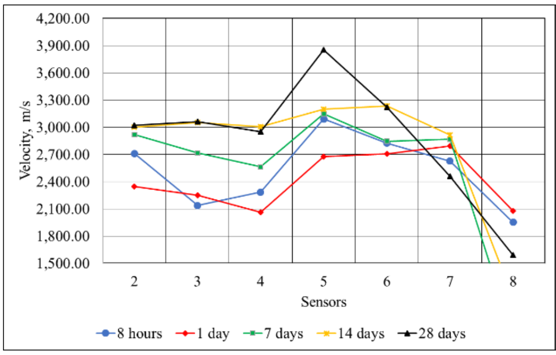

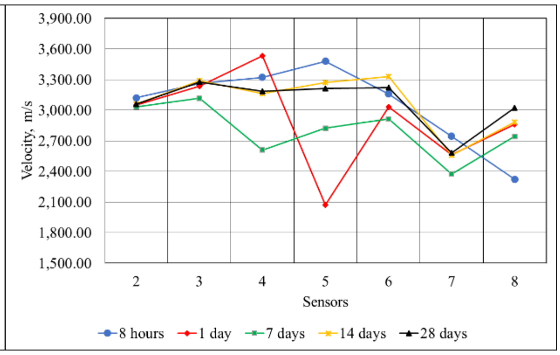

(a) Wet sand (0% cement) (b) 5% cement

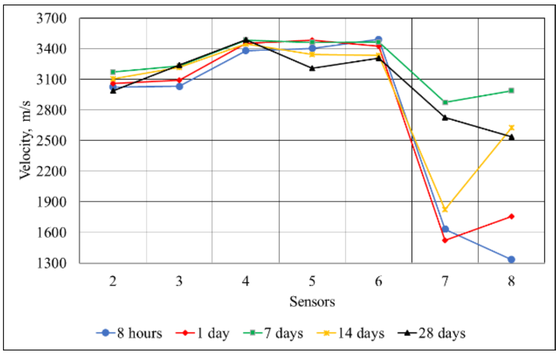

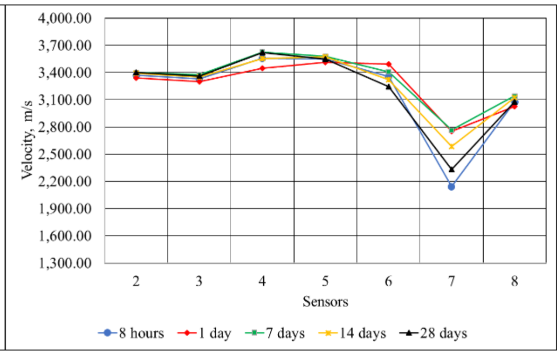

(c) 10% cement (d) 15% cement

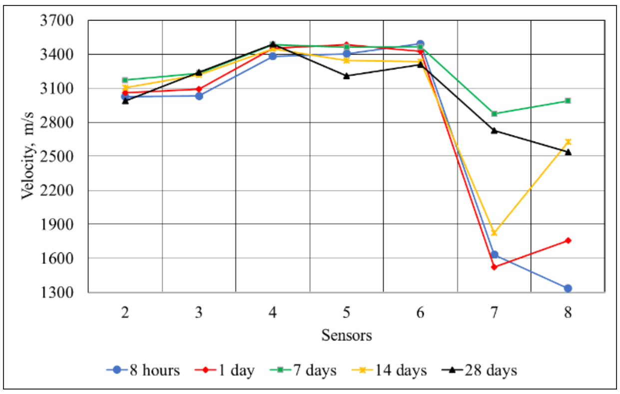

(e) 20% cement

Figure 20. Backfill effect on seismic wave velocity for 375 mm concrete cube with 125 mm diameter hole (a) wet sand (b) 5% cement (c) 10% cement (d) 15% cement (e) 20% cement backfill

Figure 21 shows the results of the impact of backfilled cement content with time on wave velocities at sensors attached to the 450 mm cubes with a void of 150 mm diameter at different locations relative to the source and void. In Figure 21a for wet sand with 0% cement, the velocities show lower values at sensors 2, 3, 7 and 8. This is due to the sensor locations relative to the void and source.

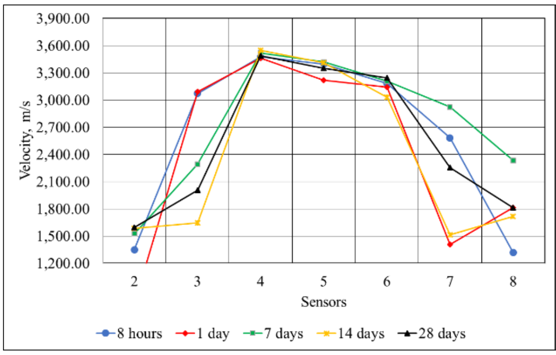

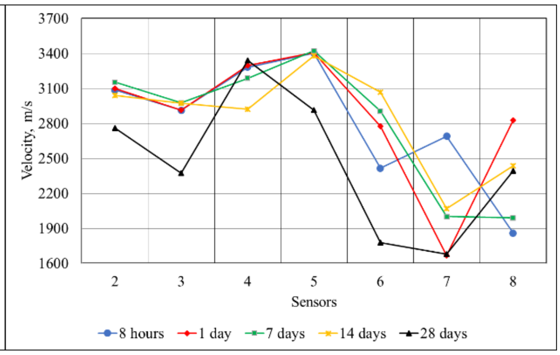

(a) Wet sand (0% cement)

(b) 15% cement

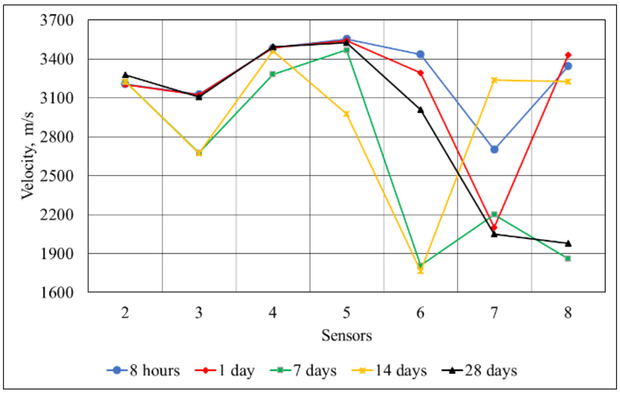

(c) 20% cement

Figure 21. Backfill effect on seismic wave velocity for 450 mm concrete cube with 150 mm diameter hole (a) wet sand (b) 15% cement (c) 20% cement backfill

4.3.4. Fracture effect on seismic wave velocity

After the fracturing of rock and concrete cubes the SCA was removed from the holes. Fractured pieces were methodically re-assembled tied together with a tape, where necessary. Figure 22 shows the locations of both the source and the sensors in relation to the cracks in the concrete samples.

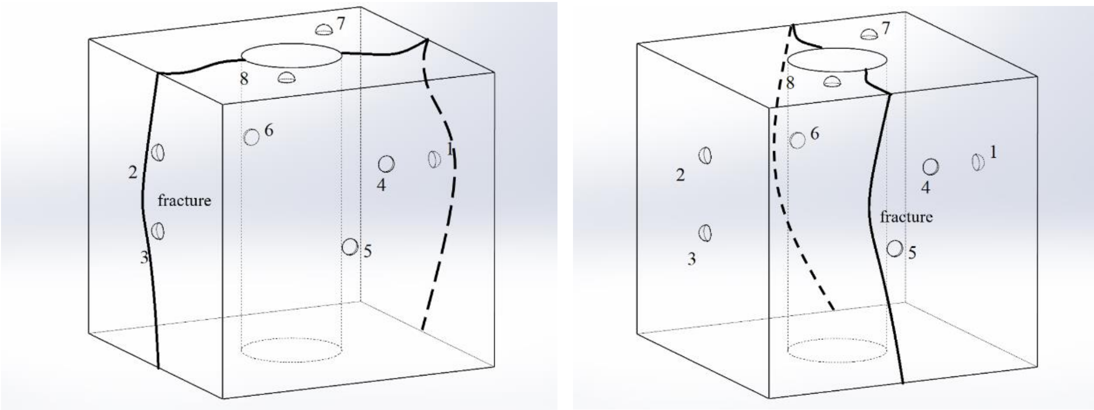

(a) (b)

Figure 22. The projected source and sensors' locations for a) 225 mm with hole diameter 75 mm b) 375 mm with hole diameter 125 mm concrete sample

Figure 23 shows the seismic wave velocity in fractured cube with backfill. Sensors 1, 5, and 7 located prior to cracks detected the signal as expected. In contrast, sensors 3, 4, and 6 were not able to receive the signal or received a weak signal because of the attenuation of the signal in the cracks.

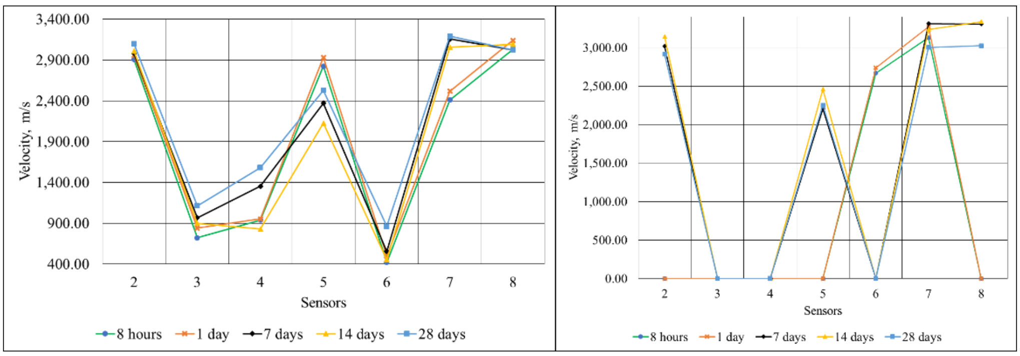

(a) 5% cement (b) 20% cement

Figure 23. Fracture effect on seismic wave velocity for 150 mm concrete cube with 50 mm diameter hole (a) 5% cement (b) 20% cement backfill

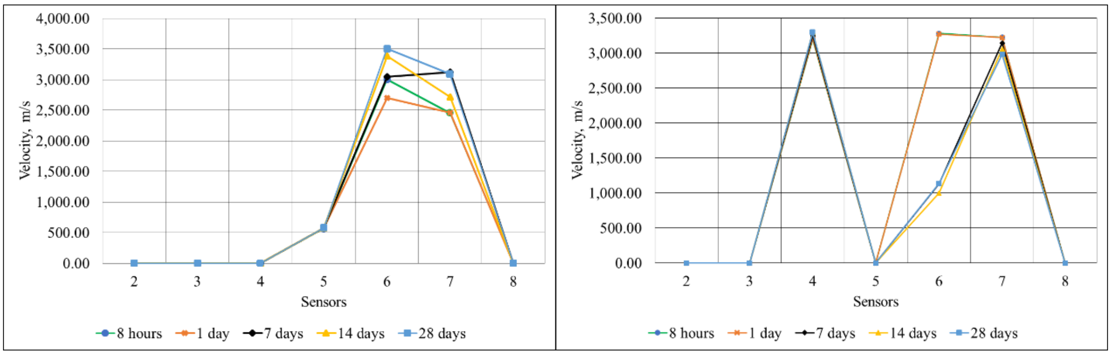

(a) 5% cement (b) 20% cement

Figure 24. Fracture effect on seismic wave velocity for 225 mm concrete cube with 75 mm diameter hole (a) 5% cement (b) 20% cement backfill

When the fractured 225 mm sample was filled with backfill, the cube had 2 cracks relative to sensors. Figure 24a shows that only sensors 5, 6 and 7 were able to receive the signal. Note sensor 5 is across the hole relative to the source, but it could receive the signal with delayed arrival time due to the crack, which is visible from lower wave velocity of 500 m/s. It is very likely that the fracture had some infilling from the backfill to enable it to transmit the pulse signal across the fracture in the location of this sensor.

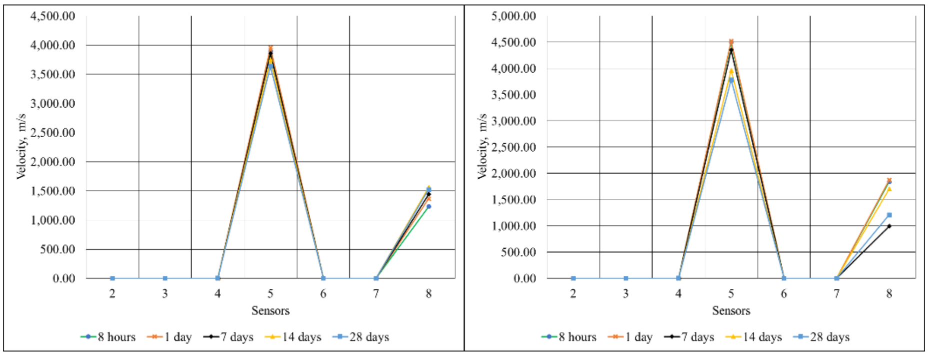

(a) 5% cement (b) 20% cement

Figure 25. Fracture effect on seismic wave velocity for 300 mm granite cube with 100 mm diameter hole (a) 5% cement (b) 20% cement backfill

In 300 mm granite cube only sensor 5 could receive a full signal without attenuation and sensor 8 received a weak signal due to location prior to the crack, other 5 sensors could not receive a signal due to the full signal attenuation in the crack.

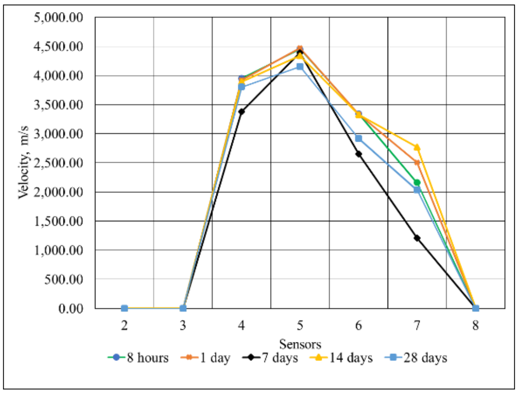

Figure 26. Fracture effect on seismic wave velocity for 375 mm concrete cube with 125 mm diameter hole filled with 15 % cement backfill

There were 2 cracks in the 375 mm cubes with 15% cement backfill. Figure 26 shows the seismic wave velocity in fractured cube with backfill. Sensors 4, 5, 6, and 7 located prior to cracks detected the signal as expected. In contrast, sensors 2, 3, and 8 were not able to receive the signal because of the full attenuation of the signal in the cracks.

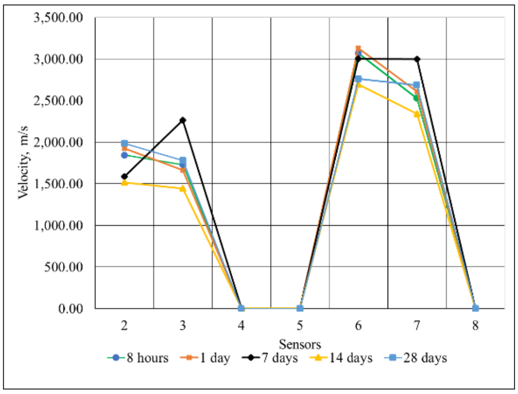

Figure 27. Fracture effect on seismic wave velocity for 450 mm concrete cube with 150 mm diameter hole filled with wet sand backfill

In the 450 mm cube 2 cracks were observed. Figure 27 presents the seismic wave velocities in a 450 mm cube with fractures filled with backfill. Sensors 2, 3, 6, and 7, located ahead of the cracks, captured the signal as predicted. On the other hand, sensors 4, 5, and 8 did not receive the signal, attributed to the total attenuation of the signal by the cracks.

4.4. Rating of fractured blocks

The evaluation of two commonly used rock mass classification systems, namely RMR and Q, was conducted to determine their appropriateness for application to the given fractured blocks. The choice for selecting a classification system was its capacity to seamlessly transition from field-scale implementation to laboratory-scale utilization. Among other factors in the decision process RMR offers an advantage by encompassing the rock mass uniaxial compressive strength as a pivotal parameter. This attribute holds particular significance in discerning between weak and strong rock formations exhibiting similar structural characteristics. Based on these considerations, RMR emerged as the preferred choice for the purpose of rating the fractured blocks in the laboratory. RMR system shown in Table 8 (Bieniawski, 1989) was used to rate the block qualities after they were fractured. Before the calculation of RMR following the procedures were undertaken in accordance with RMR determination procedure outlined by (Bieniawski, 1989):

- Counting of all fractures in the block
- Measuring the apertures of the fractures
- Measuring the lengths of all fractures
- Determination of the roughness of each fracture

Table 4. RMR system (Bieniawski, 1989)

Parameter	RMR							
	1973	1974	1976	1979	1989	2011	2013	2014
Intact rock strength	10-0	10-0	15-0	15-0	15-0	15-0	15-0	15-0

(MPa)									
RQD (%)		16-3	20-3	20-3	20-3	20-3	20-0	-	-
Joint spacing (mm)		30-5	30-5	30-5	20-5	20-5	20-0		
Discontinuity density (Joints per meter)		-	-	-	-	-	-	40-0	40-0
Separation of joints (mm)		5-1	-	-	-	-	-	-	-
Continuity of joints (m)		5-0	-	-	-	-	-	-	-
Weathering		9-1	-	-	-	-	-	-	-
Condition of joints		-	15-0	25-0	30-0	30-0	30-0	30-0	20-0
Groundwater		10-2	10-2	10-0	15-0	15-0	15-0	15-0	15-0
Alterability (%)		-	-	-	-	-	-	-	10-0
Adjustment	F_0	15-3	15-3	0-(-12)	0-(-12)	0-(-12)	0-(-12)	0-(-12)	0-(-12)
	F_e	-	-	-	-	-	-	-	1.32-1
	F_s	-	-	-	-	-	-	-	1.3-1

F_o - adjustment factor for the orientation of tunnel axis, F_e - adjustment factor to account for an excavation method and F_s - adjustment factor considering stress-strain behavior of the rock mass at the tunnel face.

4.4.1. Scaling of RMR parameters

Xu et al. (2021) highlighted the importance of ensuring that results from a physical model can be accurately scaled up to match real-world mining conditions. They noted that achieving complete similarity between physical models and actual mines is challenging, but geometric resemblance is the key factor and is relatively straightforward to achieve in a physical simulation. In order to accurately represent the size of concrete blocks that simulate mining conditions, parameters like Rock Quality Designation (RQD), fracture length, and spacing need to be adjusted.

Geometric similarity emerged as the most critical aspect in scaled physical models, as emphasized by (Xu et al., 2021). The study implemented specific scaling adjustments for fractures, focusing on the following measures:

$$l_m = \emptyset * l_d \tag{4}$$

Where l_m represents the length fracture within the mimicked in situ rock mass, ϕ denotes the length scale coefficient and l_d corresponds to the length of discontinuity utilized in RMR system rating in situ.

$$s_m = \beta * s_d \tag{5}$$

s_m represents the spacing of fractures in mimic model, s_d is the spacing of discontinuities in RMR system rating and β corresponds to the length scale coefficient. Table 6 presents the adjusted values for individual cube sizes, computed utilizing the length scaling coefficients derived from equations 4 and 5, as per the joint condition rating system outlined by (Bieniawski, 1989) for in-situ rock formations. The RMR parameters requiring scaling from in situ to laboratory scale models are RQD and fracture characteristics.

4.4.1.1.1. RQD scaling

In 1967, Deere (Deere & Miller, 1966) initially introduced the Rock Quality Designation (RQD) framework as a uniparameter system for characterizing rock masses. RQD is an adapted measure of core recovery percentage whereby the cumulative length of intact core specimens exceeding 100 mm is divided by the total length of the core traverse. The sensitivity of RQD to the extent of the core traverse is duly acknowledged, prompting the recommendation, as posited by Deere and Deere (1988), for its computation to be rooted in actual field-derived drill lengths, preferably limited to 1.5 meters.

In 1982, Palmstrom introduced the volumetric joint count (Jv) concept, for the quantification of joint occurrences in rock masses (Palmstrom, 1982). Jv is the number of joints per cubic meter and can be calculated by counting the number of joints in each area and dividing them by the area (Palmstrom, 1982). Palmstrom (2005) provided Equation (6) relating Jv to RQD.

$$RQD = 110 - 2.5J_v \tag{6}$$

In this research the J_v concept was adopted for determining RQD in fractured blocks. Details for calculating the scaled RQD from the fractured blocks are presented in Section 4.5.4.

(a) 3 fractures in 150mm cube (b) 2 fractures in 375mm cube

Figure 28. Fractured cubes with different fracture patterns and densities

4.4.1.2. Calculations of the scaled RQD

Palmstrom (2005) notes that where there is no borehole or scanline logging data available as in this study, Equation (6) could be used find RQD from J_v, where RQD is required in the Q and the RMR classification systems. Equation (6) can be rewritten as in Equation (7):

$$RQD = 110 - 2.5(K.J_s) \quad (7)$$

Where J_s represents the count of joints per unit area (in a 2-dimensional context) determined through window mapping. The conversion of J_s to J_v (in a 3-dimensional context) is achieved through the factor K, whereby J_v=K*J_s. The value of K typically falls between 1.25 and 1.35 under standard conditions, while with uniformly distributed joints in all directions, it ranges from 1.15 to 1.5, according to Palmstrom (1982). Palmstrom (2005) established that Equation (7) remains valid for Jv values within the range of 4 to 44. Beyond this range, the Rock Quality Designation (RQD) parameter becomes less sensitive to joint frequency. This alignment between J_v and RQD validates concerns previously raised by Palmstrom in 2005, as well as by

Milne et al. (1998) and Grenon and Hadjigeorgiou (2003). However, in the absence of an alternative, RQD persists as a pivotal element in rock mass classification systems.

In this study, the count of fractures was assessed from a plan-view of each cube. Table 5 outlines the fracture count per unit area for the various cube sizes, along with the parameters requisite for RQD computation. The size of each cube's plan view dictates the dimensions of the encompassing window utilized for fracture counting.

The ensuing phase necessitates the determination of suitable scaling coefficients to effectively scale the field's window mapping area to the plan view area of the laboratory's cubes. The eventual size of the window employed in mining geotechnical contexts hinges on an array of factors, encompassing project-specific objectives, data type, available resources, and equipment. Generally, window sizes can span from a few centimeters to several meters, contingent upon the mining project's scale and the desired level of intricacy for mapping and geotechnical endeavors. The dimensions of the window for RQD computation are contingent upon the excavation's size and the exposed surface area.

4.4.1.3. Scaling cube fracture area density from field window mapping practice characteristics

To calculate Js in Equation (7), it is necessary to adjust the fracture density from the plan view area of the laboratory scale cubes to match the mapping window sizes for in situ rock mass window mapping.

Munfakh et al. (1998) discussed how to map geological features for assessing the stability of slopes. They suggested that, depending on the available area for mapping, the window used for mapping should usually be around 10 meters long. When mapping open pit areas with extensive exposed rock, larger window sizes ranging from tens to hundreds of meters are often used. Wu et al. (2011) and Huo et al. (2020) employed window dimensions of

90 meters by 45 meters up to 130 meters by 65 meters to study the reliability of slope stability. They concluded that using rectangular windows for mapping was better than using circular ones. Another study by Bandpey et al. (2019) used smaller window sizes, of 1.9 meters by 2.2 meters for excavations that ranged from 3 meters by 4 meters to 6 meters by 6 meters in size. They also used a 1 meter by 1 meter window based on the findings of Zhang and Einstein (2000). Wylie (1999) based on Munfakh et al. (1998) work, provided guidelines for determining window size in slope stability mapping. Wylie (1999) suggested that roughness of discontinuities should ideally be measured on exposed surfaces with lengths of at least 2 meters, if possible. Kulatilake and Wu (1984) used a window that was 1 meter by 0.67 meters in size on a rock outcrop. Munfakh et al. (1998) also stressed that measuring roughness on exposed surfaces with lengths of at least 2 meters in the field could be a basis for determining an appropriate window size. Circular window mapping (Umili et al., 2013) has been suggested as well, but this study focused solely on rectangular or square shapes and didn't consider circular windows.

Lemy and Hadjigeorgiou (2004) used window sizes of 1.8 meters by 1.8 meters in an underground hard rock mine. In addition to the size of underground excavations dictating window size, Medinac (2019) observed that the height of mapping is usually limited to around 2 meters. This is because it is unlikely that a person can safely reach above 2 meters in contact mapping, regardless of the overall accessibility of the rock exposure.

4.4.1.4. Scaled RMR for fractured cubes

Considering the window size options and practices discussed above, it is reasonable to suggest that a window size of 2 meters by 2 meters is suitable and appropriate for underground mapping to determine fracture density (Js). This window size allows the laboratory-scale cubes to be scaled up to the size of the field window. Table 5 provides the conversion factors for different cube sizes used in this study.

Table 5. Conversion factors for scaling laboratory-scale plan view fracture densities (Jls) to field-scale fracture densities (Js) and RQDs.

Cube side length (m)	Window size (plan view): Area (m^2)	Scaling factor	Number of fractures	J_{ls}	J_s	J_v	RQD (%)
0.150	0.0225	1:13	3	133	10.2	13.4	77
0.225	0.0506	1:9	3	59.3	6.59	8.56	89
0.225	0.0506	1.9	2	39.5	4.39	5.71	96
0.300	0.0900	1:7	2	22.2	3.17	4.17	100
0.300	0.0900	1.7	3	33.3	4.75	6.18	95
0.300	0.0900	1.7	8	88.9	12.7	16.51	69
0.375	0.1406	1:5	2	14.2	2.84	3.70	100
0.450	0.2025	1:4	2	9.9	2.47	3.21	100

Drawing from Section E of the table proposed by Bieniawski, (1989) concerning factors for Rock Mass Rating (RMR), all fractures within the cubes are characterized as dry, rough, unweathered, and devoid of infilling. These attributes correspond to ratings of 0, 5, 6, and 6, respectively, resulting in a cumulative rating of 17. Table 6 presents the factor ratings for RMR and their respective values for the analyzed mortar cubes.

Subsequent to a curing period of 28 days, core samples were extracted from the mortar cubes, subsequently subjected to fracturing. These samples were then subjected to uniaxial compressive strength (UCS) tests. The obtained uniaxial compressive strength values for the fractured cubes are included in Table 6, revealing a certain degree of variability in the strengths of the mortar cubes. Additionally, fracture spacing, lengths, and apertures were gauged in each fractured block from a plan view perspective.

Table 6. RMR calculations for each fractured cube.

Cube side length (mm)	RQD		Fracture spacing		Fracture aperture		Fracture length		UCS		RMR
	(%)	Rating	(m)	Rating	(mm)	Rating	(m	Rating	MPa	Rating	
150	77	17	0.65-1.30	15	0.1-1.0	4	0.98-1.95	4	34	4	61
225	89	17	0.68-1.35	15	1-5	1	1.0-2.03	4	19	2	56
225	96	20	0.68-2.1	15	1-5	1	1.0-2.03	4	32	4	61
300	100	20	0.70-2.10	15	1-5	1	1.05-2.10	4	26	4	61
300	95	20	0.14-0.28	10	5.56	0	0.28-0.91	6	32	4	57
300	69	13	0.035-0.28	10	2.47	1	0.14-0.91	6	32	4	51
375	100	20	0.63-1.88	15	>5	0	1.31-2.63	4	24	2	58
450	100	20	0.60-1.80	15	1-5	1	0.90-1.80	4	12	2	59

The results show RMR for the fractured concrete blocks, based on the scaling of the in situ RMR system to laboratory scale physical models is feasible. Scaled RMR values will be further used to rate fractured cubes to see the effect of fracture intensity on seismic wave velocity.

4.5. Summary

The experimental study in Chapter 4 was conducted to investigate the AE signal propagation characteristics towards signal receivers under these adverse conditions taking advantage of the laboratory physical models, mimicking the complex mining environment. The following conclusions are derived from the AE measurements taken for various concrete and granite sample conditions:

- in isotropic homogeneous (intact) blocks, the straight raypath assumption is valid, and constant and layered velocity models can be safely used in the presence of voids and cemented backfills;
- void and backfill effect on AE signal travel time is negligible in small 150 mm blocks. However, with increasing block size and void diameter and with backfill in the voids, the signal travel time to sensors increase;
- fracture presence caused a signal attenuation depending on the sensors location towards the crack and the source.

Also, it was necessary to fracture the block models to simulate stress-induced fracturing caused by mining. Depending on the quality of the sample the SCA cracked the samples to different degrees. To compare the qualities of the fractured samples it was decided to use the rock mass classifications approach. RMR was selected for this purpose because the parameters constituting RMR can be scaled. The RMR parameters requiring scaling from in situ to laboratory scale models are RQD and fracture characteristics. The results show RMR for the fractured blocks, based on the scaling of the in situ RMR system to laboratory scale physical models is feasible.

5. DYNAMIC NUMERICAL MODELING

Laboratory experiments with concrete cubes and AE was simulated through dynamic numerical modeling in FLAC3D to better understand the wave propagation characteristics and its sensitivity to various factors in media.

5.1. Model Construction and Input Parameters

The model was not subjected to external loading implying that no initial stresses were applied to the model. This is because in the laboratory AE tests, the blocks were not subjected to external loading. For a solid cube without hole, a brick of a side length of 300 mm was used as the geometry. For the cube with hole, a cylindrical brick with two reflections at both ends was imposed on the solid cube to represent a cube with an empty hole. Sensor number 1 emitting the signal is shown on the model as a red dot based on the known geometry and location (Figure 29) in the laboratory tests. The constructed model was used to study the impact of various factors on seismic wave velocity (sensitivity study) through the granite and concrete cubes and to understand the physics of the problem. The input parameters of the model were varied to represent other rock types to understand the impact of different rocks on seismic wave velocity.

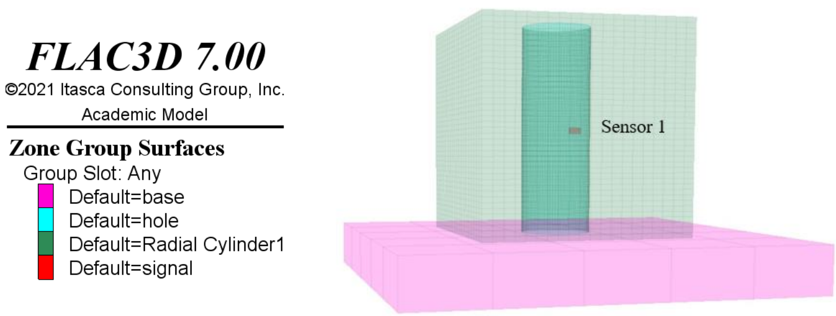

Figure 29. Geometry of the granite cube, with and without hole. Without hole, the green cylinder and the rest of the block have the same properties and with hole it is assigned the properties according to the code guidelines.

Elastic properties of granite and concrete samples were obtained from the laboratory experiments. Table 7 shows the model input parameters.

Table 7. Granite and concrete properties

Parameter	Concrete	Granite
UCS	25 MPa	153.3 MPa
Young's modulus	18.3 GPa	66.56 GPa
Poisson's ratio	0.28	0.23
Shear modulus	11.7 GPa	27.01 GPa
Bulk modulus	17.8 GPa	41.1 GPa
Density	2.4 g/cm3	2.7 g/cm3

Damping should be applied to a system subjected to dynamic loading, otherwise the system will oscillate indefinitely. FLAC 3D has three options of damping embedded in the code, namely Rayleigh damping, local damping, and artificial viscosity damping. Local damping was chosen for this research. Local damping is embodied in the FLAC 3D static solution and may be used for dynamic analysis, when input time history is not complex. The critical damping ratio is typically 2%–5% or obtained in a laboratory test; 5% was used in this analysis.

5.2. Boundary Conditions

In dynamic analyses, the application of boundaries to the model may cause the applied propagating waves to reflect into the model. Using a larger model may minimize this problem but as a consequence, a large computational time becomes a problem. An alternative is to use silent (quiet or viscous or absorbing) boundary to overcome the problem. Silent boundary operates in the time domain and was based on the use of independent dashpots in the normal and shear directions applied at the model boundaries. ITASCA (2022) states that a silent boundary is effective at absorbing the propagating waves for waves arriving at angles of incidence larger than 30°. Silent boundary is best suited for dynamic source applied within a grid. It should not be used along the side boundaries of a model when the dynamic source is applied at the top or bottom boundaries because the propagating wave will leak out of the side boundaries. For this case, silent boundary was applied to the bottom, and free-field boundary used for the other sides of the cube.

5.3. Model Meshing

Mesh creation in FLAC is relatively straightforward for this configuration. Maximum grid size is limited in the dynamic configuration to ensure proper seismic wave travel. Based on the work of (Kuhlemeyer & Lysmer, 1973) Itasca recommends that the element dimension, Δl, be no larger than $\Delta l < \frac{\lambda}{10}$. The specified wavelength, λ, is that which is associated with the highest frequency component of the input ground motion which contains significant energy.

The maximum size of the finite difference grid was calculated based on Equation 8, where Δl is the spatial element size, λ and f are the wavelength and frequency associated with the highest frequency component that contains appreciable energy, respectively, and V_s is the average velocity calculated from AE experiments in Equation 8:

$$\Delta l < \frac{\lambda}{10}$$

$$f < \frac{V_s}{10 \times \Delta l} \tag{8}$$

In equation 8, V_s = 3000 m/s, Δl< 2.29 mm.

5.4. Applied Signals and Histories

Acoustic Emission (AE) analysis employs a range of parameters to quantify the characteristics of AE signals, including the number of AE events, amplitude, ringing count, impact technique, rise time, duration, and others (Wu et al., 2018). The amplitude of an AE signal, which is its maximum value, is used to classify the type of AE source. The energy of an AE event is quantified by the area enclosed between the waveform envelope and the threshold voltage line. The ringing count reflects the intensity and frequency of the AE signal and is calculated as the number of peaks crossing the threshold. The duration of the AE signal, from threshold to threshold time, encompasses all AE activities during this period, thus providing insight into changes in the local stress characteristics of materials. These parameters are shown in Figure 31 and calculated for the two cases in Table 8.

Based on the laboratory work done with the AE system two wave signals were derived. AE is a wave generated by a sudden release of energy. After amplification and digitizing, an AE signal is represented as a voltage vs. time plot. Figure 30 presents the AE signal obtained for the solid cube case.

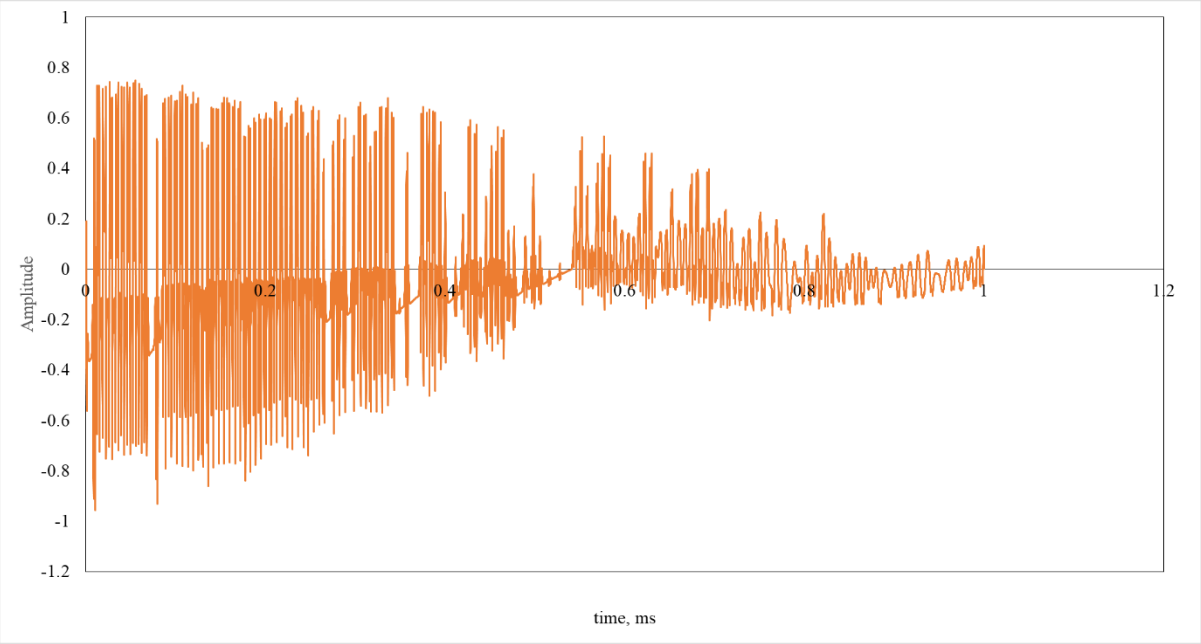

Figure 30. AE signal for solid cube case

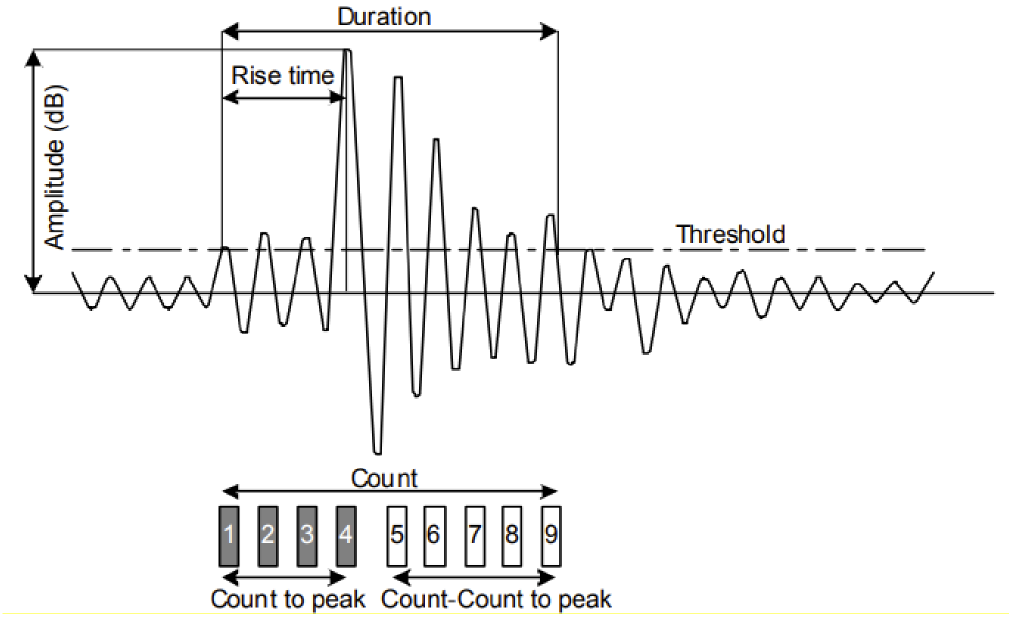

Figure 31. Definition of AE signal features (Grosse, Ohtsu Masayasu, Aggelis, & Shiotani, 2022)

Table 8. Results from Channel 1

Experiment	Amplitude	Counts	Rise Time	Duration	Energy
Solid Cube	59.6	251	3	123	4.05
Empty Hole	59.4	323	3	975	4.593

The time history may be used as an internal dynamic loading at internal grid points or as an external dynamic loading at the model boundary. There are four basic methods that dynamic loading can be applied to, namely as a time history of an acceleration, as a velocity, as a stress (or pressure), as a force. According to FLAC the first and second alternatives, should be used in cases with rigid bases, while the third and fourth options should be used in cases with flexible bases (Girsang, 2001).

Due to the nature of the discrete measurement of the initial load, the input time history may exhibit a high peak velocity, a brief rise-time, and a substantial high-frequency component. This can pose a challenge for simulation calculations, as the element dimension, Δl, must be less than 1/10 the wavelength (λ) to accurately represent the high-frequency component. Thus, the higher the frequency, the finer the grid generation required in FLAC. To mitigate this issue, a filtering process can be applied to the input time history, removing the high frequency components, which enables FLAC to utilize a coarser grid generation without sacrificing the precision of the results. This study employed the Bandpass computer code to filter the time history and eliminate low and high frequencies from it, thus addressing the aforementioned challenge (ITASCA, 2022b).

The following procedure was used to prepare the data for the filtering process:

1. The SWAE software (comes together with AE equipment) displays the raw data for acceleration, velocity, and displacement over time, along with their corresponding frequency spectrums.

2. The raw data is processed using a Butterworth filter, which is an Infinite Impulse Response (IIR) method that gives accurate results and has a smooth frequency response with a gradual change in amplitude.

3. Low frequency components are removed to eliminate motions that last longer than the shake, as these long-lasting motions lead to non-zero velocities and persistent movement at the end of the velocity and displacement measurements.

The filtering process was achieved through a Fourier transformation. Fourier transformation converts the input signal into a combination of sinusoidal waves with varying amplitude, frequency, and phase. The resulting plot of amplitude vs. frequency is known as the Fourier amplitude spectrum and the phase angle plot is known as the Fourier phase spectrum. The dominant frequency of the original wave is identified from the Fourier amplitude. Figure 32 displays the FFT analysis results for granite cubes.

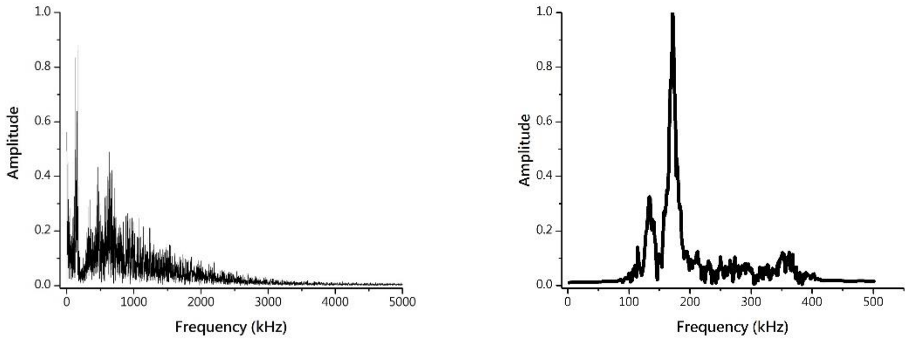

a) b)

Figure 32. FFT analysis for a) granite material b) concrete material

A baseline correction was then performed to force both the residual velocity and displacement to be zero. The purpose of this procedure is to prevent FLAC from exhibiting continuing velocity or residual displacements after the motion has finished.

5.5. Parametric analysis

The validation of the model was achieved through a comparison between the data generated by the model and the results obtained from experiments. This comparison included key wave parameters such as velocity, amplitude, and attenuation. Following the validation of the model using experimental data, the elastic characteristics and wave frequency of granite were altered to those of concrete and sandstone. This adjustment aimed to observe the resultant changes in wave velocity in the different materials. Figure 33 illustrates the location of sensors from the source. Tables 9 and 10 show the calculated wave velocity at each sensor for granite cube with empty hole and solid granite cube accordingly based on experimental data collected from the laboratory tests with the AE equipment. According to the Tables 9 and 10, sensors 2 and 3 show the lowest velocities due to the location at the furthest distance from the source that causes higher signal attenuation.

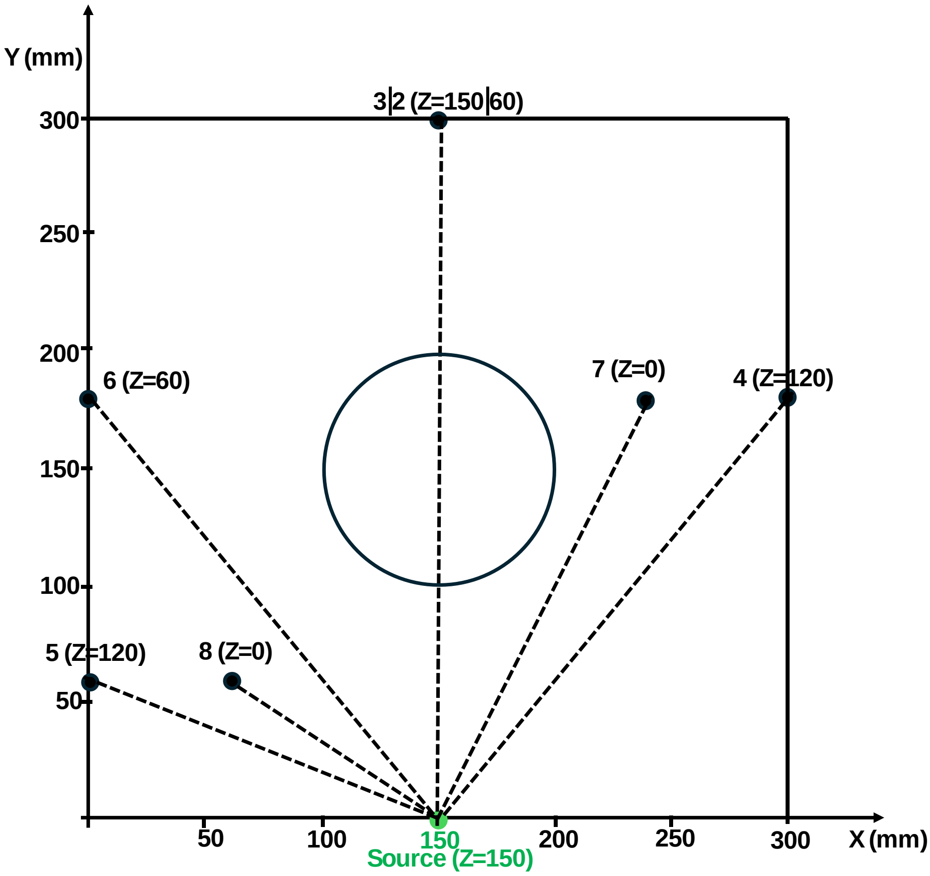

Figure 33. Location of sensors from the source (plan view of 300-mm cube: hole diameter is 100 mm)

Table 9. Calculated wave velocity at each sensor in granite cube with empty hole

Sensor	Velocity, m/s
1	Source
2	2378
3	1923
4	3786
5	2564
6	2733
7	4031
8	2554

Table 10. Calculated wave velocity at each sensor in solid granite cube

Sensor	Velocity, m/s
1	Source
2	3343
3	3442
4	4209
5	3906
6	4076
7	3936
8	3857

The numerical model was augmented with two checkpoints corresponding to the coordinates of sensors 2 and 5 to evaluate velocities at those specific locations. The graphs presented in Figure 34 depict both experimental and modeled data for granite cube with empty hole at sensors 2 and 5. Figure 35 illustrates experimental and modeled data for solid granite cube. The experimental data, obtained from AE test results, provides a singular arrival time at each sensor with known locations. Leveraging this information allows for the computation of velocity at each sensor. The velocity graph for the experimental data was generated through interpolation of initial and final points concerning velocity and time.

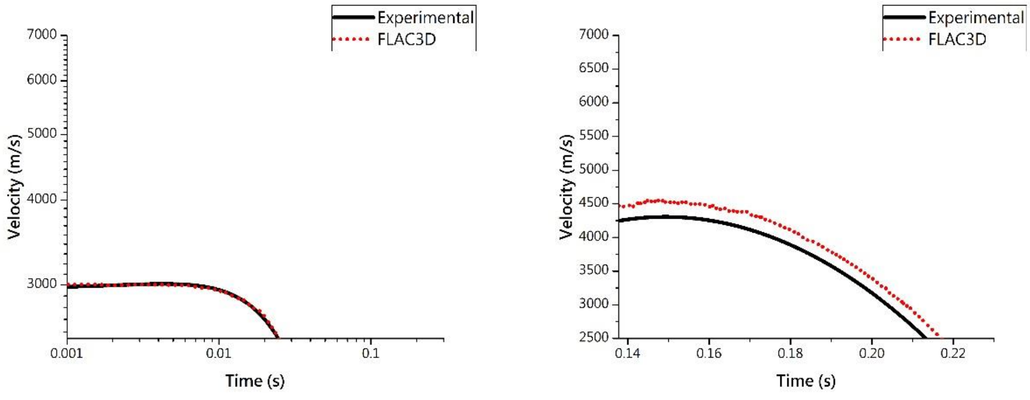

a) b)

Figure 34. Experimental versus modelled velocity in granite cube with empty hole at sensors a) 2 and b) 5

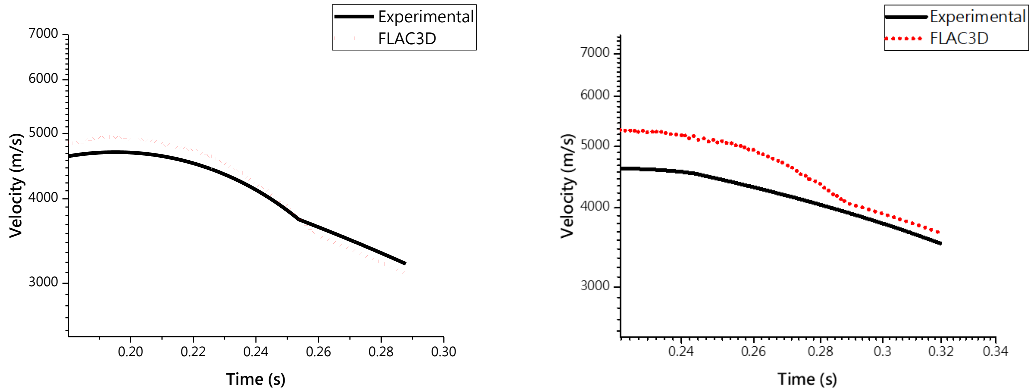

a) b)

Figure 35. Experimental versus modelled velocity in solid granite cube at sensors a) 2 and b) 5

Dynamic modelling results of the solid granite cube illustrated in Figure 36 shows wave propagation in time shots of 0.1 ms and 1 ms after wave generation across the cube from the source.

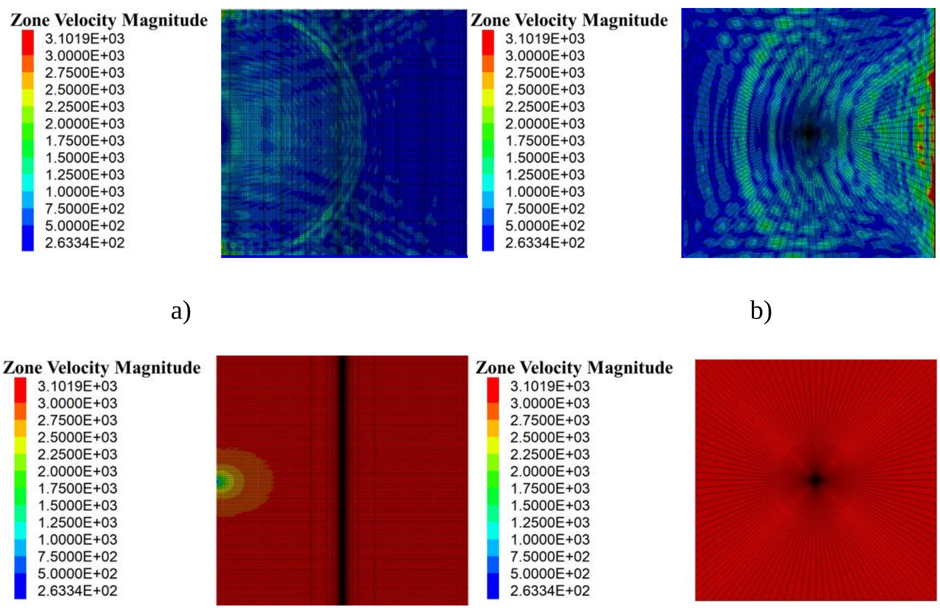

Figure 36. Wave velocity in solid granite cube after 0.1 ms a) section view b) top view and 1 ms c) section view d) top view

Figure 37 presents dynamic modeling outcomes of a granite cube with an empty hole. The illustrations encompass wave propagation snapshots at 0.1 ms and 1 ms, featuring both top and section views. In correlation with the findings from Figures 36 and 37, it is evident that the introduction of a void has a notable impact on wave velocity. The introduction of a void leads to signal attenuation, resulting in a decrease in velocity.

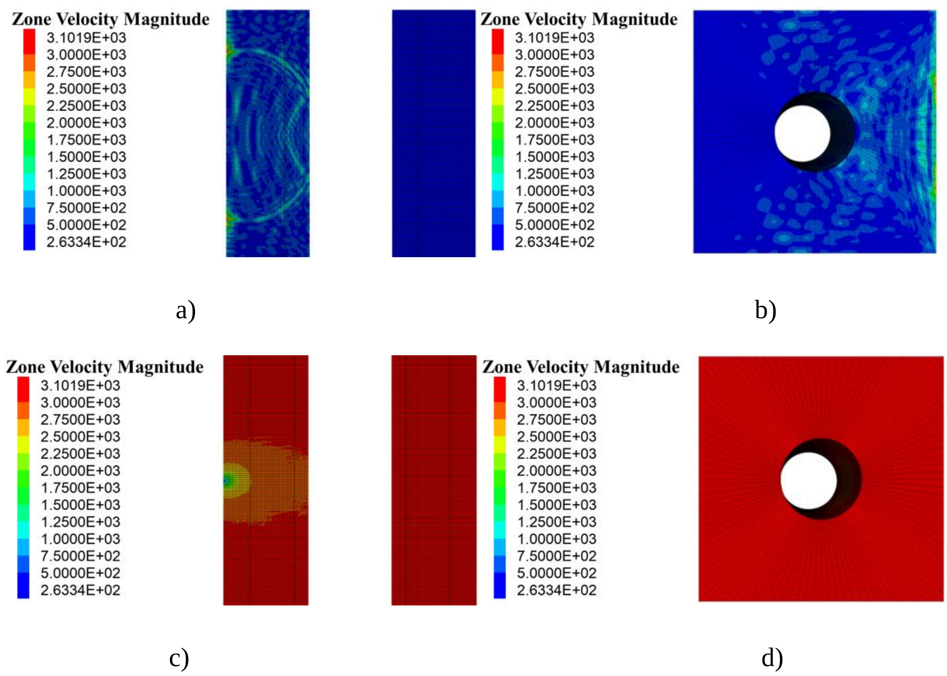

Figure 37. Wave velocity in granite cube with empty hole after 0.1 ms a) section view b) top view and 1 ms c) section view d) top view

Figures 38 and 39 depict analogous modeling results for concrete material, with alterations made to material properties as specified in Table 7. The visual representations capture wave propagation snapshots at 0.1 ms and 1 ms, incorporating both top and section views. In alignment with the observations from Figures 38 and 39, it is apparent that the presence of a void significantly influences wave velocity, mirroring the observed trend in the case of granite material.

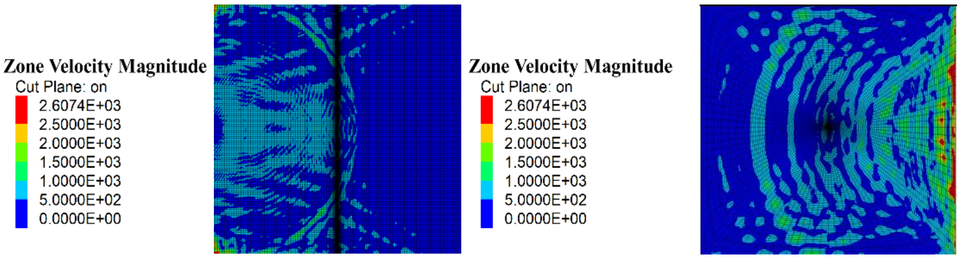

a) b)

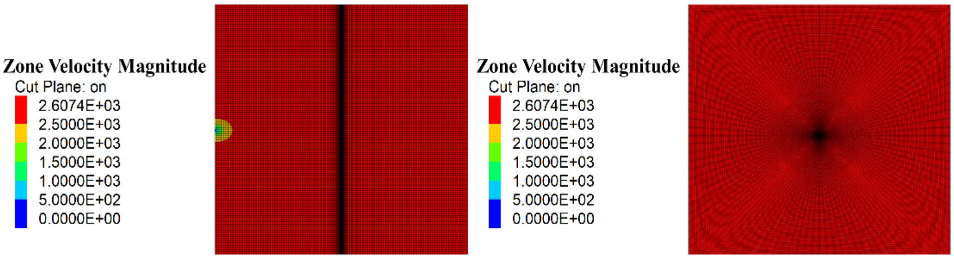

c) d)

Figure 38. Wave velocity in solid concrete cube after 0.1 ms a) section view b) top view and 1 ms c) section view d) top view

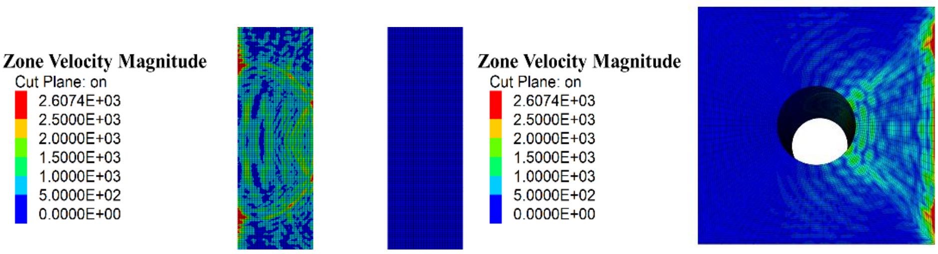

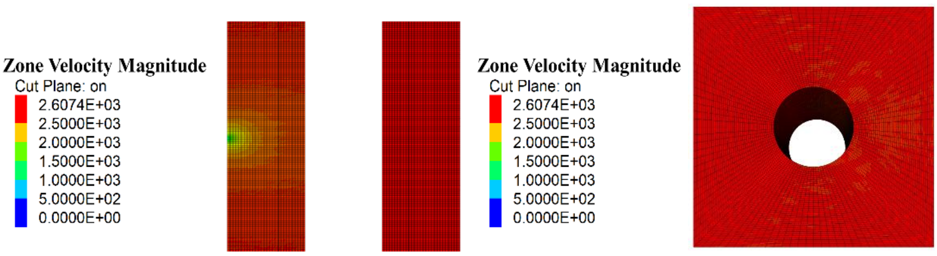

c) d)

Figure 39. Wave velocity in concrete cube with empty hole after 0.1 ms a) section view b) top view and 1 ms c) section view d) top view

The alteration in material also led to a change in average velocity, exhibiting a decrease in the case of concrete material. The average velocity in concrete registered at 2700 m/s, whereas in granite, it was approximately 3100 m/s.

In the third modeling scenario, sandstone material was utilized, and Table 11 provides the parameters employed for the modeling process. The average velocity for sandstone is approximately 1700 m/s (Zhang & Guo, 2022).

Table 11. Sandstone properties (Zhang & Guo, 2022).

Shear modulus	5 GPa
Bulk modulus	15 GPa
Density	2.6 g/cm3

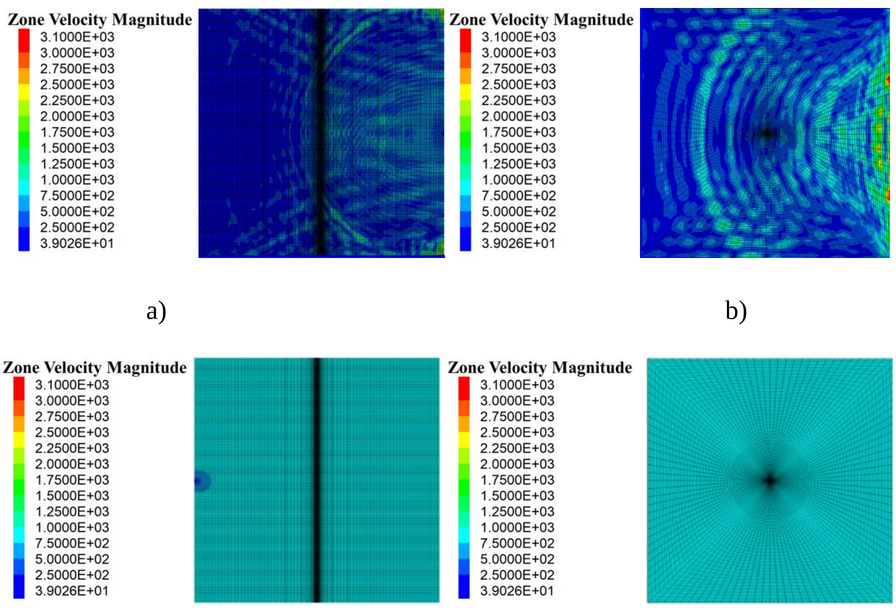

c) d)

Figure 40. Wave velocity in solid sandstone cube after 0.1 ms a) section view b) top view and 1 ms c) section view d) top view

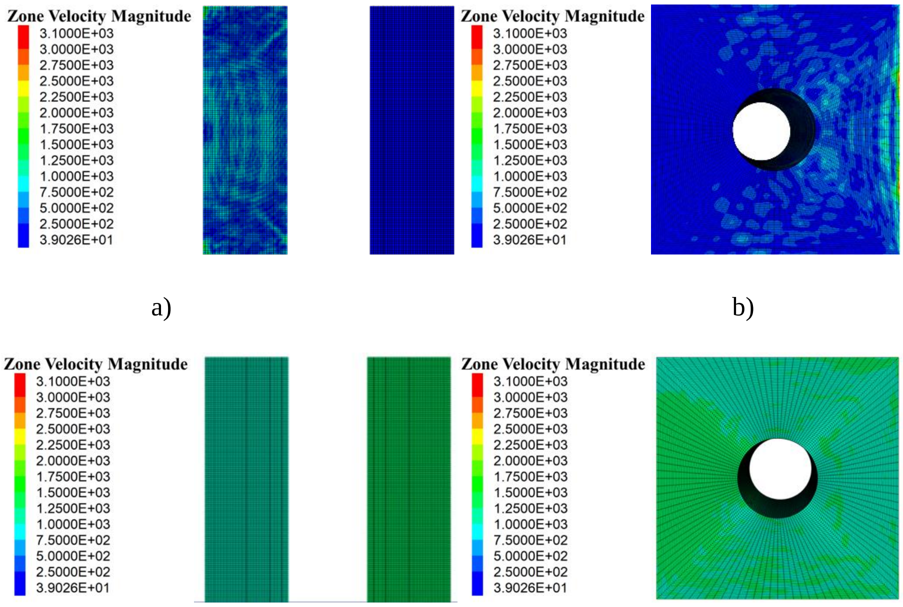

Figure 41. Wave velocity in sandstone cube with empty hole after 0.1 ms a) section view b) top view and 1 ms c) section view d) top view

5.6. Sensitivity analysis

A sensitivity analysis was conducted using the material properties of granite provided in Table 7. The geometric configuration was modified to a cube with dimensions of 450 mm and a hole diameter of 150 mm. Figures 42-43 display models with varying frequencies for configurations with and without holes. The observed results show different velocities at distinct points within the sample, depending on the frequency of the emitted signal as the wave propagates. The higher the frequency, the more the attenuation of wave energy from the source as seen in Figure 42 to 43. In Acoustic Emission (AE), a higher sampling rate enhances signal accuracy. The introduction of a hole results in increased attenuation of wave energy around the hole, as evident in the results of the 450 mm cube with a 150 mm diameter hole in Figure 43.

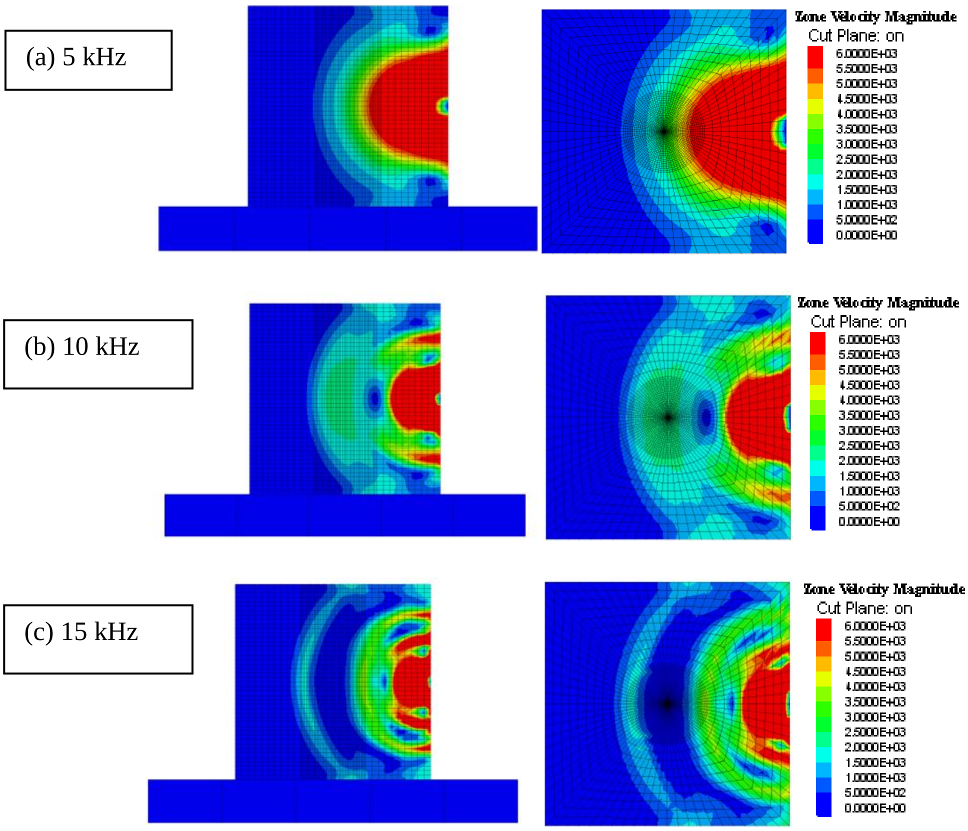

Figure 42. Velocity magnitude with different frequencies for solid 450 mm granite cube without hole. Section view at the middle of the sample and top view at 0.1 ms

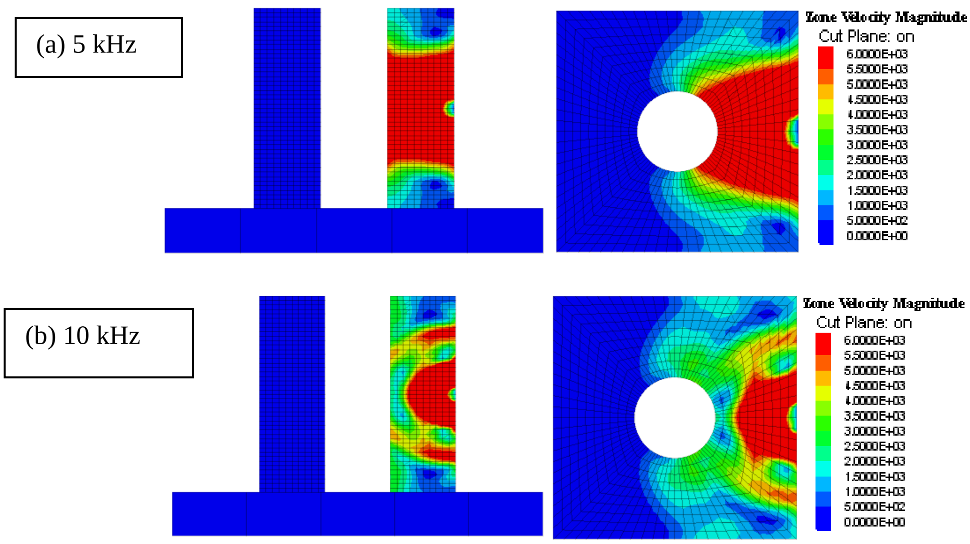

(c) 15 kHz

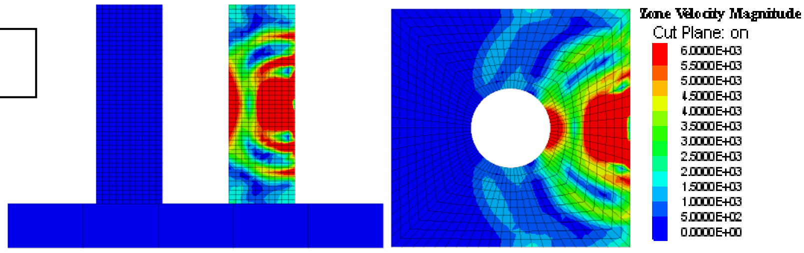

Figure 43. Velocity magnitude with different frequencies for 450 mm granite cube with hole diameter of 150 mm. Section view at the middle of the sample and top view at 0.1 ms

Additional factors influencing the wave propagation pattern include material density and elastic parameters. Figure 44 illustrates those variations in density, ranging from weakly compacted materials such as soil to more densely compacted materials. For a density of 1700 kg/m3 there is a higher wave attenuation compared with densities greater than or equal to 220 kg/m3. Hence, it can be concluded that density has an impact on seismic wave attenuation.

(a) 1700 kg/m^3

(b) 2200 kg/m^3

(c) 2700 kg/m^3

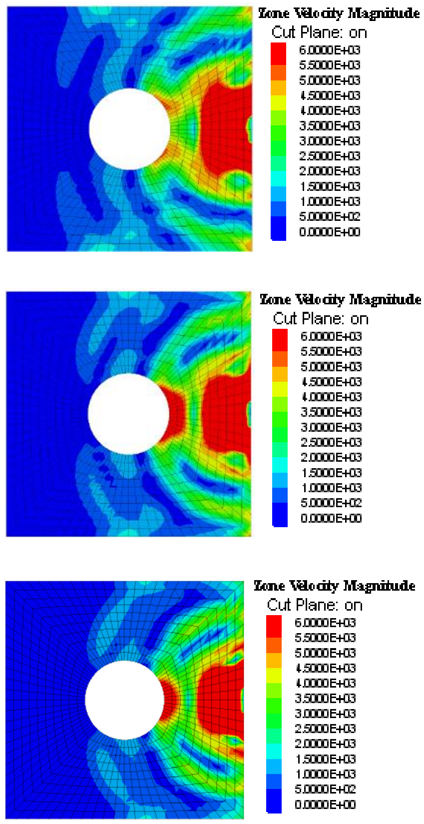

Figure 44. Velocity magnitude with different densities for 450 mm granite cube with hole diameter of 150 mm. Top view of a cut at the middle of the sample at 0.1 ms

Properly characterizing the elastic parameters of the sample is also crucial. Figure 45 illustrates the significant impact of elastic parameters on wave propagation. The model incorporates parameters outlined in Table 7. Specifically, Figure 45(a) was executed using half of the parameters from Table 7, while Figure 45(c) utilized double those values.

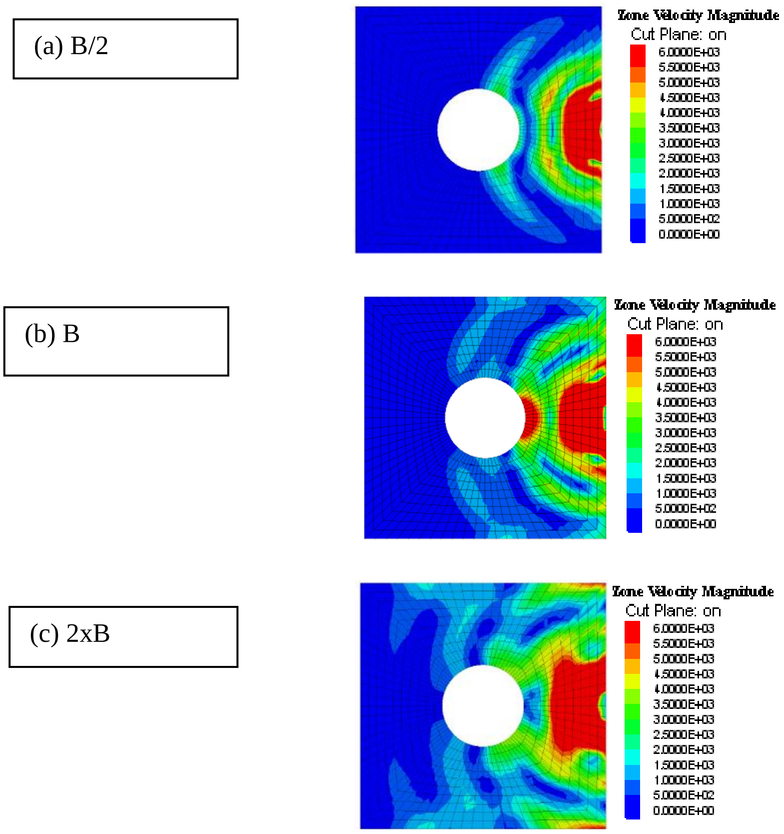

Figure 45. Velocity magnitude with different elastic parameters for 450 mm granite cube with hole diameter of 150 mm. Top view of a cut at the middle of the sample at 0.1 ms

Based on the modeling results illustrated on figure 45 velocity and elastic properties has strong positive correlation.

5.7. Summary

The study explored how voids impact seismic waves using various materials and configurations, revealing increased attenuation with void introduction. Notably, seismic wave velocity responded to material properties, especially changes in density and elastic parameters. Higher material density and increased elastic parameters contribute to faster seismic wave velocity, offering insights into forecasting events like rockbursts and stress variations in mining scenarios.

Additionally, the strong agreement between experimental and modeled data affirms the reliability of the modeling approach. Successful validation enhances confidence in the accuracy of predictions, providing valuable insights for geomechanics and applications in seismic hazard assessment and mine safety.

6. MACHINE LEARNING

Machine learning (ML) is the broader category of artificial intelligence, aiming to empower computers to solve complex issues without needing to be directly programmed for each task. Within ML, the term "training" refers to the process of learning from past data. The ability to learn and adapt by drawing on past experiences to enhance or acquire new skills sets ML apart from the conventional approach of programming computers to execute specific tasks. Traditional computer programming depends on clearly defining a problem through the known physical laws of the system being analyzed. Conversely, ML focuses on examining data to forecast the behavior of complex systems that are difficult to define with standard methods. The training in ML can be supervised, where the system learns from a dataset that includes correct answers, or unsupervised, which involves identifying patterns without prior knowledge of outcomes (Jooshaki et al., 2021).

6.1. Data exploration

Data exploration involves extracting knowledge from data to quickly identify relevant data elements. To ensure reliable exploration results, the raw data needs to undergo thorough selection and cleaning. This is similar to seismic data management at mine sites where normally there will be a dedicated person responsible for cleaning the seismic data to get rid of blasting events and other related sources that are not responses of the ground due to mining. Several dataset-handling techniques, including one-hot encoding, handling missing values, managing recurring parameters, standardizing data types, and normalization, were applied to guarantee data integrity and quality.

6.2. Initial data

The laboratory test results generated in Chapter 4 served as the database for the machine learning application. The dataset provided information such as the coordinates of the source and receiving sensors, arrival times of the wave at each sensor, quality parameters of the backfill affecting wave velocity, and the quality of fractured and unfractured cubes, represented by RMR scores and corresponding wave velocities.

Initially, the dataset consisted of 64 different parameters and a total of 1070 records, of which 166 did not contain any sensor data. Some parameters contained a mix of qualitative and quantitative data, while others had missing values. Duplicate parameters, such as the average velocity values from all sensors for each record provided. Furthermore, the data format exhibited inconsistencies, with numeric values sometimes in floating-point format and sometimes in text format.

Table 12 provides a list of the variables utilized for training the models. It is important to note that the sensor coordinates, distance to the source, and arrival time parameters differ depending on the sensor or channel. Consequently, there are seven datasets for each sensor, labeled from 2 to 8, with channel 1 being the source channel. However, the remaining parameters remain consistent across all datasets.

Table 12. Variables used in training the models.

Variable	Unit	Description
Sample	[-]	The type of the experimental cube (concrete or granite)
Block size	[mm]	The type of the experimental cube (concrete or granite)
RMR	[-]	Rock mass rating, the fractured block quality
Hole	[-]	Boolean value that represents the presence of the hole in the cube
Hole Diameter	[mm]	The diameter of the cylindrical hole in the cube

Cement Content	[%]	Percentage of the cement mixture in the hole
Curing time	[ms]	The time elapsed after the hole was filled
Backfill strength	[MPa]	Backfill material quality
Source coordinates	[m, m, m]	Source coordinates in 3D space
Sensor coordinates	[m, m, m]	Sensor coordinates in 3D space
Arrival time	[ms]	The time at which the sensor captures the wave
Distance to source	[m]	The distance from the sensor to the source
UCS	[MPa]	Uniaxial compressive strength of the sample

6.2.1. Dataset handling techniques

To address parameters with a combination of qualitative and numeric values, a segregation was performed, separating qualitative and numeric data into distinct parameters. Each qualitative value was transformed into a binary parameter, adopting values of 0 or 1 to signify the absence or presence of the respective attribute. For instance, the original parameter encapsulating cement content, initially encompassing various content types and percentages within a single column, underwent decomposition. We established distinct Boolean parameters for different content types, while the cement content column retained solely the percentage values. Qualitative data was replaced with 0, denoting the absence of cement content.

To handle missing values in the dataset, imputation was carried out using the mean value of the corresponding field. For example, if certain records lacked information regarding backfill strength, the missing values were substituted with the mean value derived from other known backfill strength values associated with the same curing time. In the case of a missing value for a 7-day cured backfill, it was imputed with the average value of known 7-day cured backfill samples. Given the dataset's comprehensive mining-related information, redundancy in parameters was addressed to enhance the stability of machine learning training. Redundant parameters were either sorted or removed. For instance, a separate parameter titled 'qualitative data,' summarizing information on block description, hole presence, diameter, block size, and backfill type, was eliminated as these parameters were already present as independent fields.

The laboratory-generated data encompassed both numeric and textual formats. To facilitate the application of machine learning algorithms and ensure valid results, all data formats were standardized to a consistent float type. This involved converting qualitative data, such as cement content, into binary representations and transforming textual data, like '272.8,' into floating-point numbers (e.g., 272.8).

Normalization was subsequently applied to the preprocessed dataset to enhance the stability of model training. This process involved shifting and scaling inputs to achieve a distribution centered on 0, with a standard deviation of 1. The mean value and variance of the data were precomputed, and Equation 9 was employed during runtime to effectuate the normalization process.

$$(input - mean)/\sqrt{var} \tag{9}$$

After cleaning the dataset using the aforementioned techniques, a total of 730 records with 60 different parameters was derived.

6.3. Machine learning methods

This research is targeted at determining the seismic event location in underground mines that is a complex task challenged by the constantly changing ground condition due to mining. Our approach is a novel three-pronged method involving the application of machine learning techniques for velocity prediction and seismic event source location, using the simplex method. The solution architecture is presented in Figure 46.

Deep learning (DL) intuitively has a high potential in improving the accuracy of microseismic event source location due to its ability to discover hidden patterns to eliminate the need for extensive feature engineering. Various DL-based solutions utilizing convolutional neural networks (CNN) have been proposed for microseismic and seismic wave denoising, waveform processing, event detection, classification, and location (Ma et al., 2019; Pham et al., 2020; Zhu et al., 2019). However, the geological model's uncertainty adds complexity to the task of detecting, classifying, and locating events, which can be performed using either time of arrival picking or raw waveforms. Prominent solutions include Bayesian networks and CNNs, which output location information based on channel impulse response (Cao et al., 2020; Niitsoo et al., 2018; Zhu & Beroza, 2019).

6.4. Seismic event source location prediction

6.4.1. Velocity prediction

The first phase of seismic event source location prediction centers on predicting the velocity of seismic waves given various conditions using machine learning algorithms. Specifically, Linear Regression, Artificial Neural Networks (ANN), and Decision Trees (inclusive of ensemble methods such as Random Forest and Gradient Boosted Trees) were employed to identify the best-performing model. In ANN models, the Rectified Linear Unit (ReLU) activation function is incorporated, and twelve different configurations are tested, varying the number of hidden layers and neurons per layer. The performance of these models is evaluated using key metrics like Mean Absolute Error (MAE).

6.4.2. Initial seismic event source location

The second phase involves the application of the simplex method, a well-known optimization algorithm, for the preliminary location of the seismic event sources. The simplex method is used to optimize an objective function representing the seismic wave travel time (dependent on the predicted velocities) and the potential seismic event locations.

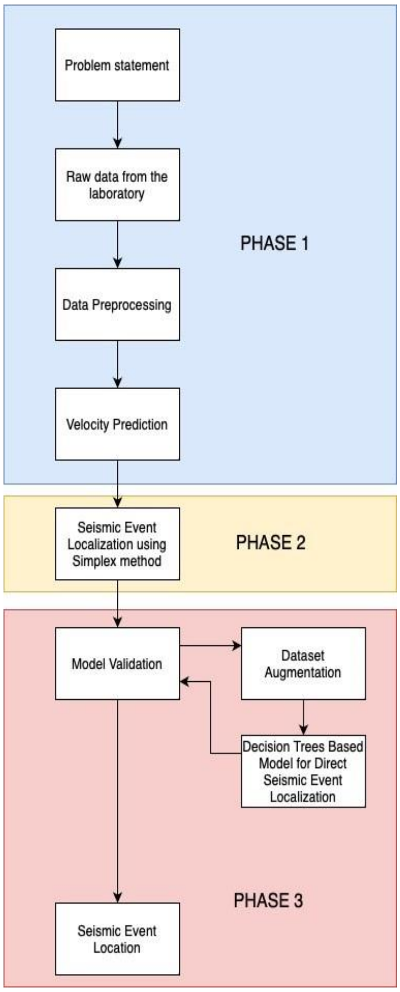

Figure 46. Solution Architecture for velocity real-time velocity prediction and improved seismic event source location determination

6.4.3. Refined seismic event source location

To address the errors identified in the second phase, a third phase was introduced, leveraging machine learning techniques for the refinement of seismic event location. In this phase, the model is not solely trained on the disparities between the locations derived from the simplex method and the actual seismic event locations. Instead, both the original dataset and an augmented dataset are utilized to train a machine learning model explicitly for predicting the seismic event location. The objective of this phase is to provide a more precise and accurate prediction of the seismic event source location.

6.5. Machine learning implementation

6.5.1. Velocity prediction and simplex method

Linear Regression uses a straightforward model to estimate the dependent variable by considering independent parameters, aiming to minimize the difference between predicted and actual values. Its simplicity, interpretability, and scalability make it suitable for various applications. In this research, Linear Regression is utilized to forecast velocity using data from 22 concrete blocks and wave arrival times from seven sensors placed at known locations on concrete and granite cubes.

Another alternative, Artificial Neural Networks (ANNs) (Figure 47), imitate human neuron behavior through signal transmission with assigned weights, forming the basis for neural networks. Deep learning, an advanced form of machine learning, heavily relies on these networks, detecting intricate correlations and patterns among features that may be overlooked in other methods. In this study, various neural network architectures with varying numbers of hidden layers and neurons per layer were tested. The rectified linear unit (ReLU) function served as the activation function, and a total of 12 diverse neural network configurations were assessed.

Decision Trees (DTs), specifically Random Forest and Gradient Boosted DT, were also employed in our study due to their prediction accuracy and efficiency. DTs replicate decision-making processes but may overfit data, resulting in less generalizable models. Random Forest addresses this by integrating multiple decision trees, promoting collective intelligence at the expense of interpretability and computational speed. Gradient Boosted DT enhances this approach by constructing trees sequentially to improve on previous models' shortcomings and minimize loss.

Following velocity prediction, the next step involves determining the event source location using the Simplex method. Widely used in seismic monitoring systems, the Simplex method efficiently solves non-linear equations. In the context of seismic event source location calculation, the simplex method is applied to solve a system of equations derived from velocity measurements and time differences of seismic wave arrivals at multiple sensors.

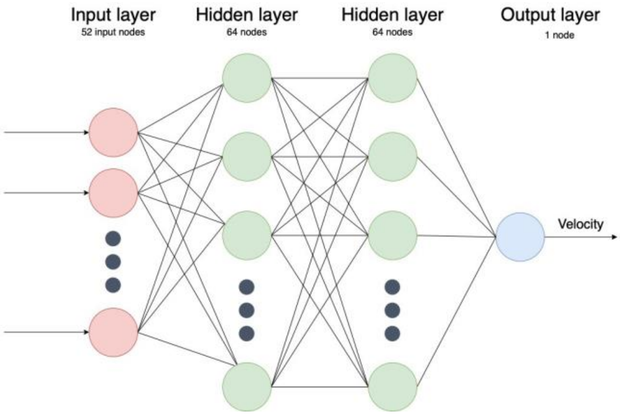

Figure 47. Deep Neural Network with 2 hidden layers

The approach formulates the problem as a system of nonlinear equations based on the following algebraic expression:

$$v.t + \sqrt{(X - a_1)^2 + (Y - b_1)^2 + (Z - c_1)^2} = \sqrt{(X - a_i)^2 + (Y - b_i)^2 + (Z - c_i)^2} \quad (10)$$

Where a_1, b_1, c_1 are coordinates of the nearest sensor a_i, b_i, c_i are the i^{th} sensor's coordinates t is the time difference between sensors v is the velocity and X, Y, Z are the event source coordinates.

The implementation of the Simplex method in this study has the following architecture:

- Input: The code takes as input the coordinates of seismic sensors, the predicted velocities of seismic waves at the receiving sensor, and the time differences of seismic wave arrivals.
- Objective Function: The code defines an objective function that represents the difference between the predicted and observed time differences. This objective function is a measure of the error or residual in the seismic event location estimation.
- Initialization: An initial guess for the seismic event coordinates is provided to start the optimization process. This initial guess can be set to (0, 0, 0) or any other suitable value.
- Iterative Optimization: The code uses the simplex method to iteratively update the seismic event coordinates and minimize the objective function. It starts with the initial guess and iteratively adjusts the coordinates to reduce the difference between predicted and observed time differences.
- Convergence: The optimization process continues until the objective function reaches a minimum or a specified stopping criterion is met. This ensures that the solution is as close as possible to the true seismic event location.
- Output: The code returns the estimated seismic event coordinates, which represent the calculated epicenter of the seismic event based on the simplex method optimization.

By applying the simplex method for seismic event location calculation, the code aims to identify coordinates that minimize the discrepancy between predicted and observed time differences at seismic sensors. The objective is to theoretically achieve precise estimation of the seismic event's epicenter. However, practical datasets often incorporate noise, rendering certain systems of equations unsolvable when exact solutions are sought. Consequently, an approach emphasizing approximate solutions was pursued. Despite these efforts, the method still yielded an error margin approximating 100%. As a consequence, the introduction of Direct Seismic Event location was deemed necessary.

6.5.2. Direct seismic event source location

To predict the location of the seismic event source, multioutput regression was necessary. Random Forest (Jin et al., 2020), XGBoost (Chen & Guestrin, 2016), and Gradient Boosted Decision Trees (Natekin & Knoll, 2013) paired with skcikit-learn Multi Output Regressor was used to run regression.

Each model exhibited significant overfitting, primarily attributed to the limited diversity in the source location data, resulting in a prediction error of 0 cm for each coordinate. Recognizing the potential unreliability of such models in real-world scenarios, a strategic decision was made to introduce greater realism and robustness by randomly sampling a holdout dataset and incorporating noisy data.

Initially, the seismic dataset is imported into a Pandas DataFrame, encompassing information about seismic events slated for location. To fortify the robustness and accuracy of the model, the dataset is stratified into five equal segments. Within each segment, random sampling is executed, where approximately half of the data is randomly chosen as a holdout test set, while the remaining half is retained for model training and testing. The determination of the number of random samples involves dividing the segment length by 2 and rounding up to ensure a representative data subset. The resulting holdout segments are amalgamated and stored for the ultimate testing phase of trained models. Additionally, datasets are saved as CSV files, thereby ensuring reproducibility.

Iterating this process five times yields five distinct holdout and training datasets, each featuring diverse seismic events for training and testing. This iterative approach guarantees that the model undergoes training and evaluation on varied subsets of the dataset, contributing to a more robust assessment and instilling greater confidence in the model's performance. This methodology serves as a countermeasure against the pronounced overfitting tendencies observed in models.

6.5.2.1. Data Augmentation

To enhance the training data and optimize the performance of the direct seismic event localization model, two distinct augmentation methods—Gaussian augmentation and augmentation with Generative Adversarial Networks (GANs)—are employed.

The first technique, Gaussian Augmentation, introduces synthetic seismic events into the training set by applying Gaussian noise to the existing data. This noise, derived from a Gaussian distribution, introduces variations, simulating the inherent variability of seismic signals. Each dataset row undergoes slight modifications to create new data points. The integration of this augmented data into the training set enhances the model's resilience to noise and improves its ability to generalize to unseen seismic events with diverse characteristics.

The second augmentation method leverages GANs, comprising a generator and a discriminator. The generator produces synthetic seismic events, while the discriminator learns to differentiate between real and synthetic events. Through adversarial training, the generator refines its ability to generate realistic synthetic seismic events that challenge the discriminator's ability to discern them from real events. The generated events are subsequently incorporated into the training set, providing additional diverse examples for the model to learn from. These augmentation methods are sequentially employed to generate more robust synthetic data for training. Through data augmentation, the training dataset size is quadrupled, totaling approximately 2500 rows.

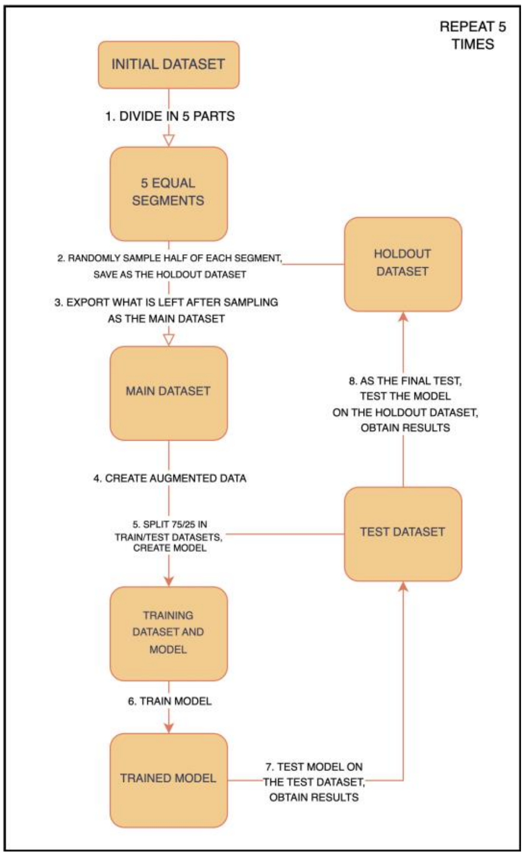

Figure 48. Data Preparation and Model training process

6.5.2.2. Building models and hyperparameter tuning

The training dataset, comprising remaining data post-random sampling and newly generated data, is utilized for model training. Subsequently, this training dataset undergoes further division into testing and training subsets, with a proportion of 75/25.

XGBoost, Random Forest, and Gradient Boosted Decision Trees models are employed to predict the source location, utilizing scikit-learn Multiple Output Regressor. In the initial attempt, these models are run on default parameters, resulting in an average error of 7 cm on the training dataset, which is deemed considerable.

To decrease error, Grid Search cross-validation to tune models' hyperparameters was used. A range of relevant parameters is set for each respective model and Grid Search cross-validation is performed. After the tuning is completed, Random Forest shows the best results with 4cm error on average, which is a 75% decrease compared to default parameters. When tested on the holdout dataset, the error is about 1 cm, which is more realistic than the 0 cm the model was predicting before the data augmentation.

6.5.3. Experimental results

Maksut et al. (2022) used newly designed models for algorithms based on neural networks and employed and used Decision Trees. Moreover, instead of predicting a single velocity based on collective sensor data, velocities were predicted independently for each sensor. This strategy was aimed at enhancing the accuracy of predictions compared to the previous study, and at pinpointing potentially unreliable sensors.

$$MAE = \frac{\sum_{i=1}^{D} |x_i - y_i|}{n} \tag{11}$$

The Mean Absolute Error (MAE), given in Equation (13), was chosen as the performance metric to assess the accuracy of our models. The most efficient version of each algorithm was selected, with their respective performances tabulated in Table 13. As per the results obtained by Maksut et al. (2022), the highest accuracy recorded was 34.770 m/s. However, the research produced markedly enhanced results, with the highest accuracy reaching 7.146 m/s for sensor 2. Considering the extensive range of records analyzed, an average velocity of 1615.386 m/s was computed. This average serves as a central value, providing a generalized estimate of the velocities observed in this context.

Table 13. Model Performance

Model	Unit	#2	#3	#4	#5	#6	#7	#8
Linear Regression	[m/s]	618.25	591.09	624.4	478.43	628.08	674.04	673.1
DNN 6 128	[m/s]	22.02	20.46	29.46	42.99	26.95	27.88	21.39
GBDT	[m/s]	9.74	7.15	13.5	7.32	7.97	10.25	12.33

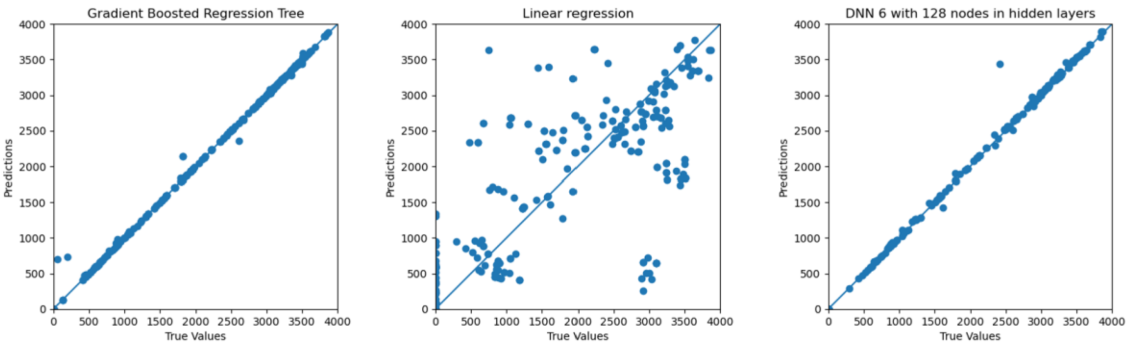

Figure 49. Training and validation losses of the models

Acknowledging that a single metric may not comprehensively capture the entire distribution or potential outliers, it serves as a valuable benchmark for assessing the model's errors. Considering the average velocity, the observed discrepancies in the models are relatively modest, indicating a favorable proximity to this central benchmark. Consequently, these findings enhance confidence in asserting that the models demonstrate commendable accuracy in predicting velocities.

Subsequently, for validation, recourse was made to the simplex method. However, even minor noise can render the system of equations unsolvable due to inherent contradictions. To mitigate this challenge, a least squares approximation was employed to determine the coordinates. However, as indicated in Table 12, the Mean Absolute Error (MAE) for each coordinate is substantial, often surpassing the actual values.

6.6. Summary

In this chapter, ML was employed to predict seismic wave velocities from data generated under specific discrete block conditions. This data served as input for a seismic source location algorithm, aimed at determining source locations. Among the tested ML models, the Random Forest methodology emerged as the most accurate predictive model, exhibiting a minimal error margin of just 1mm. A variety of ML models, including deep learning techniques, were applied to the data generated under various block conditions to identify the optimal model. The task of the model was to predict an equivalent ground condition velocity to a given set of conditions. Among the ML models tested, the Gradient Boosted Decision Tree model distinguished itself by having an error rate of 7.15 m/s, in contrast to the average target velocity of 1615.39 m/s. The level of accuracy achieved in predicting velocity within a dynamic mining environment significantly enhances the precision in identifying the source locations of seismic events. Additionally, the study led to the development of an algorithm based on the simplex method. This algorithm, grounded in the concept of least squares approximation, calculates the x, y, and z coordinates in 3D space.

7. CONCLUSIONS AND RECOMMENDATIONS

7.1. Conclusions

The research goal of the thesis was to predict the most suitable velocity model in real-time for use in seismic source location calculations in seismic monitoring systems. The objective was motivated by the problem of predicting the exact location of rockburst occurrence. The literature review showed that significant source of uncertainty affecting source location accuracy lies in the velocity model utilized in the location algorithm. Establishing a reliable velocity model in mining is challenging due to encountering multiple rock types and the constant changes in rock mass conditions resulting from the creation of voids and stress alterations. This complexity necessitates a continuously changing velocity model, which contrasts with the current assumptions of using single (homogeneous rock mass assumption) or variable static constant velocity models (layered rocks assumption) in seismic monitoring systems for seismic source location calculations.

The research consisted of three main stages. The first step was imitation of underground mine conditions in a controlled laboratory environment. It involved the novel use of discrete physical models as analogues, representing different stages in the mining process, including increasing mine maturity, increasing mine extraction, and mining induced fracturing. AE tests were performed on each discrete block under various conditions to assess the impact of each condition on seismic wave velocity. The results showed that in isotropic homogeneous blocks the size effect showed negligible effect on seismic wave velocity. Void and backfill effect on AE signal travel time is negligible in small 150 mm blocks. However, with increasing block size and void diameter and with backfill in the voids, the signal travel time to sensors increase thereby decreasing seismic wave velocity. Fracture presence caused a signal attenuation depending on the sensors location relative to the crack and the source. RMR system by Bieniawski (1973) was scaled to suit laboratory samples.

The second step was to analyze the sensitivity of seismic wave velocity to various factors in underground mining environments by dynamic modelling in FLAC3D. The modeling results showed voids impact on seismic waves, revealing increased attenuation with void introduction. Moreover, seismic wave velocity responded to material properties, especially changes in density and elastic parameters. Higher material density and increased elastic parameters contribute to faster seismic wave velocity, offering insights into forecasting events like rockbursts and stress variations in mining scenarios.

The third step was application of ML for real-time seismic wave velocity prediction for various underground mine conditions in seismic event source locations determination. Among the ML models tested, the Gradient Boosted Decision Tree model distinguished itself by having an error rate of 7.15 m/s, in contrast to the average target velocity of 1615.39 m/s. The level of accuracy achieved in predicting velocity within a dynamic mining environment significantly enhances the precision in identifying the source locations of seismic events. Moreover, the study led to the development of an algorithm based on the Simplex method grounded in the concept of least squares approximation, calculates the x, y, and z coordinates in 3D space.

The integration of numerical modeling, laboratory experiments, and advanced monitoring in a holistic approach enhances comprehension of seismic activities in mining. This comprehensive understanding, validated through strong agreement between experimental and modeled data, not only advances mining safety and efficiency but also underscores the necessity of addressing seismic risks in complex mining projects. The study establishes a robust framework considering stress, energy, and loading systems for predicting seismic energy release in mining activities.

The findings presented in this thesis provide valuable insights into the challenges and complexities associated with accurately determining seismic event source locations in dynamic underground mining environments. The development of a continuously changing velocity model using discrete physical models as analogues represents a significant advancement in addressing the limitations of current approaches.

7.2. Recommendations

Based on the obtained results, it is strongly recommended that further work be undertaken to bridge the gap between theoretical advancements and practical implementation. Specifically, the focus should be on integrating the developed velocity model into microseismic monitoring systems used in underground mines to enable real time velocity prediction coupled with simplex method. This implementation would serve to validate the effectiveness of the continuously changing velocity model in real-world scenarios and contribute to the evolution of seismic monitoring practices in the mining industry.

Another vital aspect that could benefit future research yet was overlooked by the author due to time constraints, is the impact of confined stress on seismic wave velocity. The study operated under the assumption of a straight ray-path. However, this element could be explored deeper to gain a comprehensive understanding of the wave travel path through the application of ray tracing theory.

REFERENCES

Ammon, C. J., Velasco, A. A., Lay, T., & Wallace, T. C. (2021). Earth motions & seismometry. In *Foundations of Modern Global Seismology*. https://doi.org/10.1016/b978-0-12-815679-7.00011-2

Aster, R., Borchers, B., & Thurber, C. (2018). Parameter Estimation and Inverse Problems (3rd ed.). Elsevier.

Bandpey, A. K., Shahriar, K., Sharifzadeh, M., & Marefvand, P. (2019). Comparison of methods for calculating geometrical characteristics of discontinuities in a cavern of the Rudbar Lorestan power plant. *Bulletin of Engineering Geology and the Environment*, *78*(2), 1073–1093. https://doi.org/10.1007/s10064-017-1145-x

Barton, N., Grimstad, E. (1993). Updating the Q-system for NMT. International Symposium on Sprayed Concrete, January 1993, 46–66.

Bieniawski, Z. T. (1989). *Engineering Rock Mass Classifications*. A wiley-interscience publication.

Blake, W., & Leighton, F. (1970). Recent developments and applications of the microseismic method in deep mines. Proc. 11th Symposium on Rock Mechanics, 429–433.

Blake, W., Leighton, FW., & Duvall, W. (1974). *Microseismic techniques for monitoring the behaviour of rock structures*. U.S. Bureau of Mines.

C109/109M-16a, A. (2016). Standard test method for compressive strength of hydraulic cement mortars (Using 2-in. or cube specimens). *Annual Book of ASTM Standards*, 1–10. https://doi.org/10.1520/C0109

Cai, M. (2013). Principles of rock support in burst-prone ground. *Tunnelling and Underground Space Technology*, *36*, 46–56. https://doi.org/10.1016/j.tust.2013.02.003

Cai, M. (2016). Prediction and prevention of rockburst in metal mines - A case study of Sanshandao gold mine. *Journal of Rock Mechanics and Geotechnical Engineering*, *8*(2), 204–211. https://doi.org/10.1016/j.jrmge.2015.11.002

Cai, W., Dou, L., Cao, A., Gong, S., & Li, Z. (2014). Application of seismic velocity tomography in underground coal mines: A case study of Yima mining area, Henan, China. *Journal of Applied Geophysics*, *109*, 140–149. https://doi.org/10.1016/j.jappgeo.2014.07.021

Cai, W., Dou, L., Gong, S., Li, Z., & Yuan, S. (2015). Quantitative analysis of seismic velocity tomography in rock burst hazard assessment. *Natural Hazards*, *75*(3), 2453–2465. https://doi.org/10.1007/s11069-014-1443-6

Cai, W., Dou, L.-M., Li, Z.-L., Liu, J., Gong, S.-Y., & He, J. (2014). Microseismic multidimensional information identification and spatio-temporal forecasting of rock burst:A case study of Yima Yuejin coal mine, Henan, China. *Acta Geophysica Sinica*, *57*(8), 2687–2700. https://doi.org/10.6038/cjg20140827

CAMIRO. (1996). *Canadian Rockbursts Handbook* (Volume 6). Mining Research Directory.

Cao, R., Earp, S., De Ridder, S. A. L., Curtis, A., & Galetti, E. (2020). Near-real-time near-surface 3D seismic velocity and uncertainty models by wavefield gradiometry and neural network inversion of ambient seismic noise. *Geophysics*, *85*(1), KS13–KS27. https://doi.org/10.1190/geo2018-0562.1

Chen, T., & Guestrin, C. (2016). The 22nd ACM sigkdd international conference on knowledge discovery and data mining. *A Scalable Tree Boosting System*, 785–794.

Deere, D. U., & Deere, D. W. (1988). *Deere_1988_The_Rock_Quality_Designation.pdf* (pp. 91–101).

Deere, D. U., & Miller, R. P. (1966). *Engineering Classification and Index Properties for Intact Rock*. University of Illinois Urbana-Champaign.

Di Benedetti, M., Loreto, G., Matta, F., & Nanni, A. (2014). Acoustic Emission Historic Index and Frequency Spectrum of Reinforced Concrete under Accelerated Corrosion. *Journal of Materials in Civil Engineering*, *26*(9). https://doi.org/10.1061/(asce)mt.1943-5533.0000954

Dong, L., & Li, X. (2013). A microseismic/acoustic emission source location method using arrival times of PS waves for unknown velocity system. *International Journal of Distributed Sensor Networks*, *2013*. https://doi.org/10.1155/2013/307489

Dong, L., Sun, D., Li, X., & Du, K. (2017). Theoretical and Experimental Studies of Localization Methodology for AE and Microseismic Sources Without Pre-Measured Wave Velocity in Mines. *IEEE Access*, *5*, 16818–16828. https://doi.org/10.1109/ACCESS.2017.2743115

Fall, M., Célestin, J. C., Pokharel, M., & Touré, M. (2010). A contribution to understanding the effects of curing temperature on the mechanical properties of mine cemented tailings backfill. *Engineering Geology*, *114*(3–4), 397–413. https://doi.org/10.1016/j.enggeo.2010.05.016

Feng, X. T., Yu, Y., Feng, G. L., Xiao, Y. X., Chen, B. rui, & Jiang, Q. (2016). Fractal behaviour of the microseismic energy associated with immediate rockbursts in deep, hard rock tunnels. *Tunnelling and Underground Space Technology*, *51*, 98–107. https://doi.org/10.1016/j.tust.2015.10.002

Feng, X., Xiao, Y., Feng, G., Yao, Z., Chen, B., Yang, C., & Su, G. (2019). Study on the development process of rockbursts. *Yanshilixue Yu Gongcheng Xuebao/Chinese Journal of Rock Mechanics and Engineering*, *38*(4), 649–673. https://doi.org/10.13722/j.cnki.jrme.2019.0103

Gao, F., Kaiser, P. K., Stead, D., Eberhardt, E., & Elmo, D. (2019). Numerical simulation of strainbursts using a novel initiation method. *Computers and Geotechnics*, *106*(July 2018), 117–127. https://doi.org/10.1016/j.compgeo.2018.10.018

Grenon, M., & Hadjigeorgiou, J. (2003). Evaluating discontinuity network characterization tools through mining case studies. *Soil Rock America*, *1*, 137–142.

Grosse, C. U., Ohtsu Masayasu, Aggelis, D. G., & Shiotani, T. (2022). *Acoustic Emission Testing Basics for Research – Applications in Engineering* (second). Springer. http://www.springer.com/series/15088

Hauquin, T., Gunzburger, Y., & Deck, O. (2018). Predicting pillar burst by an explicit modelling of kinetic energy. International Journal of Rock Mechanics and Mining Sciences, 107(November 2017), 159–171. https://doi.org/10.1016/j.ijrmms.2018.05.004

Hedley, D. (1992). *Rockburst handbook for Ontario hardrock mines* (volume 92,). Canmet.

Aster, R., Borchers, B., & Thurber, C. (2018). *Parameter Estimation and Inverse Problems* (3rd ed.). Elsevier.

Barton, N., Grimstad, E. (1993). Updating the Q-system for NMT. *International Symposium on Sprayed Concrete, January 1993*, 46–66.

Blake, W., & Leighton, F. (1970). Recent developments and applications of the microseismic method in deep mines. *Proc. 11th Symposium on Rock Mechanics*, 429–433.

Hauquin, T., Gunzburger, Y., & Deck, O. (2018). Predicting pillar burst by an explicit modelling of kinetic energy. *International Journal of Rock Mechanics and Mining Sciences*, *107*(November 2017), 159–171. https://doi.org/10.1016/j.ijrmms.2018.05.004

He, M. C., Miao, J. L., & Feng, J. L. (2010). Rock burst process of limestone and its acoustic emission characteristics under true-triaxial unloading conditions. *International Journal of Rock Mechanics and Mining Sciences*, *47*(2), 286–298. https://doi.org/10.1016/j.ijrmms.2009.09.003

KSGidro. (2022). *No Title*. https://ksgidro.ru/katalog/materialyi/smesi-dlya-razrusheniya-betona/nevzryivchataya-smes-nrs-1.html

Mohsin, A., Alsmadi, Y., Arshad Uppal, A., & Gulfam, S. M. (2021). A modified simplex based direct search optimization algorithm for adaptive transversal FIR filters. *Science Progress*, *104*(2), 1–19. https://doi.org/10.1177/00368504211025409

Nelder, J. A., & Mead, R. (1965). A Simplex Method for Function Minimization. *The Computer Journal*, *7*(4), 308–313. https://doi.org/10.1093/comjnl/7.4.308

Shirani Faradonbeh, R., Taheri, A., Ribeiro e Sousa, L., & Karakus, M. (2020). Rockburst assessment in deep geotechnical conditions using true-triaxial tests and data-driven approaches. *International Journal of Rock Mechanics and Mining Sciences*, *128*(February), 104279. https://doi.org/10.1016/j.ijrmms.2020.104279

Song, Y., Zhao, Y., Zhang, Y., Deng, W., & Lu, C. (2023). Research on microseismic localization algorithm with global search and local optimization. *Heliyon*, *9*(9), e19251. https://doi.org/10.1016/j.heliyon.2023.e19251

Spall, J. C. (2003). *Introduction to Stochastic Search and Optimization: Estimation, Simulation, and Control*. https://doi.org/10.1002/0471722138

Xu, S., Hou, P., Li, R., & Suorineni, F. T. (2022). An improved outer pipe method for expansive pressure measurement of static cracking agents. *International Journal of Mining Science and Technology*, *32*(1), 27–39. https://doi.org/10.1016/j.ijmst.2021.11.011

Zhang, H., & Guo, W. (2022). Acoustic Emission Waveform Characteristics of Red Sandstone Failure under Uniaxial Compression after Thermal Damage. *Sustainability (Switzerland)*, *14*(20). https://doi.org/10.3390/su142013285

Huo, X., Wu, Q., Tang, H., Meng, Z., Wang, D., Liu, Y., & Li, S. (2020). A new approach for estimating rock discontinuity trace intensity based on rectangular sampling windows. *Advances in Civil Engineering*, *2020*. https://doi.org/10.1155/2020/8834861

ITASCA. (2022a). *Itasca's FLAC3D Documentation*.

ITASCA. (2022b). *Itasca's FLAC3D Documentation*.

Jiang, Q., Feng, X. T., Xiang, T. B., & Su, G. S. (2010). Rockburst characteristics and numerical simulation based on a new energy index: A case study of a tunnel at 2,500 m depth. *Bulletin of Engineering Geology and the Environment*, *69*(3), 381–388. https://doi.org/10.1007/s10064-010-0275-1

Jin, Z., Shang, J., Zhu, Q., Ling, C., Xie, W., & Qiang, B. (2020). RFRSF: Employee Turnover Prediction Based on Random Forests and Survival Analysis. *Lecture Notes in Computer Science (Including Subseries Lecture Notes in Artificial Intelligence and Lecture Notes in Bioinformatics)*, *12343 LNCS*, 503–515. https://doi.org/10.1007/978-3-030-62008-0_35

Jing, L. (2003). A review of techniques, advances and outstanding issues in numerical modelling for rock mechanics and rock engineering. *International Journal of Rock Mechanics and Mining Sciences*, *40*(3), 283–353. https://doi.org/10.1016/S1365-1609(03)00013-3

Jing, L., & Hudson, J. A. (2002). Numerical methods in rock mechanics. *International Journal of Rock Mechanics and Mining Sciences*, *39*(4), 409–427. https://doi.org/10.1016/S1365-1609(02)00065-5

Jooshaki, M., Nad, A., & Michaux, S. (2021). A systematic review on the application of machine learning in exploiting mineralogical data in mining and mineral industry. *Minerals*, *11*(8), 816. https://doi.org/10.3390/min11080816

Kaiser, P. K., & Cai, M. (2012). Design of rock support system under rockburst condition. *Journal of Rock Mechanics and Geotechnical Engineering*, *4*(3), 215–227. https://doi.org/10.3724/sp.j.1235.2012.00215

Kaiser, P. K., McCreath, D. R., & Tannant, D. D. (1996). *Canadian Rockburst Support Handbook*. *January*, 314.

Kennett, B. L. N., Marson-Pidgeon, K., & SAmbridge, M. S. (2000). *GEOPHYSICAL RESEARCH LETTERS*.

KSGidro. (2022). No Title. https://ksgidro.ru/katalog/materialyi/smesi-dlya-razrusheniya-betona/nevzryivchataya-smes-nrs-1.html

Kuhlemeyer, R. L., & Lysmer, J. (1973). Finite Element Method Accuracy for Wave Propagation Problems. *Journal of the Soil Dynamics Division*, *99*, 421–427.

Kulatilake, P. H. S. W., & Wu, T. H. (1984). Sampling bias on orientation of discontinuities. *Rock Mechanics and Rock Engineering*, *17*, 243–253. https://doi.org/https://doi.org/10.1007/BF01032337

Lemy, F., & Hadjigeorgiou, J. (2004). A digital face mapping case study in an underground hard rock mine. *Canadian Geotechnical Journal*, *41*(6), 1011–1025. https://doi.org/10.1139/t04-046

Li, Z., He, S., Song, D., He, X., Dou, L., Chen, J., Liu, X., & Feng, P. (2021). Microseismic temporal-spatial precursory characteristics and early warning method of rockburst in steeply inclined and extremely thick coal seam. *Energies*, *14*(4). https://doi.org/10.3390/en14041186

Liang, Z., Xue, R., Xu, N., & Li, W. (2020). Characterizing rockbursts and analysis on frequency-spectrum evolutionary law of rockburst precursor based on microseismic monitoring. *Tunnelling and Underground Space Technology*, *105*(November 2019), 103564. https://doi.org/10.1016/j.tust.2020.103564

Ma, Y., Cao, S., Rector, J. W., & Zhang, Z. (2019). Automatic first arrival picking for borehole seismic data using a pixel-level network. *SEG Technical Program Expanded Abstracts*, 2463–2467. https://doi.org/10.1190/segam2019-3216775.1

Maksut, Z., Meiramov, R., Yazici, A., & Suorineni, F. (2022). A Machine Learning-based Microseismic Event Location and Wave Velocity Prediction. *56th U.S. Rock Mechanics/Geomechanics Symposium*. https://doi.org/10.56952/arma-2022-0166

Malek, F., Espley, S., Yao, M., Trifu, C., & Suorineni, F. (2008). Management of High Stress and Seismicity at Vale Inco Creighton Mine. *The 42nd U.S. Rock Mechanics Symposium (USRMS), 29 June-2 July*, *January*, 8.

Manouchehrian, A., & Cai, M. (2017). Analysis of rockburst in tunnels subjected to static and dynamic loads. *Journal of Rock Mechanics and Geotechnical Engineering*, *9*(6), 1031–1040. https://doi.org/10.1016/j.jrmge.2017.07.001

Manouchehrian, A., & Cai, M. (2018). Numerical modeling of rockburst near fault zones in deep tunnels. *Tunnelling and Underground Space Technology*, *80*(June), 164–180. https://doi.org/10.1016/j.tust.2018.06.015

Medinac, F. (2019). *Advances in Pit Wall Mapping and Slope Assessment using Unmanned Aerial Vehicle Technology*. University of Toronto.

Milne, D., Hadjigeorgiou, J., & Pakalnis, R. (1998). Rock mass characterization for underground hard rock mines. *Tunnelling and Underground Space Technology*, *13*(4), 383–391. https://doi.org/10.1016/S0886-7798(98)00081-9

Mohsin, A., Alsmadi, Y., Arshad Uppal, A., & Gulfam, S. M. (2021). A modified simplex based direct search optimization algorithm for adaptive transversal FIR filters. Science Progress, 104(2), 1–19. https://doi.org/10.1177/00368504211025409

Mondal, D., & Roy, P. N. S. (2019). Fractal and seismic b-value study during dynamic roof displacements (roof fall and surface blasting) for enhancing safety in the longwall coal mines. *Engineering Geology*, *253*(March), 184–204. https://doi.org/10.1016/j.enggeo.2019.03.018

Morkel, I., Wesseloo, J., & Potvin, Y. (2022). *Seismic event location uncertainty in mining with reference to caving*. *2015*, 445–460. https://doi.org/10.36487/acg_repo/2205_30

Munfakh, G., Wylie, D., & CW, M. (1998). *Training Course in Geotechnical* (Issue 13235).

Natekin, A., & Knoll, A. (2013). Gradient boosting machines, a tutorial. *Frontiers in Neurorobotics*, *7*(DEC). https://doi.org/10.3389/fnbot.2013.00021

Nelder, J. A., & Mead, R. (1965). A Simplex Method for Function Minimization. The Computer Journal, 7(4), 308–313. https://doi.org/10.1093/comjnl/7.4.308

Niitsoo, A., Edelhäußer, T., & Mutschler, C. (2018). Convolutional Neural Networks for Position Estimation in TDoA-Based Locating Systems. *IPIN 2018 - 9th International Conference on Indoor Positioning and Indoor Navigation*, *September*, 24–27. https://doi.org/10.1109/IPIN.2018.8533766

Palei, S. K., & Das, S. K. (2009). Logistic regression model for prediction of roof fall risks in bord and pillar workings in coal mines: An approach. *Safety Science*, *47*(1), 88–96. https://doi.org/10.1016/j.ssci.2008.01.002

Palmstrom, A. (1982). The Volumetric Joint Count—A Useful and Simple Measure of the Degree of Rock Jointing. *Proceedings of 4th International Association of Engineering Geology*, 221–228.

Palmstrom, A. (2005). Measurements of and correlations between block size and rock quality designation (RQD). *Tunnelling and Underground Space Technology*, *20*(4), 362–377. https://doi.org/10.1016/j.tust.2005.01.005

Peng, P., Jiang, Y., Wang, L., He, Z., & Tu, S. (2020). A fast ray-tracing method for locating mining-induced seismicity by considering underground voids. *Applied Sciences (Switzerland)*, *10*(19), 1–15. https://doi.org/10.3390/app10196763

Pham, N., Merzlikin, D., Fomel, S., & Chen, Y. (2020). SEG Technical Program Expanded Abstracts. *Passive Seismic Signal Denoising Using Convolutional Neural Network Convolutional Neural Network*.

Qian, Q. H. (2014). Definition, mechanism, classification and quantitative forecast model for rockburst and pressure bump. *Yantu Lixue/Rock and Soil Mechanics*, *35*(1), 1–6.

Qin, Z., Li, T., Li, Q., Chen, G., & Cao, B. (2019). Combined Early Warning Method for Rock Burst and Its Engineering Application. *Advances in Civil Engineering*, *2019*. https://doi.org/10.1155/2019/1269537

Ranjith, P. G., Zhao, J., Ju, M., De Silva, R. V. S., Rathnaweera, T. D., & Bandara, A. K. M. S. (2017). Opportunities and Challenges in Deep Mining: A Brief Review. *Engineering*, *3*(4), 546–551. https://doi.org/10.1016/J.ENG.2017.04.024

Salamon, A., & Kazár, G. (1993). Epidemiology of hand injuries in Vas County based on a survey. *Magyar Traumatológia, Ortopédia, Kézsebészet, Plasztikai Sebészet*, *36*(3), 297–300.

Shi, X., Jing, H., Yin, Q., Zhao, Z., Han, G., & Gao, Y. (2020). Investigation on physical and mechanical properties of bedded sandstone after high-temperature exposure. *Bulletin of Engineering Geology and the Environment*, *79*(5), 2591–2606. https://doi.org/10.1007/s10064-020-01729-7

Shirani Faradonbeh, R., Taheri, A., Ribeiro e Sousa, L., & Karakus, M. (2020). Rockburst assessment in deep geotechnical conditions using true-triaxial tests and data-driven approaches. *International Journal of Rock Mechanics and Mining Sciences*, 128(February), 104279. https://doi.org/10.1016/j.ijrmms.2020.104279

Sirois, F., & Grilli, F. (2015). Potential and limits of numerical modelling for supporting the development of HTS devices. *Superconductor Science and Technology*, *28*(4), 43002. https://doi.org/10.1088/0953-2048/28/4/043002

Spall, J. C. (2003). Introduction to Stochastic Search and Optimization: Estimation, Simulation, and Control. https://doi.org/10.1002/0471722138

Song, Y., Zhao, Y., Zhang, Y., Deng, W., & Lu, C. (2023). Research on microseismic localization algorithm with global search and local optimization. Heliyon, 9(9), e19251. https://doi.org/10.1016/j.heliyon.2023.e19251

Trifu, C. I., & Shumila, V. (2010). Geometrical and inhomogeneous raypath effects on the characterization of open-pit seismicity. *44th US Rock Mechanics Symposium - 5th US/Canada Rock Mechanics Symposium*.

Trifu, C. I., & Suorineni, F. T. (2009). Use of Microseismic Monitoring for Rockburst Management At Vale Inco Mines. *Controlling Seismic Hazard And Sustainable Development Of Deep Mines: 7th International Symposium on Rockburst And Seismicity In Mines*, *January 2009*, 1105–1114.

Umili, G., Ferrero, A., & Einstein, H. H. (2013). A new method for automatic discontinuity traces sampling on rock mass 3D model. *Computers and Geosciences*, *51*, 182–192. https://doi.org/10.1016/j.cageo.2012.07.026

Wang, G., Gong, S., Dou, L., Wang, H., Cai, W., & Cao, A. (2018). Rockburst characteristics in syncline regions and microseismic precursors based on energy density clouds. *Tunnelling and Underground Space Technology*, *81*(April), 83–93. https://doi.org/10.1016/j.tust.2018.06.026

Wang, J., Apel, D. B., Pu, Y., Hall, R., Wei, C., & Sepehri, M. (2021). Numerical modeling for rockbursts: A state-of-the-art review. *Journal of Rock Mechanics and Geotechnical Engineering*, *13*(2), 457–478. https://doi.org/10.1016/j.jrmge.2020.09.011

Wu, Q., Kulatilake, P. H. S. W., & Tang, H. ming. (2011). Comparison of rock discontinuity mean trace length and density estimation methods using discontinuity data from an outcrop in Wenchuan area, China. *Computers and Geotechnics*, *38*(2), 258–268. https://doi.org/10.1016/j.compgeo.2010.12.003

Wylie, D. C. (1999). *Foundations on Rock: Engineering Practice* (second). E&FN Spon.

Xie, H., Gao, F., & Ju, Y. (2015). Research and development of rock mechanics in deep ground engineering. *Yanshilixue Yu Gongcheng Xuebao/Chinese Journal of Rock Mechanics and Engineering*, *34*(11), 2161–2178. https://doi.org/10.13722/j.cnki.jrme.2015.1369

Xu, S., Liang, R., Suorineni, F. T., & Li, Y. (2021). Evaluation of the use of sublevel open stoping in the mining of moderately dipping medium-thick orebodies. *International Journal of Mining Science and Technology*, *31*(2), 333–346. https://doi.org/10.1016/j.ijmst.2020.12.002

Xu, S., Hou, P., Li, R., & Suorineni, F. T. (2022). An improved outer pipe method for expansive pressure measurement of static cracking agents. International Journal of Mining Science and Technology, 32(1), 27–39. https://doi.org/10.1016/j.ijmst.2021.11.011

Xue, R., Liang, Z., Xu, N., & Dong, L. (2020). Rockburst prediction and stability analysis of the access tunnel in the main powerhouse of a hydropower station based on microseismic monitoring. *International Journal of Rock Mechanics and Mining Sciences*, *126*(March 2019), 104174. https://doi.org/10.1016/j.ijrmms.2019.104174

Xue, Y., Song, D., Chen, J., Li, Z., He, X., Wang, H., Zhou, C., & Sobolev, A. (2023). Integrated rockburst hazard estimation methodology based on spatially smoothed seismicity model and Mann-Kendall trend test. *International Journal of Rock Mechanics and Mining Sciences*, *163*(May 2022), 105329. https://doi.org/10.1016/j.ijrmms.2023.105329

Yu, Q., Zhao, D., Xia, Y., Jin, S., Zheng, J., Meng, Q., Mu, C., & Zhao, J. (2022). Multivariate Early Warning Method for Rockburst Monitoring Based on Microseismic Activity

Characteristics. *Frontiers in Earth Science*, *10*(January), 1–15. https://doi.org/10.3389/feart.2022.837333

Yuyama, S., Yokoyama, K., Niitani, K., Ohtsu, M., & Uomoto, T. (2007). Detection and evaluation of failures in high-strength tendon of prestressed concrete bridges by acoustic emission. *Construction and Building Materials*, *21*(3), 491–500. https://doi.org/10.1016/j.conbuildmat.2006.04.010

Zhang, C., Feng, X. T., Zhou, H., Qiu, S., & Wu, W. (2012). Case histories of four extremely intense rockbursts in deep tunnels. *Rock Mechanics and Rock Engineering*, *45*(3), 275–288. https://doi.org/10.1007/s00603-011-0218-6

Zhang, C., Jin, G., Liu, C., Li, S., Xue, J., Cheng, R., Wang, X., & Zeng, X. (2021). Prediction of rockbursts in a typical island working face of a coal mine through microseismic monitoring technology. *Tunnelling and Underground Space Technology*, *113*(February), 103972. https://doi.org/10.1016/j.tust.2021.103972

Zhang, L., & Einstein, H. H. (2000). Estimating the intensity of rock discontinuities. *International Journal of Rock Mechanics and Mining Sciences*, *37*(5), 819–837. https://doi.org/10.1016/s1365-1609(00)00022-8

Zhang, H., & Guo, W. (2022). Acoustic Emission Waveform Characteristics of Red Sandstone Failure under Uniaxial Compression after Thermal Damage. *Sustainability (Switzerland)*, *14*(20). https://doi.org/10.3390/su142013285

Zhou, J., Li, X., & Mitri, H. S. (2018). Evaluation method of rockburst: State-of-the-art literature review. *Tunnelling and Underground Space Technology*, *81*(October 2017), 632–659. https://doi.org/10.1016/j.tust.2018.08.029

Zhu, W., & Beroza, G. C. (2019). PhaseNet: A deep-neural-network-based seismic arrival-time picking method. *Geophysical Journal International*, *216*(1), 261–273. https://doi.org/10.1093/gji/ggy423

Zhu, W., Mousavi, S. M., & Beroza, G. C. (2019). Seismic Signal Denoising and Decomposition Using Deep Neural Networks. *IEEE Transactions on Geoscience and Remote Sensing*, *57*(11), 9476–9488. https://doi.org/10.1109/TGRS.2019.2926772

APPENDIX 1

				Block description		
Sample	Block Size, mm	RMR	Hole	Hole diameter (mm)	Quality data	
						Cement content (%)
concrete	150.00	100.00	no	50.00	no hole block size: 150mm cube	No hole
concrete	150.00	100.00	yes	50.00	hole diameter: 50mm backfill type: no backfill block size: 150mm cube	No backfill in hole
concrete	150.00	100.00	yes	50.00	hole diameter: 50mm backfill type: dry sand block size: 150mm cube	dry sand
concrete	150.00	100.00	yes	50.00	hole diameter: 50mm backfill type: water saturated sand block size: 150mm cube	water saturated sand

concrete	150.00	100.00	yes	50.00	hole diameter: 50mm backfill type: 10% cement block size: 150mm cube	5 %
concrete	150.00	100.00	yes	50.00	hole diameter: 50mm backfill type: 10% cement block size: 150mm cube	10 %
concrete	150.00	100.00	yes	50.00	hole diameter: 50mm backfill type: 15% cement block size: 150mm cube	15 %

concrete	150.00	100.00	yes	50.00	hole diameter: 50mm backfill type: 20% cement block size: 150mm cube	20 %
concrete	225.00	100.00	no	75.00	no hole block size: 225 mm cube	No hole
concrete	225.00		yes	75.00	hole diameter: 75 mm backfill type: no backfill block size: 225 mm cube	No backfill in hole
concrete	225.00		yes	75.00	hole diameter: 75 mm backfill type: dry sand block size: 225 mm cube	dry sand

concrete	225.00	100.00	yes	75.00	hole diameter: 75 mm backfill type: water saturated sand block size: 225 mm cube	water saturated sand
concrete	225.00	100.00	yes	75.00	hole diameter: 75 mm backfill type: 10% cement block size: 225 mm cube	5 %

concrete	225.00	100.00	yes	75.00	hole diameter: 75 mm backfill type: 10% cement block size: 225 mm cube	10 %
concrete	225.00	100.00	yes	75.00	hole diameter: 75 mm backfill type: 15% cement block size: 225 mm cube	15 %
concrete	225.00	100.00	yes	75.00	hole diameter: 75 mm backfill type: 20% cement block size: 225 mm cube	20 %

granite	300.00	100.00	no	100.00	no hole block size: 300mm cube	No hole
granite	300.00	100.00	yes	100.00	hole diameter: 100mm backfill type: no backfill block size: 300mm cube	No backfill in hole
granite	300.00	100.00	yes	100.00	hole diameter: 100mm backfill type: dry sand block size: 300mm cube	dry sand
concrete	300.00	100.00	yes	100.00	hole diameter: 100mm backfill type: water saturated sand block size: 300mm cube	**Water Saturated Sand**
		100.00	yes	100.00	hole diameter: 100mm backfill type: water saturated sand block size: 300mm cube	
		100.00	yes	100.00	hole diameter: 100mm backfill type: water saturated sand block size: 300mm cube	
		100.00	yes	100.00	hole diameter: 100mm backfill type: water saturated sand block size: 300mm cube	
		100.00	yes	100.00	hole diameter: 100mm backfill type: water saturated sand block size: 300mm cube	
		100.00	yes	100.00	hole diameter: 100mm backfill type: water saturated sand	

concrete	300.00				saturated sand block size: 300mm cube	5 %
		100.00	yes	100.00	hole diameter: 100mm backfill type: water saturated sand block size: 300mm cube	
		100.00	yes	100.00	hole diameter: 100mm backfill type: water saturated sand block size: 300mm cube	
		100.00	yes	100.00	hole diameter: 100mm backfill type: water saturated sand block size: 300mm cube	
		100.00	yes	100.00	hole diameter: 100mm backfill type: water saturated sand block size: 300mm cube	
concrete	300.00	100.00	yes	100.00	hole diameter: 100mm backfill type: water saturated sand block size: 300mm cube	10 %
		100.00	yes	100.00	hole diameter: 100mm backfill type: water saturated sand block size: 300mm cube	
		100.00	yes	100.00	hole diameter: 100mm backfill type: water saturated sand block size: 300mm cube	
		100.00	yes	100.00	hole diameter: 100mm backfill type: water saturated sand block size: 300mm cube	
		100.00	yes	100.00	hole diameter: 100mm backfill type: water saturated sand block size: 300mm cube	
		100.00	yes	100.00	hole diameter: 100mm backfill type: water saturated sand block size: 300mm cube	
					hole diameter: 100mm backfill type: water	

concrete	300.00	100.00	yes	100.00	type: water saturated sand block size: 300mm cube	**15 %**
		100.00	yes	100.00	hole diameter: 100mm backfill type: water saturated sand block size: 300mm cube	
		100.00	yes	100.00	hole diameter: 100mm backfill type: water saturated sand block size: 300mm cube	
		100.00	yes	100.00	hole diameter: 100mm backfill type: water saturated sand block size: 300mm cube	
concrete	300.00	100.00	yes	100.00	hole diameter: 100mm backfill type: water saturated sand block size: 300mm cube	**20 %**
		100.00	yes	100.00	hole diameter: 100mm backfill type: water saturated sand block size: 300mm cube	
		100.00	yes	100.00	hole diameter: 100mm backfill type: water saturated sand block size: 300mm cube	
		100.00	yes	100.00	hole diameter: 100mm backfill type: water saturated sand block size: 300mm cube	
		100.00	yes	100.00	hole diameter: 100mm backfill type: water saturated sand block size: 300mm cube	
Concrete	375.00	100.00	no	125.00	no hole block size: 300mm cube	No hole
Concrete	375.00	100.00	yes	125.00	hole diameter: 100mm backfill type: no backfill block size: 300mm cube	No backfill in hole

Concrete	375.00	100.00	yes	125.00	no hole block size: 300mm cube	dry sand
Concrete	375.00	100.00	yes	125.00	hole diameter: 100mm backfill type: no backfill block size: 300mm cube	**wet sand**
		100.00	no	125.00	no hole block size: 300mm cube	
		100.00	yes	125.00	hole diameter: 100mm backfill type: no backfill block size: 300mm cube	
		100.00	yes	125.00	no hole block size: 300mm cube	
		100.00	yes	125.00	hole diameter: 100mm backfill type: no backfill block size: 300mm cube	
Concrete	375.00	100.00	yes	125.00	no hole block size: 300mm cube	**5 %**
		100.00	yes	125.00	hole diameter: 100mm backfill type: no backfill block size: 300mm cube	
		100.00	yes	125.00	no hole block size: 300mm cube	
		100.00	yes	125.00	hole diameter: 100mm backfill type: no backfill block size: 300mm cube	
		100.00	yes	125.00	hole diameter: 100mm backfill type: no backfill block size: 300mm cube	

		100.00	yes	125.00	no hole block size: 300mm cube	
		100.00	yes	125.00	hole diameter: 100mm backfill type: no backfill block size: 300mm cube	
Concrete	375.00	100.00	yes	125.00	no hole block size: 300mm cube	**10 %**
		100.00	yes	125.00	hole diameter: 100mm backfill type: no backfill block size: 300mm cube	
		100.00	yes	125.00	hole diameter: 100mm backfill type: no backfill block size: 300mm cube	
		100.00	yes	125.00	no hole block size: 300mm cube	
		100.00	yes	125.00	hole diameter: 100mm backfill type: no backfill block size: 300mm cube	
Concrete	375.00	100.00	yes	125.00	no hole block size: 300mm cube	**15 %**
		100.00	yes	125.00	hole diameter: 100mm backfill type: no backfill block size: 300mm cube	
		100.00	yes	125.00	hole diameter: 100mm backfill type: no backfill block size: 300mm cube	
			yes	125.00	hole diameter: 125mm backfill type: 20% cement block size: 375mm cube	
					hole diameter:	

			yes	125.00	125mm backfill type: 20% cement block size: 375mm cube	
Concrete	375.00	100.00	yes	125.00	hole diameter: 125mm backfill type: 20% cement block size: 375mm cube	**20 %**
			yes	125.00	hole diameter: 125mm backfill type: 20% cement block size: 375mm cube	
			yes	125.00	hole diameter: 125mm backfill type: 20% cement block size: 375mm cube	
Concrete	450.00	100.00	no	150.00	no hole block size: 450mm cube	No hole
Concrete	450.00	100.00	yes	150.00	hole diameter: 150 mm backfill type: no backfill block size: 450mm cube	No backfill in hole
Concrete	450.00	100.00	yes	150.00	hole diameter: 150 mm backfill type: dry sand block size: 450 mm cube	Dry sand
		100.00	yes	150.00	hole diameter: 150 mm backfill type: wet sand cement block size: 450 mm cube	
		100.00	yes	150.00	hole diameter: 150 mm backfill type: wet sand cement block size: 450 mm cube	
Concrete	450.00	100.00	yes	150.00	hole diameter: 150 mm backfill type: wet sand cement block size: 450 mm cube	**Wet Sand**
		100.00	yes	150.00	hole diameter: 150 mm backfill type: wet sand cement block size: 450 mm cube	
					hole diameter: 150	

		100.00	yes	150.00	mm backfill type: wet sand cement block size: 450 mm cube	
		100.00	yes	150.00	hole diameter: 150 mm backfill type: 5% cement block size: 450 mm cube	
		100.00	yes	150.00	hole diameter: 150 mm backfill type: 5% cement block size: 450 mm cube	
Concrete	450.00	100.00	yes	150.00	hole diameter: 150 mm backfill type: 5% cement block size: 450 mm cube	**5 %**
		100.00	yes	150.00	hole diameter: 150 mm backfill type: 5% cement block size: 450 mm cube	
		100.00	yes	150.00	hole diameter: 150 mm backfill type: 5% cement block size: 450 mm cube	
		100.00	yes	150.00	hole diameter: 150 mm backfill type: 10% cement block size: 450 mm cube	
		100.00	yes	150.00	hole diameter: 150 mm backfill type: 10% cement block size: 450 mm cube	
Concrete	450.00	100.00	yes	150.00	hole diameter: 150 mm backfill type: 10% cement block size: 450 mm cube	**10 %**
		100.00	yes	150.00	hole diameter: 150 mm backfill type: 10% cement block size: 450 mm cube	
		100.00	yes	150.00	hole diameter: 150 mm backfill type: 10% cement block size: 450 mm cube	
					hole diameter: 150	

		100.00	yes	150.00	hole diameter: 150 mm backfill type: 15% cement block size: 450 mm cube	
		100.00	yes	150.00	hole diameter: 150 mm backfill type: 15% cement block size: 450 mm cube	
Concrete	450.00	100.00	yes	150.00	hole diameter: 150 mm backfill type: 15% cement block size: 450 mm cube	**15 %**
		100.00	yes	150.00	hole diameter: 150 mm backfill type: 15% cement block size: 450 mm cube	
		100.00	yes	150.00	hole diameter: 150 mm backfill type: 15% cement block size: 450 mm cube	
		100.00	yes	150.00	hole diameter: 150 mm backfill type: 20% cement block size: 450 mm cube	
		100.00	yes	150.00	hole diameter: 150 mm backfill type: 20% cement block size: 450 mm cube	
Concrete	450.00	100.00	yes	150.00	hole diameter: 150 mm backfill type: 20% cement block size: 450 mm cube	**20 %**
		100.00	yes	150.00	hole diameter: 150 mm backfill type: 20% cement block size: 450 mm cube	
		100.00	yes	150.00	hole diameter: 150 mm backfill type: 20% cement block size: 450 mm cube	

granite	300.00	100.00	yes	100.00	hole diameter: 100mm backfill type: water saturated sand block size: 300mm cube	water saturated sand
granite	300.00	100.00	yes	100.00	hole diameter: 100mm backfill type: 5% cement block size: 300mm cube	5 %
					hole diameter:	

granite	300.00	100.00	yes	100.00	100mm backfill type: 10% cement block size: 300mm cube	10 %
granite	300.00	100.00	yes	100.00	hole diameter: 100mm backfill type: 15% cement block size: 300mm cube	15 %
granite	300.00	100.00	yes	100.00	hole diameter: 100mm backfill type: 20% cement block size: 300mm cube	20 %

concrete	300.00	100.00	no	100.00	no hole block size: 300mm cube	No hole
concrete	300.00	100.00	yes	100.00	hole diameter: 100mm backfill type: no backfill block size: 300mm cube	No backfill in hole
concrete	300.00	100.00	yes	100.00	hole diameter: 100mm backfill type: dry sand block size: 300mm cube	dry sand

			Source (Chanel 1)			
			(sensor 1)			
Backfill Quality		Test #	location			Arrival time, millisecond
curing time	Backfill strength, MPa		x0	y0	zo	t1
n/a		1.00	75.00	0.00	75.00	227.30
		2.00	75.00	0.00	75.00	227.30
		3.00	75.00	0.00	75.00	227.20
		4.00	75.00	0.00	75.00	227.10
		5.00	75.00	0.00	75.00	227.00
n/a		1.00	75.00	0.00	75.00	975.60
		2.00	75.00	0.00	75.00	975.60
		3.00	75.00	0.00	75.00	975.50
		4.00	75.00	0.00	75.00	975.40
		5.00	75.00	0.00	75.00	975.30
n/a	n/a	1.00	75.00	0.00	75.00	336.10
		2.00	75.00	0.00	75.00	336.00
		3.00	75.00	0.00	75.00	335.90
		4.00	75.00	0.00	75.00	335.80
		5.00	75.00	0.00	75.00	335.70
8 hours	n/a	1.00	75.00	0.00	75.00	292.10
		2.00	75.00	0.00	75.00	292.00
		3.00	75.00	0.00	75.00	291.90
		4.00	75.00	0.00	75.00	291.80
		5.00	75.00	0.00	75.00	291.70
1 day	n/a	1.00	75.00	0.00	75.00	272.60
		2.00	75.00	0.00	75.00	272.50
		3.00	75.00	0.00	75.00	272.40
		4.00	75.00	0.00	75.00	272.30
		5.00	75.00	0.00	75.00	272.20
7 days	n/a	1.00	75.00	0.00	75.00	759.50
		2.00	75.00	0.00	75.00	759.50
		3.00	75.00	0.00	75.00	759.40
		4.00	75.00	0.00	75.00	759.30
		5.00	75.00	0.00	75.00	759.20
14 days	n/a	1.00	75.00	0.00	75.00	241.70
		2.00	75.00	0.00	75.00	241.60
		3.00	75.00	0.00	75.00	241.50
		4.00	75.00	0.00	75.00	241.40
		5.00	75.00	0.00	75.00	241.30
28 days	n/a	1.00	75.00	0.00	75.00	676.60
		2.00	75.00	0.00	75.00	676.50
		3.00	75.00	0.00	75.00	676.40
		4.00	75.00	0.00	75.00	676.30
		5.00	75.00	0.00	75.00	676.20
8 hours	n/a	1.00	75.00	0.00	75.00	346.90
		2.00	75.00	0.00	75.00	346.80
		3.00	75.00	0.00	75.00	346.70
		4.00	75.00	0.00	75.00	346.60
		5.00	75.00	0.00	75.00	346.50
1 day	0.25	1.00	75.00	0.00	75.00	336.00
		2.00	75.00	0.00	75.00	335.90
		3.00	75.00	0.00	75.00	335.80
		4.00	75.00	0.00	75.00	335.70

		5.00	75.00	0.00	75.00	335.70
7 days	0.35	1.00	75.00	0.00	75.00	449.80
		2.00	75.00	0.00	75.00	449.70
		3.00	75.00	0.00	75.00	449.60
		4.00	75.00	0.00	75.00	449.50
		5.00	75.00	0.00	75.00	449.50
14 days	0.57	1.00	75.00	0.00	75.00	418.80
		2.00	75.00	0.00	75.00	418.80
		3.00	75.00	0.00	75.00	418.70
		4.00	75.00	0.00	75.00	418.60
		5.00	75.00	0.00	75.00	418.50
28 days	0.65	1.00	75.00	0.00	75.00	440.60
		2.00	75.00	0.00	75.00	440.50
		3.00	75.00	0.00	75.00	440.40
		4.00	75.00	0.00	75.00	440.30
		5.00	75.00	0.00	75.00	440.30
8 hours		1.00	75.00	0.00	75.00	543.40
		2.00	75.00	0.00	75.00	543.40
		3.00	75.00	0.00	75.00	543.30
		4.00	75.00	0.00	75.00	543.20
		5.00	75.00	0.00	75.00	543.10
1 day	0.51	1.00	75.00	0.00	75.00	407.60
		2.00	75.00	0.00	75.00	407.50
		3.00	75.00	0.00	75.00	407.50
		4.00	75.00	0.00	75.00	407.40
		5.00	75.00	0.00	75.00	407.30
7 days	1.01	1.00	75.00	0.00	75.00	40.40
		2.00	75.00	0.00	75.00	40.30
		3.00	75.00	0.00	75.00	40.20
		4.00	75.00	0.00	75.00	40.10
		5.00	75.00	0.00	75.00	40.00
14 days	1.39	1.00	75.00	0.00	75.00	335.80
		2.00	75.00	0.00	75.00	335.70
		3.00	75.00	0.00	75.00	335.60
		4.00	75.00	0.00	75.00	335.50
		5.00	75.00	0.00	75.00	335.40
28 days	1.62	1.00	75.00	0.00	75.00	331.70
		2.00	75.00	0.00	75.00	331.60
		3.00	75.00	0.00	75.00	331.50
		4.00	75.00	0.00	75.00	331.40
		5.00	75.00	0.00	75.00	331.30
8 hours		1.00	75.00	0.00	75.00	579.20
		2.00	75.00	0.00	75.00	579.10
		3.00	75.00	0.00	75.00	579.00
		4.00	75.00	0.00	75.00	578.90
		5.00	75.00	0.00	75.00	578.80
1 day	0.68	1.00	75.00	0.00	75.00	251.10
		2.00	75.00	0.00	75.00	251.00
		3.00	75.00	0.00	75.00	250.90
		4.00	75.00	0.00	75.00	250.80
		5.00	75.00	0.00	75.00	250.70
7 days	2.00	1.00	75.00	0.00	75.00	579.00
		2.00	75.00	0.00	75.00	578.90
		3.00	75.00	0.00	75.00	578.80
		4.00	75.00	0.00	75.00	578.70

		5.00	75.00	0.00	75.00	578.70
14 days	2.26	1.00	75.00	0.00	75.00	468.00
		2.00	75.00	0.00	75.00	467.90
		3.00	75.00	0.00	75.00	467.80
		4.00	75.00	0.00	75.00	467.70
		5.00	75.00	0.00	75.00	467.60
28 days	2.56	1.00	75.00	0.00	75.00	901.80
		2.00	75.00	0.00	75.00	901.70
		3.00	75.00	0.00	75.00	901.60
		4.00	75.00	0.00	75.00	901.50
		5.00	75.00	0.00	75.00	901.50
8 hours		1.00	75.00	0.00	75.00	36.00
		2.00	75.00	0.00	75.00	35.90
		3.00	75.00	0.00	75.00	35.80
		4.00	75.00	0.00	75.00	35.80
		5.00	75.00	0.00	75.00	35.70
1 day	1.07	1.00	75.00	0.00	75.00	846.60
		2.00	75.00	0.00	75.00	846.50
		3.00	75.00	0.00	75.00	846.40
		4.00	75.00	0.00	75.00	846.40
		5.00	75.00	0.00	75.00	846.30
7 days	3.10	1.00	75.00	0.00	75.00	733.00
		2.00	75.00	0.00	75.00	732.90
		3.00	75.00	0.00	75.00	732.80
		4.00	75.00	0.00	75.00	732.70
		5.00	75.00	0.00	75.00	732.60
14 days	4.42	1.00	75.00	0.00	75.00	398.50
		2.00	75.00	0.00	75.00	398.40
		3.00	75.00	0.00	75.00	398.30
		4.00	75.00	0.00	75.00	398.30
		5.00	75.00	0.00	75.00	398.20
28 days	5.25	1.00	75.00	0.00	75.00	990.30
		2.00	75.00	0.00	75.00	990.30
		3.00	75.00	0.00	75.00	990.20
		4.00	75.00	0.00	75.00	990.10
		5.00	75.00	0.00	75.00	990.00
n/a		1.00	120.00	0.00	90.00	25.90
		2.00	120.00	0.00	90.00	25.80
		3.00	120.00	0.00	90.00	25.70
		4.00	120.00	0.00	90.00	25.60
		5.00	120.00	0.00	90.00	25.60
n/a		1.00	120.00	0.00	90.00	297.10
		2.00	120.00	0.00	90.00	297.10
		3.00	120.00	0.00	90.00	297.00
		4.00	120.00	0.00	90.00	296.90
		5.00	120.00	0.00	90.00	296.80
n/a	n/a	1.00	120.00	0.00	90.00	86.80
		2.00	120.00	0.00	90.00	86.70
		3.00	120.00	0.00	90.00	86.60
		4.00	120.00	0.00	90.00	86.50
		5.00	120.00	0.00	90.00	86.40
8 hours	n/a	1.00	120.00	0.00	90.00	173.30
		2.00	120.00	0.00	90.00	173.20
		3.00	120.00	0.00	90.00	173.20
		4.00	120.00	0.00	90.00	173.10

		5.00	120.00	0.00	90.00	173.00
1 day	n/a	1.00	120.00	0.00	90.00	12.50
		2.00	120.00	0.00	90.00	12.40
		3.00	120.00	0.00	90.00	12.30
		4.00	120.00	0.00	90.00	12.20
		5.00	120.00	0.00	90.00	12.10
7 days	n/a	1.00	120.00	0.00	90.00	69.40
		2.00	120.00	0.00	90.00	69.30
		3.00	120.00	0.00	90.00	69.30
		4.00	120.00	0.00	90.00	69.10
		5.00	120.00	0.00	90.00	69.10
14 days	n/a	1.00	120.00	0.00	90.00	18.50
		2.00	120.00	0.00	90.00	18.40
		3.00	120.00	0.00	90.00	18.30
		4.00	120.00	0.00	90.00	18.20
		5.00	120.00	0.00	90.00	18.10
28 days	n/a	1.00	120.00	0.00	90.00	670.00
		2.00	120.00	0.00	90.00	670.00
		3.00	120.00	0.00	90.00	669.90
		4.00	120.00	0.00	90.00	669.80
		5.00	120.00	0.00	90.00	669.70
8 hours	n/a	1.00	120.00	0.00	90.00	62.60
		2.00	120.00	0.00	90.00	62.50
		3.00	120.00	0.00	90.00	62.50
		4.00	120.00	0.00	90.00	62.40
			120.00	0.00	90.00	62.30
1 day	0.25	1.00	120.00	0.00	90.00	947.20
		2.00	120.00	0.00	90.00	947.10
		3.00	120.00	0.00	90.00	947.00
		4.00	120.00	0.00	90.00	946.90
		5.00	120.00	0.00	90.00	946.80
7 days	0.35	1.00	120.00	0.00	90.00	709.00
		2.00	120.00	0.00	90.00	709.00
		3.00	120.00	0.00	90.00	708.90
		4.00	120.00	0.00	90.00	708.80
		5.00	120.00	0.00	90.00	708.70
14 days	0.57	1.00	120.00	0.00	90.00	406.40
		2.00	120.00	0.00	90.00	406.30
		3.00	120.00	0.00	90.00	406.20
		4.00	120.00	0.00	90.00	406.10
		5.00	120.00	0.00	90.00	406.10
28 days	0.65	1.00	120.00	0.00	90.00	660.50
		2.00	120.00	0.00	90.00	660.40
		3.00	120.00	0.00	90.00	660.30
		4.00	120.00	0.00	90.00	660.30
		5.00	120.00	0.00	90.00	660.20
8 hours		1.00	120.00	0.00	90.00	179.50
		2.00	120.00	0.00	90.00	179.40
		3.00	120.00	0.00	90.00	179.40
		4.00	120.00	0.00	90.00	179.30
		5.00	120.00	0.00	90.00	179.20
1 day	0.51	1.00	120.00	0.00	90.00	916.60
		2.00	120.00	0.00	90.00	916.50
		3.00	120.00	0.00	90.00	916.40
		4.00	120.00	0.00	90.00	916.40

		5.00	120.00	0.00	90.00	916.30
7 days	1.01	1.00	120.00	0.00	90.00	757.30
		2.00	120.00	0.00	90.00	757.30
		3.00	120.00	0.00	90.00	757.20
		4.00	120.00	0.00	90.00	757.10
		5.00	120.00	0.00	90.00	757.00
14 days	1.39	1.00	120.00	0.00	90.00	123.10
		2.00	120.00	0.00	90.00	123.00
		3.00	120.00	0.00	90.00	122.90
		4.00	120.00	0.00	90.00	122.90
		5.00	120.00	0.00	90.00	122.80
28 days	1.62	1.00	120.00	0.00	90.00	874.60
		2.00	120.00	0.00	90.00	874.50
		3.00	120.00	0.00	90.00	874.40
		4.00	120.00	0.00	90.00	874.30
		5.00	120.00	0.00	90.00	874.20
8 hours		1.00	120.00	0.00	90.00	453.30
		2.00	120.00	0.00	90.00	453.20
		3.00	120.00	0.00	90.00	453.10
		4.00	120.00	0.00	90.00	453.00
		5.00	120.00	0.00	90.00	452.90
1 day	0.68	1.00	120.00	0.00	90.00	284.10
		2.00	120.00	0.00	90.00	284.00
		3.00	120.00	0.00	90.00	283.90
		4.00	120.00	0.00	90.00	283.80
		5.00	120.00	0.00	90.00	283.70
7 days	2.00	1.00	120.00	0.00	90.00	355.10
		2.00	120.00	0.00	90.00	355.00
		3.00	120.00	0.00	90.00	354.90
		4.00	120.00	0.00	90.00	354.80
		5.00	120.00	0.00	90.00	354.70
14 days	2.26	1.00	120.00	0.00	90.00	103.60
		2.00	120.00	0.00	90.00	103.50
		3.00	120.00	0.00	90.00	103.40
		4.00	120.00	0.00	90.00	103.40
		5.00	120.00	0.00	90.00	103.30
28 days	2.56	1.00	120.00	0.00	90.00	901.70
		2.00	120.00	0.00	90.00	901.60
		3.00	120.00	0.00	90.00	901.50
		4.00	120.00	0.00	90.00	901.40
		5.00	120.00	0.00	90.00	901.40
8 hours		1.00	120.00	0.00	90.00	517.00
		2.00	120.00	0.00	90.00	516.90
		3.00	120.00	0.00	90.00	516.80
		4.00	120.00	0.00	90.00	516.80
		5.00	120.00	0.00	90.00	516.70
1 day	1.07	1.00	120.00	0.00	90.00	98.70
		2.00	120.00	0.00	90.00	98.60
		3.00	120.00	0.00	90.00	98.50
		4.00	120.00	0.00	90.00	98.40
		5.00	120.00	0.00	90.00	98.40
7 days	3.10	1.00	120.00	0.00	90.00	726.40
		2.00	120.00	0.00	90.00	726.30
		3.00	120.00	0.00	90.00	726.20
		4.00	120.00	0.00	90.00	726.10

		5.00	120.00	0.00	90.00	726.00
14 days	4.42	1.00	120.00	0.00	90.00	156.70
		2.00	120.00	0.00	90.00	156.60
		3.00	120.00	0.00	90.00	156.50
		4.00	120.00	0.00	90.00	156.50
		5.00	120.00	0.00	90.00	156.40
28 days	5.25	1.00	120.00	0.00	90.00	548.90
		2.00	120.00	0.00	90.00	548.80
		3.00	120.00	0.00	90.00	548.70
		4.00	120.00	0.00	90.00	548.70
		5.00	120.00	0.00	90.00	548.60
n/a		1.00	150.00	0.00	150.00	356.50
		2.00	150.00	0.00	150.00	356.40
		3.00	150.00	0.00	150.00	356.30
		4.00	150.00	0.00	150.00	356.30
		5.00	150.00	0.00	150.00	356.20
n/a		1.00	150.00	0.00	150.00	162.80
		2.00	150.00	0.00	150.00	162.70
		3.00	150.00	0.00	150.00	162.60
		4.00	150.00	0.00	150.00	162.50
		5.00	150.00	0.00	150.00	162.40
n/a	n/a	1.00	150.00	0.00	150.00	200.00
		2.00	150.00	0.00	150.00	199.90
		3.00	150.00	0.00	150.00	199.80
		4.00	150.00	0.00	150.00	199.70
		5.00	150.00	0.00	150.00	199.60
8 hours	n/a	1.00	150.00	0.00	150.00	512.40
		2.00	150.00	0.00	150.00	512.30
		3.00	150.00	0.00	150.00	512.30
		4.00	150.00	0.00	150.00	512.10
		5.00	150.00	0.00	150.00	512.10
1 day	n/a	1.00	150.00	0.00	150.00	392.90
		2.00	150.00	0.00	150.00	392.80
		3.00	150.00	0.00	150.00	392.70
		4.00	150.00	0.00	150.00	392.60
		5.00	150.00	0.00	150.00	392.50
7 days	n/a	1.00	150.00	0.00	150.00	273.00
		2.00	150.00	0.00	150.00	273.00
		3.00	150.00	0.00	150.00	272.90
		4.00	150.00	0.00	150.00	272.80
		5.00	150.00	0.00	150.00	272.70
14 days	n/a	1.00	150.00	0.00	150.00	160,00
		2.00	150.00	0.00	150.00	159,90
		3.00	150.00	0.00	150.00	159,80
		4.00	150.00	0.00	150.00	159,70
		5.00	150.00	0.00	150.00	159,60
28 days	n/a	1.00	150.00	0.00	150.00	82,50
		2.00	150.00	0.00	150.00	82,40
		3.00	150.00	0.00	150.00	82,30
		4.00	150.00	0.00	150.00	82,20
		5.00	150.00	0.00	150.00	82,10
8 hours	n/a	1.00	150.00	0.00	150.00	284.40
		2.00	150.00	0.00	150.00	287.40
		3.00	150.00	0.00	150.00	287.40

		4.00	150.00	0.00	150.00	287.40
		5.00	150.00	0.00	150.00	283.40
1 day	0.25	1.00	150.00	0.00	150.00	569.60
		2.00	150.00	0.00	150.00	565.60
		3.00	150.00	0.00	150.00	565.60
		4.00	150.00	0.00	150.00	565.60
		5.00	150.00	0.00	150.00	565.60
7 days	0.35	1.00	150.00	0.00	150.00	795.80
		2.00	150.00	0.00	150.00	795.80
		3.00	150.00	0.00	150.00	795.80
		4.00	150.00	0.00	150.00	795.80
		5.00	150.00	0.00	150.00	794.80
14 days	0.57	1.00	150.00	0.00	150.00	604.60
		2.00	150.00	0.00	150.00	603.60
		3.00	150.00	0.00	150.00	603.60
		4.00	150.00	0.00	150.00	603.60
		5.00	150.00	0.00	150.00	603.60
28 days	0.65	1.00	150.00	0.00	150.00	335.60
		2.00	150.00	0.00	150.00	335.60
		3.00	150.00	0.00	150.00	334.60
		4.00	150.00	0.00	150.00	334.60
		5.00	150.00	0.00	150.00	334.60
8 hours		1.00	150.00	0.00	150.00	223.70
		2.00	150.00	0.00	150.00	223.70
		3.00	150.00	0.00	150.00	223.70
		4.00	150.00	0.00	150.00	223.70
		5.00	150.00	0.00	150.00	223.70
1 day	0.51	1.00	150.00	0.00	150.00	90.00
		2.00	150.00	0.00	150.00	87.00
		3.00	150.00	0.00	150.00	90.00
		4.00	150.00	0.00	150.00	86.00
		5.00	150.00	0.00	150.00	86.00
7 days	1.01	1.00	150.00	0.00	150.00	747.60
		2.00	150.00	0.00	150.00	747.60
		3.00	150.00	0.00	150.00	747.60
		4.00	150.00	0.00	150.00	747.60
		5.00	150.00	0.00	150.00	747.60
14 days	1.39	1.00	150.00	0.00	150.00	861.50
		2.00	150.00	0.00	150.00	861.50
		3.00	150.00	0.00	150.00	861.50
		4.00	150.00	0.00	150.00	861.50
		5.00	150.00	0.00	150.00	861.50
28 days	1.62	1.00	150.00	0.00	150.00	71.30
		2.00	150.00	0.00	150.00	71.30
		3.00	150.00	0.00	150.00	70.30
		4.00	150.00	0.00	150.00	70.30
		5.00	150.00	0.00	150.00	70.30
8 hours		1.00	150.00	0.00	150.00	881.50
		2.00	150.00	0.00	150.00	885.50
		3.00	150.00	0.00	150.00	881.50
		4.00	150.00	0.00	150.00	884.50
		5.00	150.00	0.00	150.00	880.50
		1.00	150.00	0.00	150.00	506.90
		2.00	150.00	0.00	150.00	506.90

1 day	0.68	3.00	150.00	0.00	150.00	506.90
		4.00	150.00	0.00	150.00	506.90
		5.00	150.00	0.00	150.00	506.90
7 days	2.00	1.00	150.00	0.00	150.00	829.90
		2.00	150.00	0.00	150.00	829.90
		3.00	150.00	0.00	150.00	833.90
		4.00	150.00	0.00	150.00	829.90
		5.00	150.00	0.00	150.00	833.90
14 days	2.26	1.00	150.00	0.00	150.00	621.20
		2.00	150.00	0.00	150.00	617.20
		3.00	150.00	0.00	150.00	617.20
		4.00	150.00	0.00	150.00	616.20
		5.00	150.00	0.00	150.00	616.20
28 days	2.56	1.00	150.00	0.00	150.00	611.10
		2.00	150.00	0.00	150.00	611.10
		3.00	150.00	0.00	150.00	611.10
		4.00	150.00	0.00	150.00	611.10
		5.00	150.00	0.00	150.00	611.10
8 hours		1.00	150.00	0.00	150.00	801.80
		2.00	150.00	0.00	150.00	801.80
		3.00	150.00	0.00	150.00	801.70
		4.00	150.00	0.00	150.00	801.60
		5.00	150.00	0.00	150.00	801.50
1 day	1.07	1.00	150.00	0.00	150.00	739.40
		2.00	150.00	0.00	150.00	739.30
		3.00	150.00	0.00	150.00	739.20
		4.00	150.00	0.00	150.00	739.10
		5.00	150.00	0.00	150.00	739.10
7 days	3.10	1.00	150.00	0.00	150.00	963.60
		2.00	150.00	0.00	150.00	963.50
		3.00	150.00	0.00	150.00	963.40
		4.00	150.00	0.00	150.00	963.30
		5.00	150.00	0.00	150.00	963.20
14 days	4.42	1.00	150.00	0.00	150.00	592,80
		2.00	150.00	0.00	150.00	592,70
		3.00	150.00	0.00	150.00	592,60
		4.00	150.00	0.00	150.00	592,50
		5.00	150.00	0.00	150.00	592,40
28 days	5.25	1.00	150.00	0.00	150.00	82,50
		2.00	150.00	0.00	150.00	82,40
		3.00	150.00	0.00	150.00	82,30
		4.00	150.00	0.00	150.00	82,20
		5.00	150.00	0.00	150.00	82,10
n/a		1.00	200.00	0.00	150.00	405.90
		2.00	200.00	0.00	150.00	409.90
		3.00	200.00	0.00	150.00	409.90
		4.00	200.00	0.00	150.00	409.90
		5.00	200.00	0.00	150.00	409.90
n/a		1.00	200.00	0.00	150.00	757.60
		2.00	200.00	0.00	150.00	757.60
		3.00	200.00	0.00	150.00	761.60
		4.00	200.00	0.00	150.00	761.60
		5.00	200.00	0.00	150.00	762.60
		1.00	200.00	0.00	150.00	154.20

n/a	n/a	2.00	200.00	0.00	150.00	154.20
		3.00	200.00	0.00	150.00	154.20
		4.00	200.00	0.00	150.00	154.20
		5.00	200.00	0.00	150.00	154.20
8 hours	n/a	1.00	200.00	0.00	150.00	252.40
		2.00	200.00	0.00	150.00	256.40
		3.00	200.00	0.00	150.00	252.40
		4.00	200.00	0.00	150.00	256.40
		5.00	200.00	0.00	150.00	256.40
1 day	n/a	1.00	200.00	0.00	150.00	818.80
		2.00	200.00	0.00	150.00	818.80
		3.00	200.00	0.00	150.00	814.80
		4.00	200.00	0.00	150.00	818.80
		5.00	200.00	0.00	150.00	818.80
7 days	n/a	1.00	200.00	0.00	150.00	480.20
		2.00	200.00	0.00	150.00	480.20
		3.00	200.00	0.00	150.00	484.20
		4.00	200.00	0.00	150.00	484.20
		5.00	200.00	0.00	150.00	484.20
14 days	n/a	1.00	200.00	0.00	150.00	574.00
		2.00	200.00	0.00	150.00	574.00
		3.00	200.00	0.00	150.00	574.00
		4.00	200.00	0.00	150.00	574.00
		5.00	200.00	0.00	150.00	574.00
28 days	n/a	1.00	200.00	0.00	150.00	892.00
		2.00	200.00	0.00	150.00	892.00
		3.00	200.00	0.00	150.00	892.00
		4.00	200.00	0.00	150.00	892.00
		5.00	200.00	0.00	150.00	892.00
8 hours	n/a	1.00	200.00	0.00	150.00	76.20
		2.00	200.00	0.00	150.00	76.20
		3.00	200.00	0.00	150.00	76.20
		4.00	200.00	0.00	150.00	76.20
		5.00	200.00	0.00	150.00	75.20
1 day	0.25	1.00	200.00	0.00	150.00	523.10
		2.00	200.00	0.00	150.00	523.10
		3.00	200.00	0.00	150.00	523.10
		4.00	200.00	0.00	150.00	523.10
		5.00	200.00	0.00	150.00	523.10
7 days	0.35	1.00	200.00	0.00	150.00	859.70
		2.00	200.00	0.00	150.00	863.70
		3.00	200.00	0.00	150.00	859.70
		4.00	200.00	0.00	150.00	863.70
		5.00	200.00	0.00	150.00	860.70
14 days	0.57	1.00	200.00	0.00	150.00	552.30
		2.00	200.00	0.00	150.00	552.30
		3.00	200.00	0.00	150.00	551.30
		4.00	200.00	0.00	150.00	551.30
		5.00	200.00	0.00	150.00	551.30
28 days	0.65	1.00	200.00	0.00	150.00	4.90
		2.00	200.00	0.00	150.00	4.90
		3.00	200.00	0.00	150.00	3.90
		4.00	200.00	0.00	150.00	3.90
		5.00	200.00	0.00	150.00	3.90
		1.00	200.00	0.00	150.00	717.70

8 hours		2.00	200.00	0.00	150.00	717.70
		3.00	200.00	0.00	150.00	713.70
		4.00	200.00	0.00	150.00	713.70
		5.00	200.00	0.00	150.00	713.70
1 day	0.51	1.00	200.00	0.00	150.00	642.10
		2.00	200.00	0.00	150.00	642.10
		3.00	200.00	0.00	150.00	642.10
		4.00	200.00	0.00	150.00	642.10
		5.00	200.00	0.00	150.00	642.10
7 days	1.01	1.00	200.00	0.00	150.00	407.00
		2.00	200.00	0.00	150.00	403.00
		3.00	200.00	0.00	150.00	407.00
		4.00	200.00	0.00	150.00	403.00
		5.00	200.00	0.00	150.00	407.00
14 days	1.39	1.00	200.00	0.00	150.00	226.00
		2.00	200.00	0.00	150.00	226.00
		3.00	200.00	0.00	150.00	226.00
		4.00	200.00	0.00	150.00	226.00
		5.00	200.00	0.00	150.00	226.00
28 days	1.62	1.00	200.00	0.00	150.00	967.00
		2.00	200.00	0.00	150.00	967.00
		3.00	200.00	0.00	150.00	967.00
		4.00	200.00	0.00	150.00	966.00
		5.00	200.00	0.00	150.00	966.00
8 hours		1.00	200.00	0.00	150.00	490.30
		2.00	200.00	0.00	150.00	490.30
		3.00	200.00	0.00	150.00	490.20
		4.00	200.00	0.00	150.00	490.10
		5.00	200.00	0.00	150.00	490.00
1 day	0.68	1.00	200.00	0.00	150.00	376,70
		2.00	200.00	0.00	150.00	376,70
		3.00	200.00	0.00	150.00	376,60
		4.00	200.00	0.00	150.00	376,50
		5.00	200.00	0.00	150.00	376,40
7 days	2.00	1.00	200.00	0.00	150.00	258,30
		2.00	200.00	0.00	150.00	258,20
		3.00	200.00	0.00	150.00	258,10
		4.00	200.00	0.00	150.00	258,10
		5.00	200.00	0.00	150.00	258,00
14 days	2.26	1.00	200.00	0.00	150.00	666,90
		2.00	200.00	0.00	150.00	666,80
		3.00	200.00	0.00	150.00	666,70
		4.00	200.00	0.00	150.00	666,70
		5.00	200.00	0.00	150.00	666,60
28 days	2.56	1.00	200.00	0.00	150.00	426,10
		2.00	200.00	0.00	150.00	426,00
		3.00	200.00	0.00	150.00	425,90
		4.00	200.00	0.00	150.00	425,80
		5.00	200.00	0.00	150.00	425,70
8 hours		1.00	200.00	0.00	150.00	167,90
		2.00	200.00	0.00	150.00	167,80
		3.00	200.00	0.00	150.00	167,70
		4.00	200.00	0.00	150.00	167,70
		5.00	200.00	0.00	150.00	167,50
		1.00	200.00	0.00	150.00	328,30

1 day	1.07	2.00	200.00	0.00	150.00	328,20
		3.00	200.00	0.00	150.00	328,10
		4.00	200.00	0.00	150.00	328,00
		5.00	200.00	0.00	150.00	328,00
7 days	3.10	1.00	200.00	0.00	150.00	112,00
		2.00	200.00	0.00	150.00	112,00
		3.00	200.00	0.00	150.00	111,90
		4.00	200.00	0.00	150.00	111,80
		5.00	200.00	0.00	150.00	111,70
14 days	4.42	1.00	200.00	0.00	150.00	782,20
		2.00	200.00	0.00	150.00	782,10
		3.00	200.00	0.00	150.00	782,00
		4.00	200.00	0.00	150.00	781,90
		5.00	200.00	0.00	150.00	781,80
28 days	5.25	1.00	200.00	0.00	150.00	261,50
		2.00	200.00	0.00	150.00	261,40
		3.00	200.00	0.00	150.00	261,40
		4.00	200.00	0.00	150.00	261,30
		5.00	200.00	0.00	150.00	261,20
n/a		1.00	240.00	0.00	180.00	799.90
		2.00	240.00	0.00	180.00	799.90
		3.00	240.00	0.00	180.00	800.90
		4.00	240.00	0.00	180.00	803.90
		5.00	240.00	0.00	180.00	803.90
n/a		1.00	240.00	0.00	180.00	972.50
		2.00	240.00	0.00	180.00	972.50
		3.00	240.00	0.00	180.00	976.50
		4.00	240.00	0.00	180.00	976.50
		5.00	240.00	0.00	180.00	976.50
n/a	n/a	1.00	240.00	0.00	180.00	404,10
		2.00	240.00	0.00	180.00	404,00
		3.00	240.00	0.00	180.00	403,90
		4.00	240.00	0.00	180.00	403,80
		5.00	240.00	0.00	180.00	403,80
8 hours	n/a	1.00	240.00	0.00	180.00	921,20
		2.00	240.00	0.00	180.00	921,10
		3.00	240.00	0.00	180.00	921,10
		4.00	240.00	0.00	180.00	921,00
		5.00	240.00	0.00	180.00	920,90
1 day	n/a	1.00	240.00	0.00	180.00	294,10
		2.00	240.00	0.00	180.00	294,00
		3.00	240.00	0.00	180.00	293,90
		4.00	240.00	0.00	180.00	293,90
		5.00	240.00	0.00	180.00	293,80
7 days	n/a	1.00	240.00	0.00	180.00	192,00
		2.00	240.00	0.00	180.00	191,90
		3.00	240.00	0.00	180.00	191,80
		4.00	240.00	0.00	180.00	191,70
		5.00	240.00	0.00	180.00	191,60
14 days	n/a	1.00	240.00	0.00	180.00	476,30
		2.00	240.00	0.00	180.00	476,20
		3.00	240.00	0.00	180.00	476,10
		4.00	240.00	0.00	180.00	476,00
		5.00	240.00	0.00	180.00	476,00
		1.00	240.00	0.00	180.00	963,40

28 days	n/a	2.00	240.00	0.00	180.00	963,30
		3.00	240.00	0.00	180.00	963,20
		4.00	240.00	0.00	180.00	963,20
		5.00	240.00	0.00	180.00	963,10
8 hours	n/a	1.00	240.00	0.00	180.00	312,50
		2.00	240.00	0.00	180.00	312,40
		3.00	240.00	0.00	180.00	312,30
		4.00	240.00	0.00	180.00	312,20
		5.00	240.00	0.00	180.00	312,10
1 day	0.25	1.00	240.00	0.00	180.00	36,30
		2.00	240.00	0.00	180.00	36,20
		3.00	240.00	0.00	180.00	36,20
		4.00	240.00	0.00	180.00	36,10
		5.00	240.00	0.00	180.00	30,40
7 days	0.35	1.00	240.00	0.00	180.00	825,50
		2.00	240.00	0.00	180.00	825,40
		3.00	240.00	0.00	180.00	825,30
		4.00	240.00	0.00	180.00	825,20
		5.00	240.00	0.00	180.00	825,10
14 days	0.57	1.00	240.00	0.00	180.00	857.00
		2.00	240.00	0.00	180.00	856.90
		3.00	240.00	0.00	180.00	856.80
		4.00	240.00	0.00	180.00	856.70
		5.00	240.00	0.00	180.00	856.70
28 days	0.65	1.00	240.00	0.00	180.00	269.50
		2.00	240.00	0.00	180.00	269.40
		3.00	240.00	0.00	180.00	269.30
		4.00	240.00	0.00	180.00	269.20
		5.00	240.00	0.00	180.00	269.10
8 hours		1.00	240.00	0.00	180.00	936,50
		2.00	240.00	0.00	180.00	936,40
		3.00	240.00	0.00	180.00	936,30
		4.00	240.00	0.00	180.00	936,20
		5.00	240.00	0.00	180.00	936,10
1 day	0.51	1.00	240.00	0.00	180.00	187,30
		2.00	240.00	0.00	180.00	187,30
		3.00	240.00	0.00	180.00	187,20
		4.00	240.00	0.00	180.00	187,10
		5.00	240.00	0.00	180.00	187,00
7 days	1.01	1.00	240.00	0.00	180.00	275,10
		2.00	240.00	0.00	180.00	275,00
		3.00	240.00	0.00	180.00	274,90
		4.00	240.00	0.00	180.00	274,80
		5.00	240.00	0.00	180.00	274,70
14 days	1.39	1.00	240.00	0.00	180.00	892.40
		2.00	240.00	0.00	180.00	892.30
		3.00	240.00	0.00	180.00	892.20
		4.00	240.00	0.00	180.00	892.10
		5.00	240.00	0.00	180.00	892.00
28 days	1.62	1.00	240.00	0.00	180.00	50.90
		2.00	240.00	0.00	180.00	50.80
		3.00	240.00	0.00	180.00	50.70
		4.00	240.00	0.00	180.00	50.60
		5.00	240.00	0.00	180.00	50.50
		1.00	240.00	0.00	180.00	677,30

8 hours		2.00	240.00	0.00	180.00	677,20
		3.00	240.00	0.00	180.00	677,10
		4.00	240.00	0.00	180.00	677,00
		5.00	240.00	0.00	180.00	676,90
1 day	0.68	1.00	240.00	0.00	180.00	221,00
		2.00	240.00	0.00	180.00	220,90
		3.00	240.00	0.00	180.00	220,90
		4.00	240.00	0.00	180.00	220,80
		5.00	240.00	0.00	180.00	220,70
7 days	2.00	1.00	240.00	0.00	180.00	953,70
		2.00	240.00	0.00	180.00	953,60
		3.00	240.00	0.00	180.00	953,50
		4.00	240.00	0.00	180.00	953,40
		5.00	240.00	0.00	180.00	953,40
14 days	2.26	1.00	240.00	0.00	180.00	952.20
		2.00	240.00	0.00	180.00	952.10
		3.00	240.00	0.00	180.00	952.00
		4.00	240.00	0.00	180.00	951.90
		5.00	240.00	0.00	180.00	951.80
28 days	2.56	1.00	240.00	0.00	180.00	108.90
		2.00	240.00	0.00	180.00	108.80
		3.00	240.00	0.00	180.00	108.70
		4.00	240.00	0.00	180.00	108.60
		5.00	240.00	0.00	180.00	108.50
8 hours		1.00	240.00	0.00	180.00	384,20
		2.00	240.00	0.00	180.00	384,10
		3.00	240.00	0.00	180.00	384,10
		4.00	240.00	0.00	180.00	384,00
		5.00	240.00	0.00	180.00	383,90
1 day	1.07	1.00	240.00	0.00	180.00	950,70
		2.00	240.00	0.00	180.00	950,70
		3.00	240.00	0.00	180.00	950,60
		4.00	240.00	0.00	180.00	950,50
		5.00	240.00	0.00	180.00	950,40
7 days	3.10	1.00	240.00	0.00	180.00	475,70
		2.00	240.00	0.00	180.00	475,60
		3.00	240.00	0.00	180.00	475,50
		4.00	240.00	0.00	180.00	475,40
		5.00	240.00	0.00	180.00	475,30
14 days	4.42	1.00	240.00	0.00	180.00	47.30
		2.00	240.00	0.00	180.00	47.20
		3.00	240.00	0.00	180.00	47.10
		4.00	240.00	0.00	180.00	47.00
		5.00	240.00	0.00	180.00	46.90
28 days	5.25	1.00	240.00	0.00	180.00	226.70
		2.00	240.00	0.00	180.00	226.70
		3.00	240.00	0.00	180.00	226.60
		4.00	240.00	0.00	180.00	226.50
		5.00	240.00	0.00	180.00	226.40
8 hours	n/a	1.00	150.00	0.00	150.00	220.50
		2.00	150.00	0.00	150.00	220.40
		3.00	150.00	0.00	150.00	220.30
		4.00	150.00	0.00	150.00	220.20
		5.00	150.00	0.00	150.00	220.10
		1.00	150.00	0.00	150.00	403.60

1 day	n/a	2.00	150.00	0.00	150.00	403.50
		3.00	150.00	0.00	150.00	403.40
		4.00	150.00	0.00	150.00	403.40
		5.00	150.00	0.00	150.00	403.30
7 days	n/a	1.00	150.00	0.00	150.00	666.80
		2.00	150.00	0.00	150.00	666.70
		3.00	150.00	0.00	150.00	666.70
		4.00	150.00	0.00	150.00	666.60
		5.00	150.00	0.00	150.00	666.50
14 days	n/a	1.00	150.00	0.00	150.00	840.80
		2.00	150.00	0.00	150.00	840.70
		3.00	150.00	0.00	150.00	840.60
		4.00	150.00	0.00	150.00	840.60
		5.00	150.00	0.00	150.00	840.40
28 days	n/a	1.00	150.00	0.00	150.00	763.00
		2.00	150.00	0.00	150.00	762.90
		3.00	150.00	0.00	150.00	762.90
		4.00	150.00	0.00	150.00	762.80
		5.00	150.00	0.00	150.00	762.70
8 hours	n/a	1.00	150.00	0.00	150.00	351.90
		2.00	150.00	0.00	150.00	351.80
		3.00	150.00	0.00	150.00	351.80
		4.00	150.00	0.00	150.00	351.70
		5.00	150.00	0.00	150.00	351.60
1 day	0.25	1.00	150.00	0.00	150.00	531.20
		2.00	150.00	0.00	150.00	531.20
		3.00	150.00	0.00	150.00	531.10
		4.00	150.00	0.00	150.00	531.00
		5.00	150.00	0.00	150.00	530.90
7 days	0.35	1.00	150.00	0.00	150.00	717.20
		2.00	150.00	0.00	150.00	717.10
		3.00	150.00	0.00	150.00	717.00
		4.00	150.00	0.00	150.00	716.90
		5.00	150.00	0.00	150.00	716.80
14 days	0.57	1.00	150.00	0.00	150.00	353.40
		2.00	150.00	0.00	150.00	353.30
		3.00	150.00	0.00	150.00	353.20
		4.00	150.00	0.00	150.00	353.20
		5.00	150.00	0.00	150.00	353.00
28 days	0.65	1.00	150.00	0.00	150.00	915.50
		2.00	150.00	0.00	150.00	915.50
		3.00	150.00	0.00	150.00	915.40
		4.00	150.00	0.00	150.00	915.30
		5.00	150.00	0.00	150.00	915.20
8 hours		1.00	150.00	0.00	150.00	592.20
		2.00	150.00	0.00	150.00	592.10
		3.00	150.00	0.00	150.00	592.10
		4.00	150.00	0.00	150.00	592.00
		5.00	150.00	0.00	150.00	591.90
1 day	0.51	1.00	150.00	0.00	150.00	893.00
		2.00	150.00	0.00	150.00	892.90
		3.00	150.00	0.00	150.00	892.80
		4.00	150.00	0.00	150.00	892.70
		5.00	150.00	0.00	150.00	892.70
		1.00	150.00	0.00	150.00	411.70

7 days	1.01	2.00	150.00	0.00	150.00	411.60
		3.00	150.00	0.00	150.00	411.60
		4.00	150.00	0.00	150.00	411.50
		5.00	150.00	0.00	150.00	411.40
14 days	1.39	1.00	150.00	0.00	150.00	927.50
		2.00	150.00	0.00	150.00	927.40
		3.00	150.00	0.00	150.00	927.30
		4.00	150.00	0.00	150.00	927.20
		5.00	150.00	0.00	150.00	927.10
28 days	1.62	1.00	150.00	0.00	150.00	76.40
		2.00	150.00	0.00	150.00	76.30
		3.00	150.00	0.00	150.00	76.20
		4.00	150.00	0.00	150.00	76.10
		5.00	150.00	0.00	150.00	76.00
8 hours		1.00	150.00	0.00	150.00	490.50
		2.00	150.00	0.00	150.00	490.40
		3.00	150.00	0.00	150.00	490.30
		4.00	150.00	0.00	150.00	490.20
		5.00	150.00	0.00	150.00	490.10
1 day	0.68	1.00	150.00	0.00	150.00	757.30
		2.00	150.00	0.00	150.00	757.30
		3.00	150.00	0.00	150.00	757.20
		4.00	150.00	0.00	150.00	757.10
		5.00	150.00	0.00	150.00	757.00
7 days	2.00	1.00	150.00	0.00	150.00	982.60
		2.00	150.00	0.00	150.00	982.50
		3.00	150.00	0.00	150.00	982.50
		4.00	150.00	0.00	150.00	982.40
		5.00	150.00	0.00	150.00	982.20
14 days	2.26	1.00	150.00	0.00	150.00	391.40
		2.00	150.00	0.00	150.00	391.40
		3.00	150.00	0.00	150.00	391.30
		4.00	150.00	0.00	150.00	391.20
		5.00	150.00	0.00	150.00	391.10
28 days	2.56	1.00	150.00	0.00	150.00	949.40
		2.00	150.00	0.00	150.00	949.30
		3.00	150.00	0.00	150.00	949.20
		4.00	150.00	0.00	150.00	949.10
		5.00	150.00	0.00	150.00	949.00
8 hours		1.00	150.00	0.00	150.00	759.00
		2.00	150.00	0.00	150.00	758.90
		3.00	150.00	0.00	150.00	758.80
		4.00	150.00	0.00	150.00	758.70
		5.00	150.00	0.00	150.00	758.60
1 day	1.07	1.00	150.00	0.00	150.00	270.50
		2.00	150.00	0.00	150.00	270.40
		3.00	150.00	0.00	150.00	270.30
		4.00	150.00	0.00	150.00	270.20
		5.00	150.00	0.00	150.00	270.10
7 days	3.10	1.00	150.00	0.00	150.00	405.50
		2.00	150.00	0.00	150.00	405.40
		3.00	150.00	0.00	150.00	405.40
		4.00	150.00	0.00	150.00	405.30
		5.00	150.00	0.00	150.00	405.20
		1.00	150.00	0.00	150.00	238.20

14 days	4.42	2.00	150.00	0.00	150.00	238.10
		3.00	150.00	0.00	150.00	238.10
		4.00	150.00	0.00	150.00	238.00
		5.00	150.00	0.00	150.00	237.90
28 days	5.25	1.00	150.00	0.00	150.00	797.50
		2.00	150.00	0.00	150.00	797.40
		3.00	150.00	0.00	150.00	797.30
		4.00	150.00	0.00	150.00	797.20
		5.00	150.00	0.00	150.00	797.10
		1.00	150.00	0.00	150.00	661.90
		2.00	150.00	0.00	150.00	661.80
		3.00	150.00	0.00	150.00	661.70
		4.00	150.00	0.00	150.00	661.60
		5.00	150.00	0.00	150.00	661.50
		1.00	150.00	0.00	150.00	471.20
		2.00	150.00	0.00	150.00	471.10
		3.00	150.00	0.00	150.00	471.00
		4.00	150.00	0.00	150.00	470.90
		5.00	150.00	0.00	150.00	470.80
	n/a	1.00	150.00	0.00	150.00	199.20
		2.00	150.00	0.00	150.00	199.10
		3.00	150.00	0.00	150.00	199.00
		4.00	150.00	0.00	150.00	199.00
		5.00	150.00	0.00	150.00	198.90

Channel 2						
(sensor 2)						
location			Distance	Velocity	Average velocity for sensor 2	Arrival time, millisecond
x2	y2	z2	(mm)	m/s	m/s	t2
0.00	90.00	60.00	118.11	3,005.35	3,017.65	266.60
0.00	90.00	60.00	118.11	3,020.72		266.40
0.00	90.00	60.00	118.11	3,028.46		266.20
0.00	90.00	60.00	118.11	3,013.01		266.30
0.00	90.00	60.00	118.11	3,020.72		266.10
0.00	90.00	60.00	118.11	3,289.98	3,289.98	1,011.50
0.00	90.00	60.00	118.11	3,289.98		1,011.50
0.00	90.00	60.00	118.11	3,289.98		1,011.40
0.00	90.00	60.00	118.11	3,289.98		1,011.30
0.00	90.00	60.00	118.11	3,289.98		1,011.20
0.00	90.00	60.00	118.11	3,289.98	3,289.98	372.00
0.00	90.00	60.00	118.11	3,289.98		371.90
0.00	90.00	60.00	118.11	3,289.98		371.80
0.00	90.00	60.00	118.11	3,289.98		371.70
0.00	90.00	60.00	118.11	3,289.98		371.60
0.00	90.00	60.00	118.11	3,289.98	3,282.67	328.00
0.00	90.00	60.00	118.11	3,280.84		328.00
0.00	90.00	60.00	118.11	3,289.98		327.80
0.00	90.00	60.00	118.11	3,280.84		327.80
0.00	90.00	60.00	118.11	3,271.75		327.80
0.00	90.00	60.00	118.11	3,271.75	3,266.33	308.70
0.00	90.00	60.00	118.11	3,262.71		308.70
0.00	90.00	60.00	118.11	3,271.75		308.50
0.00	90.00	60.00	118.11	3,262.71		308.50
0.00	90.00	60.00	118.11	3,262.71		308.40
0.00	90.00	60.00	118.11	3,124.61	3,127.92	797.30
0.00	90.00	60.00	118.11	3,124.61		797.30
0.00	90.00	60.00	118.11	3,132.89		797.10
0.00	90.00	60.00	118.11	3,132.89		797.00
0.00	90.00	60.00	118.11	3,124.61		797.00
0.00	90.00	60.00	118.11	3,218.26	3,213.01	278.40
0.00	90.00	60.00	118.11	3,209.51		278.40
0.00	90.00	60.00	118.11	3,209.51		278.30
0.00	90.00	60.00	118.11	3,218.26		278.10
0.00	90.00	60.00	118.11	3,209.51		278.10
0.00	90.00	60.00	118.11	3,183.56	3,180.14	713.70
0.00	90.00	60.00	118.11	3,183.56		713.60
0.00	90.00	60.00	118.11	3,183.56		713.50
0.00	90.00	60.00	118.11	3,175.00		713.50
0.00	90.00	60.00	118.11	3,175.00		713.40
0.00	90.00	60.00	118.11	3,075.78	3,077.39	385.30
0.00	90.00	60.00	118.11	3,083.82		385.10
0.00	90.00	60.00	118.11	3,075.78		385.10
0.00	90.00	60.00	118.11	3,075.78		385.00
0.00	90.00	60.00	118.11	3,075.78		384.90
0.00	90.00	60.00	118.11	2,975.07	2,978.07	375.70
0.00	90.00	60.00	118.11	2,975.07		375.60
0.00	90.00	60.00	118.11	2,982.58		375.40
0.00	90.00	60.00	118.11	2,975.07		375.40

0.00	90.00	60.00	118.11	2,982.58		375.30
0.00	90.00	60.00	118.11	2,916.30		490.30
0.00	90.00	60.00	118.11	2,923.52		490.10
0.00	90.00	60.00	118.11	2,909.12	2,920.64	490.20
0.00	90.00	60.00	118.11	2,923.52		489.90
0.00	90.00	60.00	118.11	2,930.77		489.80
0.00	90.00	60.00	118.11	2,894.86		459.60
0.00	90.00	60.00	118.11	2,901.97		459.50
0.00	90.00	60.00	118.11	2,901.97	2,900.55	459.40
0.00	90.00	60.00	118.11	2,901.97		459.30
0.00	90.00	60.00	118.11	2,901.97		459.20
0.00	90.00	60.00	118.11	3,108.16		478.60
0.00	90.00	60.00	118.11	3,108.16		478.50
0.00	90.00	60.00	118.11	3,108.16	3,108.16	478.40
0.00	90.00	60.00	118.11	3,108.16		478.30
0.00	90.00	60.00	118.11	3,108.16		478.30
0.00	90.00	60.00	118.11	3,100.00		581.50
0.00	90.00	60.00	118.11	3,108.16		581.40
0.00	90.00	60.00	118.11	3,108.16	3,106.53	581.30
0.00	90.00	60.00	118.11	3,108.16		581.20
0.00	90.00	60.00	118.11	3,108.16		581.10
0.00	90.00	60.00	118.11	4,374.45		434.60
0.00	90.00	60.00	118.11	4,374.45		434.50
0.00	90.00	60.00	118.11	4,374.45	4,380.95	434.50
0.00	90.00	60.00	118.11	4,390.71		434.30
0.00	90.00	60.00	118.11	4,390.71		434.20
0.00	90.00	60.00	118.11	2,529.12		87.10
0.00	90.00	60.00	118.11	2,507.65		87.40
0.00	90.00	60.00	118.11	2,507.65	2,515.17	87.30
0.00	90.00	60.00	118.11	2,529.12		86.80
0.00	90.00	60.00	118.11	2,502.33		87.20
0.00	90.00	60.00	118.11	2,545.48		382.20
0.00	90.00	60.00	118.11	2,550.97		382.00
0.00	90.00	60.00	118.11	2,545.48	2,544.39	382.00
0.00	90.00	60.00	118.11	2,545.48		381.90
0.00	90.00	60.00	118.11	2,534.55		382.00
0.00	90.00	60.00	118.11	3,158.02		369.10
0.00	90.00	60.00	118.11	3,158.02		369.00
0.00	90.00	60.00	118.11	3,158.02	3,159.72	368.90
0.00	90.00	60.00	118.11	3,158.02		368.80
0.00	90.00	60.00	118.11	3,166.49		368.60
0.00	90.00	60.00	118.11	2,997.72		618.60
0.00	90.00	60.00	118.11	3,005.35		618.40
0.00	90.00	60.00	118.11	2,997.72	3,000.77	618.40
0.00	90.00	60.00	118.11	3,005.35		618.20
0.00	90.00	60.00	118.11	2,997.72		618.20
0.00	90.00	60.00	118.11	3,013.01		290.30
0.00	90.00	60.00	118.11	3,013.01		290.20
0.00	90.00	60.00	118.11	3,020.72	3,014.55	290.00
0.00	90.00	60.00	118.11	3,013.01		290.00
0.00	90.00	60.00	118.11	3,013.01		289.90
0.00	90.00	60.00	118.11	2,990.13		618.50
0.00	90.00	60.00	118.11	2,997.72		618.30
0.00	90.00	60.00	118.11	2,990.13	2,994.69	618.30
0.00	90.00	60.00	118.11	2,990.13		618.20

0.00	90.00	60.00	118.11	3,005.35		618.00
0.00	90.00	60.00	118.11	3,280.84	3,275.38	504.00
0.00	90.00	60.00	118.11	3,271.75		504.00
0.00	90.00	60.00	118.11	3,271.75		503.90
0.00	90.00	60.00	118.11	3,280.84		503.70
0.00	90.00	60.00	118.11	3,271.75		503.70
0.00	90.00	60.00	118.11	3,020.72	3,020.73	940.90
0.00	90.00	60.00	118.11	3,020.72		940.80
0.00	90.00	60.00	118.11	3,013.01		940.80
0.00	90.00	60.00	118.11	3,020.72		940.60
0.00	90.00	60.00	118.11	3,028.46		940.50
0.00	90.00	60.00	118.11	3,028.46	3,030.02	75.00
0.00	90.00	60.00	118.11	3,028.46		74.90
0.00	90.00	60.00	118.11	3,028.46		74.80
0.00	90.00	60.00	118.11	3,028.46		74.80
0.00	90.00	60.00	118.11	3,036.25		74.60
0.00	90.00	60.00	118.11	3,083.82	3,079.00	884.90
0.00	90.00	60.00	118.11	3,075.78		884.90
0.00	90.00	60.00	118.11	3,075.78		884.80
0.00	90.00	60.00	118.11	3,083.82		884.70
0.00	90.00	60.00	118.11	3,075.78		884.70
0.00	90.00	60.00	118.11	3,100.00	3,093.51	771.10
0.00	90.00	60.00	118.11	3,091.89		771.10
0.00	90.00	60.00	118.11	3,091.89		771.00
0.00	90.00	60.00	118.11	3,091.89		770.90
0.00	90.00	60.00	118.11	3,091.89		770.80
0.00	90.00	60.00	118.11	3,116.36	3,116.37	436.40
0.00	90.00	60.00	118.11	3,108.16		436.40
0.00	90.00	60.00	118.11	3,116.36		436.20
0.00	90.00	60.00	118.11	3,124.61		436.10
0.00	90.00	60.00	118.11	3,116.36		436.10
0.00	90.00	60.00	118.11	2,997.72	2,997.72	1,029.70
0.00	90.00	60.00	118.11	2,997.72		1,029.70
0.00	90.00	60.00	118.11	2,997.72		1,029.60
0.00	90.00	60.00	118.11	2,997.72		1,029.50
0.00	90.00	60.00	118.11	2,997.72		1,029.40
120.00	225.00	60.00	226.99	3,362.83	3,359.85	93.40
120.00	225.00	60.00	226.99	3,362.83		93.30
120.00	225.00	60.00	226.99	3,357.86		93.30
120.00	225.00	60.00	226.99	3,357.86		93.20
120.00	225.00	60.00	226.99	3,357.86		93.20
120.00	225.00	60.00	226.99	3,275.49	3,276.44	366.40
120.00	225.00	60.00	226.99	3,280.22		366.30
120.00	225.00	60.00	226.99	3,280.22		366.20
120.00	225.00	60.00	226.99	3,275.49		366.20
120.00	225.00	60.00	226.99	3,270.77		366.20
120.00	225.00	60.00	226.99	3,284.97	3,279.28	155.90
120.00	225.00	60.00	226.99	3,275.49		156.00
120.00	225.00	60.00	226.99	3,275.49		155.90
120.00	225.00	60.00	226.99	3,280.22		155.70
120.00	225.00	60.00	226.99	3,280.22		155.60
120.00	225.00	60.00	226.99	3,270.77	3,272.66	242.70
120.00	225.00	60.00	226.99	3,266.06		242.70
120.00	225.00	60.00	226.99	3,275.49		242.50
120.00	225.00	60.00	226.99	3,275.49		242.40

120.00	225.00	60.00	226.99	3,275.49		242.30
120.00	225.00	60.00	226.99	3,299.29		81.30
120.00	225.00	60.00	226.99	3,304.09		81.10
120.00	225.00	60.00	226.99	3,299.29	3,299.29	81.10
120.00	225.00	60.00	226.99	3,294.50		81.10
120.00	225.00	60.00	226.99	3,299.29		80.90
120.00	225.00	60.00	226.99	2,978.89		145.60
120.00	225.00	60.00	226.99	2,982.80		145.40
120.00	225.00	60.00	226.99	2,990.66	2,982.02	145.20
120.00	225.00	60.00	226.99	2,978.89		145.30
120.00	225.00	60.00	226.99	2,978.89		145.30
120.00	225.00	60.00	226.99	3,352.90		86.20
120.00	225.00	60.00	226.99	3,367.82		85.80
120.00	225.00	60.00	226.99	3,352.90	3,355.88	86.00
120.00	225.00	60.00	226.99	3,352.90		85.90
120.00	225.00	60.00	226.99	3,352.90		85.80
120.00	225.00	60.00	226.99	3,318.58		738.40
120.00	225.00	60.00	226.99	3,308.91		738.60
120.00	225.00	60.00	226.99	3,318.58	3,321.52	738.30
120.00	225.00	60.00	226.99	3,328.32		738.00
120.00	225.00	60.00	226.99	3,333.20		737.80
120.00	225.00	60.00	226.99	3,092.52		136.00
120.00	225.00	60.00	226.99	3,084.12		136.10
120.00	225.00	60.00	226.99	3,088.32	3,090.00	136.00
120.00	225.00	60.00	226.99	3,096.74		135.70
120.00	225.00	60.00	226.99	3,088.32		135.80
120.00	225.00	60.00	226.99	3,092.52		1,020.60
120.00	225.00	60.00	226.99	3,079.93		1,020.80
120.00	225.00	60.00	226.99	3,075.76	3,086.66	1,020.80
120.00	225.00	60.00	226.99	3,084.12		1,020.50
120.00	225.00	60.00	226.99	3,100.97		1,020.00
120.00	225.00	60.00	226.99	1,792.98		835.60
120.00	225.00	60.00	226.99	1,792.98		835.60
120.00	225.00	60.00	226.99	1,795.82	1,794.40	835.30
120.00	225.00	60.00	226.99	1,800.09		834.90
120.00	225.00	60.00	226.99	1,790.15		835.50
120.00	225.00	60.00	226.99	2,895.30		484.80
120.00	225.00	60.00	226.99	2,898.99		484.60
120.00	225.00	60.00	226.99	2,898.99	2,898.25	484.50
120.00	225.00	60.00	226.99	2,898.99		484.40
120.00	225.00	60.00	226.99	2,898.99		484.40
120.00	225.00	60.00	226.99	2,928.92		738.00
120.00	225.00	60.00	226.99	3,030.59		735.30
120.00	225.00	60.00	226.99	2,925.14	2,976.96	737.90
120.00	225.00	60.00	226.99	2,932.70		737.70
120.00	225.00	60.00	226.99	3,067.45		734.20
120.00	225.00	60.00	226.99	3,338.11		247.50
120.00	225.00	60.00	226.99	3,343.02		247.30
120.00	225.00	60.00	226.99	3,347.95	3,343.02	247.20
120.00	225.00	60.00	226.99	3,343.02		247.20
120.00	225.00	60.00	226.99	3,343.02		247.10
120.00	225.00	60.00	226.99	3,266.06		986.10
120.00	225.00	60.00	226.99	3,284.97		985.60
120.00	225.00	60.00	226.99	3,289.73	3,275.52	985.40
120.00	225.00	60.00	226.99	3,270.77		985.80

120.00	225.00	60.00	226.99	3,266.06		985.80
120.00	225.00	60.00	226.99	3,434.06		823.40
120.00	225.00	60.00	226.99	3,454.96		823.00
120.00	225.00	60.00	226.99	3,465.51	3,455.01	822.70
120.00	225.00	60.00	226.99	3,470.81		822.50
120.00	225.00	60.00	226.99	3,449.71		822.80
120.00	225.00	60.00	226.99	3,343.02		191.00
120.00	225.00	60.00	226.99	3,338.11		191.00
120.00	225.00	60.00	226.99	3,347.95	3,344.01	190.70
120.00	225.00	60.00	226.99	3,347.95		190.70
120.00	225.00	60.00	226.99	3,343.02		190.70
120.00	225.00	60.00	226.99	3,372.83		941.90
120.00	225.00	60.00	226.99	3,377.85		941.70
120.00	225.00	60.00	226.99	3,367.82	3,369.85	941.80
120.00	225.00	60.00	226.99	3,377.85		941.50
120.00	225.00	60.00	226.99	3,352.90		941.90
120.00	225.00	60.00	226.99	1,590.69		596.00
120.00	225.00	60.00	226.99	1,589.57		596.00
120.00	225.00	60.00	226.99	1,589.57	1,590.02	595.90
120.00	225.00	60.00	226.99	1,590.69		595.70
120.00	225.00	60.00	226.99	1,589.57		595.70
120.00	225.00	60.00	226.99	1,871.32		405.40
120.00	225.00	60.00	226.99	1,871.32		405.30
120.00	225.00	60.00	226.99	1,874.41	1,872.87	405.00
120.00	225.00	60.00	226.99	1,872.86		405.00
120.00	225.00	60.00	226.99	1,874.41		404.80
120.00	225.00	60.00	226.99	2,648.67		440.80
120.00	225.00	60.00	226.99	56.02		4,407.00
120.00	225.00	60.00	226.99	2,648.67	2,128.91	440.60
120.00	225.00	60.00	226.99	2,648.67		440.50
120.00	225.00	60.00	226.99	2,642.51		440.60
120.00	225.00	60.00	226.99	2,561.98		192.20
120.00	225.00	60.00	226.99	2,553.33		192.40
120.00	225.00	60.00	226.99	2,559.09	2,556.79	192.10
120.00	225.00	60.00	226.99	2,559.09		192.10
120.00	225.00	60.00	226.99	2,550.46		192.30
120.00	225.00	60.00	226.99	1,961.89		1,017.40
120.00	225.00	60.00	226.99	1,960.20		1,017.40
120.00	225.00	60.00	226.99	1,961.89	2,073.04	1,017.20
120.00	225.00	60.00	226.99	2,519.33		991.50
120.00	225.00	60.00	226.99	1,961.89		1,017.10
120.00	225.00	60.00	226.99	3,152.66		589.00
120.00	225.00	60.00	226.99	3,157.04		588.80
120.00	225.00	60.00	226.99	3,152.66	3,155.29	588.80
120.00	225.00	60.00	226.99	3,157.04		588.70
120.00	225.00	60.00	226.99	3,157.04		588.60
120.00	225.00	60.00	226.99	3,113.73		171.60
120.00	225.00	60.00	226.99	3,109.47		171.60
120.00	225.00	60.00	226.99	3,118.01	3,113.74	171.30
120.00	225.00	60.00	226.99	3,113.73		171.30
120.00	225.00	60.00	226.99	3,113.73		171.30
120.00	225.00	60.00	226.99	3,170.27		798.00
120.00	225.00	60.00	226.99	3,170.27		797.90
120.00	225.00	60.00	226.99	3,284.97	3,220.86	795.30
120.00	225.00	60.00	226.99	3,304.09		794.80

120.00	225.00	60.00	226.99	3,174.70		797.50
120.00	225.00	60.00	226.99	3,161.44	3,234.62	228.50
120.00	225.00	60.00	226.99	3,275.49		225.90
120.00	225.00	60.00	226.99	3,161.44		228.30
120.00	225.00	60.00	226.99	3,280.22		225.70
120.00	225.00	60.00	226.99	3,294.50		225.30
120.00	225.00	60.00	226.99	3,130.91	3,130.92	621.40
120.00	225.00	60.00	226.99	3,130.91		621.30
120.00	225.00	60.00	226.99	3,130.91		621.20
120.00	225.00	60.00	226.99	3,135.24		621.10
120.00	225.00	60.00	226.99	3,126.60		621.20
0.00	180.00	120.00	236.22	3,840.98	3,906.12	418.00
0.00	180.00	120.00	236.22	3,840.98		417.90
0.00	180.00	120.00	236.22	3,840.98		417.80
0.00	180.00	120.00	236.22	3,983.48		415.60
0.00	180.00	120.00	236.22	4,024.19		414.90
0.00	180.00	120.00	236.22	3,584.53	3,583.45	228.70
0.00	180.00	120.00	236.22	3,584.53		228.60
0.00	180.00	120.00	236.22	3,584.53		228.50
0.00	180.00	120.00	236.22	3,573.68		228.60
0.00	180.00	120.00	236.22	3,589.97		228.20
0.00	180.00	120.00	236.22	3,345.90	3,386.04	270.60
0.00	180.00	120.00	236.22	3,453.51		268.30
0.00	180.00	120.00	236.22	3,341.16		270.50
0.00	180.00	120.00	236.22	3,448.47		268.20
0.00	180.00	120.00	236.22	3,341.16		270.30
0.00	180.00	120.00	236.22	3,091.89	3,091.89	588.80
0.00	180.00	120.00	236.22	3,091.89		588.70
0.00	180.00	120.00	236.22	3,095.94		588.60
0.00	180.00	120.00	236.22	3,091.89		588.50
0.00	180.00	120.00	236.22	3,087.85		588.60
0.00	180.00	120.00	236.22	3,055.89	3,050.37	470.20
0.00	180.00	120.00	236.22	3,051.94		470.20
0.00	180.00	120.00	236.22	3,048.00		470.20
0.00	180.00	120.00	236.22	3,048.00		470.10
0.00	180.00	120.00	236.22	3,048.00		470.00
0.00	180.00	120.00	236.22	3,213.88	3,213.01	346.50
0.00	180.00	120.00	236.22	3,209.51		346.60
0.00	180.00	120.00	236.22	3,213.88		346.40
0.00	180.00	120.00	236.22	3,218.26		346.20
0.00	180.00	120.00	236.22	3,209.51		346.30
0.00	180.00	120.00	236,22	3285,40	3288,15	231,90
0.00	180.00	120.00	236,22	3294,56		231,60
0.00	180.00	120.00	236,22	3285,40		231,70
0.00	180.00	120.00	236,22	3285,40		231,60
0.00	180.00	120.00	236,22	3289,98		231,40
0.00	180.00	120.00	236,22	3175,00	3173,30	156,90
0.00	180.00	120.00	236,22	3175,00		156,80
0.00	180.00	120.00	236,22	3175,00		156,70
0.00	180.00	120.00	236,22	3170,74		156,70
0.00	180.00	120.00	236,22	3170,74		156,60
0.00	180.00	120.00	236.22	3,149.60		359.40
0.00	180.00	120.00	236.22	3,327.05		358.40
0.00	180.00	120.00	236.22	3,327.05	3,256.07	358.40

0.00	180.00	120.00	236.22	3,327.05		358.40
0.00	180.00	120.00	236.22	3,149.60		358.40
0.00	180.00	120.00	236.22	3,192.17		643.60
0.00	180.00	120.00	236.22	3,028.46		643.60
0.00	180.00	120.00	236.22	3,028.46	3,061.20	643.60
0.00	180.00	120.00	236.22	3,028.46		643.60
0.00	180.00	120.00	236.22	3,028.46		643.60
0.00	180.00	120.00	236.22	2,540.00		888.80
0.00	180.00	120.00	236.22	2,540.00		888.80
0.00	180.00	120.00	236.22	2,540.00	2,534.60	888.80
0.00	180.00	120.00	236.22	2,540.00		888.80
0.00	180.00	120.00	236.22	2,512.98		888.80
0.00	180.00	120.00	236.22	792.69		902.60
0.00	180.00	120.00	236.22	790.03		902.60
0.00	180.00	120.00	236.22	792.69	792.16	901.60
0.00	180.00	120.00	236.22	792.69		901.60
0.00	180.00	120.00	236.22	792.69		901.60
0.00	180.00	120.00	236.22	811.75		626.60
0.00	180.00	120.00	236.22	811.75		626.60
0.00	180.00	120.00	236.22	808.97	810.09	626.60
0.00	180.00	120.00	236.22	808.97		626.60
0.00	180.00	120.00	236.22	808.97		626.60
0.00	180.00	120.00	236.22	3,280.84		295.70
0.00	180.00	120.00	236.22	3,280.84		295.70
0.00	180.00	120.00	236.22	3,280.84	3,280.84	295.70
0.00	180.00	120.00	236.22	3,280.84		295.70
0.00	180.00	120.00	236.22	3,280.84		295.70
0.00	180.00	120.00	236.22	2,654.16		179.00
0.00	180.00	120.00	236.22	2,567.61		179.00
0.00	180.00	120.00	236.22	2,654.16	2,596.71	179.00
0.00	180.00	120.00	236.22	2,540.00		179.00
0.00	180.00	120.00	236.22	2,567.61		178.00
0.00	180.00	120.00	236.22	2,779.06		832.60
0.00	180.00	120.00	236.22	2,779.06		832.60
0.00	180.00	120.00	236.22	2,779.06	2,779.06	832.60
0.00	180.00	120.00	236.22	2,779.06		832.60
0.00	180.00	120.00	236.22	2,779.06		832.60
0.00	180.00	120.00	236.22	2,654.16		950.50
0.00	180.00	120.00	236.22	2,779.06		946.50
0.00	180.00	120.00	236.22	2,779.06	2,754.08	946.50
0.00	180.00	120.00	236.22	2,779.06		946.50
0.00	180.00	120.00	236.22	2,779.06		946.50
0.00	180.00	120.00	236.22	620.00		452.30
0.00	180.00	120.00	236.22	620.00		452.30
0.00	180.00	120.00	236.22	618.38	619.03	452.30
0.00	180.00	120.00	236.22	618.38		452.30
0.00	180.00	120.00	236.22	618.38		452.30
0.00	180.00	120.00	236.22	3,192.17		955.50
0.00	180.00	120.00	236.22	3,374.57		955.50
0.00	180.00	120.00	236.22	3,192.17	3,247.11	955.50
0.00	180.00	120.00	236.22	3,327.05		955.50
0.00	180.00	120.00	236.22	3,149.60		955.50
0.00	180.00	120.00	236.22	3,327.05		577.90
0.00	180.00	120.00	236.22	3,473.83		574.90

0.00	180.00	120.00	236.22	3,473.83	3,444.47	574.90
0.00	180.00	120.00	236.22	3,473.83		574.90
0.00	180.00	120.00	236.22	3,473.83		574.90
0.00	180.00	120.00	236.22	3,149.60		904.90
0.00	180.00	120.00	236.22	3,149.60		904.90
0.00	180.00	120.00	236.22	3,327.05	3,220.58	904.90
0.00	180.00	120.00	236.22	3,149.60		904.90
0.00	180.00	120.00	236.22	3,327.05		904.90
0.00	180.00	120.00	236.22	4,144.21		678.20
0.00	180.00	120.00	236.22	3,634.16		682.20
0.00	180.00	120.00	236.22	3,634.16	3,714.14	682.20
0.00	180.00	120.00	236.22	3,579.09		682.20
0.00	180.00	120.00	236.22	3,579.09		682.20
0.00	180.00	120.00	236.22	3,579.09		677.10
0.00	180.00	120.00	236.22	3,579.09		677.10
0.00	180.00	120.00	236.22	3,579.09	3,601.12	677.10
0.00	180.00	120.00	236.22	3,634.16		676.10
0.00	180.00	120.00	236.22	3,634.16		676.10
0.00	180.00	120.00	236.22	3,322.37		872.90
0.00	180.00	120.00	236.22	3,331.74		872.70
0.00	180.00	120.00	236.22	3,327.05	3,328.93	872.70
0.00	180.00	120.00	236.22	3,331.74		872.50
0.00	180.00	120.00	236.22	3,331.74		872.40
0.00	180.00	120.00	236.22	3,253.72		812.00
0.00	180.00	120.00	236.22	3,249.25		812.00
0.00	180.00	120.00	236.22	3,244.78	3,249.25	812.00
0.00	180.00	120.00	236.22	3,244.78		811.90
0.00	180.00	120.00	236.22	3,253.72		811.70
0.00	180.00	120.00	236.22	3,355.40		1,034.00
0.00	180.00	120.00	236.22	3,355.40		1,033.90
0.00	180.00	120.00	236.22	3,355.40	3,354.45	1,033.80
0.00	180.00	120.00	236.22	3,355.40		1,033.70
0.00	180.00	120.00	236.22	3,350.64		1,033.70
0.00	180.00	120.00	236,22	3433,43		661,60
0.00	180.00	120.00	236,22	3433,43		661,50
0.00	180.00	120.00	236,22	3433,43	3433,44	661,40
0.00	180.00	120.00	236,22	3438,43		661,20
0.00	180.00	120.00	236,22	3428,45		661,30
0.00	180.00	120.00	236,22	3175,00		156,90
0.00	180.00	120.00	236,22	3175,00		156,80
0.00	180.00	120.00	236,22	3175,00	3173,30	156,70
0.00	180.00	120.00	236,22	3170,74		156,70
0.00	180.00	120.00	236,22	3170,74		156,60
200.00	375.00	100.00	378.32	3,377.85		517.90
200.00	375.00	100.00	378.32	3,502.95		517.90
200.00	375.00	100.00	378.32	3,502.95	3,477.93	517.90
200.00	375.00	100.00	378.32	3,502.95		517.90
200.00	375.00	100.00	378.32	3,502.95		517.90
200.00	375.00	100.00	378.32	2,910.14	2,929.24	887.60
200.00	375.00	100.00	378.32	2,910.14		887.60
200.00	375.00	100.00	378.32	3,002.53		887.60
200.00	375.00	100.00	378.32	2,978.89		888.60
200.00	375.00	100.00	378.32	2,844.50		895.60
200.00	375.00	100.00	378.32	2,349.81		315.20

200.00	375.00	100.00	378.32	2,394.42		312.20
200.00	375.00	100.00	378.32	2,349.81	2,367.65	315.20
200.00	375.00	100.00	378.32	2,349.81		315.20
200.00	375.00	100.00	378.32	2,394.42		312.20
200.00	375.00	100.00	378.32	2,664.22		394.40
200.00	375.00	100.00	378.32	2,741.44		394.40
200.00	375.00	100.00	378.32	2,664.22	2,710.55	394.40
200.00	375.00	100.00	378.32	2,741.44		394.40
200.00	375.00	100.00	378.32	2,741.44		394.40
200.00	375.00	100.00	378.32	2,349.81		979.80
200.00	375.00	100.00	378.32	2,349.81		979.80
200.00	375.00	100.00	378.32	2,292.84	2,347.34	979.80
200.00	375.00	100.00	378.32	2,349.81		979.80
200.00	375.00	100.00	378.32	2,394.42		976.80
200.00	375.00	100.00	378.32	2,866.05		612.20
200.00	375.00	100.00	378.32	2,866.05		612.20
200.00	375.00	100.00	378.32	2,955.61	2,919.79	612.20
200.00	375.00	100.00	378.32	2,955.61		612.20
200.00	375.00	100.00	378.32	2,955.61		612.20
200.00	375.00	100.00	378.32	3,002.53		700.00
200.00	375.00	100.00	378.32	3,002.53		700.00
200.00	375.00	100.00	378.32	3,002.53	3,002.53	700.00
200.00	375.00	100.00	378.32	3,002.53		700.00
200.00	375.00	100.00	378.32	3,002.53		700.00
200.00	375.00	100.00	378.32	3,026.55		1,017.00
200.00	375.00	100.00	378.32	3,002.53		1,018.00
200.00	375.00	100.00	378.32	3,026.55	3,021.75	1,017.00
200.00	375.00	100.00	378.32	3,026.55		1,017.00
200.00	375.00	100.00	378.32	3,026.55		1,017.00
200.00	375.00	100.00	378.32	3,126.60		197.20
200.00	375.00	100.00	378.32	3,126.60		197.20
200.00	375.00	100.00	378.32	3,126.60	3,121.47	197.20
200.00	375.00	100.00	378.32	3,126.60		197.20
200.00	375.00	100.00	378.32	3,100.97		197.20
200.00	375.00	100.00	378.32	3,050.96		647.10
200.00	375.00	100.00	378.32	3,050.96		647.10
200.00	375.00	100.00	378.32	3,050.96	3,050.96	647.10
200.00	375.00	100.00	378.32	3,050.96		647.10
200.00	375.00	100.00	378.32	3,050.96		647.10
200.00	375.00	100.00	378.32	2,932.70		988.70
200.00	375.00	100.00	378.32	3,100.97		985.70
200.00	375.00	100.00	378.32	3,002.53	3,032.75	985.70
200.00	375.00	100.00	378.32	3,100.97		985.70
200.00	375.00	100.00	378.32	3,026.55		985.70
200.00	375.00	100.00	378.32	3,075.76		675.30
200.00	375.00	100.00	378.32	3,075.76		675.30
200.00	375.00	100.00	378.32	3,050.96	3,060.88	675.30
200.00	375.00	100.00	378.32	3,050.96		675.30
200.00	375.00	100.00	378.32	3,050.96		675.30
200.00	375.00	100.00	378.32	3,075.76		127.90
200.00	375.00	100.00	378.32	3,075.76		127.90
200.00	375.00	100.00	378.32	3,050.96	3,060.88	127.90
200.00	375.00	100.00	378.32	3,050.96		127.90
200.00	375.00	100.00	378.32	3,050.96		127.90
200.00	375.00	100.00	378.32	3,206.09		835.70

200.00	375.00	100.00	378.32	3,206.09	2,991.32	835.70
200.00	375.00	100.00	378.32	3,100.97		835.70
200.00	375.00	100.00	378.32	2,721.72		852.70
200.00	375.00	100.00	378.32	2,721.72		852.70
200.00	375.00	100.00	378.32	2,910.14	3,087.71	772.10
200.00	375.00	100.00	378.32	3,206.09		760.10
200.00	375.00	100.00	378.32	3,206.09		760.10
200.00	375.00	100.00	378.32	2,910.14		772.10
200.00	375.00	100.00	378.32	3,206.09		760.10
200.00	375.00	100.00	378.32	2,265.38	2,271.63	574.00
200.00	375.00	100.00	378.32	2,225.40		573.00
200.00	375.00	100.00	378.32	2,320.97		570.00
200.00	375.00	100.00	378.32	2,225.40		573.00
200.00	375.00	100.00	378.32	2,320.97		570.00
200.00	375.00	100.00	378.32	3,347.95	3,347.95	339.00
200.00	375.00	100.00	378.32	3,347.95		339.00
200.00	375.00	100.00	378.32	3,347.95		339.00
200.00	375.00	100.00	378.32	3,347.95		339.00
200.00	375.00	100.00	378.32	3,347.95		339.00
200.00	375.00	100.00	378.32	3,289.73	3,278.38	1,082.00
200.00	375.00	100.00	378.32	3,289.73		1,082.00
200.00	375.00	100.00	378.32	3,289.73		1,082.00
200.00	375.00	100.00	378.32	3,261.37		1,082.00
200.00	375.00	100.00	378.32	3,261.37		1,082.00
200.00	375.00	100.00	378.32	3,368.82	3,370.02	602.60
200.00	375.00	100.00	378.32	3,368.82		602.60
200.00	375.00	100.00	378.32	3,368.82		602.50
200.00	375.00	100.00	378.32	3,371.82		602.30
200.00	375.00	100.00	378.32	3,371.82		602.20
200.00	375.00	100.00	378,32	3342,04	3342,04	489,90
200.00	375.00	100.00	378,32	3342,04		489,90
200.00	375.00	100.00	378,32	3342,04		489,80
200.00	375.00	100.00	378,32	3342,04		489,70
200.00	375.00	100.00	378,32	3342,04		489,60
200.00	375.00	100.00	378,32	3399,09	3399,70	369,60
200.00	375.00	100.00	378,32	3396,04		369,60
200.00	375.00	100.00	378,32	3399,09		369,40
200.00	375.00	100.00	378,32	3402,15		369,30
200.00	375.00	100.00	378,32	3402,15		369,20
200.00	375.00	100.00	378,32	3389,95	3389,35	778,50
200.00	375.00	100.00	378,32	3386,92		778,50
200.00	375.00	100.00	378,32	3389,95		778,30
200.00	375.00	100.00	378,32	3389,95		778,30
200.00	375.00	100.00	378,32	3389,95		778,20
200.00	375.00	100.00	378,32	3402,15	3403,98	537,30
200.00	375.00	100.00	378,32	3408,28		537,00
200.00	375.00	100.00	378,32	3402,15		537,10
200.00	375.00	100.00	378,32	3405,21		536,90
200.00	375.00	100.00	378,32	3402,15		536,90
200.00	375.00	100.00	378,32	3024,13	3026,07	293,00
200.00	375.00	100.00	378,32	3026,55		292,80
200.00	375.00	100.00	378,32	3024,13		292,80
200.00	375.00	100.00	378,32	3031,40		292,50
200.00	375.00	100.00	378,32	3024,13		292,60
200.00	375.00	100.00	378,32	3058,36		452,00

200.00	375.00	100.00	378,32	3058,36	3058,36	451,90
200.00	375.00	100.00	378,32	3055,89		451,90
200.00	375.00	100.00	378,32	3055,89		451,80
200.00	375.00	100.00	378,32	3063,31		451,50
200.00	375.00	100.00	378,32	3173,81	3171,16	231,20
200.00	375.00	100.00	378,32	3160,56		231,70
200.00	375.00	100.00	378,32	3173,81		231,10
200.00	375.00	100.00	378,32	3171,15		231,10
200.00	375.00	100.00	378,32	3176,48		230,80
200.00	375.00	100.00	378,32	3106,06	3105,55	904,00
200.00	375.00	100.00	378,32	3106,06		903,90
200.00	375.00	100.00	378,32	3106,06		903,80
200.00	375.00	100.00	378,32	3103,52		903,80
200.00	375.00	100.00	378,32	3106,06		903,60
200.00	375.00	100.00	378,32	2990,66	2989,25	388,00
200.00	375.00	100.00	378,32	2988,30		388,00
200.00	375.00	100.00	378,32	2990,66		387,90
200.00	375.00	100.00	378,32	2993,03		387,70
200.00	375.00	100.00	378,32	2983,59		388,00
240.00	450.00	120.00	453.98	3,439.26	3,471.25	931.90
240.00	450.00	120.00	453.98	3,439.26		931.90
240.00	450.00	120.00	453.98	3,439.26		932.90
240.00	450.00	120.00	453.98	3,519.24		932.90
240.00	450.00	120.00	453.98	3,519.24		932.90
240.00	450.00	120.00	453.98	3,026.55	3,067.84	1,122.50
240.00	450.00	120.00	453.98	3,026.55		1,122.50
240.00	450.00	120.00	453.98	3,109.47		1,122.50
240.00	450.00	120.00	453.98	3,088.32		1,123.50
240.00	450.00	120.00	453.98	3,088.32		1,123.50
240.00	450.00	120.00	453,98	1935,13	1932,50	638,70
240.00	450.00	120.00	453,98	1931,02		639,10
240.00	450.00	120.00	453,98	1934,31		638,60
240.00	450.00	120.00	453,98	1931,84		638,80
240.00	450.00	120.00	453,98	1930,20		639,00
240.00	450.00	120.00	453,98	928,01	1349,55	1410,40
240.00	450.00	120.00	453,98	1492,87		1225,20
240.00	450.00	120.00	453,98	1440,30		1236,30
240.00	450.00	120.00	453,98	1442,59		1235,70
240.00	450.00	120.00	453,98	1443,96		1235,30
240.00	450.00	120.00	453,98	754,25	754,42	896,00
240.00	450.00	120.00	453,98	754,37		895,80
240.00	450.00	120.00	453,98	754,62		895,50
240.00	450.00	120.00	453,98	754,37		895,70
240.00	450.00	120.00	453,98	754,50		895,50
240.00	450.00	120.00	453,98	1525,48	1525,99	489,60
240.00	450.00	120.00	453,98	1528,56		488,90
240.00	450.00	120.00	453,98	1524,45		489,60
240.00	450.00	120.00	453,98	1527,02		489,00
240.00	450.00	120.00	453,98	1524,45		489,40
240.00	450.00	120.00	453,98	1587,35	1587,35	762,30
240.00	450.00	120.00	453,98	1587,91		762,10
240.00	450.00	120.00	453,98	1587,35		762,10
240.00	450.00	120.00	453,98	1586,80		762,10
240.00	450.00	120.00	453,98	1587,35		762,00
240.00	450.00	120.00	453,98	1595,72		1247,90

240.00	450.00	120.00	453,98	1594,60		1248,00
240.00	450.00	120.00	453,98	1595,72	1595,27	1247,70
240.00	450.00	120.00	453,98	1596,28		1247,60
240.00	450.00	120.00	453,98	1594,04		1247,90
240.00	450.00	120.00	453,98	3210,63		453,90
240.00	450.00	120.00	453,98	3215,17		453,60
240.00	450.00	120.00	453,98	3206,09	3211,09	453,90
240.00	450.00	120.00	453,98	3206,09		453,80
240.00	450.00	120.00	453,98	3217,45		453,20
240.00	450.00	120.00	453,98	3228,89		176,90
240.00	450.00	120.00	453,98	3224,31		177,00
240.00	450.00	120.00	453,98	3226,60	3201,93	176,90
240.00	450.00	120.00	453,98	3228,89		176,70
240.00	450.00	120.00	453,98	3100,97		176,80
240.00	450.00	120.00	453,98	1949,26		1058,40
240.00	450.00	120.00	453,98	1949,26		1058,30
240.00	450.00	120.00	453,98	1950,10	1949,76	1058,10
240.00	450.00	120.00	453,98	1950,93		1057,90
240.00	450.00	120.00	453,98	1949,26		1058,00
240.00	450.00	120.00	453.98	1,201.01		1,235.00
240.00	450.00	120.00	453.98	1,198.79		1,235.60
240.00	450.00	120.00	453.98	1,200.06	1,199.93	1,235.10
240.00	450.00	120.00	453.98	1,199.74		1,235.10
240.00	450.00	120.00	453.98	1,200.06		1,235.00
240.00	450.00	120.00	453.98	3,233.49		409.90
240.00	450.00	120.00	453.98	3,228.89		410.00
240.00	450.00	120.00	453.98	3,226.60	3,229.35	410.00
240.00	450.00	120.00	453.98	3,226.60		409.90
240.00	450.00	120.00	453.98	3,231.19		409.60
240.00	450.00	120.00	453,98	3210,63		1077,90
240.00	450.00	120.00	453,98	3206,09		1078,00
240.00	450.00	120.00	453,98	3210,63	3208,81	1077,70
240.00	450.00	120.00	453,98	3212,90		1077,50
240.00	450.00	120.00	453,98	3203,83		1077,80
240.00	450.00	120.00	453,98	3289,73		325,30
240.00	450.00	120.00	453,98	3292,11		325,20
240.00	450.00	120.00	453,98	3289,73	3290,20	325,20
240.00	450.00	120.00	453,98	3289,73		325,10
240.00	450.00	120.00	453,98	3289,73		325,00
240.00	450.00	120.00	453,98	1815,93		525,10
240.00	450.00	120.00	453,98	1820,30		524,40
240.00	450.00	120.00	453,98	1815,20	1819,28	525,00
240.00	450.00	120.00	453,98	1821,76		524,00
240.00	450.00	120.00	453,98	1823,22		523,70
240.00	450.00	120.00	453.98	1,472.06		1,200.80
240.00	450.00	120.00	453.98	1,476.85		1,199.70
240.00	450.00	120.00	453.98	1,261.76	1,524.17	1,252.00
240.00	450.00	120.00	453.98	2,015.91		1,117.30
240.00	450.00	120.00	453.98	1,394.29		1,217.60
240.00	450.00	120.00	453.98	1,248.92		414.40
240.00	450.00	120.00	453.98	1,247.89		414.60
240.00	450.00	120.00	453.98	1,247.89	1,249.13	414.50
240.00	450.00	120.00	453.98	1,251.33		413.40
240.00	450.00	120.00	453.98	1,249.61		413.80
240.00	450.00	120.00	453,98	3088,32		824,30

240.00	450.00	120.00	453,98	3084,12	3085,80	824,40
240.00	450.00	120.00	453,98	3084,12		824,30
240.00	450.00	120.00	453,98	3084,12		824,20
240.00	450.00	120.00	453,98	3088,32		823,90
240.00	450.00	120.00	453,98	3094,63	3097,17	367,70
240.00	450.00	120.00	453,98	3094,63		367,60
240.00	450.00	120.00	453,98	3100,97		367,30
240.00	450.00	120.00	453,98	3098,86		367,30
240.00	450.00	120.00	453,98	3096,74		367,30
240.00	450.00	120.00	453,98	3150,47	3153,53	1097,80
240.00	450.00	120.00	453,98	3152,66		1097,60
240.00	450.00	120.00	453,98	3157,04		1097,30
240.00	450.00	120.00	453,98	3154,85		1097,30
240.00	450.00	120.00	453,98	3152,66		1097,40
240.00	450.00	120.00	453.98	3,024.53	3,038.92	1,102.30
240.00	450.00	120.00	453.98	3,028.57		1,102.00
240.00	450.00	120.00	453.98	3,090.42		1,098.90
240.00	450.00	120.00	453.98	3,024.53		1,102.00
240.00	450.00	120.00	453.98	3,026.55		1,101.80
240.00	450.00	120.00	453.98	2,260.87	2,392.97	309.70
240.00	450.00	120.00	453.98	2,615.11		282.40
240.00	450.00	120.00	453.98	2,609.09		282.70
240.00	450.00	120.00	453.98	2,294.00		306.50
240.00	450.00	120.00	453.98	2,185.76		316.20
240.00	450.00	120.00	453,98	3201,57	3207,45	526,00
240.00	450.00	120.00	453,98	3206,09		525,70
240.00	450.00	120.00	453,98	3210,63		525,50
240.00	450.00	120.00	453,98	3210,63		525,40
240.00	450.00	120.00	453,98	3208,36		525,40
240.00	450.00	120.00	453,98	3201,57	3202,93	1092,50
240.00	450.00	120.00	453,98	3199,31		1092,60
240.00	450.00	120.00	453,98	3203,83		1092,30
240.00	450.00	120.00	453,98	3201,57		1092,30
240.00	450.00	120.00	453,98	3208,36		1091,90
240.00	450.00	120.00	453,98	3224,31	3224,31	616,50
240.00	450.00	120.00	453,98	3224,31		616,40
240.00	450.00	120.00	453,98	3222,02		616,40
240.00	450.00	120.00	453,98	3226,60		616,10
240.00	450.00	120.00	453,98	3224,31		616,10
240.00	450.00	120.00	453.98	3,219.73	3,224.78	188.30
240.00	450.00	120.00	453.98	3,217.45		188.30
240.00	450.00	120.00	453.98	3,226.60		187.80
240.00	450.00	120.00	453.98	3,224.31		187.80
240.00	450.00	120.00	453.98	3,235.80		187.20
240.00	450.00	120.00	453.98	3,277.85	3,277.86	365.20
240.00	450.00	120.00	453.98	3,273.12		365.40
240.00	450.00	120.00	453.98	3,280.22		365.00
240.00	450.00	120.00	453.98	3,273.12		365.20
240.00	450.00	120.00	453.98	3,284.97		364.60
0.00	180.00	120.00	236.22	3,685.18	3,688.64	284.60
0.00	180.00	120.00	236.22	3,690.94		284.40
0.00	180.00	120.00	236.22	3,685.18		284.40
0.00	180.00	120.00	236.22	3,696.72		284.10
0.00	180.00	120.00	236.22	3,685.18		284.20
0.00	180.00	120.00	236.22	2,415.34		501.40

0.00	180.00	120.00	236.22	3,509.96	3,313.21	470.80
0.00	180.00	120.00	236.22	3,536.23		470.20
0.00	180.00	120.00	236.22	3,568.28		469.60
0.00	180.00	120.00	236.22	3,536.23		470.10
0.00	180.00	120.00	236.22	3,379.40	3,388.16	736.70
0.00	180.00	120.00	236.22	3,403.75		736.10
0.00	180.00	120.00	236.22	3,374.57		736.70
0.00	180.00	120.00	236.22	3,389.10		736.30
0.00	180.00	120.00	236.22	3,393.97		736.10
0.00	180.00	120.00	236.22	2,241.18	1,988.25	946.20
0.00	180.00	120.00	236.22	1,817.08		970.70
0.00	180.00	120.00	236.22	1,825.50		970.00
0.00	180.00	120.00	236.22	2,234.82		946.30
0.00	180.00	120.00	236.22	1,822.69		970.00
0.00	180.00	120.00	236.22	3,509.96	3,505.80	830.30
0.00	180.00	120.00	236.22	3,509.96		830.20
0.00	180.00	120.00	236.22	3,494.38		830.50
0.00	180.00	120.00	236.22	3,509.96		830.10
0.00	180.00	120.00	236.22	3,504.75		830.10
0.00	180.00	120.00	236.22	3,515.18	3,607.94	419.10
0.00	180.00	120.00	236.22	3,662.33		416.30
0.00	180.00	120.00	236.22	3,520.42		418.90
0.00	180.00	120.00	236.22	3,679.44		415.90
0.00	180.00	120.00	236.22	3,662.33		416.10
0.00	180.00	120.00	236.22	3,623.01	3,628.58	596.40
0.00	180.00	120.00	236.22	3,634.16		596.20
0.00	180.00	120.00	236.22	3,628.58		596.20
0.00	180.00	120.00	236.22	3,628.58		596.10
0.00	180.00	120.00	236.22	3,628.58		596.00
0.00	180.00	120.00	236.22	3,423.48	3,428.48	786.20
0.00	180.00	120.00	236.22	3,428.45		786.00
0.00	180.00	120.00	236.22	3,443.44		785.60
0.00	180.00	120.00	236.22	3,413.59		786.10
0.00	180.00	120.00	236.22	3,433.43		785.60
0.00	180.00	120.00	236.22	2,230.60	2,228.10	459.30
0.00	180.00	120.00	236.22	2,239.05		458.80
0.00	180.00	120.00	236.22	2,213.87		459.90
0.00	180.00	120.00	236.22	2,230.60		459.10
0.00	180.00	120.00	236.22	2,226.39		459.10
0.00	180.00	120.00	236.22	3,634.16	3,630.81	980.50
0.00	180.00	120.00	236.22	3,634.16		980.50
0.00	180.00	120.00	236.22	3,623.01		980.60
0.00	180.00	120.00	236.22	3,628.58		980.40
0.00	180.00	120.00	236.22	3,634.16		980.20
0.00	180.00	120.00	236.22	3,651.01	3,662.34	656.90
0.00	180.00	120.00	236.22	3,668.02		656.50
0.00	180.00	120.00	236.22	3,668.02		656.50
0.00	180.00	120.00	236.22	3,662.33		656.50
0.00	180.00	120.00	236.22	3,662.33		656.40
0.00	180.00	120.00	236.22	3,859.81	3,854.80	954.20
0.00	180.00	120.00	236.22	3,840.98		954.40
0.00	180.00	120.00	236.22	3,866.12		953.90
0.00	180.00	120.00	236.22	3,840.98		954.20
0.00	180.00	120.00	236.22	3,866.12		953.80
0.00	180.00	120.00	236.22	3,557.53		478.10

0.00	180.00	120.00	236.22	3,541.53		478.30
0.00	180.00	120.00	236.22	3,546.85	3,545.80	478.20
0.00	180.00	120.00	236.22	3,541.53		478.20
0.00	180.00	120.00	236.22	3,541.53		478.10
0.00	180.00	120.00	236.22	3,393.97		997.10
0.00	180.00	120.00	236.22	3,369.76		997.50
0.00	180.00	120.00	236.22	3,393.97	3,381.37	996.90
0.00	180.00	120.00	236.22	3,379.40		997.10
0.00	180.00	120.00	236.22	3,369.76		997.20
0.00	180.00	120.00	236.22	3,468.73		144.50
0.00	180.00	120.00	236.22	3,453.51		144.70
0.00	180.00	120.00	236.22	3,463.64	3,460.60	144.40
0.00	180.00	120.00	236.22	3,458.57		144.40
0.00	180.00	120.00	236.22	3,458.57		144.30
0.00	180.00	120.00	236.22	3,536.23		557.30
0.00	180.00	120.00	236.22	3,541.53		557.10
0.00	180.00	120.00	236.22	3,530.95	3,539.42	557.20
0.00	180.00	120.00	236.22	3,552.18		556.70
0.00	180.00	120.00	236.22	3,536.23		556.90
0.00	180.00	120.00	236.22	3,573.68		823.40
0.00	180.00	120.00	236.22	3,595.44		823.00
0.00	180.00	120.00	236.22	3,606.42	3,595.49	822.70
0.00	180.00	120.00	236.22	3,611.93		822.50
0.00	180.00	120.00	236.22	3,589.97		822.80
0.00	180.00	120.00	236.22	3,525.68		1,049.60
0.00	180.00	120.00	236.22	3,536.23		1,049.30
0.00	180.00	120.00	236.22	3,552.18	3,536.25	1,049.00
0.00	180.00	120.00	236.22	3,536.23		1,049.20
0.00	180.00	120.00	236.22	3,530.95		1,049.10
0.00	180.00	120.00	236.22	3,595.44		457.10
0.00	180.00	120.00	236.22	3,606.42		456.90
0.00	180.00	120.00	236.22	3,600.92	3,600.92	456.90
0.00	180.00	120.00	236.22	3,595.44		456.90
0.00	180.00	120.00	236.22	3,606.42		456.60
0.00	180.00	120.00	236.22	3,509.96		1,016.70
0.00	180.00	120.00	236.22	3,515.18		1,016.50
0.00	180.00	120.00	236.22	3,504.75	3,509.97	1,016.60
0.00	180.00	120.00	236.22	3,499.56		1,016.60
0.00	180.00	120.00	236.22	3,520.42		1,016.10
0.00	180.00	120.00	236.22	3,755.49		821.90
0.00	180.00	120.00	236.22	3,749.53		821.90
0.00	180.00	120.00	236.22	3,755.49	3,750.72	821.70
0.00	180.00	120.00	236.22	3,749.53		821.70
0.00	180.00	120.00	236.22	3,743.59		821.70
0.00	180.00	120.00	236.22	3,828.53		332.20
0.00	180.00	120.00	236.22	3,816.16		332.30
0.00	180.00	120.00	236.22	3,822.33	3,821.11	332.10
0.00	180.00	120.00	236.22	3,828.53		331.90
0.00	180.00	120.00	236.22	3,810.00		332.10
0.00	180.00	120.00	236.22	3,536.23		472.30
0.00	180.00	120.00	236.22	3,536.23		472.20
0.00	180.00	120.00	236.22	3,541.53	3,542.63	472.10
0.00	180.00	120.00	236.22	3,562.90		471.60
0.00	180.00	120.00	236.22	3,536.23		472.00
0.00	180.00	120.00	236.22	3,494.38		305.80

0.00	180.00	120.00	236.22	3,345.90	3,419.69	308.70
0.00	180.00	120.00	236.22	3,473.83		306.10
0.00	180.00	120.00	236.22	3,438.43		306.70
0.00	180.00	120.00	236.22	3,345.90		308.50
0.00	180.00	120.00	236.22	3,584.53	3,578.01	863.40
0.00	180.00	120.00	236.22	3,579.09		863.40
0.00	180.00	120.00	236.22	3,573.68		863.40
0.00	180.00	120.00	236.22	3,573.68		863.30
0.00	180.00	120.00	236.22	3,579.09		863.10
0.00	180.00	120.00	236.22	3,568.28	3,570.44	728.10
0.00	180.00	120.00	236.22	3,568.28		728.00
0.00	180.00	120.00	236.22	3,568.28		727.90
0.00	180.00	120.00	236.22	3,573.68		727.70
0.00	180.00	120.00	236.22	3,573.68		727.60
0.00	180.00	120.00	236.22	3,276.29	3,274.47	543.30
0.00	180.00	120.00	236.22	3,276.29		543.20
0.00	180.00	120.00	236.22	3,271.75		543.20
0.00	180.00	120.00	236.22	3,276.29		543.00
0.00	180.00	120.00	236.22	3,271.75		543.00
0.00	180.00	120.00	236.22	3,276.29	3,276.29	271.30
0.00	180.00	120.00	236.22	3,276.29		271.20
0.00	180.00	120.00	236.22	3,276.29		271.10
0.00	180.00	120.00	236.22	3,276.29		271.10
0.00	180.00	120.00	236.22	3,276.29		271.00

Channel 3						
(sensor 3)						
location			Distance	Velocity	Average velocity for sensor 3	Arrival time, millisecond
x3	y3	z3	(mm)	m/s	m/s	t3
75.00	150.00	75.00	150.00	3,030.30	3,034.00	276.80
75.00	150.00	75.00	150.00	3,030.30		276.80
75.00	150.00	75.00	150.00	3,048.78		276.40
75.00	150.00	75.00	150.00	3,030.30		276.60
75.00	150.00	75.00	150.00	3,030.30		276.50
75.00	150.00	75.00	150.00	2,958.58	2,959.76	1,026.30
75.00	150.00	75.00	150.00	2,964.43		1,026.20
75.00	150.00	75.00	150.00	2,958.58		1,026.20
75.00	150.00	75.00	150.00	2,952.76		1,026.20
75.00	150.00	75.00	150.00	2,964.43		1,025.90
75.00	150.00	75.00	150.00	2,964.43	2,958.59	386.70
75.00	150.00	75.00	150.00	2,958.58		386.70
75.00	150.00	75.00	150.00	2,958.58		386.60
75.00	150.00	75.00	150.00	2,958.58		386.50
75.00	150.00	75.00	150.00	2,952.76		386.50
75.00	150.00	75.00	150.00	2,970.30	2,966.78	342.60
75.00	150.00	75.00	150.00	2,970.30		342.50
75.00	150.00	75.00	150.00	2,958.58		342.60
75.00	150.00	75.00	150.00	2,964.43		342.40
75.00	150.00	75.00	150.00	2,970.30		342.20
75.00	150.00	75.00	150.00	3,184.71	3,176.63	319.70
75.00	150.00	75.00	150.00	3,171.25		319.80
75.00	150.00	75.00	150.00	3,177.97		319.60
75.00	150.00	75.00	150.00	3,177.97		319.50
75.00	150.00	75.00	150.00	3,171.25		319.50
75.00	150.00	75.00	150.00	3,125.00	3,127.61	807.50
75.00	150.00	75.00	150.00	3,125.00		807.50
75.00	150.00	75.00	150.00	3,131.52		807.30
75.00	150.00	75.00	150.00	3,125.00		807.30
75.00	150.00	75.00	150.00	3,131.52		807.10
75.00	150.00	75.00	150.00	3,184.71	3,191.52	288.80
75.00	150.00	75.00	150.00	3,191.49		288.60
75.00	150.00	75.00	150.00	3,205.13		288.30
75.00	150.00	75.00	150.00	3,198.29		288.30
75.00	150.00	75.00	150.00	3,177.97		288.50
75.00	150.00	75.00	150.00	3,157.89	3,161.89	724.10
75.00	150.00	75.00	150.00	3,157.89		724.00
75.00	150.00	75.00	150.00	3,164.56		723.80
75.00	150.00	75.00	150.00	3,164.56		723.70
75.00	150.00	75.00	150.00	3,164.56		723.60
75.00	150.00	75.00	150.00	2,918.29	2,914.89	398.30
75.00	150.00	75.00	150.00	2,912.62		398.30
75.00	150.00	75.00	150.00	2,918.29		398.10
75.00	150.00	75.00	150.00	2,912.62		398.10
75.00	150.00	75.00	150.00	2,912.62		398.00
75.00	150.00	75.00	150.00	2,895.75	2,901.38	387.80
75.00	150.00	75.00	150.00	2,901.35		387.60
75.00	150.00	75.00	150.00	2,918.29		387.20
75.00	150.00	75.00	150.00	2,901.35		387.40

75.00	150.00	75.00	150.00	2,890.17		387.60
75.00	150.00	75.00	150.00	2,742.23		504.50
75.00	150.00	75.00	150.00	2,742.23		504.40
75.00	150.00	75.00	150.00	2,846.30	2,761.05	502.30
75.00	150.00	75.00	150.00	2,732.24		504.40
75.00	150.00	75.00	150.00	2,742.23		504.20
75.00	150.00	75.00	150.00	2,895.75		470.60
75.00	150.00	75.00	150.00	2,895.75		470.60
75.00	150.00	75.00	150.00	2,895.75	2,893.52	470.50
75.00	150.00	75.00	150.00	2,890.17		470.50
75.00	150.00	75.00	150.00	2,890.17		470.40
75.00	150.00	75.00	150.00	2,958.58		491.30
75.00	150.00	75.00	150.00	2,952.76		491.30
75.00	150.00	75.00	150.00	2,952.76	2,958.59	491.20
75.00	150.00	75.00	150.00	2,958.58		491.00
75.00	150.00	75.00	150.00	2,970.30		490.80
75.00	150.00	75.00	150.00	3,061.22		592.40
75.00	150.00	75.00	150.00	3,061.22		592.40
75.00	150.00	75.00	150.00	3,061.22	3,061.22	592.30
75.00	150.00	75.00	150.00	3,061.22		592.20
75.00	150.00	75.00	150.00	3,061.22		592.10
75.00	150.00	75.00	150.00	3,740.65		447.70
75.00	150.00	75.00	150.00	3,750.00		447.50
75.00	150.00	75.00	150.00	3,750.00	3,746.26	447.50
75.00	150.00	75.00	150.00	3,740.65		447.50
75.00	150.00	75.00	150.00	3,750.00		447.30
75.00	150.00	75.00	150.00	3,856.04		79.30
75.00	150.00	75.00	150.00	3,875.97		79.00
75.00	150.00	75.00	150.00	3,846.15	3,858.05	79.20
75.00	150.00	75.00	150.00	3,856.04		79.00
75.00	150.00	75.00	150.00	3,856.04		78.90
75.00	150.00	75.00	150.00	3,807.11		375.20
75.00	150.00	75.00	150.00	3,797.47		375.20
75.00	150.00	75.00	150.00	3,807.11	3,807.12	375.00
75.00	150.00	75.00	150.00	3,816.79		374.80
75.00	150.00	75.00	150.00	3,807.11		374.80
75.00	150.00	75.00	150.00	3,118.50		379.80
75.00	150.00	75.00	150.00	3,112.03		379.80
75.00	150.00	75.00	150.00	3,118.50	3,115.92	379.60
75.00	150.00	75.00	150.00	3,118.50		379.50
75.00	150.00	75.00	150.00	3,112.03		379.50
75.00	150.00	75.00	150.00	2,664.30		635.50
75.00	150.00	75.00	150.00	2,659.57		635.50
75.00	150.00	75.00	150.00	2,659.57	2,661.46	635.40
75.00	150.00	75.00	150.00	2,659.57		635.30
75.00	150.00	75.00	150.00	2,664.30		635.10
75.00	150.00	75.00	150.00	2,678.57		307.10
75.00	150.00	75.00	150.00	2,673.80		307.10
75.00	150.00	75.00	150.00	2,673.80	2,695.55	307.00
75.00	150.00	75.00	150.00	2,673.80		306.90
75.00	150.00	75.00	150.00	2,777.78		304.70
75.00	150.00	75.00	150.00	2,851.71		631.60
75.00	150.00	75.00	150.00	2,857.14		631.40
75.00	150.00	75.00	150.00	2,846.30	2,851.72	631.50
75.00	150.00	75.00	150.00	2,851.71		631.30

75.00	150.00	75.00	150.00	2,851.71		631.30
75.00	150.00	75.00	150.00	2,654.87	2,652.99	524.50
75.00	150.00	75.00	150.00	2,654.87		524.40
75.00	150.00	75.00	150.00	2,650.18		524.40
75.00	150.00	75.00	150.00	2,654.87		524.20
75.00	150.00	75.00	150.00	2,650.18		524.20
75.00	150.00	75.00	150.00	2,645.50	2,642.71	958.50
75.00	150.00	75.00	150.00	2,645.50		958.40
75.00	150.00	75.00	150.00	2,636.20		958.50
75.00	150.00	75.00	150.00	2,640.85		958.30
75.00	150.00	75.00	150.00	2,645.50		958.20
75.00	150.00	75.00	150.00	2,762.43	2,767.54	90.30
75.00	150.00	75.00	150.00	2,762.43		90.20
75.00	150.00	75.00	150.00	2,777.78		89.80
75.00	150.00	75.00	150.00	2,767.53		90.00
75.00	150.00	75.00	150.00	2,767.53		89.90
75.00	150.00	75.00	150.00	2,793.30	2,803.75	900.30
75.00	150.00	75.00	150.00	2,803.74		900.00
75.00	150.00	75.00	150.00	2,803.74		899.90
75.00	150.00	75.00	150.00	2,808.99		899.80
75.00	150.00	75.00	150.00	2,808.99		899.70
75.00	150.00	75.00	150.00	2,664.30	2,662.41	789.30
75.00	150.00	75.00	150.00	2,664.30		789.20
75.00	150.00	75.00	150.00	2,659.57		789.20
75.00	150.00	75.00	150.00	2,664.30		789.00
75.00	150.00	75.00	150.00	2,659.57		789.00
75.00	150.00	75.00	150.00	2,835.54	2,839.85	451.40
75.00	150.00	75.00	150.00	2,840.91		451.20
75.00	150.00	75.00	150.00	2,835.54		451.20
75.00	150.00	75.00	150.00	2,835.54		451.20
75.00	150.00	75.00	150.00	2,851.71		450.80
75.00	150.00	75.00	150.00	2,814.26	2,820.61	1,043.60
75.00	150.00	75.00	150.00	2,819.55		1,043.50
75.00	150.00	75.00	150.00	2,824.86		1,043.30
75.00	150.00	75.00	150.00	2,824.86		1,043.20
75.00	150.00	75.00	150.00	2,819.55		1,043.20
120.00	225.00	120.00	226.99	3,408.28	3,407.25	92.50
120.00	225.00	120.00	226.99	3,408.28		92.40
120.00	225.00	120.00	226.99	3,408.28		92.30
120.00	225.00	120.00	226.99	3,403.17		92.30
120.00	225.00	120.00	226.99	3,408.28		92.20
120.00	225.00	120.00	226.99	3,210.63	3,207.00	367.80
120.00	225.00	120.00	226.99	3,197.06		368.10
120.00	225.00	120.00	226.99	3,210.63		367.70
120.00	225.00	120.00	226.99	3,206.09		367.70
120.00	225.00	120.00	226.99	3,210.63		367.50
120.00	225.00	120.00	226.99	3,210.63	3,214.26	157.50
120.00	225.00	120.00	226.99	3,215.17		157.30
120.00	225.00	120.00	226.99	3,215.17		157.20
120.00	225.00	120.00	226.99	3,215.17		157.10
120.00	225.00	120.00	226.99	3,215.17		157.00
120.00	225.00	120.00	226.99	3,219.73	3,218.82	243.80
120.00	225.00	120.00	226.99	3,215.17		243.80
120.00	225.00	120.00	226.99	3,219.73		243.70
120.00	225.00	120.00	226.99	3,219.73		243.60

120.00	225.00	120.00	226.99	3,219.73		243.50
120.00	225.00	120.00	226.99	3,247.37	3,245.51	82.40
120.00	225.00	120.00	226.99	3,247.37		82.30
120.00	225.00	120.00	226.99	3,242.73		82.30
120.00	225.00	120.00	226.99	3,242.73		82.20
120.00	225.00	120.00	226.99	3,247.37		82.00
120.00	225.00	120.00	226.99	3,063.31	3,093.18	143.50
120.00	225.00	120.00	226.99	3,071.60		143.20
120.00	225.00	120.00	226.99	3,183.61		140.60
120.00	225.00	120.00	226.99	3,075.76		142.90
120.00	225.00	120.00	226.99	3,071.60		143.00
120.00	225.00	120.00	226.99	3,096.74	3,095.06	91.80
120.00	225.00	120.00	226.99	3,100.97		91.60
120.00	225.00	120.00	226.99	3,096.74		91.60
120.00	225.00	120.00	226.99	3,088.32		91.70
120.00	225.00	120.00	226.99	3,092.52		91.50
120.00	225.00	120.00	226.99	3,256.69	3,255.79	739.70
120.00	225.00	120.00	226.99	3,247.37		739.90
120.00	225.00	120.00	226.99	3,252.02		739.70
120.00	225.00	120.00	226.99	3,247.37		739.70
120.00	225.00	120.00	226.99	3,275.49		739.00
120.00	225.00	120.00	226.99	3,118.01	3,118.87	135.40
120.00	225.00	120.00	226.99	3,113.73		135.40
120.00	225.00	120.00	226.99	3,118.01		135.30
120.00	225.00	120.00	226.99	3,122.30		135.10
120.00	225.00	120.00	226.99	3,122.30		135.00
120.00	225.00	120.00	226.99	3,118.01	3,122.32	1,020.00
120.00	225.00	120.00	226.99	3,130.91		1,019.60
120.00	225.00	120.00	226.99	3,126.60		1,019.60
120.00	225.00	120.00	226.99	3,109.47		1,019.90
120.00	225.00	120.00	226.99	3,126.60		1,019.40
120.00	225.00	120.00	226.99	3,109.47	3,112.04	782.00
120.00	225.00	120.00	226.99	3,122.30		781.70
120.00	225.00	120.00	226.99	3,100.97		782.10
120.00	225.00	120.00	226.99	3,109.47		781.80
120.00	225.00	120.00	226.99	3,118.01		781.50
120.00	225.00	120.00	226.99	2,967.21	2,970.31	482.90
120.00	225.00	120.00	226.99	2,974.98		482.60
120.00	225.00	120.00	226.99	2,967.21		482.70
120.00	225.00	120.00	226.99	2,971.09		482.50
120.00	225.00	120.00	226.99	2,971.09		482.50
120.00	225.00	120.00	226.99	3,148.28	3,149.17	732.60
120.00	225.00	120.00	226.99	3,152.66		732.40
120.00	225.00	120.00	226.99	3,139.57		732.60
120.00	225.00	120.00	226.99	3,143.92		732.50
120.00	225.00	120.00	226.99	3,161.44		732.00
120.00	225.00	120.00	226.99	2,404.57	2,406.61	273.90
120.00	225.00	120.00	226.99	2,407.12		273.70
120.00	225.00	120.00	226.99	2,407.12		273.70
120.00	225.00	120.00	226.99	2,407.12		273.60
120.00	225.00	120.00	226.99	2,407.12		273.50
120.00	225.00	120.00	226.99	3,242.73	3,160.01	986.60
120.00	225.00	120.00	226.99	3,228.89		986.80
120.00	225.00	120.00	226.99	3,105.21		989.50
120.00	225.00	120.00	226.99	3,113.73		989.30

120.00	225.00	120.00	226.99	3,109.47		989.30
120.00	225.00	120.00	226.99	965.51		992.40
120.00	225.00	120.00	226.99	972.96		990.60
120.00	225.00	120.00	226.99	980.52	974.83	988.70
120.00	225.00	120.00	226.99	975.89		989.70
120.00	225.00	120.00	226.99	979.25		988.80
120.00	225.00	120.00	226.99	3,294.50		192.00
120.00	225.00	120.00	226.99	3,308.91		191.60
120.00	225.00	120.00	226.99	3,299.29	3,303.15	191.70
120.00	225.00	120.00	226.99	3,313.74		191.40
120.00	225.00	120.00	226.99	3,299.29		191.60
120.00	225.00	120.00	226.99	3,343.02		942.50
120.00	225.00	120.00	226.99	3,343.02		942.40
120.00	225.00	120.00	226.99	3,343.02	3,344.01	942.30
120.00	225.00	120.00	226.99	3,352.90		942.00
120.00	225.00	120.00	226.99	3,338.11		942.20
120.00	225.00	120.00	226.99	2,967.21		529.80
120.00	225.00	120.00	226.99	2,971.09		529.60
120.00	225.00	120.00	226.99	2,967.21	2,967.98	529.60
120.00	225.00	120.00	226.99	2,967.21		529.50
120.00	225.00	120.00	226.99	2,967.21		529.40
120.00	225.00	120.00	226.99	2,959.47		360.80
120.00	225.00	120.00	226.99	2,959.47		360.70
120.00	225.00	120.00	226.99	2,959.47	2,958.70	360.60
120.00	225.00	120.00	226.99	2,959.47		360.50
120.00	225.00	120.00	226.99	2,955.61		360.50
120.00	225.00	120.00	226.99	3,109.47		428.10
120.00	225.00	120.00	226.99	3,118.01		427.80
120.00	225.00	120.00	226.99	3,122.30	3,115.45	427.60
120.00	225.00	120.00	226.99	3,113.73		427.70
120.00	225.00	120.00	226.99	3,113.73		427.60
120.00	225.00	120.00	226.99	3,071.60		177.50
120.00	225.00	120.00	226.99	3,071.60		177.40
120.00	225.00	120.00	226.99	3,067.45	3,036.82	177.40
120.00	225.00	120.00	226.99	2,986.73		179.40
120.00	225.00	120.00	226.99	2,986.73		179.30
120.00	225.00	120.00	226.99	927.25		1,146.50
120.00	225.00	120.00	226.99	926.87		1,146.50
120.00	225.00	120.00	226.99	927.63	927.48	1,146.20
120.00	225.00	120.00	226.99	927.25		1,146.20
120.00	225.00	120.00	226.99	928.39		1,145.90
120.00	225.00	120.00	226.99	3,100.97		590.20
120.00	225.00	120.00	226.99	3,096.74		590.20
120.00	225.00	120.00	226.99	3,100.97	3,102.67	590.00
120.00	225.00	120.00	226.99	3,109.47		589.80
120.00	225.00	120.00	226.99	3,105.21		589.80
120.00	225.00	120.00	226.99	2,472.67		190.50
120.00	225.00	120.00	226.99	2,469.98		190.50
120.00	225.00	120.00	226.99	2,475.37	2,471.60	190.20
120.00	225.00	120.00	226.99	2,467.30		190.40
120.00	225.00	120.00	226.99	2,472.67		190.20
120.00	225.00	120.00	226.99	3,143.92		798.60
120.00	225.00	120.00	226.99	3,139.57		798.60
120.00	225.00	120.00	226.99	3,261.37	3,211.65	795.80
120.00	225.00	120.00	226.99	3,261.37		795.70

120.00	225.00	120.00	226.99	3,252.02		795.80
120.00	225.00	120.00	226.99	2,851.65		236.30
120.00	225.00	120.00	226.99	2,862.44		235.90
120.00	225.00	120.00	226.99	3,006.51	2,916.47	232.00
120.00	225.00	120.00	226.99	2,855.24		236.00
120.00	225.00	120.00	226.99	3,006.51		231.90
120.00	225.00	120.00	226.99	3,238.11		619.00
120.00	225.00	120.00	226.99	3,126.60		621.40
120.00	225.00	120.00	226.99	3,242.73	3,219.51	618.70
120.00	225.00	120.00	226.99	3,238.11		618.80
120.00	225.00	120.00	226.99	3,252.02		618.40
150.00	300.00	150.00	300.00	4,070.56		430.20
150.00	300.00	150.00	300.00	4,070.56		430.10
150.00	300.00	150.00	300.00	4,076.09	4,076.11	429.90
150.00	300.00	150.00	300.00	4,092.77		429.60
150.00	300.00	150.00	300.00	4,070.56		429.90
150.00	300.00	150.00	300.00	3,051.88		261.10
150.00	300.00	150.00	300.00	3,054.99		260.90
150.00	300.00	150.00	300.00	3,042.60	3,050.03	261.20
150.00	300.00	150.00	300.00	3,058.10		260.60
150.00	300.00	150.00	300.00	3,042.60		261.00
150.00	300.00	150.00	300.00	2,561.91		317.10
150.00	300.00	150.00	300.00	2,555.37		317.30
150.00	300.00	150.00	300.00	2,568.49	2,561.92	316.60
150.00	300.00	150.00	300.00	2,557.54		317.00
150.00	300.00	150.00	300.00	2,566.30		316.50
150.00	300.00	150.00	300.00	2,323.78		641.50
150.00	300.00	150.00	300.00	2,314.81		642.00
150.00	300.00	150.00	300.00	2,325.58	2,325.24	641.40
150.00	300.00	150.00	300.00	2,331.00		641.10
150.00	300.00	150.00	300.00	2,331.00		641.10
150.00	300.00	150.00	300.00	2,901.35		496.30
150.00	300.00	150.00	300.00	2,904.16		496.20
150.00	300.00	150.00	300.00	2,906.98	2,906.42	496.10
150.00	300.00	150.00	300.00	2,906.98		496.10
150.00	300.00	150.00	300.00	2,912.62		495.90
150.00	300.00	150.00	300.00	2,161.38		411.80
150.00	300.00	150.00	300.00	2,175.49		410.90
150.00	300.00	150.00	300.00	2,169.20	2,170.47	411.30
150.00	300.00	150.00	300.00	2,170.77		411.20
150.00	300.00	150.00	300.00	2,175.49		410.90
150.00	300.00	150.00	300,00	1642,94		342,60
150.00	300.00	150.00	300,00	1643,84		342,50
150.00	300.00	150.00	300,00	1643,84	1643,48	342,50
150.00	300.00	150.00	300,00	1643,84		342,50
150.00	300.00	150.00	300,00	1642,94		342,60
150.00	300.00	150.00	300,00	1676,91		261,40
150.00	300.00	150.00	300,00	1675,04		261,60
150.00	300.00	150.00	300,00	1674,11	1675,79	261,70
150.00	300.00	150.00	300,00	1678,79		261,20
150.00	300.00	150.00	300,00	1674,11		261,70
150.00	300.00	150.00	300.00	2,830.19		390.40
150.00	300.00	150.00	300.00	2,830.19		390.40
150.00	300.00	150.00	300.00	2,830.19	2,830.19	390.40

150.00	300.00	150.00	300.00	2,830.19		390.40
150.00	300.00	150.00	300.00	2,830.19		390.40
150.00	300.00	150.00	300.00	2,857.14		674.60
150.00	300.00	150.00	300.00	2,752.29		674.60
150.00	300.00	150.00	300.00	2,752.29	2,773.26	674.60
150.00	300.00	150.00	300.00	2,752.29		674.60
150.00	300.00	150.00	300.00	2,752.29		674.60
150.00	300.00	150.00	300.00	2,654.87		908.80
150.00	300.00	150.00	300.00	2,654.87		908.80
150.00	300.00	150.00	300.00	2,654.87	2,654.87	908.80
150.00	300.00	150.00	300.00	2,654.87		908.80
150.00	300.00	150.00	300.00	2,654.87		908.80
150.00	300.00	150.00	300.00	2,884.62		708.60
150.00	300.00	150.00	300.00	2,884.62		708.60
150.00	300.00	150.00	300.00	2,884.62	2,884.62	708.60
150.00	300.00	150.00	300.00	2,884.62		708.60
150.00	300.00	150.00	300.00	2,884.62		708.60
150.00	300.00	150.00	300.00	2,884.62		439.60
150.00	300.00	150.00	300.00	2,884.62		439.60
150.00	300.00	150.00	300.00	2,884.62	2,895.82	439.60
150.00	300.00	150.00	300.00	2,912.62		438.60
150.00	300.00	150.00	300.00	2,912.62		438.60
150.00	300.00	150.00	300.00	3,125.00		319.70
150.00	300.00	150.00	300.00	3,125.00		319.70
150.00	300.00	150.00	300.00	3,125.00	3,125.00	319.70
150.00	300.00	150.00	300.00	3,125.00		319.70
150.00	300.00	150.00	300.00	3,125.00		319.70
150.00	300.00	150.00	300.00	2,727.27		200.00
150.00	300.00	150.00	300.00	2,654.87		200.00
150.00	300.00	150.00	300.00	2,654.87	2,669.35	203.00
150.00	300.00	150.00	300.00	2,654.87		199.00
150.00	300.00	150.00	300.00	2,654.87		199.00
150.00	300.00	150.00	300.00	1,744.19		919.60
150.00	300.00	150.00	300.00	1,744.19		919.60
150.00	300.00	150.00	300.00	1,744.19	1,706.23	919.60
150.00	300.00	150.00	300.00	1,744.19		919.60
150.00	300.00	150.00	300.00	1,554.40		940.60
150.00	300.00	150.00	300.00	3,030.30		960.50
150.00	300.00	150.00	300.00	3,030.30		960.50
150.00	300.00	150.00	300.00	3,030.30	3,042.67	960.50
150.00	300.00	150.00	300.00	3,061.22		959.50
150.00	300.00	150.00	300.00	3,061.22		959.50
150.00	300.00	150.00	300.00	3,030.30		170.30
150.00	300.00	150.00	300.00	3,030.30		170.30
150.00	300.00	150.00	300.00	3,030.30	3,036.49	170.30
150.00	300.00	150.00	300.00	3,030.30		170.30
150.00	300.00	150.00	300.00	3,061.22		169.30
150.00	300.00	150.00	300.00	3,000.00		981.50
150.00	300.00	150.00	300.00	3,000.00		981.50
150.00	300.00	150.00	300.00	3,000.00	3,000.00	981.50
150.00	300.00	150.00	300.00	3,000.00		981.50
150.00	300.00	150.00	300.00	3,000.00		981.50
150.00	300.00	150.00	300.00	3,125.00		602.90
150.00	300.00	150.00	300.00	3,061.22		604.90

150.00	300.00	150.00	300.00	3,061.22	3,073.98	604.90
150.00	300.00	150.00	300.00	3,061.22		604.90
150.00	300.00	150.00	300.00	3,061.22		604.90
150.00	300.00	150.00	300.00	2,912.62	2,912.62	932.90
150.00	300.00	150.00	300.00	2,912.62		932.90
150.00	300.00	150.00	300.00	2,912.62		932.90
150.00	300.00	150.00	300.00	2,912.62		932.90
150.00	300.00	150.00	300.00	2,912.62		932.90
150.00	300.00	150.00	300.00	3,333.33	3,348.31	711.20
150.00	300.00	150.00	300.00	3,333.33		711.20
150.00	300.00	150.00	300.00	3,333.33		711.20
150.00	300.00	150.00	300.00	3,370.79		710.20
150.00	300.00	150.00	300.00	3,370.79		710.20
150.00	300.00	150.00	300.00	3,191.49	3,191.49	705.10
150.00	300.00	150.00	300.00	3,191.49		705.10
150.00	300.00	150.00	300.00	3,191.49		705.10
150.00	300.00	150.00	300.00	3,191.49		705.10
150.00	300.00	150.00	300.00	3,191.49		705.10
150.00	300.00	150.00	300.00	3,089.60	3,093.43	898.90
150.00	300.00	150.00	300.00	3,089.60		898.90
150.00	300.00	150.00	300.00	3,092.78		898.80
150.00	300.00	150.00	300.00	3,099.17		898.60
150.00	300.00	150.00	300.00	3,095.98		898.70
150.00	300.00	150.00	300.00	1,086.17	1,086.01	1,015.60
150.00	300.00	150.00	300.00	1,085.78		1,015.70
150.00	300.00	150.00	300.00	1,085.78		1,015.70
150.00	300.00	150.00	300.00	1,085.38		1,015.80
150.00	300.00	150.00	300.00	1,086.96		1,015.40
150.00	300.00	150.00	300.00	3,128.26	3,130.87	1,059.50
150.00	300.00	150.00	300.00	3,128.26		1,059.50
150.00	300.00	150.00	300.00	3,131.52		1,059.40
150.00	300.00	150.00	300.00	3,134.80		1,059.30
150.00	300.00	150.00	300.00	3,131.52		1,059.40
150.00	300.00	150.00	300,00	3131,52	3135,46	688,60
150.00	300.00	150.00	300,00	3131,52		688,60
150.00	300.00	150.00	300,00	3134,80		688,50
150.00	300.00	150.00	300,00	3141,36		688,30
150.00	300.00	150.00	300,00	3138,08		688,40
150.00	300.00	150.00	300,00	1676,91	1675,79	261,40
150.00	300.00	150.00	300,00	1675,04		261,60
150.00	300.00	150.00	300,00	1674,11		261,70
150.00	300.00	150.00	300,00	1678,79		261,20
150.00	300.00	150.00	300,00	1674,11		261,70
200.00	375.00	200.00	378.32	3,377.85	3,477.93	517.90
200.00	375.00	200.00	378.32	3,502.95		517.90
200.00	375.00	200.00	378.32	3,502.95		517.90
200.00	375.00	200.00	378.32	3,502.95		517.90
200.00	375.00	200.00	378.32	3,502.95		517.90
200.00	375.00	200.00	378.32	1,380.72	1,569.55	1,031.60
200.00	375.00	200.00	378.32	1,609.87		992.60
200.00	375.00	200.00	378.32	1,616.75		995.60
200.00	375.00	200.00	378.32	1,616.75		995.60
200.00	375.00	200.00	378.32	1,623.69		995.60
200.00	375.00	200.00	378.32	1,882.18		355.20

200.00	375.00	200.00	378.32	1,882.18		355.20
200.00	375.00	200.00	378.32	1,882.18	1,882.18	355.20
200.00	375.00	200.00	378.32	1,882.18		355.20
200.00	375.00	200.00	378.32	1,882.18		355.20
200.00	375.00	200.00	378.32	2,137.39		429.40
200.00	375.00	200.00	378.32	2,137.39		429.40
200.00	375.00	200.00	378.32	2,137.39	2,137.39	429.40
200.00	375.00	200.00	378.32	2,137.39		429.40
200.00	375.00	200.00	378.32	2,137.39		429.40
200.00	375.00	200.00	378.32	2,265.38		985.80
200.00	375.00	200.00	378.32	2,238.57		987.80
200.00	375.00	200.00	378.32	2,186.81	2,249.76	987.80
200.00	375.00	200.00	378.32	2,279.03		984.80
200.00	375.00	200.00	378.32	2,279.03		984.80
200.00	375.00	200.00	378.32	2,488.94		632.20
200.00	375.00	200.00	378.32	2,425.12		636.20
200.00	375.00	200.00	378.32	2,887.93	2,715.57	611.20
200.00	375.00	200.00	378.32	2,887.93		611.20
200.00	375.00	200.00	378.32	2,887.93		611.20
200.00	375.00	200.00	378.32	3,050.96		698.00
200.00	375.00	200.00	378.32	3,050.96		698.00
200.00	375.00	200.00	378.32	3,050.96	3,050.96	698.00
200.00	375.00	200.00	378.32	3,050.96		698.00
200.00	375.00	200.00	378.32	3,050.96		698.00
200.00	375.00	200.00	378.32	3,050.96		1,016.00
200.00	375.00	200.00	378.32	3,050.96		1,016.00
200.00	375.00	200.00	378.32	3,050.96	3,060.88	1,016.00
200.00	375.00	200.00	378.32	3,075.76		1,015.00
200.00	375.00	200.00	378.32	3,075.76		1,015.00
200.00	375.00	200.00	378.32	3,261.37		192.20
200.00	375.00	200.00	378.32	3,261.37		192.20
200.00	375.00	200.00	378.32	3,261.37	3,261.37	192.20
200.00	375.00	200.00	378.32	3,261.37		192.20
200.00	375.00	200.00	378.32	3,261.37		192.20
200.00	375.00	200.00	378.32	3,233.49		640.10
200.00	375.00	200.00	378.32	3,233.49		640.10
200.00	375.00	200.00	378.32	3,233.49	3,233.49	640.10
200.00	375.00	200.00	378.32	3,233.49		640.10
200.00	375.00	200.00	378.32	3,233.49		640.10
200.00	375.00	200.00	378.32	3,075.76		982.70
200.00	375.00	200.00	378.32	3,126.60		980.70
200.00	375.00	200.00	378.32	3,126.60	3,116.43	980.70
200.00	375.00	200.00	378.32	3,126.60		980.70
200.00	375.00	200.00	378.32	3,126.60		980.70
200.00	375.00	200.00	378.32	3,289.73		667.30
200.00	375.00	200.00	378.32	3,289.73		667.30
200.00	375.00	200.00	378.32	3,289.73	3,289.73	667.30
200.00	375.00	200.00	378.32	3,289.73		667.30
200.00	375.00	200.00	378.32	3,289.73		667.30
200.00	375.00	200.00	378.32	3,261.37		120.90
200.00	375.00	200.00	378.32	3,261.37		120.90
200.00	375.00	200.00	378.32	3,289.73	3,278.38	119.90
200.00	375.00	200.00	378.32	3,289.73		119.90
200.00	375.00	200.00	378.32	3,289.73		119.90
200.00	375.00	200.00	378.32	2,409.67		874.70

200.00	375.00	200.00	378.32	2,409.67		874.70
200.00	375.00	200.00	378.32	2,409.67	2,409.67	874.70
200.00	375.00	200.00	378.32	2,409.67		874.70
200.00	375.00	200.00	378.32	2,409.67		874.70
200.00	375.00	200.00	378.32	1,666.60		869.10
200.00	375.00	200.00	378.32	1,666.60		869.10
200.00	375.00	200.00	378.32	1,666.60	1,666.60	869.10
200.00	375.00	200.00	378.32	1,666.60		869.10
200.00	375.00	200.00	378.32	1,666.60		869.10
200.00	375.00	200.00	378.32	1,719.63		627.00
200.00	375.00	200.00	378.32	1,719.63		627.00
200.00	375.00	200.00	378.32	1,719.63	1,721.37	627.00
200.00	375.00	200.00	378.32	1,696.50		630.00
200.00	375.00	200.00	378.32	1,751.48		623.00
200.00	375.00	200.00	378.32	2,887.93		357.00
200.00	375.00	200.00	378.32	2,887.93		357.00
200.00	375.00	200.00	378.32	2,887.93	2,887.93	357.00
200.00	375.00	200.00	378.32	2,887.93		357.00
200.00	375.00	200.00	378.32	2,887.93		357.00
200.00	375.00	200.00	378.32	3,179.15		1,086.00
200.00	375.00	200.00	378.32	3,179.15		1,086.00
200.00	375.00	200.00	378.32	3,179.15	3,179.15	1,086.00
200.00	375.00	200.00	378.32	3,179.15		1,086.00
200.00	375.00	200.00	378.32	3,179.15		1,086.00
200.00	375.00	200.00	378.32	3,324.42		604.10
200.00	375.00	200.00	378.32	3,324.42		604.10
200.00	375.00	200.00	378.32	3,330.27	3,328.52	603.90
200.00	375.00	200.00	378.32	3,330.27		603.90
200.00	375.00	200.00	378.32	3,333.20		603.80
200.00	375.00	200.00	378,32	3295,46		491,50
200.00	375.00	200.00	378,32	3298,33		491,40
200.00	375.00	200.00	378,32	3298,33	3298,91	491,40
200.00	375.00	200.00	378,32	3298,33		491,40
200.00	375.00	200.00	378,32	3304,09		491,20
200.00	375.00	200.00	378,32	3371,82		370,50
200.00	375.00	200.00	378,32	3377,85		370,30
200.00	375.00	200.00	378,32	3374,83	3375,44	370,40
200.00	375.00	200.00	378,32	3371,82		370,50
200.00	375.00	200.00	378,32	3380,86		370,20
200.00	375.00	200.00	378,32	3342,04		780,10
200.00	375.00	200.00	378,32	3350,92		779,80
200.00	375.00	200.00	378,32	3350,92	3350,33	779,80
200.00	375.00	200.00	378,32	3353,89		779,70
200.00	375.00	200.00	378,32	3353,89		779,70
200.00	375.00	200.00	378,32	3353,89		538,90
200.00	375.00	200.00	378,32	3359,85		538,70
200.00	375.00	200.00	378,32	3362,83	3361,64	538,60
200.00	375.00	200.00	378,32	3365,82		538,50
200.00	375.00	200.00	378,32	3365,82		538,50
200.00	375.00	200.00	378,32	3026,55		292,90
200.00	375.00	200.00	378,32	3028,97		292,80
200.00	375.00	200.00	378,32	3031,40	3030,92	292,70
200.00	375.00	200.00	378,32	3033,83		292,60
200.00	375.00	200.00	378,32	3033,83		292,60
200.00	375.00	200.00	378,32	3085,80		450,90

200.00	375.00	200.00	378,32	3090,84	3092,87	450,70
200.00	375.00	200.00	378,32	3093,37		450,60
200.00	375.00	200.00	378,32	3095,90		450,50
200.00	375.00	200.00	378,32	3098,43		450,40
200.00	375.00	200.00	378,32	3230,73	3233,49	229,10
200.00	375.00	200.00	378,32	3230,73		229,10
200.00	375.00	200.00	378,32	3233,49		229,00
200.00	375.00	200.00	378,32	3236,26		228,90
200.00	375.00	200.00	378,32	3236,26		228,90
200.00	375.00	200.00	378,32	3211,53	3219,75	900,00
200.00	375.00	200.00	378,32	3211,53		900,00
200.00	375.00	200.00	378,32	3219,73		899,70
200.00	375.00	200.00	378,32	3227,97		899,40
200.00	375.00	200.00	378,32	3227,97		899,40
200.00	375.00	200.00	378,32	3230,73	3239,59	378,60
200.00	375.00	200.00	378,32	3239,03		378,30
200.00	375.00	200.00	378,32	3239,03		378,30
200.00	375.00	200.00	378,32	3247,37		378,00
200.00	375.00	200.00	378,32	3241,81		378,20
240.00	450.00	240.00	453.98	3,439.26	3,444.99	931.90
240.00	450.00	240.00	453.98	3,387.93		933.90
240.00	450.00	240.00	453.98	3,413.40		933.90
240.00	450.00	240.00	453.98	3,492.17		933.90
240.00	450.00	240.00	453.98	3,492.17		933.90
240.00	450.00	240.00	453.98	3,067.45	3,118.57	1,120.50
240.00	450.00	240.00	453.98	3,067.45		1,120.50
240.00	450.00	240.00	453.98	3,152.66		1,120.50
240.00	450.00	240.00	453.98	3,152.66		1,120.50
240.00	450.00	240.00	453.98	3,152.66		1,120.50
240.00	450.00	240.00	453,98	2187,87	2251,55	611,60
240.00	450.00	240.00	453,98	2426,42		591,20
240.00	450.00	240.00	453,98	2026,71		628,10
240.00	450.00	240.00	453,98	2422,53		591,50
240.00	450.00	240.00	453,98	2194,21		611,00
240.00	450.00	240.00	453,98	3053,01	3073,12	1069,90
240.00	450.00	240.00	453,98	3063,31		1069,40
240.00	450.00	240.00	453,98	3059,18		1069,60
240.00	450.00	240.00	453,98	3130,91		1066,20
240.00	450.00	240.00	453,98	3059,18		1069,60
240.00	450.00	240.00	453,98	3086,22	3091,26	441,20
240.00	450.00	240.00	453,98	3090,42		441,00
240.00	450.00	240.00	453,98	3092,52		440,90
240.00	450.00	240.00	453,98	3092,52		440,90
240.00	450.00	240.00	453,98	3094,63		440,80
240.00	450.00	240.00	453,98	2290,53	2294,46	390,20
240.00	450.00	240.00	453,98	2296,32		389,70
240.00	450.00	240.00	453,98	2294,00		389,90
240.00	450.00	240.00	453,98	2295,16		389,80
240.00	450.00	240.00	453,98	2296,32		389,70
240.00	450.00	240.00	453,98	1643,08	1644,86	752,60
240.00	450.00	240.00	453,98	1644,27		752,40
240.00	450.00	240.00	453,98	1645,46		752,20
240.00	450.00	240.00	453,98	1645,46		752,20
240.00	450.00	240.00	453,98	1646,06		752,10
240.00	450.00	240.00	453,98	1856,02		1208,00

240.00	450.00	240.00	453,98	2221,05	2004,49	1167,80
240.00	450.00	240.00	453,98	2226,50		1167,30
240.00	450.00	240.00	453,98	1860,58		1207,40
240.00	450.00	240.00	453,98	1858,30		1207,70
240.00	450.00	240.00	453,98	3179,15	3183,61	455,30
240.00	450.00	240.00	453,98	3179,15		455,30
240.00	450.00	240.00	453,98	3185,84		455,00
240.00	450.00	240.00	453,98	3185,84		455,00
240.00	450.00	240.00	453,98	3188,08		454,90
240.00	450.00	240.00	453,98	3210,63	3215,18	177,70
240.00	450.00	240.00	453,98	3212,90		177,60
240.00	450.00	240.00	453,98	3215,17		177,50
240.00	450.00	240.00	453,98	3217,45		177,40
240.00	450.00	240.00	453,98	3219,73		177,30
240.00	450.00	240.00	453,98	3231,19	3237,65	966,00
240.00	450.00	240.00	453,98	3235,80		965,80
240.00	450.00	240.00	453,98	3238,11		965,70
240.00	450.00	240.00	453,98	3240,42		965,60
240.00	450.00	240.00	453,98	3242,73		965,50
240.00	450.00	240.00	453.98	3,280.22	3,286.40	995.40
240.00	450.00	240.00	453.98	3,284.97		995.20
240.00	450.00	240.00	453.98	3,287.35		995.10
240.00	450.00	240.00	453.98	3,292.11		994.90
240.00	450.00	240.00	453.98	3,287.35		995.10
240.00	450.00	240.00	453.98	3,313.74	3,322.48	406.50
240.00	450.00	240.00	453.98	3,328.32		405.90
240.00	450.00	240.00	453.98	3,321.01		406.20
240.00	450.00	240.00	453.98	3,323.44		406.10
240.00	450.00	240.00	453.98	3,325.88		406.00
240.00	450.00	240.00	453,98	2601,62	2687,54	1111,00
240.00	450.00	240.00	453,98	2944,11		1090,70
240.00	450.00	240.00	453,98	2604,60		1110,80
240.00	450.00	240.00	453,98	2946,02		1090,60
240.00	450.00	240.00	453,98	2341,32		1130,40
240.00	450.00	240.00	453,98	3194,81	3202,93	329,40
240.00	450.00	240.00	453,98	3201,57		329,10
240.00	450.00	240.00	453,98	3203,83		329,00
240.00	450.00	240.00	453,98	3206,09		328,90
240.00	450.00	240.00	453,98	3208,36		328,80
240.00	450.00	240.00	453,98	1340,37	1341,95	613,80
240.00	450.00	240.00	453,98	1341,95		613,40
240.00	450.00	240.00	453,98	1342,35		613,30
240.00	450.00	240.00	453,98	1342,75		613,20
240.00	450.00	240.00	453,98	1342,35		613,30
240.00	450.00	240.00	453.98	962.23	986.16	1,364.20
240.00	450.00	240.00	453.98	961.62		1,364.50
240.00	450.00	240.00	453.98	963.66		1,363.50
240.00	450.00	240.00	453.98	961.83		1,364.40
240.00	450.00	240.00	453.98	1,081.43		1,312.20
240.00	450.00	240.00	453.98	804.22	801.28	615.40
240.00	450.00	240.00	453.98	787.21		627.60
240.00	450.00	240.00	453.98	803.08		616.20
240.00	450.00	240.00	453.98	805.36		614.60
240.00	450.00	240.00	453.98	806.51		613.80
240.00	450.00	240.00	453,98	2906,42		833,50

240.00	450.00	240.00	453,98	2913,88	2913,14	833,10
240.00	450.00	240.00	453,98	2913,88		833,10
240.00	450.00	240.00	453,98	2913,88		833,10
240.00	450.00	240.00	453,98	2917,62		832,90
240.00	450.00	240.00	453,98	2912,01	2913,51	376,90
240.00	450.00	240.00	453,98	2915,75		376,70
240.00	450.00	240.00	453,98	2913,88		376,80
240.00	450.00	240.00	453,98	2910,14		377,00
240.00	450.00	240.00	453,98	2915,75		376,70
240.00	450.00	240.00	453,98	2971,09	2974,99	1106,50
240.00	450.00	240.00	453,98	2971,09		1106,50
240.00	450.00	240.00	453,98	2973,03		1106,40
240.00	450.00	240.00	453,98	2974,98		1106,30
240.00	450.00	240.00	453,98	2984,76		1105,80
240.00	450.00	240.00	453.98	2,973.03	2,974.20	1,104.90
240.00	450.00	240.00	453.98	2,974.98		1,104.80
240.00	450.00	240.00	453.98	2,971.09		1,105.00
240.00	450.00	240.00	453.98	2,976.93		1,104.70
240.00	450.00	240.00	453.98	2,974.98		1,104.80
240.00	450.00	240.00	453.98	2,741.44	2,757.79	274.50
240.00	450.00	240.00	453.98	2,769.87		272.80
240.00	450.00	240.00	453.98	2,761.45		273.30
240.00	450.00	240.00	453.98	2,761.45		273.30
240.00	450.00	240.00	453.98	2,754.75		273.70
240.00	450.00	240.00	453,98	3122,30	3127,03	529,60
240.00	450.00	240.00	453,98	3124,45		529,50
240.00	450.00	240.00	453,98	3128,76		529,30
240.00	450.00	240.00	453,98	3128,76		529,30
240.00	450.00	240.00	453,98	3130,91		529,20
240.00	450.00	240.00	453,98	3122,30	3123,16	1096,10
240.00	450.00	240.00	453,98	3120,15		1096,20
240.00	450.00	240.00	453,98	3122,30		1096,10
240.00	450.00	240.00	453,98	3124,45		1096,00
240.00	450.00	240.00	453,98	3126,60		1095,90
240.00	450.00	240.00	453,98	2858,83	2676,58	634,50
240.00	450.00	240.00	453,98	1952,61		708,20
240.00	450.00	240.00	453,98	2880,60		633,30
240.00	450.00	240.00	453,98	2855,24		634,70
240.00	450.00	240.00	453,98	2835,62		635,80
240.00	450.00	240.00	453.98	2,857.03	2,672.86	206.20
240.00	450.00	240.00	453.98	1,948.42		280.30
240.00	450.00	240.00	453.98	2,844.50		206.90
240.00	450.00	240.00	453.98	2,837.39		207.30
240.00	450.00	240.00	453.98	2,876.95		205.10
240.00	450.00	240.00	453.98	3,098.86	3,105.23	373.20
240.00	450.00	240.00	453.98	3,111.60		372.60
240.00	450.00	240.00	453.98	3,098.86		373.20
240.00	450.00	240.00	453.98	3,105.21		372.90
240.00	450.00	240.00	453.98	3,111.60		372.60
150.00	300.00	150.00	300.00	2,967.36	2,934.49	321.60
150.00	300.00	150.00	300.00	2,906.98		323.60
150.00	300.00	150.00	300.00	2,904.16		323.60
150.00	300.00	150.00	300.00	2,955.67		321.70
150.00	300.00	150.00	300.00	2,938.30		322.20
150.00	300.00	150.00	300.00	1,708.43		579.20

150.00	300.00	150.00	300.00	1,713.31		578.60
150.00	300.00	150.00	300.00	1,711.35	1,710.96	578.70
150.00	300.00	150.00	300.00	1,709.40		578.90
150.00	300.00	150.00	300.00	1,712.33		578.50
150.00	300.00	150.00	300.00	1,195.70		917.70
150.00	300.00	150.00	300.00	1,193.79		918.00
150.00	300.00	150.00	300.00	1,193.32	1,193.98	918.10
150.00	300.00	150.00	300.00	1,193.32		918.00
150.00	300.00	150.00	300.00	1,193.79		917.80
150.00	300.00	150.00	300.00	2,964.43		942.00
150.00	300.00	150.00	300.00	2,944.06		942.60
150.00	300.00	150.00	300.00	2,722.32	2,911.35	950.80
150.00	300.00	150.00	300.00	2,964.43		941.80
150.00	300.00	150.00	300.00	2,961.50		941.70
150.00	300.00	150.00	300.00	2,884.62		867.00
150.00	300.00	150.00	300.00	2,892.96		866.60
150.00	300.00	150.00	300.00	2,895.75	2,830.52	866.50
150.00	300.00	150.00	300.00	2,597.40		878.30
150.00	300.00	150.00	300.00	2,881.84		866.80
150.00	300.00	150.00	300.00	2,734.73		461.60
150.00	300.00	150.00	300.00	2,742.23		461.20
150.00	300.00	150.00	300.00	2,732.24	2,734.74	461.60
150.00	300.00	150.00	300.00	2,732.24		461.50
150.00	300.00	150.00	300.00	2,732.24		461.40
150.00	300.00	150.00	300.00	1,858.74		692.60
150.00	300.00	150.00	300.00	1,865.67		692.00
150.00	300.00	150.00	300.00	1,853.00	1,859.44	693.00
150.00	300.00	150.00	300.00	1,861.04		692.20
150.00	300.00	150.00	300.00	1,858.74		692.30
150.00	300.00	150.00	300.00	2,149.00		856.80
150.00	300.00	150.00	300.00	2,243.83		850.80
150.00	300.00	150.00	300.00	2,150.54	2,187.47	856.50
150.00	300.00	150.00	300.00	2,155.17		856.10
150.00	300.00	150.00	300.00	2,238.81		850.80
150.00	300.00	150.00	300.00	2,228.83		488.00
150.00	300.00	150.00	300.00	2,225.52		488.10
150.00	300.00	150.00	300.00	2,343.75	2,308.30	481.20
150.00	300.00	150.00	300.00	2,506.27		472.90
150.00	300.00	150.00	300.00	2,237.14		487.10
150.00	300.00	150.00	300.00	2,835.54		1,021.30
150.00	300.00	150.00	300.00	2,859.87		1,020.40
150.00	300.00	150.00	300.00	2,840.91	2,843.13	1,021.00
150.00	300.00	150.00	300.00	2,857.14		1,020.30
150.00	300.00	150.00	300.00	2,822.20		1,021.50
150.00	300.00	150.00	300.00	2,693.00		703.60
150.00	300.00	150.00	300.00	2,680.97		704.00
150.00	300.00	150.00	300.00	2,707.58	2,690.14	702.90
150.00	300.00	150.00	300.00	2,678.57		704.00
150.00	300.00	150.00	300.00	2,690.58		703.40
150.00	300.00	150.00	300.00	2,979.15		993.70
150.00	300.00	150.00	300.00	2,994.01		993.10
150.00	300.00	150.00	300.00	2,985.07	2,946.21	993.30
150.00	300.00	150.00	300.00	2,790.70		1,000.20
150.00	300.00	150.00	300.00	2,982.11		993.30
150.00	300.00	150.00	300.00	2,553.19		529.20

150.00	300.00	150.00	300.00	2,542.37	2,545.84	529.60
150.00	300.00	150.00	300.00	2,546.69		529.40
150.00	300.00	150.00	300.00	2,548.85		529.20
150.00	300.00	150.00	300.00	2,538.07		529.60
150.00	300.00	150.00	300.00	2,555.37	2,548.43	1,044.90
150.00	300.00	150.00	300.00	2,544.53		1,045.30
150.00	300.00	150.00	300.00	2,546.69		1,045.10
150.00	300.00	150.00	300.00	2,544.53		1,045.10
150.00	300.00	150.00	300.00	2,551.02		1,044.70
150.00	300.00	150.00	300.00	2,568.49	2,564.98	193.20
150.00	300.00	150.00	300.00	2,564.10		193.30
150.00	300.00	150.00	300.00	2,564.10		193.20
150.00	300.00	150.00	300.00	2,568.49		192.90
150.00	300.00	150.00	300.00	2,559.73		193.20
150.00	300.00	150.00	300.00	1,292.55	1,275.13	722.60
150.00	300.00	150.00	300.00	1,294.78		722.10
150.00	300.00	150.00	300.00	1,293.66		722.20
150.00	300.00	150.00	300.00	1,204.34		739.30
150.00	300.00	150.00	300.00	1,290.32		722.60
150.00	300.00	150.00	300.00	1,276.05	1,288.37	992.40
150.00	300.00	150.00	300.00	1,285.90		990.60
150.00	300.00	150.00	300.00	1,295.90		988.70
150.00	300.00	150.00	300.00	1,289.77		989.70
150.00	300.00	150.00	300.00	1,294.22		988.80
150.00	300.00	150.00	300.00	2,734.73	2,737.36	1,092.30
150.00	300.00	150.00	300.00	2,729.75		1,092.40
150.00	300.00	150.00	300.00	2,744.74		1,091.80
150.00	300.00	150.00	300.00	2,767.53		1,090.80
150.00	300.00	150.00	300.00	2,710.03		1,092.90
150.00	300.00	150.00	300.00	3,030.30	3,036.45	490.40
150.00	300.00	150.00	300.00	3,033.37		490.30
150.00	300.00	150.00	300.00	3,036.44		490.10
150.00	300.00	150.00	300.00	3,045.69		489.70
150.00	300.00	150.00	300.00	3,036.44		489.90
150.00	300.00	150.00	300.00	3,000.00	3,010.86	1,049.40
150.00	300.00	150.00	300.00	3,009.03		1,049.00
150.00	300.00	150.00	300.00	3,018.11		1,048.60
150.00	300.00	150.00	300.00	3,021.15		1,048.40
150.00	300.00	150.00	300.00	3,006.01		1,048.80
150.00	300.00	150.00	300.00	2,764.98	2,758.37	867.50
150.00	300.00	150.00	300.00	2,759.89		867.60
150.00	300.00	150.00	300.00	2,759.89		867.50
150.00	300.00	150.00	300.00	2,752.29		867.70
150.00	300.00	150.00	300.00	2,754.82		867.50
150.00	300.00	150.00	300.00	3,024.19	3,030.92	369.70
150.00	300.00	150.00	300.00	3,027.25		369.50
150.00	300.00	150.00	300.00	3,036.44		369.10
150.00	300.00	150.00	300.00	3,033.37		369.10
150.00	300.00	150.00	300.00	3,033.37		369.00
150.00	300.00	150.00	300.00	2,349.26	2,320.96	533.20
150.00	300.00	150.00	300.00	2,272.73		537.40
150.00	300.00	150.00	300.00	2,345.58		533.30
150.00	300.00	150.00	300.00	2,369.67		531.90
150.00	300.00	150.00	300.00	2,267.57		537.50
150.00	300.00	150.00	300.00	2,542.37		356.20

150.00	300.00	150.00	300.00	2,540.22	2,548.45	356.20
150.00	300.00	150.00	300.00	2,557.54		355.40
150.00	300.00	150.00	300.00	2,561.91		355.10
150.00	300.00	150.00	300.00	2,540.22		356.00
150.00	300.00	150.00	300.00	2,909.80	2,908.12	900.60
150.00	300.00	150.00	300.00	2,912.62		900.40
150.00	300.00	150.00	300.00	2,898.55		900.80
150.00	300.00	150.00	300.00	2,904.16		900.50
150.00	300.00	150.00	300.00	2,915.45		900.00
150.00	300.00	150.00	300.00	3,597.12	3,594.53	745.30
150.00	300.00	150.00	300.00	3,592.81		745.30
150.00	300.00	150.00	300.00	3,592.81		745.20
150.00	300.00	150.00	300.00	3,592.81		745.10
150.00	300.00	150.00	300.00	3,597.12		744.90
150.00	300.00	150.00	300.00	2,991.03	2,985.67	571.50
150.00	300.00	150.00	300.00	2,985.07		571.60
150.00	300.00	150.00	300.00	2,979.15		571.70
150.00	300.00	150.00	300.00	2,988.05		571.30
150.00	300.00	150.00	300.00	2,985.07		571.30
150.00	300.00	150.00	300.00	2,982.11	2,988.05	299.80
150.00	300.00	150.00	300.00	2,988.05		299.50
150.00	300.00	150.00	300.00	2,988.05		299.40
150.00	300.00	150.00	300.00	2,991.03		299.30
150.00	300.00	150.00	300.00	2,991.03		299.20

Channel 4 (sensor 4)						
location			Distance	Velocity	Average velocity for sensor 4	Arrival time, millisecond
x4	y4	z4	(mm)	m/s	m/s	t4
75.00	150.00	30.00	156.60	3,151.00	3,156.09	277.00
75.00	150.00	30.00	156.60	3,157.35		276.90
75.00	150.00	30.00	156.60	3,163.73		276.70
75.00	150.00	30.00	156.60	3,157.35		276.70
75.00	150.00	30.00	156.60	3,151.00		276.70
75.00	150.00	30.00	156.60	3,023.25	3,025.59	1,027.40
75.00	150.00	30.00	156.60	3,029.10		1,027.30
75.00	150.00	30.00	156.60	3,023.25		1,027.30
75.00	150.00	30.00	156.60	3,023.25		1,027.20
75.00	150.00	30.00	156.60	3,029.10		1,027.00
75.00	150.00	30.00	156.60	3,023.25	3,022.09	387.90
75.00	150.00	30.00	156.60	3,023.25		387.80
75.00	150.00	30.00	156.60	3,023.25		387.70
75.00	150.00	30.00	156.60	3,023.25		387.60
75.00	150.00	30.00	156.60	3,017.43		387.60
75.00	150.00	30.00	156.60	3,034.97	3,033.80	343.70
75.00	150.00	30.00	156.60	3,034.97		343.60
75.00	150.00	30.00	156.60	3,040.87		343.40
75.00	150.00	30.00	156.60	3,029.10		343.50
75.00	150.00	30.00	156.60	3,029.10		343.40
75.00	150.00	30.00	156.60	3,176.56	3,184.32	321.90
75.00	150.00	30.00	156.60	3,183.02		321.70
75.00	150.00	30.00	156.60	3,183.02		321.60
75.00	150.00	30.00	156.60	3,189.50		321.40
75.00	150.00	30.00	156.60	3,189.50		321.30
75.00	150.00	30.00	156.60	3,094.95	3,084.02	810.10
75.00	150.00	30.00	156.60	3,088.85		810.20
75.00	150.00	30.00	156.60	3,088.85		810.10
75.00	150.00	30.00	156.60	3,082.77		810.10
75.00	150.00	30.00	156.60	3,064.67		810.30
75.00	150.00	30.00	156.60	3,144.67	3,135.93	291.50
75.00	150.00	30.00	156.60	3,113.41		291.90
75.00	150.00	30.00	156.60	3,138.37		291.40
75.00	150.00	30.00	156.60	3,157.35		291.00
75.00	150.00	30.00	156.60	3,125.84		291.40
75.00	150.00	30.00	156.60	3,144.67	3,138.37	726.40
75.00	150.00	30.00	156.60	3,138.37		726.40
75.00	150.00	30.00	156.60	3,138.37		726.30
75.00	150.00	30.00	156.60	3,138.37		726.20
75.00	150.00	30.00	156.60	3,132.09		726.20
75.00	150.00	30.00	156.60	2,752.28	2,748.41	403.80
75.00	150.00	30.00	156.60	2,747.45		403.80
75.00	150.00	30.00	156.60	2,747.45		403.70
75.00	150.00	30.00	156.60	2,747.45		403.60
75.00	150.00	30.00	156.60	2,747.45		403.50
75.00	150.00	30.00	156.60	2,910.87	2,915.20	389.80
75.00	150.00	30.00	156.60	2,916.29		389.60
75.00	150.00	30.00	156.60	2,916.29		389.50
75.00	150.00	30.00	156.60	2,916.29		389.40

75.00	150.00	30.00	156.60	2,916.29		389.40
75.00	150.00	30.00	156.60	2,700.08	2,694.58	507.80
75.00	150.00	30.00	156.60	2,700.08		507.70
75.00	150.00	30.00	156.60	2,672.43		508.20
75.00	150.00	30.00	156.60	2,686.19		507.80
75.00	150.00	30.00	156.60	2,714.12		507.20
75.00	150.00	30.00	156.60	2,723.56	2,728.31	476.30
75.00	150.00	30.00	156.60	2,728.30		476.20
75.00	150.00	30.00	156.60	2,733.06		476.00
75.00	150.00	30.00	156.60	2,728.30		476.00
75.00	150.00	30.00	156.60	2,728.30		475.90
75.00	150.00	30.00	156.60	2,752.28	2,749.38	497.50
75.00	150.00	30.00	156.60	2,747.45		497.50
75.00	150.00	30.00	156.60	2,752.28		497.30
75.00	150.00	30.00	156.60	2,747.45		497.30
75.00	150.00	30.00	156.60	2,747.45		497.30
75.00	150.00	30.00	156.60	2,900.09	2,982.22	597.40
75.00	150.00	30.00	156.60	3,029.10		595.10
75.00	150.00	30.00	156.60	3,052.72		594.60
75.00	150.00	30.00	156.60	3,029.10		594.90
75.00	150.00	30.00	156.60	2,900.09		597.10
75.00	150.00	30.00	156.60	3,058.68	3,075.53	458.80
75.00	150.00	30.00	156.60	3,076.71		458.40
75.00	150.00	30.00	156.60	3,082.77		458.30
75.00	150.00	30.00	156.60	3,082.77		458.20
75.00	150.00	30.00	156.60	3,076.71		458.20
75.00	150.00	30.00	156.60	2,900.09	2,891.53	94.40
75.00	150.00	30.00	156.60	2,894.72		94.40
75.00	150.00	30.00	156.60	2,889.38		94.40
75.00	150.00	30.00	156.60	2,884.06		94.40
75.00	150.00	30.00	156.60	2,889.38		94.20
75.00	150.00	30.00	156.60	2,781.61	2,776.69	392.10
75.00	150.00	30.00	156.60	2,771.76		392.20
75.00	150.00	30.00	156.60	2,786.56		391.80
75.00	150.00	30.00	156.60	2,766.87		392.10
75.00	150.00	30.00	156.60	2,776.68		391.80
75.00	150.00	30.00	156.60	2,253.30	2,251.38	401.20
75.00	150.00	30.00	156.60	2,243.62		401.40
75.00	150.00	30.00	156.60	2,243.62		401.30
75.00	150.00	30.00	156.60	2,263.07		400.60
75.00	150.00	30.00	156.60	2,253.30		400.80
75.00	150.00	30.00	156.60	1,694.85	1,982.89	671.60
75.00	150.00	30.00	156.60	2,424.22		643.70
75.00	150.00	30.00	156.60	1,691.19		671.60
75.00	150.00	30.00	156.60	2,409.30		643.90
75.00	150.00	30.00	156.60	1,694.85		671.20
75.00	150.00	30.00	156.60	2,667.88	2,656.15	309.80
75.00	150.00	30.00	156.60	2,640.89		310.30
75.00	150.00	30.00	156.60	2,663.34		309.70
75.00	150.00	30.00	156.60	2,654.32		309.80
75.00	150.00	30.00	156.60	2,654.32		309.70
75.00	150.00	30.00	156.60	2,852.54	2,848.40	633.90
75.00	150.00	30.00	156.60	2,852.54		633.80
75.00	150.00	30.00	156.60	2,842.19		633.90
75.00	150.00	30.00	156.60	2,842.19		633.80

75.00	150.00	30.00	156.60	2,852.54		633.60
75.00	150.00	30.00	156.60	2,723.56		525.50
75.00	150.00	30.00	156.60	2,723.56		525.40
75.00	150.00	30.00	156.60	2,723.56	2,723.56	525.30
75.00	150.00	30.00	156.60	2,723.56		525.20
75.00	150.00	30.00	156.60	2,723.56		525.10
75.00	150.00	30.00	156.60	2,718.83		959.40
75.00	150.00	30.00	156.60	2,718.83		959.30
75.00	150.00	30.00	156.60	2,709.42	2,717.90	959.40
75.00	150.00	30.00	156.60	2,714.12		959.20
75.00	150.00	30.00	156.60	2,728.30		958.90
75.00	150.00	30.00	156.60	2,816.63		91.60
75.00	150.00	30.00	156.60	2,847.36		90.90
75.00	150.00	30.00	156.60	2,842.19	2,844.34	90.90
75.00	150.00	30.00	156.60	2,852.54		90.70
75.00	150.00	30.00	156.60	2,862.97		90.40
75.00	150.00	30.00	156.60	2,894.72		900.70
75.00	150.00	30.00	156.60	2,900.09		900.50
75.00	150.00	30.00	156.60	2,894.72	2,895.80	900.50
75.00	150.00	30.00	156.60	2,894.72		900.50
75.00	150.00	30.00	156.60	2,894.72		900.40
75.00	150.00	30.00	156.60	2,842.19		788.10
75.00	150.00	30.00	156.60	2,714.12		790.60
75.00	150.00	30.00	156.60	2,709.42	2,795.20	790.60
75.00	150.00	30.00	156.60	2,852.54		787.60
75.00	150.00	30.00	156.60	2,857.75		787.40
75.00	150.00	30.00	156.60	2,932.67		451.90
75.00	150.00	30.00	156.60	2,921.73		452.00
75.00	150.00	30.00	156.60	2,921.73	2,927.21	451.90
75.00	150.00	30.00	156.60	2,938.17		451.60
75.00	150.00	30.00	156.60	2,921.73		451.80
75.00	150.00	30.00	156.60	2,686.19		1,048.60
75.00	150.00	30.00	156.60	2,690.80		1,048.50
75.00	150.00	30.00	156.60	2,686.19	2,688.95	1,048.50
75.00	150.00	30.00	156.60	2,690.80		1,048.30
75.00	150.00	30.00	156.60	2,690.80		1,048.20
225.00	90.00	60.00	141.51	3,369.28		67.90
225.00	90.00	60.00	141.51	3,369.28		67.80
225.00	90.00	60.00	141.51	3,353.31	3,364.48	67.90
225.00	90.00	60.00	141.51	3,369.28		67.60
225.00	90.00	60.00	141.51	3,361.28		67.70
225.00	90.00	60.00	141.51	3,377.32		339.00
225.00	90.00	60.00	141.51	3,385.40		338.90
225.00	90.00	60.00	141.51	3,385.40	3,383.78	338.80
225.00	90.00	60.00	141.51	3,385.40		338.70
225.00	90.00	60.00	141.51	3,385.40		338.60
225.00	90.00	60.00	141.51	3,385.40		128.60
225.00	90.00	60.00	141.51	3,377.32		128.60
225.00	90.00	60.00	141.51	3,377.32	3,377.33	128.50
225.00	90.00	60.00	141.51	3,377.32		128.40
225.00	90.00	60.00	141.51	3,369.28		128.40
225.00	90.00	60.00	141.51	3,230.82		217.10
225.00	90.00	60.00	141.51	3,230.82		217.00
225.00	90.00	60.00	141.51	3,230.82	3,232.29	217.00
225.00	90.00	60.00	141.51	3,230.82		216.90

225.00	90.00	60.00	141.51	3,238.21		216.70
225.00	90.00	60.00	141.51	3,245.64		56.10
225.00	90.00	60.00	141.51	3,245.64		56.00
225.00	90.00	60.00	141.51	3,238.21	3,241.18	56.00
225.00	90.00	60.00	141.51	3,238.21		55.90
225.00	90.00	60.00	141.51	3,238.21		55.80
225.00	90.00	60.00	141.51	3,158.70		114.20
225.00	90.00	60.00	141.51	3,130.75		114.50
225.00	90.00	60.00	141.51	132.29	2,545.04	1,139.00
225.00	90.00	60.00	141.51	3,137.69		114.20
225.00	90.00	60.00	141.51	3,165.77		113.80
225.00	90.00	60.00	141.51	3,069.63		64.60
225.00	90.00	60.00	141.51	3,030.19		65.10
225.00	90.00	60.00	141.51	3,083.00	3,055.23	64.20
225.00	90.00	60.00	141.51	3,069.63		64.30
225.00	90.00	60.00	141.51	3,023.71		64.90
225.00	90.00	60.00	141.51	2,700.57		722.40
225.00	90.00	60.00	141.51	2,710.91		722.20
225.00	90.00	60.00	141.51	2,726.58	2,715.10	721.80
225.00	90.00	60.00	141.51	2,721.34		721.80
225.00	90.00	60.00	141.51	2,716.12		721.80
225.00	90.00	60.00	141.51	3,208.84		106.70
225.00	90.00	60.00	141.51	3,208.84		106.60
225.00	90.00	60.00	141.51	3,223.46	3,217.61	106.40
225.00	90.00	60.00	141.51	3,223.46		106.30
225.00	90.00	60.00	141.51	3,223.46		106.20
225.00	90.00	60.00	141.51	3,187.16		991.60
225.00	90.00	60.00	141.51	3,187.16		991.50
225.00	90.00	60.00	141.51	3,187.16	3,187.16	991.40
225.00	90.00	60.00	141.51	3,194.35		991.20
225.00	90.00	60.00	141.51	3,179.99		991.30
225.00	90.00	60.00	141.51	2,954.27		756.90
225.00	90.00	60.00	141.51	2,966.66		756.70
225.00	90.00	60.00	141.51	2,985.44	2,955.67	756.30
225.00	90.00	60.00	141.51	2,917.73		757.30
225.00	90.00	60.00	141.51	2,954.27		756.60
225.00	90.00	60.00	141.51	2,406.63		465.20
225.00	90.00	60.00	141.51	2,410.73		465.00
225.00	90.00	60.00	141.51	2,448.27	2,434.98	464.00
225.00	90.00	60.00	141.51	2,461.04		463.60
225.00	90.00	60.00	141.51	2,448.27		463.90
225.00	90.00	60.00	141.51	1,579.35		750.10
225.00	90.00	60.00	141.51	2,461.04		717.90
225.00	90.00	60.00	141.51	1,593.58	1,763.17	749.10
225.00	90.00	60.00	141.51	1,598.98		748.80
225.00	90.00	60.00	141.51	1,582.88		749.60
225.00	90.00	60.00	141.51	2,742.44		231.10
225.00	90.00	60.00	141.51	2,675.04		232.30
225.00	90.00	60.00	141.51	2,763.86	2,729.01	230.60
225.00	90.00	60.00	141.51	2,726.58		231.20
225.00	90.00	60.00	141.51	2,737.13		230.90
225.00	90.00	60.00	141.51	3,083.00		962.50
225.00	90.00	60.00	141.51	3,056.37		962.80
225.00	90.00	60.00	141.51	3,076.30	3,074.99	962.40
225.00	90.00	60.00	141.51	3,076.30		962.40

225.00	90.00	60.00	141.51	3,083.00		962.20
225.00	90.00	60.00	141.51	726.06		952.20
225.00	90.00	60.00	141.51	654.53		973.50
225.00	90.00	60.00	141.51	655.14	667.93	973.20
225.00	90.00	60.00	141.51	650.62		974.60
225.00	90.00	60.00	141.51	653.32		973.60
225.00	90.00	60.00	141.51	3,216.13		167.10
225.00	90.00	60.00	141.51	3,216.13		167.00
225.00	90.00	60.00	141.51	3,223.46	3,224.95	166.80
225.00	90.00	60.00	141.51	3,238.21		166.60
225.00	90.00	60.00	141.51	3,230.82		166.60
225.00	90.00	60.00	141.51	3,158.70		919.40
225.00	90.00	60.00	141.51	3,137.69		919.60
225.00	90.00	60.00	141.51	3,158.70	3,151.69	919.20
225.00	90.00	60.00	141.51	3,158.70		919.10
225.00	90.00	60.00	141.51	3,144.66		919.20
225.00	90.00	60.00	141.51	2,452.51		511.00
225.00	90.00	60.00	141.51	2,456.77		510.80
225.00	90.00	60.00	141.51	2,456.77	2,454.21	510.70
225.00	90.00	60.00	141.51	2,448.27		510.80
225.00	90.00	60.00	141.51	2,456.77		510.50
225.00	90.00	60.00	141.51	2,456.77		341.70
225.00	90.00	60.00	141.51	2,444.04		341.90
225.00	90.00	60.00	141.51	2,448.27	2,451.67	341.70
225.00	90.00	60.00	141.51	2,448.27		341.60
225.00	90.00	60.00	141.51	2,461.04		341.20
225.00	90.00	60.00	141.51	2,504.60		411.60
225.00	90.00	60.00	141.51	2,509.04		411.40
225.00	90.00	60.00	141.51	2,504.60	2,504.60	411.40
225.00	90.00	60.00	141.51	2,504.60		411.30
225.00	90.00	60.00	141.51	2,500.17		411.30
225.00	90.00	60.00	141.51	2,495.76		160.30
225.00	90.00	60.00	141.51	2,500.17		160.10
225.00	90.00	60.00	141.51	2,500.17	2,499.29	160.00
225.00	90.00	60.00	141.51	2,500.17		160.00
225.00	90.00	60.00	141.51	2,500.17		159.90
225.00	90.00	60.00	141.51	2,242.63		964.80
225.00	90.00	60.00	141.51	2,235.54		964.90
225.00	90.00	60.00	141.51	2,242.63	2,238.37	964.60
225.00	90.00	60.00	141.51	2,235.54		964.70
225.00	90.00	60.00	141.51	2,235.54		964.70
225.00	90.00	60.00	141.51	3,089.73		562.80
225.00	90.00	60.00	141.51	3,096.49		562.60
225.00	90.00	60.00	141.51	3,103.28	3,096.50	562.40
225.00	90.00	60.00	141.51	3,089.73		562.60
225.00	90.00	60.00	141.51	3,103.28		562.30
225.00	90.00	60.00	141.51	3,069.63		144.80
225.00	90.00	60.00	141.51	3,062.98		144.80
225.00	90.00	60.00	141.51	3,069.63	3,068.30	144.60
225.00	90.00	60.00	141.51	3,062.98		144.60
225.00	90.00	60.00	141.51	3,076.30		144.40
225.00	90.00	60.00	141.51	3,137.69		771.50
225.00	90.00	60.00	141.51	3,130.75		771.50
225.00	90.00	60.00	141.51	3,123.83	3,133.53	771.50
225.00	90.00	60.00	141.51	3,130.75		771.30

225.00	90.00	60.00	141.51	3,144.66		771.00
225.00	90.00	60.00	141.51	3,103.28		202.30
225.00	90.00	60.00	141.51	3,096.49		202.30
225.00	90.00	60.00	141.51	3,103.28	3,100.57	202.10
225.00	90.00	60.00	141.51	3,096.49		202.20
225.00	90.00	60.00	141.51	3,103.28		202.00
225.00	90.00	60.00	141.51	3,030.19		595.60
225.00	90.00	60.00	141.51	3,017.26		595.70
225.00	90.00	60.00	141.51	3,036.69	3,027.62	595.30
225.00	90.00	60.00	141.51	3,036.69		595.30
225.00	90.00	60.00	141.51	3,017.26		595.50
150.00	300.00	60.00	313.21	4,215.47		430.80
150.00	300.00	60.00	313.21	4,204.15		430.90
150.00	300.00	60.00	313.21	4,204.15	4,209.81	430.80
150.00	300.00	60.00	313.21	4,215.47		430.60
150.00	300.00	60.00	313.21	4,209.80		430.60
150.00	300.00	60.00	313.21	3,189.50		261.00
150.00	300.00	60.00	313.21	3,189.50		260.90
150.00	300.00	60.00	313.21	3,196.01	3,190.80	260.60
150.00	300.00	60.00	313.21	3,189.50		260.70
150.00	300.00	60.00	313.21	3,189.50		260.60
150.00	300.00	60.00	313.21	2,623.19		319.40
150.00	300.00	60.00	313.21	2,616.62		319.60
150.00	300.00	60.00	313.21	2,607.90	2,612.27	319.90
150.00	300.00	60.00	313.21	2,612.25		319.60
150.00	300.00	60.00	313.21	2,601.41		320.00
150.00	300.00	60.00	313.21	1,518.96		718.60
150.00	300.00	60.00	313.21	1,518.96		718.60
150.00	300.00	60.00	313.21	1,516.75	1,518.67	718.90
150.00	300.00	60.00	313.21	1,521.17		718.30
150.00	300.00	60.00	313.21	1,517.49		718.80
150.00	300.00	60.00	313.21	1,289.46		635.80
150.00	300.00	60.00	313.21	1,290.52		635.60
150.00	300.00	60.00	313.21	1,290.52	1,310.24	635.60
150.00	300.00	60.00	313.21	1,290.52		635.60
150.00	300.00	60.00	313.21	1,390.19		618.20
150.00	300.00	60.00	313.21	1,148.97		545.60
150.00	300.00	60.00	313.21	1,149.39		545.50
150.00	300.00	60.00	313.21	1,149.39	1,149.39	545.50
150.00	300.00	60.00	313.21	1,149.39		545.50
150.00	300.00	60.00	313.21	1,149.81		545.40
150.00	300.00	60.00	313,21	1437,40		377,90
150.00	300.00	60.00	313,21	1438,72		377,70
150.00	300.00	60.00	313,21	1438,06	1438,46	377,80
150.00	300.00	60.00	313,21	1438,72		377,70
150.00	300.00	60.00	313,21	1439,38		377,60
150.00	300.00	60.00	313,21	1695,77		267,20
150.00	300.00	60.00	313,21	1707,79		265,90
150.00	300.00	60.00	313,21	1708,72	1705,02	265,80
150.00	300.00	60.00	313,21	1704,08		266,30
150.00	300.00	60.00	313,21	1708,72		265,80
150.00	300.00	60.00	313.21	2,847.36		394.40
150.00	300.00	60.00	313.21	2,847.36		394.40
150.00	300.00	60.00	313.21	2,847.36	2,847.36	394.40

150.00	300.00	60.00	313.21	2,847.36		394.40
150.00	300.00	60.00	313.21	2,847.36		394.40
150.00	300.00	60.00	313.21	2,900.09	2,817.23	677.60
150.00	300.00	60.00	313.21	2,796.51		677.60
150.00	300.00	60.00	313.21	2,796.51		677.60
150.00	300.00	60.00	313.21	2,796.51		677.60
150.00	300.00	60.00	313.21	2,796.51		677.60
150.00	300.00	60.00	313.21	2,821.70	2,837.10	906.80
150.00	300.00	60.00	313.21	2,821.70		906.80
150.00	300.00	60.00	313.21	2,847.36		905.80
150.00	300.00	60.00	313.21	2,847.36		905.80
150.00	300.00	60.00	313.21	2,847.36		905.80
150.00	300.00	60.00	313.21	2,927.19	2,927.19	711.60
150.00	300.00	60.00	313.21	2,927.19		711.60
150.00	300.00	60.00	313.21	2,927.19		711.60
150.00	300.00	60.00	313.21	2,927.19		711.60
150.00	300.00	60.00	313.21	2,927.19		711.60
150.00	300.00	60.00	313.21	2,821.70	2,821.70	446.60
150.00	300.00	60.00	313.21	2,821.70		446.60
150.00	300.00	60.00	313.21	2,821.70		446.60
150.00	300.00	60.00	313.21	2,821.70		446.60
150.00	300.00	60.00	313.21	2,821.70		446.60
150.00	300.00	60.00	313.21	2,320.07	2,320.07	358.70
150.00	300.00	60.00	313.21	2,320.07		358.70
150.00	300.00	60.00	313.21	2,320.07		358.70
150.00	300.00	60.00	313.21	2,320.07		358.70
150.00	300.00	60.00	313.21	2,320.07		358.70
150.00	300.00	60.00	313.21	2,610.08	2,563.67	210.00
150.00	300.00	60.00	313.21	2,546.42		210.00
150.00	300.00	60.00	313.21	2,610.08		210.00
150.00	300.00	60.00	313.21	2,525.88		210.00
150.00	300.00	60.00	313.21	2,525.88		210.00
150.00	300.00	60.00	313.21	1,385.88	1,385.76	973.60
150.00	300.00	60.00	313.21	1,385.88		973.60
150.00	300.00	60.00	313.21	1,385.27		973.70
150.00	300.00	60.00	313.21	1,385.88		973.60
150.00	300.00	60.00	313.21	1,385.88		973.60
150.00	300.00	60.00	313.21	2,900.09	2,933.23	969.50
150.00	300.00	60.00	313.21	2,982.94		966.50
150.00	300.00	60.00	313.21	2,900.09		969.50
150.00	300.00	60.00	313.21	2,982.94		966.50
150.00	300.00	60.00	313.21	2,900.09		969.50
150.00	300.00	60.00	313.21	2,954.80	2,927.60	177.30
150.00	300.00	60.00	313.21	2,954.80		177.30
150.00	300.00	60.00	313.21	2,873.48		180.30
150.00	300.00	60.00	313.21	2,954.80		177.30
150.00	300.00	60.00	313.21	2,900.09		179.30
150.00	300.00	60.00	313.21	2,982.94	2,982.94	986.50
150.00	300.00	60.00	313.21	2,982.94		986.50
150.00	300.00	60.00	313.21	2,982.94		986.50
150.00	300.00	60.00	313.21	2,982.94		986.50
150.00	300.00	60.00	313.21	2,982.94		986.50
150.00	300.00	60.00	313.21	3,101.08		607.90
150.00	300.00	60.00	313.21	3,101.08		607.90

150.00	300.00	60.00	313.21	3,101.08	3,113.49	607.90
150.00	300.00	60.00	313.21	3,132.09		606.90
150.00	300.00	60.00	313.21	3,132.09		606.90
150.00	300.00	60.00	313.21	2,821.70	2,831.97	940.90
150.00	300.00	60.00	313.21	2,821.70		940.90
150.00	300.00	60.00	313.21	2,821.70		940.90
150.00	300.00	60.00	313.21	2,847.36		939.90
150.00	300.00	60.00	313.21	2,847.36		939.90
150.00	300.00	60.00	313.21	3,332.01	3,332.01	715.20
150.00	300.00	60.00	313.21	3,332.01		715.20
150.00	300.00	60.00	313.21	3,332.01		715.20
150.00	300.00	60.00	313.21	3,332.01		715.20
150.00	300.00	60.00	313.21	3,332.01		715.20
150.00	300.00	60.00	313.21	3,196.01	3,196.01	709.10
150.00	300.00	60.00	313.21	3,196.01		709.10
150.00	300.00	60.00	313.21	3,196.01		709.10
150.00	300.00	60.00	313.21	3,196.01		709.10
150.00	300.00	60.00	313.21	3,196.01		709.10
150.00	300.00	60.00	313.21	2,974.45	2,978.41	907.10
150.00	300.00	60.00	313.21	2,977.27		907.00
150.00	300.00	60.00	313.21	2,980.11		906.90
150.00	300.00	60.00	313.21	2,980.11		906.90
150.00	300.00	60.00	313.21	2,980.11		906.90
150.00	300.00	60.00	313.21	1,922.71	1,925.08	902.30
150.00	300.00	60.00	313.21	1,923.89		902.20
150.00	300.00	60.00	313.21	1,929.82		901.70
150.00	300.00	60.00	313.21	1,922.71		902.30
150.00	300.00	60.00	313.21	1,926.26		902.00
150.00	300.00	60.00	313.21	3,061.67	3,066.47	1,065.90
150.00	300.00	60.00	313.21	3,064.67		1,065.80
150.00	300.00	60.00	313.21	3,064.67		1,065.80
150.00	300.00	60.00	313.21	3,070.68		1,065.60
150.00	300.00	60.00	313.21	3,070.68		1,065.60
150.00	300.00	60.00	313,21	3055,70	3057,49	695,30
150.00	300.00	60.00	313,21	3055,70		695,30
150.00	300.00	60.00	313,21	3055,70		695,30
150.00	300.00	60.00	313,21	3058,68		695,20
150.00	300.00	60.00	313,21	3061,67		695,10
150.00	300.00	60.00	313,21	1695,77	1705,02	267,20
150.00	300.00	60.00	313,21	1707,79		265,90
150.00	300.00	60.00	313,21	1708,72		265,80
150.00	300.00	60.00	313,21	1704,08		266,30
150.00	300.00	60.00	313,21	1708,72		265,80
375.00	150.00	100.00	235.85	3,187.16	3,332.85	479.90
375.00	150.00	100.00	235.85	3,369.28		479.90
375.00	150.00	100.00	235.85	3,369.28		479.90
375.00	150.00	100.00	235.85	3,369.28		479.90
375.00	150.00	100.00	235.85	3,369.28		479.90
375.00	150.00	100.00	235.85	3,468.38	3,587.10	825.60
375.00	150.00	100.00	235.85	3,468.38		825.60
375.00	150.00	100.00	235.85	3,685.15		825.60
375.00	150.00	100.00	235.85	3,628.45		826.60
375.00	150.00	100.00	235.85	3,685.15		826.60
375.00	150.00	100.00	235.85	2,841.56		237.20

375.00	150.00	100.00	235.85	2,841.56		237.20
375.00	150.00	100.00	235.85	2,841.56	2,841.56	237.20
375.00	150.00	100.00	235.85	2,841.56		237.20
375.00	150.00	100.00	235.85	2,841.56		237.20
375.00	150.00	100.00	235.85	2,312.25		354.40
375.00	150.00	100.00	235.85	2,246.19		357.40
375.00	150.00	100.00	235.85	2,267.78	2,285.83	356.40
375.00	150.00	100.00	235.85	2,267.78		356.40
375.00	150.00	100.00	235.85	2,335.14		353.40
375.00	150.00	100.00	235.85	2,068.86		932.80
375.00	150.00	100.00	235.85	2,068.86		932.80
375.00	150.00	100.00	235.85	1,998.72	2,062.15	932.80
375.00	150.00	100.00	235.85	2,087.16		931.80
375.00	150.00	100.00	235.85	2,087.16		931.80
375.00	150.00	100.00	235.85	2,563.58		572.20
375.00	150.00	100.00	235.85	2,563.58		572.20
375.00	150.00	100.00	235.85	2,563.58	2,563.58	572.20
375.00	150.00	100.00	235.85	2,563.58		572.20
375.00	150.00	100.00	235.85	2,563.58		572.20
375.00	150.00	100.00	235.85	2,985.44		653.00
375.00	150.00	100.00	235.85	2,985.44		653.00
375.00	150.00	100.00	235.85	3,023.71	3,008.40	652.00
375.00	150.00	100.00	235.85	3,023.71		652.00
375.00	150.00	100.00	235.85	3,023.71		652.00
375.00	150.00	100.00	235.85	2,948.12		972.00
375.00	150.00	100.00	235.85	2,948.12		972.00
375.00	150.00	100.00	235.85	2,948.12	2,948.12	972.00
375.00	150.00	100.00	235.85	2,948.12		972.00
375.00	150.00	100.00	235.85	2,948.12		972.00
375.00	150.00	100.00	235.85	3,321.82		147.20
375.00	150.00	100.00	235.85	3,321.82		147.20
375.00	150.00	100.00	235.85	3,321.82	3,321.82	147.20
375.00	150.00	100.00	235.85	3,321.82		147.20
375.00	150.00	100.00	235.85	3,321.82		147.20
375.00	150.00	100.00	235.85	3,468.38		591.10
375.00	150.00	100.00	235.85	3,468.38		591.10
375.00	150.00	100.00	235.85	3,628.45	3,532.41	588.10
375.00	150.00	100.00	235.85	3,468.38		591.10
375.00	150.00	100.00	235.85	3,628.45		588.10
375.00	150.00	100.00	235.85	2,620.55		949.70
375.00	150.00	100.00	235.85	2,620.55		949.70
375.00	150.00	100.00	235.85	2,620.55	2,609.16	949.70
375.00	150.00	100.00	235.85	2,620.55		949.70
375.00	150.00	100.00	235.85	2,563.58		951.70
375.00	150.00	100.00	235.85	3,144.66		627.30
375.00	150.00	100.00	235.85	3,144.66		627.30
375.00	150.00	100.00	235.85	3,144.66	3,161.66	627.30
375.00	150.00	100.00	235.85	3,187.16		626.30
375.00	150.00	100.00	235.85	3,187.16		626.30
375.00	150.00	100.00	235.85	3,187.16		78.90
375.00	150.00	100.00	235.85	3,187.16		78.90
375.00	150.00	100.00	235.85	3,187.16	3,187.16	78.90
375.00	150.00	100.00	235.85	3,187.16		78.90
375.00	150.00	100.00	235.85	3,187.16		78.90
375.00	150.00	100.00	235.85	3,520.14		784.70

375.00	150.00	100.00	235.85	3,520.14		784.70
375.00	150.00	100.00	235.85	3,520.14	3,520.14	784.70
375.00	150.00	100.00	235.85	3,520.14		784.70
375.00	150.00	100.00	235.85	3,520.14		784.70
375.00	150.00	100.00	235.85	1,857.08		769.10
375.00	150.00	100.00	235.85	1,857.08		769.10
375.00	150.00	100.00	235.85	1,857.08	1,860.03	769.10
375.00	150.00	100.00	235.85	1,857.08		769.10
375.00	150.00	100.00	235.85	1,871.82		768.10
375.00	150.00	100.00	235.85	3,144.66		482.00
375.00	150.00	100.00	235.85	3,062.98		484.00
375.00	150.00	100.00	235.85	3,187.16	3,128.99	481.00
375.00	150.00	100.00	235.85	3,062.98		484.00
375.00	150.00	100.00	235.85	3,187.16		481.00
375.00	150.00	100.00	235.85	3,520.14		293.00
375.00	150.00	100.00	235.85	3,520.14		293.00
375.00	150.00	100.00	235.85	3,520.14	3,541.48	293.00
375.00	150.00	100.00	235.85	3,573.48		292.00
375.00	150.00	100.00	235.85	3,573.48		292.00
375.00	150.00	100.00	235.85	3,520.14		1,034.00
375.00	150.00	100.00	235.85	3,520.14		1,034.00
375.00	150.00	100.00	235.85	3,520.14	3,530.81	1,034.00
375.00	150.00	100.00	235.85	3,520.14		1,034.00
375.00	150.00	100.00	235.85	3,573.48		1,033.00
375.00	150.00	100.00	235.85	3,557.31		556.60
375.00	150.00	100.00	235.85	3,546.61		556.80
375.00	150.00	100.00	235.85	3,562.68	3,558.40	556.50
375.00	150.00	100.00	235.85	3,557.31		556.60
375.00	150.00	100.00	235.85	3,568.07		556.40
375.00	150.00	100.00	235,85	3443,06		445,20
375.00	150.00	100.00	235,85	3438,04		445,30
375.00	150.00	100.00	235,85	3443,06	3447,10	445,20
375.00	150.00	100.00	235,85	3453,14		445,00
375.00	150.00	100.00	235,85	3458,20		444,90
375.00	150.00	100.00	235,85	3617,32		323,50
375.00	150.00	100.00	235,85	3622,88		323,40
375.00	150.00	100.00	235,85	3628,45	3627,35	323,30
375.00	150.00	100.00	235,85	3634,05		323,20
375.00	150.00	100.00	235,85	3634,05		323,20
375.00	150.00	100.00	235,85	3546,61		733,40
375.00	150.00	100.00	235,85	3546,61		733,40
375.00	150.00	100.00	235,85	3557,31	3555,18	733,20
375.00	150.00	100.00	235,85	3562,68		733,10
375.00	150.00	100.00	235,85	3562,68		733,10
375.00	150.00	100.00	235,85	3611,78		491,40
375.00	150.00	100.00	235,85	3617,32		491,30
375.00	150.00	100.00	235,85	3622,88	3620,66	491,20
375.00	150.00	100.00	235,85	3622,88		491,20
375.00	150.00	100.00	235,85	3628,45		491,10
375.00	150.00	100.00	235,85	3378,93		237,70
375.00	150.00	100.00	235,85	3378,93		237,70
375.00	150.00	100.00	235,85	3378,93	3381,84	237,70
375.00	150.00	100.00	235,85	3383,78		237,60
375.00	150.00	100.00	235,85	3388,64		237,50
375.00	150.00	100.00	235,85	3448,09		396,70

375.00	150.00	100.00	235,85	3443,06	3452,15	396,80
375.00	150.00	100.00	235,85	3448,09		396,70
375.00	150.00	100.00	235,85	3458,20		396,50
375.00	150.00	100.00	235,85	3463,28		396,40
375.00	150.00	100.00	235,85	3483,74	3485,81	179,70
375.00	150.00	100.00	235,85	3478,61		179,80
375.00	150.00	100.00	235,85	3483,74		179,70
375.00	150.00	100.00	235,85	3488,90		179,60
375.00	150.00	100.00	235,85	3494,07		179,50
375.00	150.00	100.00	235,85	3438,04	3449,13	850,80
375.00	150.00	100.00	235,85	3438,04		850,80
375.00	150.00	100.00	235,85	3453,14		850,50
375.00	150.00	100.00	235,85	3458,20		850,40
375.00	150.00	100.00	235,85	3458,20		850,40
375.00	150.00	100.00	235,85	3473,48	3486,85	329,40
375.00	150.00	100.00	235,85	3483,74		329,20
375.00	150.00	100.00	235,85	3488,90		329,10
375.00	150.00	100.00	235,85	3494,07		329,00
375.00	150.00	100.00	235,85	3494,07		329,00
450.00	180.00	120.00	283.02	3,110.10	3,174.21	890.90
450.00	180.00	120.00	283.02	3,110.10		890.90
450.00	180.00	120.00	283.02	3,144.66		890.90
450.00	180.00	120.00	283.02	3,253.10		890.90
450.00	180.00	120.00	283.02	3,253.10		890.90
450.00	180.00	120.00	283.02	3,451.46	3,557.66	1,054.50
450.00	180.00	120.00	283.02	3,451.46		1,054.50
450.00	180.00	120.00	283.02	3,628.45		1,054.50
450.00	180.00	120.00	283.02	3,628.45		1,054.50
450.00	180.00	120.00	283.02	3,628.45		1,054.50
450.00	180.00	120.00	283,02	3481,17	3485,47	485,40
450.00	180.00	120.00	283,02	3481,17		485,40
450.00	180.00	120.00	283,02	3489,76		485,20
450.00	180.00	120.00	283,02	3481,17		485,40
450.00	180.00	120.00	283,02	3494,07		485,10
450.00	180.00	120.00	283,02	3464,13	3476,92	1002,90
450.00	180.00	120.00	283,02	3476,90		1002,60
450.00	180.00	120.00	283,02	3481,17		1002,50
450.00	180.00	120.00	283,02	3472,63		1002,70
450.00	180.00	120.00	283,02	3489,76		1002,30
450.00	180.00	120.00	283,02	3447,25	3463,30	376,20
450.00	180.00	120.00	283,02	3464,13		375,80
450.00	180.00	120.00	283,02	3464,13		375,80
450.00	180.00	120.00	283,02	3472,63		375,60
450.00	180.00	120.00	283,02	3468,38		375,70
450.00	180.00	120.00	283,02	3507,06	3518,41	272,70
450.00	180.00	120.00	283,02	3515,77		272,50
450.00	180.00	120.00	283,02	3520,14		272,40
450.00	180.00	120.00	283,02	3520,14		272,40
450.00	180.00	120.00	283,02	3528,92		272,20
450.00	180.00	120.00	283,02	3537,74	3548,41	556,30
450.00	180.00	120.00	283,02	3542,17		556,20
450.00	180.00	120.00	283,02	3546,61		556,10
450.00	180.00	120.00	283,02	3555,52		555,90
450.00	180.00	120.00	283,02	3559,99		555,80
450.00	180.00	120.00	283,02	3476,90		1044,80

450.00	180.00	120.00	283,02	3485,46	3487,19	1044,60
450.00	180.00	120.00	283,02	3489,76		1044,50
450.00	180.00	120.00	283,02	3489,76		1044,50
450.00	180.00	120.00	283,02	3494,07		1044,40
450.00	180.00	120.00	283,02	3459,90	3469,24	394,30
450.00	180.00	120.00	283,02	3464,13		394,20
450.00	180.00	120.00	283,02	3468,38		394,10
450.00	180.00	120.00	283,02	3476,90		393,90
450.00	180.00	120.00	283,02	3476,90		393,90
450.00	180.00	120.00	283,02	3353,31	3362,08	120,70
450.00	180.00	120.00	283,02	3361,28		120,50
450.00	180.00	120.00	283,02	3361,28		120,50
450.00	180.00	120.00	283,02	3365,27		120,40
450.00	180.00	120.00	283,02	3369,28		120,30
450.00	180.00	120.00	283,02	3357,29	3367,69	909,80
450.00	180.00	120.00	283,02	3365,27		909,60
450.00	180.00	120.00	283,02	3369,28		909,50
450.00	180.00	120.00	283,02	3373,29		909,40
450.00	180.00	120.00	283,02	3373,29		909,40
450.00	180.00	120.00	283.02	3,349.34	3,314.39	941.50
450.00	180.00	120.00	283.02	3,361.28		941.20
450.00	180.00	120.00	283.02	3,283.29		943.20
450.00	180.00	120.00	283.02	3,287.10		943.10
450.00	180.00	120.00	283.02	3,290.92		943.00
450.00	180.00	120.00	283.02	3,393.52	3,399.23	352.90
450.00	180.00	120.00	283.02	3,393.52		352.90
450.00	180.00	120.00	283.02	3,397.59		352.80
450.00	180.00	120.00	283.02	3,405.77		352.60
450.00	180.00	120.00	283.02	3,405.77		352.60
450.00	180.00	120.00	283,02	3345,38	3350,93	1021,10
450.00	180.00	120.00	283,02	3349,34		1021,00
450.00	180.00	120.00	283,02	3349,34		1021,00
450.00	180.00	120.00	283,02	3353,31		1020,90
450.00	180.00	120.00	283,02	3357,29		1020,80
450.00	180.00	120.00	283,02	3443,06	3450,62	269,50
450.00	180.00	120.00	283,02	3447,25		269,40
450.00	180.00	120.00	283,02	3455,67		269,20
450.00	180.00	120.00	283,02	3451,46		269,30
450.00	180.00	120.00	283,02	3455,67		269,20
450.00	180.00	120.00	283,02	2074,92	2074,32	411,50
450.00	180.00	120.00	283,02	2074,92		411,50
450.00	180.00	120.00	283,02	2070,37		411,80
450.00	180.00	120.00	283,02	2076,44		411,40
450.00	180.00	120.00	283,02	2074,92		411,50
450.00	180.00	120.00	283.02	1,479.45	1,481.63	1,083.70
450.00	180.00	120.00	283.02	1,483.33		1,083.20
450.00	180.00	120.00	283.02	1,479.45		1,083.70
450.00	180.00	120.00	283.02	1,480.23		1,083.60
450.00	180.00	120.00	283.02	1,485.67		1,082.90
450.00	180.00	120.00	283.02	2,017.24	2,018.12	191.20
450.00	180.00	120.00	283.02	2,010.08		191.70
450.00	180.00	120.00	283.02	2,023.01		190.80
450.00	180.00	120.00	283.02	2,015.81		191.30
450.00	180.00	120.00	283.02	2,024.46		190.70
450.00	180.00	120.00	283,02	3279,48		763,60

450.00	180.00	120.00	283,02	3271,90		763,80
450.00	180.00	120.00	283,02	3279,48	3281,78	763,60
450.00	180.00	120.00	283,02	3287,10		763,40
450.00	180.00	120.00	283,02	3290,92		763,30
450.00	180.00	120.00	283,02	3287,10		307,10
450.00	180.00	120.00	283,02	3294,75		306,90
450.00	180.00	120.00	283,02	3298,59	3296,30	306,80
450.00	180.00	120.00	283,02	3298,59		306,80
450.00	180.00	120.00	283,02	3302,44		306,70
450.00	180.00	120.00	283,02	3179,99		1042,70
450.00	180.00	120.00	283,02	3179,99		1042,70
450.00	180.00	120.00	283,02	3187,16	3187,17	1042,50
450.00	180.00	120.00	283,02	3194,35		1042,30
450.00	180.00	120.00	283,02	3194,35		1042,30
450.00	180.00	120.00	283.02	2,969.77		1,047.50
450.00	180.00	120.00	283.02	2,972.89		1,047.40
450.00	180.00	120.00	283.02	2,963.55	2,921.37	1,047.70
450.00	180.00	120.00	283.02	2,705.73		1,056.80
450.00	180.00	120.00	283.02	2,994.91		1,046.70
450.00	180.00	120.00	283.02	2,410.73		226.30
450.00	180.00	120.00	283.02	2,304.72		231.70
450.00	180.00	120.00	283.02	2,297.24	2,372.85	232.10
450.00	180.00	120.00	283.02	2,297.24		232.10
450.00	180.00	120.00	283.02	2,554.33		219.70
450.00	180.00	120.00	283,02	3476,90		465,60
450.00	180.00	120.00	283,02	3481,17		465,50
450.00	180.00	120.00	283,02	3485,46	3485,47	465,40
450.00	180.00	120.00	283,02	3489,76		465,30
450.00	180.00	120.00	283,02	3494,07		465,20
450.00	180.00	120.00	283,02	3476,90		1032,10
450.00	180.00	120.00	283,02	3481,17		1032,00
450.00	180.00	120.00	283,02	3489,76	3486,33	1031,80
450.00	180.00	120.00	283,02	3489,76		1031,80
450.00	180.00	120.00	283,02	3494,07		1031,70
450.00	180.00	120.00	283,02	3279,48		562,00
450.00	180.00	120.00	283,02	3275,69		562,10
450.00	180.00	120.00	283,02	3275,69	3281,01	562,10
450.00	180.00	120.00	283,02	3283,29		561,90
450.00	180.00	120.00	283,02	3290,92		561,70
450.00	180.00	120.00	283.02	3,455.67		129.20
450.00	180.00	120.00	283.02	3,459.90		129.10
450.00	180.00	120.00	283.02	3,455.67	3,462.45	129.20
450.00	180.00	120.00	283.02	3,472.63		128.80
450.00	180.00	120.00	283.02	3,468.38		128.90
450.00	180.00	120.00	283.02	3,489.76		307.80
450.00	180.00	120.00	283.02	3,489.76		307.80
450.00	180.00	120.00	283.02	3,494.07	3,492.35	307.70
450.00	180.00	120.00	283.02	3,489.76		307.80
450.00	180.00	120.00	283.02	3,498.39		307.60
150.00	300.00	60.00	313.21	2,716.47		335.80
150.00	300.00	60.00	313.21	2,718.83		335.60
150.00	300.00	60.00	313.21	2,718.83	2,716.01	335.50
150.00	300.00	60.00	313.21	2,718.83		335.40
150.00	300.00	60.00	313.21	2,707.08		335.80
150.00	300.00	60.00	313.21	2,427.98		532.60

150.00	300.00	60.00	313.21	2,429.86		532.40
150.00	300.00	60.00	313.21	2,427.98	2,426.10	532.40
150.00	300.00	60.00	313.21	2,418.60		532.90
150.00	300.00	60.00	313.21	2,426.10		532.40
150.00	300.00	60.00	313.21	1,619.49		860.20
150.00	300.00	60.00	313.21	1,618.65		860.20
150.00	300.00	60.00	313.21	1,620.33	1,619.66	860.00
150.00	300.00	60.00	313.21	1,620.33		859.90
150.00	300.00	60.00	313.21	1,619.49		859.90
150.00	300.00	60.00	313.21	2,424.22		970.00
150.00	300.00	60.00	313.21	2,378.20		972.40
150.00	300.00	60.00	313.21	2,376.40	2,366.66	972.40
150.00	300.00	60.00	313.21	2,420.47		970.00
150.00	300.00	60.00	313.21	2,234.02		980.60
150.00	300.00	60.00	313.21	1,979.83		921.20
150.00	300.00	60.00	313.21	1,977.33		921.30
150.00	300.00	60.00	313.21	1,973.59	1,977.08	921.60
150.00	300.00	60.00	313.21	1,978.58		921.10
150.00	300.00	60.00	313.21	1,976.08		921.20
150.00	300.00	60.00	313.21	2,837.04		462.30
150.00	300.00	60.00	313.21	2,834.47		462.30
150.00	300.00	60.00	313.21	2,844.77	2,840.65	461.90
150.00	300.00	60.00	313.21	2,842.19		461.90
150.00	300.00	60.00	313.21	2,844.77		461.70
150.00	300.00	60.00	313.21	2,837.04		641.60
150.00	300.00	60.00	313.21	2,842.19		641.40
150.00	300.00	60.00	313.21	2,844.77	2,842.19	641.20
150.00	300.00	60.00	313.21	2,842.19		641.20
150.00	300.00	60.00	313.21	2,844.77		641.00
150.00	300.00	60.00	313.21	2,381.82		848.70
150.00	300.00	60.00	313.21	2,279.54		854.50
150.00	300.00	60.00	313.21	2,346.14	2,350.30	850.50
150.00	300.00	60.00	313.21	2,387.27		848.10
150.00	300.00	60.00	313.21	2,356.73		849.70
150.00	300.00	60.00	313.21	2,237.21		493.40
150.00	300.00	60.00	313.21	2,245.23		492.80
150.00	300.00	60.00	313.21	2,234.02	2,305.98	493.40
150.00	300.00	60.00	313.21	2,577.85		474.70
150.00	300.00	60.00	313.21	2,235.61		493.10
150.00	300.00	60.00	313.21	1,688.46		1,101.00
150.00	300.00	60.00	313.21	1,852.21		1,084.60
150.00	300.00	60.00	313.21	1,683.92	1,721.21	1,101.40
150.00	300.00	60.00	313.21	1,689.37		1,100.70
150.00	300.00	60.00	313.21	1,692.11		1,100.30
150.00	300.00	60.00	313.21	2,271.28		730.10
150.00	300.00	60.00	313.21	2,269.63		730.10
150.00	300.00	60.00	313.21	2,378.20	2,292.99	723.80
150.00	300.00	60.00	313.21	2,272.93		729.80
150.00	300.00	60.00	313.21	2,272.93		729.70
150.00	300.00	60.00	313.21	2,714.12		1,008.40
150.00	300.00	60.00	313.21	2,714.12		1,008.30
150.00	300.00	60.00	313.21	2,752.28	2,780.16	1,006.60
150.00	300.00	60.00	313.21	2,725.93		1,007.60
150.00	300.00	60.00	313.21	2,994.35		997.30
150.00	300.00	60.00	313.21	2,546.42		534.70

150.00	300.00	60.00	313.21	2,309.80		547.20
150.00	300.00	60.00	313.21	2,523.85	2,484.80	535.70
150.00	300.00	60.00	313.21	2,542.28		534.70
150.00	300.00	60.00	313.21	2,501.67		536.60
150.00	300.00	60.00	313.21	2,291.22		1,064.20
150.00	300.00	60.00	313.21	2,491.72		1,053.10
150.00	300.00	60.00	313.21	2,507.68	2,446.17	1,052.20
150.00	300.00	60.00	313.21	2,477.92		1,053.60
150.00	300.00	60.00	313.21	2,462.34		1,054.30
150.00	300.00	60.00	313.21	2,511.70		201.10
150.00	300.00	60.00	313.21	2,507.68		201.20
150.00	300.00	60.00	313.21	2,505.67	2,508.49	201.20
150.00	300.00	60.00	313.21	2,515.74		200.60
150.00	300.00	60.00	313.21	2,501.67		201.20
150.00	300.00	60.00	313.21	1,083.02		779.70
150.00	300.00	60.00	313.21	1,082.64		779.70
150.00	300.00	60.00	313.21	1,083.77	994.13	779.30
150.00	300.00	60.00	313.21	638.94		980.40
150.00	300.00	60.00	313.21	1,082.27		779.50
150.00	300.00	60.00	313.21	1,607.03		952.20
150.00	300.00	60.00	313.21	1,448.70		973.50
150.00	300.00	60.00	313.21	1,450.04	1,478.37	973.20
150.00	300.00	60.00	313.21	1,440.04		974.60
150.00	300.00	60.00	313.21	1,446.03		973.60
150.00	300.00	60.00	313.21	2,499.67		1,107.90
150.00	300.00	60.00	313.21	2,497.68		1,107.90
150.00	300.00	60.00	313.21	2,505.67	2,498.50	1,107.50
150.00	300.00	60.00	313.21	2,485.79		1,108.40
150.00	300.00	60.00	313.21	2,503.67		1,107.30
150.00	300.00	60.00	313.21	2,819.16		502.50
150.00	300.00	60.00	313.21	2,971.62		496.80
150.00	300.00	60.00	313.21	2,971.62	2,910.16	496.70
150.00	300.00	60.00	313.21	2,794.02		503.30
150.00	300.00	60.00	313.21	2,994.35		495.70
150.00	300.00	60.00	313.21	2,774.22		1,062.30
150.00	300.00	60.00	313.21	2,894.72		1,057.50
150.00	300.00	60.00	313.21	2,764.42	2,820.11	1,062.50
150.00	300.00	60.00	313.21	2,902.77		1,057.00
150.00	300.00	60.00	313.21	2,764.42		1,062.30
150.00	300.00	60.00	313.21	2,757.12		872.60
150.00	300.00	60.00	313.21	2,774.22		871.80
150.00	300.00	60.00	313.21	2,774.22	2,773.26	871.70
150.00	300.00	60.00	313.21	2,776.68		871.50
150.00	300.00	60.00	313.21	2,784.08		871.10
150.00	300.00	60.00	313.21	2,771.76		383.50
150.00	300.00	60.00	313.21	2,769.31		383.50
150.00	300.00	60.00	313.21	2,769.31	2,771.29	383.40
150.00	300.00	60.00	313.21	2,761.99		383.60
150.00	300.00	60.00	313.21	2,784.08		382.60
150.00	300.00	60.00	313.21	2,335.64		539.60
150.00	300.00	60.00	313.21	2,360.28		538.10
150.00	300.00	60.00	313.21	2,277.89	2,321.33	542.90
150.00	300.00	60.00	313.21	2,354.96		538.30
150.00	300.00	60.00	313.21	2,277.89		542.70
150.00	300.00	60.00	313.21	2,573.62		359.90

150.00	300.00	60.00	313.21	2,597.09		358.70
150.00	300.00	60.00	313.21	2,582.10	2,585.97	359.40
150.00	300.00	60.00	313.21	2,584.23		359.20
150.00	300.00	60.00	313.21	2,592.79		358.70
150.00	300.00	60.00	313.21	2,686.19		914.10
150.00	300.00	60.00	313.21	2,679.29		914.30
150.00	300.00	60.00	313.21	2,681.59	2,685.27	914.10
150.00	300.00	60.00	313.21	2,690.80		913.60
150.00	300.00	60.00	313.21	2,688.49		913.60
150.00	300.00	60.00	313.21	3,579.54		749.40
150.00	300.00	60.00	313.21	3,575.46		749.40
150.00	300.00	60.00	313.21	3,575.46	3,577.09	749.30
150.00	300.00	60.00	313.21	3,579.54		749.10
150.00	300.00	60.00	313.21	3,575.46		749.10
150.00	300.00	60.00	313.21	3,029.10		574.60
150.00	300.00	60.00	313.21	3,026.18		574.60
150.00	300.00	60.00	313.21	3,023.25	3,024.43	574.60
150.00	300.00	60.00	313.21	3,020.34		574.60
150.00	300.00	60.00	313.21	3,023.25		574.40
150.00	300.00	60.00	313.21	3,026.18		302.70
150.00	300.00	60.00	313.21	3,026.18		302.60
150.00	300.00	60.00	313.21	3,029.10	3,027.94	302.40
150.00	300.00	60.00	313.21	3,023.25		302.60
150.00	300.00	60.00	313.21	3,034.97		302.10

Channel 5						
(sensor 5)						
location			Distance	Velocity	Average velocity for sensor 5	Arrival time, millisecond
x5	y5	z5	(mm)	m/s	m/s	t5
150.00	30.00	60.00	82.16	2,842.85	2,854.74	256.20
150.00	30.00	60.00	82.16	2,862.66		256.00
150.00	30.00	60.00	82.16	2,862.66		255.90
150.00	30.00	60.00	82.16	2,862.66		255.80
150.00	30.00	60.00	82.16	2,842.85		255.90
150.00	30.00	60.00	82.16	3,286.34	3,296.89	1,000.60
150.00	30.00	60.00	82.16	3,299.53		1,000.50
150.00	30.00	60.00	82.16	3,299.53		1,000.40
150.00	30.00	60.00	82.16	3,299.53		1,000.30
150.00	30.00	60.00	82.16	3,299.53		1,000.20
150.00	30.00	60.00	82.16	3,299.53	3,296.89	361.00
150.00	30.00	60.00	82.16	3,299.53		360.90
150.00	30.00	60.00	82.16	3,286.34		360.90
150.00	30.00	60.00	82.16	3,299.53		360.70
150.00	30.00	60.00	82.16	3,299.53		360.60
150.00	30.00	60.00	82.16	3,312.84	3,296.92	316.90
150.00	30.00	60.00	82.16	3,299.53		316.90
150.00	30.00	60.00	82.16	3,286.34		316.90
150.00	30.00	60.00	82.16	3,299.53		316.70
150.00	30.00	60.00	82.16	3,286.34		316.70
150.00	30.00	60.00	82.16	3,286.34	3,281.10	297.60
150.00	30.00	60.00	82.16	3,273.24		297.60
150.00	30.00	60.00	82.16	3,286.34		297.40
150.00	30.00	60.00	82.16	3,286.34		297.30
150.00	30.00	60.00	82.16	3,273.24		297.30
150.00	30.00	60.00	82.16	3,234.58	3,242.25	784.90
150.00	30.00	60.00	82.16	3,247.37		784.80
150.00	30.00	60.00	82.16	3,247.37		784.70
150.00	30.00	60.00	82.16	3,247.37		784.60
150.00	30.00	60.00	82.16	3,234.58		784.60
150.00	30.00	60.00	82.16	3,234.58	3,239.70	267.10
150.00	30.00	60.00	82.16	3,234.58		267.00
150.00	30.00	60.00	82.16	3,247.37		266.80
150.00	30.00	60.00	82.16	3,234.58		266.80
150.00	30.00	60.00	82.16	3,247.37		266.60
150.00	30.00	60.00	82.16	3,221.90	3,211.83	702.10
150.00	30.00	60.00	82.16	3,209.31		702.10
150.00	30.00	60.00	82.16	3,209.31		702.00
150.00	30.00	60.00	82.16	3,209.31		701.90
150.00	30.00	60.00	82.16	3,209.31		701.80
150.00	30.00	60.00	82.16	1,782.18	1,779.86	393.00
150.00	30.00	60.00	82.16	1,782.18		392.90
150.00	30.00	60.00	82.16	1,778.32		392.90
150.00	30.00	60.00	82.16	1,778.32		392.80
150.00	30.00	60.00	82.16	1,778.32		392.70
150.00	30.00	60.00	82.16	1,965.51	1,968.36	377.80
150.00	30.00	60.00	82.16	1,965.51		377.70
150.00	30.00	60.00	82.16	1,960.82		377.70
150.00	30.00	60.00	82.16	1,979.72		377.20

150.00	30.00	60.00	82.16	1,970.23		377.40
150.00	30.00	60.00	82.16	1,607.80	1,606.54	500.90
150.00	30.00	60.00	82.16	1,607.80		500.80
150.00	30.00	60.00	82.16	1,604.66		500.80
150.00	30.00	60.00	82.16	1,607.80		500.60
150.00	30.00	60.00	82.16	1,604.66		500.70
150.00	30.00	60.00	82.16	1,423.89	1,424.88	476.50
150.00	30.00	60.00	82.16	1,426.36		476.40
150.00	30.00	60.00	82.16	1,423.89		476.40
150.00	30.00	60.00	82.16	1,426.36		476.20
150.00	30.00	60.00	82.16	1,423.89		476.20
150.00	30.00	60.00	82.16	2,327.43	2,322.18	475.90
150.00	30.00	60.00	82.16	2,314.32		476.00
150.00	30.00	60.00	82.16	2,320.86		475.80
150.00	30.00	60.00	82.16	2,320.86		475.70
150.00	30.00	60.00	82.16	2,327.43		475.60
150.00	30.00	60.00	82.16	3,339.77	3,347.95	568.00
150.00	30.00	60.00	82.16	3,353.40		567.90
150.00	30.00	60.00	82.16	3,353.40		567.80
150.00	30.00	60.00	82.16	3,339.77		567.80
150.00	30.00	60.00	82.16	3,353.40		567.60
150.00	30.00	60.00	82.16	1,666.50	1,667.86	456.90
150.00	30.00	60.00	82.16	1,666.50		456.80
150.00	30.00	60.00	82.16	1,666.50		456.80
150.00	30.00	60.00	82.16	1,669.89		456.60
150.00	30.00	60.00	82.16	1,669.89		456.50
150.00	30.00	60.00	82.16	2,388.33	2,405.18	74.80
150.00	30.00	60.00	82.16	2,402.29		74.50
150.00	30.00	60.00	82.16	2,395.29		74.50
150.00	30.00	60.00	82.16	2,416.42		74.10
150.00	30.00	60.00	82.16	2,423.55		73.90
150.00	30.00	60.00	82.16	2,437.93	2,433.62	369.50
150.00	30.00	60.00	82.16	2,437.93		369.40
150.00	30.00	60.00	82.16	2,430.72		369.40
150.00	30.00	60.00	82.16	2,437.93		369.20
150.00	30.00	60.00	82.16	2,423.55		369.30
150.00	30.00	60.00	82.16	3,247.37	3,242.25	357.00
150.00	30.00	60.00	82.16	3,247.37		356.90
150.00	30.00	60.00	82.16	3,234.58		356.90
150.00	30.00	60.00	82.16	3,234.58		356.80
150.00	30.00	60.00	82.16	3,247.37		356.60
150.00	30.00	60.00	82.16	1,279.73	1,280.53	643.40
150.00	30.00	60.00	82.16	1,283.72		643.10
150.00	30.00	60.00	82.16	1,281.72		643.10
150.00	30.00	60.00	82.16	1,277.74		643.20
150.00	30.00	60.00	82.16	1,279.73		643.00
150.00	30.00	60.00	82.16	1,295.87	1,297.93	314.50
150.00	30.00	60.00	82.16	1,299.97		314.20
150.00	30.00	60.00	82.16	1,299.97		314.10
150.00	30.00	60.00	82.16	1,291.80		314.40
150.00	30.00	60.00	82.16	1,302.03		313.80
150.00	30.00	60.00	82.16	2,934.23	2,925.87	607.00
150.00	30.00	60.00	82.16	2,923.79		607.00
150.00	30.00	60.00	82.16	2,923.79		606.90
150.00	30.00	60.00	82.16	2,923.79		606.80

150.00	30.00	60.00	82.16	2,923.79		606.80
150.00	30.00	60.00	82.16	1,362.49		528.30
150.00	30.00	60.00	82.16	1,362.49		528.20
150.00	30.00	60.00	82.16	1,362.49	1,361.59	528.10
150.00	30.00	60.00	82.16	1,360.24		528.10
150.00	30.00	60.00	82.16	1,360.24		528.00
150.00	30.00	60.00	82.16	1,485.69		957.10
150.00	30.00	60.00	82.16	1,402.02		960.30
150.00	30.00	60.00	82.16	1,397.25	1,416.37	960.40
150.00	30.00	60.00	82.16	1,397.25		960.30
150.00	30.00	60.00	82.16	1,399.63		960.20
150.00	30.00	60.00	82.16	2,133.98		74.50
150.00	30.00	60.00	82.16	2,117.48		74.70
150.00	30.00	60.00	82.16	2,122.96	2,132.94	74.50
150.00	30.00	60.00	82.16	2,145.13		74.10
150.00	30.00	60.00	82.16	2,145.13		74.00
150.00	30.00	60.00	82.16	1,620.48		897.30
150.00	30.00	60.00	82.16	1,626.90		897.00
150.00	30.00	60.00	82.16	1,636.62	1,627.56	896.60
150.00	30.00	60.00	82.16	1,626.90		896.90
150.00	30.00	60.00	82.16	1,626.90		896.80
150.00	30.00	60.00	82.16	1,633.37		783.30
150.00	30.00	60.00	82.16	1,626.90		783.40
150.00	30.00	60.00	82.16	1,633.37	1,632.08	783.10
150.00	30.00	60.00	82.16	1,639.89		782.80
150.00	30.00	60.00	82.16	1,626.90		783.10
150.00	30.00	60.00	82.16	1,919.59		441.30
150.00	30.00	60.00	82.16	2,117.48		437.20
150.00	30.00	60.00	82.16	1,906.23	1,952.93	441.40
150.00	30.00	60.00	82.16	1,915.11		441.20
150.00	30.00	60.00	82.16	1,906.23		441.30
150.00	30.00	60.00	82.16	2,862.66		1,019.00
150.00	30.00	60.00	82.16	2,872.67		1,018.90
150.00	30.00	60.00	82.16	2,872.67	2,870.67	1,018.80
150.00	30.00	60.00	82.16	2,872.67		1,018.70
150.00	30.00	60.00	82.16	2,872.67		1,018.60
225.00	120.00	120.00	162.25	3,373.18		74.00
225.00	120.00	120.00	162.25	3,366.18		74.00
225.00	120.00	120.00	162.25	3,366.18	3,366.18	73.90
225.00	120.00	120.00	162.25	3,359.21		73.90
225.00	120.00	120.00	162.25	3,366.18		73.80
225.00	120.00	120.00	162.25	3,380.20		345.10
225.00	120.00	120.00	162.25	3,380.20		345.10
225.00	120.00	120.00	162.25	3,387.26	3,383.03	344.90
225.00	120.00	120.00	162.25	3,380.20		344.90
225.00	120.00	120.00	162.25	3,387.26		344.70
225.00	120.00	120.00	162.25	3,394.35		134.60
225.00	120.00	120.00	162.25	3,380.20		134.70
225.00	120.00	120.00	162.25	3,387.26	3,385.86	134.50
225.00	120.00	120.00	162.25	3,387.26		134.40
225.00	120.00	120.00	162.25	3,380.20		134.40
225.00	120.00	120.00	162.25	3,264.58		223.00
225.00	120.00	120.00	162.25	3,251.50		223.10
225.00	120.00	120.00	162.25	3,264.58	3,261.97	222.90
225.00	120.00	120.00	162.25	3,264.58		222.80

225.00	120.00	120.00	162.25	3,264.58		222.70
225.00	120.00	120.00	162.25	3,271.17	3,271.17	62.10
225.00	120.00	120.00	162.25	3,271.17		62.00
225.00	120.00	120.00	162.25	3,271.17		61.90
225.00	120.00	120.00	162.25	3,271.17		61.80
225.00	120.00	120.00	162.25	3,271.17		61.70
225.00	120.00	120.00	162.25	3,212.87	3,247.75	119.90
225.00	120.00	120.00	162.25	3,245.00		119.30
225.00	120.00	120.00	162.25	3,284.41		118.70
225.00	120.00	120.00	162.25	3,245.00		119.10
225.00	120.00	120.00	162.25	3,251.50		119.00
225.00	120.00	120.00	162.25	3,193.89	3,206.54	69.30
225.00	120.00	120.00	162.25	3,206.52		69.00
225.00	120.00	120.00	162.25	3,219.24		68.70
225.00	120.00	120.00	162.25	3,206.52		68.80
225.00	120.00	120.00	162.25	3,206.52		68.70
225.00	120.00	120.00	162.25	3,258.03	3,250.20	719.80
225.00	120.00	120.00	162.25	3,245.00		720.00
225.00	120.00	120.00	162.25	3,251.50		719.80
225.00	120.00	120.00	162.25	3,245.00		719.80
225.00	120.00	120.00	162.25	3,251.50		719.60
225.00	120.00	120.00	162.25	3,206.52	3,200.20	113.20
225.00	120.00	120.00	162.25	3,193.89		113.30
225.00	120.00	120.00	162.25	3,200.19		113.20
225.00	120.00	120.00	162.25	3,200.19		113.10
225.00	120.00	120.00	162.25	3,200.19		113.00
225.00	120.00	120.00	162.25	3,175.14	3,180.14	998.30
225.00	120.00	120.00	162.25	3,175.14		998.20
225.00	120.00	120.00	162.25	3,181.37		998.00
225.00	120.00	120.00	162.25	3,193.89		997.70
225.00	120.00	120.00	162.25	3,175.14		997.90
225.00	120.00	120.00	162.25	3,044.09	3,036.12	762.30
225.00	120.00	120.00	162.25	3,027.05		762.60
225.00	120.00	120.00	162.25	3,038.39		762.30
225.00	120.00	120.00	162.25	3,032.71		762.30
225.00	120.00	120.00	162.25	3,038.39		762.10
225.00	120.00	120.00	162.25	3,055.55	3,033.89	459.50
225.00	120.00	120.00	162.25	3,021.41		460.00
225.00	120.00	120.00	162.25	3,038.39		459.60
225.00	120.00	120.00	162.25	3,027.05		459.70
225.00	120.00	120.00	162.25	3,027.05		459.70
225.00	120.00	120.00	162.25	3,114.20	3,123.81	712.60
225.00	120.00	120.00	162.25	3,120.19		712.40
225.00	120.00	120.00	162.25	3,126.20		712.20
225.00	120.00	120.00	162.25	3,132.24		712.10
225.00	120.00	120.00	162.25	3,126.20		712.10
225.00	120.00	120.00	162.25	3,277.77	3,283.10	229.00
225.00	120.00	120.00	162.25	3,277.77		228.90
225.00	120.00	120.00	162.25	3,297.76		228.60
225.00	120.00	120.00	162.25	3,284.41		228.70
225.00	120.00	120.00	162.25	3,277.77		228.70
225.00	120.00	120.00	162.25	3,238.52	3,226.96	966.70
225.00	120.00	120.00	162.25	3,225.64		966.80
225.00	120.00	120.00	162.25	3,206.52		967.00
225.00	120.00	120.00	162.25	3,232.07		966.60

225.00	120.00	120.00	162.25	3,232.07		966.50
225.00	120.00	120.00	162.25	4,016.08		797.70
225.00	120.00	120.00	162.25	3,996.30		797.90
225.00	120.00	120.00	162.25	4,046.13	4,020.13	797.30
225.00	120.00	120.00	162.25	4,026.05		797.40
225.00	120.00	120.00	162.25	4,016.08		797.40
225.00	120.00	120.00	162.25	3,304.48		172.20
225.00	120.00	120.00	162.25	3,291.07		172.30
225.00	120.00	120.00	162.25	3,304.48	3,307.21	172.00
225.00	120.00	120.00	162.25	3,311.22		171.90
225.00	120.00	120.00	162.25	3,324.79		171.60
225.00	120.00	120.00	162.25	3,271.17		924.20
225.00	120.00	120.00	162.25	3,264.58		924.20
225.00	120.00	120.00	162.25	3,264.58	3,267.22	924.10
225.00	120.00	120.00	162.25	3,271.17		923.90
225.00	120.00	120.00	162.25	3,264.58		923.90
225.00	120.00	120.00	162.25	2,759.35		512.10
225.00	120.00	120.00	162.25	2,768.77		511.80
225.00	120.00	120.00	162.25	2,759.35	2,762.17	511.90
225.00	120.00	120.00	162.25	2,764.05		511.70
225.00	120.00	120.00	162.25	2,759.35		511.70
225.00	120.00	120.00	162.25	2,754.67		343.00
225.00	120.00	120.00	162.25	2,754.67		342.90
225.00	120.00	120.00	162.25	2,750.00	2,752.80	342.90
225.00	120.00	120.00	162.25	2,754.67		342.70
225.00	120.00	120.00	162.25	2,750.00		342.70
225.00	120.00	120.00	162.25	2,816.84		412.70
225.00	120.00	120.00	162.25	2,768.77		413.60
225.00	120.00	120.00	162.25	2,764.05	2,776.50	413.60
225.00	120.00	120.00	162.25	2,764.05		413.50
225.00	120.00	120.00	162.25	2,768.77		413.30
225.00	120.00	120.00	162.25	2,745.34		162.70
225.00	120.00	120.00	162.25	2,887.01		159.70
225.00	120.00	120.00	162.25	2,740.71	2,771.82	162.60
225.00	120.00	120.00	162.25	2,745.34		162.50
225.00	120.00	120.00	162.25	2,740.71		162.50
225.00	120.00	120.00	162.25	2,759.35		960.50
225.00	120.00	120.00	162.25	2,754.67		960.50
225.00	120.00	120.00	162.25	2,750.00	2,754.67	960.50
225.00	120.00	120.00	162.25	2,750.00		960.40
225.00	120.00	120.00	162.25	2,759.35		960.20
225.00	120.00	120.00	162.25	3,156.61		568.40
225.00	120.00	120.00	162.25	3,144.38		568.50
225.00	120.00	120.00	162.25	3,156.61	3,157.86	568.20
225.00	120.00	120.00	162.25	3,162.76		568.10
225.00	120.00	120.00	162.25	3,168.94		567.90
225.00	120.00	120.00	162.25	3,238.52		148.80
225.00	120.00	120.00	162.25	3,238.52		148.70
225.00	120.00	120.00	162.25	3,238.52	3,239.81	148.60
225.00	120.00	120.00	162.25	3,238.52		148.50
225.00	120.00	120.00	162.25	3,245.00		148.40
225.00	120.00	120.00	162.25	3,232.07		776.60
225.00	120.00	120.00	162.25	3,232.07		776.50
225.00	120.00	120.00	162.25	3,232.07	3,232.07	776.40
225.00	120.00	120.00	162.25	3,232.07		776.30

225.00	120.00	120.00	162.25	3,232.07		776.20
225.00	120.00	120.00	162.25	3,232.07		206.90
225.00	120.00	120.00	162.25	3,232.07		206.80
225.00	120.00	120.00	162.25	3,225.64	3,234.66	206.80
225.00	120.00	120.00	162.25	3,238.52		206.60
225.00	120.00	120.00	162.25	3,245.00		206.40
225.00	120.00	120.00	162.25	3,206.52		599.50
225.00	120.00	120.00	162.25	3,200.19		599.50
225.00	120.00	120.00	162.25	3,200.19	3,206.53	599.40
225.00	120.00	120.00	162.25	3,206.52		599.30
225.00	120.00	120.00	162.25	3,219.24		599.00
300.00	60.00	120.00	164.32	3,346.57		405.60
300.00	60.00	120.00	164.32	3,333.00		405.70
300.00	60.00	120.00	164.32	3,353.40	3,343.86	405.30
300.00	60.00	120.00	164.32	3,346.57		405.40
300.00	60.00	120.00	164.32	3,339.77		405.40
300.00	60.00	120.00	164.32	3,857.20		205.40
300.00	60.00	120.00	164.32	3,866.28		205.20
300.00	60.00	120.00	164.32	3,848.17	3,857.22	205.30
300.00	60.00	120.00	164.32	3,866.28		205.00
300.00	60.00	120.00	164.32	3,848.17		205.10
300.00	60.00	120.00	164.32	3,619.31		245.40
300.00	60.00	120.00	164.32	3,603.44		245.50
300.00	60.00	120.00	164.32	3,627.30	3,617.74	245.10
300.00	60.00	120.00	164.32	3,619.31		245.10
300.00	60.00	120.00	164.32	3,619.31		245.00
300.00	60.00	120.00	164.32	3,459.30		559.90
300.00	60.00	120.00	164.32	3,466.60		559.80
300.00	60.00	120.00	164.32	3,473.93	3,472.48	559.70
300.00	60.00	120.00	164.32	3,481.29		559.60
300.00	60.00	120.00	164.32	3,481.29		559.60
300.00	60.00	120.00	164.32	3,595.55		438.60
300.00	60.00	120.00	164.32	3,603.44		438.50
300.00	60.00	120.00	164.32	3,611.36	3,609.79	438.40
300.00	60.00	120.00	164.32	3,619.31		438.30
300.00	60.00	120.00	164.32	3,619.31		438.30
300.00	60.00	120.00	164.32	3,541.31		319.40
300.00	60.00	120.00	164.32	3,548.96		319.30
300.00	60.00	120.00	164.32	3,564.36	3,558.22	319.10
300.00	60.00	120.00	164.32	3,564.36		319.10
300.00	60.00	120.00	164.32	3,572.10		319.00
300.00	60.00	120.00	164,32	3503,56		206,90
300.00	60.00	120.00	164,32	3518,56		206,70
300.00	60.00	120.00	164,32	3526,11	3523,13	206,60
300.00	60.00	120.00	164,32	3526,11		206,60
300.00	60.00	120.00	164,32	3541,31		206,40
300.00	60.00	120.00	164,32	3587,70		128,30
300.00	60.00	120.00	164,32	3572,10		128,50
300.00	60.00	120.00	164,32	3587,70	3589,30	128,30
300.00	60.00	120.00	164,32	3595,55		128,20
300.00	60.00	120.00	164,32	3603,44		128,10
300.00	60.00	120.00	164.32	2,857.68		341.90
300.00	60.00	120.00	164.32	2,857.68		341.90
300.00	60.00	120.00	164.32	2,761.63	2,838.47	343.90

300.00	60.00	120.00	164.32	2,857.68		341.90
300.00	60.00	120.00	164.32	2,857.68		341.90
300.00	60.00	120.00	164.32	2,456.15		636.50
300.00	60.00	120.00	164.32	2,317.58		636.50
300.00	60.00	120.00	164.32	2,317.58	2,345.30	636.50
300.00	60.00	120.00	164.32	2,317.58		636.50
300.00	60.00	120.00	164.32	2,317.58		636.50
300.00	60.00	120.00	164.32	2,738.61		855.80
300.00	60.00	120.00	164.32	2,738.61		855.80
300.00	60.00	120.00	164.32	2,934.23	2,835.75	851.80
300.00	60.00	120.00	164.32	2,934.23		851.80
300.00	60.00	120.00	164.32	2,833.05		853.80
300.00	60.00	120.00	164.32	2,908.26		661.10
300.00	60.00	120.00	164.32	2,960.66		660.10
300.00	60.00	120.00	164.32	2,960.66	2,950.18	660.10
300.00	60.00	120.00	164.32	2,960.66		660.10
300.00	60.00	120.00	164.32	2,960.66		660.10
300.00	60.00	120.00	164.32	3,172.14		387.40
300.00	60.00	120.00	164.32	3,437.59		383.40
300.00	60.00	120.00	164.32	3,437.59	3,413.88	383.40
300.00	60.00	120.00	164.32	3,511.04		382.40
300.00	60.00	120.00	164.32	3,511.04		382.40
300.00	60.00	120.00	164.32	3,381.00		272.30
300.00	60.00	120.00	164.32	3,381.00		272.30
300.00	60.00	120.00	164.32	3,381.00	3,381.00	272.30
300.00	60.00	120.00	164.32	3,381.00		272.30
300.00	60.00	120.00	164.32	3,381.00		272.30
300.00	60.00	120.00	164.32	2,808.83		148.50
300.00	60.00	120.00	164.32	2,671.82		148.50
300.00	60.00	120.00	164.32	2,808.83	2,709.52	148.50
300.00	60.00	120.00	164.32	2,629.07		148.50
300.00	60.00	120.00	164.32	2,629.07		148.50
300.00	60.00	120.00	164.32	2,898.00		804.30
300.00	60.00	120.00	164.32	2,898.00		804.30
300.00	60.00	120.00	164.32	2,898.00	2,908.41	804.30
300.00	60.00	120.00	164.32	2,898.00		804.30
300.00	60.00	120.00	164.32	2,950.03		803.30
300.00	60.00	120.00	164.32	3,466.60		908.90
300.00	60.00	120.00	164.32	3,260.25		911.90
300.00	60.00	120.00	164.32	3,541.31	3,413.94	907.90
300.00	60.00	120.00	164.32	3,541.31		907.90
300.00	60.00	120.00	164.32	3,260.25		911.90
300.00	60.00	120.00	164.32	3,159.94		123.30
300.00	60.00	120.00	164.32	3,159.94		123.30
300.00	60.00	120.00	164.32	3,159.94	3,159.94	123.30
300.00	60.00	120.00	164.32	3,159.94		123.30
300.00	60.00	120.00	164.32	3,159.94		123.30
300.00	60.00	120.00	164.32	2,966.01		936.90
300.00	60.00	120.00	164.32	2,966.01		936.90
300.00	60.00	120.00	164.32	2,966.01	2,976.91	936.90
300.00	60.00	120.00	164.32	2,966.01		936.90
300.00	60.00	120.00	164.32	3,020.53		935.90
300.00	60.00	120.00	164.32	3,234.58		557.70
300.00	60.00	120.00	164.32	3,234.58		557.70

300.00	60.00	120.00	164.32	3,234.58	3,234.58	557.70
300.00	60.00	120.00	164.32	3,234.58		557.70
300.00	60.00	120.00	164.32	3,234.58		557.70
300.00	60.00	120.00	164.32	2,756.99		889.50
300.00	60.00	120.00	164.32	2,756.99		889.50
300.00	60.00	120.00	164.32	2,804.04	2,785.22	888.50
300.00	60.00	120.00	164.32	2,804.04		888.50
300.00	60.00	120.00	164.32	2,804.04		888.50
300.00	60.00	120.00	164.32	3,437.59		669.00
300.00	60.00	120.00	164.32	3,511.04		668.00
300.00	60.00	120.00	164.32	3,511.04	3,496.35	668.00
300.00	60.00	120.00	164.32	3,511.04		668.00
300.00	60.00	120.00	164.32	3,511.04		668.00
300.00	60.00	120.00	164.32	3,100.32		664.10
300.00	60.00	120.00	164.32	3,100.32		664.10
300.00	60.00	120.00	164.32	3,100.32	3,100.32	664.10
300.00	60.00	120.00	164.32	3,100.32		664.10
300.00	60.00	120.00	164.32	3,100.32		664.10
300.00	60.00	120.00	164.32	3,253.80		852.30
300.00	60.00	120.00	164.32	3,260.25		852.20
300.00	60.00	120.00	164.32	3,266.73	3,266.76	852.10
300.00	60.00	120.00	164.32	3,273.24		852.00
300.00	60.00	120.00	164.32	3,279.78		851.90
300.00	60.00	120.00	164.32	3,240.96		790.10
300.00	60.00	120.00	164.32	3,247.37		790.00
300.00	60.00	120.00	164.32	3,253.80	3,251.24	789.90
300.00	60.00	120.00	164.32	3,253.80		789.90
300.00	60.00	120.00	164.32	3,260.25		789.80
300.00	60.00	120.00	164.32	3,209.31		1,014.80
300.00	60.00	120.00	164.32	3,209.31		1,014.80
300.00	60.00	120.00	164.32	3,215.59	3,216.87	1,014.70
300.00	60.00	120.00	164.32	3,221.90		1,014.60
300.00	60.00	120.00	164.32	3,228.23		1,014.50
300.00	60.00	120.00	164,32	3215,59		643,90
300.00	60.00	120.00	164,32	3228,23		643,70
300.00	60.00	120.00	164,32	3228,23	3226,97	643,70
300.00	60.00	120.00	164,32	3228,23		643,70
300.00	60.00	120.00	164,32	3234,58		643,60
300.00	60.00	120.00	164,32	3587,70		128,30
300.00	60.00	120.00	164,32	3572,10		128,50
300.00	60.00	120.00	164,32	3587,70	3589,30	128,30
300.00	60.00	120.00	164,32	3595,55		128,20
300.00	60.00	120.00	164,32	3603,44		128,10
375.00	200.00	200.00	270.42	3,346.74		486.70
375.00	200.00	200.00	270.42	3,346.74		490.70
375.00	200.00	200.00	270.42	3,346.74	3,346.74	490.70
375.00	200.00	200.00	270.42	3,346.74		490.70
375.00	200.00	200.00	270.42	3,346.74		490.70
375.00	200.00	200.00	270.42	3,422.99		836.60
375.00	200.00	200.00	270.42	3,380.20		837.60
375.00	200.00	200.00	270.42	3,558.11	3,504.99	837.60
375.00	200.00	200.00	270.42	3,558.11		837.60
375.00	200.00	200.00	270.42	3,605.55		837.60
375.00	200.00	200.00	270.42	3,649.34		228.30

375.00	200.00	200.00	270.42	3,649.34		228.30
375.00	200.00	200.00	270.42	3,649.34	3,649.34	228.30
375.00	200.00	200.00	270.42	3,649.34		228.30
375.00	200.00	200.00	270.42	3,649.34		228.30
375.00	200.00	200.00	270.42	3,090.47		339.90
375.00	200.00	200.00	270.42	3,090.47		339.90
375.00	200.00	200.00	270.42	3,090.47	3,090.47	339.90
375.00	200.00	200.00	270.42	3,090.47		339.90
375.00	200.00	200.00	270.42	3,090.47		339.90
375.00	200.00	200.00	270.42	2,664.20		920.30
375.00	200.00	200.00	270.42	2,664.20		920.30
375.00	200.00	200.00	270.42	2,638.21	2,675.23	917.30
375.00	200.00	200.00	270.42	2,664.20		920.30
375.00	200.00	200.00	270.42	2,745.34		917.30
375.00	200.00	200.00	270.42	3,148.04		566.10
375.00	200.00	200.00	270.42	3,148.04		566.10
375.00	200.00	200.00	270.42	3,148.04	3,148.04	566.10
375.00	200.00	200.00	270.42	3,148.04		566.10
375.00	200.00	200.00	270.42	3,148.04		566.10
375.00	200.00	200.00	270.42	3,192.64		658.70
375.00	200.00	200.00	270.42	3,192.64		658.70
375.00	200.00	200.00	270.42	3,192.64	3,200.27	658.70
375.00	200.00	200.00	270.42	3,192.64		658.70
375.00	200.00	200.00	270.42	3,230.78		657.70
375.00	200.00	200.00	270.42	3,819.44		962.80
375.00	200.00	200.00	270.42	3,874.16		961.80
375.00	200.00	200.00	270.42	3,819.44	3,852.27	962.80
375.00	200.00	200.00	270.42	3,874.16		961.80
375.00	200.00	200.00	270.42	3,874.16		961.80
375.00	200.00	200.00	270.42	3,480.26		153.90
375.00	200.00	200.00	270.42	3,480.26		153.90
375.00	200.00	200.00	270.42	3,480.26	3,480.26	153.90
375.00	200.00	200.00	270.42	3,480.26		153.90
375.00	200.00	200.00	270.42	3,480.26		153.90
375.00	200.00	200.00	270.42	2,073.74		653.50
375.00	200.00	200.00	270.42	2,073.74		653.50
375.00	200.00	200.00	270.42	2,073.74	2,073.74	653.50
375.00	200.00	200.00	270.42	2,073.74		653.50
375.00	200.00	200.00	270.42	2,073.74		653.50
375.00	200.00	200.00	270.42	2,945.71		951.50
375.00	200.00	200.00	270.42	2,793.56		956.50
375.00	200.00	200.00	270.42	2,793.56	2,823.99	956.50
375.00	200.00	200.00	270.42	2,793.56		956.50
375.00	200.00	200.00	270.42	2,793.56		956.50
375.00	200.00	200.00	270.42	3,261.96		635.20
375.00	200.00	200.00	270.42	3,261.96		635.20
375.00	200.00	200.00	270.42	3,261.96	3,269.92	635.20
375.00	200.00	200.00	270.42	3,261.96		635.20
375.00	200.00	200.00	270.42	3,301.79		634.20
375.00	200.00	200.00	270.42	3,211.60		89.10
375.00	200.00	200.00	270.42	3,211.60		89.10
375.00	200.00	200.00	270.42	3,211.60	3,211.60	89.10
375.00	200.00	200.00	270.42	3,211.60		89.10
375.00	200.00	200.00	270.42	3,211.60		89.10
375.00	200.00	200.00	270.42	3,380.20		797.70

375.00	200.00	200.00	270.42	3,380.20		797.70
375.00	200.00	200.00	270.42	3,380.20	3,380.20	797.70
375.00	200.00	200.00	270.42	3,380.20		797.70
375.00	200.00	200.00	270.42	3,380.20		797.70
375.00	200.00	200.00	270.42	3,338.47		723.10
375.00	200.00	200.00	270.42	3,338.47		723.10
375.00	200.00	200.00	270.42	3,338.47	3,314.63	723.10
375.00	200.00	200.00	270.42	3,338.47		723.10
375.00	200.00	200.00	270.42	3,219.24		726.10
375.00	200.00	200.00	270.42	3,137.08		493.20
375.00	200.00	200.00	270.42	3,137.08		493.20
375.00	200.00	200.00	270.42	3,250.20	3,182.33	490.20
375.00	200.00	200.00	270.42	3,137.08		493.20
375.00	200.00	200.00	270.42	3,250.20		490.20
375.00	200.00	200.00	270.42	3,431.68		304.80
375.00	200.00	200.00	270.42	3,431.68		304.80
375.00	200.00	200.00	270.42	3,431.68	3,440.50	304.80
375.00	200.00	200.00	270.42	3,431.68		304.80
375.00	200.00	200.00	270.42	3,475.79		303.80
375.00	200.00	200.00	270.42	3,699.27		1,040.10
375.00	200.00	200.00	270.42	3,699.27		1,040.10
375.00	200.00	200.00	270.42	3,699.27	3,699.27	1,040.10
375.00	200.00	200.00	270.42	3,699.27		1,040.10
375.00	200.00	200.00	270.42	3,699.27		1,040.10
375.00	200.00	200.00	270.42	3,539.48		566.70
375.00	200.00	200.00	270.42	3,544.12		566.60
375.00	200.00	200.00	270.42	3,548.77	3,548.78	566.50
375.00	200.00	200.00	270.42	3,553.43		566.40
375.00	200.00	200.00	270.42	3,558.11		566.30
375.00	200.00	200.00	270,42	3511,90		453,70
375.00	200.00	200.00	270,42	3502,80		453,90
375.00	200.00	200.00	270,42	3511,90	3514,66	453,70
375.00	200.00	200.00	270,42	3521,05		453,50
375.00	200.00	200.00	270,42	3525,64		453,40
375.00	200.00	200.00	270,42	3567,50		334,10
375.00	200.00	200.00	270,42	3572,21		334,00
375.00	200.00	200.00	270,42	3586,42	3578,85	333,70
375.00	200.00	200.00	270,42	3581,67		333,80
375.00	200.00	200.00	270,42	3586,42		333,70
375.00	200.00	200.00	270,42	3558,11		742,90
375.00	200.00	200.00	270,42	3567,50		742,70
375.00	200.00	200.00	270,42	3572,21	3572,24	742,60
375.00	200.00	200.00	270,42	3576,94		742,50
375.00	200.00	200.00	270,42	3586,42		742,30
375.00	200.00	200.00	270,42	3539,48		502,50
375.00	200.00	200.00	270,42	3544,12		502,40
375.00	200.00	200.00	270,42	3548,77	3549,72	502,30
375.00	200.00	200.00	270,42	3558,11		502,10
375.00	200.00	200.00	270,42	3558,11		502,10
375.00	200.00	200.00	270,42	3401,46		247,40
375.00	200.00	200.00	270,42	3401,46		247,40
375.00	200.00	200.00	270,42	3397,19	3403,18	247,50
375.00	200.00	200.00	270,42	3405,75		247,30
375.00	200.00	200.00	270,42	3410,04		247,20
375.00	200.00	200.00	270,42	3480,26		406,00

375.00	200.00	200.00	270,42	3475,79	3483,86	406,10
375.00	200.00	200.00	270,42	3480,26		406,00
375.00	200.00	200.00	270,42	3493,75		405,70
375.00	200.00	200.00	270,42	3489,24		405,80
375.00	200.00	200.00	270,42	3449,19	3462,45	190,40
375.00	200.00	200.00	270,42	3462,44		190,10
375.00	200.00	200.00	270,42	3462,44		190,10
375.00	200.00	200.00	270,42	3466,88		190,00
375.00	200.00	200.00	270,42	3471,33		189,90
375.00	200.00	200.00	270,42	3334,36	3341,80	863,30
375.00	200.00	200.00	270,42	3334,36		863,30
375.00	200.00	200.00	270,42	3342,60		863,10
375.00	200.00	200.00	270,42	3359,21		862,70
375.00	200.00	200.00	270,42	3338,47		863,20
375.00	200.00	200.00	270,42	3203,99	3207,79	345,90
375.00	200.00	200.00	270,42	3207,79		345,80
375.00	200.00	200.00	270,42	3207,79		345,80
375.00	200.00	200.00	270,42	3211,60		345,70
375.00	200.00	200.00	270,42	3207,79		345,80
450.00	240.00	240.00	324.50	3,297.76	3,360.43	898.30
450.00	240.00	240.00	324.50	3,297.76		898.30
450.00	240.00	240.00	324.50	3,331.62		898.30
450.00	240.00	240.00	324.50	3,437.50		898.30
450.00	240.00	240.00	324.50	3,437.50		898.30
450.00	240.00	240.00	324.50	3,569.85	3,635.19	1,063.40
450.00	240.00	240.00	324.50	3,531.01		1,064.40
450.00	240.00	240.00	324.50	3,691.69		1,064.40
450.00	240.00	240.00	324.50	3,691.69		1,064.40
450.00	240.00	240.00	324.50	3,691.69		1,064.40
450.00	240.00	240.00	324,50	3415,79	3415,79	499,10
450.00	240.00	240.00	324,50	3412,19		499,20
450.00	240.00	240.00	324,50	3419,38		499,00
450.00	240.00	240.00	324,50	3419,38		499,00
450.00	240.00	240.00	324,50	3412,19		499,20
450.00	240.00	240.00	324,50	3394,35	3396,48	1016,80
450.00	240.00	240.00	324,50	3394,35		1016,80
450.00	240.00	240.00	324,50	3390,80		1016,90
450.00	240.00	240.00	324,50	3401,46		1016,60
450.00	240.00	240.00	324,50	3401,46		1016,60
450.00	240.00	240.00	324,50	3212,87	3217,33	395,10
450.00	240.00	240.00	324,50	3212,87		395,10
450.00	240.00	240.00	324,50	3219,24		394,90
450.00	240.00	240.00	324,50	3222,44		394,80
450.00	240.00	240.00	324,50	3219,24		394,90
450.00	240.00	240.00	324,50	3419,38	3420,11	286,90
450.00	240.00	240.00	324,50	3415,79		287,00
450.00	240.00	240.00	324,50	3419,38		286,90
450.00	240.00	240.00	324,50	3422,99		286,80
450.00	240.00	240.00	324,50	3422,99		286,80
450.00	240.00	240.00	324,50	3405,03	3410,77	571,60
450.00	240.00	240.00	324,50	3405,03		571,60
450.00	240.00	240.00	324,50	3412,19		571,40
450.00	240.00	240.00	324,50	3415,79		571,30
450.00	240.00	240.00	324,50	3415,79		571,30
450.00	240.00	240.00	324,50	3345,36		1060,40

450.00	240.00	240.00	324,50	3352,27		1060,20
450.00	240.00	240.00	324,50	3345,36	3351,59	1060,40
450.00	240.00	240.00	324,50	3355,74		1060,10
450.00	240.00	240.00	324,50	3359,21		1060,00
450.00	240.00	240.00	324,50	3338,47		409,70
450.00	240.00	240.00	324,50	3341,91		409,60
450.00	240.00	240.00	324,50	3345,36	3345,36	409,50
450.00	240.00	240.00	324,50	3352,27		409,30
450.00	240.00	240.00	324,50	3348,81		409,40
450.00	240.00	240.00	324,50	2952,68		146,20
450.00	240.00	240.00	324,50	2955,37		146,10
450.00	240.00	240.00	324,50	2955,37	2955,91	146,10
450.00	240.00	240.00	324,50	2955,37		146,10
450.00	240.00	240.00	324,50	2960,76		145,90
450.00	240.00	240.00	324,50	2963,47		935,00
450.00	240.00	240.00	324,50	2971,61		934,70
450.00	240.00	240.00	324,50	2968,89	2970,53	934,80
450.00	240.00	240.00	324,50	2974,33		934,60
450.00	240.00	240.00	324,50	2974,33		934,60
450.00	240.00	240.00	324.50	2,990.78		965.50
450.00	240.00	240.00	324.50	3,099.33		961.70
450.00	240.00	240.00	324.50	2,999.07	3,043.31	965.20
450.00	240.00	240.00	324.50	3,117.19		961.10
450.00	240.00	240.00	324.50	3,010.20		964.80
450.00	240.00	240.00	324.50	3,485.50		362.60
450.00	240.00	240.00	324.50	3,481.76		362.70
450.00	240.00	240.00	324.50	3,481.76	3,482.50	362.70
450.00	240.00	240.00	324.50	3,481.76		362.70
450.00	240.00	240.00	324.50	3,481.76		362.70
450.00	240.00	240.00	324,50	3380,20		1032,50
450.00	240.00	240.00	324,50	3380,20		1032,50
450.00	240.00	240.00	324,50	3383,73	3383,73	1032,40
450.00	240.00	240.00	324,50	3387,26		1032,30
450.00	240.00	240.00	324,50	3387,26		1032,30
450.00	240.00	240.00	324,50	3463,18		281,00
450.00	240.00	240.00	324,50	3470,58		280,80
450.00	240.00	240.00	324,50	3470,58	3473,57	280,80
450.00	240.00	240.00	324,50	3481,76		280,50
450.00	240.00	240.00	324,50	3481,76		280,50
450.00	240.00	240.00	324,50	3132,24		378,70
450.00	240.00	240.00	324,50	3132,24		378,70
450.00	240.00	240.00	324,50	3138,29	3137,69	378,50
450.00	240.00	240.00	324,50	3141,33		378,40
450.00	240.00	240.00	324,50	3144,38		378,30
450.00	240.00	240.00	324.50	3,232.07		992.80
450.00	240.00	240.00	324.50	3,216.05		993.30
450.00	240.00	240.00	324.50	3,225.64	3,225.67	993.00
450.00	240.00	240.00	324.50	3,216.05		993.30
450.00	240.00	240.00	324.50	3,238.52		992.60
450.00	240.00	240.00	324.50	2,126.47		203.50
450.00	240.00	240.00	324.50	2,119.53		204.00
450.00	240.00	240.00	324.50	2,127.87	2,123.98	203.40
450.00	240.00	240.00	324.50	2,115.38		204.30
450.00	240.00	240.00	324.50	2,130.66		203.20
450.00	240.00	240.00	324,50	3397,90		772,80

450.00	240.00	240.00	324,50	3397,90	3402,18	772,80
450.00	240.00	240.00	324,50	3401,46		772,70
450.00	240.00	240.00	324,50	3405,03		772,60
450.00	240.00	240.00	324,50	3408,61		772,50
450.00	240.00	240.00	324,50	3397,90	3405,04	316,50
450.00	240.00	240.00	324,50	3401,46		316,40
450.00	240.00	240.00	324,50	3405,03		316,30
450.00	240.00	240.00	324,50	3408,61		316,20
450.00	240.00	240.00	324,50	3412,19		316,10
450.00	240.00	240.00	324,50	3415,79	3422,28	1048,70
450.00	240.00	240.00	324,50	3419,38		1048,60
450.00	240.00	240.00	324,50	3422,99		1048,50
450.00	240.00	240.00	324,50	3422,99		1048,50
450.00	240.00	240.00	324,50	3430,23		1048,30
450.00	240.00	240.00	324.50	3,373.18	3,378.82	1,048.40
450.00	240.00	240.00	324.50	3,373.18		1,048.40
450.00	240.00	240.00	324.50	3,376.69		1,048.30
450.00	240.00	240.00	324.50	3,394.35		1,047.80
450.00	240.00	240.00	324.50	3,376.69		1,048.30
450.00	240.00	240.00	324.50	3,324.79	3,340.56	206.50
450.00	240.00	240.00	324.50	3,341.91		206.00
450.00	240.00	240.00	324.50	3,341.91		206.00
450.00	240.00	240.00	324.50	3,352.27		205.70
450.00	240.00	240.00	324.50	3,341.91		206.00
450.00	240.00	240.00	324,50	3550,32	3553,44	475,60
450.00	240.00	240.00	324,50	3546,44		475,70
450.00	240.00	240.00	324,50	3554,21		475,50
450.00	240.00	240.00	324,50	3554,21		475,50
450.00	240.00	240.00	324,50	3562,02		475,30
450.00	240.00	240.00	324,50	3534,85	3540,26	1042,50
450.00	240.00	240.00	324,50	3534,85		1042,50
450.00	240.00	240.00	324,50	3542,57		1042,30
450.00	240.00	240.00	324,50	3542,57		1042,30
450.00	240.00	240.00	324,50	3546,44		1042,20
450.00	240.00	240.00	324,50	3463,18	3468,36	569,40
450.00	240.00	240.00	324,50	3466,88		569,30
450.00	240.00	240.00	324,50	3470,58		569,20
450.00	240.00	240.00	324,50	3466,88		569,30
450.00	240.00	240.00	324,50	3474,30		569,10
450.00	240.00	240.00	324.50	3,489.24	3,496.02	140.30
450.00	240.00	240.00	324.50	3,489.24		140.30
450.00	240.00	240.00	324.50	3,493.00		140.20
450.00	240.00	240.00	324.50	3,500.54		140.00
450.00	240.00	240.00	324.50	3,508.10		139.80
450.00	240.00	240.00	324.50	3,519.52	3,524.11	318.90
450.00	240.00	240.00	324.50	3,527.17		318.70
450.00	240.00	240.00	324.50	3,515.71		319.00
450.00	240.00	240.00	324.50	3,527.17		318.70
450.00	240.00	240.00	324.50	3,531.01		318.60
300.00	60.00	120.00	164.32	3,839.18	3,833.81	263.30
300.00	60.00	120.00	164.32	3,839.18		263.20
300.00	60.00	120.00	164.32	3,830.23		263.20
300.00	60.00	120.00	164.32	3,830.23		263.10
300.00	60.00	120.00	164.32	3,830.23		263.00
300.00	60.00	120.00	164.32	3,830.23		446.50

300.00	60.00	120.00	164.32	3,821.32	3,824.88	446.50
300.00	60.00	120.00	164.32	3,821.32		446.40
300.00	60.00	120.00	164.32	3,830.23		446.30
300.00	60.00	120.00	164.32	3,821.32		446.30
300.00	60.00	120.00	164.32	3,848.17	3,848.18	709.50
300.00	60.00	120.00	164.32	3,848.17		709.40
300.00	60.00	120.00	164.32	3,857.20		709.30
300.00	60.00	120.00	164.32	3,848.17		709.30
300.00	60.00	120.00	164.32	3,839.18		709.30
300.00	60.00	120.00	164.32	3,848.17	3,823.16	883.50
300.00	60.00	120.00	164.32	3,803.63		883.90
300.00	60.00	120.00	164.32	3,830.23		883.50
300.00	60.00	120.00	164.32	3,821.32		883.60
300.00	60.00	120.00	164.32	3,812.45		883.50
300.00	60.00	120.00	164.32	3,684.23	3,697.52	807.60
300.00	60.00	120.00	164.32	3,709.18		807.20
300.00	60.00	120.00	164.32	3,709.18		807.20
300.00	60.00	120.00	164.32	3,692.51		807.30
300.00	60.00	120.00	164.32	3,692.51		807.20
300.00	60.00	120.00	164.32	3,675.99	3,676.00	396.60
300.00	60.00	120.00	164.32	3,667.78		396.60
300.00	60.00	120.00	164.32	3,675.99		396.50
300.00	60.00	120.00	164.32	3,684.23		396.30
300.00	60.00	120.00	164.32	3,675.99		396.30
300.00	60.00	120.00	164.32	3,839.18	3,846.38	574.00
300.00	60.00	120.00	164.32	3,848.17		573.90
300.00	60.00	120.00	164.32	3,839.18		573.90
300.00	60.00	120.00	164.32	3,848.17		573.70
300.00	60.00	120.00	164.32	3,857.20		573.50
300.00	60.00	120.00	164.32	3,931.02	3,919.83	759.00
300.00	60.00	120.00	164.32	3,903.01		759.20
300.00	60.00	120.00	164.32	3,903.01		759.10
300.00	60.00	120.00	164.32	3,921.64		758.80
300.00	60.00	120.00	164.32	3,940.45		758.50
300.00	60.00	120.00	164.32	3,857.20	3,871.77	396.00
300.00	60.00	120.00	164.32	3,884.56		395.60
300.00	60.00	120.00	164.32	3,875.40		395.60
300.00	60.00	120.00	164.32	3,875.40		395.60
300.00	60.00	120.00	164.32	3,866.28		395.50
300.00	60.00	120.00	164.32	3,839.18	3,832.03	958.30
300.00	60.00	120.00	164.32	3,830.23		958.40
300.00	60.00	120.00	164.32	3,839.18		958.20
300.00	60.00	120.00	164.32	3,821.32		958.30
300.00	60.00	120.00	164.32	3,830.23		958.10
300.00	60.00	120.00	164.32	3,884.56	3,895.64	634.50
300.00	60.00	120.00	164.32	3,884.56		634.40
300.00	60.00	120.00	164.32	3,893.76		634.30
300.00	60.00	120.00	164.32	3,912.30		634.00
300.00	60.00	120.00	164.32	3,903.01		634.00
300.00	60.00	120.00	164.32	4,170.48	4,174.76	932.40
300.00	60.00	120.00	164.32	4,170.48		932.30
300.00	60.00	120.00	164.32	4,170.48		932.20
300.00	60.00	120.00	164.32	4,159.92		932.20
300.00	60.00	120.00	164.32	4,202.47		931.80
300.00	60.00	120.00	164.32	3,988.27		452.90

300.00	60.00	120.00	164.32	3,978.61	3,998.01	452.90
300.00	60.00	120.00	164.32	4,007.73		452.60
300.00	60.00	120.00	164.32	4,007.73		452.50
300.00	60.00	120.00	164.32	4,007.73		452.40
300.00	60.00	120.00	164.32	3,903.01	3,897.48	969.60
300.00	60.00	120.00	164.32	3,884.56		969.70
300.00	60.00	120.00	164.32	3,893.76		969.50
300.00	60.00	120.00	164.32	3,912.30		969.20
300.00	60.00	120.00	164.32	3,893.76		969.30
300.00	60.00	120.00	164.32	3,912.30	3,901.17	118.40
300.00	60.00	120.00	164.32	3,903.01		118.40
300.00	60.00	120.00	164.32	3,903.01		118.30
300.00	60.00	120.00	164.32	3,893.76		118.30
300.00	60.00	120.00	164.32	3,893.76		118.20
300.00	60.00	120.00	164.32	3,893.76	3,910.47	532.70
300.00	60.00	120.00	164.32	3,921.64		532.30
300.00	60.00	120.00	164.32	3,912.30		532.30
300.00	60.00	120.00	164.32	3,903.01		532.30
300.00	60.00	120.00	164.32	3,921.64		532.00
300.00	60.00	120.00	164.32	4,067.25	4,071.34	797.70
300.00	60.00	120.00	164.32	4,047.21		797.90
300.00	60.00	120.00	164.32	4,097.67		797.30
300.00	60.00	120.00	164.32	4,077.34		797.40
300.00	60.00	120.00	164.32	4,067.25		797.40
300.00	60.00	120.00	164.32	3,893.76	3,910.50	1,024.80
300.00	60.00	120.00	164.32	3,921.64		1,024.40
300.00	60.00	120.00	164.32	3,912.30		1,024.50
300.00	60.00	120.00	164.32	3,931.02		1,024.20
300.00	60.00	120.00	164.32	3,893.76		1,024.40
300.00	60.00	120.00	164.32	3,912.30	3,912.30	433.40
300.00	60.00	120.00	164.32	3,912.30		433.40
300.00	60.00	120.00	164.32	3,912.30		433.30
300.00	60.00	120.00	164.32	3,912.30		433.20
300.00	60.00	120.00	164.32	3,912.30		433.10
300.00	60.00	120.00	164.32	3,884.56	3,888.28	991.70
300.00	60.00	120.00	164.32	3,893.76		991.50
300.00	60.00	120.00	164.32	3,912.30		991.20
300.00	60.00	120.00	164.32	3,875.40		991.50
300.00	60.00	120.00	164.32	3,875.40		991.40
300.00	60.00	120.00	164.32	3,848.17	3,849.99	801.70
300.00	60.00	120.00	164.32	3,848.17		801.60
300.00	60.00	120.00	164.32	3,866.28		801.30
300.00	60.00	120.00	164.32	3,848.17		801.40
300.00	60.00	120.00	164.32	3,839.18		801.40
300.00	60.00	120.00	164.32	3,839.18	3,833.83	313.30
300.00	60.00	120.00	164.32	3,821.32		313.40
300.00	60.00	120.00	164.32	3,821.32		313.30
300.00	60.00	120.00	164.32	3,848.17		312.90
300.00	60.00	120.00	164.32	3,839.18		312.90
300.00	60.00	120.00	164.32	3,760.11	3,765.28	449.20
300.00	60.00	120.00	164.32	3,768.73		449.00
300.00	60.00	120.00	164.32	3,768.73		449.00
300.00	60.00	120.00	164.32	3,768.73		448.90
300.00	60.00	120.00	164.32	3,760.11		448.90
300.00	60.00	120.00	164.32	3,751.52		282.00

300.00	60.00	120.00	164.32	3,726.00	3,744.73	282.20
300.00	60.00	120.00	164.32	3,734.47		282.10
300.00	60.00	120.00	164.32	3,760.11		281.70
300.00	60.00	120.00	164.32	3,751.52		281.70
300.00	60.00	120.00	164.32	3,848.17	3,846.37	840.20
300.00	60.00	120.00	164.32	3,848.17		840.10
300.00	60.00	120.00	164.32	3,848.17		840.00
300.00	60.00	120.00	164.32	3,848.17		839.90
300.00	60.00	120.00	164.32	3,839.18		839.90
300.00	60.00	120.00	164.32	3,388.04	3,382.46	710.40
300.00	60.00	120.00	164.32	3,381.07		710.40
300.00	60.00	120.00	164.32	3,381.07		710.30
300.00	60.00	120.00	164.32	3,381.07		710.20
300.00	60.00	120.00	164.32	3,381.07		710.10
300.00	60.00	120.00	164.32	3,106.18	3,101.49	524.10
300.00	60.00	120.00	164.32	3,100.32		524.10
300.00	60.00	120.00	164.32	3,100.32		524.00
300.00	60.00	120.00	164.32	3,100.32		523.90
300.00	60.00	120.00	164.32	3,100.32		523.80
300.00	60.00	120.00	164.32	3,106.18	3,103.83	252.10
300.00	60.00	120.00	164.32	3,100.32		252.10
300.00	60.00	120.00	164.32	3,100.32		252.00
300.00	60.00	120.00	164.32	3,106.18		251.90
300.00	60.00	120.00	164.32	3,106.18		251.80

Channel 6 (Sensor 6)						
location			Distance	Velocity	Average velocity for sensor 6	Arrival time, millisecond
x6	y6	z6	(mm)	m/s	m/s	t6
150.00	90.00	30.00	125.50	3,024.07	3,022.62	268.80
150.00	90.00	30.00	125.50	3,024.07		268.80
150.00	90.00	30.00	125.50	3,024.07		268.70
150.00	90.00	30.00	125.50	3,024.07		268.60
150.00	90.00	30.00	125.50	3,016.80		268.60
150.00	90.00	30.00	125.50	3,302.61	3,299.14	1,013.60
150.00	90.00	30.00	125.50	3,302.61		1,013.60
150.00	90.00	30.00	125.50	3,302.61		1,013.50
150.00	90.00	30.00	125.50	3,293.94		1,013.50
150.00	90.00	30.00	125.50	3,293.94		1,013.40
150.00	90.00	30.00	125.50	3,293.94	3,297.41	374.20
150.00	90.00	30.00	125.50	3,293.94		374.10
150.00	90.00	30.00	125.50	3,302.61		373.90
150.00	90.00	30.00	125.50	3,293.94		373.90
150.00	90.00	30.00	125.50	3,302.61		373.70
150.00	90.00	30.00	125.50	3,302.61	3,300.87	330.10
150.00	90.00	30.00	125.50	3,302.61		330.00
150.00	90.00	30.00	125.50	3,302.61		329.90
150.00	90.00	30.00	125.50	3,302.61		329.80
150.00	90.00	30.00	125.50	3,293.94		329.80
150.00	90.00	30.00	125.50	3,447.77	3,459.21	309.00
150.00	90.00	30.00	125.50	3,466.82		308.70
150.00	90.00	30.00	125.50	3,457.27		308.70
150.00	90.00	30.00	125.50	3,447.77		308.70
150.00	90.00	30.00	125.50	3,476.43		308.30
150.00	90.00	30.00	125.50	3,391.86	3,399.22	796.50
150.00	90.00	30.00	125.50	3,401.06		796.40
150.00	90.00	30.00	125.50	3,401.06		796.30
150.00	90.00	30.00	125.50	3,401.06		796.20
150.00	90.00	30.00	125.50	3,401.06		796.10
150.00	90.00	30.00	125.50	3,419.59	3,421.47	278.40
150.00	90.00	30.00	125.50	3,428.93		278.20
150.00	90.00	30.00	125.50	3,419.59		278.20
150.00	90.00	30.00	125.50	3,410.30		278.20
150.00	90.00	30.00	125.50	3,428.93		277.90
150.00	90.00	30.00	125.50	3,545.17	3,541.18	712.00
150.00	90.00	30.00	125.50	3,545.17		711.90
150.00	90.00	30.00	125.50	3,545.17		711.80
150.00	90.00	30.00	125.50	3,535.18		711.80
150.00	90.00	30.00	125.50	3,535.18		711.70
150.00	90.00	30.00	125.50	2,587.61	2,584.41	395.40
150.00	90.00	30.00	125.50	2,587.61		395.30
150.00	90.00	30.00	125.50	2,582.28		395.30
150.00	90.00	30.00	125.50	2,582.28		395.20
150.00	90.00	30.00	125.50	2,582.28		395.10
150.00	90.00	30.00	125.50	2,598.32	2,630.30	384.30
150.00	90.00	30.00	125.50	2,598.32		384.20
150.00	90.00	30.00	125.50	2,598.32		384.10
150.00	90.00	30.00	125.50	2,758.22		381.20

150.00	90.00	30.00	125.50	2,598.32		384.00
150.00	90.00	30.00	125.50	2,067.53	2,404.73	510.50
150.00	90.00	30.00	125.50	2,509.98		499.70
150.00	90.00	30.00	125.50	2,455.95		500.70
150.00	90.00	30.00	125.50	2,480.22		500.10
150.00	90.00	30.00	125.50	2,509.98		499.50
150.00	90.00	30.00	125.50	1,834.78	1,836.39	487.20
150.00	90.00	30.00	125.50	1,837.47		487.10
150.00	90.00	30.00	125.50	1,837.47		487.00
150.00	90.00	30.00	125.50	1,837.47		486.90
150.00	90.00	30.00	125.50	1,834.78		486.90
150.00	90.00	30.00	125.50	2,576.98	2,583.36	489.30
150.00	90.00	30.00	125.50	2,592.95		488.90
150.00	90.00	30.00	125.50	2,582.28		489.00
150.00	90.00	30.00	125.50	2,576.98		489.00
150.00	90.00	30.00	125.50	2,587.61		488.80
150.00	90.00	30.00	125.50	3,226.20	3,231.20	582.30
150.00	90.00	30.00	125.50	3,242.87		582.10
150.00	90.00	30.00	125.50	3,226.20		582.20
150.00	90.00	30.00	125.50	3,234.51		582.00
150.00	90.00	30.00	125.50	3,226.20		582.00
150.00	90.00	30.00	125.50	3,259.71	3,266.51	446.10
150.00	90.00	30.00	125.50	3,259.71		446.00
150.00	90.00	30.00	125.50	3,276.74		445.80
150.00	90.00	30.00	125.50	3,268.20		445.80
150.00	90.00	30.00	125.50	3,268.20		445.70
150.00	90.00	30.00	125.50	2,653.26	2,656.64	87.70
150.00	90.00	30.00	125.50	2,658.88		87.50
150.00	90.00	30.00	125.50	2,658.88		87.40
150.00	90.00	30.00	125.50	2,647.66		87.50
150.00	90.00	30.00	125.50	2,664.52		87.10
150.00	90.00	30.00	125.50	2,614.56	2,612.40	383.80
150.00	90.00	30.00	125.50	2,603.71		383.90
150.00	90.00	30.00	125.50	2,620.02		383.50
150.00	90.00	30.00	125.50	2,609.13		383.60
150.00	90.00	30.00	125.50	2,614.56		383.40
150.00	90.00	30.00	125.50	3,302.61	3,307.84	369.70
150.00	90.00	30.00	125.50	3,302.61		369.60
150.00	90.00	30.00	125.50	3,311.32		369.40
150.00	90.00	30.00	125.50	3,320.08		369.20
150.00	90.00	30.00	125.50	3,302.61		369.30
150.00	90.00	30.00	125.50	1,072.64	1,072.27	696.20
150.00	90.00	30.00	125.50	1,072.64		696.10
150.00	90.00	30.00	125.50	1,072.64		696.00
150.00	90.00	30.00	125.50	1,071.73		696.00
150.00	90.00	30.00	125.50	1,071.73		695.90
150.00	90.00	30.00	125.50	1,541.76	1,542.90	332.50
150.00	90.00	30.00	125.50	1,543.65		332.30
150.00	90.00	30.00	125.50	1,545.55		332.10
150.00	90.00	30.00	125.50	1,539.87		332.30
150.00	90.00	30.00	125.50	1,543.65		332.00
150.00	90.00	30.00	125.50	3,068.44	3,063.94	619.90
150.00	90.00	30.00	125.50	3,060.95		619.90
150.00	90.00	30.00	125.50	3,060.95		619.80
150.00	90.00	30.00	125.50	3,060.95		619.70

150.00	90.00	30.00	125.50	3,068.44		619.60
150.00	90.00	30.00	125.50	1,462.69	1,266.11	553.80
150.00	90.00	30.00	125.50	1,218.44		570.90
150.00	90.00	30.00	125.50	1,217.26		570.90
150.00	90.00	30.00	125.50	1,216.08		570.90
150.00	90.00	30.00	125.50	1,216.08		570.80
150.00	90.00	30.00	125.50	1,691.36	1,688.64	976.00
150.00	90.00	30.00	125.50	1,682.29		976.30
150.00	90.00	30.00	125.50	1,691.36		975.80
150.00	90.00	30.00	125.50	1,686.81		975.90
150.00	90.00	30.00	125.50	1,691.36		975.70
150.00	90.00	30.00	125.50	2,795.08	2,796.33	80.90
150.00	90.00	30.00	125.50	2,801.32		80.70
150.00	90.00	30.00	125.50	2,795.08		80.70
150.00	90.00	30.00	125.50	2,795.08		80.70
150.00	90.00	30.00	125.50	2,795.08		80.60
150.00	90.00	30.00	125.50	2,001.58	2,024.86	909.30
150.00	90.00	30.00	125.50	1,998.39		909.30
150.00	90.00	30.00	125.50	1,992.05		909.40
150.00	90.00	30.00	125.50	2,130.71		905.30
150.00	90.00	30.00	125.50	2,001.58		909.00
150.00	90.00	30.00	125.50	1,845.57	1,847.77	801.00
150.00	90.00	30.00	125.50	1,853.75		800.60
150.00	90.00	30.00	125.50	1,851.02		800.60
150.00	90.00	30.00	125.50	1,851.02		800.50
150.00	90.00	30.00	125.50	1,837.47		800.90
150.00	90.00	30.00	125.50	2,540.47	2,540.47	447.90
150.00	90.00	30.00	125.50	2,540.47		447.80
150.00	90.00	30.00	125.50	2,540.47		447.70
150.00	90.00	30.00	125.50	2,540.47		447.70
150.00	90.00	30.00	125.50	2,540.47		447.60
150.00	90.00	30.00	125.50	3,038.72	3,038.72	1,031.60
150.00	90.00	30.00	125.50	3,038.72		1,031.60
150.00	90.00	30.00	125.50	3,038.72		1,031.50
150.00	90.00	30.00	125.50	3,038.72		1,031.40
150.00	90.00	30.00	125.50	3,038.72		1,031.30
0.00	90.00	90.00	150.00	3,253.80	3,260.90	72.00
0.00	90.00	90.00	150.00	3,267.97		71.70
0.00	90.00	90.00	150.00	3,260.87		71.70
0.00	90.00	90.00	150.00	3,275.11		71.40
0.00	90.00	90.00	150.00	3,246.75		71.80
0.00	90.00	90.00	150.00	3,340.76	3,343.74	342.00
0.00	90.00	90.00	150.00	3,340.76		342.00
0.00	90.00	90.00	150.00	3,340.76		341.90
0.00	90.00	90.00	150.00	3,348.21		341.70
0.00	90.00	90.00	150.00	3,348.21		341.60
0.00	90.00	90.00	150.00	3,355.70	3,348.22	131.50
0.00	90.00	90.00	150.00	3,348.21		131.50
0.00	90.00	90.00	150.00	3,340.76		131.50
0.00	90.00	90.00	150.00	3,348.21		131.30
0.00	90.00	90.00	150.00	3,348.21		131.20
0.00	90.00	90.00	150.00	3,218.88	3,217.51	219.90
0.00	90.00	90.00	150.00	3,211.99		219.90
0.00	90.00	90.00	150.00	3,225.81		219.70
0.00	90.00	90.00	150.00	3,218.88		219.70

0.00	90.00	90.00	150.00	3,211.99		219.70
0.00	90.00	90.00	150.00	3,225.81		59.00
0.00	90.00	90.00	150.00	3,225.81		58.90
0.00	90.00	90.00	150.00	3,225.81	3,225.81	58.80
0.00	90.00	90.00	150.00	3,225.81		58.70
0.00	90.00	90.00	150.00	3,225.81		58.60
0.00	90.00	90.00	150.00	2,702.70		124.90
0.00	90.00	90.00	150.00	2,332.81		133.60
0.00	90.00	90.00	150.00	2,347.42	2,485.41	133.20
0.00	90.00	90.00	150.00	2,693.00		124.80
0.00	90.00	90.00	150.00	2,351.10		132.90
0.00	90.00	90.00	150.00	2,722.32		73.60
0.00	90.00	90.00	150.00	2,722.32		73.50
0.00	90.00	90.00	150.00	2,737.23	2,720.39	73.10
0.00	90.00	90.00	150.00	2,712.48		73.50
0.00	90.00	90.00	150.00	2,707.58		73.50
0.00	90.00	90.00	150.00	2,737.23		724.80
0.00	90.00	90.00	150.00	2,737.23		724.80
0.00	90.00	90.00	150.00	2,742.23	2,735.25	724.60
0.00	90.00	90.00	150.00	2,722.32		724.90
0.00	90.00	90.00	150.00	2,737.23		724.50
0.00	90.00	90.00	150.00	3,131.52		110.50
0.00	90.00	90.00	150.00	3,131.52		110.40
0.00	90.00	90.00	150.00	3,151.26	3,135.47	110.10
0.00	90.00	90.00	150.00	3,131.52		110.30
0.00	90.00	90.00	150.00	3,131.52		110.20
0.00	90.00	90.00	150.00	3,138.08		995.00
0.00	90.00	90.00	150.00	3,131.52		995.00
0.00	90.00	90.00	150.00	3,125.00	3,130.24	995.00
0.00	90.00	90.00	150.00	3,138.08		994.70
0.00	90.00	90.00	150.00	3,118.50		994.90
0.00	90.00	90.00	150.00	3,099.17		757.40
0.00	90.00	90.00	150.00	3,112.03		757.20
0.00	90.00	90.00	150.00	3,105.59	3,109.47	757.20
0.00	90.00	90.00	150.00	3,118.50		756.90
0.00	90.00	90.00	150.00	3,112.03		756.90
0.00	90.00	90.00	150.00	3,144.65		454.10
0.00	90.00	90.00	150.00	3,138.08		454.10
0.00	90.00	90.00	150.00	3,144.65	3,144.66	453.90
0.00	90.00	90.00	150.00	3,144.65		453.80
0.00	90.00	90.00	150.00	3,151.26		453.70
0.00	90.00	90.00	150.00	3,112.03		708.70
0.00	90.00	90.00	150.00	3,112.03		708.60
0.00	90.00	90.00	150.00	3,105.59	3,112.04	708.60
0.00	90.00	90.00	150.00	3,112.03		708.50
0.00	90.00	90.00	150.00	3,118.50		708.30
0.00	90.00	90.00	150.00	2,946.95		230.40
0.00	90.00	90.00	150.00	2,912.62		230.90
0.00	90.00	90.00	150.00	2,923.98	2,927.44	230.70
0.00	90.00	90.00	150.00	2,929.69		230.50
0.00	90.00	90.00	150.00	2,923.98		230.50
0.00	90.00	90.00	150.00	2,555.37		975.30
0.00	90.00	90.00	150.00	2,564.10		975.00
0.00	90.00	90.00	150.00	2,546.69	2,557.12	975.30
0.00	90.00	90.00	150.00	2,559.73		975.00

0.00	90.00	90.00	150.00	2,559.73		974.90
0.00	90.00	90.00	150.00	1,594.05	1,777.23	851.40
0.00	90.00	90.00	150.00	2,049.18		830.50
0.00	90.00	90.00	150.00	1,597.44		851.10
0.00	90.00	90.00	150.00	2,054.79		830.10
0.00	90.00	90.00	150.00	1,590.67		851.30
0.00	90.00	90.00	150.00	2,946.95	2,937.75	174.00
0.00	90.00	90.00	150.00	2,923.98		174.30
0.00	90.00	90.00	150.00	2,946.95		173.80
0.00	90.00	90.00	150.00	2,935.42		174.00
0.00	90.00	90.00	150.00	2,935.42		173.90
0.00	90.00	90.00	150.00	3,024.19	3,006.07	924.20
0.00	90.00	90.00	150.00	3,012.05		924.30
0.00	90.00	90.00	150.00	2,994.01		924.50
0.00	90.00	90.00	150.00	2,988.05		924.50
0.00	90.00	90.00	150.00	3,012.05		924.00
0.00	90.00	90.00	150.00	3,099.17	3,096.62	501.70
0.00	90.00	90.00	150.00	3,099.17		501.60
0.00	90.00	90.00	150.00	3,099.17		501.50
0.00	90.00	90.00	150.00	3,092.78		501.50
0.00	90.00	90.00	150.00	3,092.78		501.40
0.00	90.00	90.00	150.00	3,118.50	3,112.04	332.20
0.00	90.00	90.00	150.00	3,112.03		332.20
0.00	90.00	90.00	150.00	3,112.03		332.10
0.00	90.00	90.00	150.00	3,112.03		332.00
0.00	90.00	90.00	150.00	3,105.59		332.00
0.00	90.00	90.00	150.00	3,080.08	3,078.82	403.80
0.00	90.00	90.00	150.00	3,080.08		403.70
0.00	90.00	90.00	150.00	3,080.08		403.60
0.00	90.00	90.00	150.00	3,073.77		403.60
0.00	90.00	90.00	150.00	3,080.08		403.40
0.00	90.00	90.00	150.00	3,092.78	3,094.06	152.10
0.00	90.00	90.00	150.00	3,092.78		152.00
0.00	90.00	90.00	150.00	3,092.78		151.90
0.00	90.00	90.00	150.00	3,092.78		151.90
0.00	90.00	90.00	150.00	3,099.17		151.70
0.00	90.00	90.00	150.00	2,982.11	2,971.49	952.00
0.00	90.00	90.00	150.00	2,970.30		952.10
0.00	90.00	90.00	150.00	2,964.43		952.10
0.00	90.00	90.00	150.00	2,970.30		951.90
0.00	90.00	90.00	150.00	2,970.30		951.90
0.00	90.00	90.00	150.00	2,678.57	2,679.53	573.00
0.00	90.00	90.00	150.00	2,678.57		572.90
0.00	90.00	90.00	150.00	2,673.80		572.90
0.00	90.00	90.00	150.00	2,683.36		572.70
0.00	90.00	90.00	150.00	2,683.36		572.60
0.00	90.00	90.00	150.00	2,636.20	2,635.29	155.60
0.00	90.00	90.00	150.00	2,636.20		155.50
0.00	90.00	90.00	150.00	2,626.97		155.60
0.00	90.00	90.00	150.00	2,636.20		155.30
0.00	90.00	90.00	150.00	2,640.85		155.20
0.00	90.00	90.00	150.00	2,664.30	2,739.04	782.70
0.00	90.00	90.00	150.00	2,862.60		778.70
0.00	90.00	90.00	150.00	2,830.19		779.20
0.00	90.00	90.00	150.00	2,664.30		782.40

0.00	90.00	90.00	150.00	2,673.80		782.10
0.00	90.00	90.00	150.00	2,572.90	2,570.26	215.00
0.00	90.00	90.00	150.00	2,568.49		215.00
0.00	90.00	90.00	150.00	2,568.49		214.90
0.00	90.00	90.00	150.00	2,568.49		214.90
0.00	90.00	90.00	150.00	2,572.90		214.70
0.00	90.00	90.00	150.00	2,688.17	2,692.04	604.70
0.00	90.00	90.00	150.00	2,697.84		604.40
0.00	90.00	90.00	150.00	2,697.84		604.30
0.00	90.00	90.00	150.00	2,693.00		604.40
0.00	90.00	90.00	150.00	2,683.36		604.50
300.00	180.00	60.00	251.00	3,438.33	3,442.10	429.50
300.00	180.00	60.00	251.00	3,438.33		429.40
300.00	180.00	60.00	251.00	3,443.05		429.20
300.00	180.00	60.00	251.00	3,443.05		429.20
300.00	180.00	60.00	251.00	3,447.77		429.00
300.00	180.00	60.00	251.00	3,642.93	3,647.21	231.70
300.00	180.00	60.00	251.00	3,642.93		231.60
300.00	180.00	60.00	251.00	3,648.23		231.40
300.00	180.00	60.00	251.00	3,632.39		231.60
300.00	180.00	60.00	251.00	3,669.56		230.80
300.00	180.00	60.00	251.00	3,433.63	3,455.06	273.10
300.00	180.00	60.00	251.00	3,550.18		270.60
300.00	180.00	60.00	251.00	3,433.63		272.90
300.00	180.00	60.00	251.00	3,428.93		272.90
300.00	180.00	60.00	251.00	3,428.93		272.80
300.00	180.00	60.00	251.00	2,661.70	2,666.23	606.70
300.00	180.00	60.00	251.00	2,667.35		606.50
300.00	180.00	60.00	251.00	2,661.70		606.70
300.00	180.00	60.00	251.00	2,670.19		606.40
300.00	180.00	60.00	251.00	2,670.19		606.40
300.00	180.00	60.00	251.00	2,096.89	2,099.00	512.60
300.00	180.00	60.00	251.00	2,098.65		512.50
300.00	180.00	60.00	251.00	2,098.65		512.50
300.00	180.00	60.00	251.00	2,096.89		512.60
300.00	180.00	60.00	251.00	2,103.92		512.20
300.00	180.00	60.00	251.00	749.02	749.34	608.10
300.00	180.00	60.00	251.00	749.47		607.90
300.00	180.00	60.00	251.00	748.80		608.20
300.00	180.00	60.00	251.00	749.25		608.00
300.00	180.00	60.00	251.00	750.14		607.60
300.00	180.00	60.00	251,00	718,57	719,40	509,30
300.00	180.00	60.00	251,00	719,19		509,00
300.00	180.00	60.00	251,00	719,40		508,90
300.00	180.00	60.00	251,00	719,40		508,90
300.00	180.00	60.00	251,00	720,43		508,40
300.00	180.00	60.00	251,00	660,00	660,24	462,80
300.00	180.00	60.00	251,00	660,00		462,80
300.00	180.00	60.00	251,00	660,17		462,70
300.00	180.00	60.00	251,00	660,69		462,40
300.00	180.00	60.00	251,00	660,35		462,60
300.00	180.00	60.00	251.00	3,042.40		366.90
300.00	180.00	60.00	251.00	3,042.40		366.90
300.00	180.00	60.00	251.00	3,042.40	3,057.33	366.90

300.00	180.00	60.00	251.00	3,079.73		365.90
300.00	180.00	60.00	251.00	3,079.73		365.90
300.00	180.00	60.00	251.00	2,956.40		654.50
300.00	180.00	60.00	251.00	2,823.37		654.50
300.00	180.00	60.00	251.00	2,823.37	2,849.98	654.50
300.00	180.00	60.00	251.00	2,823.37		654.50
300.00	180.00	60.00	251.00	2,823.37		654.50
300.00	180.00	60.00	251.00	2,952.92		880.80
300.00	180.00	60.00	251.00	2,952.92		880.80
300.00	180.00	60.00	251.00	2,952.92	2,952.92	880.80
300.00	180.00	60.00	251.00	2,952.92		880.80
300.00	180.00	60.00	251.00	2,952.92		880.80
300.00	180.00	60.00	251.00	3,238.68		682.10
300.00	180.00	60.00	251.00	3,238.68		682.10
300.00	180.00	60.00	251.00	3,281.02	3,264.09	681.10
300.00	180.00	60.00	251.00	3,281.02		681.10
300.00	180.00	60.00	251.00	3,281.02		681.10
300.00	180.00	60.00	251.00	3,068.44		417.40
300.00	180.00	60.00	251.00	3,068.44		417.40
300.00	180.00	60.00	251.00	3,068.44	3,083.63	417.40
300.00	180.00	60.00	251.00	3,106.41		416.40
300.00	180.00	60.00	251.00	3,106.41		416.40
300.00	180.00	60.00	251.00	3,320.08		299.30
300.00	180.00	60.00	251.00	3,320.08		299.30
300.00	180.00	60.00	251.00	3,320.08	3,320.08	299.30
300.00	180.00	60.00	251.00	3,320.08		299.30
300.00	180.00	60.00	251.00	3,320.08		299.30
300.00	180.00	60.00	251.00	3,157.21		169.50
300.00	180.00	60.00	251.00	3,042.40		169.50
300.00	180.00	60.00	251.00	3,157.21	3,088.32	169.50
300.00	180.00	60.00	251.00	3,042.40		168.50
300.00	180.00	60.00	251.00	3,042.40		168.50
300.00	180.00	60.00	251.00	2,798.19		837.30
300.00	180.00	60.00	251.00	2,798.19		837.30
300.00	180.00	60.00	251.00	2,895.02	2,856.29	834.30
300.00	180.00	60.00	251.00	2,895.02		834.30
300.00	180.00	60.00	251.00	2,895.02		834.30
300.00	180.00	60.00	251.00	3,373.63		935.90
300.00	180.00	60.00	251.00	3,373.63		935.90
300.00	180.00	60.00	251.00	3,373.63	3,373.63	935.90
300.00	180.00	60.00	251.00	3,373.63		935.90
300.00	180.00	60.00	251.00	3,373.63		935.90
300.00	180.00	60.00	251.00	3,302.61		147.30
300.00	180.00	60.00	251.00	3,302.61		147.30
300.00	180.00	60.00	251.00	3,302.61	3,302.61	147.30
300.00	180.00	60.00	251.00	3,302.61		147.30
300.00	180.00	60.00	251.00	3,302.61		147.30
300.00	180.00	60.00	251.00	3,009.57		964.90
300.00	180.00	60.00	251.00	3,009.57		964.90
300.00	180.00	60.00	251.00	3,046.09	3,031.48	963.90
300.00	180.00	60.00	251.00	3,046.09		963.90
300.00	180.00	60.00	251.00	3,046.09		963.90
300.00	180.00	60.00	251.00	3,185.25		585.70
300.00	180.00	60.00	251.00	3,185.25		585.70

300.00	180.00	60.00	251.00	3,185.25	3,185.25	585.70
300.00	180.00	60.00	251.00	3,185.25		585.70
300.00	180.00	60.00	251.00	3,185.25		585.70
300.00	180.00	60.00	251.00	2,653.26	2,653.26	924.50
300.00	180.00	60.00	251.00	2,653.26		924.50
300.00	180.00	60.00	251.00	2,653.26		924.50
300.00	180.00	60.00	251.00	2,653.26		924.50
300.00	180.00	60.00	251.00	2,653.26		924.50
300.00	180.00	60.00	251.00	3,545.17	3,565.49	692.00
300.00	180.00	60.00	251.00	3,545.17		692.00
300.00	180.00	60.00	251.00	3,545.17		692.00
300.00	180.00	60.00	251.00	3,595.96		691.00
300.00	180.00	60.00	251.00	3,595.96		691.00
300.00	180.00	60.00	251.00	3,217.92	3,234.64	689.10
300.00	180.00	60.00	251.00	3,217.92		689.10
300.00	180.00	60.00	251.00	3,217.92		689.10
300.00	180.00	60.00	251.00	3,259.71		688.10
300.00	180.00	60.00	251.00	3,259.71		688.10
300.00	180.00	60.00	251.00	3,364.58	3,380.94	876.40
300.00	180.00	60.00	251.00	3,373.63		876.20
300.00	180.00	60.00	251.00	3,387.29		875.90
300.00	180.00	60.00	251.00	3,382.72		876.00
300.00	180.00	60.00	251.00	3,396.45		875.70
300.00	180.00	60.00	251.00	3,382.72	3,386.39	813.60
300.00	180.00	60.00	251.00	3,378.17		813.70
300.00	180.00	60.00	251.00	3,382.72		813.60
300.00	180.00	60.00	251.00	3,387.29		813.50
300.00	180.00	60.00	251.00	3,401.06		813.20
300.00	180.00	60.00	251.00	3,410.30	3,414.02	1,037.20
300.00	180.00	60.00	251.00	3,414.94		1,037.10
300.00	180.00	60.00	251.00	3,410.30		1,037.20
300.00	180.00	60.00	251.00	3,424.26		1,036.90
300.00	180.00	60.00	251.00	3,410.30		1,037.20
300.00	180.00	60.00	251,00	3133,56	3140,63	672,90
300.00	180.00	60.00	251,00	3133,56		672,90
300.00	180.00	60.00	251,00	3141,40		672,70
300.00	180.00	60.00	251,00	3145,34		672,60
300.00	180.00	60.00	251,00	3149,28		672,50
300.00	180.00	60.00	251,00	660,00	660,28	462,80
300.00	180.00	60.00	251,00	660,17		462,70
300.00	180.00	60.00	251,00	660,69		462,40
300.00	180.00	60.00	251,00	660,35		462,60
300.00	180.00	60.00	251,00	660,17		462,70
0.00	150.00	150.00	250.00	3,132.83	3,164.64	485.70
0.00	150.00	150.00	250.00	3,172.59		488.70
0.00	150.00	150.00	250.00	3,172.59		488.70
0.00	150.00	150.00	250.00	3,172.59		488.70
0.00	150.00	150.00	250.00	3,172.59		488.70
0.00	150.00	150.00	250.00	3,623.19	3,768.99	826.60
0.00	150.00	150.00	250.00	3,623.19		826.60
0.00	150.00	150.00	250.00	3,846.15		826.60
0.00	150.00	150.00	250.00	3,846.15		826.60
0.00	150.00	150.00	250.00	3,906.25		826.60
0.00	150.00	150.00	250.00	3,160.56		233.30

0.00	150.00	150.00	250.00	3,160.56		233.30
0.00	150.00	150.00	250.00	3,160.56	3,160.56	233.30
0.00	150.00	150.00	250.00	3,160.56		233.30
0.00	150.00	150.00	250.00	3,160.56		233.30
0.00	150.00	150.00	250.00	2,824.86		340.90
0.00	150.00	150.00	250.00	2,824.86		340.90
0.00	150.00	150.00	250.00	2,824.86	2,824.86	340.90
0.00	150.00	150.00	250.00	2,824.86		340.90
0.00	150.00	150.00	250.00	2,824.86		340.90
0.00	150.00	150.00	250.00	2,732.24		910.30
0.00	150.00	150.00	250.00	2,732.24		910.30
0.00	150.00	150.00	250.00	2,617.80	2,709.35	910.30
0.00	150.00	150.00	250.00	2,732.24		910.30
0.00	150.00	150.00	250.00	2,732.24		910.30
0.00	150.00	150.00	250.00	2,844.14		568.10
0.00	150.00	150.00	250.00	2,844.14		568.10
0.00	150.00	150.00	250.00	2,844.14	2,844.14	568.10
0.00	150.00	150.00	250.00	2,844.14		568.10
0.00	150.00	150.00	250.00	2,844.14		568.10
0.00	150.00	150.00	250.00	3,217.50		651.70
0.00	150.00	150.00	250.00	3,217.50		651.70
0.00	150.00	150.00	250.00	3,217.50	3,234.28	651.70
0.00	150.00	150.00	250.00	3,259.45		650.70
0.00	150.00	150.00	250.00	3,259.45		650.70
0.00	150.00	150.00	250.00	3,213.37		969.80
0.00	150.00	150.00	250.00	3,213.37		969.80
0.00	150.00	150.00	250.00	3,213.37	3,221.74	969.80
0.00	150.00	150.00	250.00	3,213.37		969.80
0.00	150.00	150.00	250.00	3,255.21		968.80
0.00	150.00	150.00	250.00	3,136.76		155.90
0.00	150.00	150.00	250.00	3,136.76		155.90
0.00	150.00	150.00	250.00	3,176.62	3,160.68	154.90
0.00	150.00	150.00	250.00	3,176.62		154.90
0.00	150.00	150.00	250.00	3,176.62		154.90
0.00	150.00	150.00	250.00	3,033.98		605.50
0.00	150.00	150.00	250.00	3,033.98		605.50
0.00	150.00	150.00	250.00	3,033.98	3,033.98	605.50
0.00	150.00	150.00	250.00	3,033.98		605.50
0.00	150.00	150.00	250.00	3,033.98		605.50
0.00	150.00	150.00	250.00	2,913.75		945.50
0.00	150.00	150.00	250.00	2,913.75		945.50
0.00	150.00	150.00	250.00	2,913.75	2,913.75	945.50
0.00	150.00	150.00	250.00	2,913.75		945.50
0.00	150.00	150.00	250.00	2,913.75		945.50
0.00	150.00	150.00	250.00	3,293.81		628.20
0.00	150.00	150.00	250.00	3,337.78		627.20
0.00	150.00	150.00	250.00	3,337.78	3,328.99	627.20
0.00	150.00	150.00	250.00	3,337.78		627.20
0.00	150.00	150.00	250.00	3,337.78		627.20
0.00	150.00	150.00	250.00	3,196.93		83.10
0.00	150.00	150.00	250.00	3,196.93		83.10
0.00	150.00	150.00	250.00	3,238.34	3,221.78	82.10
0.00	150.00	150.00	250.00	3,238.34		82.10
0.00	150.00	150.00	250.00	3,238.34		82.10
0.00	150.00	150.00	250.00	3,571.43		787.70

0.00	150.00	150.00	250.00	3,623.19		786.70
0.00	150.00	150.00	250.00	3,623.19	3,612.84	786.70
0.00	150.00	150.00	250.00	3,623.19		786.70
0.00	150.00	150.00	250.00	3,623.19		786.70
0.00	150.00	150.00	250.00	3,571.43		712.10
0.00	150.00	150.00	250.00	3,571.43		712.10
0.00	150.00	150.00	250.00	3,571.43	3,571.43	712.10
0.00	150.00	150.00	250.00	3,571.43		712.10
0.00	150.00	150.00	250.00	3,571.43		712.10
0.00	150.00	150.00	250.00	3,561.25		477.20
0.00	150.00	150.00	250.00	3,561.25		477.20
0.00	150.00	150.00	250.00	3,561.25	3,561.25	477.20
0.00	150.00	150.00	250.00	3,561.25		477.20
0.00	150.00	150.00	250.00	3,561.25		477.20
0.00	150.00	150.00	250.00	3,687.32		293.80
0.00	150.00	150.00	250.00	3,687.32		293.80
0.00	150.00	150.00	250.00	3,687.32	3,687.32	293.80
0.00	150.00	150.00	250.00	3,687.32		293.80
0.00	150.00	150.00	250.00	3,687.32		293.80
0.00	150.00	150.00	250.00	2,548.42		1,065.10
0.00	150.00	150.00	250.00	2,378.69		1,072.10
0.00	150.00	150.00	250.00	2,472.80	2,469.10	1,068.10
0.00	150.00	150.00	250.00	2,472.80		1,068.10
0.00	150.00	150.00	250.00	2,472.80		1,068.10
0.00	150.00	150.00	250.00	3,351.21		564.90
0.00	150.00	150.00	250.00	3,351.21		564.90
0.00	150.00	150.00	250.00	3,355.70	3,355.71	564.80
0.00	150.00	150.00	250.00	3,360.22		564.70
0.00	150.00	150.00	250.00	3,360.22		564.70
0.00	150.00	150.00	250,00	3486,75		448,40
0.00	150.00	150.00	250,00	3491,62		448,30
0.00	150.00	150.00	250,00	3496,50	3495,54	448,20
0.00	150.00	150.00	250,00	3496,50		448,20
0.00	150.00	150.00	250,00	3506,31		448,00
0.00	150.00	150.00	250,00	3401,36		331,80
0.00	150.00	150.00	250,00	3405,99		331,70
0.00	150.00	150.00	250,00	3405,99	3407,86	331,70
0.00	150.00	150.00	250,00	3410,64		331,60
0.00	150.00	150.00	250,00	3415,30		331,50
0.00	150.00	150.00	250,00	3306,88		742,50
0.00	150.00	150.00	250,00	3315,65		742,30
0.00	150.00	150.00	250,00	3320,05	3318,30	742,20
0.00	150.00	150.00	250,00	3324,47		742,10
0.00	150.00	150.00	250,00	3324,47		742,10
0.00	150.00	150.00	250,00	3238,34		503,30
0.00	150.00	150.00	250,00	3238,34		503,30
0.00	150.00	150.00	250,00	3246,75	3245,08	503,10
0.00	150.00	150.00	250,00	3246,75		503,10
0.00	150.00	150.00	250,00	3255,21		502,90
0.00	150.00	150.00	250,00	3486,75		239,60
0.00	150.00	150.00	250,00	3481,89		239,70
0.00	150.00	150.00	250,00	3496,50	3492,61	239,40
0.00	150.00	150.00	250,00	3496,50		239,40
0.00	150.00	150.00	250,00	3501,40		239,30
0.00	150.00	150.00	250,00	3424,66		401,30

0.00	150.00	150.00	250,00	3419,97	3426,54	401,40
0.00	150.00	150.00	250,00	3424,66		401,30
0.00	150.00	150.00	250,00	3429,36		401,20
0.00	150.00	150.00	250,00	3434,07		401,10
0.00	150.00	150.00	250,00	3453,04	3464,54	184,40
0.00	150.00	150.00	250,00	3467,41		184,10
0.00	150.00	150.00	250,00	3462,60		184,20
0.00	150.00	150.00	250,00	3467,41		184,10
0.00	150.00	150.00	250,00	3472,22		184,00
0.00	150.00	150.00	250,00	3328,89	3336,90	857,30
0.00	150.00	150.00	250,00	3337,78		857,10
0.00	150.00	150.00	250,00	3337,78		857,10
0.00	150.00	150.00	250,00	3337,78		857,10
0.00	150.00	150.00	250,00	3342,25		857,00
0.00	150.00	150.00	250,00	3302,51	3309,51	337,20
0.00	150.00	150.00	250,00	3311,26		337,00
0.00	150.00	150.00	250,00	3311,26		337,00
0.00	150.00	150.00	250,00	3311,26		337,00
0.00	150.00	150.00	250,00	3311,26		337,00
0.00	180.00	180.00	300.00	3,282.28	3,349.62	891.30
0.00	180.00	180.00	300.00	3,282.28		891.30
0.00	180.00	180.00	300.00	3,318.58		891.30
0.00	180.00	180.00	300.00	3,432.49		891.30
0.00	180.00	180.00	300.00	3,432.49		891.30
0.00	180.00	180.00	300.00	3,064.35	3,122.47	1,070.40
0.00	180.00	180.00	300.00	3,064.35		1,070.40
0.00	180.00	180.00	300.00	3,161.22		1,071.40
0.00	180.00	180.00	300.00	3,161.22		1,071.40
0.00	180.00	180.00	300.00	3,161.22		1,071.40
0.00	180.00	180.00	300,00	3181,34	3194,22	498,40
0.00	180.00	180.00	300,00	3191,49		498,10
0.00	180.00	180.00	300,00	3198,29		497,90
0.00	180.00	180.00	300,00	3198,29		497,90
0.00	180.00	180.00	300,00	3201,71		497,80
0.00	180.00	180.00	300,00	3171,25	3185,41	1015,80
0.00	180.00	180.00	300,00	3188,10		1015,30
0.00	180.00	180.00	300,00	3188,10		1015,30
0.00	180.00	180.00	300,00	3191,49		1015,20
0.00	180.00	180.00	300,00	3188,10		1015,30
0.00	180.00	180.00	300,00	3134,80	3144,01	389,80
0.00	180.00	180.00	300,00	3141,36		389,60
0.00	180.00	180.00	300,00	3141,36		389,60
0.00	180.00	180.00	300,00	3151,26		389,30
0.00	180.00	180.00	300,00	3151,26		389,30
0.00	180.00	180.00	300,00	3201,71	3207,87	285,70
0.00	180.00	180.00	300,00	3205,13		285,60
0.00	180.00	180.00	300,00	3208,56		285,50
0.00	180.00	180.00	300,00	3211,99		285,40
0.00	180.00	180.00	300,00	3211,99		285,40
0.00	180.00	180.00	300,00	3027,25	3032,15	575,40
0.00	180.00	180.00	300,00	3030,30		575,30
0.00	180.00	180.00	300,00	3030,30		575,30
0.00	180.00	180.00	300,00	3036,44		575,10
0.00	180.00	180.00	300,00	3036,44		575,10
0.00	180.00	180.00	300,00	3246,75		1055,80

0.00	180.00	180.00	300,00	3239,74		1056,00
0.00	180.00	180.00	300,00	3243,24	3246,06	1055,90
0.00	180.00	180.00	300,00	3250,27		1055,70
0.00	180.00	180.00	300,00	3250,27		1055,70
0.00	180.00	180.00	300,00	3579,95		396,30
0.00	180.00	180.00	300,00	3588,52		396,10
0.00	180.00	180.00	300,00	3592,81	3589,38	396,00
0.00	180.00	180.00	300,00	3588,52		396,10
0.00	180.00	180.00	300,00	3597,12		395,90
0.00	180.00	180.00	300,00	3592,81		119,80
0.00	180.00	180.00	300,00	3690,04		117,60
0.00	180.00	180.00	300,00	3597,12	3637,02	119,70
0.00	180.00	180.00	300,00	3601,44		119,60
0.00	180.00	180.00	300,00	3703,70		117,30
0.00	180.00	180.00	300,00	3448,28		912,50
0.00	180.00	180.00	300,00	3460,21		912,20
0.00	180.00	180.00	300,00	3456,22	3459,43	912,30
0.00	180.00	180.00	300,00	3460,21		912,20
0.00	180.00	180.00	300,00	3472,22		911,90
0.00	180.00	180.00	300.00	2,949.85		958.70
0.00	180.00	180.00	300.00	2,961.50		958.30
0.00	180.00	180.00	300.00	2,952.76	2,955.68	958.60
0.00	180.00	180.00	300.00	2,949.85		958.70
0.00	180.00	180.00	300.00	2,964.43		958.20
0.00	180.00	180.00	300.00	3,712.87		350.30
0.00	180.00	180.00	300.00	3,690.04		350.80
0.00	180.00	180.00	300.00	3,699.14	3,702.81	350.60
0.00	180.00	180.00	300.00	3,708.28		350.40
0.00	180.00	180.00	300.00	3,703.70		350.50
0.00	180.00	180.00	300,00	3157,89		1031,50
0.00	180.00	180.00	300,00	3161,22		1031,40
0.00	180.00	180.00	300,00	3164,56	3163,90	1031,30
0.00	180.00	180.00	300,00	3171,25		1031,10
0.00	180.00	180.00	300,00	3164,56		1031,30
0.00	180.00	180.00	300,00	3278,69		278,80
0.00	180.00	180.00	300,00	3282,28		278,70
0.00	180.00	180.00	300,00	3289,47	3286,60	278,50
0.00	180.00	180.00	300,00	3293,08		278,40
0.00	180.00	180.00	300,00	3289,47		278,50
0.00	180.00	180.00	300,00	3177,97		369,50
0.00	180.00	180.00	300,00	3171,25		369,70
0.00	180.00	180.00	300,00	3181,34	3177,97	369,40
0.00	180.00	180.00	300,00	3174,60		369,60
0.00	180.00	180.00	300,00	3184,71		369,30
0.00	180.00	180.00	300.00	3,318.58		982.80
0.00	180.00	180.00	300.00	3,333.33		982.40
0.00	180.00	180.00	300.00	3,337.04	3,309.83	982.30
0.00	180.00	180.00	300.00	3,211.99		985.80
0.00	180.00	180.00	300.00	3,348.21		982.00
0.00	180.00	180.00	300.00	3,141.36		146.40
0.00	180.00	180.00	300.00	3,161.22		145.80
0.00	180.00	180.00	300.00	3,144.65	3,157.95	146.30
0.00	180.00	180.00	300.00	3,167.90		145.60
0.00	180.00	180.00	300.00	3,174.60		145.40
0.00	180.00	180.00	300,00	2413,52		801,60

0.00	180.00	180.00	300,00	2411,58		801,70
0.00	180.00	180.00	300,00	2415,46	2415,08	801,50
0.00	180.00	180.00	300,00	2423,26		801,10
0.00	180.00	180.00	300,00	2411,58		801,70
0.00	180.00	180.00	300,00	3138,08		316,60
0.00	180.00	180.00	300,00	3144,65		316,40
0.00	180.00	180.00	300,00	2744,74	2776,76	330,30
0.00	180.00	180.00	300,00	2427,18		344,60
0.00	180.00	180.00	300,00	2429,15		344,50
0.00	180.00	180.00	300,00	3086,42		1050,90
0.00	180.00	180.00	300,00	3080,08		1051,10
0.00	180.00	180.00	300,00	2159,83	2904,95	1092,60
0.00	180.00	180.00	300,00	3108,81		1050,20
0.00	180.00	180.00	300,00	3089,60		1050,80
0.00	180.00	180.00	300.00	3,102.38		1,048.90
0.00	180.00	180.00	300.00	3,067.48		1,050.00
0.00	180.00	180.00	300.00	3,102.38	3,066.89	1,048.90
0.00	180.00	180.00	300.00	2,946.95		1,054.00
0.00	180.00	180.00	300.00	3,115.26		1,048.50
0.00	180.00	180.00	300.00	2,938.30		211.00
0.00	180.00	180.00	300.00	2,801.12		216.00
0.00	180.00	180.00	300.00	2,949.85	2,912.02	210.60
0.00	180.00	180.00	300.00	2,935.42		211.10
0.00	180.00	180.00	300.00	2,935.42		211.10
0.00	180.00	180.00	300,00	3432,49		471,60
0.00	180.00	180.00	300,00	3432,49		471,60
0.00	180.00	180.00	300,00	3440,37	3435,64	471,40
0.00	180.00	180.00	300,00	3432,49		471,60
0.00	180.00	180.00	300,00	3440,37		471,40
0.00	180.00	180.00	300,00	3285,87		1042,00
0.00	180.00	180.00	300,00	3285,87		1042,00
0.00	180.00	180.00	300,00	3293,08	3291,65	1041,80
0.00	180.00	180.00	300,00	3296,70		1041,70
0.00	180.00	180.00	300,00	3296,70		1041,70
0.00	180.00	180.00	300,00	1805,05		641,90
0.00	180.00	180.00	300,00	1806,14		641,80
0.00	180.00	180.00	300,00	1807,23	1807,89	641,70
0.00	180.00	180.00	300,00	1809,41		641,50
0.00	180.00	180.00	300,00	1811,59		641,30
0.00	180.00	180.00	300.00	3,015.08		146.80
0.00	180.00	180.00	300.00	3,024.19		146.50
0.00	180.00	180.00	300.00	3,000.00	2,977.44	147.30
0.00	180.00	180.00	300.00	2,832.86		153.20
0.00	180.00	180.00	300.00	3,015.08		146.80
0.00	180.00	180.00	300.00	3,048.78		325.10
0.00	180.00	180.00	300.00	3,006.01		326.50
0.00	180.00	180.00	300.00	2,985.07	3,007.39	327.20
0.00	180.00	180.00	300.00	2,988.05		327.10
0.00	180.00	180.00	300.00	3,009.03		326.40
300.00	180.00	60.00	251.00	3,535.18		291.50
300.00	180.00	60.00	251.00	3,530.21		291.50
300.00	180.00	60.00	251.00	3,535.18	3,533.19	291.30
300.00	180.00	60.00	251.00	3,530.21		291.30
300.00	180.00	60.00	251.00	3,535.18		291.10
300.00	180.00	60.00	251.00	3,530.21		474.70

300.00	180.00	60.00	251.00	3,530.21	3,531.21	474.60
300.00	180.00	60.00	251.00	3,530.21		474.50
300.00	180.00	60.00	251.00	3,530.21		474.50
300.00	180.00	60.00	251.00	3,535.18		474.30
300.00	180.00	60.00	251.00	3,373.63	3,365.52	741.20
300.00	180.00	60.00	251.00	3,369.10		741.20
300.00	180.00	60.00	251.00	3,346.64		741.70
300.00	180.00	60.00	251.00	3,373.63		741.00
300.00	180.00	60.00	251.00	3,364.58		741.10
300.00	180.00	60.00	251.00	3,520.31	3,524.32	912.10
300.00	180.00	60.00	251.00	3,550.18		911.40
300.00	180.00	60.00	251.00	3,525.25		911.80
300.00	180.00	60.00	251.00	3,510.46		912.10
300.00	180.00	60.00	251.00	3,515.38		911.80
300.00	180.00	60.00	251.00	3,337.74	3,343.08	838.20
300.00	180.00	60.00	251.00	3,337.74		838.10
300.00	180.00	60.00	251.00	3,342.18		838.00
300.00	180.00	60.00	251.00	3,346.64		837.80
300.00	180.00	60.00	251.00	3,351.11		837.60
300.00	180.00	60.00	251.00	3,664.20	3,664.21	420.40
300.00	180.00	60.00	251.00	3,658.86		420.40
300.00	180.00	60.00	251.00	3,664.20		420.30
300.00	180.00	60.00	251.00	3,664.20		420.20
300.00	180.00	60.00	251.00	3,669.56		420.00
300.00	180.00	60.00	251.00	3,680.32	3,678.17	599.40
300.00	180.00	60.00	251.00	3,674.93		599.50
300.00	180.00	60.00	251.00	3,674.93		599.40
300.00	180.00	60.00	251.00	3,680.32		599.20
300.00	180.00	60.00	251.00	3,680.32		599.10
300.00	180.00	60.00	251.00	3,601.12	3,606.30	786.90
300.00	180.00	60.00	251.00	3,606.29		786.70
300.00	180.00	60.00	251.00	3,606.29		786.60
300.00	180.00	60.00	251.00	3,601.12		786.60
300.00	180.00	60.00	251.00	3,616.69		786.20
300.00	180.00	60.00	251.00	3,520.31	3,521.33	424.70
300.00	180.00	60.00	251.00	3,515.38		424.70
300.00	180.00	60.00	251.00	3,520.31		424.50
300.00	180.00	60.00	251.00	3,540.17		424.10
300.00	180.00	60.00	251.00	3,510.46		424.50
300.00	180.00	60.00	251.00	3,729.54	3,714.12	982.80
300.00	180.00	60.00	251.00	3,724.01		982.90
300.00	180.00	60.00	251.00	3,702.04		983.20
300.00	180.00	60.00	251.00	3,702.04		983.10
300.00	180.00	60.00	251.00	3,712.99		982.80
300.00	180.00	60.00	251.00	3,560.26	3,564.30	662.70
300.00	180.00	60.00	251.00	3,565.31		662.50
300.00	180.00	60.00	251.00	3,560.26		662.60
300.00	180.00	60.00	251.00	3,570.38		662.30
300.00	180.00	60.00	251.00	3,565.31		662.30
300.00	180.00	60.00	251.00	3,832.03	3,739.60	958.50
300.00	180.00	60.00	251.00	3,808.77		958.80
300.00	180.00	60.00	251.00	3,685.73		960.90
300.00	180.00	60.00	251.00	3,680.32		960.90
300.00	180.00	60.00	251.00	3,691.15		960.70
300.00	180.00	60.00	251.00	3,590.82		481.60

300.00	180.00	60.00	251.00	3,616.69		481.00
300.00	180.00	60.00	251.00	3,648.23	3,619.91	480.40
300.00	180.00	60.00	251.00	3,627.14		480.70
300.00	180.00	60.00	251.00	3,616.69		480.80
300.00	180.00	60.00	251.00	3,471.62		999.80
300.00	180.00	60.00	251.00	3,500.67		999.10
300.00	180.00	60.00	251.00	3,500.67	3,437.73	999.00
300.00	180.00	60.00	251.00	3,355.59		1,002.00
300.00	180.00	60.00	251.00	3,360.08		1,001.80
300.00	180.00	60.00	251.00	3,580.57		146.50
300.00	180.00	60.00	251.00	3,595.96		146.10
300.00	180.00	60.00	251.00	3,580.57	3,587.75	146.30
300.00	180.00	60.00	251.00	3,590.82		146.00
300.00	180.00	60.00	251.00	3,590.82		145.90
300.00	180.00	60.00	251.00	3,486.08		562.50
300.00	180.00	60.00	251.00	3,476.43		562.60
300.00	180.00	60.00	251.00	3,447.77	3,468.79	563.10
300.00	180.00	60.00	251.00	3,471.62		562.50
300.00	180.00	60.00	251.00	3,462.04		562.60
300.00	180.00	60.00	251.00	2,667.35		851.40
300.00	180.00	60.00	251.00	3,428.93		830.50
300.00	180.00	60.00	251.00	2,673.04	2,973.87	851.10
300.00	180.00	60.00	251.00	3,438.33		830.10
300.00	180.00	60.00	251.00	2,661.70		851.30
300.00	180.00	60.00	251.00	3,378.17		1,056.90
300.00	180.00	60.00	251.00	3,382.72		1,056.70
300.00	180.00	60.00	251.00	3,387.29	3,415.13	1,056.60
300.00	180.00	60.00	251.00	3,540.17		1,053.30
300.00	180.00	60.00	251.00	3,387.29		1,056.30
300.00	180.00	60.00	251.00	3,550.18		462.10
300.00	180.00	60.00	251.00	3,560.26		461.90
300.00	180.00	60.00	251.00	3,565.31	3,560.26	461.70
300.00	180.00	60.00	251.00	3,560.26		461.70
300.00	180.00	60.00	251.00	3,565.31		461.50
300.00	180.00	60.00	251.00	3,616.69		1,018.80
300.00	180.00	60.00	251.00	3,606.29		1,018.90
300.00	180.00	60.00	251.00	3,611.48	3,606.31	1,018.70
300.00	180.00	60.00	251.00	3,595.96		1,018.90
300.00	180.00	60.00	251.00	3,601.12		1,018.70
300.00	180.00	60.00	251.00	3,855.58		824.10
300.00	180.00	60.00	251.00	3,849.66		824.10
300.00	180.00	60.00	251.00	3,855.58	3,852.03	823.90
300.00	180.00	60.00	251.00	3,849.66		823.90
300.00	180.00	60.00	251.00	3,849.66		823.80
300.00	180.00	60.00	251.00	3,837.89		335.90
300.00	180.00	60.00	251.00	3,861.51		335.40
300.00	180.00	60.00	251.00	3,867.46	3,850.88	335.20
300.00	180.00	60.00	251.00	3,843.77		335.50
300.00	180.00	60.00	251.00	3,843.77		335.40
300.00	180.00	60.00	251.00	3,685.73		473.60
300.00	180.00	60.00	251.00	3,642.93		474.30
300.00	180.00	60.00	251.00	3,664.20	3,672.87	473.90
300.00	180.00	60.00	251.00	3,680.32		473.50
300.00	180.00	60.00	251.00	3,691.15		473.20
300.00	180.00	60.00	251.00	3,601.12		307.90

300.00	180.00	60.00	251.00	3,632.39	3,609.46	307.20
300.00	180.00	60.00	251.00	3,590.82		308.00
300.00	180.00	60.00	251.00	3,606.29		307.60
300.00	180.00	60.00	251.00	3,616.69		307.30
300.00	180.00	60.00	251.00	3,685.73	3,679.25	865.60
300.00	180.00	60.00	251.00	3,680.32		865.60
300.00	180.00	60.00	251.00	3,674.93		865.60
300.00	180.00	60.00	251.00	3,674.93		865.50
300.00	180.00	60.00	251.00	3,680.32		865.30
300.00	180.00	60.00	251.00	3,481.25	3,482.22	734.00
300.00	180.00	60.00	251.00	3,481.25		733.90
300.00	180.00	60.00	251.00	3,486.08		733.70
300.00	180.00	60.00	251.00	3,486.08		733.60
300.00	180.00	60.00	251.00	3,476.43		733.70
300.00	180.00	60.00	251.00	3,328.89	3,328.89	546.60
300.00	180.00	60.00	251.00	3,328.89		546.50
300.00	180.00	60.00	251.00	3,328.89		546.40
300.00	180.00	60.00	251.00	3,328.89		546.30
300.00	180.00	60.00	251.00	3,328.89		546.20
300.00	180.00	60.00	251.00	3,337.74	3,335.97	274.40
300.00	180.00	60.00	251.00	3,333.31		274.40
300.00	180.00	60.00	251.00	3,333.31		274.30
300.00	180.00	60.00	251.00	3,337.74		274.20
300.00	180.00	60.00	251.00	3,337.74		274.10

Channel 7						
(sensor 7)						
location			Distance	Velocity	Average velocity for sensor 7	Arrival time, millisecond
x7	y7	z7	(mm)	m/s	m/s	t7
30.00	90.00	0.00	125.50	3,137.48	3,135.91	267.30
30.00	90.00	0.00	125.50	3,137.48		267.30
30.00	90.00	0.00	125.50	3,137.48		267.20
30.00	90.00	0.00	125.50	3,137.48		267.10
30.00	90.00	0.00	125.50	3,129.65		267.10
30.00	90.00	0.00	125.50	3,337.74	3,339.53	1,013.20
30.00	90.00	0.00	125.50	3,346.64		1,013.10
30.00	90.00	0.00	125.50	3,337.74		1,013.10
30.00	90.00	0.00	125.50	3,328.89		1,013.10
30.00	90.00	0.00	125.50	3,346.64		1,012.80
30.00	90.00	0.00	125.50	3,346.64	3,339.53	373.60
30.00	90.00	0.00	125.50	3,337.74		373.60
30.00	90.00	0.00	125.50	3,346.64		373.40
30.00	90.00	0.00	125.50	3,337.74		373.40
30.00	90.00	0.00	125.50	3,328.89		373.40
30.00	90.00	0.00	125.50	3,346.64	3,348.43	329.60
30.00	90.00	0.00	125.50	3,346.64		329.50
30.00	90.00	0.00	125.50	3,346.64		329.40
30.00	90.00	0.00	125.50	3,355.59		329.20
30.00	90.00	0.00	125.50	3,346.64		329.20
30.00	90.00	0.00	125.50	3,364.58	3,359.20	309.90
30.00	90.00	0.00	125.50	3,346.64		310.00
30.00	90.00	0.00	125.50	3,355.59		309.80
30.00	90.00	0.00	125.50	3,364.58		309.60
30.00	90.00	0.00	125.50	3,364.58		309.50
30.00	90.00	0.00	125.50	3,209.69	3,211.35	798.60
30.00	90.00	0.00	125.50	3,217.92		798.50
30.00	90.00	0.00	125.50	3,209.69		798.50
30.00	90.00	0.00	125.50	3,217.92		798.30
30.00	90.00	0.00	125.50	3,201.51		798.40
30.00	90.00	0.00	125.50	2,752.17	2,738.97	287.30
30.00	90.00	0.00	125.50	2,740.15		287.40
30.00	90.00	0.00	125.50	2,734.18		287.40
30.00	90.00	0.00	125.50	2,734.18		287.30
30.00	90.00	0.00	125.50	2,734.18		287.20
30.00	90.00	0.00	125.50	2,871.83	2,869.21	720.30
30.00	90.00	0.00	125.50	2,865.27		720.30
30.00	90.00	0.00	125.50	2,871.83		720.10
30.00	90.00	0.00	125.50	2,871.83		720.00
30.00	90.00	0.00	125.50	2,865.27		720.00
30.00	90.00	0.00	125.50	2,451.15	2,451.16	398.10
30.00	90.00	0.00	125.50	2,451.15		398.00
30.00	90.00	0.00	125.50	2,455.95		397.80
30.00	90.00	0.00	125.50	2,451.15		397.80
30.00	90.00	0.00	125.50	2,446.37		397.80
30.00	90.00	0.00	125.50	2,625.50	2,622.23	383.80
30.00	90.00	0.00	125.50	2,609.13		384.00
30.00	90.00	0.00	125.50	2,620.02		383.70
30.00	90.00	0.00	125.50	2,631.01		383.40

30.00	90.00	0.00	125.50	2,625.50		383.50
30.00	90.00	0.00	125.50	2,561.20		498.80
30.00	90.00	0.00	125.50	2,576.98		498.40
30.00	90.00	0.00	125.50	2,566.44	2,564.37	498.50
30.00	90.00	0.00	125.50	2,550.79		498.70
30.00	90.00	0.00	125.50	2,566.44		498.40
30.00	90.00	0.00	125.50	1,719.16		491.80
30.00	90.00	0.00	125.50	1,719.16		491.80
30.00	90.00	0.00	125.50	1,723.89	1,720.11	491.50
30.00	90.00	0.00	125.50	1,719.16		491.60
30.00	90.00	0.00	125.50	1,719.16		491.50
30.00	90.00	0.00	125.50	1,957.86		504.70
30.00	90.00	0.00	125.50	1,960.92		504.50
30.00	90.00	0.00	125.50	1,957.86	1,958.48	504.50
30.00	90.00	0.00	125.50	1,954.81		504.50
30.00	90.00	0.00	125.50	1,960.92		504.30
30.00	90.00	0.00	125.50	3,169.17		583.00
30.00	90.00	0.00	125.50	3,201.51		582.60
30.00	90.00	0.00	125.50	3,193.36	3,188.53	582.60
30.00	90.00	0.00	125.50	3,185.25		582.60
30.00	90.00	0.00	125.50	3,193.36		582.40
30.00	90.00	0.00	125.50	0.00		0.00
30.00	90.00	0.00	125.50	0.00		0.00
30.00	90.00	0.00	125.50	0.00	0.00	0.00
30.00	90.00	0.00	125.50	0.00		0.00
30.00	90.00	0.00	125.50	0.00		0.00
30.00	90.00	0.00	125.50	2,658.88		87.60
30.00	90.00	0.00	125.50	2,653.26		87.60
30.00	90.00	0.00	125.50	2,693.11	2,669.13	86.80
30.00	90.00	0.00	125.50	2,670.19		87.10
30.00	90.00	0.00	125.50	2,670.19		87.00
30.00	90.00	0.00	125.50	2,614.56		383.80
30.00	90.00	0.00	125.50	2,636.53		383.30
30.00	90.00	0.00	125.50	2,609.13	2,620.09	383.70
30.00	90.00	0.00	125.50	2,603.71		383.70
30.00	90.00	0.00	125.50	2,636.53		383.00
30.00	90.00	0.00	125.50	3,053.50		372.80
30.00	90.00	0.00	125.50	3,083.51		372.30
30.00	90.00	0.00	125.50	3,060.95	3,053.61	372.50
30.00	90.00	0.00	125.50	3,031.38		372.80
30.00	90.00	0.00	125.50	3,038.72		372.60
30.00	90.00	0.00	125.50	2,561.20		628.20
30.00	90.00	0.00	125.50	1,760.15		650.40
30.00	90.00	0.00	125.50	1,760.15	1,920.36	650.30
30.00	90.00	0.00	125.50	1,760.15		650.20
30.00	90.00	0.00	125.50	1,760.15		650.10
30.00	90.00	0.00	125.50	2,609.13		299.20
30.00	90.00	0.00	125.50	2,603.71		299.20
30.00	90.00	0.00	125.50	2,603.71	2,603.72	299.10
30.00	90.00	0.00	125.50	2,598.32		299.10
30.00	90.00	0.00	125.50	2,603.71		298.90
30.00	90.00	0.00	125.50	2,658.88		626.20
30.00	90.00	0.00	125.50	2,647.66		626.30
30.00	90.00	0.00	125.50	2,653.26	2,654.39	626.10
30.00	90.00	0.00	125.50	2,647.66		626.10

30.00	90.00	0.00	125.50	2,664.52		625.80
30.00	90.00	0.00	125.50	1,735.81		540.30
30.00	90.00	0.00	125.50	1,735.81		540.20
30.00	90.00	0.00	125.50	1,735.81	1,735.33	540.10
30.00	90.00	0.00	125.50	1,735.81		540.00
30.00	90.00	0.00	125.50	1,733.41		540.00
30.00	90.00	0.00	125.50	1,797.98		971.60
30.00	90.00	0.00	125.50	1,795.41		971.60
30.00	90.00	0.00	125.50	2,341.40	1,906.15	955.20
30.00	90.00	0.00	125.50	1,795.41		971.40
30.00	90.00	0.00	125.50	1,800.56		971.20
30.00	90.00	0.00	125.50	3,009.57		77.70
30.00	90.00	0.00	125.50	3,009.57		77.60
30.00	90.00	0.00	125.50	2,995.20	3,006.70	77.70
30.00	90.00	0.00	125.50	3,009.57		77.50
30.00	90.00	0.00	125.50	3,009.57		77.40
30.00	90.00	0.00	125.50	3,068.44		887.50
30.00	90.00	0.00	125.50	3,075.96		887.30
30.00	90.00	0.00	125.50	3,060.95	3,069.95	887.40
30.00	90.00	0.00	125.50	3,068.44		887.30
30.00	90.00	0.00	125.50	3,075.96		887.10
30.00	90.00	0.00	125.50	3,038.72		774.30
30.00	90.00	0.00	125.50	3,046.09		774.10
30.00	90.00	0.00	125.50	3,031.38	3,038.73	774.20
30.00	90.00	0.00	125.50	3,046.09		773.90
30.00	90.00	0.00	125.50	3,031.38		774.00
30.00	90.00	0.00	125.50	3,177.19		438.00
30.00	90.00	0.00	125.50	3,169.17		438.00
30.00	90.00	0.00	125.50	3,169.17	3,173.98	437.90
30.00	90.00	0.00	125.50	3,177.19		437.80
30.00	90.00	0.00	125.50	3,177.19		437.70
30.00	90.00	0.00	125.50	2,587.61		1,038.80
30.00	90.00	0.00	125.50	2,592.95		1,038.70
30.00	90.00	0.00	125.50	2,592.95	2,590.82	1,038.60
30.00	90.00	0.00	125.50	2,592.95		1,038.50
30.00	90.00	0.00	125.50	2,587.61		1,038.50
60.00	60.00	0.00	123.69	3,255.08		63.90
60.00	60.00	0.00	123.69	3,272.31		63.60
60.00	60.00	0.00	123.69	3,272.31	3,261.97	63.50
60.00	60.00	0.00	123.69	3,255.08		63.60
60.00	60.00	0.00	123.69	3,255.08		63.60
60.00	60.00	0.00	123.69	3,379.59		333.70
60.00	60.00	0.00	123.69	3,379.59		333.70
60.00	60.00	0.00	123.69	3,388.85	3,381.45	333.50
60.00	60.00	0.00	123.69	3,379.59		333.50
60.00	60.00	0.00	123.69	3,379.59		333.40
60.00	60.00	0.00	123.69	3,398.16		123.20
60.00	60.00	0.00	123.69	3,388.85		123.20
60.00	60.00	0.00	123.69	3,379.59	3,388.86	123.20
60.00	60.00	0.00	123.69	3,388.85		123.00
60.00	60.00	0.00	123.69	3,388.85		122.90
60.00	60.00	0.00	123.69	3,221.18		211.70
60.00	60.00	0.00	123.69	3,221.18		211.60
60.00	60.00	0.00	123.69	3,229.59	3,222.86	211.50
60.00	60.00	0.00	123.69	3,221.18		211.50

60.00	60.00	0.00	123.69	3,221.18		211.40
60.00	60.00	0.00	123.69	3,238.04	3,227.91	50.70
60.00	60.00	0.00	123.69	3,229.59		50.70
60.00	60.00	0.00	123.69	3,221.18		50.70
60.00	60.00	0.00	123.69	3,221.18		50.60
60.00	60.00	0.00	123.69	3,229.59		50.40
60.00	60.00	0.00	123.69	3,179.77	3,189.64	108.30
60.00	60.00	0.00	123.69	3,204.49		107.90
60.00	60.00	0.00	123.69	3,196.21		108.00
60.00	60.00	0.00	123.69	3,179.77		108.00
60.00	60.00	0.00	123.69	3,187.97		107.90
60.00	60.00	0.00	123.69	3,263.67	3,261.96	56.40
60.00	60.00	0.00	123.69	3,272.31		56.20
60.00	60.00	0.00	123.69	3,255.08		56.30
60.00	60.00	0.00	123.69	3,255.08		56.20
60.00	60.00	0.00	123.69	3,263.67		56.00
60.00	60.00	0.00	123.69	3,171.62	3,174.89	709.00
60.00	60.00	0.00	123.69	3,179.77		708.90
60.00	60.00	0.00	123.69	3,179.77		708.80
60.00	60.00	0.00	123.69	3,179.77		708.70
60.00	60.00	0.00	123.69	3,163.51		708.80
60.00	60.00	0.00	123.69	3,238.04	2,979.36	100.80
60.00	60.00	0.00	123.69	2,566.25		110.70
60.00	60.00	0.00	123.69	3,255.08		100.50
60.00	60.00	0.00	123.69	2,582.32		110.30
60.00	60.00	0.00	123.69	3,255.08		100.30
60.00	60.00	0.00	123.69	3,229.59	3,231.28	985.50
60.00	60.00	0.00	123.69	3,229.59		985.40
60.00	60.00	0.00	123.69	3,229.59		985.30
60.00	60.00	0.00	123.69	3,229.59		985.20
60.00	60.00	0.00	123.69	3,238.04		985.00
60.00	60.00	0.00	123.69	3,123.56	3,131.50	748.60
60.00	60.00	0.00	123.69	3,123.56		748.60
60.00	60.00	0.00	123.69	3,147.41		748.20
60.00	60.00	0.00	123.69	3,131.47		748.30
60.00	60.00	0.00	123.69	3,131.47		748.20
60.00	60.00	0.00	123.69	3,123.56	3,120.43	446.00
60.00	60.00	0.00	123.69	3,107.87		446.10
60.00	60.00	0.00	123.69	3,115.70		445.90
60.00	60.00	0.00	123.69	3,123.56		445.70
60.00	60.00	0.00	123.69	3,131.47		445.60
60.00	60.00	0.00	123.69	3,139.42	3,142.62	699.90
60.00	60.00	0.00	123.69	3,139.42		699.80
60.00	60.00	0.00	123.69	3,139.42		699.70
60.00	60.00	0.00	123.69	3,147.41		699.60
60.00	60.00	0.00	123.69	3,147.41		699.50
60.00	60.00	0.00	123.69	3,204.49	3,214.50	218.10
60.00	60.00	0.00	123.69	3,204.49		218.00
60.00	60.00	0.00	123.69	3,221.18		217.80
60.00	60.00	0.00	123.69	3,221.18		217.70
60.00	60.00	0.00	123.69	3,221.18		217.60
60.00	60.00	0.00	123.69	3,155.44	3,145.82	955.80
60.00	60.00	0.00	123.69	3,147.41		955.80
60.00	60.00	0.00	123.69	3,147.41		955.70
60.00	60.00	0.00	123.69	3,139.42		955.80

60.00	60.00	0.00	123.69	3,139.42		955.70
60.00	60.00	0.00	123.69	1,787.47		826.50
60.00	60.00	0.00	123.69	1,795.26		826.20
60.00	60.00	0.00	123.69	1,792.65	1,793.18	826.20
60.00	60.00	0.00	123.69	1,792.65		826.10
60.00	60.00	0.00	123.69	1,797.87		825.80
60.00	60.00	0.00	123.69	3,163.51		162.20
60.00	60.00	0.00	123.69	3,163.51		162.10
60.00	60.00	0.00	123.69	3,155.44	3,163.52	162.10
60.00	60.00	0.00	123.69	3,171.62		161.90
60.00	60.00	0.00	123.69	3,163.51		161.90
60.00	60.00	0.00	123.69	2,876.59		917.60
60.00	60.00	0.00	123.69	2,883.29		917.40
60.00	60.00	0.00	123.69	2,890.03	2,879.29	917.20
60.00	60.00	0.00	123.69	2,863.27		917.50
60.00	60.00	0.00	123.69	2,883.29		917.10
60.00	60.00	0.00	123.69	3,031.70		494.10
60.00	60.00	0.00	123.69	3,024.28		494.10
60.00	60.00	0.00	123.69	3,024.28	3,025.77	494.00
60.00	60.00	0.00	123.69	3,024.28		493.90
60.00	60.00	0.00	123.69	3,024.28		493.80
60.00	60.00	0.00	123.69	3,046.63		324.70
60.00	60.00	0.00	123.69	3,046.63		324.60
60.00	60.00	0.00	123.69	3,039.14	3,045.13	324.60
60.00	60.00	0.00	123.69	3,046.63		324.40
60.00	60.00	0.00	123.69	3,046.63		324.30
60.00	60.00	0.00	123.69	3,084.62		395.20
60.00	60.00	0.00	123.69	3,084.62		395.10
60.00	60.00	0.00	123.69	3,084.62	3,084.62	395.00
60.00	60.00	0.00	123.69	3,084.62		394.90
60.00	60.00	0.00	123.69	3,084.62		394.80
60.00	60.00	0.00	123.69	3,076.94		143.80
60.00	60.00	0.00	123.69	3,076.94		143.70
60.00	60.00	0.00	123.69	3,084.62	3,078.48	143.50
60.00	60.00	0.00	123.69	3,076.94		143.60
60.00	60.00	0.00	123.69	3,076.94		143.50
60.00	60.00	0.00	123.69	1,581.75		979.90
60.00	60.00	0.00	123.69	1,508.45		983.60
60.00	60.00	0.00	123.69	1,506.62	1,537.77	983.60
60.00	60.00	0.00	123.69	1,510.30		983.30
60.00	60.00	0.00	123.69	1,581.75		979.60
60.00	60.00	0.00	123.69	2,626.18		564.10
60.00	60.00	0.00	123.69	2,626.18		564.00
60.00	60.00	0.00	123.69	2,631.77	2,629.53	563.80
60.00	60.00	0.00	123.69	2,631.77		563.80
60.00	60.00	0.00	123.69	2,631.77		563.70
60.00	60.00	0.00	123.69	2,626.18		145.80
60.00	60.00	0.00	123.69	2,626.18		145.70
60.00	60.00	0.00	123.69	2,626.18	2,626.19	145.60
60.00	60.00	0.00	123.69	2,620.62		145.60
60.00	60.00	0.00	123.69	2,631.77		145.40
60.00	60.00	0.00	123.69	2,598.60		774.00
60.00	60.00	0.00	123.69	2,609.56		773.70
60.00	60.00	0.00	123.69	2,598.60	2,599.70	773.80
60.00	60.00	0.00	123.69	2,593.15		773.80

60.00	60.00	0.00	123.69	2,598.60		773.60
60.00	60.00	0.00	123.69	2,576.94		204.70
60.00	60.00	0.00	123.69	2,582.32		204.50
60.00	60.00	0.00	123.69	2,576.94	2,580.17	204.50
60.00	60.00	0.00	123.69	2,587.72		204.30
60.00	60.00	0.00	123.69	2,576.94		204.40
60.00	60.00	0.00	123.69	2,550.37		597.40
60.00	60.00	0.00	123.69	2,550.37		597.30
60.00	60.00	0.00	123.69	2,550.37	2,554.62	597.20
60.00	60.00	0.00	123.69	2,550.37		597.20
60.00	60.00	0.00	123.69	2,571.58		596.70
60.00	180.00	0.00	251.00	3,927.98		420.40
60.00	180.00	0.00	251.00	3,946.51		420.00
60.00	180.00	0.00	251.00	3,927.98	3,936.64	420.20
60.00	180.00	0.00	251.00	3,952.72		419.80
60.00	180.00	0.00	251.00	3,927.98		420.10
60.00	180.00	0.00	251.00	3,757.46		229.60
60.00	180.00	0.00	251.00	3,774.41		229.20
60.00	180.00	0.00	251.00	3,768.74	3,760.86	229.20
60.00	180.00	0.00	251.00	3,746.24		229.50
60.00	180.00	0.00	251.00	3,757.46		229.20
60.00	180.00	0.00	251.00	2,207.55		313.70
60.00	180.00	0.00	251.00	2,207.55		313.60
60.00	180.00	0.00	251.00	2,205.61	2,207.16	313.60
60.00	180.00	0.00	251.00	2,209.49		313.30
60.00	180.00	0.00	251.00	2,205.61		313.40
60.00	180.00	0.00	251.00	1,096.06		741.40
60.00	180.00	0.00	251.00	1,098.94		740.80
60.00	180.00	0.00	251.00	1,100.87	1,099.52	740.40
60.00	180.00	0.00	251.00	1,099.90		740.60
60.00	180.00	0.00	251.00	1,101.84		740.20
60.00	180.00	0.00	251.00	1,512.95		558.80
60.00	180.00	0.00	251.00	1,514.77		558.60
60.00	180.00	0.00	251.00	1,516.60	1,515.87	558.40
60.00	180.00	0.00	251.00	1,517.52		558.30
60.00	180.00	0.00	251.00	1,517.52		558.30
60.00	180.00	0.00	251.00	1,634.10		426.60
60.00	180.00	0.00	251.00	1,656.75		424.50
60.00	180.00	0.00	251.00	1,642.66	1,650.10	425.80
60.00	180.00	0.00	251.00	1,645.89		425.50
60.00	180.00	0.00	251.00	1,671.09		423.20
60.00	180.00	0.00	251,00	1291,14		354,40
60.00	180.00	0.00	251,00	1288,49		354,80
60.00	180.00	0.00	251,00	1392,11	1340,49	340,30
60.00	180.00	0.00	251,00	1339,37		347,40
60.00	180.00	0.00	251,00	1391,34		340,40
60.00	180.00	0.00	251,00	1391,34		262,90
60.00	180.00	0.00	251,00	1393,66		262,60
60.00	180.00	0.00	251,00	1392,11	1392,58	262,80
60.00	180.00	0.00	251,00	1394,43		262,50
60.00	180.00	0.00	251,00	1391,34		262,90
60.00	180.00	0.00	251.00	2,773.46		374.90
60.00	180.00	0.00	251.00	2,773.46		374.90
60.00	180.00	0.00	251.00	2,773.46	2,773.46	374.90

60.00	180.00	0.00	251.00	2,773.46		374.90
60.00	180.00	0.00	251.00	2,773.46		374.90
60.00	180.00	0.00	251.00	2,617.29		665.50
60.00	180.00	0.00	251.00	2,512.49		665.50
60.00	180.00	0.00	251.00	2,512.49	2,533.45	665.50
60.00	180.00	0.00	251.00	2,512.49		665.50
60.00	180.00	0.00	251.00	2,512.49		665.50
60.00	180.00	0.00	251.00	2,324.06		903.80
60.00	180.00	0.00	251.00	2,324.06		903.80
60.00	180.00	0.00	251.00	2,324.06	2,311.49	903.80
60.00	180.00	0.00	251.00	2,324.06		903.80
60.00	180.00	0.00	251.00	2,261.24		906.80
60.00	180.00	0.00	251.00	1,317.57		795.10
60.00	180.00	0.00	251.00	1,317.57		795.10
60.00	180.00	0.00	251.00	1,317.57	1,317.57	795.10
60.00	180.00	0.00	251.00	1,317.57		795.10
60.00	180.00	0.00	251.00	1,317.57		795.10
60.00	180.00	0.00	251.00	1,237.66		538.40
60.00	180.00	0.00	251.00	1,237.66		538.40
60.00	180.00	0.00	251.00	1,237.66	1,237.66	538.40
60.00	180.00	0.00	251.00	1,237.66		538.40
60.00	180.00	0.00	251.00	1,237.66		538.40
60.00	180.00	0.00	251.00	2,134.34		341.30
60.00	180.00	0.00	251.00	2,134.34		341.30
60.00	180.00	0.00	251.00	2,152.64	2,145.32	340.30
60.00	180.00	0.00	251.00	2,152.64		340.30
60.00	180.00	0.00	251.00	2,152.64		340.30
60.00	180.00	0.00	251.00	1,498.50		257.50
60.00	180.00	0.00	251.00	1,472.13		257.50
60.00	180.00	0.00	251.00	1,438.38	1,457.16	264.50
60.00	180.00	0.00	251.00	1,438.38		260.50
60.00	180.00	0.00	251.00	1,438.38		260.50
60.00	180.00	0.00	251.00	1,479.07		917.30
60.00	180.00	0.00	251.00	1,479.07		917.30
60.00	180.00	0.00	251.00	1,479.07	1,433.98	917.30
60.00	180.00	0.00	251.00	1,366.35		931.30
60.00	180.00	0.00	251.00	1,366.35		931.30
60.00	180.00	0.00	251.00	2,868.55		949.00
60.00	180.00	0.00	251.00	2,868.55		949.00
60.00	180.00	0.00	251.00	2,839.34	2,862.05	949.90
60.00	180.00	0.00	251.00	2,865.27		949.10
60.00	180.00	0.00	251.00	2,868.55		949.00
60.00	180.00	0.00	251.00	933.08		340.30
60.00	180.00	0.00	251.00	933.08		340.30
60.00	180.00	0.00	251.00	922.79	920.36	343.30
60.00	180.00	0.00	251.00	922.79		343.30
60.00	180.00	0.00	251.00	890.06		353.30
60.00	180.00	0.00	251.00	2,871.83		968.90
60.00	180.00	0.00	251.00	2,807.58		970.90
60.00	180.00	0.00	251.00	2,807.58	2,846.28	970.90
60.00	180.00	0.00	251.00	2,839.34		969.90
60.00	180.00	0.00	251.00	2,905.07		967.90
60.00	180.00	0.00	251.00	3,031.38		589.70
60.00	180.00	0.00	251.00	3,031.38		589.70

60.00	180.00	0.00	251.00	3,031.38	3,038.79	589.70
60.00	180.00	0.00	251.00	3,031.38		589.70
60.00	180.00	0.00	251.00	3,068.44		588.70
60.00	180.00	0.00	251.00	2,801.32	2,801.32	919.50
60.00	180.00	0.00	251.00	2,801.32		919.50
60.00	180.00	0.00	251.00	2,801.32		919.50
60.00	180.00	0.00	251.00	2,801.32		919.50
60.00	180.00	0.00	251.00	2,801.32		919.50
60.00	180.00	0.00	251.00	3,068.44	3,098.82	703.00
60.00	180.00	0.00	251.00	3,106.41		702.00
60.00	180.00	0.00	251.00	3,106.41		702.00
60.00	180.00	0.00	251.00	3,106.41		702.00
60.00	180.00	0.00	251.00	3,106.41		702.00
60.00	180.00	0.00	251.00	2,852.25	2,852.25	699.10
60.00	180.00	0.00	251.00	2,852.25		699.10
60.00	180.00	0.00	251.00	2,852.25		699.10
60.00	180.00	0.00	251.00	2,852.25		699.10
60.00	180.00	0.00	251.00	2,852.25		699.10
60.00	180.00	0.00	251.00	2,592.95	2,818.04	898.60
60.00	180.00	0.00	251.00	2,878.42		889.00
60.00	180.00	0.00	251.00	2,881.72		888.90
60.00	180.00	0.00	251.00	2,868.55		889.30
60.00	180.00	0.00	251.00	2,868.55		889.30
60.00	180.00	0.00	251.00	2,522.59	2,528.19	838.90
60.00	180.00	0.00	251.00	2,530.22		838.60
60.00	180.00	0.00	251.00	2,522.59		838.90
60.00	180.00	0.00	251.00	2,532.78		838.50
60.00	180.00	0.00	251.00	2,532.78		838.50
60.00	180.00	0.00	251.00	2,939.09	2,949.47	1,049.00
60.00	180.00	0.00	251.00	2,945.99		1,048.80
60.00	180.00	0.00	251.00	2,942.53		1,048.90
60.00	180.00	0.00	251.00	2,959.88		1,048.40
60.00	180.00	0.00	251.00	2,959.88		1,048.40
60.00	180.00	0.00	251,00	2076,08	2081,25	713,70
60.00	180.00	0.00	251,00	2081,24		713,40
60.00	180.00	0.00	251,00	2082,97		713,30
60.00	180.00	0.00	251,00	2082,97		713,30
60.00	180.00	0.00	251,00	2082,97		713,30
60.00	180.00	0.00	251,00	1391,34	1392,58	262,90
60.00	180.00	0.00	251,00	1393,66		262,60
60.00	180.00	0.00	251,00	1392,11		262,80
60.00	180.00	0.00	251,00	1394,43		262,50
60.00	180.00	0.00	251,00	1391,34		262,90
100.00	100.00	0.00	206.16	2,831.80	2,963.52	478.70
100.00	100.00	0.00	206.16	2,996.44		478.70
100.00	100.00	0.00	206.16	2,996.44		478.70
100.00	100.00	0.00	206.16	2,996.44		478.70
100.00	100.00	0.00	206.16	2,996.44		478.70
100.00	100.00	0.00	206.16	3,221.18	3,350.02	821.60
100.00	100.00	0.00	206.16	3,221.18		821.60
100.00	100.00	0.00	206.16	3,435.92		821.60
100.00	100.00	0.00	206.16	3,435.92		821.60
100.00	100.00	0.00	206.16	3,435.92		822.60
100.00	100.00	0.00	206.16	2,673.87		231.30

100.00	100.00	0.00	206.16	2,573.72		234.30
100.00	100.00	0.00	206.16	2,673.87	2,653.84	231.30
100.00	100.00	0.00	206.16	2,673.87		231.30
100.00	100.00	0.00	206.16	2,673.87		231.30
100.00	100.00	0.00	206.16	2,626.18		330.90
100.00	100.00	0.00	206.16	2,626.18		330.90
100.00	100.00	0.00	206.16	2,626.18	2,626.18	330.90
100.00	100.00	0.00	206.16	2,626.18		330.90
100.00	100.00	0.00	206.16	2,626.18		330.90
100.00	100.00	0.00	206.16	2,843.52		891.30
100.00	100.00	0.00	206.16	2,730.53		894.30
100.00	100.00	0.00	206.16	2,626.18	2,793.36	893.30
100.00	100.00	0.00	206.16	2,883.29		890.30
100.00	100.00	0.00	206.16	2,883.29		890.30
100.00	100.00	0.00	206.16	2,867.25		552.10
100.00	100.00	0.00	206.16	2,867.25		552.10
100.00	100.00	0.00	206.16	2,867.25	2,867.25	552.10
100.00	100.00	0.00	206.16	2,867.25		552.10
100.00	100.00	0.00	206.16	2,867.25		552.10
100.00	100.00	0.00	206.16	2,915.92		644.70
100.00	100.00	0.00	206.16	2,915.92		644.70
100.00	100.00	0.00	206.16	2,915.92	2,915.92	644.70
100.00	100.00	0.00	206.16	2,915.92		644.70
100.00	100.00	0.00	206.16	2,915.92		644.70
100.00	100.00	0.00	206.16	2,460.09		975.80
100.00	100.00	0.00	206.16	2,460.09		975.80
100.00	100.00	0.00	206.16	2,460.09	2,460.09	975.80
100.00	100.00	0.00	206.16	2,460.09		975.80
100.00	100.00	0.00	206.16	2,460.09		975.80
100.00	100.00	0.00	206.16	2,723.32		151.90
100.00	100.00	0.00	206.16	2,723.32		151.90
100.00	100.00	0.00	206.16	2,723.32	2,745.80	151.90
100.00	100.00	0.00	206.16	2,723.32		151.90
100.00	100.00	0.00	206.16	2,835.70		148.90
100.00	100.00	0.00	206.16	2,564.12		603.50
100.00	100.00	0.00	206.16	2,564.12		603.50
100.00	100.00	0.00	206.16	2,564.12	2,564.12	603.50
100.00	100.00	0.00	206.16	2,564.12		603.50
100.00	100.00	0.00	206.16	2,564.12		603.50
100.00	100.00	0.00	206.16	2,375.06		946.50
100.00	100.00	0.00	206.16	2,375.06		946.50
100.00	100.00	0.00	206.16	2,375.06	2,375.06	946.50
100.00	100.00	0.00	206.16	2,375.06		946.50
100.00	100.00	0.00	206.16	2,375.06		946.50
100.00	100.00	0.00	206.16	2,548.27		633.20
100.00	100.00	0.00	206.16	2,548.27		633.20
100.00	100.00	0.00	206.16	2,548.27	2,561.03	633.20
100.00	100.00	0.00	206.16	2,580.17		632.20
100.00	100.00	0.00	206.16	2,580.17		632.20
100.00	100.00	0.00	206.16	2,570.51		85.10
100.00	100.00	0.00	206.16	2,570.51		85.10
100.00	100.00	0.00	206.16	2,570.51	2,583.50	85.10
100.00	100.00	0.00	206.16	2,602.97		84.10
100.00	100.00	0.00	206.16	2,602.97		84.10
100.00	100.00	0.00	206.16	3,031.70		785.70

100.00	100.00	0.00	206.16	3,031.70		785.70
100.00	100.00	0.00	206.16	3,031.70	3,031.70	785.70
100.00	100.00	0.00	206.16	3,031.70		785.70
100.00	100.00	0.00	206.16	3,031.70		785.70
100.00	100.00	0.00	206.16	2,483.80		725.10
100.00	100.00	0.00	206.16	2,483.80		725.10
100.00	100.00	0.00	206.16	2,483.80	2,483.80	725.10
100.00	100.00	0.00	206.16	2,483.80		725.10
100.00	100.00	0.00	206.16	2,483.80		725.10
100.00	100.00	0.00	206.16	2,855.34		479.20
100.00	100.00	0.00	206.16	2,855.34		479.20
100.00	100.00	0.00	206.16	2,855.34	2,855.34	479.20
100.00	100.00	0.00	206.16	2,855.34		479.20
100.00	100.00	0.00	206.16	2,855.34		479.20
100.00	100.00	0.00	206.16	2,871.24		297.80
100.00	100.00	0.00	206.16	2,871.24		297.80
100.00	100.00	0.00	206.16	2,871.24	2,871.24	297.80
100.00	100.00	0.00	206.16	2,871.24		297.80
100.00	100.00	0.00	206.16	2,871.24		297.80
100.00	100.00	0.00	206.16	1,702.36		1,088.10
100.00	100.00	0.00	206.16	1,702.36		1,088.10
100.00	100.00	0.00	206.16	1,702.36	1,708.03	1,088.10
100.00	100.00	0.00	206.16	1,716.53		1,087.10
100.00	100.00	0.00	206.16	1,716.53		1,087.10
100.00	100.00	0.00	206.16	2,138.54		586.70
100.00	100.00	0.00	206.16	2,140.76		586.60
100.00	100.00	0.00	206.16	2,142.99	2,143.44	586.50
100.00	100.00	0.00	206.16	2,145.22		586.40
100.00	100.00	0.00	206.16	2,149.69		586.20
100.00	100.00	0.00	206,16	2745,08		451,80
100.00	100.00	0.00	206,16	2748,74		451,70
100.00	100.00	0.00	206,16	2752,41	2750,21	451,60
100.00	100.00	0.00	206,16	2748,74		451,70
100.00	100.00	0.00	206,16	2756,09		451,50
100.00	100.00	0.00	206,16	2763,48		332,90
100.00	100.00	0.00	206,16	2763,48		332,90
100.00	100.00	0.00	206,16	2767,18	2767,19	332,80
100.00	100.00	0.00	206,16	2770,90		332,70
100.00	100.00	0.00	206,16	2770,90		332,70
100.00	100.00	0.00	206,16	2576,94		746,90
100.00	100.00	0.00	206,16	2580,17		746,80
100.00	100.00	0.00	206,16	2583,40	2584,06	746,70
100.00	100.00	0.00	206,16	2583,40		746,70
100.00	100.00	0.00	206,16	2596,41		746,30
100.00	100.00	0.00	206,16	2326,81		514,70
100.00	100.00	0.00	206,16	2321,57		514,90
100.00	100.00	0.00	206,16	2334,71	2333,16	514,40
100.00	100.00	0.00	206,16	2342,67		514,10
100.00	100.00	0.00	206,16	2340,01		514,20
100,0	100,0	0,0	206,16	1416,87		313,40
100,0	100,0	0,0	206,16	1677,42		290,80
100,0	100,0	0,0	206,16	1691,18	1631,08	289,80
100,0	100,0	0,0	206,16	1687,03		290,10
100,0	100,0	0,0	206,16	1682,90		290,40
100.00	100.00	0.00	206,16	1521,44		463,80

100.00	100.00	0.00	206,16	1519,20	1520,77	464,00
100.00	100.00	0.00	206,16	1518,08		464,10
100.00	100.00	0.00	206,16	1521,44		463,80
100.00	100.00	0.00	206,16	1523,69		463,60
100.00	100.00	0.00	206,16	2863,27	2873,66	184,00
100.00	100.00	0.00	206,16	2875,25		183,70
100.00	100.00	0.00	206,16	2879,26		183,60
100.00	100.00	0.00	206,16	2871,24		183,80
100.00	100.00	0.00	206,16	2879,26		183,60
100.00	100.00	0.00	206,16	1821,16	1823,42	895,40
100.00	100.00	0.00	206,16	1821,16		895,40
100.00	100.00	0.00	206,16	1822,77		895,30
100.00	100.00	0.00	206,16	1826,00		895,10
100.00	100.00	0.00	206,16	1826,00		895,10
100.00	100.00	0.00	206,16	2763,48	2727,28	336,10
100.00	100.00	0.00	206,16	2643,02		339,50
100.00	100.00	0.00	206,16	2643,02		339,50
100.00	100.00	0.00	206,16	2789,65		335,40
100.00	100.00	0.00	206,16	2797,22		335,20
120.00	120.00	0.00	247.39	2,966.26	3,033.24	883.30
120.00	120.00	0.00	247.39	2,966.26		883.30
120.00	120.00	0.00	247.39	3,002.26		883.30
120.00	120.00	0.00	247.39	3,115.70		883.30
120.00	120.00	0.00	247.39	3,115.70		883.30
120.00	120.00	0.00	247.39	2,879.93	2,935.84	1,058.40
120.00	120.00	0.00	247.39	2,846.79		1,059.40
120.00	120.00	0.00	247.39	2,984.15		1,059.40
120.00	120.00	0.00	247.39	2,984.15		1,059.40
120.00	120.00	0.00	247.39	2,984.15		1,059.40
120.00	120.00	0.00	247,39	2856,66	2867,94	490,70
120.00	120.00	0.00	247,39	2876,59		490,10
120.00	120.00	0.00	247,39	2859,96		490,60
120.00	120.00	0.00	247,39	2869,91		490,30
120.00	120.00	0.00	247,39	2876,59		490,10
120.00	120.00	0.00	247,39	2587,72	2583,97	1016,80
120.00	120.00	0.00	247,39	2590,43		1016,70
120.00	120.00	0.00	247,39	2587,72		1016,80
120.00	120.00	0.00	247,39	2587,72		1016,80
120.00	120.00	0.00	247,39	2566,25		1017,60
120.00	120.00	0.00	247,39	1386,69	1406,34	472,50
120.00	120.00	0.00	247,39	1385,92		472,60
120.00	120.00	0.00	247,39	1484,91		460,70
120.00	120.00	0.00	247,39	1387,47		472,40
120.00	120.00	0.00	247,39	1386,69		472,50
120.00	120.00	0.00	247,39	2920,74	2922,12	276,70
120.00	120.00	0.00	247,39	2924,19		276,60
120.00	120.00	0.00	247,39	2917,29		276,80
120.00	120.00	0.00	247,39	2920,74		276,70
120.00	120.00	0.00	247,39	2927,65		276,50
120.00	120.00	0.00	247,39	1510,30	1512,51	640,10
120.00	120.00	0.00	247,39	1510,30		640,10
120.00	120.00	0.00	247,39	1513,99		639,70
120.00	120.00	0.00	247,39	1513,99		639,70
120.00	120.00	0.00	247,39	1513,99		639,70
120.00	120.00	0.00	247,39	2255,12		1073,10

120.00	120.00	0.00	247,39	2255,12		1073,10
120.00	120.00	0.00	247,39	2253,06	2255,94	1073,20
120.00	120.00	0.00	247,39	2257,17		1073,00
120.00	120.00	0.00	247,39	2259,24		1072,90
120.00	120.00	0.00	247,39	1932,71		440,50
120.00	120.00	0.00	247,39	1937,25		440,20
120.00	120.00	0.00	247,39	1941,81	1938,47	439,90
120.00	120.00	0.00	247,39	1940,29		440,00
120.00	120.00	0.00	247,39	1940,29		440,00
120.00	120.00	0.00	247,39	3147,41		114,90
120.00	120.00	0.00	247,39	3139,42		115,10
120.00	120.00	0.00	247,39	3155,44	3152,24	114,70
120.00	120.00	0.00	247,39	3159,47		114,60
120.00	120.00	0.00	247,39	3159,47		114,60
120.00	120.00	0.00	247,39	2054,70		945,90
120.00	120.00	0.00	247,39	2051,30		946,10
120.00	120.00	0.00	247,39	2054,70	2054,36	945,90
120.00	120.00	0.00	247,39	2054,70		945,90
120.00	120.00	0.00	247,39	2056,41		945,80
120.00	120.00	0.00	247.39	1,525.19		1,019.20
120.00	120.00	0.00	247.39	1,526.13		1,019.10
120.00	120.00	0.00	247.39	1,528.02	1,527.08	1,018.90
120.00	120.00	0.00	247.39	1,528.96		1,018.80
120.00	120.00	0.00	247.39	1,527.08		1,019.00
120.00	120.00	0.00	247.39	2,519.21		367.70
120.00	120.00	0.00	247.39	2,532.10		367.20
120.00	120.00	0.00	247.39	2,017.83	2,320.77	392.10
120.00	120.00	0.00	247.39	2,521.78		367.60
120.00	120.00	0.00	247.39	2,012.91		392.40
120.00	120.00	0.00	247,39	2202,91		1048,80
120.00	120.00	0.00	247,39	2208,81		1048,50
120.00	120.00	0.00	247,39	2208,81	2207,23	1048,50
120.00	120.00	0.00	247,39	2208,81		1048,50
120.00	120.00	0.00	247,39	2206,84		1048,60
120.00	120.00	0.00	247,39	2850,07		274,10
120.00	120.00	0.00	247,39	2850,07		274,10
120.00	120.00	0.00	247,39	2863,27	2857,33	273,70
120.00	120.00	0.00	247,39	2856,66		273,90
120.00	120.00	0.00	247,39	2866,59		273,60
120.00	120.00	0.00	247,39	1779,76		414,10
120.00	120.00	0.00	247,39	1781,04		414,00
120.00	120.00	0.00	247,39	1782,32	1781,30	413,90
120.00	120.00	0.00	247,39	1779,76		414,10
120.00	120.00	0.00	247,39	1783,61		413,80
120.00	120.00	0.00	247.39	2,259.24		1,001.90
120.00	120.00	0.00	247.39	2,259.24		1,001.90
120.00	120.00	0.00	247.39	2,265.44	2,265.87	1,001.60
120.00	120.00	0.00	247.39	2,271.68		1,001.30
120.00	120.00	0.00	247.39	2,273.77		1,001.20
120.00	120.00	0.00	247.39	1,665.90		199.40
120.00	120.00	0.00	247.39	2,187.32		164.00
120.00	120.00	0.00	247.39	1,665.90	1,772.44	199.40
120.00	120.00	0.00	247.39	1,670.40		199.00
120.00	120.00	0.00	247.39	1,672.66		198.80
120.00	120.00	0.00	247,39	2683,15		769,50

120.00	120.00	0.00	247,39	2686,06	2689,58	769,40
120.00	120.00	0.00	247,39	2688,98		769,30
120.00	120.00	0.00	247,39	2691,91		769,20
120.00	120.00	0.00	247,39	2697,78		769,00
120.00	120.00	0.00	247,39	1665,90	1667,47	369,50
120.00	120.00	0.00	247,39	1665,90		369,50
120.00	120.00	0.00	247,39	1667,02		369,40
120.00	120.00	0.00	247,39	1669,27		369,20
120.00	120.00	0.00	247,39	1669,27		369,20
120.00	120.00	0.00	247,39	2486,29	2001,42	1053,20
120.00	120.00	0.00	247,39	1876,98		1085,50
120.00	120.00	0.00	247,39	1881,26		1085,20
120.00	120.00	0.00	247,39	1878,41		1085,40
120.00	120.00	0.00	247,39	1884,13		1085,00
120.00	120.00	0.00	247.39	1,788.77	2,071.02	1,090.50
120.00	120.00	0.00	247.39	2,493.81		1,051.40
120.00	120.00	0.00	247.39	1,787.47		1,090.60
120.00	120.00	0.00	247.39	2,498.85		1,051.20
120.00	120.00	0.00	247.39	1,786.18		1,090.70
120.00	120.00	0.00	247.39	1,772.11	1,776.95	248.50
120.00	120.00	0.00	247.39	1,778.48		248.00
120.00	120.00	0.00	247.39	1,775.92		248.20
120.00	120.00	0.00	247.39	1,783.61		247.60
120.00	120.00	0.00	247.39	1,774.65		248.30
120.00	120.00	0.00	247,39	2677,34	2700,54	476,60
120.00	120.00	0.00	247,39	2767,18		473,60
120.00	120.00	0.00	247,39	2683,15		476,40
120.00	120.00	0.00	247,39	2686,06		476,30
120.00	120.00	0.00	247,39	2688,98		476,20
120.00	120.00	0.00	247,39	2098,27	2100,06	1068,60
120.00	120.00	0.00	247,39	2098,27		1068,60
120.00	120.00	0.00	247,39	2100,05		1068,50
120.00	120.00	0.00	247,39	2100,05		1068,50
120.00	120.00	0.00	247,39	2103,63		1068,30
120.00	120.00	0.00	247,39	1295,22	1296,44	666,70
120.00	120.00	0.00	247,39	1296,57		666,50
120.00	120.00	0.00	247,39	1297,25		666,40
120.00	120.00	0.00	247,39	1295,89		666,60
120.00	120.00	0.00	247,39	1297,25		666,40
120.00	120.00	0.00	247.39	1,556.87	1,766.58	206.20
120.00	120.00	0.00	247.39	1,975.93		172.50
120.00	120.00	0.00	247.39	2,185.39		160.50
120.00	120.00	0.00	247.39	1,557.85		206.10
120.00	120.00	0.00	247.39	1,556.87		206.20
120.00	120.00	0.00	247.39	2,019.48	2,050.75	349.20
120.00	120.00	0.00	247.39	2,175.78		340.40
120.00	120.00	0.00	247.39	2,011.27		349.70
120.00	120.00	0.00	247.39	2,024.44		348.90
120.00	120.00	0.00	247.39	2,022.78		349.00
60.00	180.00	0.00	251.00	3,575.47	3,557.25	290.70
60.00	180.00	0.00	251.00	3,550.18		291.10
60.00	180.00	0.00	251.00	3,555.21		290.90
60.00	180.00	0.00	251.00	3,550.18		290.90
60.00	180.00	0.00	251.00	3,555.21		290.70
60.00	180.00	0.00	251.00	2,439.24		506.50

60.00	180.00	0.00	251.00	2,441.61	2,440.67	506.30
60.00	180.00	0.00	251.00	2,441.61		506.20
60.00	180.00	0.00	251.00	2,439.24		506.30
60.00	180.00	0.00	251.00	2,441.61		506.10
60.00	180.00	0.00	251.00	3,410.30	3,424.28	740.40
60.00	180.00	0.00	251.00	3,428.93		739.90
60.00	180.00	0.00	251.00	3,419.59		740.10
60.00	180.00	0.00	251.00	3,433.63		739.70
60.00	180.00	0.00	251.00	3,428.93		739.70
60.00	180.00	0.00	251.00	3,486.08	3,492.92	912.80
60.00	180.00	0.00	251.00	3,500.67		912.40
60.00	180.00	0.00	251.00	3,471.62		912.90
60.00	180.00	0.00	251.00	3,505.56		912.20
60.00	180.00	0.00	251.00	3,500.67		912.10
60.00	180.00	0.00	251.00	3,268.20	3,267.36	839.80
60.00	180.00	0.00	251.00	3,263.95		839.80
60.00	180.00	0.00	251.00	3,263.95		839.80
60.00	180.00	0.00	251.00	3,272.46		839.50
60.00	180.00	0.00	251.00	3,268.20		839.50
60.00	180.00	0.00	251.00	3,820.37	3,819.20	417.60
60.00	180.00	0.00	251.00	3,820.37		417.50
60.00	180.00	0.00	251.00	3,820.37		417.50
60.00	180.00	0.00	251.00	3,814.56		417.50
60.00	180.00	0.00	251.00	3,820.37		417.30
60.00	180.00	0.00	251.00	3,873.43	3,863.90	596.00
60.00	180.00	0.00	251.00	3,873.43		596.00
60.00	180.00	0.00	251.00	3,861.51		596.10
60.00	180.00	0.00	251.00	3,855.58		596.10
60.00	180.00	0.00	251.00	3,855.58		596.00
60.00	180.00	0.00	251.00	3,691.15	3,682.49	785.20
60.00	180.00	0.00	251.00	3,680.32		785.30
60.00	180.00	0.00	251.00	3,685.73		785.10
60.00	180.00	0.00	251.00	3,680.32		785.10
60.00	180.00	0.00	251.00	3,674.93		785.10
60.00	180.00	0.00	251.00	3,606.29	3,606.30	423.00
60.00	180.00	0.00	251.00	3,611.48		422.80
60.00	180.00	0.00	251.00	3,606.29		422.80
60.00	180.00	0.00	251.00	3,611.48		422.70
60.00	180.00	0.00	251.00	3,595.96		422.80
60.00	180.00	0.00	251.00	3,820.37	3,839.11	981.20
60.00	180.00	0.00	251.00	3,832.03		981.00
60.00	180.00	0.00	251.00	3,861.51		980.40
60.00	180.00	0.00	251.00	3,837.89		980.70
60.00	180.00	0.00	251.00	3,843.77		980.50
60.00	180.00	0.00	251.00	1,716.81	1,716.58	738.40
60.00	180.00	0.00	251.00	1,714.47		738.50
60.00	180.00	0.00	251.00	1,717.99		738.20
60.00	180.00	0.00	251.00	1,715.64		738.30
60.00	180.00	0.00	251.00	1,717.99		738.00
60.00	180.00	0.00	251.00	1,956.34	1,944.18	1,021.30
60.00	180.00	0.00	251.00	2,029.09		1,016.60
60.00	180.00	0.00	251.00	1,813.57		1,031.20
60.00	180.00	0.00	251.00	1,968.61		1,020.20
60.00	180.00	0.00	251.00	1,953.29		1,021.20
60.00	180.00	0.00	251.00	2,035.67		535.00

60.00	180.00	0.00	251.00	2,035.67	2,121.68	534.90
60.00	180.00	0.00	251.00	2,037.32		534.80
60.00	180.00	0.00	251.00	2,460.76		513.50
60.00	180.00	0.00	251.00	2,038.98		534.50
60.00	180.00	0.00	251.00	1,628.80	1,629.43	1,081.60
60.00	180.00	0.00	251.00	1,629.86		1,081.40
60.00	180.00	0.00	251.00	1,627.74		1,081.50
60.00	180.00	0.00	251.00	1,630.92		1,081.10
60.00	180.00	0.00	251.00	1,629.86		1,081.10
60.00	180.00	0.00	251.00	1,976.36	1,976.67	203.40
60.00	180.00	0.00	251.00	1,976.36		203.30
60.00	180.00	0.00	251.00	1,976.36		203.20
60.00	180.00	0.00	251.00	1,977.92		203.00
60.00	180.00	0.00	251.00	1,976.36		203.00
60.00	180.00	0.00	251.00	3,565.31	3,579.57	560.90
60.00	180.00	0.00	251.00	3,585.69		560.40
60.00	180.00	0.00	251.00	3,575.47		560.50
60.00	180.00	0.00	251.00	3,580.57		560.30
60.00	180.00	0.00	251.00	3,590.82		560.00
60.00	180.00	0.00	251.00	3,627.14	3,638.72	826.50
60.00	180.00	0.00	251.00	3,642.93		826.20
60.00	180.00	0.00	251.00	3,637.65		826.20
60.00	180.00	0.00	251.00	3,637.65		826.10
60.00	180.00	0.00	251.00	3,648.23		825.80
60.00	180.00	0.00	251.00	3,333.31	3,326.25	1,057.90
60.00	180.00	0.00	251.00	3,315.69		1,058.20
60.00	180.00	0.00	251.00	3,324.48		1,058.00
60.00	180.00	0.00	251.00	3,328.89		1,057.80
60.00	180.00	0.00	251.00	3,328.89		1,057.60
60.00	180.00	0.00	251.00	3,560.26	3,565.34	461.90
60.00	180.00	0.00	251.00	3,570.38		461.70
60.00	180.00	0.00	251.00	3,570.38		461.60
60.00	180.00	0.00	251.00	3,550.18		461.90
60.00	180.00	0.00	251.00	3,575.47		461.30
60.00	180.00	0.00	251.00	2,418.09	2,414.84	1,053.20
60.00	180.00	0.00	251.00	2,415.77		1,053.20
60.00	180.00	0.00	251.00	2,413.44		1,053.20
60.00	180.00	0.00	251.00	2,411.12		1,053.20
60.00	180.00	0.00	251.00	2,415.77		1,052.90
60.00	180.00	0.00	251.00	2,422.76	2,424.64	862.60
60.00	180.00	0.00	251.00	2,420.42		862.60
60.00	180.00	0.00	251.00	2,427.45		862.20
60.00	180.00	0.00	251.00	2,422.76		862.30
60.00	180.00	0.00	251.00	2,429.80		861.90
60.00	180.00	0.00	251.00	2,522.59	2,589.86	370.00
60.00	180.00	0.00	251.00	2,628.25		365.90
60.00	180.00	0.00	251.00	2,631.01		365.70
60.00	180.00	0.00	251.00	2,522.59		369.70
60.00	180.00	0.00	251.00	2,644.87		365.00
60.00	180.00	0.00	251.00	1,864.77	1,867.55	540.10
60.00	180.00	0.00	251.00	1,866.16		539.90
60.00	180.00	0.00	251.00	1,870.33		539.60
60.00	180.00	0.00	251.00	1,867.54		539.70
60.00	180.00	0.00	251.00	1,868.94		539.50
60.00	180.00	0.00	251.00	2,381.39		343.60

60.00	180.00	0.00	251.00	2,372.38	2,382.30	343.90
60.00	180.00	0.00	251.00	2,381.39		343.50
60.00	180.00	0.00	251.00	2,388.18		343.10
60.00	180.00	0.00	251.00	2,388.18		343.00
60.00	180.00	0.00	251.00	2,764.30	2,774.09	888.30
60.00	180.00	0.00	251.00	2,770.40		888.00
60.00	180.00	0.00	251.00	2,782.68		887.50
60.00	180.00	0.00	251.00	2,773.46		887.70
60.00	180.00	0.00	251.00	2,779.60		887.40
60.00	180.00	0.00	251.00	3,481.25	3,477.40	734.00
60.00	180.00	0.00	251.00	3,476.43		734.00
60.00	180.00	0.00	251.00	3,481.25		733.80
60.00	180.00	0.00	251.00	3,471.62		733.90
60.00	180.00	0.00	251.00	3,476.43		733.70
60.00	180.00	0.00	251.00	3,247.06	3,247.07	548.50
60.00	180.00	0.00	251.00	3,251.27		548.30
60.00	180.00	0.00	251.00	3,242.87		548.40
60.00	180.00	0.00	251.00	3,247.06		548.20
60.00	180.00	0.00	251.00	3,247.06		548.10
60.00	180.00	0.00	251.00	3,251.27	3,249.59	276.40
60.00	180.00	0.00	251.00	3,247.06		276.40
60.00	180.00	0.00	251.00	3,251.27		276.20
60.00	180.00	0.00	251.00	3,247.06		276.30
60.00	180.00	0.00	251.00	3,251.27		276.10

Channel 8						
(Sensor 8)						
location			Distance	Velocity	Average velocity for sensor 8	Arrival time, millisecond
x8	y8	z8	(mm)	m/s	m/s	t8
120.00	30.00	0.00	92.47	2,944.78	2,944.78	258.70
120.00	30.00	0.00	92.47	2,944.78		258.70
120.00	30.00	0.00	92.47	2,944.78		258.60
120.00	30.00	0.00	92.47	2,944.78		258.50
120.00	30.00	0.00	92.47	2,944.78		258.40
120.00	30.00	0.00	92.47	3,155.84	3,151.55	1,004.90
120.00	30.00	0.00	92.47	3,155.84		1,004.90
120.00	30.00	0.00	92.47	3,145.11		1,004.90
120.00	30.00	0.00	92.47	3,145.11		1,004.80
120.00	30.00	0.00	92.47	3,155.84		1,004.60
120.00	30.00	0.00	92.47	3,155.84	3,155.84	365.40
120.00	30.00	0.00	92.47	3,155.84		365.30
120.00	30.00	0.00	92.47	3,155.84		365.20
120.00	30.00	0.00	92.47	3,155.84		365.10
120.00	30.00	0.00	92.47	3,155.84		365.00
120.00	30.00	0.00	92.47	3,155.84	3,151.56	321.40
120.00	30.00	0.00	92.47	3,155.84		321.30
120.00	30.00	0.00	92.47	3,155.84		321.20
120.00	30.00	0.00	92.47	3,155.84		321.10
120.00	30.00	0.00	92.47	3,134.45		321.20
120.00	30.00	0.00	92.47	3,399.49	3,389.53	299.80
120.00	30.00	0.00	92.47	3,387.04		299.80
120.00	30.00	0.00	92.47	3,387.04		299.70
120.00	30.00	0.00	92.47	3,387.04		299.60
120.00	30.00	0.00	92.47	3,387.04		299.50
120.00	30.00	0.00	92.47	3,233.08	3,239.89	788.10
120.00	30.00	0.00	92.47	3,244.43		788.00
120.00	30.00	0.00	92.47	3,233.08		788.00
120.00	30.00	0.00	92.47	3,244.43		787.80
120.00	30.00	0.00	92.47	3,244.43		787.70
120.00	30.00	0.00	92.47	3,233.08	3,230.85	270.30
120.00	30.00	0.00	92.47	3,233.08		270.20
120.00	30.00	0.00	92.47	3,221.82		270.20
120.00	30.00	0.00	92.47	3,221.82		270.10
120.00	30.00	0.00	92.47	3,244.43		269.80
120.00	30.00	0.00	92.47	3,290.61	3,290.68	704.70
120.00	30.00	0.00	92.47	3,267.36		704.80
120.00	30.00	0.00	92.47	3,314.20		704.30
120.00	30.00	0.00	92.47	3,290.61		704.40
120.00	30.00	0.00	92.47	3,290.61		704.30
120.00	30.00	0.00	92.47	2,283.12	2,271.92	387.40
120.00	30.00	0.00	92.47	2,260.79		387.70
120.00	30.00	0.00	92.47	2,266.33		387.50
120.00	30.00	0.00	92.47	2,277.49		387.20
120.00	30.00	0.00	92.47	2,271.90		387.20
120.00	30.00	0.00	92.47	2,335.01	2,331.48	375.60
120.00	30.00	0.00	92.47	2,335.01		375.50
120.00	30.00	0.00	92.47	2,323.27		375.60
120.00	30.00	0.00	92.47	2,329.12		375.40

120.00	30.00	0.00	92.47	2,335.01		375.30
120.00	30.00	0.00	92.47	1,699.75		504.20
120.00	30.00	0.00	92.47	1,687.34		504.50
120.00	30.00	0.00	92.47	1,687.34	1,691.68	504.40
120.00	30.00	0.00	92.47	1,687.34		504.30
120.00	30.00	0.00	92.47	1,696.63		504.00
120.00	30.00	0.00	92.47	2,277.49		459.40
120.00	30.00	0.00	92.47	2,305.89		458.90
120.00	30.00	0.00	92.47	2,277.49	2,287.69	459.30
120.00	30.00	0.00	92.47	2,283.12		459.10
120.00	30.00	0.00	92.47	2,294.45		458.80
120.00	30.00	0.00	92.47	2,401.72		479.10
120.00	30.00	0.00	92.47	2,389.31		479.20
120.00	30.00	0.00	92.47	2,395.50	2,396.75	479.00
120.00	30.00	0.00	92.47	2,395.50		478.90
120.00	30.00	0.00	92.47	2,401.72		478.80
120.00	30.00	0.00	92.47	3,092.52		573.30
120.00	30.00	0.00	92.47	3,092.52		573.30
120.00	30.00	0.00	92.47	3,102.89	3,094.59	573.10
120.00	30.00	0.00	92.47	3,092.52		573.10
120.00	30.00	0.00	92.47	3,092.52		573.00
120.00	30.00	0.00	92.47	3,041.65		438.00
120.00	30.00	0.00	92.47	3,041.65		437.90
120.00	30.00	0.00	92.47	3,061.80	3,047.69	437.70
120.00	30.00	0.00	92.47	3,051.69		437.70
120.00	30.00	0.00	92.47	3,041.65		437.70
120.00	30.00	0.00	92.47	2,836.39		73.00
120.00	30.00	0.00	92.47	2,827.71		73.00
120.00	30.00	0.00	92.47	2,827.71	2,824.29	72.90
120.00	30.00	0.00	92.47	2,819.09		72.90
120.00	30.00	0.00	92.47	2,810.52		72.90
120.00	30.00	0.00	92.47	2,862.73		368.10
120.00	30.00	0.00	92.47	2,845.11		368.20
120.00	30.00	0.00	92.47	2,845.11	2,846.89	368.10
120.00	30.00	0.00	92.47	2,845.11		368.00
120.00	30.00	0.00	92.47	2,836.39		368.00
120.00	30.00	0.00	92.47	3,123.86		361.30
120.00	30.00	0.00	92.47	3,123.86		361.20
120.00	30.00	0.00	92.47	3,123.86	3,128.11	361.10
120.00	30.00	0.00	92.47	3,123.86		361.00
120.00	30.00	0.00	92.47	3,145.11		360.70
120.00	30.00	0.00	92.47	1,541.10		639.20
120.00	30.00	0.00	92.47	1,538.54		639.20
120.00	30.00	0.00	92.47	1,528.37	1,538.05	639.50
120.00	30.00	0.00	92.47	1,543.68		638.80
120.00	30.00	0.00	92.47	1,538.54		638.90
120.00	30.00	0.00	92.47	1,572.55		309.90
120.00	30.00	0.00	92.47	1,572.55		309.80
120.00	30.00	0.00	92.47	1,572.55	1,572.02	309.70
120.00	30.00	0.00	92.47	1,572.55		309.60
120.00	30.00	0.00	92.47	1,569.88		309.60
120.00	30.00	0.00	92.47	3,041.65		609.40
120.00	30.00	0.00	92.47	3,031.68		609.40
120.00	30.00	0.00	92.47	3,031.68	3,035.67	609.30
120.00	30.00	0.00	92.47	3,031.68		609.20

120.00	30.00	0.00	92.47	3,041.65		609.10
120.00	30.00	0.00	92.47	1,451.59		531.70
120.00	30.00	0.00	92.47	1,447.05		531.80
120.00	30.00	0.00	92.47	1,451.59	1,449.77	531.50
120.00	30.00	0.00	92.47	1,447.05		531.60
120.00	30.00	0.00	92.47	1,451.59		531.30
120.00	30.00	0.00	92.47	2,317.45		941.70
120.00	30.00	0.00	92.47	2,311.66		941.70
120.00	30.00	0.00	92.47	2,340.92	2,329.22	941.10
120.00	30.00	0.00	92.47	2,352.83		940.80
120.00	30.00	0.00	92.47	2,323.27		941.30
120.00	30.00	0.00	92.47	2,201.58		78.00
120.00	30.00	0.00	92.47	2,201.58		77.90
120.00	30.00	0.00	92.47	2,201.58	2,202.63	77.80
120.00	30.00	0.00	92.47	2,201.58		77.80
120.00	30.00	0.00	92.47	2,206.83		77.60
120.00	30.00	0.00	92.47	1,853.03		896.50
120.00	30.00	0.00	92.47	1,660.08		902.20
120.00	30.00	0.00	92.47	1,672.08	1,743.41	901.70
120.00	30.00	0.00	92.47	1,675.11		901.60
120.00	30.00	0.00	92.47	1,856.75		896.10
120.00	30.00	0.00	92.47	1,795.46		784.50
120.00	30.00	0.00	92.47	1,768.00		785.20
120.00	30.00	0.00	92.47	1,795.46	1,744.49	784.30
120.00	30.00	0.00	92.47	1,798.95		784.10
120.00	30.00	0.00	92.47	1,564.57		791.70
120.00	30.00	0.00	92.47	2,001.43		444.70
120.00	30.00	0.00	92.47	2,001.43		444.60
120.00	30.00	0.00	92.47	2,266.33	2,056.15	439.10
120.00	30.00	0.00	92.47	2,005.77		444.40
120.00	30.00	0.00	92.47	2,005.77		444.30
120.00	30.00	0.00	92.47	2,862.73		1,022.60
120.00	30.00	0.00	92.47	2,880.57		1,022.40
120.00	30.00	0.00	92.47	2,880.57	2,875.21	1,022.30
120.00	30.00	0.00	92.47	2,871.62		1,022.30
120.00	30.00	0.00	92.47	2,880.57		1,022.10
180.00	150.00	0.00	184.93	3,261.59		82.60
180.00	150.00	0.00	184.93	3,267.36		82.40
180.00	150.00	0.00	184.93	3,250.13	3,255.87	82.60
180.00	150.00	0.00	184.93	3,250.13		82.50
180.00	150.00	0.00	184.93	3,250.13		82.50
180.00	150.00	0.00	184.93	3,412.04		351.30
180.00	150.00	0.00	184.93	3,424.67		351.10
180.00	150.00	0.00	184.93	3,418.34	3,413.31	351.10
180.00	150.00	0.00	184.93	3,405.75		351.20
180.00	150.00	0.00	184.93	3,405.75		351.10
180.00	150.00	0.00	184.93	3,412.04		141.00
180.00	150.00	0.00	184.93	3,418.34		140.80
180.00	150.00	0.00	184.93	3,418.34	3,414.56	140.70
180.00	150.00	0.00	184.93	3,418.34		140.60
180.00	150.00	0.00	184.93	3,405.75		140.70
180.00	150.00	0.00	184.93	3,255.85		230.10
180.00	150.00	0.00	184.93	3,255.85		230.00
180.00	150.00	0.00	184.93	3,255.85	3,254.71	230.00
180.00	150.00	0.00	184.93	3,250.13		230.00

180.00	150.00	0.00	184.93	3,255.85		229.80
180.00	150.00	0.00	184.93	3,284.77		68.80
180.00	150.00	0.00	184.93	3,278.94		68.80
180.00	150.00	0.00	184.93	3,284.77	3,281.28	68.60
180.00	150.00	0.00	184.93	3,284.77		68.50
180.00	150.00	0.00	184.93	3,273.14		68.60
180.00	150.00	0.00	184.93	3,233.08		126.60
180.00	150.00	0.00	184.93	3,238.75		126.40
180.00	150.00	0.00	184.93	3,233.08	3,241.04	126.50
180.00	150.00	0.00	184.93	3,250.13		126.00
180.00	150.00	0.00	184.93	3,250.13		126.00
180.00	150.00	0.00	184.93	3,332.12		74.00
180.00	150.00	0.00	184.93	3,350.23		73.60
180.00	150.00	0.00	184.93	3,344.17	3,336.95	73.60
180.00	150.00	0.00	184.93	3,326.12		73.80
180.00	150.00	0.00	184.93	3,332.12		73.60
180.00	150.00	0.00	184.93	3,233.08		727.20
180.00	150.00	0.00	184.93	3,238.75		727.10
180.00	150.00	0.00	184.93	3,233.08	3,238.75	727.10
180.00	150.00	0.00	184.93	3,244.43		726.80
180.00	150.00	0.00	184.93	3,244.43		726.70
180.00	150.00	0.00	184.93	3,296.48		118.70
180.00	150.00	0.00	184.93	3,267.36		119.10
180.00	150.00	0.00	184.93	3,273.14	3,275.50	119.00
180.00	150.00	0.00	184.93	3,278.94		118.80
180.00	150.00	0.00	184.93	3,261.59		119.00
180.00	150.00	0.00	184.93	3,250.13		1,004.10
180.00	150.00	0.00	184.93	3,273.14		1,003.60
180.00	150.00	0.00	184.93	3,261.59	3,260.46	1,003.70
180.00	150.00	0.00	184.93	3,255.85		1,003.70
180.00	150.00	0.00	184.93	3,261.59		1,003.50
180.00	150.00	0.00	184.93	3,172.08		767.30
180.00	150.00	0.00	184.93	3,172.08		767.30
180.00	150.00	0.00	184.93	3,183.00	3,180.86	767.00
180.00	150.00	0.00	184.93	3,205.07		766.50
180.00	150.00	0.00	184.93	3,172.08		767.00
180.00	150.00	0.00	184.93	3,123.86		465.60
180.00	150.00	0.00	184.93	3,123.86		465.50
180.00	150.00	0.00	184.93	3,123.86	3,124.92	465.40
180.00	150.00	0.00	184.93	3,134.45		465.10
180.00	150.00	0.00	184.93	3,118.59		465.40
180.00	150.00	0.00	184.93	3,166.65		718.90
180.00	150.00	0.00	184.93	3,172.08		718.70
180.00	150.00	0.00	184.93	3,161.24	3,168.83	718.80
180.00	150.00	0.00	184.93	3,172.08		718.60
180.00	150.00	0.00	184.93	3,172.08		718.50
180.00	150.00	0.00	184.93	3,267.36		236.10
180.00	150.00	0.00	184.93	3,278.94		235.80
180.00	150.00	0.00	184.93	3,284.77	3,277.79	235.70
180.00	150.00	0.00	184.93	3,278.94		235.70
180.00	150.00	0.00	184.93	3,278.94		235.60
180.00	150.00	0.00	184.93	3,227.44		973.90
180.00	150.00	0.00	184.93	3,210.63		974.10
180.00	150.00	0.00	184.93	3,221.82	3,222.96	973.80
180.00	150.00	0.00	184.93	3,233.08		973.60

180.00	150.00	0.00	184.93	3,221.82		973.70
180.00	150.00	0.00	184.93	4,082.39		802.60
180.00	150.00	0.00	184.93	4,100.50		802.40
180.00	150.00	0.00	184.93	4,118.76	4,095.09	802.10
180.00	150.00	0.00	184.93	4,091.43		802.30
180.00	150.00	0.00	184.93	4,082.39		802.30
180.00	150.00	0.00	184.93	3,296.48		179.20
180.00	150.00	0.00	184.93	3,290.61		179.20
180.00	150.00	0.00	184.93	3,296.48	3,289.46	179.00
180.00	150.00	0.00	184.93	3,278.94		179.30
180.00	150.00	0.00	184.93	3,284.77		179.10
180.00	150.00	0.00	184.93	3,250.13		931.50
180.00	150.00	0.00	184.93	3,250.13		931.40
180.00	150.00	0.00	184.93	3,255.85	3,247.87	931.20
180.00	150.00	0.00	184.93	3,250.13		931.20
180.00	150.00	0.00	184.93	3,233.08		931.40
180.00	150.00	0.00	184.93	2,867.17		517.80
180.00	150.00	0.00	184.93	2,871.62		517.60
180.00	150.00	0.00	184.93	2,871.62	2,870.73	517.50
180.00	150.00	0.00	184.93	2,871.62		517.40
180.00	150.00	0.00	184.93	2,871.62		517.30
180.00	150.00	0.00	184.93	2,876.09		348.40
180.00	150.00	0.00	184.93	2,880.57		348.20
180.00	150.00	0.00	184.93	2,880.57	2,877.88	348.10
180.00	150.00	0.00	184.93	2,876.09		348.10
180.00	150.00	0.00	184.93	2,876.09		348.00
180.00	150.00	0.00	184.93	3,031.68		416.10
180.00	150.00	0.00	184.93	3,011.93		416.40
180.00	150.00	0.00	184.93	3,031.68	3,028.74	415.90
180.00	150.00	0.00	184.93	3,046.66		415.50
180.00	150.00	0.00	184.93	3,021.77		415.90
180.00	150.00	0.00	184.93	3,056.73		164.10
180.00	150.00	0.00	184.93	3,071.97		163.70
180.00	150.00	0.00	184.93	3,041.65	3,058.79	164.20
180.00	150.00	0.00	184.93	3,066.87		163.70
180.00	150.00	0.00	184.93	3,056.73		163.80
180.00	150.00	0.00	184.93	2,862.73		966.30
180.00	150.00	0.00	184.93	2,858.31		966.30
180.00	150.00	0.00	184.93	2,853.90	2,859.19	966.30
180.00	150.00	0.00	184.93	2,858.31		966.10
180.00	150.00	0.00	184.93	2,862.73		966.00
180.00	150.00	0.00	184.93	3,205.07		574.70
180.00	150.00	0.00	184.93	3,194.00		574.80
180.00	150.00	0.00	184.93	3,199.52	3,201.74	574.60
180.00	150.00	0.00	184.93	3,205.07		574.50
180.00	150.00	0.00	184.93	3,205.07		574.40
180.00	150.00	0.00	184.93	3,183.00		156.80
180.00	150.00	0.00	184.93	3,177.53		156.80
180.00	150.00	0.00	184.93	3,188.49	3,184.10	156.50
180.00	150.00	0.00	184.93	3,183.00		156.50
180.00	150.00	0.00	184.93	3,188.49		156.40
180.00	150.00	0.00	184.93	3,267.36		783.00
180.00	150.00	0.00	184.93	3,261.59		783.00
180.00	150.00	0.00	184.93	3,250.13	3,255.87	783.10
180.00	150.00	0.00	184.93	3,255.85		782.90

180.00	150.00	0.00	184.93	3,244.43		783.00
180.00	150.00	0.00	184.93	3,002.15	3,007.04	218.30
180.00	150.00	0.00	184.93	3,011.93		218.00
180.00	150.00	0.00	184.93	3,002.15		218.10
180.00	150.00	0.00	184.93	3,011.93		217.90
180.00	150.00	0.00	184.93	3,007.03		217.90
180.00	150.00	0.00	184.93	3,002.15	3,003.13	610.50
180.00	150.00	0.00	184.93	3,002.15		610.40
180.00	150.00	0.00	184.93	3,002.15		610.30
180.00	150.00	0.00	184.93	3,002.15		610.30
180.00	150.00	0.00	184.93	3,007.03		610.10
240.00	60.00	0.00	184.93	3,860.80	3,857.58	404.40
240.00	60.00	0.00	184.93	3,852.76		404.40
240.00	60.00	0.00	184.93	3,852.76		404.30
240.00	60.00	0.00	184.93	3,860.80		404.20
240.00	60.00	0.00	184.93	3,860.80		404.10
240.00	60.00	0.00	184.93	4,046.66	4,043.13	208.50
240.00	60.00	0.00	184.93	4,046.66		208.40
240.00	60.00	0.00	184.93	4,037.83		208.40
240.00	60.00	0.00	184.93	4,037.83		208.30
240.00	60.00	0.00	184.93	4,046.66		208.10
240.00	60.00	0.00	184.93	3,662.03	3,662.03	250.50
240.00	60.00	0.00	184.93	3,662.03		250.40
240.00	60.00	0.00	184.93	3,662.03		250.30
240.00	60.00	0.00	184.93	3,662.03		250.20
240.00	60.00	0.00	184.93	3,662.03		250.10
240.00	60.00	0.00	184.93	3,026.72	3,036.67	573.50
240.00	60.00	0.00	184.93	3,031.68		573.40
240.00	60.00	0.00	184.93	3,036.66		573.30
240.00	60.00	0.00	184.93	3,041.65		573.20
240.00	60.00	0.00	184.93	3,046.66		573.10
240.00	60.00	0.00	184.93	3,134.45	3,139.78	451.90
240.00	60.00	0.00	184.93	3,134.45		451.90
240.00	60.00	0.00	184.93	3,134.45		451.90
240.00	60.00	0.00	184.93	3,150.47		451.60
240.00	60.00	0.00	184.93	3,145.11		451.70
240.00	60.00	0.00	184.93	3,041.65	3,051.71	333.80
240.00	60.00	0.00	184.93	3,046.66		333.70
240.00	60.00	0.00	184.93	3,051.69		333.60
240.00	60.00	0.00	184.93	3,056.73		333.50
240.00	60.00	0.00	184.93	3,061.80		333.40
240.00	60.00	0.00	184,93	3077,08	3085,31	220,10
240.00	60.00	0.00	184,93	3082,21		220,00
240.00	60.00	0.00	184,93	3087,35		219,90
240.00	60.00	0.00	184,93	3082,21		220,00
240.00	60.00	0.00	184,93	3097,70		219,70
240.00	60.00	0.00	184,93	3102,89	3113,37	142,10
240.00	60.00	0.00	184,93	3108,11		142,00
240.00	60.00	0.00	184,93	3108,11		142,00
240.00	60.00	0.00	184,93	3123,86		141,70
240.00	60.00	0.00	184,93	3123,86		141,70
240.00	60.00	0.00	184.93	2,699.74	2,731.74	352.90
240.00	60.00	0.00	184.93	2,739.74		351.90
240.00	60.00	0.00	184.93	2,739.74		351.90

240.00	60.00	0.00	184.93	2,739.74		351.90
240.00	60.00	0.00	184.93	2,739.74		351.90
240.00	60.00	0.00	184.93	2,572.08		641.50
240.00	60.00	0.00	184.93	2,436.53		641.50
240.00	60.00	0.00	184.93	2,469.06	2,483.16	640.50
240.00	60.00	0.00	184.93	2,469.06		640.50
240.00	60.00	0.00	184.93	2,469.06		640.50
240.00	60.00	0.00	184.93	2,499.09		869.80
240.00	60.00	0.00	184.93	2,499.09		869.80
240.00	60.00	0.00	184.93	2,499.09	2,499.09	869.80
240.00	60.00	0.00	184.93	2,499.09		869.80
240.00	60.00	0.00	184.93	2,499.09		869.80
240.00	60.00	0.00	184.93	2,780.94		671.10
240.00	60.00	0.00	184.93	2,780.94		671.10
240.00	60.00	0.00	184.93	2,780.94	2,797.92	671.10
240.00	60.00	0.00	184.93	2,823.40		670.10
240.00	60.00	0.00	184.93	2,823.40		670.10
240.00	60.00	0.00	184.93	2,810.52		401.40
240.00	60.00	0.00	184.93	2,810.52		401.40
240.00	60.00	0.00	184.93	2,810.52	2,810.52	401.40
240.00	60.00	0.00	184.93	2,810.52		401.40
240.00	60.00	0.00	184.93	2,810.52		401.40
240.00	60.00	0.00	184.93	2,907.74		287.30
240.00	60.00	0.00	184.93	2,907.74		287.30
240.00	60.00	0.00	184.93	3,051.69	2,936.53	284.30
240.00	60.00	0.00	184.93	2,907.74		287.30
240.00	60.00	0.00	184.93	2,907.74		287.30
240.00	60.00	0.00	184.93	2,780.94		156.50
240.00	60.00	0.00	184.93	2,660.90		156.50
240.00	60.00	0.00	184.93	2,780.94	2,693.82	156.50
240.00	60.00	0.00	184.93	2,623.15		156.50
240.00	60.00	0.00	184.93	2,623.15		156.50
240.00	60.00	0.00	184.93	2,509.26		821.30
240.00	60.00	0.00	184.93	2,509.26		821.30
240.00	60.00	0.00	184.93	2,509.26	2,509.26	821.30
240.00	60.00	0.00	184.93	2,509.26		821.30
240.00	60.00	0.00	184.93	2,509.26		821.30
240.00	60.00	0.00	184.93	2,827.71		926.90
240.00	60.00	0.00	184.93	2,827.71		926.90
240.00	60.00	0.00	184.93	2,827.71	2,827.71	926.90
240.00	60.00	0.00	184.93	2,827.71		926.90
240.00	60.00	0.00	184.93	2,827.71		926.90
240.00	60.00	0.00	184.93	2,889.57		135.30
240.00	60.00	0.00	184.93	2,889.57		135.30
240.00	60.00	0.00	184.93	2,889.57	2,889.57	135.30
240.00	60.00	0.00	184.93	2,889.57		135.30
240.00	60.00	0.00	184.93	2,889.57		135.30
240.00	60.00	0.00	184.93	2,452.68		956.90
240.00	60.00	0.00	184.93	2,452.68		956.90
240.00	60.00	0.00	184.93	2,452.68	2,452.68	956.90
240.00	60.00	0.00	184.93	2,452.68		956.90
240.00	60.00	0.00	184.93	2,452.68		956.90
240.00	60.00	0.00	184.93	1,853.03		606.70
240.00	60.00	0.00	184.93	1,853.03		606.70

240.00	60.00	0.00	184.93	1,853.03	1,856.78	606.70
240.00	60.00	0.00	184.93	1,853.03		606.70
240.00	60.00	0.00	184.93	1,871.79		605.70
240.00	60.00	0.00	184.93	2,266.33		911.50
240.00	60.00	0.00	184.93	2,478.99		904.50
240.00	60.00	0.00	184.93	2,294.45	2,349.08	910.50
240.00	60.00	0.00	184.93	2,352.83		908.50
240.00	60.00	0.00	184.93	2,352.83		908.50
240.00	60.00	0.00	184.93	3,255.85		678.00
240.00	60.00	0.00	184.93	3,255.85		678.00
240.00	60.00	0.00	184.93	3,255.85	3,255.85	678.00
240.00	60.00	0.00	184.93	3,255.85		678.00
240.00	60.00	0.00	184.93	3,255.85		678.00
240.00	60.00	0.00	184.93	2,935.44		674.10
240.00	60.00	0.00	184.93	2,935.44		674.10
240.00	60.00	0.00	184.93	2,982.78	2,963.84	673.10
240.00	60.00	0.00	184.93	2,982.78		673.10
240.00	60.00	0.00	184.93	2,982.78		673.10
240.00	60.00	0.00	184.93	3,066.87		862.10
240.00	60.00	0.00	184.93	3,061.80		862.20
240.00	60.00	0.00	184.93	3,077.08	3,074.03	861.90
240.00	60.00	0.00	184.93	3,082.21		861.80
240.00	60.00	0.00	184.93	3,082.21		861.80
240.00	60.00	0.00	184.93	2,921.52		802.70
240.00	60.00	0.00	184.93	3,118.59		798.70
240.00	60.00	0.00	184.93	2,926.15	2,966.50	802.60
240.00	60.00	0.00	184.93	2,930.78		802.50
240.00	60.00	0.00	184.93	2,935.44		802.40
240.00	60.00	0.00	184.93	2,958.92		1,026.10
240.00	60.00	0.00	184.93	2,958.92		1,026.10
240.00	60.00	0.00	184.93	2,963.66	2,965.58	1,026.00
240.00	60.00	0.00	184.93	2,968.42		1,025.90
240.00	60.00	0.00	184.93	2,977.98		1,025.70
240.00	60.00	0.00	184,93	3155,84		651,40
240.00	60.00	0.00	184,93	3166,65		651,20
240.00	60.00	0.00	184,93	3166,65	3169,94	651,20
240.00	60.00	0.00	184,93	3177,53		651,00
240.00	60.00	0.00	184,93	3183,00		650,90
240.00	60.00	0.00	184,93	3102,89		142,10
240.00	60.00	0.00	184,93	3108,11		142,00
240.00	60.00	0.00	184,93	3108,11	3113,37	142,00
240.00	60.00	0.00	184,93	3123,86		141,70
240.00	60.00	0.00	184,93	3123,86		141,70
300.00	250.00	0.00	308.22	2,969.37		509.70
300.00	250.00	0.00	308.22	3,088.38		509.70
300.00	250.00	0.00	308.22	3,088.38	3,064.58	509.70
300.00	250.00	0.00	308.22	3,088.38		509.70
300.00	250.00	0.00	308.22	3,088.38		509.70
300.00	250.00	0.00	308.22	3,082.21		857.60
300.00	250.00	0.00	308.22	3,082.21		857.60
300.00	250.00	0.00	308.22	3,210.63	3,166.02	857.60
300.00	250.00	0.00	308.22	3,210.63		857.60
300.00	250.00	0.00	308.22	3,244.43		857.60
300.00	250.00	0.00	308.22	1,481.12		362.30

300.00	250.00	0.00	308.22	1,481.12		362.30
300.00	250.00	0.00	308.22	1,481.12	1,483.98	362.30
300.00	250.00	0.00	308.22	1,488.27		361.30
300.00	250.00	0.00	308.22	1,488.27		361.30
300.00	250.00	0.00	308.22	1,944.61		410.90
300.00	250.00	0.00	308.22	1,944.61		410.90
300.00	250.00	0.00	308.22	1,956.96	1,952.02	409.90
300.00	250.00	0.00	308.22	1,956.96		409.90
300.00	250.00	0.00	308.22	1,956.96		409.90
300.00	250.00	0.00	308.22	2,089.63		966.30
300.00	250.00	0.00	308.22	2,089.63		966.30
300.00	250.00	0.00	308.22	2,034.46	2,078.60	966.30
300.00	250.00	0.00	308.22	2,089.63		966.30
300.00	250.00	0.00	308.22	2,089.63		966.30
300.00	250.00	0.00	308.22	686.61		929.10
300.00	250.00	0.00	308.22	692.79		925.10
300.00	250.00	0.00	308.22	692.79	691.55	925.10
300.00	250.00	0.00	308.22	692.79		925.10
300.00	250.00	0.00	308.22	692.79		925.10
300.00	250.00	0.00	308.22	1,113.92		850.70
300.00	250.00	0.00	308.22	1,113.92		850.70
300.00	250.00	0.00	308.22	1,130.26	1,123.72	846.70
300.00	250.00	0.00	308.22	1,130.26		846.70
300.00	250.00	0.00	308.22	1,130.26		846.70
300.00	250.00	0.00	308.22	1,590.41		1,085.80
300.00	250.00	0.00	308.22	1,590.41		1,085.80
300.00	250.00	0.00	308.22	1,590.41	1,590.41	1,085.80
300.00	250.00	0.00	308.22	1,590.41		1,085.80
300.00	250.00	0.00	308.22	1,590.41		1,085.80
300.00	250.00	0.00	308.22	2,322.69		208.90
300.00	250.00	0.00	308.22	2,322.69		208.90
300.00	250.00	0.00	308.22	2,322.69	2,322.69	208.90
300.00	250.00	0.00	308.22	2,322.69		208.90
300.00	250.00	0.00	308.22	2,322.69		208.90
300.00	250.00	0.00	308.22	2,869.84		630.50
300.00	250.00	0.00	308.22	2,817.37		632.50
300.00	250.00	0.00	308.22	2,817.37	2,859.64	632.50
300.00	250.00	0.00	308.22	2,896.81		629.50
300.00	250.00	0.00	308.22	2,896.81		629.50
300.00	250.00	0.00	308.22	2,756.89		971.50
300.00	250.00	0.00	308.22	2,756.89		971.50
300.00	250.00	0.00	308.22	2,708.44	2,742.49	973.50
300.00	250.00	0.00	308.22	2,708.44		973.50
300.00	250.00	0.00	308.22	2,781.78		970.50
300.00	250.00	0.00	308.22	2,883.26		659.20
300.00	250.00	0.00	308.22	2,883.26		659.20
300.00	250.00	0.00	308.22	2,883.26	2,883.26	659.20
300.00	250.00	0.00	308.22	2,883.26		659.20
300.00	250.00	0.00	308.22	2,883.26		659.20
300.00	250.00	0.00	308.22	3,015.86		107.10
300.00	250.00	0.00	308.22	3,015.86		107.10
300.00	250.00	0.00	308.22	3,015.86	3,021.82	107.10
300.00	250.00	0.00	308.22	3,015.86		107.10
300.00	250.00	0.00	308.22	3,045.66		106.10
300.00	250.00	0.00	308.22	3,082.21		817.70

300.00	250.00	0.00	308.22	3,082.21		817.70
300.00	250.00	0.00	308.22	3,082.21	3,082.21	817.70
300.00	250.00	0.00	308.22	3,082.21		817.70
300.00	250.00	0.00	308.22	3,082.21		817.70
300.00	250.00	0.00	308.22	2,727.62		755.10
300.00	250.00	0.00	308.22	2,727.62		755.10
300.00	250.00	0.00	308.22	2,727.62	2,737.36	755.10
300.00	250.00	0.00	308.22	2,751.97		754.10
300.00	250.00	0.00	308.22	2,751.97		754.10
300.00	250.00	0.00	308.22	2,929.85		512.20
300.00	250.00	0.00	308.22	3,015.86		509.20
300.00	250.00	0.00	308.22	3,015.86	2,998.66	509.20
300.00	250.00	0.00	308.22	3,015.86		509.20
300.00	250.00	0.00	308.22	3,015.86		509.20
300.00	250.00	0.00	308.22	3,217.34		321.80
300.00	250.00	0.00	308.22	3,119.64		324.80
300.00	250.00	0.00	308.22	3,119.64	3,139.18	324.80
300.00	250.00	0.00	308.22	3,119.64		324.80
300.00	250.00	0.00	308.22	3,119.64		324.80
300.00	250.00	0.00	308.22	3,110.20		1,066.10
300.00	250.00	0.00	308.22	3,110.20		1,066.10
300.00	250.00	0.00	308.22	3,110.20	3,110.20	1,066.10
300.00	250.00	0.00	308.22	3,110.20		1,066.10
300.00	250.00	0.00	308.22	3,110.20		1,066.10
300.00	250.00	0.00	308.22	3,069.93		590.70
300.00	250.00	0.00	308.22	3,072.99		590.60
300.00	250.00	0.00	308.22	3,076.05	3,075.45	590.50
300.00	250.00	0.00	308.22	3,079.13		590.40
300.00	250.00	0.00	308.22	3,079.13		590.40
300.00	250.00	0.00	308,22	3066,87		477,20
300.00	250.00	0.00	308,22	3072,99		477,00
300.00	250.00	0.00	308,22	2995,34	3025,76	479,60
300.00	250.00	0.00	308,22	2995,34		479,60
300.00	250.00	0.00	308,22	2998,26		479,50
300.00	250.00	0.00	308,22	3135,51		356,60
300.00	250.00	0.00	308,22	3135,51		356,60
300.00	250.00	0.00	308,22	3141,90	3140,63	356,40
300.00	250.00	0.00	308,22	3141,90		356,40
300.00	250.00	0.00	308,22	3148,32		356,20
300.00	250.00	0.00	308,22	3132,32		765,30
300.00	250.00	0.00	308,22	3141,90		765,00
300.00	250.00	0.00	308,22	3125,97	3123,15	765,50
300.00	250.00	0.00	308,22	3154,77		764,60
300.00	250.00	0.00	308,22	3060,78		767,60
300.00	250.00	0.00	308,22	3054,71		527,00
300.00	250.00	0.00	308,22	3054,71		527,00
300.00	250.00	0.00	308,22	3057,75	3077,84	526,90
300.00	250.00	0.00	308,22	3060,78		526,80
300.00	250.00	0.00	308,22	3161,24		523,60
300.00	250.00	0.00	308,22	1343,01		397,40
300.00	250.00	0.00	308,22	1316,62		402,00
300.00	250.00	0.00	308,22	1345,35	1333,95	397,00
300.00	250.00	0.00	308,22	1344,77		397,10
300.00	250.00	0.00	308,22	1320,00		401,40
300.00	250.00	0.00	308,22	1527,36		530,10

300.00	250.00	0.00	308,22	1524,34	1755,45	530,50
300.00	250.00	0.00	308,22	2666,27		443,90
300.00	250.00	0.00	308,22	1531,15		529,60
300.00	250.00	0.00	308,22	1528,11		530,00
300.00	250.00	0.00	308,22	2983,74	2988,38	215,30
300.00	250.00	0.00	308,22	2983,74		215,30
300.00	250.00	0.00	308,22	2989,53		215,10
300.00	250.00	0.00	308,22	2992,43		215,00
300.00	250.00	0.00	308,22	2992,43		215,00
300.00	250.00	0.00	308,22	2625,39	2628,53	899,60
300.00	250.00	0.00	308,22	2625,39		899,60
300.00	250.00	0.00	308,22	2629,87		899,40
300.00	250.00	0.00	308,22	2632,12		899,30
300.00	250.00	0.00	308,22	2629,87		899,40
300.00	250.00	0.00	308,22	2616,47	2537,23	379,30
300.00	250.00	0.00	308,22	2614,26		379,40
300.00	250.00	0.00	308,22	2215,82		400,60
300.00	250.00	0.00	308,22	2620,92		379,10
300.00	250.00	0.00	308,22	2618,70		379,20
360.00	300.00	0.00	369.86	3,150.47	3,200.33	917.30
360.00	300.00	0.00	369.86	3,150.47		917.30
360.00	300.00	0.00	369.86	3,177.53		917.30
360.00	300.00	0.00	369.86	3,261.59		917.30
360.00	300.00	0.00	369.86	3,261.59		917.30
360.00	300.00	0.00	369.86	2,387.77	2,387.77	1,127.40
360.00	300.00	0.00	369.86	2,387.77		1,127.40
360.00	300.00	0.00	369.86	2,387.77		1,131.40
360.00	300.00	0.00	369.86	2,387.77		1,131.40
360.00	300.00	0.00	369.86	2,387.77		1,131.40
360.00	300.00	0.00	369,86	2164,22	2236,98	575,00
360.00	300.00	0.00	369,86	2210,79		571,40
360.00	300.00	0.00	369,86	2489,00		552,70
360.00	300.00	0.00	369,86	2155,39		575,70
360.00	300.00	0.00	369,86	2165,49		574,90
360.00	300.00	0.00	369,86	1070,83	1321,10	1266,60
360.00	300.00	0.00	369,86	1570,55		1156,70
360.00	300.00	0.00	369,86	1390,99		1187,10
360.00	300.00	0.00	369,86	1501,68		1167,50
360.00	300.00	0.00	369,86	1071,45		1266,40
360.00	300.00	0.00	369,86	1810,40	1812,18	498,40
360.00	300.00	0.00	369,86	1811,29		498,30
360.00	300.00	0.00	369,86	1811,29		498,30
360.00	300.00	0.00	369,86	1813,06		498,10
360.00	300.00	0.00	369,86	1814,84		497,90
360.00	300.00	0.00	369,86	3110,72	2333,69	310,90
360.00	300.00	0.00	369,86	1812,17		396,10
360.00	300.00	0.00	369,86	1813,06		396,00
360.00	300.00	0.00	369,86	1811,29		396,20
360.00	300.00	0.00	369,86	3121,22		310,50
360.00	300.00	0.00	369,86	1716,31	1718,22	691,80
360.00	300.00	0.00	369,86	1717,90		691,60
360.00	300.00	0.00	369,86	1717,90		691,60
360.00	300.00	0.00	369,86	1719,50		691,40
360.00	300.00	0.00	369,86	1719,50		691,40
360.00	300.00	0.00	369,86	1812,17		1167,50

360.00	300.00	0.00	369,86	1808,63		1167,90
360.00	300.00	0.00	369,86	1812,17	1811,64	1167,50
360.00	300.00	0.00	369,86	1811,29		1167,60
360.00	300.00	0.00	369,86	1813,95		1167,30
360.00	300.00	0.00	369,86	3158,54		429,60
360.00	300.00	0.00	369,86	3161,24		429,50
360.00	300.00	0.00	369,86	3163,94	3163,41	429,40
360.00	300.00	0.00	369,86	3163,94		429,40
360.00	300.00	0.00	369,86	3169,36		429,20
360.00	300.00	0.00	369,86	3311,23		148,00
360.00	300.00	0.00	369,86	3308,27		148,10
360.00	300.00	0.00	369,86	3311,23	3313,02	148,00
360.00	300.00	0.00	369,86	3317,17		147,80
360.00	300.00	0.00	369,86	3317,17		147,80
360.00	300.00	0.00	369,86	3311,23		937,20
360.00	300.00	0.00	369,86	3320,15		936,90
360.00	300.00	0.00	369,86	3320,15	3320,76	936,90
360.00	300.00	0.00	369,86	3329,12		936,60
360.00	300.00	0.00	369,86	3323,13		936,80
360.00	300.00	0.00	369.86	3,287.69		969.50
360.00	300.00	0.00	369.86	3,296.48		969.20
360.00	300.00	0.00	369.86	3,293.54	3,294.13	969.30
360.00	300.00	0.00	369.86	3,296.48		969.20
360.00	300.00	0.00	369.86	3,296.48		969.20
360.00	300.00	0.00	369.86	3,284.77		382.10
360.00	300.00	0.00	369.86	3,281.85		382.20
360.00	300.00	0.00	369.86	3,281.85	3,284.19	382.20
360.00	300.00	0.00	369.86	3,281.85		382.20
360.00	300.00	0.00	369.86	3,290.61		381.90
360.00	300.00	0.00	369,86	1837,38		1137,80
360.00	300.00	0.00	369,86	1840,12		1137,50
360.00	300.00	0.00	369,86	1840,12	1840,49	1137,50
360.00	300.00	0.00	369,86	1841,96		1137,30
360.00	300.00	0.00	369,86	1842,87		1137,20
360.00	300.00	0.00	369,86	2878,33		315,80
360.00	300.00	0.00	369,86	2889,57		315,30
360.00	300.00	0.00	369,86	2887,31	2787,15	315,40
360.00	300.00	0.00	369,86	2395,50		341,70
360.00	300.00	0.00	369,86	2885,06		315,50
360.00	300.00	0.00	369,86	813,07		730,00
360.00	300.00	0.00	369,86	813,25		729,90
360.00	300.00	0.00	369,86	812,89	812,96	730,10
360.00	300.00	0.00	369,86	812,89		730,10
360.00	300.00	0.00	369,86	812,71		730,20
360.00	300.00	0.00	369.86	1,967.37		1,080.40
360.00	300.00	0.00	369.86	1,516.46		1,136.30
360.00	300.00	0.00	369.86	1,563.91	1,707.61	1,128.90
360.00	300.00	0.00	369.86	1,517.71		1,136.10
360.00	300.00	0.00	369.86	1,972.61		1,079.90
360.00	300.00	0.00	369.86	1,573.89		285.90
360.00	300.00	0.00	369.86	1,456.16		304.90
360.00	300.00	0.00	369.86	1,577.25	1,393.84	285.40
360.00	300.00	0.00	369.86	910.32		457.20
360.00	300.00	0.00	369.86	1,451.59		305.70
360.00	300.00	0.00	369,86	1856,75		876,50

360.00	300.00	0.00	369,86	1860,49	1859,18	876,10
360.00	300.00	0.00	369,86	1858,62		876,30
360.00	300.00	0.00	369,86	1861,42		876,00
360.00	300.00	0.00	369,86	1858,62		876,30
360.00	300.00	0.00	369,86	2819,09	2826,86	352,20
360.00	300.00	0.00	369,86	2827,71		351,80
360.00	300.00	0.00	369,86	2821,24		352,10
360.00	300.00	0.00	369,86	2829,88		351,70
360.00	300.00	0.00	369,86	2836,39		351,40
360.00	300.00	0.00	369,86	1873,68	1988,66	1151,10
360.00	300.00	0.00	369,86	2433,32		1105,70
360.00	300.00	0.00	369,86	1878,44		1150,60
360.00	300.00	0.00	369,86	1877,49		1150,70
360.00	300.00	0.00	369,86	1880,35		1150,40
360.00	300.00	0.00	369.86	3,139.77	2,436.85	1,070.00
360.00	300.00	0.00	369.86	3,166.65		1,069.00
360.00	300.00	0.00	369.86	1,889.96		1,147.90
360.00	300.00	0.00	369.86	1,946.66		1,142.20
360.00	300.00	0.00	369.86	2,041.20		1,133.40
360.00	300.00	0.00	369.86	1,638.75	1,676.70	334.60
360.00	300.00	0.00	369.86	1,483.61		358.20
360.00	300.00	0.00	369.86	2,136.71		282.00
360.00	300.00	0.00	369.86	1,484.21		358.10
360.00	300.00	0.00	369.86	1,640.20		334.40
360.00	300.00	0.00	369,86	3341,15	3344,78	494,90
360.00	300.00	0.00	369,86	3341,15		494,90
360.00	300.00	0.00	369,86	3344,17		494,80
360.00	300.00	0.00	369,86	3350,23		494,60
360.00	300.00	0.00	369,86	3347,19		494,70
360.00	300.00	0.00	369,86	3450,23	3429,02	1057,90
360.00	300.00	0.00	369,86	3371,60		1060,40
360.00	300.00	0.00	369,86	3466,40		1057,40
360.00	300.00	0.00	369,86	3472,91		1057,20
360.00	300.00	0.00	369,86	3383,94		1060,00
360.00	300.00	0.00	369,86	1903,58	1860,26	670,00
360.00	300.00	0.00	369,86	1721,90		690,50
360.00	300.00	0.00	369,86	1976,83		662,80
360.00	300.00	0.00	369,86	1977,89		662,70
360.00	300.00	0.00	369,86	1721,10		690,60
360.00	300.00	0.00	369.86	3,235.91	3,235.40	161.60
360.00	300.00	0.00	369.86	3,255.85		160.90
360.00	300.00	0.00	369.86	3,224.63		162.00
360.00	300.00	0.00	369.86	3,241.58		161.40
360.00	300.00	0.00	369.86	3,219.02		162.20
360.00	300.00	0.00	369.86	1,976.83	1,977.46	413.80
360.00	300.00	0.00	369.86	1,975.77		413.90
360.00	300.00	0.00	369.86	1,980.00		413.50
360.00	300.00	0.00	369.86	1,976.83		413.80
360.00	300.00	0.00	369.86	1,977.89		413.70
240.00	60.00	0.00	184.93	3,736.01	3,733.00	270.00
240.00	60.00	0.00	184.93	3,736.01		269.90
240.00	60.00	0.00	184.93	3,728.48		269.90
240.00	60.00	0.00	184.93	3,728.48		269.80
240.00	60.00	0.00	184.93	3,736.01		269.60
240.00	60.00	0.00	184.93	3,836.77		451.80

240.00	60.00	0.00	184.93	3,820.92	3,824.11	451.90
240.00	60.00	0.00	184.93	3,828.83		451.70
240.00	60.00	0.00	184.93	3,805.19		452.00
240.00	60.00	0.00	184.93	3,828.83		451.60
240.00	60.00	0.00	184.93	3,535.99	3,544.13	719.10
240.00	60.00	0.00	184.93	3,542.77		718.90
240.00	60.00	0.00	184.93	3,549.57		718.80
240.00	60.00	0.00	184.93	3,549.57		718.70
240.00	60.00	0.00	184.93	3,542.77		718.70
240.00	60.00	0.00	184.93	3,789.60	3,780.32	889.60
240.00	60.00	0.00	184.93	3,774.13		889.70
240.00	60.00	0.00	184.93	3,789.60		889.40
240.00	60.00	0.00	184.93	3,774.13		889.60
240.00	60.00	0.00	184.93	3,774.13		889.40
240.00	60.00	0.00	184.93	3,443.81	3,450.27	816.70
240.00	60.00	0.00	184.93	3,437.41		816.70
240.00	60.00	0.00	184.93	3,456.68		816.40
240.00	60.00	0.00	184.93	3,443.81		816.50
240.00	60.00	0.00	184.93	3,469.65		816.00
240.00	60.00	0.00	184.93	4,020.27	4,036.10	397.90
240.00	60.00	0.00	184.93	4,037.83		397.60
240.00	60.00	0.00	184.93	4,037.83		397.60
240.00	60.00	0.00	184.93	4,029.03		397.60
240.00	60.00	0.00	184.93	4,055.54		397.20
240.00	60.00	0.00	184.93	4,109.61	4,116.94	576.20
240.00	60.00	0.00	184.93	4,118.76		576.10
240.00	60.00	0.00	184.93	4,118.76		576.00
240.00	60.00	0.00	184.93	4,127.96		575.80
240.00	60.00	0.00	184.93	4,109.61		575.90
240.00	60.00	0.00	184.93	4,037.83	4,041.39	763.00
240.00	60.00	0.00	184.93	4,029.03		763.00
240.00	60.00	0.00	184.93	4,055.54		762.60
240.00	60.00	0.00	184.93	4,029.03		762.80
240.00	60.00	0.00	184.93	4,055.54		762.40
240.00	60.00	0.00	184.93	4,029.03	4,002.96	399.30
240.00	60.00	0.00	184.93	4,011.55		399.40
240.00	60.00	0.00	184.93	4,011.55		399.30
240.00	60.00	0.00	184.93	3,977.04		399.70
240.00	60.00	0.00	184.93	3,985.61		399.40
240.00	60.00	0.00	184.93	4,020.27	4,027.28	961.50
240.00	60.00	0.00	184.93	4,029.03		961.40
240.00	60.00	0.00	184.93	4,029.03		961.30
240.00	60.00	0.00	184.93	4,037.83		961.10
240.00	60.00	0.00	184.93	4,020.27		961.20
240.00	60.00	0.00	184.93	3,876.99	3,860.82	639.90
240.00	60.00	0.00	184.93	3,860.80		640.00
240.00	60.00	0.00	184.93	3,852.76		640.10
240.00	60.00	0.00	184.93	3,860.80		639.90
240.00	60.00	0.00	184.93	3,852.76		639.90
240.00	60.00	0.00	184.93	4,212.58	4,206.84	936.90
240.00	60.00	0.00	184.93	4,203.01		936.90
240.00	60.00	0.00	184.93	4,203.01		936.80
240.00	60.00	0.00	184.93	4,203.01		936.70
240.00	60.00	0.00	184.93	4,212.58		936.60
240.00	60.00	0.00	184.93	4,055.54		457.30

240.00	60.00	0.00	184.93	4,046.66	4,064.49	457.30
240.00	60.00	0.00	184.93	4,064.45		457.10
240.00	60.00	0.00	184.93	4,073.40		456.90
240.00	60.00	0.00	184.93	4,082.39		456.70
240.00	60.00	0.00	184.93	3,766.44	3,777.28	976.60
240.00	60.00	0.00	184.93	3,805.19		976.00
240.00	60.00	0.00	184.93	3,781.85		976.20
240.00	60.00	0.00	184.93	3,774.13		976.20
240.00	60.00	0.00	184.93	3,758.79		976.30
240.00	60.00	0.00	184.93	3,852.76	3,865.66	124.40
240.00	60.00	0.00	184.93	3,868.88		124.10
240.00	60.00	0.00	184.93	3,868.88		124.00
240.00	60.00	0.00	184.93	3,860.80		124.00
240.00	60.00	0.00	184.93	3,876.99		123.70
240.00	60.00	0.00	184.93	4,002.87	3,995.97	536.70
240.00	60.00	0.00	184.93	4,002.87		536.60
240.00	60.00	0.00	184.93	4,002.87		536.50
240.00	60.00	0.00	184.93	3,994.22		536.50
240.00	60.00	0.00	184.93	3,977.04		536.60
240.00	60.00	0.00	184.93	4,082.39	4,095.09	802.60
240.00	60.00	0.00	184.93	4,100.50		802.40
240.00	60.00	0.00	184.93	4,118.76		802.10
240.00	60.00	0.00	184.93	4,091.43		802.30
240.00	60.00	0.00	184.93	4,082.39		802.30
240.00	60.00	0.00	184.93	3,828.83	3,824.10	1,030.90
240.00	60.00	0.00	184.93	3,820.92		1,030.90
240.00	60.00	0.00	184.93	3,820.92		1,030.90
240.00	60.00	0.00	184.93	3,836.77		1,030.60
240.00	60.00	0.00	184.93	3,813.04		1,030.70
240.00	60.00	0.00	184.93	3,844.75	3,851.18	439.50
240.00	60.00	0.00	184.93	3,868.88		439.20
240.00	60.00	0.00	184.93	3,844.75		439.40
240.00	60.00	0.00	184.93	3,852.76		439.20
240.00	60.00	0.00	184.93	3,844.75		439.20
240.00	60.00	0.00	184.93	3,909.78	3,921.41	996.70
240.00	60.00	0.00	184.93	3,926.38		996.40
240.00	60.00	0.00	184.93	3,926.38		996.30
240.00	60.00	0.00	184.93	3,934.73		996.10
240.00	60.00	0.00	184.93	3,909.78		996.30
240.00	60.00	0.00	184.93	4,029.03	4,016.79	804.90
240.00	60.00	0.00	184.93	4,011.55		805.00
240.00	60.00	0.00	184.93	4,011.55		804.90
240.00	60.00	0.00	184.93	4,011.55		804.80
240.00	60.00	0.00	184.93	4,020.27		804.60
240.00	60.00	0.00	184.93	4,082.39	4,106.00	315.80
240.00	60.00	0.00	184.93	4,118.76		315.30
240.00	60.00	0.00	184.93	4,118.76		315.20
240.00	60.00	0.00	184.93	4,109.61		315.20
240.00	60.00	0.00	184.93	4,100.50		315.20
240.00	60.00	0.00	184.93	4,002.87	3,997.69	451.70
240.00	60.00	0.00	184.93	4,002.87		451.60
240.00	60.00	0.00	184.93	3,994.22		451.70
240.00	60.00	0.00	184.93	3,985.61		451.70
240.00	60.00	0.00	184.93	4,002.87		451.40
240.00	60.00	0.00	184.93	3,789.60		287.00

240.00	60.00	0.00	184.93	3,852.76	3,825.93	286.10
240.00	60.00	0.00	184.93	3,789.60		286.90
240.00	60.00	0.00	184.93	3,868.88		285.80
240.00	60.00	0.00	184.93	3,828.83		286.20
240.00	60.00	0.00	184.93	4,011.55	3,999.42	843.60
240.00	60.00	0.00	184.93	4,002.87		843.60
240.00	60.00	0.00	184.93	3,985.61		843.70
240.00	60.00	0.00	184.93	3,994.22		843.50
240.00	60.00	0.00	184.93	4,002.87		843.30
240.00	60.00	0.00	184.93	3,380.85	3,374.68	716.60
240.00	60.00	0.00	184.93	3,374.68		716.60
240.00	60.00	0.00	184.93	3,374.68		716.50
240.00	60.00	0.00	184.93	3,374.68		716.40
240.00	60.00	0.00	184.93	3,368.53		716.40
240.00	60.00	0.00	184.93	3,344.17	3,346.59	526.50
240.00	60.00	0.00	184.93	3,350.23		526.30
240.00	60.00	0.00	184.93	3,350.23		526.20
240.00	60.00	0.00	184.93	3,344.17		526.20
240.00	60.00	0.00	184.93	3,344.17		526.10
240.00	60.00	0.00	184.93	3,344.17	3,351.45	254.50
240.00	60.00	0.00	184.93	3,356.31		254.20
240.00	60.00	0.00	184.93	3,344.17		254.30
240.00	60.00	0.00	184.93	3,356.31		254.10
240.00	60.00	0.00	184.93	3,356.31		254.00

Average Velocity for 7 sensors
V average
v1, m/s
3,019.40
3,025.34
3,030.00
3,023.68
3,019.44
3,193.48
3,198.30
3,193.83
3,190.49
3,197.07
3,196.23
3,194.12
3,194.75
3,194.12
3,192.43
3,201.88
3,198.68
3,197.26
3,198.28
3,190.36
3,304.46
3,298.67
3,302.71
3,302.27
3,303.54
3,201.97
3,207.03
3,206.35
3,207.35
3,200.34
3,169.58
3,164.45
3,168.00
3,167.83
3,166.89
3,202.23
3,195.28
3,203.86
3,197.84
3,196.00
2,550.06
2,546.52
2,546.34
2,546.44
2,544.96
2,615.15
2,614.38
2,617.08
2,641.54

2,616.87
2,327.84
2,392.56
2,391.75
2,381.16
2,394.98
2,252.78
2,259.27
2,256.22
2,255.22
2,256.10
2,583.29
2,580.84
2,581.39
2,580.33
2,586.23
3,127.00
3,155.54
3,156.85
3,150.08
3,133.56
3,190.27
3,194.84
3,202.04
3,200.65
3,199.53
2,831.73
2,831.50
2,831.17
2,831.80
2,830.94
2,809.14
2,806.21
2,806.30
2,803.58
2,804.20
3,036.74
3,038.72
3,035.84
3,035.64
3,037.95
1,973.08
1,963.46
1,855.91
1,961.07
1,858.15
2,196.97
2,192.51
2,197.09
2,191.95
2,209.20
2,913.94
2,910.21
2,906.90
2,906.87

2,915.43
2,095.98
2,059.14
2,058.95
2,059.78
2,058.11
2,239.65
2,225.20
2,304.22
2,229.71
2,231.01
2,678.25
2,681.17
2,680.46
2,685.70
2,689.05
2,473.62
2,448.70
2,447.99
2,469.81
2,477.24
2,417.09
2,395.01
2,396.02
2,420.67
2,381.36
2,646.18
2,671.34
2,679.40
2,648.12
2,645.64
2,835.70
2,841.85
2,841.95
2,841.33
2,841.09
3,326.29
3,330.60
3,324.13
3,324.26
3,320.79
3,339.43
3,341.13
3,344.49
3,340.11
3,341.09
3,348.75
3,343.37
3,341.99
3,345.06
3,341.10
3,240.26
3,236.08
3,243.12
3,240.12

3,241.00
3,258.87
3,257.51
3,254.74
3,254.05
3,254.94
3,075.62
3,029.46
2,623.95
3,080.03
3,036.71
3,147.32
3,150.05
3,155.48
3,144.43
3,139.86
3,096.54
3,095.42
3,100.54
3,098.36
3,103.07
3,184.56
3,080.82
3,187.07
3,090.78
3,183.21
3,170.09
3,172.49
3,169.58
3,172.19
3,171.55
2,899.38
2,902.38
2,908.09
2,902.15
2,902.34
2,959.54
2,953.70
2,962.44
2,965.83
2,963.82
2,884.12
3,026.86
2,884.39
2,891.34
2,910.85
3,025.95
3,014.14
3,035.23
3,027.28
3,027.02
3,109.79
3,102.57
3,084.81
3,089.30

3,087.37
2,372.23
2,431.96
2,379.45
2,437.46
2,367.04
3,223.58
3,218.90
3,224.86
3,228.16
3,225.95
3,185.23
3,181.23
3,182.00
3,180.29
3,175.52
2,681.11
2,683.04
2,681.14
2,679.84
2,680.23
2,726.21
2,724.10
2,723.41
2,724.29
2,724.20
2,896.56
2,518.35
2,890.86
2,890.87
2,887.38
2,871.59
2,893.40
2,869.50
2,861.13
2,858.70
2,188.25
2,173.48
2,172.44
2,253.00
2,185.71
3,001.40
2,999.06
3,002.66
3,005.60
3,007.81
2,905.71
2,902.98
2,906.17
2,903.19
2,909.83
3,030.60
3,058.06
3,083.02
3,063.08

3,045.75
2,928.63
2,947.03
2,949.21
2,948.37
2,972.31
2,978.06
2,960.76
2,980.13
2,980.30
2,982.44
3,814.38
3,812.33
3,814.06
3,842.12
3,840.13
3,590.02
3,594.18
3,589.44
3,586.29
3,591.99
3,064.79
3,092.67
3,063.73
3,076.86
3,060.68
2 454.06
2 455.75
2 458.77
2 462.44
2 462.33
2 512.36
2 513.99
2 515.22
2 518.53
2 533.81
2 212.90
2 219.46
2 220.00
2 222.09
2 227.14
2136,58
2140,80
2156,04
2147,86
2160,44
2184,23
2184,53
2186,56
2189,74
2190,37
2 885.78
2 916.84
2 903.12

2 922.17
2 896.82
2,793.04
2,666.75
2,671.40
2,671.40
2,671.40
2 647.32
2 647.32
2 678.93
2 678.93
2 651.64
2 407.14
2 414.24
2 420.67
2 426.73
2 426.73
2 400.98
2 438.90
2 438.50
2 458.42
2 458.42
2 924.15
2 924.15
2 947.33
2 926.77
2 926.77
2,605.28
2,516.59
2,586.35
2,493.39
2,497.34
2 227.66
2 227.66
2 241.41
2 225.39
2 205.71
3 017.29
3 017.49
3 041.64
3 061.59
3 010.07
2 412.90
2 412.90
2 399.58
2 411.20
2 403.12
2 925.03
2 941.91
2 921.07
2 944.87
2 936.70
2,979.62
2,991.48

2,991.48
2,995.91
3,003.89
2 765.97
2 796.35
2 802.06
2 788.72
2 814.07
3 445.23
3 388.28
3 388.28
3 393.02
3 393.02
3 153.22
3 153.22
3 159.98
3 173.82
3 173.82
3 094.95
3 138.96
3 144.68
3 145.39
3 147.83
2 618.63
2 647.61
2 620.80
2 622.50
2 628.07
3 151.85
3 153.93
3 154.81
3 162.19
3 161.32
3028,82
3032,91
3034,74
3038,94
3039,72
2184,23
2184,55
2186,64
2189,69
2190,34
3,174.80
3,282.76
3,282.76
3,282.76
3,282.76
3,015.54
3,042.17
3,193.61
3,182.13
3,192.21
2 576.92

2 568.99
2 576.92
2 577.94
2 584.31
2 514.28
2 515.88
2 509.69
2 520.73
2 530.35
2,430.52
2,410.55
2,342.15
2,440.77
2,458.73
2 494.94
2 486.71
2 565.62
2 565.62
2 565.62
2 782.70
2 782.70
2 790.50
2 796.49
2 801.94
2 872.70
2 877.09
2 872.70
2 884.06
2 890.04
3 053.26
3 053.26
3 058.95
3 058.95
3 071.35
2,899.22
2,891.72
2,914.59
2,903.07
2,925.94
2 802.92
2 812.48
2 791.50
2 805.56
2 797.27
3 071.06
3 077.35
3 073.80
3 084.43
3 090.12
3 074.17
3 074.17
3 080.59
3 085.23
3 089.49
3 171.63

3 179.03
3 164.01
3 109.83
3 109.83
2,650.74
2,693.01
2,693.01
2,654.21
2,681.56
2 801.89
2 796.79
2 844.34
2 793.49
2 848.89
3 280.51
3 266.56
3 266.56
3 274.18
3 280.48
3 007.04
2 982.79
2 996.23
2 994.21
3 001.83
3 192.81
3 192.70
3 197.90
3 199.63
3 202.89
3270,17
3270,65
3262,80
3265,02
3270,09
3322,30
3324,85
3329,13
3330,45
3334,00
3264,69
3269,95
3271,40
3278,01
3267,80
3218,17
3220,60
3225,12
3228,89
3244,43
2725,39
2758,84
2766,38
2769,01
2765,85
2792,28

2790,22
2955,23
2797,96
2800,02
3233,93
3236,96
3240,70
3242,04
3246,01
2980,78
2982,05
2987,42
2992,11
2989,83
3083,05
3069,63
3013,78
3095,41
3093,49
3,240.77
3,233.44
3,261.05
3,358.83
3,358.83
3,063.91
3,053.62
3,159.34
3,156.32
3,156.32
2746,02
2789,95
2773,92
2782,65
2753,49
2524,19
2682,36
2648,32
2675,50
2602,88
2404,64
2408,62
2424,01
2413,39
2412,79
2853,66
2671,13
2670,98
2672,76
2861,94
2346,72
2348,27
2350,54
2353,36
2354,16
2512,58

2565,27
2566,54
2517,30
2518,44
3122,76
3126,77
3129,18
3130,55
3134,00
3256,71
3270,23
3260,32
3263,58
3261,58
2902,20
2907,66
2908,21
2911,86
2913,06
2 654.87
2 675.50
2 649.15
2 667.35
2 653.79
3,277.58
3,276.64
3,203.68
3,278.50
3,207.40
2819,43
2869,99
2823,11
2874,50
2786,28
3199,69
3204,78
3208,55
3139,18
3210,95
2019,18
2019,28
2020,39
2021,36
2023,70
2,098.71
2,035.27
2,013.85
2,096.48
2,113.50
1,796.86
1,852.77
1,798.52
1,705.22
1,787.16
2803,65

2803,70
2806,00
2809,53
2810,49
2902,10
2906,41
2850,21
2806,08
2808,85
2880,53
2873,36
2665,68
2801,70
2802,30
2,910.20
3,011.08
2,740.22
2,784.86
2,759.40
2,441.00
2,442.12
2,553.17
2,415.46
2,455.29
3257,44
3271,28
3263,82
3264,59
3267,41
3167,14
3155,89
3174,00
3175,43
3165,68
2547,09
2392,01
2561,46
2559,31
2522,16
2,975.65
2,910.14
3,061.40
2,952.45
2,982.88
2,918.72
2,937.03
2,909.31
2,912.08
2,919.38
3,436.41
3,424.62
3,422.47
3,430.04
3,426.74
2,884.03

3,038.17
3,042.51
3,043.02
3,043.09
2,908.95
2,915.02
2,908.75
2,915.39
2,911.82
3,182.00
3,109.71
3,077.27
3,175.88
3,088.69
3,158.34
3,161.22
3,162.25
3,120.19
3,163.45
3,466.83
3,489.12
3,470.83
3,492.27
3,494.40
3,403.05
3,408.19
3,402.96
3,406.26
3,404.97
3,316.49
3,310.07
3,312.95
3,312.59
3,330.94
3,101.35
3,104.68
3,115.03
3,188.40
3,093.92
3,366.79
3,394.50
3,368.51
3,367.74
3,365.10
3,093.41
3,091.96
3,111.22
3,096.14
3,094.99
3,389.21
3,394.35
3,353.75
3,338.50
3,414.58
3,189.63

3,153.05
3,196.44
3,257.39
3,189.58
3,001.49
3,032.33
3,036.05
3,010.68
3,003.66
3,124.42
3,124.22
3,123.18
3,123.73
3,122.56
2,979.97
2,986.51
2,978.11
2,906.41
2,980.05
2,985.84
3,078.52
2,982.78
3,083.78
2,969.97
3,313.45
3,314.95
3,321.08
3,346.63
3,309.66
3,473.20
3,503.32
3,500.25
3,472.95
3,505.01
3,301.90
3,323.02
3,307.27
3,320.10
3,298.99
3,347.59
3,344.78
3,350.06
3,344.38
3,345.91
3,415.22
3,434.65
3,438.09
3,421.15
3,436.54
3,076.37
3,064.28
3,066.07
3,084.25
3,057.82
3,162.00

3,152.39
3,158.54
3,172.58
3,152.02
3,355.75
3,353.25
3,349.32
3,351.35
3,355.00
3,496.61
3,492.84
3,494.22
3,494.20
3,492.66
3,188.96
3,188.32
3,185.21
3,186.44
3,185.79
3,189.13
3,189.64
3,188.93
3,191.12
3,193.40

APPENDIX 2

Volume 21 | Issue 4 Article 7

2022

Impact of voids and backfill on seismic wave velocity-preliminary results

Author(s) ORCID Identifier:
Zarina Mukhamedyarova: 0000-0002-3056-8110
Fidelis Suorineni: 0000-0002-7356-5446
Temirlan Aldubay: 0000-0002-1728-7920
Gylym Sapinov: 0000-0002-1853-6810

Recommended Citation

Mukhamedyarova, Zarina; Suorineni, Fidelis; Aldubay, Temirlan; and Sapinov, Gylym (2022) "Impact of voids and backfill on seismic wave velocity-preliminary results," *Journal of Sustainable Mining*: Vol. 21 : Iss. 4 , Article 7.
Available at: https://doi.org/10.46873/2300-3960.1370

Impact of voids and backfill on seismic wave velocity-preliminary results

Abstract

In this study, laboratory experiments were conducted on discrete physical models that mimic mining effects to better understand the impact of continuous changes in mining environments on seismic wave velocities. The discrete physical models are represented by concrete and granite cubic samples of different sizes with holes of different diameters filled and unfilled with cemented sand backfill of different cement-sand content ratios. The hole diameters range from 0 to 150 mm in block sizes ranging from 150 mm to 450 mm in increments of 75 mm. The increasing hole size mimics increasing extraction in the mine with time. Cemented sand fills at cement contents ranging from 0 to 20% are used to fill the voids after testing them empty and retesting the same at different backfill cured ages. The SAEU3H AE eight-channel system is used in the study. Preliminarily results show that the impact of continuous changes in mining environments significantly affects the seismic wave velocities. The impact of voids and their contents on the seismic wave velocity depends on the sensor location relative to source and void, and it backfills cement content with time.

Keywords

seismic event source location accuracy, constantly changing mine conditions, real-time seismic wave velocity, void and cemented sand backfill effect with time

Impact of Voids and Backfill on Seismic Wave Velocity-Preliminary Results

Zarina Mukhamedyarova [a], Fidelis Suorineni [a,*], Temirlan Aldubay [a], Gylym Sapinov [b]

[a] Nazarbayev University, School of Mining and Geosciences, Nur-Sultan, Kazakhstan
[b] Karaganda Technical University, Department of Development of Mineral Deposits, Karaganda, Kazakhstan

Abstract

In this study, laboratory experiments were conducted on discrete physical models that mimic mining effects to better understand the impact of continuous changes in mining environments on seismic wave velocities. The discrete physical models are represented by concrete and granite cubic samples of different sizes with holes of different diameters filled and unfilled with cemented sand backfill of different cement-sand content ratios. The hole diameters range from 0 to 150 mm in block sizes ranging from 150 mm to 450 mm in increments of 75 mm. The increasing hole size mimics increasing extraction in the mine with time. Cemented sand fills at cement contents ranging from 0 to 20% are used to fill the voids after testing them empty and retesting the same at different backfill cured ages. The SAEU3H AE eight-channel system is used in the study. Preliminarily results show that the impact of continuous changes in mining environments significantly affects the seismic wave velocities. The impact of voids and their contents on the seismic wave velocity depends on the sensor location relative to source and void, and it backfills cement content with time.

Keywords: source location, changing ground condition, seismic wave velocity, discrete physical modelling

1. Introduction

With the increasing depletion and production of mineral resources, underground mines are going deeper worldwide. High in situ stresses coupled with a complex geological environment result in rock burst, rock mass failure, and excavation deformations [1–5].

Microseismic monitoring systems are integral parts of deep underground mining. These systems help to understand mining-induced seismicity to mitigate their potential hazards in predicted locations. However, microseismic monitoring system's accuracy in predicting the event source location depends on the input velocity in the event source calculation [6].

Recent research has identified that wave velocities in rock masses in underground mining are not constant as previously often assumed in seismic monitoring systems source location algorithms. Rock masses in mining environments are continuously degraded because of mining. Hence the use of 3D velocity models based on 3D ray tracing in heterogeneous media that consider the presence of voids from mining activities is actively researched [7]. This approach shows some improvements in the accuracy of seismic event source locations. However, seismic wave velocity changes are not only due to the introduction of voids but also several other sources of rock mass degradation, including stress-induced fracturing and the state of the voids created, including their constantly changing size, shapes, and contents. Laboratory study of the seismic wave propagation through rock samples tracks properties such as sample heterogeneity and fracture intensity [8].

Abbreviations: AE, acoustic emission; UCS, uniaxial compressive strength; AET, acoustic emission technique; ASTM C-109 C, standard Test Method for Compressive Strength of Hydraulic Cement Mortars; ISRM, International Society for Rock Mechanics; , friction coefficient; ω_o, resonant frequency; m, mass; , seismic wave attenuation; Q, quality factor; CCVM, continuously changing velocity model; φ, diameter; CAMIRO, Canada Mining Innovation Research Organization,

Received 17 March 2022; revised 25 July 2022; accepted 27 July 2022.
Available online 23 November 2022

* Corresponding author.
E-mail address: fidelis.suorineni@nu.edu.kz (F. Suorineni).

https://doi.org/10.46873/2300-3960.1370

Seismic wave propagation is highly affected by rock mass structure and fluid content. Many pieces of research in recent years have shown that rock mass micro-fracturing is the critical factor affecting seismic wave velocity and attenuation. Therefore, it is crucial to understand the effect of attenuation on wave velocity due to rock mass fracturing [9].

This paper presents a novel approach and preliminary research results aimed at predicting wave velocities in real-time in the constantly changing underground mining conditions. The underground mine is challenging to control, while the laboratory is a perfect controlled condition to simulate and study seismicity. The driving force and interest in this research are to find solutions to the rockburst problem in the mining industry to improve safety and productivity. The novelty of the research is the use of discrete physical models as analogs to mimic the changing ground conditions in underground mining to capture the impact on seismic wave velocity.

In the discrete physical modelling concept, rather than using a single block and changing its condition to reflect the constantly changing ground condition in mining environments (a physically challenging approach), separate individual blocks are used with each block representing a different stage in the mining process in time, structure, and geometry.

2. Materials and methods

To understand changes in seismic wave velocity in constantly changing mining conditions, laboratory physical models that mimic constantly changing underground mining conditions were developed. The novel approach of using discrete physical models to solve a rather complex problem was strategically developed and executed in the laboratory to enable fundamental factors governing seismic wave velocity changes to be captured. This approach overcomes the complex mining environment that is somewhat more problematic to control.

2.1. Physical laboratory models mimicking the continuously changing underground mine environment

Rock (granite) and concrete block samples were used as the discrete mine models. Sample material choice was based on rock homogeneity. Sample sizes varied between 150 mm and 450 mm cubes at 75 mm side length increments (Fig. 1).

For each cube size, one cube had no hole, while another had a hole in its centre of a diameter depending on the cube size to account for the cube boundary conditions. Hole diameters varied from 50 mm in the 150 mm cubes to 150 mm diameter in the 450 mm cube at increments of 25 mm, as shown in Table 1.

The increasing hole diameters mimicked the increasing extraction and the mine maturity with time. In principle, the increasing hole diameter in the blocks of increasing size represents the total amount of voids (sum of all voids in the mine with increasing maturity) in the mine with time.

In mining practice, voids such as stopes are usually filled with backfill of various types. To mimic backfilling, the holes in the blocks were subsequently filled with a backfill (Fig. 2) with different cement to sand ratios of 0, 5, 10, 15, and 20%. The 0% cement content backfill was tested dry and wet. Each 5−20% cement backfill was cured for 8 h, 1 day, 7 days, 14 days, and 28 days and tested to account for curing time impact on seismic wave velocity.

Initially, samples with holes were tested empty to represent a mine without a backfill. In the following tests, the holes were filled with different cement to sand ratio backfills cured for 8 h, 1 day, 7 days, 14 days, and 28 days to represent a mine with different backfill types and ages. Testing after 28 days of curing was chosen since concrete gains 99% strength after 28 days [10].

Each cube was attached with eight sensors for the wave velocity determination tests, one of which was used as a source (pulse) and the other seven as receivers of the seismic wave arrival times at known coordinate locations based on established grids on each cube (Fig. 3).

2.2. Materials

Granite and concrete cubes and backfill were used in the tests. The following sections describe the details of these materials.

2.2.1. Granite cubes

The study involves laboratory experiments with homogeneous rock samples of granite. Sample homogeneity was the critical factor for the choice of rock type. The surfaces of the cubes must be polished to a tolerance of 1 mm, with each opposite face parallel to each other. The homogeneity and isotropy of the rock allowed for the results to be comparable. It was a challenge to prepare granite cubes in-house to meet these specifications. Hence, a professional stone vendor was used.

Ideally, it was planned to use only the granite cubes for the project. However, the cost of the

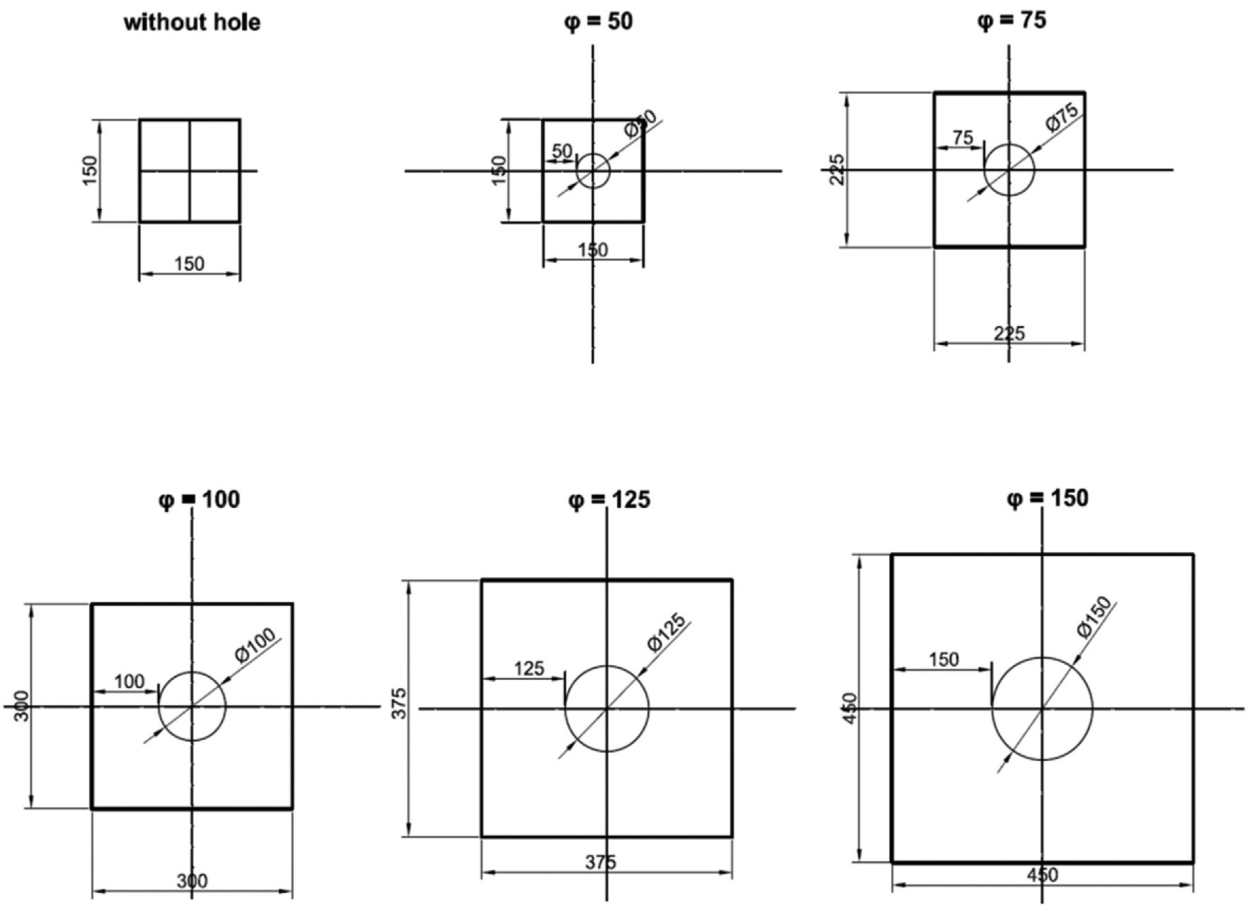

Fig. 1. Sample sizes varying between 150 and 450 mm cubes at 75 mm side length increments representing various stages of mining in time. Hole diameters represent increasing extraction with time.

granite cubes and the challenge of obtaining samples that were consistent in composition resulted in the use of synthetic rock in the form of concrete cubes.

2.2.2. Concrete cubes

The concrete cubes were moulded in the laboratory with a mixture of sand and cement to represent rock. A suitable cement to sand ratio was established through the ASTM C-109 C standard [11]. The cubes were used after curing for 28 days. Material proportions for standard mortars according to ASTM C-109 C standard:

Table 1. Block sizes and hole diameters.

Cube size (mm)	Material type	Hole diameter (mm)
150	concrete	0 (no hole)
150	concrete	50
225	concrete	0 (no hole)
225	concrete	75
300	granite	0 (no hole)
300	granite	100
375	concrete	0 (no hole)
375	concrete	125
450	concrete	0 (no hole)
450	concrete	150

Fig. 2. Granite rock samples with a cube size of 300 mm with and without holes (hole diameter is 100 mm).

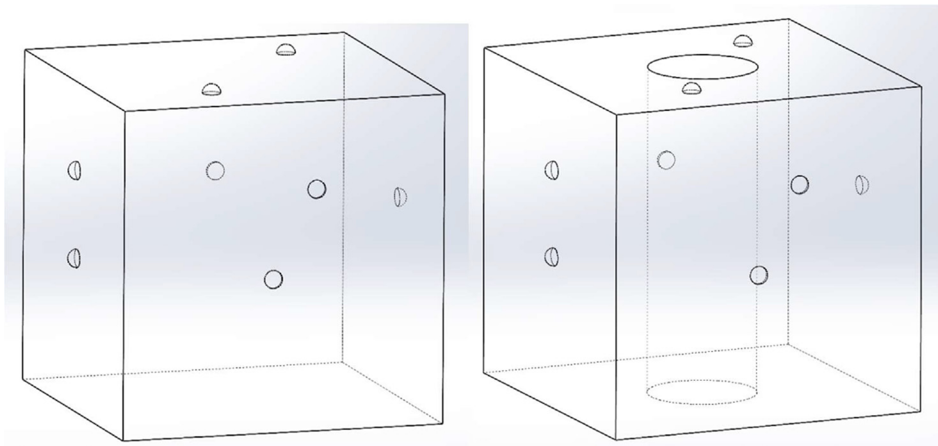

Fig. 3. Location of sensors on cubes a) without the hole and b) with the hole.

- sand to cement ratio is 2.75,
- the water to cement ratio is 0.485.

After moulding, the mixture was vibrated for 4 min for compaction and release of excess air. Samples of 37 mm diameter and 74 mm height were prepared from the same mixture for the UCS test to ensure all blocks were similar in strength as a control measure.

The cube sizes varied between 150 and 450 mm to account for boundary conditions' effect when the holes are introduced and represent increasing mine maturity with time. The cubes were with and without holes. Each hole was in the centre and through the cube's height.

2.2.3. Backfill

The holes in the blocks were filled with different cement to sand ratios to study void content's impact on wave velocity. Backfill ratios of 0% cement (100% dry sand), 0% cement (water-saturated sand), 5% cement, 10% cement 15% cement, and 20% cement content were used. The different mix ratios represent the different backfill mixes commonly used in the mining industry. Each backfill type was cured to various ages (8 h, one day, seven days, 14 days, and 28 days). ASTM C-109 C standard was used to establish the ratio of water to dry components, including sand and cement. Clay particles, large fragments, and organic materials were removed through a sieving procedure performed using the AS 200 basic vibratory sieve shaker. All fragments more than 4 mm and less than 0.002 mm were removed as oversized particles and clays, respectively.

2.3. Equipment and testing methods

Acoustic emission testing (AET) is a technique used for the non-destructive testing of materials. AET can track the changes in material behaviour. This technique allows one to observe crack propagations appearing deep inside a material.

Different terms are used to define instabilities or "events" caused by rock fracturing at different scales, as shown in Fig. 4.

CAMIRO [12] notes that in mine seismology, large events in the seismic range are often called mine tremors or mine-induced seismic events. Smaller events, often located close to active mine stopes, are

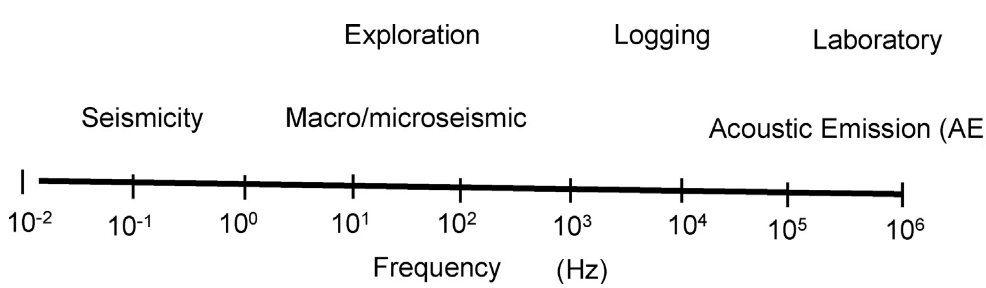

Fig. 4. Monitoring frequency ranges of earthquakes, macro/microseismic activity, acoustic emission, and associated fields of study/research domains [12].

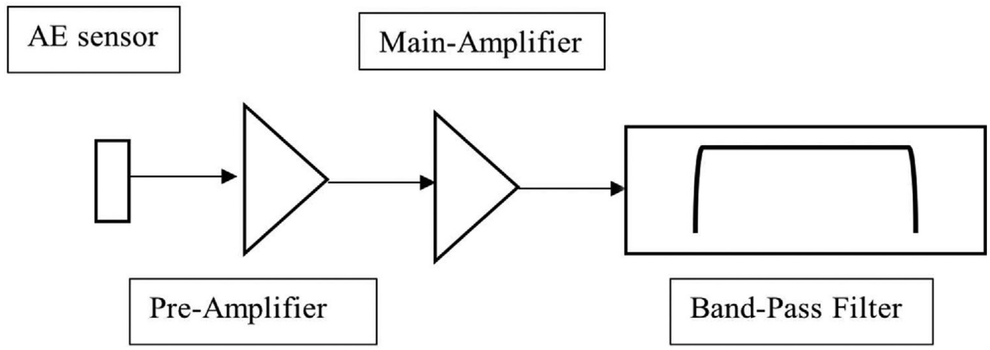

Fig. 5. AE detection system [15].

usually defined as "microseismic events" due to their much smaller magnitudes. At the lowest end of the magnitude spectrum, "acoustic emission" is often used to indicate high-frequency emissions or "rock noise" monitored in rock samples under loading in a laboratory or observed in localized failure areas within a mine. It is known that the boundaries between these different categories are not very well defined, and many authors such as Dong et al. [13] use the term "acoustic emission/microseismic" or simply "AE/MS" to refer to the latter two categories in a general manner. Therefore, microseismicity during the failure process while loading material is very similar to acoustic emission (AE). Acoustic emissions are characterized as the energy released in stressed materials. The release of localized strain energy can be due to fracturing and can be recorded on the material's surface by sensors. Therefore, AET is compared with seismological techniques since they have similar concepts but different scales.

AET has been used to track rock mass defects at the very early stage prior to complete failure. The main difference from other non-destructive tests is the type of data received and the application mechanism. For instance, in the ultrasound method, artificially created signal and source-receiver are used to determine the geometric shape of a defect in a sample. In contrast, AET can determine elastic waves going through fractures in a sample [14]. Compared to other non-destructive methods, AET requires only a few sensors under certain conditions that can have signals passing a trigger level threshold. AET does not need access to all sides of the sample, as is required for all other methods of through-transmission [14].

Fig. 5 illustrates a standard AE detection system. AE sensors transform dynamic motions into electric signals and detect AE waves at a material's surface. A preamplifier and main amplifier are used to increase weak AE signals and could provide more than 1000 times gain.

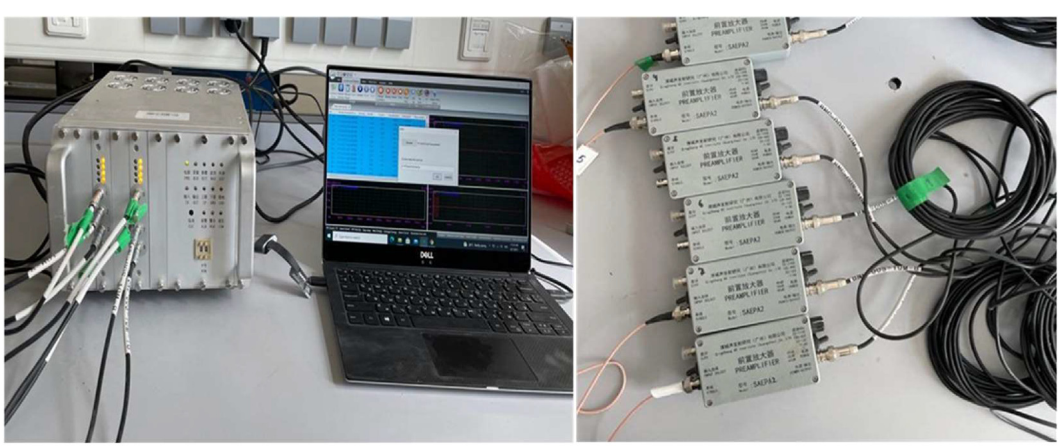

(a) AE data acquisition modules, chassis with front and rear panels, optional network communication module, laptop

(b) Preamplifiers and cables

Fig. 6. AE system and accessories.

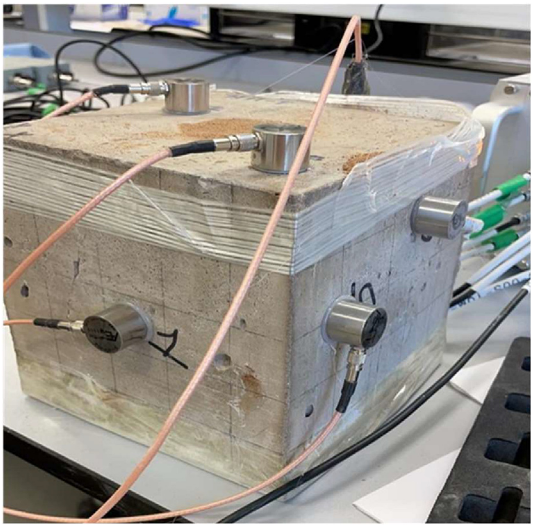

Fig. 7. AE sensors attached to the rock sample.

In Fig. 5, elastic waves generated by the source propagate in the material and are detected by AE sensors [15].

The AE method has been used to study mine seismicity by Dong and Li [16], Ge et al. [17], Kennet et al. [18], and Nivesrangsan et al. [19]. The AE system and accessories are shown in Fig. 6. In this study, the SAEU3H AE system was used. The SAEU3H AE system is a multi-channel system that consists of AE data acquisition modules, chassis with front and rear panels, an optional network communication module, a laptop, eight sensors, preamplifiers, and cables (Fig. 6).

In the laboratory tests in this research, AE sensors were attached to the surface by hot glue, as shown in Fig. 7. Eight sensors were attached to each cube, with one sensor used as a source that generated a pulse, and the other seven sensors serving as receivers that received the pulse wave. The wave was generated as a pulse from sensor number 1 placed in the middle of the front view of the cube to enable waves to go through the hole.

The sensor used in the experiments for 150 mm, 225 mm, and 300 mm cube sizes is the SR150M high-frequency broadband AE sensor. The frequency range of the sensor is 60−400 kHz; peak sensitivity is > 75 dB. SRI150 sensor type was used for larger cubes of 375 mm and 450 mm. This sensor has a built-in preamplifier with a frequency range of 60−400 kHz and a sensitivity of 40 dB. This change in sensor type was necessitated by the fact that with the SR150M sensors, wave arrival times could not be detected at the receiving sensors due to seismic wave attenuation in inelastic materials such as rocks and concrete materials used in the study. Seismic waves attenuate with time and distance in inelastic

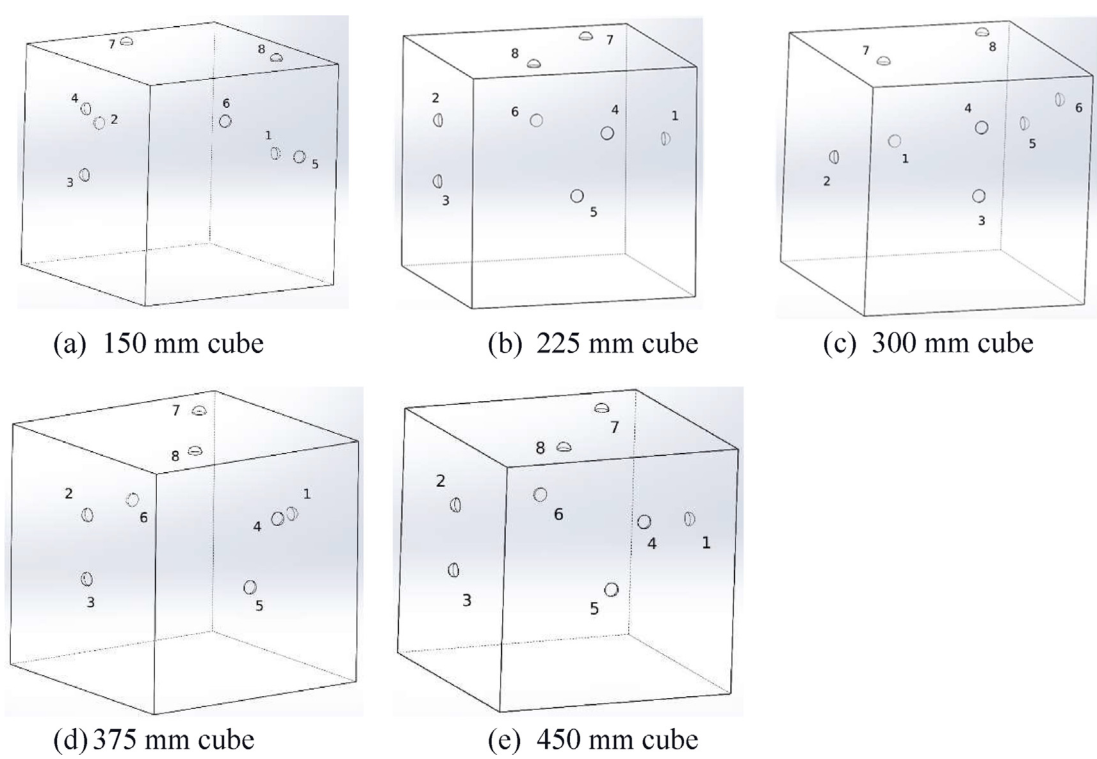

Fig. 8. Sensor positions on the various cube sizes without a hole.

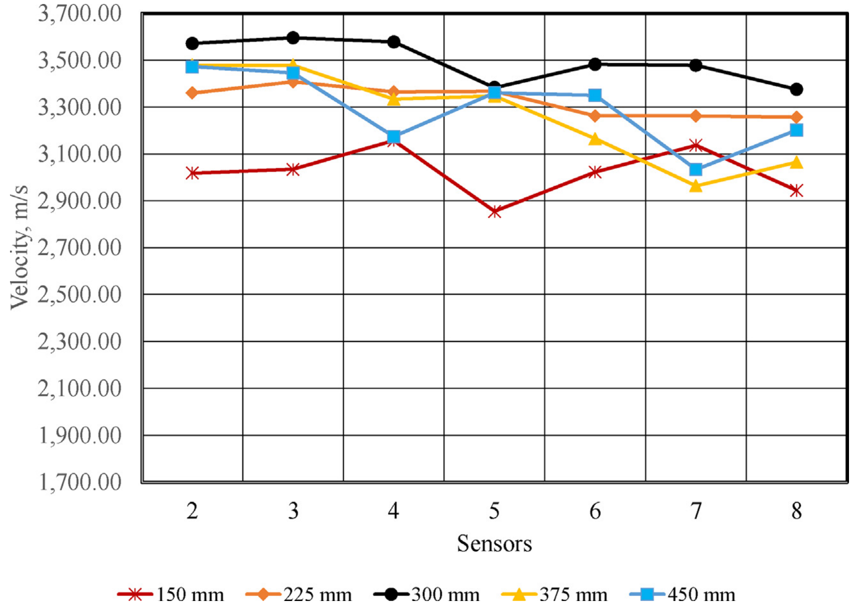

Fig. 9. Seismic wave velocities on concrete cubes without holes.

materials due to various inelastic energy loss mechanisms such as porosity, fractures and microscopic movements along mineral dislocations or shear heating at grain boundaries [20]. According to [20], seismic wave attenuation (∈) is often quantified using a quantity called the quality factor (Q) [Equation (1)].

$$\in = \frac{\gamma}{m\omega_o} = \frac{1}{2Q} \qquad (1)$$

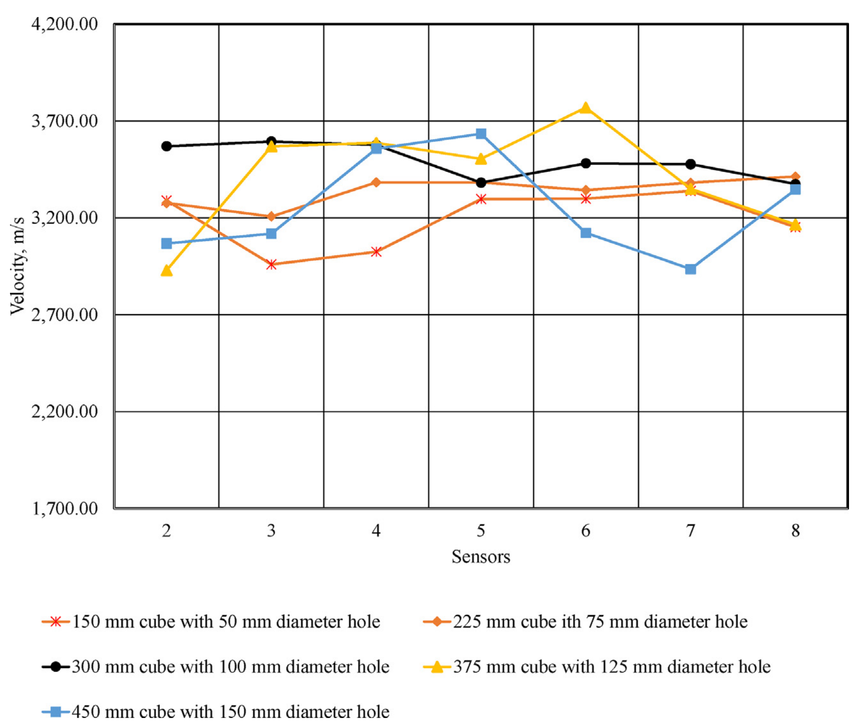

Fig. 10. Seismic wave velocities in blocks with holes of different diameters at sensor locations.

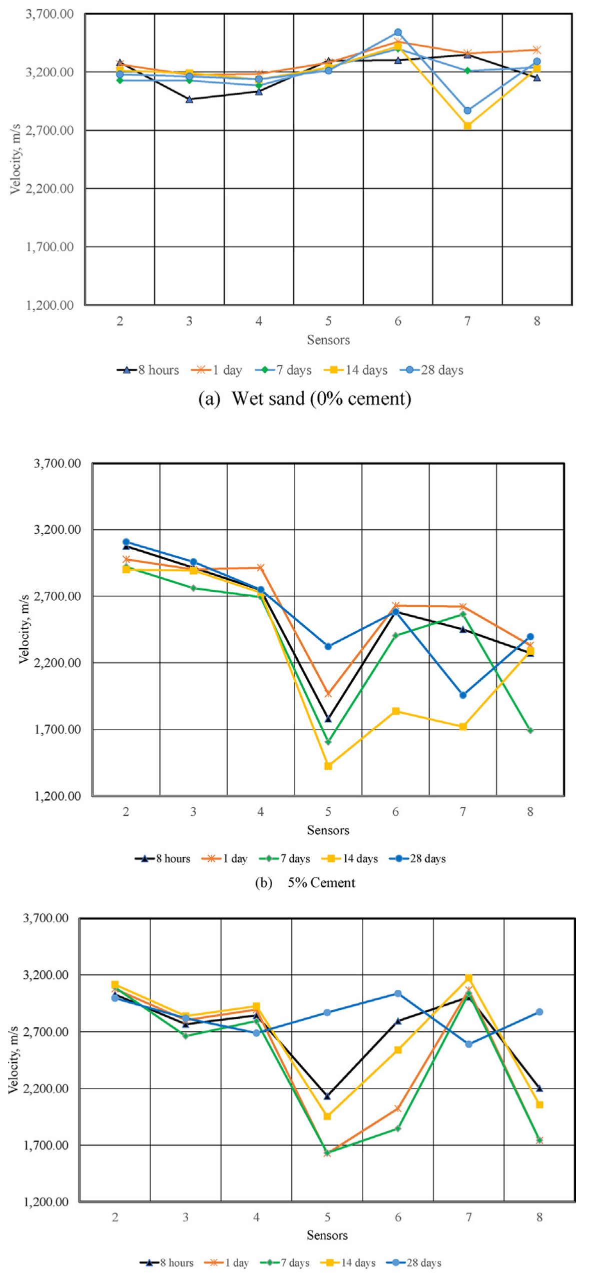

Fig. 11. Backfill effect on seismic wave velocity for 150 mm cube with 50 mm diameter hole (a) Wet sand – 0% cement (b) 5% cement (c) 20% cement backfill.

where γ = coefficient of friction, m = mass and ω_o = resonant frequency.

A low attenuation (high-quality factor Q) may indicate a tightly bound rock mass or one that can propagate a displacement pulse with little or no energy loss, thus reaching the free surface with nearly full strength, and vice versa. Hence, with the larger cubes and SR150M sensors, energy loss stopped the wave propagation before they reached the receiving sensors, therefore requiring a change to the SRI150 sensors. CAMIRO [12] notes that the properties of the rock mass affect the way seismic waves propagate through the medium. This influence is not restricted to the velocity of the waves but also includes the relative amplitude and frequency content of the signals referred to as signal degradation or attenuation. In a mining environment, seismic waves propagating through a host medium are affected by the rock type, backfill, voids, state of stress, and the type of structures (faults, shears, and joints) and their distribution.

2.4. Procedure of velocity calculation by AE equipment

Hedley [21] stated that seismic monitoring systems basically measure the arrival times of the seismic waves, and then, knowing the coordinates of the sensors and assuming a uniform velocity at which the seismic signals travel through the rock, an estimate of the source location can be determined. There are two general methods of source location based on the arrival times of the *P*-waves alone or the arrival times of both the *P*- and *S*-waves [21]. In this research, we used the direct method of source locations by Blake, Leighton, and Duvall [22] and discussed in Hedley [21].

Data derived from the AE tests provided the arrival time of the wave at each sensor. Knowing each sensor's arrival times and location coordinates, the distances from the pulse source to the receiving sensor locations were calculated. The corresponding seismic wave velocities were calculated by dividing the distance from the source to each sensor by the wave arrival time at the sensor.

The use of the AE procedure to determine the arrival time of the wave generated by the source sensor pulse includes the following steps:

1. Construction of coordinate system with grid and coordinate values on the surfaces of blocks.
2. Sensor placement around the samples at known coordinate points; the test should include at least four sensors along the different lines.
3. One of the eight sensors used as a source, while the other sensors were receivers.
4. The eight-channel SAEU3H acoustic emission system was used to collect source location and arrival times. Each cube with a drill hole had a control sample without a hole.

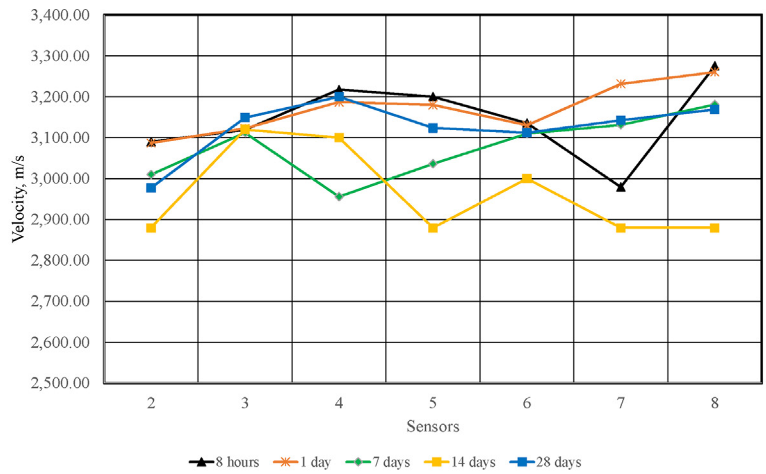

(a) 5% Cement

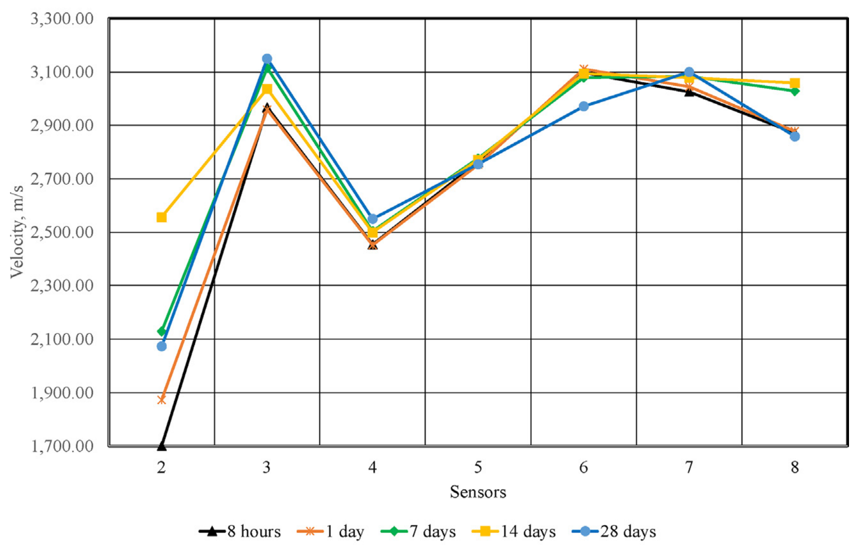

(b) 15% Cement

Fig. 12. Backfill effect on seismic wave velocity for 225 mm concrete cube with 75 mm diameter hole (a) 5% cement (b) 15% cement.

5. Based on the coordinates and wave arrival times, the wave velocity to each sensor was calculated.

Figure 8 shows the sensor positions in the various block sizes used. These blocks are without the central holes representing volumes of extraction with increasing mine life.

Following the procedure developed by Blake, Leighton, and Duval [22], the distance between the source and receiving sensors was calculated according to Equation (1):

$$d_i = \sqrt{(x_i - x_1)^2 + (y_i - y_1^2) + (z_i - z_1)^2} \quad (2)$$

where $i = 2, 3, 4, 5, 6, 7, 8$ and x, y, z – sensor coordinates.

Wave velocity was calculated by the following equation, by dividing the distance of each sensor from the source by its corresponding wave arrival time:

$$v = \frac{d_i}{\Delta t} \quad (3)$$

In Equation (3) d_i is the distance of each sensor 2, 3, 4, 5, 6, 7, 8 from the source at x_1, y_1, z_1, and Δt is the wave arrival time from the source.

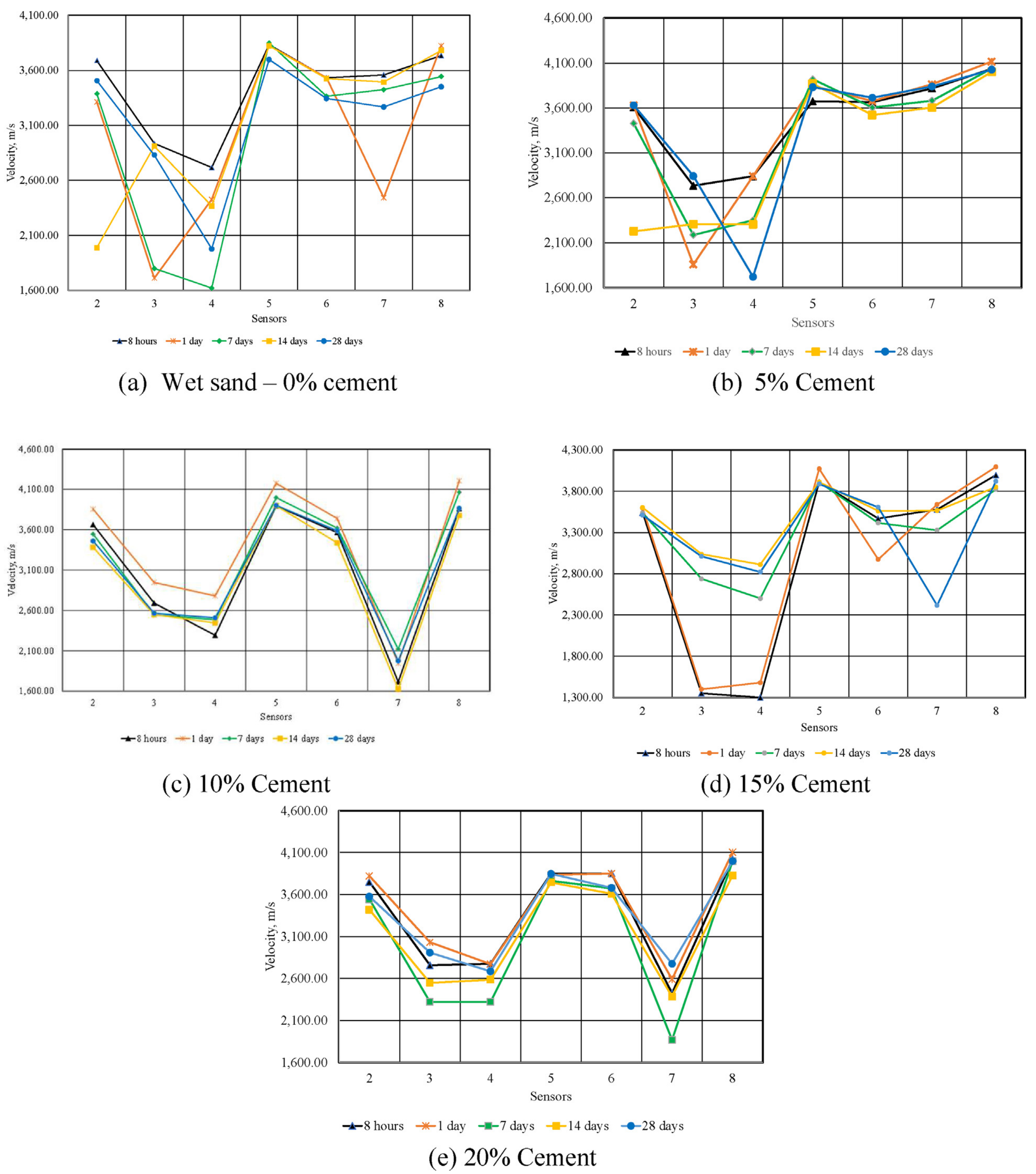

Fig. 13. Backfill effect on seismic wave velocity for 300 mm granite cube with 100 mm diameter hole (a) Wet sand – 0% cement (b) 5% cement (c) 10% cement (d) 15% cement (e) 20% cement.

The procedure described for the distance calculations assumes the material is homogeneous and without voids or fractures to affect the wave path (i.e., the procedure assumes the so-called straight ray path concept [23,24].

3. Results and discussion

3.1. Size effect on seismic wave velocity

The primary purpose of the research was to see the effect of size, voids, and different backfill content

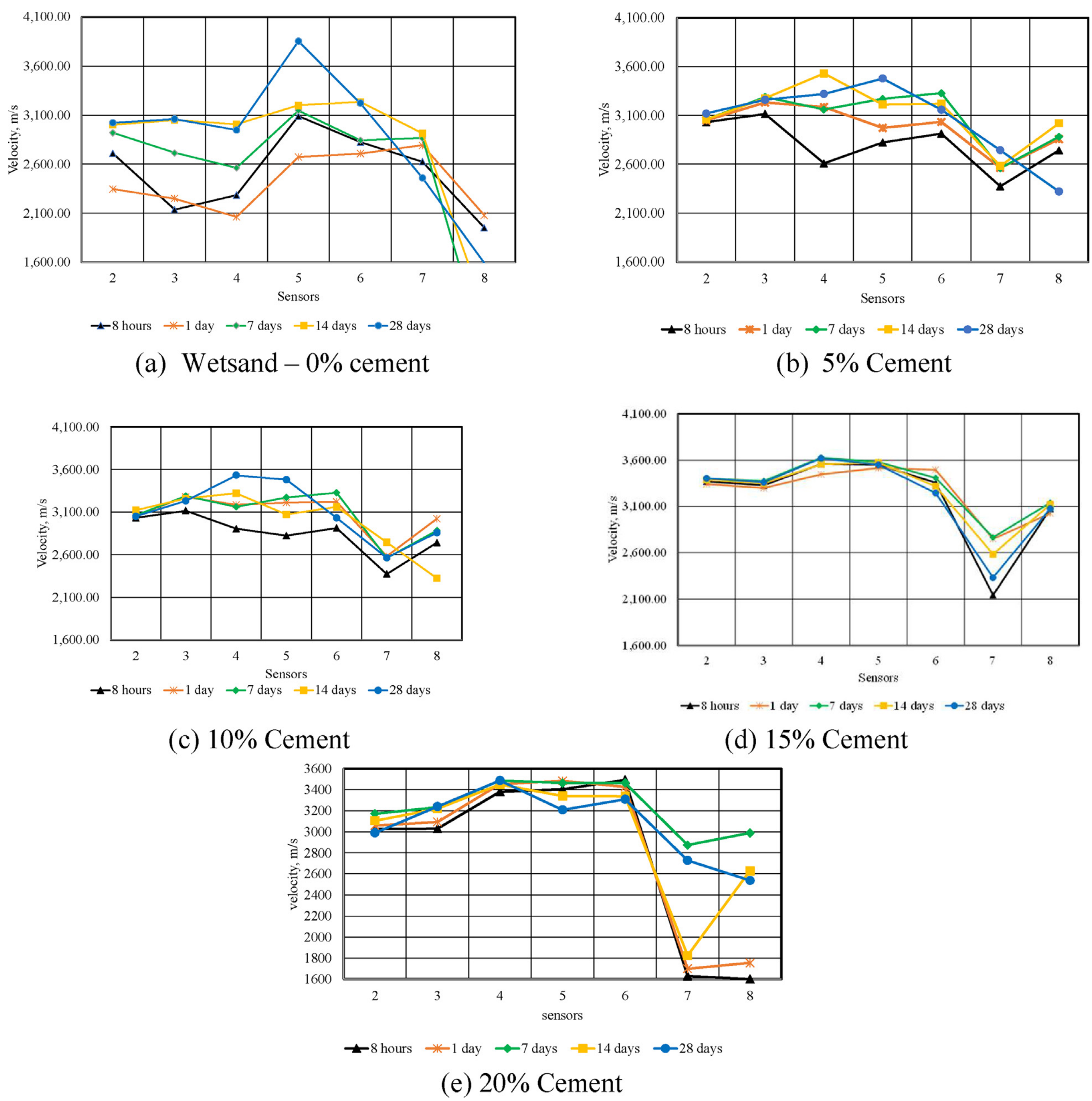

Fig. 14. Backfill effect on seismic wave velocity for 375 mm concrete cube with 125 mm diameter hole (a) wet sand (b) 5% cement (c) 10% cement (d) 15% cement (e) 20% cement backfill.

and age on seismic wave velocity. AE tests were repeated five times for each cubic sample. Fig. 9 shows seismic wave velocities for cubes of all sizes without holes. An average of 5 velocity measurements was used at each sensor to plot the graph. Based on the test results shown in Fig. 9, except at sensor 7, there is no significant difference in seismic wave velocities with increasing cube size. The range of wave velocities of between 3000–3500 m/s is within the values of 3160–3818 m/s with a standard deviation of 146 m/s determined by Lee and Oh [25]. The smaller cube of 150 mm diameter shows the lowest velocities at the sensors with the least velocity of 2855 m/s at sensor 5. The small variations in the velocities for all five cubes could be from the concrete mix quality variations and possible errors in the determination of the wave arrival times.

3.2. Hole effect on seismic wave velocity

Fig. 10 shows the results of AE tests on concrete cubes with empty holes. The hole diameter

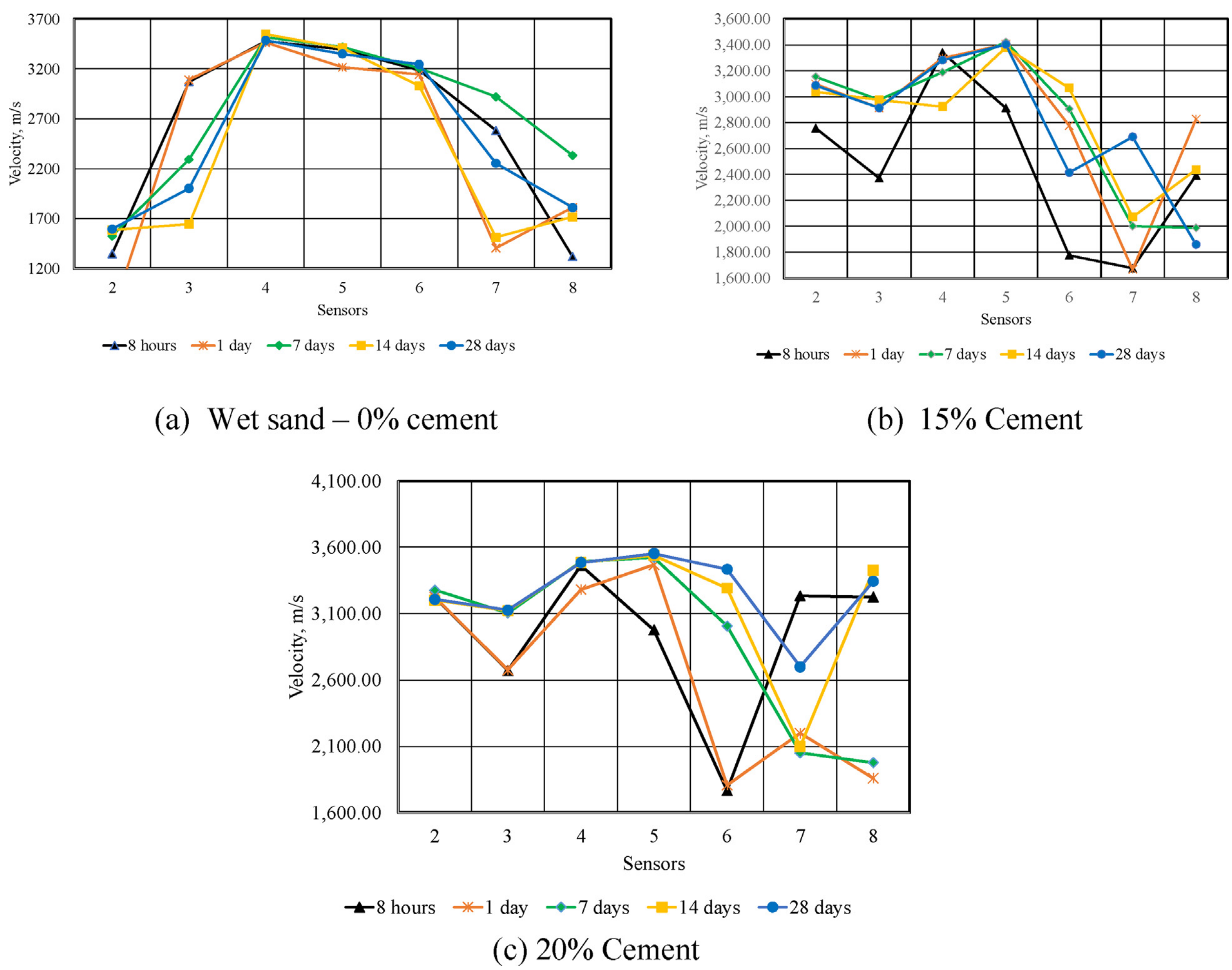

Fig. 15. Backfill effect on seismic wave velocity for 450 mm concrete cube with 150 mm diameter hole (a) wet sand (b) 15% cement (c) 20% cement backfill.

increases with increasing cube size. According to the test results in Fig. 10, the velocities in the 150-, 225-, 300- and 375-mm cubes with holes of 50-, 75-, 100- and 125-mm diameters are not significantly affected compared with their equivalent cubes without holes. For these cubes, the velocities at the sensors range between 3033 and 3577 m/s. The cube size of 450 mm with a hole diameter of 150 mm shows a significant change in the seismic wave velocity at sensors 2, 3, 6 and 7. Sensors 4 and 5 show relatively higher velocities of 3558 and 3635 m/s, respectively, implying that they are not affected by the void. Sensors 6 and 7 show the most significant drop in velocities of almost 1500 m/s from the peak value in the 450 mm cube with a hole diameter of 150 mm. The significant drop in velocities is caused by the sensors' location across the hole from the source sensor. Wave energy attenuation is high due to the empty 150 mm diameter hole and the effect of ray path tracing that is ignored in the distance calculation, resulting in longer arrival time and, therefore, lower velocities. The results show that ray paths being assumed straight in this case were not significantly affected by the holes in the smaller cubes but were impacted by the hole diameter of 150 mm in the 450 mm cube with the severity depending on the sensor location relative to the source and hole.

3.3. Backfill effect on seismic wave velocity

The effect of backfill at different ages in the holes of the blocks can be related to the effect of a layered velocity model as opposed to the uniform velocity model (straight ray paths from source) according to the Fermat principle. In the layered velocity model, the ray path from the source is a polyline with an inflection at the interface of the layers [23]. Based on these principles, waves travelling in the concrete through the backfill material will have their velocities impacted.

Fig.11 shows seismic wave velocity results for each backfill type at cured age for wet sand (0% cement), 5% and 20% cement, respectively, for a cube size of 150 mm with a hole diameter of 50 mm. Based on the positions of sensors 2, 3, 4 and 5 in Fig. 11a for wet sand, the ray paths of these sensors are not impacted by the backfill in the void, while the ray paths from the source to sensor 7 are significantly impacted by the void and its contents in days 14 and 28 when the wet sand would have been dry. For the higher cement content backfill (15% and 20% cement), there is less impact on the wave velocity at 28 days of curing time, as can be seen in Fig. 11c. In Fig. 11b, there is a general decrease in velocities for all curing times at sensors 5 to 8 that is attributed to the void and its content and the locations of these sensors relative to the source. Fig. 11c, with a backfill cement content of 20%, shows the significant impact of the void and its content on the pulse wave velocities at sensors 5, 6 and 8 because of their relative locations to the void and source. It is reasonable to say that, even though straight ray paths were assumed in the pulse wave velocity calculations, the impact of the void and its contents is visible without ray tracing but could be better with ray tracing.

Fig. 12 shows the impact of the void and backfill effect on wave velocities at the receiving sensors on the 225 mm cube with 5% and 15% cement content backfill in the void. In Fig. 12a, for 5% cement content backfill, the wave velocities for all the cured times fall within the range of 2879–3200 m/s, like in a homogeneous material. The pulse wave velocity is significantly affected from the source to the receiving sensors 2 and 4 in Fig. 12b because of the void and backfill, as can be seen in Fig. 12a (wet sand).

Fig. 13 shows the AE test results for the 300 mm granite cube with different cement content backfills at different ages. Fig. 13 a, c and e show drops in velocities at sensors 3, 4 and 7, which reflect their relative locations to the source and void. The velocities at the other sensors are not impacted. This implies that their ray paths were not affected by the void. Velocities at sensors 2, 5, 6 and 8 are not impacted and fall in the range of 3600–4100 m/s.

According to Fig. 14, sensors 7 and 8 are significantly affected by the void of 125 mm diameter and changes in backfill properties with time in the 375 mm cube. The two sensors are located at the top of the cube near the void, and wave paths to these sensors are impacted by the void and its contents to different degrees.

Fig. 15 shows the results of the impact of backfilled cement content with time on wave velocities at sensors attached to the 450 mm cubes with a void of 150 mm diameter at different locations relative to the source and void. In Fig. 15a for wet sand with 0% cement, the velocities show lower values at sensors 2, 3, 7 and 8. This is due to the sensor locations relative to the void and source.

4. Conclusions

Input velocity models in seismic monitoring systems algorithms for seismic event source locations determination affect the accuracy of the source locations in underground mining environments. Uniform velocity models assume rock masses are homogeneous. Layered velocity models, on the other hand, ignore the effect of other factors, such as voids and fractures. Recent works using 3D Velocity models and ray path tracing have shown significant improvements to seismic event source location accuracies.

Establishing a reliable velocity model in mining is a challenge, as multiple rock types are encountered, and the rock mass conditions are constantly changing due to the creation of voids that may or may not be backfilled, and stress changes that cause continuous fracturing of the rock mass. The consequence of the changing ground condition, coupled with the existence of multiple rock types and backfills, is a continuously changing velocity model (CCVM) contrary to the assumption of single (homogeneous rock mass assumption) or variable static constant velocity models (layered rocks assumption), currently used in seismic monitoring systems for the calculation of seismic source locations. One strategy often used to account for changing ground conditions in the velocity model is periodic updating of the velocity. This approach is not only cumbersome but time consuming, and most importantly event source locations in between the periodic updates will not be reliable.

The objective of this research is to develop novel means for tracking velocity changes in continuously degrading ground conditions due to mining activities in underground mining environments, for the purpose of selecting the appropriate velocity for source location calculations in seismic monitoring systems in real time.

The approach adopted in the research involves the use of discrete physical models as analogues to mimic the changing ground conditions in underground mining to capture the impact on seismic wave velocity. In the discrete physical modelling concept, rather than using a single block and changing its condition to reflect the constantly changing ground condition in mining environments (a physically challenging approach), separate individual blocks are used, with each block representing a different stage in the mining process in time, structure, and geometry.

While the study did not explicitly use the concept of ray tracing to account for travel ray path changes due to voids, the results clearly show the impact of voids and their contents on the pulse wave velocities using acoustic emission (AE) monitoring systems.

The results also show that while the straight seismic ray path method was used, depending on sensor location relative to the pulse event source, the impact of the void and its content with time were clearly visible, confirming that in mining where ground conditions are constantly changing a uniform constant or periodically changing velocity model is not appropriate for accurate seismic event source locations.

The research is ongoing and will include the effect of stress and blast-induced fracturing on the seismic wave velocity model. Eventually, machine learning (ML) or artificial intelligence (AI) will be applied to the data to enable real-time velocity prediction for use in seismic event source calculation algorithms in seismic monitoring systems for improved accuracy in seismic event source locations.

Ethical statement

The authors state that the research was conducted according to ethical standards.

Conflict of interest

The authors declare no conflict of interest.

Funding body

The authors acknowledge Nazarbayev University for support through the Collaborative Research Program Grant # OPCRP2020014.

References

[1] Palei SK, Das SK. Logistic regression model for prediction of roof fall risks in bord and pillar workings in coal mines: an approach. Saf Sci [Internet]. Elsevier 2009;vol. 47:88–96. Available from: https://doi.org/10.1016/j.ssci.2008.01.002.

[2] Fall M, Célestin JC, Pokharel M, Touré M. A contribution to understanding the effects of curing temperature on the mechanical properties of mine cemented tailings backfill. Elsevier B.V. Eng Geol Invest 2010;114:397–413. Available from: https://doi.org/10.1016/j.enggeo.2010.05.016.

[3] Shi X, Jing H, Yin Q, Zhao Z, Han G, Gao Y. Investigation on physical and mechanical properties of bedded sandstone after high-temperature exposure. Bull Eng Geol Environ. Bulletin of Engineering Geology and the Environment 2020; 79:2591–606.

[4] Ranjith PG, Zhao J, Ju M, De Silva RVS, Rathnaweera TD, Bandara AKMS. Opportunities and challenges in deep mining: a brief review. Elsevier LTD on behalf of Chinese Academy of Engineering and Higher Education Press Limited Company Engineering 2017;vol. 3:546–51. Available from: https://doi.org/10.1016/J.ENG.2017.04.024.

[5] Xie H, Gao F, Ju Y. Research and development of rock mechanics in deep ground engineering. Yanshilixue Yu Gongcheng Xuebao/Chinese J Rock Mech Eng. 2015;34: 2161–78.

[6] Collins DS, Pinnock I, Toya Y, Shumila V, Trifu CI. Seismic event location and source mechanism accounting for complex block geology and voids. 48th US Rock Mech/Geomech Symp. 2014;1:63–9.

[7] Trifu CI, Shumila V. Geometrical and inhomogeneous raypath effects on the characterization of open-pit seismicity. 44th US Rock Mech Symp - 5th US/Canada Rock Mech Symp; 2010.

[8] Vilhelm J, Ivankina T, Lokajíček T, Rudajev V. Comparison of laboratory and field measurements of P and S wave velocities of a peridotite rock. Int J Rock Mech Min Sci 2016;88: 235–41.

[9] Wulff AM, Raab S, Huenges E. Alteration of seismic wave properties and fluid permeability in sandstones due to microfracturing. Phys Chem Earth, Part A Solid Earth Geod 2000;25:141–7.

[10] Memon RP, Sam ARM, Awang AZ, Memon UI. Effect of improper curing on the properties of normal strength concrete. Eng Technol Appl Sci Res 2018;8:3536–40.

[11] C109/109M-16a A. Standard test method for compressive strength of hydraulic cement mortars (Using 2-in. or cube specimens). Annu Book ASTM Stand 2016:1–10.

[12] CAMIRO. Canadian rockbursts handbook6 Volumes. Mining Research Directorate; 1996.

[13] Dong L, Sun D, Li X, Du K. Theoretical and experimental studies of localization methodology for AE and microseismic sources without pre-measured wave velocity in mines. 2017. See, http://www.ieee.org/publications_standards/publications/rights/index.html for more information.

[14] Yassin A. ENGR 489: NDT Spring 2020 Acoustic emission testing (AET) submitted by : students' name supervised by: instructor: Dr . Ameen El Sinawi. 2020. 0–vol. 33.

[15] Grosse CU, Masayasu Ohtsu, Aggelis DG, Shiotani T. Acoustic emission testing basics for research – applications in engineering [Internet]. Springer; 2022. Available from: http://www.springer.com/series/15088.

[16] Dong L, Li X. A microseismic/acoustic emission source location method using arrival times of PS waves for unknown velocity system, 2013 using arrival times of PS waves for unknown velocity system. Int J Distributed Sens Netw 2013;2013:8. https://doi.org/10.1155/2013/307489. Article ID 307489.

[17] Ge M, Hardy Jr HR, Wang H, Wang J. Development of a simple mechanical impact system as a non-explosive seismic source. Geotech Geol Eng 2011;29(1):137–42.

[18] Kennett BLN, Marson-Pidgeon K, Sambridge MS. Seismic source characterization using a Neighbourhood Algorithm. Geophys Res Lett 2000;27(20):3401–4.

[19] Nivesrangsan P, Steel JA, Reuben RL. Source location of acoustic emission in diesel engines. Mech Syst Signal Process 2007;21(2):1103–14.

[20] Ammon CJ, Velasco AA, Lay T, Wallace TC. Foundations of seismology. 2nd ed. Academic Press; 2021.

[21] Hedley DGF. Rockburst handbook for ontario hardrocr mines. CANMET special report SP92-1E. 1992.
[22] Blake W, Leighton FW, Duvall W. Microseismic techniques for monitoring the behaviour of rock structures. Bull (Arch Am Art) 1974;vol. 665. U.S. Bureau of Mines.
[23] Peng P, Jiang Y, Wang L, He Z, Tu S. Mining-induced seismicity by considering underground voids. 2020. https://doi.org/10.3390/app10196763.
[24] Morkel IG, Wesseloo J, Potvin Y. Seismic event location uncertainty in mining with reference to caving. Adelaide, Australia: Cave2022; 2022.
[25] Lee YH, Oh T. The measurement of P-, S-, and R-wave velocities to evaluate the condition of reinforced and prestressed concrete slabs. Adv Mater Sci Eng 2016;2016:14p. https://doi.org/10.1155/2016/1548215.

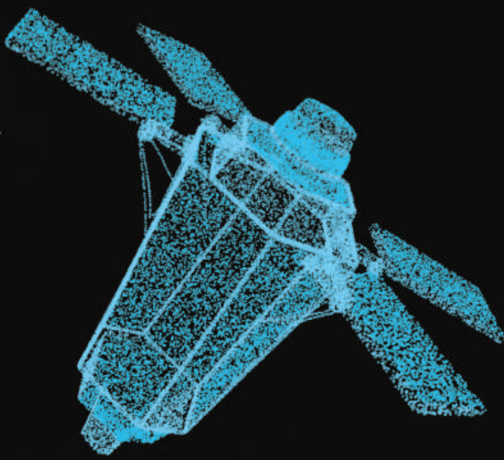

26th World Mining Congress

BRISBANE AUSTRALIA

26–29 JUNE 2023

Resourcing Tomorrow

Creating Value for Society

Proceedings

HOSTED BY

CSIRO

WMC2023.ORG

STUDY OF SEISMICITY SOURCE LOCATION ERRORS MINIMIZATION: IMPACT OF VOIDS, FRACTURES AND BACKFILL

Z. Mukhamedyarova[1], *F. Suorineni[1]

[1]School of Mining and Geosciences, Nazarbayev University, Nur-Sultan, Kazakhstan
*Corresponding author: E-mail address: fidelis.suorineni@nu.edu.kz;
cell: +7(776)1150945

ABSTRACT

The study focuses on laboratory experiments on physical models mimicking mining effects for better understanding of the effect of continuous rock mass degradation in underground mining on seismic wave velocities. Concrete cube samples of different sizes and hole diameters unfilled and filled with different cemented backfill of various cement to sand ratios. The concrete cubes sizes range from 150 mm to 375 mm in increments of 75 mm and hole diameter ranging from 50 to 150 mm in increments of 25 mm. Increasing hole diameter imitates increasing mine extraction ratio with time. Backfills with cement contents ranging from 0% to 20% were used to fill holes for curing times of 8 hours, 1 day, 14 days and 28 days. To fracture the cubes, the holes in the cubes were filled with static cracking agent (SCA).The cubes were fractured in order to investigate the effect of fractures on seismic wave velocity. An eight channel AE system was used in the study to determine the seismic wave velocities. Preliminary research results show significant effect of continuous rock mass degradation on seismic wave velocities depending on the location of a sensor relative to the source. The effect of backfill and hole on seismic wave velocity depends on sensor location relative to the source location, fractures, hole and content and backfill curing time.

KEYWORDS

Seismic event source location, continuously changing mining environment, seismic wave velocity, hole and backfill effect with time.

ISBN: 978-0-646-87565-1

1. INTRODUCTION

With increasing demand for mineral resources and their depletion, underground mines are going deeper all over the world. Complex geology of ore deposits coupled with high in situ stresses result in a number of hazards such as rockburst, rock mass caving and fracturing (Fall, Célestin, Pokharel, & Touré, 2010; Palei & Das, 2009; Ranjith et al., 2017; Shi et al., 2020; Wang et al., 2021). Microseismic monitoring systems are essential part of the underground mine safety management system and help to mitigate mining-induced seismic hazards. The accurate location of the seismic event sources is vital for the successful seismic monitoring systems. The accuracy of the seismic event source location with microseismic monitoring systems is highly dependent on ground input velocity model (Collins, Pinnock, Toya, Shumila, & Trifu, 2014). Recent studies by Bardainne and Gaucher (2010), Cong, Wang, and Cheng (2019) Zhang et al. (2016) observed that seismic wave velocities are not constant as was often assumed in event source location algorithms of microseismic monitoring systems.

In mining several changes occur, in particular, in underground mining the mine geometry is constantly changing in terms of volume and geometry, induced fracturing occur from blasting and stress redistribution, and mined out voids may be filled or unfilled depending on the mining system. The backfill used in filling the voids change in strength with time. All of these factors affect the ground condition which is constantly changing with mining. This implies that the input velocity in the microseismic monitoring system algorithm for calculation of the seismic event source locations is constantly changing as a consequence of the continuously changing mine ground condition. A single static input velocity or layered model assuming a homogeneous rock mass in an underground mining environment is far from reality, and often results in significant source location errors as evidenced in Collins et al. (2014). Reyes-Montes et al. (2016) note that one principal source of uncertainty in source location accuracy is the velocity model (VM) used to invert the location algorithm. Establishing a reliable velocity model in mining is a challenge, as multiple rock types are encountered, and the rock mass conditions are constantly changing.

The application of 3D velocity models considering the presence of voids caused by mining activities in heterogeneous media is being actively researched (Trifu & Shumila, 2010). The current approach showed improvements in seismic event source location accuracy. As previously explained, the changes in seismic wave velocity are caused by several other factors apart from voids and their condition.

Current attempts to account for changing velocities due to the changes in rock mass conditions in VMs use 3D velocity models based on 3D raytracing in heterogeneous geological units (Trifu & Shumila, 2010) that can account for the presence of voids such as mined out stopes. While this approach has resulted in some improvement in source locations accuracy, seismic monitoring systems are only periodically updated with the 3D VMs. This means that event sources located in between the velocity updates, when the ground condition would have changed will not be accurate. Also, manually increasing the frequency of updates to avoid this limitation is not only laborious, but impractical. Another proposition to overcome velocity changes in the mining environment is to use routine development blasts (Simser, Deredin, Jalbout, & Butler, 2015). The use of development blasts for the determination or calibration of 3D VMs while realistic, is not ideal for the understanding of the basic mechanics of wave propagation characteristics in a complex mining environment. Development blasts quality may also depend on shift crews, which can affect velocity calibration processes. Additionally, in matured mines, where management of seismicity is more critical, development blasts may not be regular. It could also be argued that dense monitoring sensor arrays could be a solution. Use of denser sensor array networks is not only expensive, but will also require continuous expansion as the volume of interest to be monitored increases. Drop tests have also been used in the development of 3D velocity models as discussed in Hosseini et al. (2015). Drop tests are useful for establishment of initial velocity models.

 ISBN: 978-0-646-87565-1

In this paper we present a novel approach and the study results aimed at predicting seismic wave velocities in real-time in continuously degraded underground mine environments. The underground mines are complex and difficult to control and will much more difficult to use in studying a complex problem such as velocity changes in a continuously changing mine environment. Hence, using a controlled environment which various factors can be introduced and combined to understand their effect on seismic wave velocity offers a practical alternative and the laboratory environment is identified as ideal for the study.

The novelty of the research is in the use of discrete physical models as analogues to mimic the changing ground conditions in underground mining to capture the impact on seismic wave velocity. In the discrete physical modelling concept, rather than using a single block and changing its condition to reflect the constantly changing ground condition in mining environments (a physically challenging approach), separate individual blocks are used with each block representing a different stage in the mining process in time, structure, and geometry.

2. MATERIALS AND METHODS

Laboratory experiments with discrete mimic mine models were conducted to understand constantly changing underground mine conditions. The research novelty is in using mimic mine models in a controlled laboratory conditions to investigate the effect of continuous rock mass degradation on seismic wave velocity. The novel approach helps to overcome problems with complex mine environment challenging to control.

2.1 Physical laboratory models mimicking the continuously changing underground mine environment

Discrete mine models were represented using concrete cube blocks. The size of concrete cube samples varies between 150 mm and 375 mm at increments of 75 mm. Each sample has a central cylindrical hole that increases in diameter with increasing block size representing increasing extraction ratio with time. The hole diameters varied from 50 mm in the 150 mm cubes to 125 mm-diameter in the 375 mm-cube as shown in Table 1. The hole diameters increased with cube size to account for boundary condition effects based on the theory of elasticity.

The concrete samples were moulded in laboratory conditions with a mixture of sand, cement and water. ASTM C-109 C (2016) standard was followed to find a suitable cement to sand ratio. Concrete samples used after 28 days curing, because concrete gains 99% strength after 28 days (Memon, Sam, Awang, & Memon, 2018). The material proportions for standard concrete samples according to ASTM C-109 C standard are sand to cement ratio is 2.75, the water to cement ratio is 0.485. The concrete mixture was vibrated after moulding for compression and expulsion of trapped air.

 ISBN: 978-0-646-87565-1

Table 1. Block sizes and hole diameters

Cube size (mm)	Material type	Hole diameter (mm)
150	concrete	No hole
150	concrete	50
225	concrete	No. hole
225	concrete	75
300	granite	No hole
300	granite	100
375	concrete	No. hole
375	concrete	125

In underground mines, voids are commonly filled with various backfill types. In this study, the holes in the concrete blocks were filled with different cement-sand ratios of 0%, 5%, 10%, 15%, and 20% to simulate backfill. The 0% cement backfill was tested both dry and wet. To account for the effect of backfill age on seismic wave velocity, each 5% to 20% cement backfill was cured for 8 hours, 1 day, 7 days, 14 days, and 28 days before being tested. Prior to that the samples were tested empty to mimic a mine without backfill.

2.2 Static Cracking Agent

Mining induced stresses and blasting often result in rock mass fracturing. In order to mimic this effect static cracking agent (SCA) was used. SCA is a highly expansive powdered cementitious material for the fragmentation of rocks and concrete (Habib, Vennes, & Mitri, 2022; Xu, Liang, Suorineni, & Li, 2021). After mixing with water and pouring into a hole the SCA swells and creates a pressure on the hole walls, thereby breaking them. The powder was mixed with clean water at a ratio 20% by weight. The slurry was poured into the holes of concrete samples within 5 minutes after preparation. The cracks (Figure 1) appeared after 2-3 hours after filling the hole with SCA. In the figure, the SCA was removed after fracturing the concrete cube.

Figure 1. Fractured cube with 3 joints.

ISBN: 978-0-646-87565-1

2.3 Equipment and testing methods

Acoustic Emission (AE) is one of the most effective non-destructive techniques for materials testing (Qiu et al., 2022). The AE system can track defects development in structures and monitor the structure in real-time without damaging it (Behnia, Chai, & Shiotani, 2014). AE system was used by many scholars to investigate mine seismicity including Dong and Li (2013) and Kennett et al. (2000). In current research SAEU3H AE system was used. Figure 2a shows the AE system with accessories consisting of AE data acquisition modules, chassis with front and rear panels, an optional network communication module, preamplifiers, and cables.

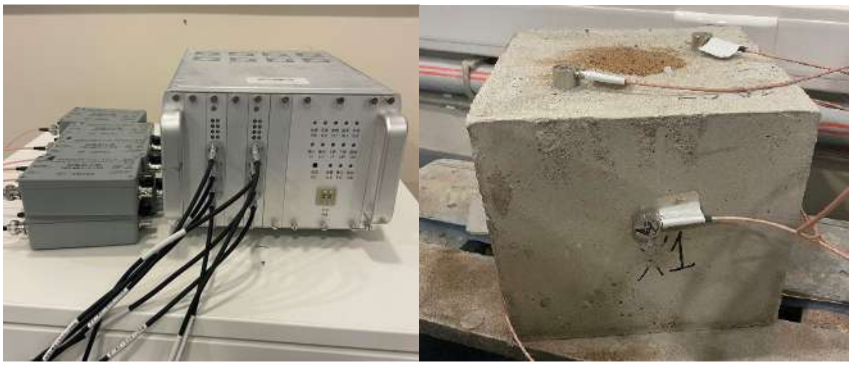

(a) (b)

Figure 2. a) AE system with accessories b) Cubic sample with attached sensors

In the study, AE sensors were attached to the sample surface with hot glue as shown in Figure 2b. Overall, 8 sensors were attached to the surface at known coordinates. Sensor number 1 was used as a source and placed in the middle of the front view of the sample to enable waves go across the hole. The other 7 were placed on the faces of the cube and acted as receivers. The SR150M High-frequency broadband AE sensor type was used in the study. The sensor characteristics are as follows as given by the Supplier (Qing Cheng AE Institute): the frequency range is 60-400 kHz, peak sensitivity is > 75 dB.

2.4 Procedure of velocity calculation by AE equipment

In this research we used the direct method of source locations based on the wave arrival time by Blake, Leighton, and Duvall (1974). Arrival time at each sensor was provided by the AE system based on its auto pick algorithm. Each cube sample was attached with 8 sensors at known coordinate locations. Distances between each sensor and the pulse source sensor were calculated based on known coordinates (Equation (1)) as given in Blake et al. (1974). Seismic wave velocities were then calculated based on the distances and respective arrival times at sensors using Equation (2).

$$d_i = \sqrt{\left(a_i - a_1\right)^2 + \left(b_i - b_1\right)^2 + \left(c_i - c_1\right)^2} \tag{1}$$

Where $i = 2, 3, 4, 5, 6, 7, 8$ and *a, b, c* – sensor coordinates.

$$v = \frac{d_i}{\Delta t} \tag{2}$$

Where d_i is the distance from the source to each sensor and Δt is deduction of wave arrival time and wave generated time.

 ISBN: 978-0-646-87565-1

The method used for distance calculation between sensors is based on the assumption that the material is homogeneous, free of voids or fractures that effect on wave path, or what is known as the "straight ray path concept" (Rawlinson, Hauser, & Sambridge, 2008).

3. RESULTS AND DISCUSSIONS

3.1 Size effect on seismic wave velocity

The ultimate goal of the research was to investigate the effect of cube size, hole, backfill content and its age and fractures on seismic wave velocity. AE pulse at the source was repeated five times and the average arrival time for the five pulses at the sensors was taken. Figure 4a illustrates the average of 5 velocities at each sensor for all cube sizes without holes. The range of wave velocities is within the values of 2854 m/s and 3594 m/s. The smallest cube with the size of 150 mm diameter shows the lowest velocities at almost all sensors with the least velocity of 2854 m/s at sensor 5. The small discrepancies in the velocities for all five cubes could be the result of inaccuracies in the estimation of the wave arrival times as well as changes in the quality of the concrete mix.

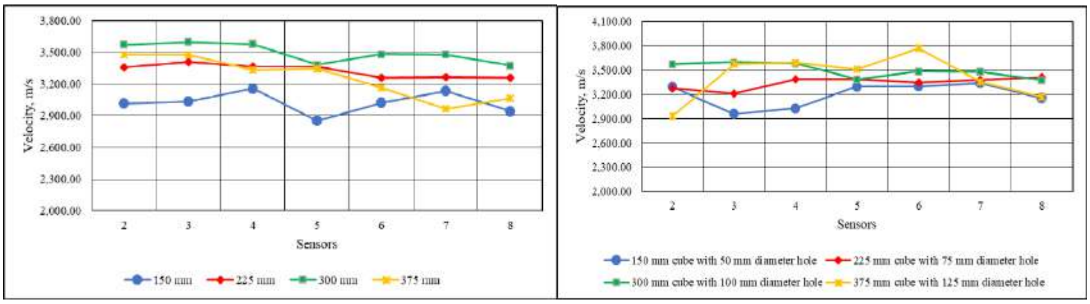

(a) (b)

Figure 4. a) Size effect on seismic wave velocity b) Hole effect on seismic wave velocity

3.2 Hole effect on seismic wave velocity

Figure 4b illustrates the results of AE tests on concrete cubes with holes without backfill to see the hole effect on seismic wave velocity. The hole diameters increase with increasing cube size. The test results show that the velocities at each cube size with diameters in the range of 50 mm – 125 mm are not significantly affected by hole introduction. The velocity at the sensors varies between 2900 m/s and 3800 m/s. The cube size of 375 mm with a hole diameter of 125 mm shows a significant change in the seismic wave velocity at sensors 2 and 8. Sensor 6shows relatively higher velocity of 3800 m/s implying that it is not affected by the void. Sensor 2 shows the most significant drop in velocity of almost 1000 m/s from the peak value in the 375 mm cube with a hole diameter of 125 mm. The significant drop in velocity is caused by the sensors' location across the hole from the source sensor. Wave energy attenuation is high due to the empty 125 mm diameter hole, resulting in longer arrival time and therefore lower velocity.

3.3 Backfill effect on seismic wave velocity

The effect of backfill at various curing times in the holes of the blocks can be likened to the effect of a layered velocity model. Based on the principle of polyline ray path in a layered velocity model, wave velocities going through the samples will be affected by backfills (Peng, Jiang, Wang, He, & Tu, 2020).

Figure 6 shows the impact of the void and backfill effect on wave velocities at the receiving sensors on the 225 mm cube with 5% and 15% cement content backfill in the void. In Figure 6a for 5% cement content backfill, the wave velocities for all the cured times fall within the range of 2870 to 3275 m/s like in the cube without holes. The wave velocity is significantly decreasing at the receiving sensors 2 and 4 in Figure 6b because of the void and backfill as can be seen Figure 6b for the sample filled with 15% cement backfill.

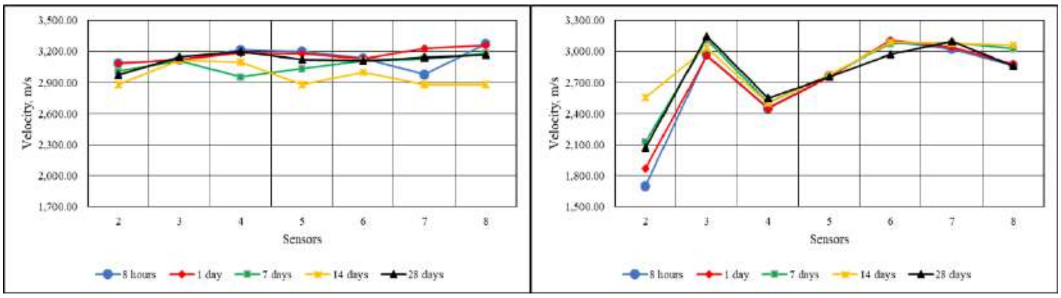

(a) (b)

Figure 6. Backfill effect on seismic wave velocity for 225 mm cube with 75 mm diameter hole (a) 5% cement (b) 15% cement backfill.

Based on the Figure 7a and b sensors 7 and 8 are significantly affected by the void of 125 mm diameter and changes in backfill properties with time in the 375 mm cube. The two sensors are located at the top of the cube near the void and wave paths to these sensors are impacted by the void and its contents to different degrees.

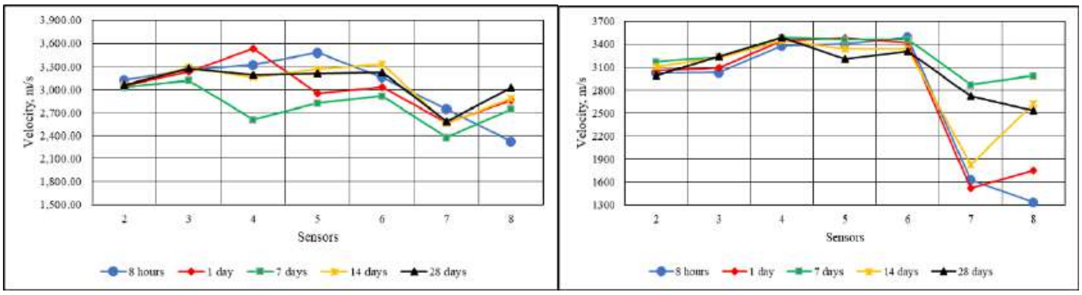

(a) (b)

Figure 7. Backfill effect on seismic wave velocity for 375 mm cube with 125 mm diameter hole (a) 5% cement (b) 20% cement

3.4. RMR calculation in fractured cubes with backfill

After the fracturing of concrete cube samples with the SCA, the SCA was removed from the holes. The fractured pieces were put together and held up with a tape, where necessary. RMR system of Bieniawski (1989) was used to rate the block qualities after they were fractured. Before the calculation of RMR the following steps were undertaken in accordance with RMR determination procedure outlined in Bieniawski (1989):

- Counting of all fractures in the block
- Measuring the apertures of the fractures
- Measuring the lengths of all fractures
- Determining the roughness of each fracture

 ISBN: 978-0-646-87565-1

3.4.1 Scaling of RMR input parameters

In order to rate the concrete blocks using the RMR system it was necessary to scale some parameters to the cube sizes relative to in situ rock masses. The following six parameters are needed in determining RMR: UCS of rock (concrete) sample, RQD, discontinuity spacing, condition of discontinuities, condition of groundwater and discontinuity orientation. RQD, fracture length and spacing are parameters that need to be scaled up to suit the concrete blocks that mimic the model mine. Geometric similarity is the most critical factor in scaled physical models (Xu et al., 2021). In this study, following measures for scaling were undertaken:

$$l_m = k * l_d \quad (3)$$

where l_m is the length of fracture in concrete cube, l_d is the length of discontinuity in RMR system rating, and k is the length scale.

$$s_m = p * s_d \quad (4)$$

where s_m is the spacing of fractures in mimic model, s_d is the spacing of discontinuities in RMR system rating and p is the length scale. The modified values for each cube size based on the length scaling coefficients are provided in Table 2.

3.4.2 Calculations

According to Palmstrom (1982), when no core is available, but discontinuity traces are visible in surface exposures, RQD can be calculated from the discontinuity number per unit volume. The equation for clay-free rock masses is as following:

$$RQD = 115 - 3.3J_v \quad (5)$$

where J_v is the sum of the number of discontinuities per unit length for all discontinuity sets.

ISBN: 978-0-646-87565-1

Table 2. Fractured concrete cube rating system input parameters

Sample	Discontinuity Spacing, mm		Discontinuity length, mm		UCS, Mpa	
	value	rating	value	rating	value	rating
150 mm	>150	20	7.5	6	>250	15
	50-150	15	7.5-22.5	4	>100-250	12
	15-50	10	22.5-75	2	>50-100	7
	4.5-15	8	75-150	1	>25-50	4
	<4.5	5	>150	0	>5-25	2
225 mm	>225	20	11.25	6	>250	15
	75-225	15	11.25-33.75	4	>100-250	12
	22.5-75	10	33.75-112.5	2	>50-100	7
	6.75-22.5	8	112.5-225	1	>25-50	4
	<6.75	5	>225	0	>5-25	2
300 mm	>300	20	15	6	>250	15
	100-300	15	15-45	4	>100-250	12
	30-100	10	45-150	2	>50-100	7
	9-30	8	150-300	1	>25-50	4
	<9	5	>300	0	>5-25	2
375 mm	>375	20	18.75	6	>250	15
	125-375	15	18.75-56.25	4	>100-250	12
	37.5-125	10	56.25-187.5	2	>50-100	7
	11.25-37.5	8	187.5-375	1	>25-50	4
	<11.25	5	>375	0	>5-25	2

RMR calculations for cubes with the size 225 mm:
Jv=2, RQD = 115-3.3*2/(225/1000)=85.6
RMR value: 69
RMR calculations for cubes with the size 375 mm:
Jv=2, RQD = 115-3.3*2/(375/1000)=97.4
RMR value: 72

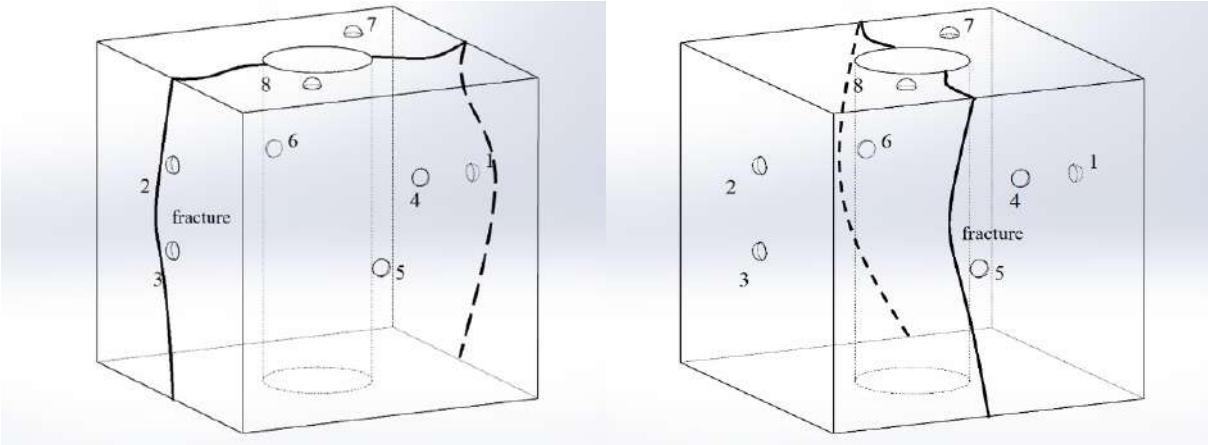

(a) (b)

Figure 8. The projected source and sensors’ locations for a) 225 mm with hole diameter 75 mm b) 375 mm with hole diameter 125 mm concrete sample

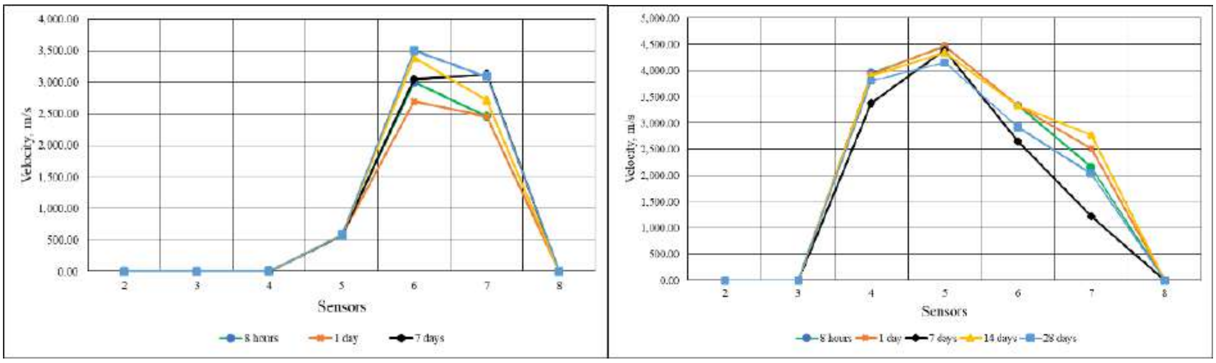

(a) (b)

Figure 9. Seismic wave velocity in fractured cubes of sizes a) 225 mm b) 375 mm with backfill

After cubes were fractured, the SCA was removed from the hole and fractured parts were tied up together with insulating tape and the hole filled with backfill. When the fractured 225 mm sample was filled with 10% cement backfill, the cube had 2 cracks relative to sensors as in Figure 8a. Figure 9a shows that only sensors 5, 6 and 7 were able to receive the signal. Note sensor 5 is across the hole relative to the source, but it could receive the signal with delayed arrival time due to the crack, which is visible from lower wave velocity of 500 m/s. It is very likely that the fracture had some infilling from the backfill to enable it transmit the pulse signal across the fracture in the location of this sensor.

 ISBN: 978-0-646-87565-1

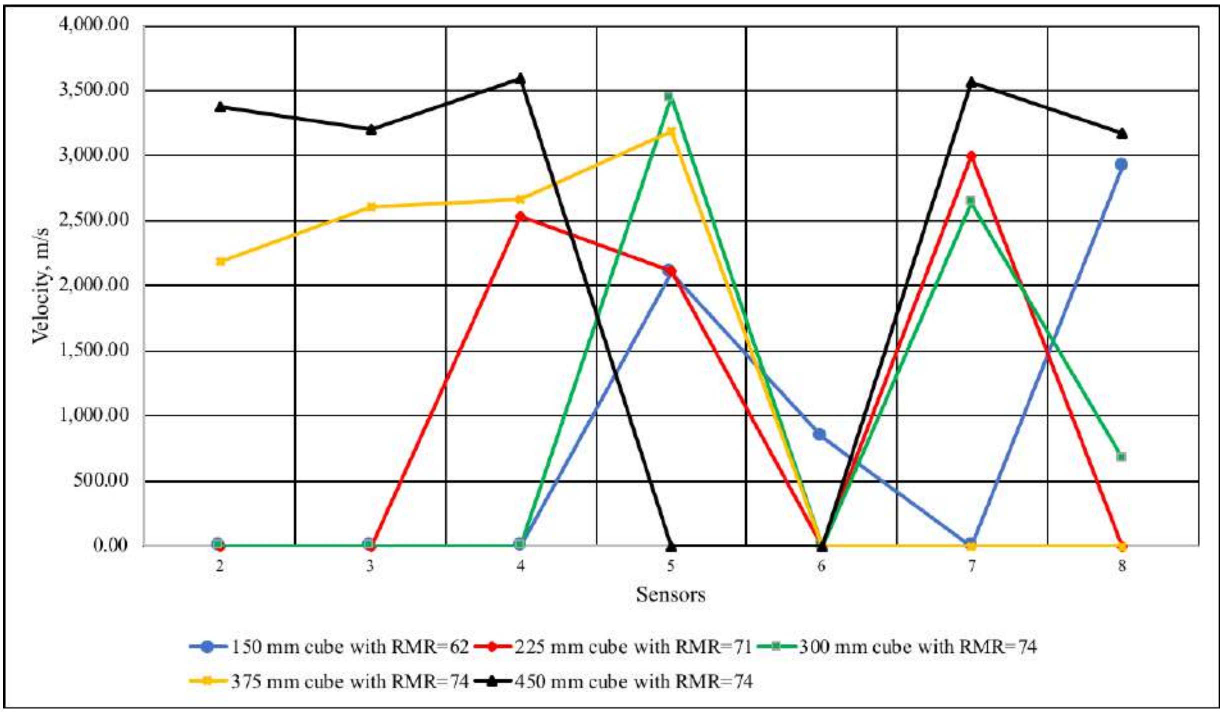

Figure 10. RMR and seismic wave velocity relationships for all cube sizes with empty hole

There were 2 cracks in the 375 mm cubes with 10% cement backfill. The approximate crack locations relative to the sensors are illustrated in Figure 8b. Figure 9b shows the seismic wave velocity in fractured cube with backfill. Sensors 4, 5, 6, and 7 located prior to cracks detected the signal as expected. In contrast, sensors 2, 3, and 8 were not able to receive the signal because of the full attenuation of the signal in the cracks

CONCLUSIONS

The objective of the study is to develop a novel approach for tracking velocity changes caused by continuously changing mining environment due to mining activities to enable real-time prediction of seismic wave velocity for accurate seismic source locations by the seismic source location algorithm in seismic monitoring systems.

The strategy used in the study comprises simulating changing ground conditions in underground mining using discrete physical models as analogues to capture the impact of mining activities on seismic wave velocity. The study results clearly show the impact of voids, their contents and fracture intensity and propagation on the wave velocities using an acoustic emission (AE) monitoring systems.

The research findings also confirm that, in mining, where ground conditions are constantly changing, a constant or periodically changing velocity model is not appropriate for location of seismic event sources. This is because, while the straight seismic ray path method was employed, depending on sensor location relative to the pulse event source, the impact of the void and its content over time, and fractures were clearly visible. Use of ray path tracing could improve the results, and this is currently in progress.

ACKNOWLEDGEMENTS

The authors acknowledge Nazarbayev University for support through the Collaborative Research Program Grant # OPCRP2020014.

REFERENCES

Bardainne, T., & Gaucher, E. (2010). Constrained tomography of realistic velocity models in microseismic monitoring using calibration shots. *Geophysical Prospecting*, *58*(5), 739–753. https://doi.org/10.1111/j.1365-2478.2010.00912.x

Behnia, A., Chai, H. K., & Shiotani, T. (2014). Advanced structural health monitoring of concrete structures with the aid of acoustic emission. *Construction and Building Materials*, *65*, 282–302. https://doi.org/10.1016/j.conbuildmat.2014.04.103

Bieniawski, Z. T. (1989). *Engineering Rock Mass Classifications*. New York: A wiley-interscience publication.

Blake, W., Leighton, F., & Duvall, W. (1974). *Microseismic techniques for monitoring the behaviour of rock structures*. U.S. Bureau of Mines.

C109/109M-16a, A. (2016). Standard test method for compressive strength of hydraulic cement mortars (Using 2-in. or cube specimens). *Annual Book of ASTM Standards*, 1–10. https://doi.org/10.1520/C0109

Collins, D. S., Pinnock, I., Toya, Y., Shumila, V., & Trifu, C. I. (2014). Seismic event location and source mechanism accounting for complex block geology and voids. *48th US Rock Mechanics / Geomechanics Symposium 2014*, *1*, 63–69.

Cong, S., Wang, Y. hong, & Cheng, J. Y. (2019). Coal mine microseismic velocity model inversion based on first arrival time difference. *Arabian Journal of Geosciences*, *12*(1). https://doi.org/10.1007/s12517-018-4172-4

Dong, L., & Li, X. (2013). A microseismic/acoustic emission source location method using arrival times of PS waves for unknown velocity system. *International Journal of Distributed Sensor Networks*, *2013*. https://doi.org/10.1155/2013/307489

Fall, M., Célestin, J. C., Pokharel, M., & Touré, M. (2010). A contribution to understanding the effects of curing temperature on the mechanical properties of mine cemented tailings backfill. *Engineering Geology*, *114*(3–4), 397–413. https://doi.org/10.1016/j.enggeo.2010.05.016

Habib, K. M., Vennes, I., & Mitri, H. (2022). Laboratory investigation into the use of soundless chemical demolitions agents for the breakage of hard rock. *International Journal of Coal Science and Technology*, *9*(1), 1–10. https://doi.org/10.1007/s40789-022-00547-4

Hosseini, Z., Collins, D., Shumila, V., Trifu, C. I., & Pinnock, I. (2015). Induced microseismic monitoring in salt caverns. *49th US Rock Mechanics / Geomechanics Symposium 2015*, *1*, 407–415.

Kennett, B. L. N., Marson-Pidgeon, K., & SAmbridge, M. S. (2000). *GEOPHYSICAL RESEARCH LETTERS*.

Memon, R. P., Sam, A. R. M., Awang, A. Z., & Memon, U. I. (2018). Effect of Improper Curing on the Properties of Normal Strength Concrete. *Engineering, Technology & Applied Science Research*, *8*(6), 3536–3540. https://doi.org/10.48084/etasr.2376

Palei, S. K., & Das, S. K. (2009). Logistic regression model for prediction of roof fall risks in bord and pillar workings in coal mines: An approach. *Safety Science*, *47*(1), 88–96. https://doi.org/10.1016/j.ssci.2008.01.002

Palmstrom, A. (1982). The Volumetric Joint Count—A Useful and Simple Measure of the Degree of Rock Jointing. *Proceedings of 4th International Association of Engineering Geology*, 221–228.

Peng, P., Jiang, Y., Wang, L., He, Z., & Tu, S. (2020). A fast ray-tracing method for locating mining-induced seismicity by considering underground voids. *Applied Sciences (Switzerland)*, *10*(19), 1–15. https://doi.org/10.3390/app10196763

Qiu, H., Zhang, F., Liu, L., Huan, C., Hou, D., & Kang, W. (2022). Experimental study on acoustic emission characteristics of cemented rock-tailings backfill. *Construction and Building Materials*, *315*(May 2021), 125278. https://doi.org/10.1016/j.conbuildmat.2021.125278

Ranjith, P. G., Zhao, J., Ju, M., De Silva, R. V. S., Rathnaweera, T. D., & Bandara, A. K. M. S. (2017). Opportunities and Challenges in Deep Mining: A Brief Review. *Engineering*, *3*(4), 546–551. https://doi.org/10.1016/J.ENG.2017.04.024

Rawlinson, N., Hauser, J., & Sambridge, M. (2008). Seismic ray tracing and wavefront tracking in laterally heterogeneous media. *Advances in Geophysics*, *49*(07), 203–273. https://doi.org/

10.1016/S0065-2687(07)49003-3
Reyes-Montes, J. M., Sainsbury, B. L., Andrews, J. R., & Young, R. P. (2016). Application of cave-scale rock degradation models in the imaging of the seismogenic zone. *CIM Journal*, *7*(2), 87–92. https://doi.org/10.15834/cimj.2016.9

Shi, X., Jing, H., Yin, Q., Zhao, Z., Han, G., & Gao, Y. (2020). Investigation on physical and mechanical properties of bedded sandstone after high-temperature exposure. *Bulletin of Engineering Geology and the Environment*, *79*(5), 2591–2606. https://doi.org/10.1007/s10064-020-01729-7

Simser, B., Deredin, R., Jalbout, A., & Butler, T. (2015). Use of microseismic monitoring data as an aid to rock mechanics decision making and mine design verification. *49th US Rock Mechanics / Geomechanics Symposium 2015*, *2*, 1093–1108.

Trifu, C. I., & Shumila, V. (2010). Geometrical and inhomogeneous raypath effects on the characterization of open-pit seismicity. *44th US Rock Mechanics Symposium - 5th US/Canada Rock Mechanics Symposium*.

Wang, J., Apel, D. B., Pu, Y., Hall, R., Wei, C., & Sepehri, M. (2021). Numerical modeling for rockbursts: A state-of-the-art review. *Journal of Rock Mechanics and Geotechnical Engineering*, *13*(2), 457–478. https://doi.org/10.1016/j.jrmge.2020.09.011

Xu, S., Liang, R., Suorineni, F. T., & Li, Y. (2021). Evaluation of the use of sublevel open stoping in the mining of moderately dipping medium-thick orebodies. *International Journal of Mining Science and Technology*, *31*(2), 333–346. https://doi.org/10.1016/j.ijmst.2020.12.002

Zhang, J., Zhang, H., Zhang, Y., & Liu, Q. (2016). Calibrating one-dimensional velocity model for downhole microseismic monitoring using station-pair differential arrival times based on the differential evolution method. *Physics of the Earth and Planetary Interiors*, *261*, 124–132. https://doi.org/10.1016/j.pepi.2016.06.003

 ISBN: 978-0-646-87565-1

THE KARAGANDA COAL BASIN MINES CHALLENGES: STATE OF THE ART OF GAS OUTBURSTS AND COAL BURSTS WITH A VIEW TO FUTURE IMPROVEMENTS

*G. Balniyazova[1], F.T. Suorineni[2], Z. Mukhamedyarova[2]

[1]Faculty of Mining Engineering, Abylkas Saginov Karaganda Technical University, Karaganda, Kazakhstan
(*Presenting author: balniyazova1983@mail.ru)
[2]School of Mining and Geosciences, Nazarbayev University, Astana 01000, Kazakhstan

ABSTRACT

Kazakhstan is the 10th producer of coal in the world and is in the 8th place among countries with coal reserves. The Karaganda Coal Basin is a vital source of coal in Kazakhstan. The coal produced in the Karaganda Coal Basin consists of both coking and thermal coal. It is established that the basin coal is extremely gassy. The main mining system used in the coal production in the basin is the longwall mining system. For decades, coal production by long wall mining in the basin has been plagued with gas outbursts and coal bursts. A review of the state-of-art of longwall mining in the basin shows that two primary factors are responsible for the frequent dynamic events in the longwall mining practiced in the basin, namely in adequate gas drainage and the complex geology associated with some of the coal seams in the basin. The geology of the basin is characterized by synclines and anticlines, and complex faults. As a mitigation measure it is established that diligent gas drainage practices using established international coal gas drainage could assist minimize the rate of gas outbursts and coal bursts in the gassy coal seams in the basin. It also determined that development and adoption of best technological practices in the coal cutting process could be of benefit. It is therefore recommended that research efforts be put in place to establish optimum shearer coal cutting speeds for use in the longwall coal mining system in the basin.

KEYWORDS

Karaganda Coal Basin, Gas outburst and Coal bursts, Gassy coal

ISBN: 978-0-646-87565-1

1. INTRODUCTION

The Karaganda Basin is a vital source of coal in Kazakhstan (Figure 1). The basin is one of the oldest and most studied coal-bearing basins in both Central Asia and the former Soviet Union. The area of the Basin is 3, 600 km^2, with a length (from East to West) of 120 km and a width of 30–50 km from North to South. The Basin is characterized by four synclines, namely: Tentek, Sherubainur, Karaganda, and Verkhnesokursk. The first three of these synclines form the industrial part of the basin and are studied to a depth of between 700 and 1300 m. Productive sediments are represented by Ashlyarik (C1), Karaganda (C1), Dolinsk (C2), and the Tentek (C2-3) series, and contain up to 30 coal seams with a total working thickness of 40 m. The US EPA puts the total coal resource in the Karaganda Coal Bain at 41.3 billion tons to a depth 1800 m.

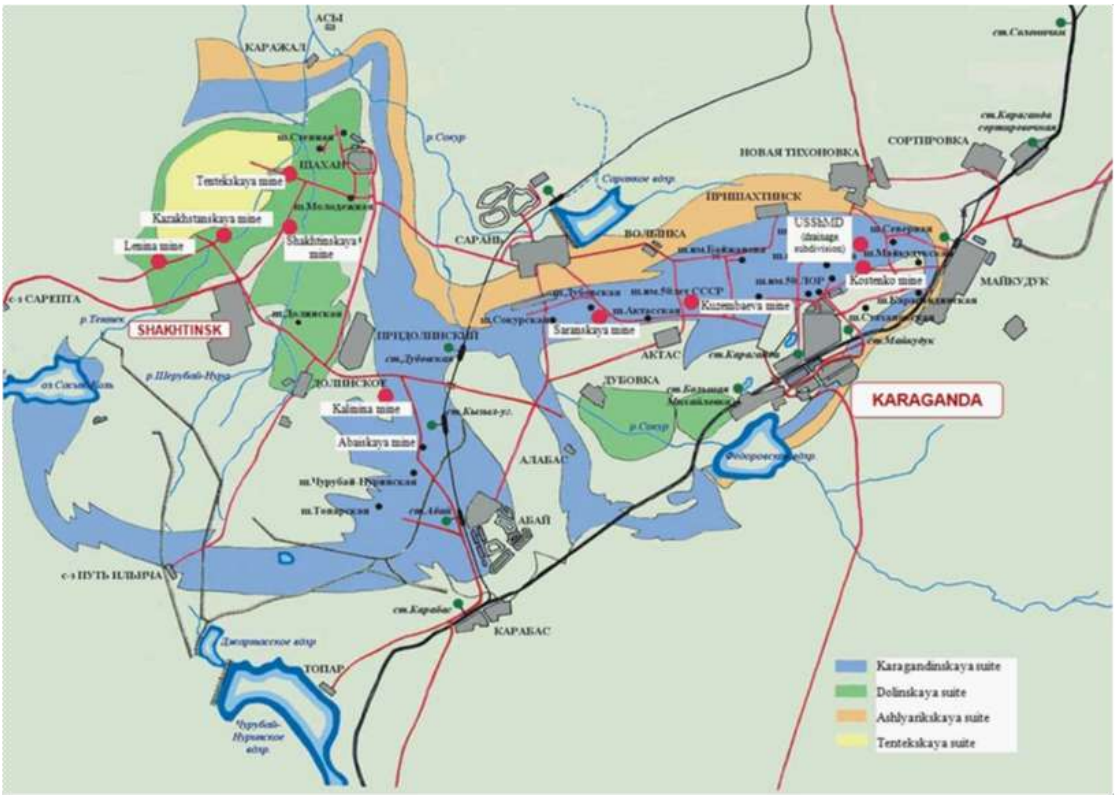

Figure 1 – Karaganda Coal Basin (US EPA, 2011)

The main coal types found in the Basin are the high volatile B bituminous coal (hvBb) to medium volatile bituminous (mvb) coal with heating values in the range of 30.2–32.6 MJ and volatile matter of 22–31% respectively. The coal in the Karaganda Basin is known to have of high gas content in the range of between 15 to 20 m^3/t in top 400 to 500 m of the methane zone and is more stabilized at depth at 22 to 27 m^3/t.

The most widespread coals are hvBb to mvb types. The Karaganda basin has high gas content, and gas content layers range from 400-500m to 15-20 m^3/t at the beginning of the methane zone and are more stabilized at a depth between 22-27 m^3/t. The gas weathering zone depth varies within the limits of 60-250 m.

The mining system used for the extraction of the Karaganda Basin coal is generally longwall mining. The leading coal mining company in the Karaganda Basin is the ArcelorMittal and owns eight underground coal mines, namely: Kostenko, Kuzembaev, Saranskaya, Abaiskaya, Kazakhstanskaya, Lenina, Shaktanskaya, and Tentekskaya. The eight mines (Figure 2) are a result of the restructuring of the fifteen mines that the company had acquired in 1996.

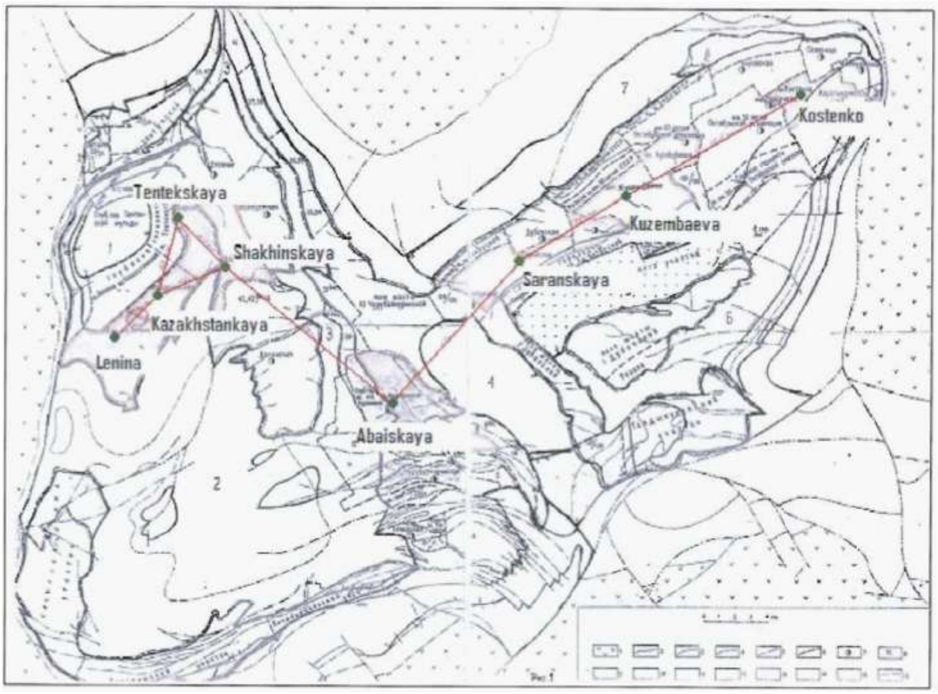

Figure 2 – The eight Coal Mines of ArcelorMittal in the Karaganda basin (https://www.globalmethane.org/documents/karaganda.pdf)

The mines produce primarily coking coal used for steelmaking at Temirtau Steel plant and thermal coal for ArcelorMittal Temirtau's power plants. For beneficiation of coking coal, two treatment plants are operated: one located close to the coal mines, and the other at the ArcelorMittal Temirtau steel plant. Excess coal is supplied to group steel plants, mainly ArcelorMittal Kryvyi Rih in Ukraine.

Kazakhstan is a major coal producer in the world. As shown in Figure 3, Kazakhstan is the 10th producer of coal in the world and is in the 8th place among countries with coal reserves.

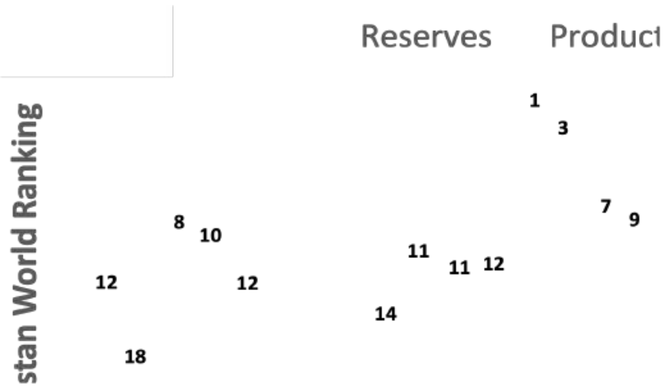

Figure 3 – Kazakhstan's place in the world in terms of natural resources (Suorineni, 2019)

26th World Mining Congress (WMC 2023) 26 – 29 JUNE BRISBANE AUSTRALIA ISBN: 978-0-646-87565-1

2. CHALLENGES IN COAL MINING IN THE KARAGANDA COAL BASIN

As stated in Section 1, the main method of coal mining in the Karaganda Coal Basin is longwall mining. It was also noted that the Karaganda Coal Basin Mines are characterized as gassy, with gas contents in the range of 15 to 27 m^3/t depending on the location in the methane zone. The high gas content in the Karaganda Basin is the main source of hazards in coal mines in the Basin.

2.1 Longwall Mining Principles

Before discussing the challenges in the mining of coal in the Karaganda Coal Basin, it is worth briefly describing the process of longwall coal mining. Barczak (2017) provides a very clear description of the longwall mining process in which it is noted that longwall mining is an underground mining system of excavating tabular seams such as coal and potash. In the case of coal large rectangular blocks of coal are defined during the development stage of the mine and are then extracted in a single continuous operation. Each defined block of coal is known as a panel. Longwall panels range in size from 3–4 km long and 150–400 m wide.

Development of the panels involves driving one, two or three gate roads down both flanks of a panel to its extremity, and then connecting these two sets of gate roads. The headings are usually connected on a regular basis with roadways referred to as cut-throughs or crosscuts. As the coal is cut, the longwall face is supported with hydraulically operated supports known as shields. The function of these supports is to provide a safe working environment by supporting the roof as coal is extracted as well as advancing the longwall equipment. There are two methods of longwall mining namely, retreat longwall mining and advance longwall mining. In retreat longwall mining, the longwall face is installed and as mining continues into the panel the entries are allowed to collapse behind the face line to form part of the gob. In advance mining, the longwall face is set up a short distance from the main development tunnels or headings. The gate entries of the longwall face are formed as the coal is mined, with roadways formed adjacent to the gob. Each coal panel is separate from the adjacent workings with a solid barrier pillar. Longwall mining is an efficient and high production mining system. A typical longwall mining layout is given in Figure 4.

The process of coal extraction is mechanical and involves the use of cutting equipment known as shearers. The shearer cuts a fresh web of coal in slices typically 0.6–1.0 m thick each time it traverses up and down the longwall face, enabling the Armored face Conveyor (AFC) to immediately advance behind the shearer.

 ISBN: 978-0-646-87565-1

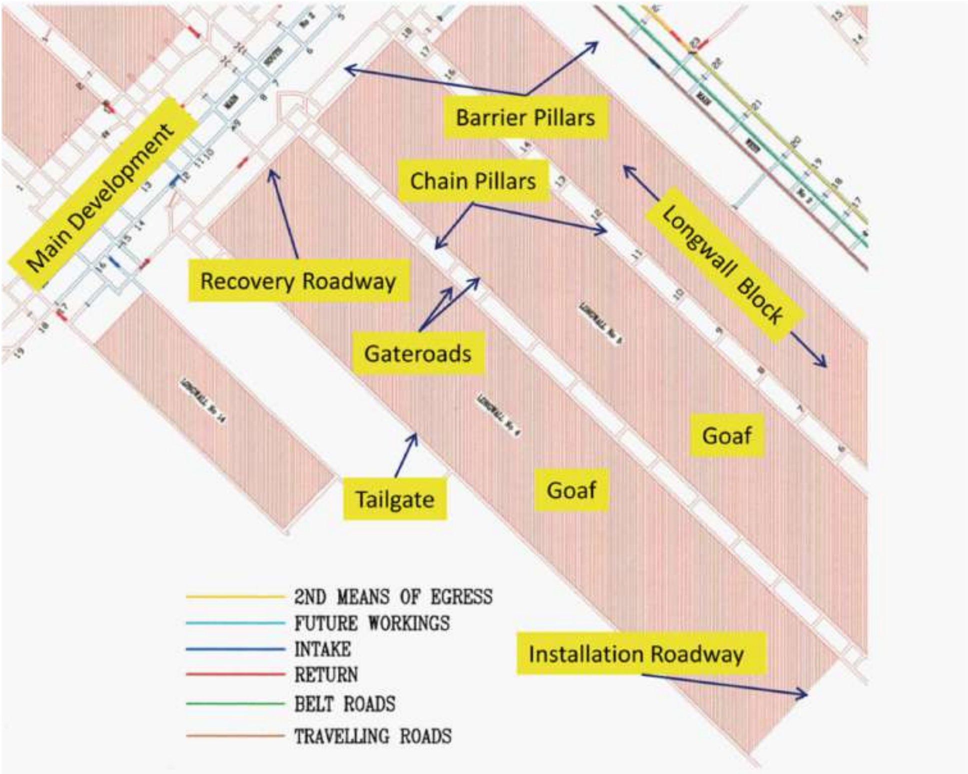

Figure 4 – Simplified longwall mining layout showing the major infrastructure

2.2 The Challenges of Longwall Coal Mining

2.2.1 Coal Mining Hazards

Coal mining comes with a number of hazards that need to be managed. The details of these risks are discussed in detail in Galvin (2016). Coal mining hazards include:

- Windblast
- Feather edging
- Top and bottom coaling
- Inclined workings
- Inrush
- Flooding of mine workings
- Bumps and pressure bursts
- Gas outbursts
- Mining through faults and dykes
- Frictional ignition involving rock
- Backfilling of bord and pillar workings
- Effect of roof falls on pillar strength
- Recovering roof falls
- Mining in the Vicinity of Convergence Channels and Paleochannels.

2.2.2 Coal burst versus Gas Outburst

These two hazards remain a challenge in other coal mining environments as may be seen in Canbulat et al. (2016) in the report entitled "A preliminary review of coal burst experiences, mechanisms and critical conditions in underground coal mines". In this report the authors define coal burst as the violent dynamic

 ISBN: 978-0-646-87565-1

failure of overstressed coal in an underground coal mine. They observed that coal bursts pose one of the highest safety and productivity risks in the mining industry with the potential to cause multiple fatalities, as was evident in a recent incident at an Australian coal mine where two miners were fatally injured.

Unlike a coal burst an outburst or gas outburst is a dynamic energy release leading to some form of coal failure primarily associated with in situ gas pressure, sometimes also accompanied by stress-related energy. Gas pressure can be a factor as a source of energy in some coal bursts, but the dominant energy source in coal or pressure bursts is stress.

A pressure bump is a dynamic release of energy within the coal mass in a coal mine, often due to intact coal failure or failure/displacement along a geological structure, that generates an audible signal, ground vibration, and potential for displacement of existing loose or fractured material into mine openings. On the other hand, a pressure bump is sometimes referred to as a bounce that actually causes consequent dynamic coal failure in the vicinity of a mine opening, resulting in high velocity expulsion of this broken/failed material into the mine opening.

Coal outbursts are generally caused by the following factors or their combinations:

- Presence of strong, massive, and rigid main roof strata overlying a coal seam
- Depth of cover or overburden thickness
- Presences of geological structures such as faults, dykes, sandstone channels and joints
- Coal mechanical properties may also make them burst prone:
    - Coal brittleness with compressive strength
    - Coal composition and texture such as detritus content and grain size. Fine grain size reduces coal bursting likelihood (Pan et al., 2005) while high amounts of detritus increases burst proneness.
    - Non-uniform coal seam thickness can be burst prone (Agapito and Goodrich, 1999; Furniss, 2009)
    - Lack of joints and cleating in the coal mass
- Operational factors such as
    - Shearer cutting rate – high cutting rate increases bursting potential
    - Pillar design
    - Retreat mining
    - Multi-seam mining

A dynamic event in coal can be attributed to coal burst or gas outburst. Brauner (1994) stated that the most characteristic features which distinguish outburst from coal bursts are mainly:

- The process is slower and less violent
- There is no or relatively little seismic reaction
- The ejected coal is broken into smaller particles
- The occurrence is predominately associated with geological disturbances and is usually in coal face or its close vicinity; and
- The seam contains enough gas (e.g., more than 10 m^3 of methane per ton of solid coal).

3. KARAGANDA COAL BASIN MINING CHALLENGES

Out of the hazards listed Section 2, the most significant hazards affecting coal mining in the Karaganda Coal Basin are gas outbursts and coal bursts. In Karaganda Basin coal mines, reports on reviewed incidents of dynamic events often fail to identify the event as either coal burst or gas outburst. In almost all cases all dynamic events in the Karaganda Coal Basin are attributed to gas bursts. This may be because of the difficulty in differentiating between coal bursts and gas outbursts as acknowledged in Canbulat et al. (2016).

The Karaganda Coal Basin Mines use external and international experts/consultants to review incidents of dynamic events. Some of these companies/experts are:

- Troshkov N.Y. - Investigate the circumstances and causes of group accidents that occurred 07.11.2021
- Khodzhaev, R. (Director of GeoMark Scientific and Engineering Center LLP) - establish the causes of the gas dynamic phenomenon in the face that occurred on November 07, 2021, in the face of the ventilation drift 35K10-c " Abayskaya mines of Arcelor Mittal Temirtau UD JSC.
- Kolikov Konstantin Sergeevich (National University of Science and Technology (NUST) MISIS Mining Institute – Investigated the accident that occurred on November 07, 2021, in the face of the 35K10-c ventilation drift of the Abayskaya UD mine of Arcelor Mittal Temirtau JSC.
- Doctor of Technical Sciences Mustafina (Saint Petersburg) Russia - Investigated a group accident that occurred on November 07 in the face of the 35K10-c Ventilation drift of the Abayskaya UD mine of Arcelor Mittal Temirtau JSC.

From the various reports gleaned during the preparation of this paper, the causes of the dynamic events in the Karaganda Coal Basin mines are often attributed to:

- Indeterminate or inconclusive
- Gas outburst due geological structures (the Upwash 10 fault)
- Gas outbursts as result of the Influence of anticlinal and synclinal folds

After analyzing the outburst hazard indicators and parameters of 60 sudden outbursts of coal and gas that occurred in the conditions of the Karaganda basin, characterizing the outbursts, several patterns, and features of sudden outbursts of coal and gas were established.

- Sudden outbursts of coal and gas in the basin occur from a depth of 200 meters from the surface. The depth varies with the complexity of the tectonic structure.
- Emissions occur only in the development workings and during the opening of the seams. The absence of emissions in production faces is due to the large discharge zone of the bottomhole part of thick and medium-sized seams and the maintenance of production operations in longwalls, after preliminary degassing of the coal mass.
- Sudden outbursts in development workings occur mainly in thick seams. Of the 47 outbursts that occurred in development workings, 43 occurred in seams with a thickness of 3.5 meters or more. When opening coal seams with cut throughs, emissions occur equally in both thick and thin seams.
- Emissions in development workings in most cases occur in horizontal workings (31 out of 47). In inclined workings, out of 16 blowouts, 10 were blown from top to bottom and only 6 were blown from rising workings. This is due to the predominant workings from top to bottom.
- All emissions of coal and gas in the basin occurred in zones of geological disturbances. Of the 60 cases, 28 occurred when workings approached faults, mainly reverse faults, and 21 blowouts occurred in zones of small tectonic disturbances, and 11 blowouts occurred in zones of changing seam thickness, in the presence of an intensely crushed coal pack, or a sharp change in seam geometry.
- A characteristic feature of sudden outbursts of coal and gas is their confinement to places of increased stress due to the influence of coal pillars left on neighboring seams. In the conditions of the basin, 28 blowouts occurred in the zone of influence of pillars of coal, 26 blowouts occurred in the unworked massif, and only 6 blowouts occurred under the mined-out space of the overlying seam at a distance between seams of more than 60 meters.
- Coal in places of emissions is characterized by reduced mechanical strength. The strength coefficient in the places of emissions varies from 0.22 to 0.6.
- With the deepening of mining operations, an increase in the number of emissions is observed, as well as an increase in the amount of coal thrown out and additionally released gas. This is due to a natural increase in gas pressure in coal seams and a decrease in coal moisture with an increase in the depth of

 ISBN: 978-0-646-87565-1

mining, which, other things being equal (gas-dynamic, strength, and other properties of coal), leads to an increase in the outburst hazard of seams and the intensity of coal and gas emissions.

- There is no direct relationship between the magnitude of the gas pressure in the coal seam and the natural gas content of coal and the probability of coal and gas outbursts. Emissions can occur at low gas pressure or low gas content of coal and do not occur at very high values, with high coal hardness and low values of the initial gas recovery rate .

Two mines, namely the Kazakhstanskaya and Abaiskaya Mines are selected as typical representatives of the Karaganda Coal Basin Mines to examine the statistics of dynamic events in the Karaganda Coal Basin and their consequences.

The Kazakhstanskaya mine has rights to develop the following coal seams: T3, T1, T11, D10, D9, D6, D5, D4, D3, and D1. Seams D6 and D11 are currently being developed, and D10 is being prepared for development. Seam D6 is the thickest and most stable seam of the Dolinskaya suite. Its effective thickness varies from 2.92 to 7.04 m, with an average thickness of 5.44m. The seam has a complex structure where up to 8-10 interlayers of strata of different thicknesses (usually not exceeding 0.2m) are being identified. The most stable seam is the waste strata interlayer of 0.05-0.20 m, appearing in the upper part of the seam. The other strata interlayers are lens shaped.

The detailed geology of the is provided in the US EPA () report and summarised here. The geological structure of the Abaiskaya mine (formerly the Kalinina mine) is represented by sedimentations of carbonic, Paleogene, neogene, and quarternary age. The carbonic section is represented by a full section of Karaganda suite divided into three sub-suites: lower (seams K1K6), middle (seams K7- K14), and upper (seams K15- K20). Lithological content of the strata is represented by interbedding of sandstones, siltstones, argillite, carbonaceous argillites, and coal seams. Thickness of the suite sedimentations is 750m. The field of the Abaiskaya mine is located in the Southern part of the north-eastern flank of Sherubai-Nurinskaya synclinal as a big tectonic block limited by a series of overlap faulting. Slope of the seam mainly varies 10 to 25° to the northwest. The area is complicated with folds and disjunctive imperfections. Results of exploratory works have indicated 91 disjunctive faults and 82 low-swing imperfections with amplitude distortion of 3-5m spreading from 50 to 300m. Zones of the imperfections have intensive cleavage of the strata with trace of drifts along sliding surfaces.

The D6 coal seam occurs in the Kazakhstanskaya, Lenin, Shakhtinskaya, Kazakh and Tentekskaya mines while the Saranskaya, Abai and Kuzembaeva mines. Figure 5 shows some statistics of the impact of dynamic events in selected mines in the D6 and K10 coal seams. The figure shows that most severe dynamic events occur at depths greater than 400 m on average.

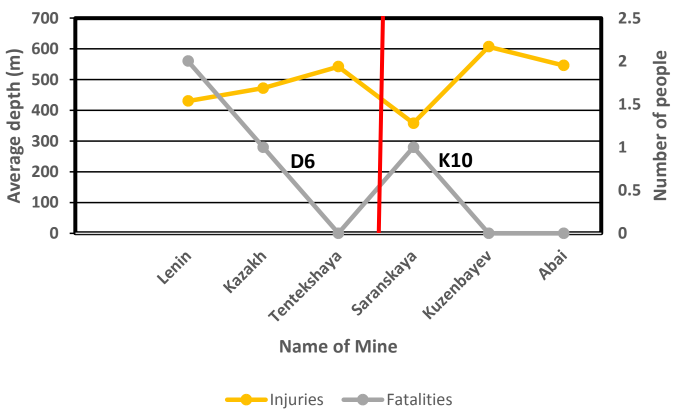

Figure 5 – Illustrative statistics of the consequences and locations of some dynamic events in selected Karaganda Coal Basin

 ISBN: 978-0-646-87565-1

4. TECHNICAL PROPOSALS FOR IMPROVING THE SAFETY OF MINING OPERATIONS ON COAL SEAMS PRONE TO GAS-DYNAMIC PHENOMENA

It is well established that the Karaganda Coal Basin is gassy. Hence, an effective approach to managing dynamic events will be efficient gas drainage. Best practice gas drainage guidelines (Hua, 2015; Hua et al. 2016; Skiba, 2019) are well established and if adopted, adhered to, and followed in the Karaganda Coal Basin Mines could help reduce the risk of gas outburst and coal bursts. In most cases interviews with miners and staff appear to point out that operational practices are not followed.

Work at the Central Mining Institute (CMI) in Poland by Eugeniusz et al. (2019) also demonstrate that shearer cutting rate impacts outbursts and coal bursts. The work shows that in gassy coal conditions a minimum shear cutting rate must be established and used to mitigate gas outbursts. It is concluded that elaboration of the tool which would be system of coal shearer speed control based on automatic methane concentration sensors measurement will have direct and significant impact on safety conditions in the exploited coal panels. This is a critical consideration to be investigated for potential use in the Karaganda Coal Basin mines.

5. SUMMARY

The paper sought to review the state-of-art of coal mining in the Karaganda Coal Basin mines with a view to future improvements on the impact of coal and gas outbursts. The coal in the Karaganda Basin is established to be gassy and sometimes occurs in complex geological structures. These characteristics have made the coal in the basin outburst and coal burst prone.

While several external experts have always been used to review dynamic events when they occur to provide guidelines for future improvements, the reports often provided seem vague and often do not differentiate between outbursts and coal bursts, apart from lack practical remedial measures that the management of the mines need.

The review has established that efficient gas drainage prior to and during longwall mining is lacking. Due diligence of gas drainage procedures established internationally if adopted and followed could assist mitigate the frequent and sometimes fatal gas outbursts and coal bursts.

It is also proposed that shearer speed monitoring to establish an optimum coal cutting speed appropriate for the coal in the Karaganda Coal Basin could benefit coal mining in the basin. This is worth further investigation.

ACKNOWLEDGEMENTS

The authors acknowledge Nazarbayev University for support through the Collaborative Research Program Grant # OPCRP2020014.

REFERENCES

Agapito, J.F.T. and Goodrich, R.R., (1999). Five Stress Factors Conducive to Bursts in Utah, USA, Coal Mines, in Proceedings 9th International Congress on Rock Mechanics (eds: Vouille, G. and Berest, P.), A.A. Balkema: Rotterdam.

Barczak, T.M., (2017). Research developments that contributed to the landscape of longwall roof support design over the past 25 years. In Advances in Coal Mining Ground Control.

Bauner, G., (1994). Rockbursts in Coal Mines and Their Prevention. AA Balkema, London.

Canbulat, I., Zhang, C., and Hebblewhite B., (2015). A preliminary review of coal burst experiences, mechanisms, and critical conditions in underground coal mines. Report Submitted to ACARP.

Eugeniusz, K, Skiba, J., and Bartłomiej, J., (2019). Mining speed control in the coal panels with high coal output concentration. Geneva, November 7-8, 2019.

Furniss, M.D., (2009). Quantitative Comparison of Seismic Velocity Tomography with Seismic Activity around a Deep Coal Longwall Panel, Master thesis, Virginia Polytechnic Institute and State University.

Galvin, J.M., (2016). Ground Engineering - Principles and Practices for Underground Coal Mining. Springer, Switzerland, 684 p.

Guo, H., Todhunter, C., Qu, Q. and Qin, Z., (2015). Longwall horizontal gas drainage through goaf pressure control. *International Journal of Coal Geology*. 150-151, 276-286.

Guo, Hua; Shen, Baotang; Qu, Qingdong; Qin, Johnny; Zhou, Binzhong; Wilkins, Andy. (2016). Fundamental studies for co-extraction of coal and coal mine methane in deep mining condition- Zhuji mine. CSIRO: N/A; 2016. csiro:EP163059.

Hua, G., (2015). Longwall Horizontal Gas Drainage through Goaf Pressure Control. International Journal of Coal Geology, Volume: pp. 150-151.

Pan, J., Meng, Z., Liu, B. (2005). Relationship between rock composition and texture of coal-bearing formation and its burst potential, Chinese Journal of Rock Mechanics, and Engineering, 24, 4422-4427.

Skiba, J., (2019). Development of Improved Methane Drainage Technologies by Stimulating Coal Seams for Major Risks Prevention and Increased Coal Output.

Suorineni, F.T. (2019). The future mining engineer – what will be the educational needs for the mine 4.0 industry? Mining Journal of Kazakhstan, Vol. 9, pp. 44-56.

US EPA, (2011). Deep Gassy Coal Mines of Karaganda Coal Basin. Prepared for the U.S. EPA Coalbed Methane Outreach Program by the Methane Center, Kazakhstan, through an Interagency Agreement with Pacific Northwest National Laboratory.

ISBN: 978-0-646-87565-1

ARMA 22–13

Strategy towards accurate location of seismic events sources in mining environments: Effect of voids and backfill

Mukhamedyarova Z., Suorineni F. and Aldubay T.
School of Mining and Geosciences, Nazarbayev University, Nur-Sultan, Kazakhstan
Sapinov G.
Department of Development of Mineral Deposits, Karaganda Technical University, Karaganda, Kazakhstan

ABSTRACT: Seismic events may occur naturally or unnaturally as a result of human activity. The focus of this research is on seismicity caused by human activities in underground mines. Despite significant technological advances in the mining industry, the phenomenon of rockburst and its mitigation measures are still controversial technique. Predicting the time of occurrence of rockbursts remains a challenge. At best we can estimate the potential location of seismic events from numerical modelling. Seismic monitoring systems play a major role in the mitigation of rockbursts by identifying their potential source locations. The accuracy of seismic event source locations depends on the reliability of the velocity model. Because the mining environment is constantly changing, a constant input velocity may result in spurious seismic event locations. In this paper physical laboratory models mimicking the continuously changing mining environment are used to investigate the impact of the changing mining environment on seismic wave velocity to provide means for predicting the seismic wave velocity in real-time to improve the accuracy of seismic source locations.

1. INTRODUCTION

Seismicity can occur naturally or be caused by human activity. This study focuses on underground mine seismicity induced by mining operations. A seismic event that occurs suddenly resulting in a damage to an excavation, equipment and or injury to personnel is known as a rockburst (Zhou, Li & Mitri, 2018). Rockbursts are a common problem in deep underground mines and affect mine operations in terms of safety, productivity and efficiency. Predicting the time of rockburst occurrence is difficult due to its complex nature. The only way to deal with the problem is to identify possible locations of rockburst occurrence through site experience or numerical modelling (Trifu & Suorineni, 2009).

Microseismic monitoring systems are common tools used for monitoring seismicity for the estimation of different hazard sources. These equipment are widely used in deep underground mines and are vital to control and mitigate the risks caused by seismicity. The microseismic monitoring system helps to detect, locate and identify seismic events in underground mines, and therefore they are essential part of the rockburst understanding mechanism.

The accuracy of predicting rockburst source location using microseismic monitoring systems is highly dependent on the velocity model in the event source location algorithm. Current practice uses a static input velocity model assuming the whole rockmass is homogeneous and does not degrade, which is far from reality. Using inappropriate input velocity model could result in inaccurate seismic event source locations (Collins, et al., 2014).

Nowadays using numerical modeling or relying on experience is the sole option to anticipate regions at risk of rockburst. Reducing the consequences of rockbursts requires discovering feasible solutions for reliable source locations.

The practice of using constant seismic wave velocities in seismic monitoring systems, while helping in the mitigation of rockburst consequences could be better improved if the corresponding velocities associated with the constantly changing mine environment are used in the source location algorithms for the calculation of the seismic source locations. The constantly changing underground mine environment is caused by several factors including stress-induced fracturing, expanding underground drift network, increasing number of voids from stoping, and changing excavation geometries and sizes. Increasing mining also means the intersection of different lithologies and structures such as faults and shear zones. Additionally, the type of backfill used, its age with time, and whether a stope is backfilled or not all affect the seismic wave velocity.

The application of 3D velocity models based on heterogeneous material on 3D ray tracing is shown to account for the presence of voids from mining operations and improved the accuracy of seismic source locations (Trifu & Shumila, 2010). However, seismic wave velocities are affected by other factors such as stress-induced fractures and the status of the voids formed, and their continually varying dimensions, geometry, and content. New lithologies and other geological structures such as faults and dykes intersected in the mining process will also impact the seismic wave velocity. The impact of these conditions is recognized by the Engineering Seismology Group (ESG), Inc., Canada and steps are being taken to overcome these issues. Such steps include periodic updating of the seismic monitoring systems input velocities through the use of in-situ experimental blasting in the concerned mines. While this approach is useful, it does not account for the continuously changing mine environment. Increasing the frequency of velocity updates could further improve the process, but, could be tedious and time-consuming. An ideal solution to the velocity updating should be in real-time.

The goal of this study is to develop a strategy based on physical modelling in a controlled environment to enable real-time seismic wave velocity prediction for inputting the microseismic monitoring systems source location algorithm for better seismic event source location determination.

The strategy of using physical models in a controlled environment is to avoid the complexities of rockbursts that are yet to be understood, and secondly, undertaking such a task remains a challenge in the complex mining environment that is constantly changing and is even more problematic. For these reasons, a novel experimental approach was made to use the physical models to mimic the underground mine environment in a controlled environment.

2. METHODOLOGY

Laboratory experiments with homogeneous rock samples (e.g. sandstone or granite) and synthetic blocks made from sand and cement are used in the study. The choice of rock types is based on sample homogeneity. There are five block sizes in the form of cubes (Table 1). Each block size is without a hole and with a hole of diameter determined based on the theory of elasticity to account for the boundary effects. Sample sizes vary from 150 mm to 450 mm at increments of 75 mm. The holes in the samples are centered with diameters varying from 50 mm in the 150 mm size cube to 150 mm in the 450 mm size cure at increments of 25 mm (Fig. 1).

Due to the high cost of the granite blocks, concrete samples molded in the laboratory were used for the most of the study. For the concrete samples used, the external faces were polished such that the deviation from planarity was less than 1mm. The increasing hole diameter mimics the increasing mine extraction ratio with time. Seismic wave velocities were determined in the cubes without holes and in the cubes with holes. The holes were tested empty to capture the impact of empty stopes and other voids in the mine on seismic wave velocity. After that, the holes were filled with different cement-sand ratios to represent mines with different backfill types. Each cement-sand ratio material was tested after curing for 8 hours, 1 day, 7 days, 14 days, and 28 days for its impact on seismic wave velocity. Backfill types used in the study include 0% cement (dry and wet sand), 5%, 10%, 15%, and 20% cement reflecting the cement to sand ratios of backfills commonly used in the mining industry.

In each of the block conditions discussed above, one sensor was used as a pulse to mimic seismicity and serve as a source. Seven other sensors were used as receivers at known coordinates. The pulse sensor location was also known. This was possible because the cube surfaces were carefully divided into grids with intersection points assigned known coordinates x, y, and z so that distances from the source to the receiving sensors could be calculated. Details of the acoustic emission (AE) equipment used in the research and the wave velocity calculation procedure are presented later in the paper.

2.1. *Rock and concrete block samples*

Laboratory investigations using homogenous synthetic rock samples are part of the research. Sample homogeneity is a key factor affecting on rock type choice. To represent a rock, concrete samples were cast in the laboratory with a mixture of sand and cement. A suitable cement to sand ratio for molding of concrete samples were established through ASTM C-109C standard (ASTM, 1966) and UCS testing of specimens from concrete mixes both for backfill and concrete samples quality assurance were conducted in accordance with ISRM/ASTM standards.

In accordance with ASTM C-109 C standard for material fraction for normal mortar:

- sand to cement ratio is 2.75
- water to cement ratio is 0.485.

After casting, vibration of the mixes was carried out for 4 minutes in order to compact and release any trapped air. The curing time was of 28 days was chosen, since concrete reaches approximate maximum strength (99%) after 28 days (Technology, 2021).

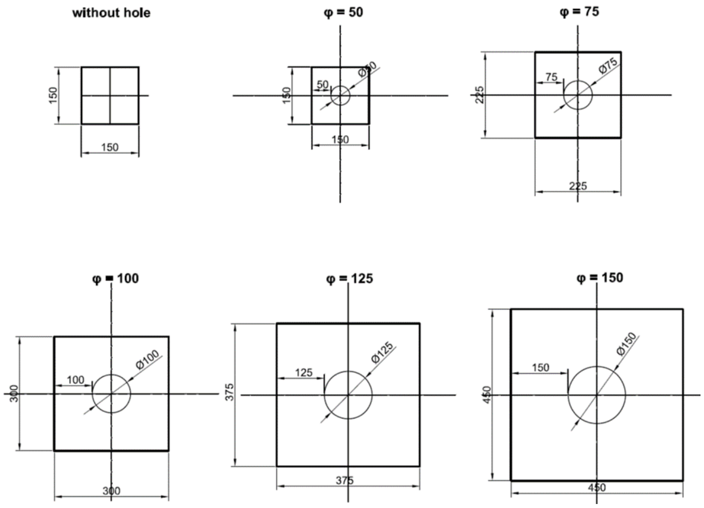

Fig. 1. Rock sample geometries representing a sample without hole and with increasing hole diameters, where ϕ is a hole diameter in mm.

Table 1. Block sizes and hole diameters

Block size			Hole diameter (mm)
Length (mm)	Width (mm)	Height (mm)	
150	150	150	0 (No hole)
150	150	150	50
225	225	225	0 (No. hole)
225	225	225	75
300	300	300	0 (No hole
300	300	300	100
375	375	375	0 (No. hole)
375	375	375	125
450	450	450	0 (No. hole)
450	450	450	150

2.2. *Backfill*

To see the effect of void content, backfill in holes in rock cubes and synthetic rock on seismic wave velocity the holes in the cubes were filled with various backfill types such as dry sand and water-saturated sand at 0% cement, 5%, 10%, 15% and 20% cement-sand proportions. Identification of mixture proportions of water to solids such as cement and sand was performed in accordance with ASTM C-109C standard. Sieving out of the sand was conducted to remove unnecessary materials such as organic materials, clay and oversize particles from the sand using AS 200 vibratory sieve shaker. Thus particles with dimensions more than 4 mm and less than 0.002 were removed.

2.3. *Equipment*

The application of acoustic emission technique (AET) is meant for non-disruptive testing of materials. Acoustic emission (AE) testing of concrete in the laboratory is about the laboratory scale monitoring of field scale seismic monitoring systems and can be used to mimic mine scale microseismic monitoring systems, with the difference that the mine scale coordinates be translated to the laboratory scale samples (Suorineni, 2000). Geometric similarity is the most critical factor and easy to implement in a scaled physical models (Xu, Liang, Suorineni and Li, 2021). There is a similarity between acoustic emissions (AE) and microseismicity in material failure processes. The discharge of energy from a strained substance is characterization of acoustic emission. Localized strain energy is released as a result of fracturing and is detected by sensors on the material's surface. Consequently, there is a comparison between seismological approaches and AET because they are based on identical principles. An illustration of a general AE identification system is shown in Figure 2. The transformation of dynamic movements at the surface of a material to electric impulses and detection of AE waves are executed by AE sensors. Preamplifier and main amplifier used to increase weak AE signals and could provide more than 1000 times gain.

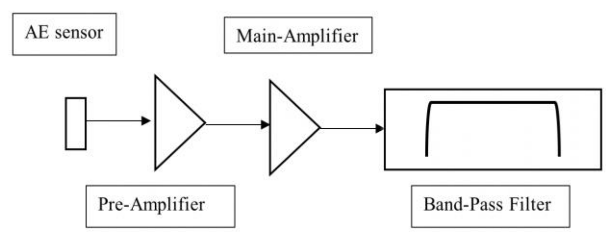

Fig. 2. AE detection system (Grosse and Ohtsu, 2022)

The source propagation in the material generates elastic waves and AE sensors record them (Grosse and Ohtsu, 2022). Hot glue gun was used to attach the AE sensors to the surface as shown in Figure 3.

The SAEU3H AE system was employed for the laboratory tests. The main components of this multi-channel system are AE data acquisition modules, a frame with forefront and back panels, a dispensable network connection module, a laptop, 8 sensors, preamplifiers, and cables (Figure 4). For testing 150 mm, 225 mm, and 300 mm rock samples, the SR150M High-frequency broadband AE sensor was used. The sensor's frequency band is between 60-400 kHz and peak sensibility is more than 75dB. For larger rock samples with dimensions of 375 mm and 450 mm, the SRI150 sensor was applied. This type of sensor has an embedded pre-amplifier with a frequency band between 60 kHz-400 kHz and a sensibility 40 dB.

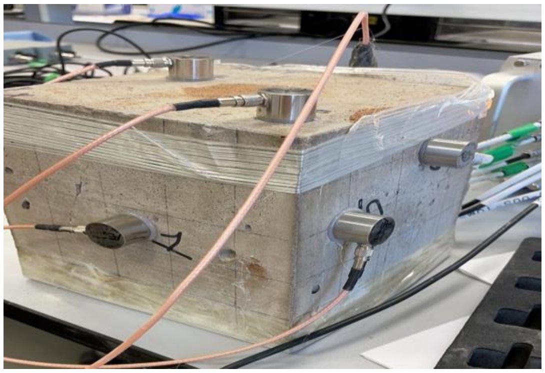

Fig. 3. AE sensors attached to the rock sample

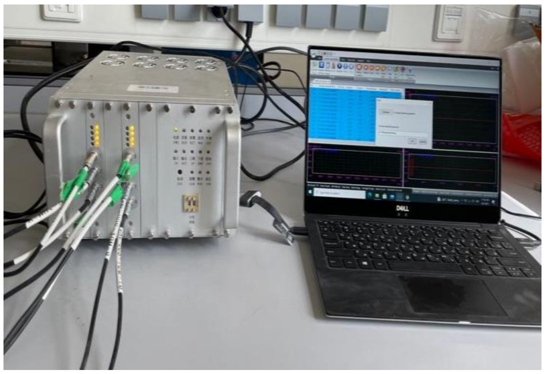

Fig. 4. SAEU3H AE system

2.4. Procedure of velocity calculation

The following steps were applied to determine the arrival time of the seismic wave:

- Generation of a coordinate system with grid and coordinate dimensions on the surfaces of the cubes
- Sensors placement on the sample surface at known coordinate; the experiment requires attaching at least four sensors lengthwise on the various sides
- Assignment of one of the sensors as a source s, and 7 sensors as receivers.
- The collection of the arrival times and source locations by the acoustic emission system is automated.
- For controlling every concrete sample to be consistent in characteristics, molding of cylindrical samples of 37 mm diameter and 74 mm height from the same concrete mixes was undertaken.
- Preparation of backfill specimens with 37 mm diameter and 74 mm height for the UCS experiment.

3. RESULTS AND DISCUSSION

3.1. AE tests

Sensor 1 was assigned as a source, which originates waves as a pulse toward a sample, and location of this sensor was in the middle of the front of the cubic sample to ensure wave travel across the hole. The determination of wave arrival times at every sensor was obtained from the AE experiments. The calculation of the distance (d_i) between receiving sensors and the source sensor was performed using the following equation:

$$d_i = \sqrt{(x_i - x_1)^2 + (y_i - y_1)^2 + (z_i - z_1)^2} \quad (1)$$

where $i = 2, 3, 4, 5, 6, 7, 8$ *and* x, y, z *are coordinates*.

The following equation was applied for seismic wave velocity (v) determination:

$$v = \frac{d_i}{\Delta t} \quad (2)$$

where $\Delta t = t_i - t_1$ and $i = 2, 3, 4, 5, 6, 7, 8$.

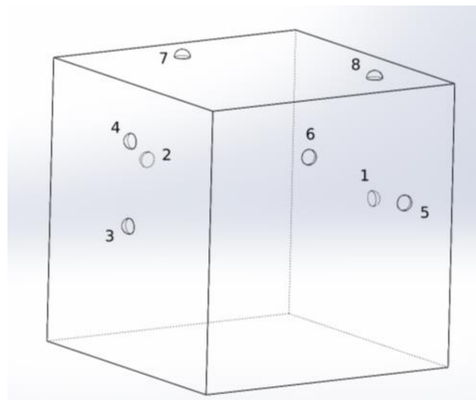

Fig. 5. Sensors location on 150 mm cube

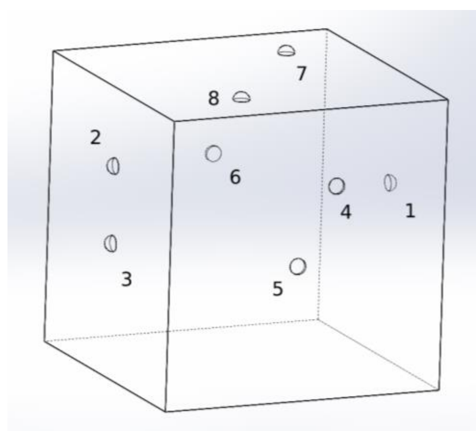

Fig. 6. Sensors location on 450 mm cube

3.2. Size effect on seismic wave velocity

The main objective of this study was to study the effect of size, hole, and various backfill content and age on seismic wave velocity. Five series of AE experiments were performed for each cubic rock and concrete sample. The seismic wave velocities for concrete samples without holes are shown in Figure 7. The mean values of 5 seismic wave velocities are used on the graph. According to obtained Figure 7, there appears to be no significant difference between the blocks without holes. It was expected that larger cubes with no holes will show relatively low velocities due to energy attenuation.

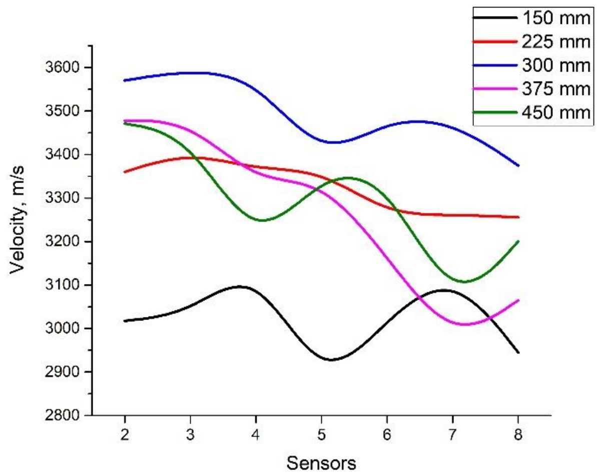

Fig. 7. Size effect on seismic wave velocity

3.3. *Hole effect on seismic wave velocity*

The outcomes of AE tests on cube samples with empty holes can be seen in Figure 8. The diameter of holes increases with increasing cube size. Figure 8 shows that apart from the larger cube size with the biggest hole diameter, there is no significant difference in the velocities of the other blocks with smaller diameter holes. Sensors 6, 7, and 8 show the largest drop in velocities in the 450 mm cube with a 150 mm hole diameter because these sensors were located across the hole for the source. We speculate that as a result of these sensor locations they suffered significant wave energy attenuation that resulted in delayed arrival times and therefore lower velocities.

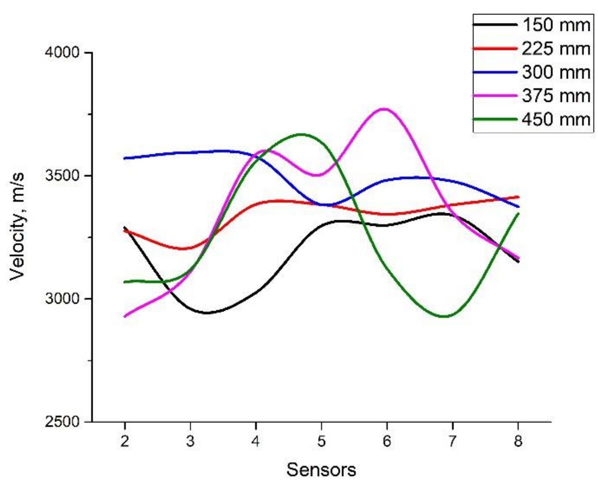

Fig. 8. Hole effect on seismic wave velocity

3.4. *Backfill effect on seismic wave velocity*

According to Figure 9 for the 150 mm cube, there is no velocity difference at the sensor locations except at sensor 7 for the 14 and 28 day curing times. One will assume that the same is located across the hole from the source. Similarly, in Figure 10 for the same cube with 20% backfill for 8 hours, 1 day, 7 days and 14 days show lower velocities at sensors 5, 6 and 8 and again attributed to wave energy attenuation across the source. Figures 11 and 12 for the 450 mm cube with cemented backfill tend to show some increase of velocities to maximum values and then drop. Such a behavior attributed to sensor locations relative to the source. According to the Figure 11, sensors 2 and 3 located opposite to the source showing the lowest velocities for the test with wet sand backfill for all curing periods.

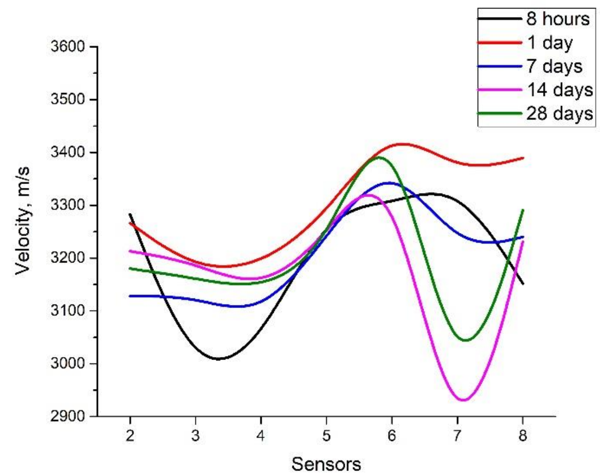

Fig. 9. 150 mm cubed filled with wet sand backfill

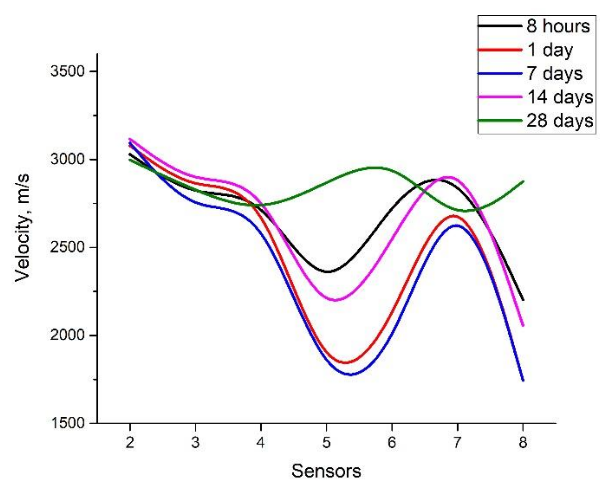

Fig. 10. 150 mm cubed filled with 20% cement backfill

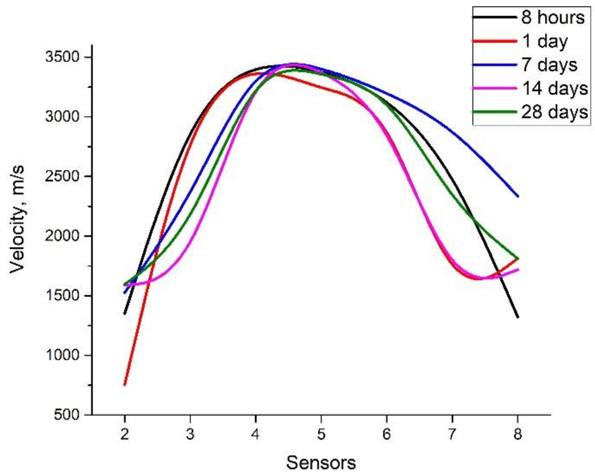

Fig. 11. 450 mm cubed filled with wet sand backfill

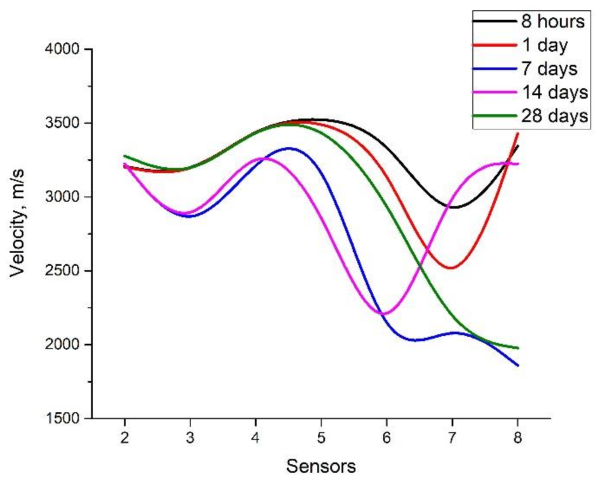

Fig. 12. 450 mm cubed filled with 20% cement backfill

4. CONCLUSIONS

Accurate seismic event source location in underground mines using seismic monitoring systems depends on the input velocity model. Consequently, it is crucial to consider the influence of the above-mentioned factors on seismic wave velocity. Through mimicking continuously changing underground mine environments with discrete physical rock and concrete models, the research outcomes demonstrate the influence of continual rockmass degradation in varying mining contexts as well as its impact on seismic wave velocity. The study results demonstrated increasing seismic wave velocity with increasing backfill strength and seismic wave velocity decrease with increasing hole size. The seismic wave velocities change depending on the location relative to the seismic source, if a void is present. The study is ongoing and future work will help clarify some inconsistencies in the data.

5. ACKNOWLEDMENTS

The authors acknowledge Nazarbayev University for support through the Collaborative Research Program Grant # OPCRP2020014

6. REFERENCES

1. Zhou, J., Li, X., & Mitri, H. (2018). Evaluation method of rockburst: State-of-the-art literature review. Tunnelling And Underground Space Technology, 81, 632-659. doi: 10.1016/j.tust.2018.08.029
2. Trifu, C., & Suorineni, F. (2009). Use of microseismic monitoring for rockburst management at Vale Inco mines, 1105-1114.
3. Collins, D., Pinnock, I., Toya, Y., Shumila, V., & Trifu, C. (2014). Seismic Event Location and Source Mechanism Accounting for Complex Block Geology and Voids. Retrieved 1 March 2022, from https://onepetro.org/ARMAUSRMS/proceedings/ARMA14/All-ARMA14/ARMA-2014-7530/123925
4. Trifu, C., & Shumila, V. (2010). Geometrical and inhomogeneous raypath effects on the characterization of open-pit seismicity. The 44th U.S. Rock Mechanics Symposium and 5th U.S.-Canada Rock Mechanics Symposium, Salt Lake City, Utah.
5. American Society for Testing and Materials. (1966). ASTM metric practice guide. Philadelphia.
6. Technology (2021). Why We Test Concrete Compressive Strength after 28 Days? Retrieved 1 March 2022, from https://theconstructor.org/concrete/why-we-test-concrete-strength-after-28-days/6060/
7. Suorineni F., 2000. Procedure for laboratory acoustic emission ae tests: esg system. Internal report, Mirarco, Laurentian University, Canada.
8. Xu, S., Liang, R., Suorineni, F., & Li, Y. (2021). Evaluation of the use of sublevel open stoping in the mining of moderately dipping medium-thick orebodies. *International Journal Of Mining Science And Technology*, *31*(2), 333-346. doi: 10.1016/j.ijmst.2020.12.002
9. Grosse, C., Ohtsu, M., Aggelis, D., & Shiotani, T. (2022). Acoustic Emission Testing. Cham: Springer International Publishing.

ARMA 23–111

Numerical modeling of seismic wave propagation in mimicked underground mine models

Mukhamedyarova, Z.
School of Mining and Geosciences, Nazarbayev University, Nur-Sultan, Kazakhstan
Suzuki Morales, K.
Department of Mining Engineering, University of Chile, Santiago, Chile
Suorineni, F., Madenova, Y.
School of Mining and Geosciences, Nazarbayev University, Nur-Sultan, Kazakhstan

ABSTRACT: Underground mines are going deeper worldwide with increasing production of mineral resources and decreasing ore grade, and this fact is creating challenging conditions. This fact makes the research into mine seismicity problem paramount. This manuscript focuses on the study of seismic wave propagation in a single material medium imitating the conditions found in underground mines. Understanding how waves propagate in a medium is fundamental to better interpret real-time information for accurate rockburst prediction. For this purpose, a numerical model is developed to represent results from laboratory experiments in which a signal of AE is transmitted through the material to measure the arrival time at different sensors located in the sample. The objective of the model is to better understand the physics of wave propagation and attenuation in the medium, which cannot be directly observed in a laboratory experiment. The model will be further used for other materials and geometries to study seismic wave propagation. The study considers two configurations: the first is a solid granite cube and the second is a solid granite cube with an empty hole in the middle. These configurations are modeled in FLAC^{3D}. The main assumptions are that materials are elastic, and the signal's waveform is sinusoidal. The study results showed wave propagation within a sample and quantified differences between modeled configurations. The model will be further used for other materials and geometries to study seismic wave propagation.

1. INTRODUCTION

With increasing production and depletion of mineral resources, underground mines are going deeper worldwide (Feng et al., 2019). Moreover, there are geotechnical engineering projects such as tunnels and underground laboratories located in very deep areas with complicated geology and ground conditions (Jiang, Feng, Xiang, & Su, 2010; Zhang, Feng, Zhou, Qiu, & Wu, 2012). Factors controlling seismic activity in the mine are not equivalent to those controlling the volume of the damage caused by seismicity. High stress is not the only factor causing seismicity; in fact, not all highly stressed areas are amenable to seismicity. There is a strong correlation between areas with a considerable decline in the volume of stored energy and seismically active regions. A threefold analysis is needed for the assessment of potential energy release that responds to mining works and major components of the analysis are stress, energy and loading system. Some of the conditions to be satisfied with seismic energy release from the rockmass are that (a) applied stresses have to exceed the strength of the rockmass, (b) a considerable volume of energy needs to be stored and released, and (c) energy release must be in a short period to initiate the dynamic, non-linear response of the rockmass (Kaiser, McCreath, & Tannant, 1996).

It is commonly observed that damage has the potential to manifest far away from the source and in unanticipated locations. Such outcomes may result from the impact of the excavation on the propagation of waves. If the propagation of waves surrounding excavations can be effectively simulated, it may become feasible to identify regions that are prone to damage in the event of potential seismic activity occurrences. This insight could then be utilized as valuable input into the mine safety design process (Hildyard & Young, 2002). The capacity to simulate the propagation of waves in the vicinity of deep underground openings holds significant potential applications in the design and stability of such excavations. This is particularly relevant for mining operations where short-term stability is imperative, as well as for other fields, such as nuclear waste disposal, where long-term stability is paramount. By using such models, it becomes possible to investigate the effects of a given excavation on wave propagation, peak motion distribution, and the mechanisms that can lead to unexpected motion amplification. Moreover, if models can accurately reproduce wave propagation patterns around excavations, then it becomes possible to forecast the probable motions and amplitudes in the event of a potential incident. This would allow the identification of areas that are likely to be impacted, and to take appropriate design measures. Another possible benefit is that the waves pass through fractured rock, and comparing recordings with models can provide valuable information about the condition of the rock in the vicinity of the excavation.

Application of numerical modelling is helpful for a better understanding of wave propagation in a material. Over the last decade significant progress has been made in using numerical modelling to simulate physical processes in rock mechanics and rock engineering at various scales (Jing, 2003). According to (Jing & Hudson, 2002) numerical modelling could help with a variety of aspects of the rockburst problem, such as the relationship between mining activities and associated seismicity, the source mechanism, and the effects of seismic waves on mining excavations.

The comparison of seismic locations, magnitudes, and mechanisms obtained from the numerical model and seismic data from the field provides additional confidence that the FDM/DEM coupled model can behave realistically, despite the obvious simplification of the reality in the model (Jing & Hudson, 2002).

Nowadays seismic signals using Acoustic Emission and signal analysis are being actively used for determination of the decomposition degree (Skipochka, Krukovskyi, Serhiienko, & Krasovskyi, 2019), elastic parameters (Nguyen, To, & Vu, 2017), microcracks (Song & Suh, 2014), character of the crack (Y. Wang & Li, 2015) and fracture depth (Kahraman & Yeken, 2008) of rocks. Static and dynamic loads effect physical characteristic of rocks differently. However, there is a strong correlation between seismic wave velocity and physical rock properties (Uyanık, Sabbağ, Uyanık, & Öncü, 2019). According to CAMIRO (1996), in the field of mine seismology, substantial seismic events are commonly referred to as "mine tremors" or "mine-induced seismic events." On the other hand, smaller seismic events located in proximity to active mine stopes are typically designated as "microseismic events," owing to their significantly reduced magnitudes. At the lower end of the magnitude spectrum, the term "acoustic emission" is often employed to describe high-frequency emissions or "rock noise" that are either recorded in laboratory-based rock samples under load or observed in localized areas of failure within a mine. It should be noted that the boundaries between these various categories are not clearly defined, and several authors, such as Dong, Sun, Li, and Du (2017), use the term "acoustic emission microseismic" or simply "AE/MS" to encompass both in a general sense.

As a result, the phenomenon of microseismicity during the failure process of materials exhibits similarities with acoustic emission (AE), which is characterized by the release of energy in stressed materials. This release of localized strain energy can lead to fracture, which can be detected by sensors on the material's surface. Hence, AET can be regarded as comparable to seismological techniques, despite the discrepancy in scale.

Numerical models can provide measurements of stress and strain changes caused by large-scale mining, when geotechnical monitoring is unavailable (Yi Wang, Shang, & Peng, 2020). Numerical models could suggest the best locations for access and proper stope sequencing. However, the rockmass response to mining that causes seismic energy release and potential damage to the excavations is complex and still not thoroughly understood. Therefore, laboratory experiments in a controlled environment are appropriate for seismicity study. The objective of this work is to develop a simple model to better understand the physics of wave propagation and attenuation in media, which cannot be easily and directly observed in a laboratory experiment. To achieve this objective, a simulation was performed on a granite cube in order to examine the impact of factors such as material density, elastic properties, and signal frequency on the propagation of seismic waves. It is essential to comprehend the influence of these diverse parameters on wave velocity and seismic wave propagation, as accurate prediction of rockburst necessitates a reliable velocity model.

2. METHODOLOGY

2.1. Laboratory test with AE system

The configuration previously used in tests with AE in concrete samples and granite properties obtained from laboratory tests are used for dynamic numerical modelling. The laboratory tests were conducted on a concrete cubic sample without a hole in the center through the block height to check the hole effect on seismic wave velocity. The cube size is 450 mm, and the hole diameter is 150 mm. Detailed settings, sensor choice, and AE data acquisition parameters are described in Mukhamedyarova et al. (2022).

2.2. Models

Fig. 1 presents the FLAC^{3D} model setup. The maximum grid size is limited in the dynamic configuration to ensure proper seismic wave travel. Based on the work of (Kuhlemeyer & Lysmer, 1973) recommended length of the element, Δl, by (ITASCA, 2022) is no larger than: 1/10 of the wavelength (λ). The specified wavelength, λ, corresponds to the highest frequency component of the input ground motion containing a large amount of energy. In this case, in order to study wave propagation in a granite sample, the element size is chosen to be at least 20 mm and results in a frequency of less than 15 kHz for granite that has a wave velocity of 3,000 m/s according to equation 1, where Δl is the spatial element size, λ and f are the wavelength and frequency associated with the highest frequency component that contains appreciable energy, respectively, and V_s is the shear wave velocity.

$$f < \frac{V_s}{10 * \Delta l} \quad (1)$$

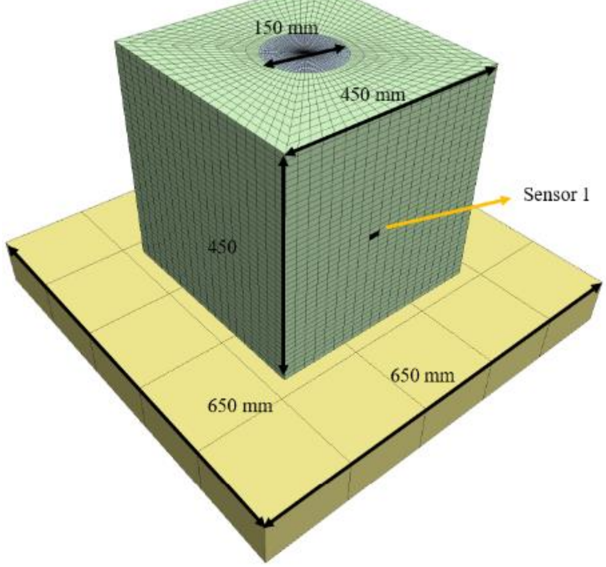

Fig. 1. Granite cube geometry.

In Fig. 1, the signal source originates waves as a pulse toward the sample in sensor 1, and the location of this sensor was in the middle of the front of the cubic sample to ensure waves travel across the hole.

2.3. Material

The model considers granite material. Table 1 presents the properties of the model, which is linear elastic because there are no stresses in the model that make the rock fail. Granite properties were determined from core samples drilled from granite cube.

Table 1. Granite properties

Young's modulus	66.56 GPa
Poisson's ratio	0.23
Shear modulus	27.01 GPa
Bulk modulus	41.10 GPa
Density	Density 2.7 g/cm^3

Damping should be applied to a system subjected to dynamic loading to simulate natural energy dissipation, otherwise, the system will oscillate indefinitely (Raffaldi & Loken, 2016). There are three damping models implemented in FLAC^{3D}: local damping, hysteretic damping and Rayleigh damping (ITASCA, 2022). Local damping, which has been widely used in many dynamic simulation studies (He et al., 2020) is chosen for this research. The critical damping ratio can typically be set as 2%–5% or obtained in a laboratory test; 5% is taken in this analysis.

2.4. Boundary conditions

Applying boundaries to the model in dynamic analysis may result in the reflection of propagating waves into the model. Model size could resolve this problem, but large model needs large computational time, which is also a problem, and in this case is not good solution since the model represents the whole system that needs to be studied and is not a volume of rock in the field. Another solution is to apply silent (quiet or absorbing) boundary to overcome the issue (Lysmer & Kuhlemeyer, 1969). However, these are not good options for the modeled configuration. For this case, to absorb wave energy reflected from the model boundary as much as possible and, thus guarantee calculation precision, static boundary conditions and free-field boundary conditions are established because the dimensions of the model represent the real laboratory configuration. Additionally, a signal source is directly applied to an element in the model to provide the input signal.

2.5. Applied signals and histories

Based on previous laboratory work done with AE system, one wave signal was assumed for the emitted signal based on the frequency considered for the model. AE is a wave generated by a sudden release of energy.

The time history may be used as an internal dynamic loading at internal grid points or as an external dynamic loading at the model border. There are four basic methods that dynamic loading can be applied: as time history of an acceleration, as a velocity, as a stress (or pressure), as a force, or all four of these. According to FLAC, the first and second alternatives should be used in cases with rigid bases, while the third and fourth options should be used in cases with flexible bases (Girsang, 2001). In this case, the assumed signal is presented in equation 2, where A is the amplitude, f is the frequency, and t is time, and it is applied for 1 ms.

$$v(t) = A \times \sin(2\pi \times f \times t) \quad (2)$$

3. RESULTS AND DISCUSSION

Figures 2-5 present the models with different frequencies for the configuration with and without hole. From these results it is possible to conclude that as wave propagates, different velocities are observed at different points in the sample which depends on the frequency of the emitted signal. Patterns are similar, but higher frequencies require smaller elements to properly propagate the wave. In AE, the higher the sampling rate, higher the accuracy of the signal, which means that higher frequencies are preferred.

Also, hole introduction causes additional wave energy attenuation around the hole, which can be seen from the results of 450 mm cube with a 150 mm diameter hole in Figure 5.

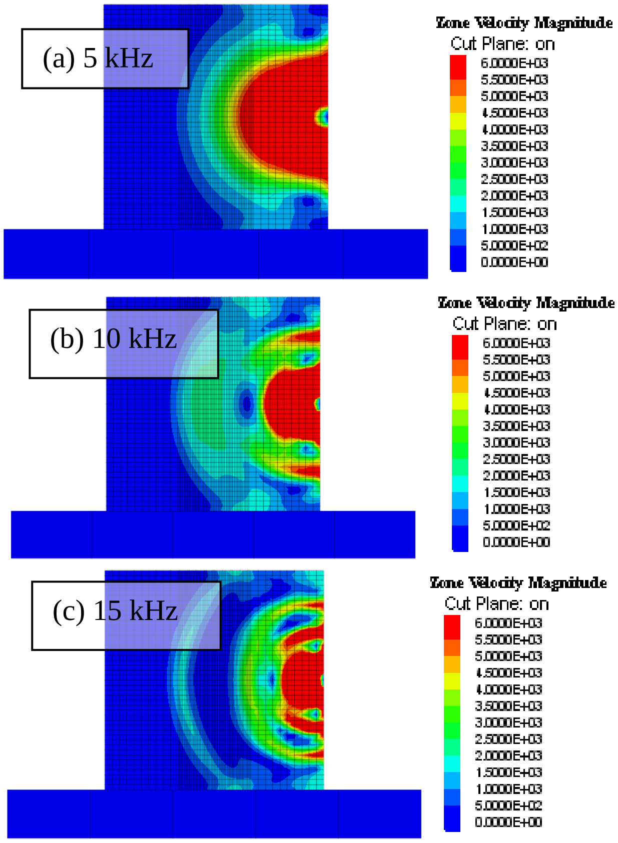

Fig. 2. Velocity magnitude with different frequencies for solid 450 mm granite cube. Section view at the middle of the sample at 0.1 ms.

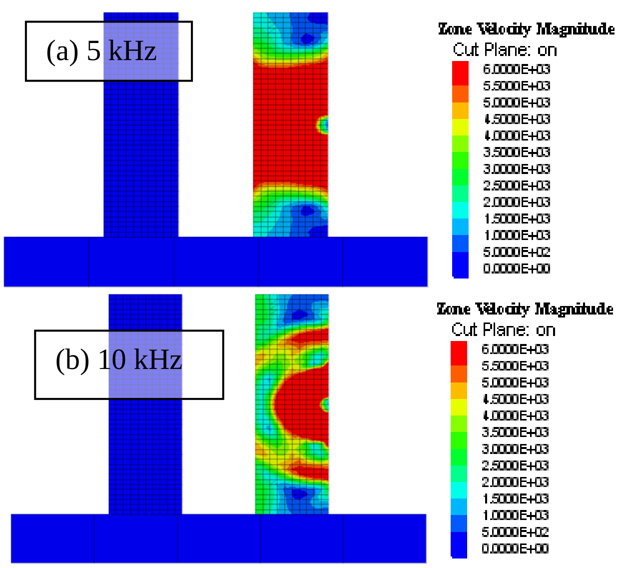

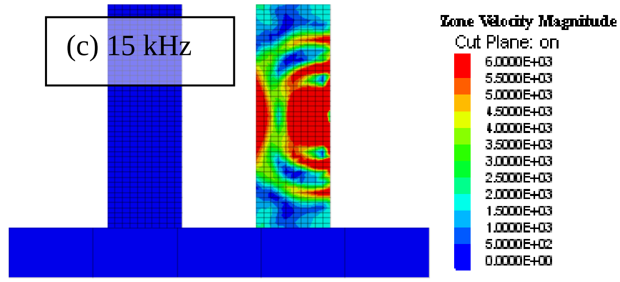

Fig. 3. Velocity magnitude with different frequencies for 450 mm granite cube with hole. Section view at the middle of the sample at 0.1 ms.

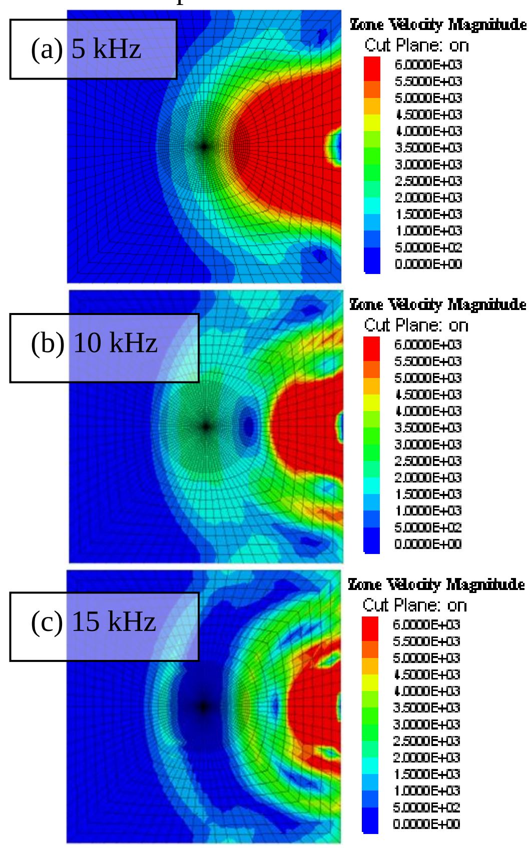

Fig. 4. Velocity magnitude with different frequencies for solid 450 mm granite cube. Top view of a cut at the middle of the sample at 0.1 ms.

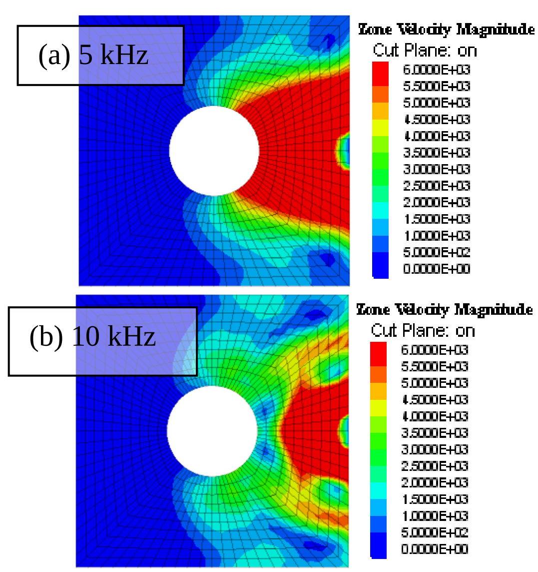

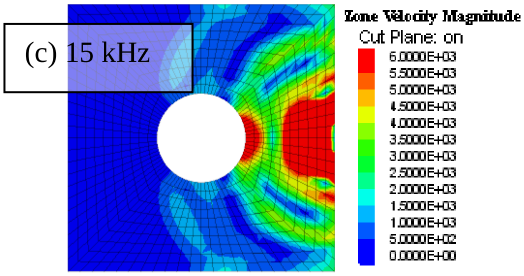

Fig. 5. Velocity magnitude with different frequencies for 450 mm granite cube with hole. Top view of a cut at the middle of the sample at 0.1 ms.

These results indicate that further research is required to better interpret results observed in receiving signal at different locations in the sample since the measured velocity will be affected by changes made in the rock.

Other parameters that affect the wave propagation pattern is the material density and elastic parameters. Figure 6 depicts that modifications in density within a spectrum spanning from sparsely compacted materials like soil to more densely compacted materials like rocks have minor impacts, but these may potentially influence the morphology of waves detected by various sensors. It is also important to properly characterize the elastic parameters of the sample. Fig. 7 shows that elastic parameters have a much significant effect on the wave propagation. The model considers parameters from Table 1. Fig. 7 (a) was run using the half of Table 1 parameters and Fig. 7 (c) using the double of those values.

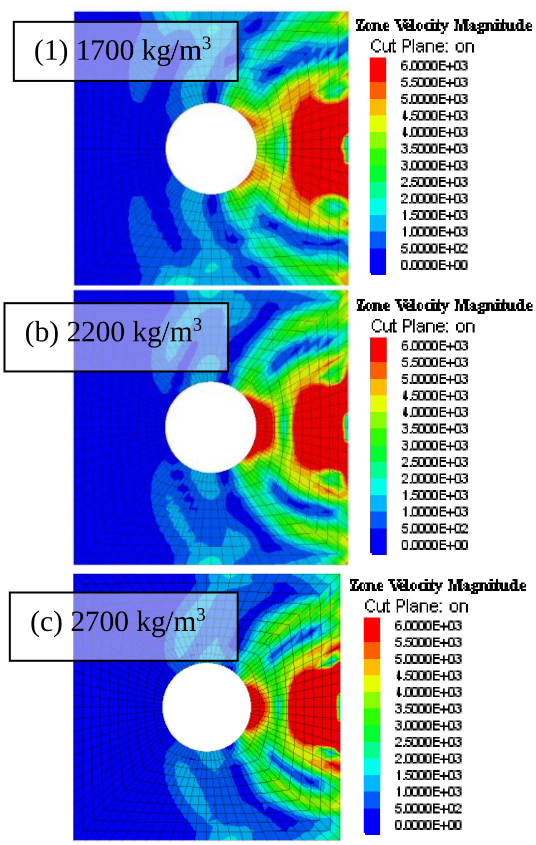

Fig. 6. Velocity magnitude with different densities for 450 mm granite cube with hole. Top view of a cut at the middle of the sample at 0.1 ms.

4. CONCLUSIONS

The findings of the study reveal that the introduction of holes resulted in an escalation in attenuation. The velocity of seismic waves varies with material properties and characteristics of the propagating waves, particularly with changes in elastic properties. The seismic wave velocity increases with higher material density and with the elevation of elastic parameters. These outcomes hold vital importance for the precise forecasting and interpretation of seismic wave velocity and energy attenuation in underground mine environments to enable accurate predictions of rockburst and stress variations. Although the research is ongoing, future work will explore the impact of additional parameters on wave velocity and attenuation in mimicked mine models.

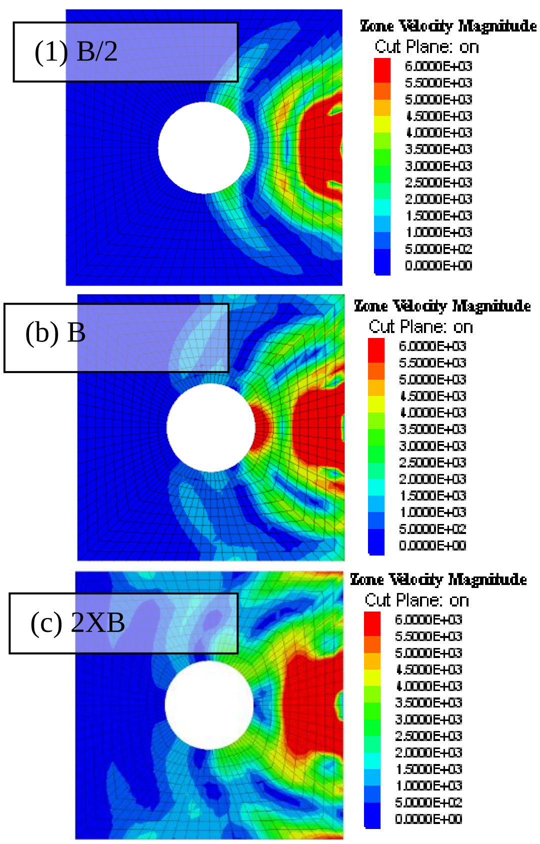

Fig. 7. Velocity magnitude with different elastic parameters for 450 mm granite cube with hole. Top view of a cut at the middle of the sample at 0.1 ms.

5. ACKNOWLEDMENTS

The authors acknowledge Nazarbayev University for support through the Collaborative Research Program Grant # OPCRP2020014.

REFERENCES

CAMIRO. (1996). *Canadian Rockbursts Handbook* (Volume 6). Mining Research Directory.

Dong, L., Sun, D., Li, X., & Du, K. (2017). Theoretical and Experimental Studies of Localization Methodology for AE and Microseismic Sources Without Pre-Measured Wave Velocity in Mines. *IEEE Access*, *5*, 16818–16828. https://doi.org/10.1109/ACCESS.2017.2743115

Feng, X., Xiao, Y., Feng, G., Yao, Z., Chen, B., Yang, C., & Su, G. (2019). Study on the development process of rockbursts. *Yanshilixue Yu Gongcheng Xuebao/Chinese Journal of Rock Mechanics and Engineering*, *38*(4), 649–673. https://doi.org/10.13722/j.cnki.jrme.2019.0103

Girsang, C. H. (2001). *A NUMERICAL INVESTIGATION OF THE SEISMIC RESPONSE OF THE AGGREGATE PIER FOUNDATION SYSTEM*.

He, S., Chen, T., Vennes, I., He, X., Song, D., Chen, J., & Mitri, H. (2020). Dynamic Modelling of Seismic Wave Propagation due to a Remote Seismic Source: A Case Study. *Rock Mechanics and Rock Engineering*, *53*(11), 5177–5201. https://doi.org/10.1007/s00603-020-02217-w

Hildyard, M. W., & Young, R. P. (2002). Modelling seismic waves around underground openings in fractured rock. *Pure and Applied Geophysics*, *159*(1–3), 247–276. https://doi.org/10.1007/PL00001253

ITASCA. (2022). Itasca's FLAC3D Documentation.

Jiang, Q., Feng, X. T., Xiang, T. B., & Su, G. S. (2010). Rockburst characteristics and numerical simulation based on a new energy index: A case study of a tunnel at 2,500 m depth. *Bulletin of Engineering Geology and the Environment*, *69*(3), 381–388. https://doi.org/10.1007/s10064-010-0275-1

Jing, L. (2003). A review of techniques, advances and outstanding issues in numerical modelling for rock mechanics and rock engineering. *International Journal of Rock Mechanics and Mining Sciences*, *40*(3), 283–353. https://doi.org/10.1016/S1365-1609(03)00013-3

Jing, L., & Hudson, J. A. (2002). Numerical methods in rock mechanics. *International Journal of Rock Mechanics and Mining Sciences*, *39*(4), 409–427. https://doi.org/10.1016/S1365-1609(02)00065-5

Kahraman, S., & Yeken, T. (2008). Determination of physical properties of carbonate rocks from P-wave velocity. *Bulletin of Engineering Geology and the Environment*, *67*(2), 277–281. https://doi.org/10.1007/s10064-008-0139-0

Kaiser, P. K., McCreath, D. R., & Tannant, D. D. (1996). *Canadian Rockburst Support Handbook*. (January), 314.

Kuhlemeyer, R. L., & Lysmer, J. (1973). Finite Element Method Accuracy for Wave Propagation Problems. *Journal of the Soil Dynamics Division*, (99), 421–427.

Lysmer, J., & Kuhlemeyer, R. L. (1969). Finite Dynamic Model for Infinite Media. *Journal of the Engineering Mechanics Division*, *95*(4).

Mukhamedyarova, Z., Suorineni, F., Aldubay, T., & Sapinov, G. (2022). Impact of Voids and Backfill on Seismic Wave Velocity-Preliminary Results. *Journal of Sustainable Mining*, *21*(4), 319–333. https://doi.org/10.46873/2300-3960.1370

Nguyen, S. T., To, Q. D., & Vu, M. N. (2017). Extended analytical solutions for effective elastic moduli of cracked porous media. *Journal of Applied Geophysics*, *140*, 34–41. https://doi.org/10.1016/j.jappgeo.2017.03.007

Raffaldi, M. J., & Loken, M. C. (2016). Framework for simulating fracture, ejection, and restraint of rock around a mine drift subjected to seismic loading. *50th US Rock Mechanics / Geomechanics Symposium 2016*, *2*(September), 1374–1390.

Skipochka, S., Krukovskyi, O., Serhiienko, V., & Krasovskyi, I. (2019). Non-destructive testing of rock bolt fastening as an element of monitoring the state of mine workings. *Mining of Mineral Deposits*, *13*(1), 16–23. https://doi.org/10.33271/mining13.01.016

Song, I., & Suh, M. (2014). Effects of foliation and microcracks on ultrasonic anisotropy in retrograde ultramafic and metamorphic rocks at shallow depths. *Journal of Applied Geophysics*, *109*, 27–35. https://doi.org/10.1016/J.JAPPGEO.2014.07.011

Uyanık, O., Sabbağ, N., Uyanık, N. A., & Öncü, Z. (2019). Prediction of mechanical and physical properties of some sedimentary rocks from ultrasonic velocities. *Bulletin of Engineering Geology and the Environment*, *78*(8), 6003–6016. https://doi.org/10.1007/s10064-019-01501-6

Wang, Y., & Li, X. (2015). Experimental study on cracking damage characteristics of a soil and rock mixture by UPV testing. *Bulletin of Engineering Geology and the Environment*, *74*(3), 775–788. https://doi.org/10.1007/s10064-014-0673-x

Wang, Yi, Shang, X., & Peng, K. (2020). Locating mine microseismic events in a 3d velocity model through the gaussian beam reverse-time migration technique. *Sensors (Switzerland)*, *20*(9). https://doi.org/10.3390/s20092676

Zhang, C., Feng, X. T., Zhou, H., Qiu, S., & Wu, W. (2012). Case histories of four extremely intense rockbursts in deep tunnels. *Rock Mechanics and Rock Engineering*, *45*(3), 275–288. https://doi.org/10.1007/s00603-011-0218-6

ARMA 23–345

Seismic source wave propagation analysis using laboratory AE monitoring system

Madenova, Y.[1,2]

[1]*Nazarbayev University, Astana, Kazakhstan*

[2]*Current affiliation: Los Alamos National Laboratory, Los Alamos, NM, USA*

Suorineni, F.T.[1] and Mukhamedyarova, Z.[1]

[1]*Nazarbayev University, Astana, Kazakhstan*

ABSTRACT: The source location algorithm in microseismic monitoring systems assumes a constant velocity model, which does not account for the effects of voids, fractures, backfills, and changing mine geometry in underground mines. This study investigated Acoustic Emission (AE) signal propagation characteristics towards signal receivers in laboratory physical models to understand the influence of various factors on seismic wave velocity. It was observed that the AE wave bypasses the voids and reflects off the backfill boundaries and follows the path of least resistance described by Fermat's principle and Snell's law. AE measurements show 1) similar signal travel time to sensors located across the void when the void in the concrete blocks was empty and when filled with various backfill types; 2) increasing backfill age had no influence on the signal travel time to the sensors. It was also found that the signal triggering behavior of the sensors in the proximity of the block voids is governed by Snell's law. This study concludes that the combination of the sensor network ray tracing method with Snell's law would be a promising solution to accurately determine applicable input wave velocities in seismic monitoring systems.

1. INTRODUCTION

The accurate location of seismic event sources is of practical importance for identifying seismic and burst-prone areas in underground mining, particularly when the ground condition and mine geometry are continuously changing. The effective tool employed by rockburst suspected underground mines to mitigate rockburst hazards is the microseismic monitoring system. The velocity model (VM) assigned to the rockmass is a fundamental parameter in microseismic monitoring systems used to define the seismic source parameters and to locate the seismic event sources. Several researchers pointed out that high uncertainties in microseismic source location come from the VM (Husen and Hardebeck, 2010; Collins et al. 2014; Reyes-Montes et al, 2016). The microseismic systems in most mines rely on a single or layered VM that is constant for source location purposes. This velocity model assumes an isotropic and homogeneous medium with the same properties throughout the volume of interest.

The single or layered VM is greatly simplified by ignoring the different geological and mine conditions underground, which affects the seismic wave velocity. For example, Horie and Aki (1982) detected velocity anomalies affected by the presence of active faults and lithological discontinuities when applying the inversion method of travel-time residuals for source location. While assigning the individual wave velocity to each rockmass type in multi-layer anisotropic rockmasses sounds a promising solution, the layered VM fails to capture the velocity changes due to mining-induced activities as noted by King (2012). Recently, Brantut (2018) developed an integrated open-source software called FaATSO (Fast Marching Acoustic Emission Tomography using Standard Optimization) that performs 3D anisotropic wave velocity tomography. The method presents a good perspective to locate the seismic sources, however, its accuracy somewhat depends on the inversion with anisotropy and p-wave arrival time picking precision.

The mining events in underground mines lead to continuous ground changes. Rock excavation, blasting, and other mining activities affect the quality of the rockmass, and results in voids, fracturing, and stress redistribution. To prevent the adverse consequences of mining-induced stress redistribution, voids created as a result of ore extraction are often backfilled. The backfill materials have different properties than the surrounding rockmass. The voids may also be unfilled. The excavated voids and the geological structures impact the wave propagation path making the single VM with straight raypath assumption inaccurate in locating the microseismic event source as shown in Collins et al.

(2014a, b) and Peng et al. (2020). The wave velocity of the seismic event is not uniform in the various underground media and changes depending on the characteristics of the wave propagation environment. Thus, the commonly used VMs are unable to account for sharp velocity contrast when locating the seismic source due to the heterogeneous medium characteristics and continuously changing ground conditions in underground mines. Because voids, fractures, backfills, and changing mine geometry in underground mining are known to impact seismic wave velocity due to the different properties of the media (Collins et al., 2014a, b; Mukhamedyarova et al., 2022), their effects on seismic wave propagation requires a close investigation to enhance the VMs to more accurately locate the seismic source.

Laboratory conditions enable the creation of a controlled mining environment in which the void and various backfill influence on the seismic wave propagation, can be explored. This paper presents the study of the Acoustic Emission (AE) signal propagation characteristics towards the signal receivers in laboratory physical models, which mimic the complex mining environment, with the objective of understanding the influence of various factors such as the excavated voids, fractures, backfills and changing mine geometry on seismic wave velocity.

2. MATERIALS AND METHODS

A complex underground mining environment associated with continuous excavation disturbances and backfilling is simulated using cast concrete cubes in the laboratory. Particularly, intact concrete cube samples with sizes of 150 mm, 225 mm, 300 mm, 375 mm, and 450 mm were used as a reference and representing ground conditions before any mining. The increasing extraction rock volume as a result of mine maturity with time was modeled by the holes in these cubic samples with the diameters of 50 mm, 75 mm, 100 mm, 125 mm, and 150 mm in the cubes of sizes 150 mm, 225 mm, 300 mm, 375 mm and 450 mm, respectively. Further, in the mining process, the resulting voids (holes) may be left empty or backfilled. To mimic the underground mine with backfilled voids, the holes of all concrete cubes were filled with backfill of different cement to sand ratios. It is also recognized that blasting and stress redistribution leads to fracturing of the rockmass. To effectively mimic this process in the physical modeling of underground mining conditions, a static cracking agent (SCA) is used to fracture the concrete blocks. For each of the conditions and blocks mimicking the underground mine, multi-channel SAEU3H AE system was used with one sensor generating a pulse to serve as a source while the other seven sensors mounted at different locations around the block surfaces served as receivers. The SR150M broadband AE sensor with peak sensitivity of more than 75 dB was used in the 150 mm, 225 mm, and 300 mm concrete blocks, while for larger blocks of 375 mm and 450 mm sizes, SRI150 sensor with a built-in preamplifier and sensitivity of 40 dB was selected. The frequency range of both sensors is 60-400 kHz (Mukhamedyarova et al., 2022). For larger concrete blocks, SR150M sensor was replaced with SRI150 sensor because the former was not capable to detect the wave arrival times in the 375 mm and 450 mm cubes likely due to the wave attenuation in inelastic concrete material. Cormier (1989) identify three seismic wave mechanisms: geometric spreading, intrinsic attenuation, and scattering attenuation. Soham and Abhishek (2016) states that geometrical spreading defines the attenuation of the seismic energy due to the distribution of wave energy over the surface of the spherical wavefront while intrinsic wave attenuation stems from the conversion of energy into heat. Scattering attenuation is the consequence of wave energy redistribution due to the presence of the heterogeneities in the medium through which the wave is propagated. Seismic wave attenuation (∈) (Ammon et al., 2021) has been quantified by Gellings (1961) and Knopoff (1964) using the term called quality factor (Q) (Eq. (1):

$$\in = \frac{\gamma}{m \times \omega_o} = \frac{1}{2Q} \quad (1)$$

where γ is coefficient of friction, m is mass, and ω_o is a resonant frequency. Eq. (1) implies that a high-quality factor Q (low attenuation) may indicate a tightly bound material which enables the propagation of displacement pulse with low or no energy loss, reaching the free surface with almost full strength, and vice versa. Furter details on seismic wave attenuation can be found in Jackson and Anderson (1970), Müller et al. (2010) and Spencer and Shine (2016).

Sensor configuration on 150 mm and 300 mm concrete blocks were similar, while the 225 mm, 375, mm and 450 mm concrete blocks also had similar sensor arrangements but different from those of the 150 mm and 300 mm blocks. The two types of sensor arrangement configurations on the 300 mm and 450 mm cubic samples with straight paths of AE signal source to receivers are illustrated in Figure 1. The AE wave arrival times at the receiving sensors were recorded for the following conditions: 1) Intact concrete cubes with no holes; 2) Concrete cubes with holes (a) empty; (b) holes filled with i) dry sand; ii) saturated sand; iii) 5% cemented sand fill; iv) 10% cemented sand fill; v) 15% cemented sand fill; vi) 20% cemented sand fill; (3) Fractured cubes with (i) no backfill and (ii) with backfill. In addition, AE signal data were collected for wet sand, and various cemented backfill cases after curing for 8 hours, 1 day, 7 days, 14 days, and 28 days. The case of the fractured cubes is beyond the scope of this paper and is discussed elsewhere in this conference.

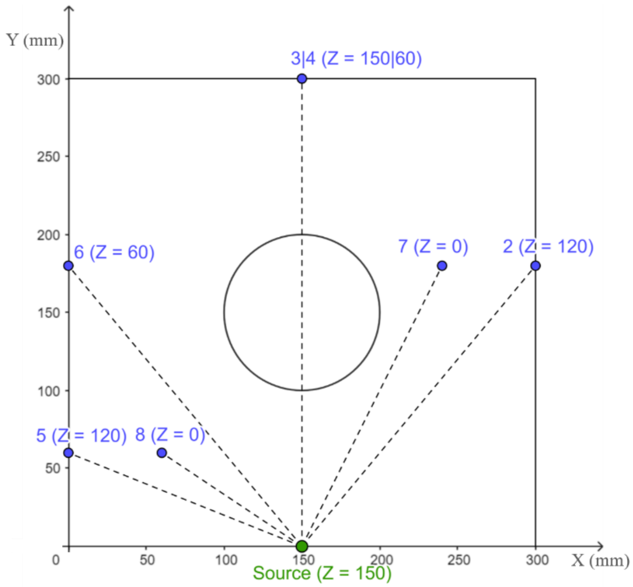

a)

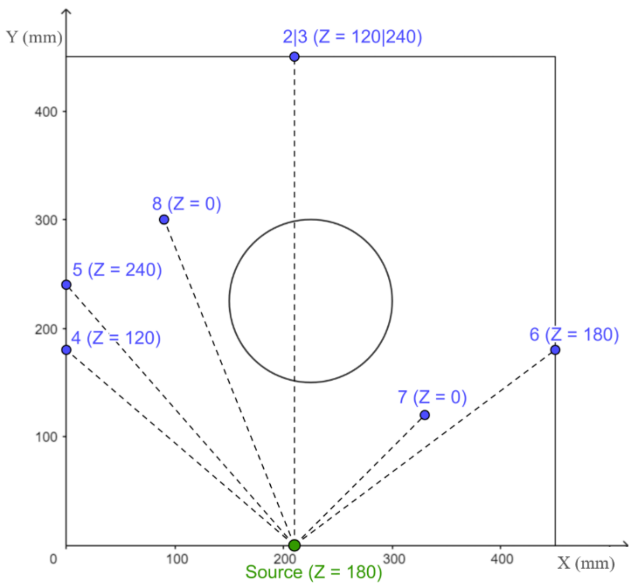

b)

Figure 1. The projected source and sensors' locations on the XY plane (plan view) for a) 300 mm block sample with hole diameter of 100 mm; and b) 450 mm block sample with hole diameter of 150 mm. Sensors 3 and 4 in the 300 mm block and sensors 2 and 3 in the 450 mm block are located across the block holes. Sensors 7 and 8 are the closest sensors to the block voids.

The AE measurements taken on the block samples are based on the first arrival time of the p-wave. These arrival times were auto determined by the AE system algorithm. The laboratory AE results were analyzed from the perspective of the wave (signal) travel time rather than the wave velocity. This is because the wave path is not explicitly known as it is affected by different factors (i.e., hole, backfill and fractures). In contrast, the wave travel time implicitly accounts for all known and unknown factors (i.e., concrete mix quality). To analyze the seismic source wave propagation, AE signal travel time (TT), from source to receivers (sensors) is calculated according to Eq. (2):

$$TT = t_a - t_o \quad (2)$$

Where t_0 is the origin time of the AE signal and t_a is AE wave first arrival time to sensor.

The conventional velocity models in the microseismic monitoring system are based either on direct or iterative solutions to locate the seismic sources (Riefenberg, 1989; Hedley, 1992; Ge, 2003). In both approaches, the distance between the source and receivers is considered a single or series of straight lines. Given the sensor configuration in Figure 1, the direct solution leads to the direct source-sensor distances shown in Table 1 for the 300 mm and 450 mm concrete blocks.

Table 1. The direct distances (straight raypaths) between source and receivers in 300 mm and 450 mm concrete blocks.

300 mm concrete block		
	Distance	Ray path across hole?
D51	164.32	no
D81	184.93	no
D21	236.22	no
D61	251.00	no
D71	251.00	no
D31	300.00	yes
D41	313.21	yes
450 mm concrete block		
	Distance	Ray path across hole?
D71	247.39	no
D41	283.02	no
D61	300.00	no
D51	324.50	no
D81	369.86	no
D21	453.98	yes
D31	453.98	yes

The source to receiver distances in Table 1 are listed from the shortest to the longest in increasing order. The increasing order of the source to sensor distances according to the straight ray path assumption is the same for the 150 mm and 300 mm and for the 225 mm, 375 mm, and 450 mm blocks because of the similar sensor configuration in these sample groups. In the 150 mm and 300 mm cubes, the AE wave traveling distance from source to sensors 6 and 7 is equal, while the assumed straight raypath from source to sensors 3 and 4 lies across the block hole. In the cases of the 225 mm, 375 mm, and 450 mm cubes, sensors 2 and 3 are located across the sample hole and the straight ray path distance from the source to these sensors is equal. The straight raypath assumption defined by the source to receiver direct distances is taken as a reference for seismic wave propagation analysis in this study.

3. RESULTS AND DISCUSSION

The AE wave arrival times recorded for each condition is presented in bar charts of the signal travel time to each sensor in Figures 2, 3, and 4. The results presented are for only the 150 mm, 300 mm and 450 mm concrete blocks. According to Figure 1 and Table 1, the assumption of straight AE wave raypath between source and sensors implies that the arrival times at the sensors should be in the order of 5, 8, 2, 6, 7, 3, and 4 for the 150 mm and 300 mm samples, while for the 450 mm sample, the signal should first be detected by sensors 7, 4, 6, 5, and then by sensors 8, 2, and 3 in that order.

In the following sections, first, the results are discussed for the cases when the blocks were solid (with no holes/voids), then with holes empty and finally with the holes filled with dry sand. This is followed by the block tested with the holes filled with saturated sand and various ratios of cement to sand. Finally, the AE signal to sensors located across the hole are analyzed.

3.1. Results for intact blocks, blocks with empty holes and with holes filled with dry sand

Figure 2 illustrates the signal TT obtained from the measurements taken on the solid concrete blocks, blocks with empty holes and holes filled with dry sand. Figures 2a and 2b show the outcome for arrival times for the 150 mm and 300 mm concrete blocks. It can be observed from these figures that the source signal was first detected by sensors 5, 8, 2, 6, 7, 3 and 4 complying with the straight raypath concept between source and receivers. The arrival times increase with distance of the receiving sensor from the event source (Sensor 1). For the 150 mm cube the travel times for the solid cube are about the same as cubes with holes empty and when filled with dry sand considering experimental errors. In particular, the solid cube, and the cube with hole were cast separately and their qualities could vary to impact the travel times. Thus, in a small 150 mm concrete block, a) the wave velocity can be calculated assuming the straight raypath and the VM can be considered constant despite the existing empty hole or hole filled with dry sand because of the same AE signal travel times in these conditions. The implication of this observation is that in the early stages of a mine with a low extraction ratio the constant velocity model could apply.

For the 300 mm cube (Figure 2b) with similar sensor arrangement to that of the 150 mm cube the travel times increase with distance from source to receiving sensors, generally, as observed in the 150 mm cube. For sensors at the same location for all cube conditions the travel times are similar, except for the case of sensors 3 and 4 that are located across the hole from the source. For these two sensors, the travel times for the cubes with hole and with hole filled with dry sand are equal and longer than for the case of the solid cube. This again reflects the effect of wave energy attenuation in traversing across the hole and due to the concrete block's inelasticity and size. The bigger the inelastic block size, the more the attenuation effect. In this case, there is no difference in the arrival times for two sensors in the case of the empty void and the void filled with loose dry sand. However, the presence of the void in this case compared with the solid cube affects the arrival time.

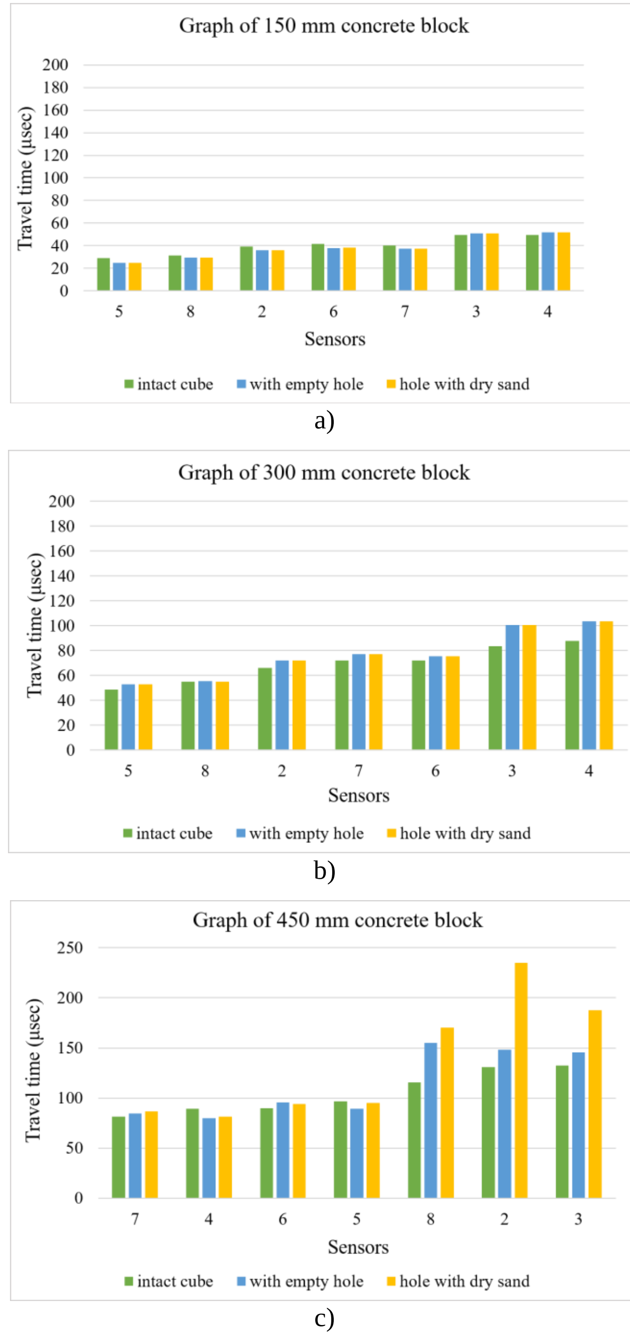

Figure 2. The graphs of the source signal travel time to sensors on a) 150 mm, b) 300 mm, and c) 450 mm concrete blocks when these blocks were intact, their holes were empty and filled with dry sand.

Considering equal signal travel time in the 300 mm blocks with empty holes and holes filled with dry sand, the explanation of an alternative signal route to sensors is reasonable and raypath tracing should apply. Practically, this means that with increased extraction the constant velocity model will no longer apply.

Figure 2c shows the AE signal travel time to sensors on the 450 mm concrete blocks with varying conditions: solid cube, cube with hole and cube with hole filled with dry sand. It can be seen that the source signal travel time to sensors 7, 4, 6, and 5 are approximately the same where the sensors were located in the intact block and not influenced by the void and its contents. However, the incremental pattern of the signal travel time to receiving sensors according to the straight raypath assumption cannot be clearly observed in the 450 mm blocks with an empty hole and a hole filled with dry sand compared to the 150 mm and 300 mm block cases. When the hole of the 450 mm block was empty, the AE signal arrival times at sensors 4, 5, 7, and 6 increases with sensor location distance from source. The wave arrival times at sensors 2, 3, 8 in the case of the block with an empty hole are about the same. The later signal arrivals at sensors 2, 3, and 8 can be explained by their further locations from the source and larger hole diameter in the 450 mm block (Figure 1b) that attenuates the signal energy increasing the signal travel time to these receivers. An empty hole in a 450 mm block presents a low velocity medium for AE wave propagation, when the AE signal straight raypath lies through the hole to sensors 2 and 3. Additionally, since sensor 8 is located close to the void of the 450 mm concrete block, the AE signal would have reached sensor 8 through the various paths reflected off the hole boundary following Snell's law. Snell's law for body waves describes the relationship between the angle of incidence of the ray and the velocity of the medium and it is widely applied in seismology as part of the ray path theory (Cervený, 2001; Amman et al., 2020). Thus, this implies that ray tracing becomes feasible to model the AE wave propagation to receivers near and across the voids when the extraction ratio (i.e., larger hole diameter) increases, and using the uniform velocity model is inappropriate.

Figure 2c depicts that when a 450 mm block hole was filled with dry sand, the AE signal travel time to sensors 2, 3, and 8 is greater than the other two cases and unlike the AE signal travel time patterns on 150 mm and 300 mm blocks. This means that the larger hole diameter in the 450 mm concrete block has more impact on the signal travel times compared to the smaller hole diameters in the 150 mm and 300 mm concrete blocks. This observation also confirms that in inelastic materials scale prolongs wave travel times through energy attenuation. Furthermore, a backfill of dry sand can be seen as a porous medium, which causes signal attenuation and slows down the AE wave propagation. The longer AE travel times to sensors 2 and 3 across the hole in the 450 mm block can be explained by the AE wave propagation path through the dry sand-filled environment.

It can be seen from Figure 2 that with increasing block and hole diameter, the signal travel time to sensors increases accordingly because of wave energy attenuation. This observation is in agreement with Zarina et al. (2022), who concluded that lower velocities observed with increasing cube size is due to a low-quality factor (Q) (Ammon et al. (2021) associated with less dense media and longer travel times.

3.2. Case for block voids filled with saturated sand

Figure 3 shows the cases of the 150 mm, 300 mm, and 450 mm concrete blocks with voids of 50 mm, 100 mm and 150 mm diameters, respectively, backfilled with the saturated sand. The AE measurements were taken at time intervals of 8 hours, 1 day, 7, 14, and 28 days after placing the fully saturated sand into the block voids and maintaining at room temperature. It is clearly seen that the source signal travel times to sensors at various backfill curing times are similar, especially for the 150 mm concrete cube, and depends on sensor locations from the source. They are also similar for sensors 5, 8, 2, and 3 in the case of the 300 mm cube. For the 450 mm cube, the arrival times are similar for sensors 7, 4, 6, 5 and 8. This implies that the saturated sand curing time has no effect on the AE signal travel time in the case of the 150 mm cube and increase with sensor location distance from the source. Similar to Figure 2a, the AE signal was detected by sensors in the order of 5-8-2-6-7-3-4 in the 150 mm block with holes filled with saturated sand (Figure 3a).

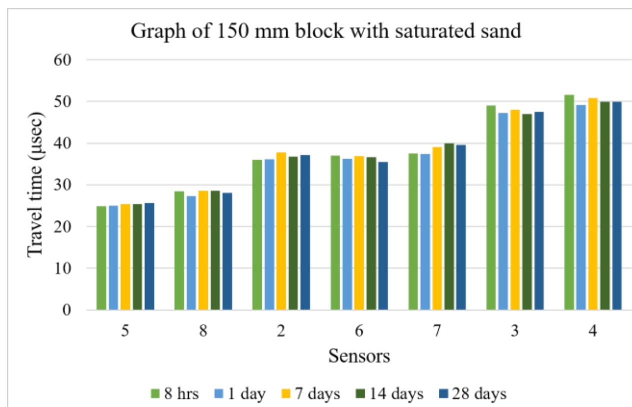

a)

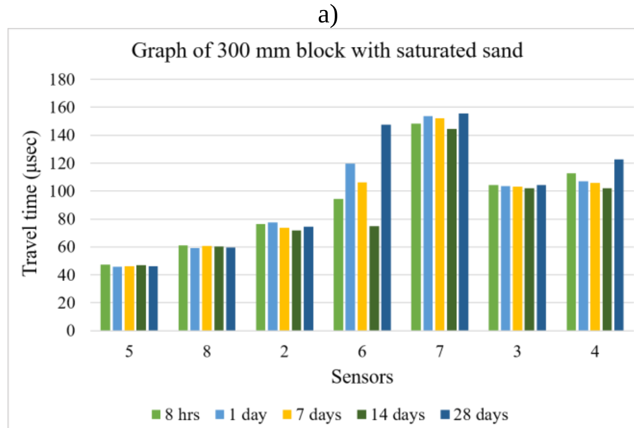

b)

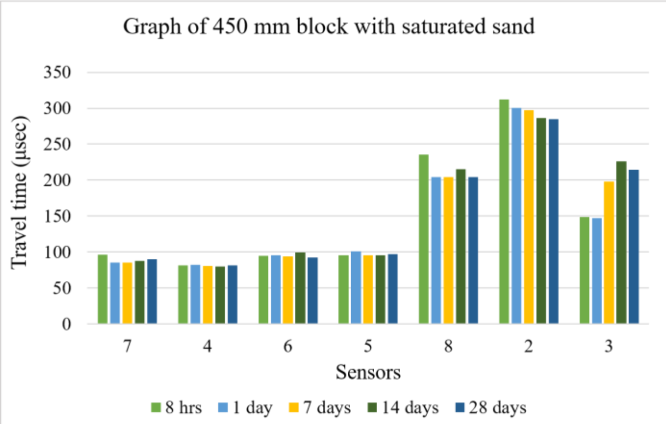

c)

Figure 3. Plots of the source signal travel time to receiving sensors when the block holes were filled with saturated sand a) 150 mm block, b) 300 mm block, and c) 450 mm block.

However, in the 300 mm block, the signal detection order is not conserved according to the straight path assumption. It can be noted that the source signal travel times to sensors close to the hole and across it from the source are considerably higher in the 300 mm and 450 mm blocks in Figures 3b and 3c, respectively. This can be the result of larger hole diameters in these blocks that cause the higher attenuation and consequently, increase in travel time. In addition, signal travel time to sensor 7 in the 300 mm block and sensor 8 in 450 mm block, which are close to the saturated sand filled holes, can be influenced by the backfilled boundary and sand saturation. Figures 3b and 3c also show anomalous arrival time spikes at several sensors at various wet sand curing times. These travel time spikes can be attributed to the arrival time picking algorithm in AE system, sand saturation, and signal reflections and refractions from the boundaries of the backfilled holes and blocks.

3.3. *Block hole filled with various backfill types*

Backfill in stopes was mimicked in the laboratory by filling voids in blocks with cement to sand ratios of 5%, 10%, 15%, and 20%. Due to the consistent and similar patterns for the various backfill conditions, only the 10% and 20% cemented sand fills in the 150 mm, 300 mm, and 450 mm concrete blocks are presented in Figure 4. If the AE first arrival wave to receiving sensors across the hole passed through the backfilled hole, then the AE signal travel time would be decreased with the increased cement content from 5% to 20% in the backfill. AE measurements were taken at backfill ages of 8 hours, 1 day, 7, 14, and 28 days. The cemented backfill gains strength with increasing curing time. Thus, backfill with higher cement content and curing age increases the velocity of the wave propagating through it, and consequently, reduces the AE signal travel time. However, this trend cannot be observed in Figures 4a-f. In Figure 4a, when the 50 mm hole of 150 mm block was filled with 10% cemented sand fill, the signal travel time to sensors was not affected by the backfill ages. Although some scattered pattern exists at various curing intervals, the difference between the signal travel times to sensors at various backfill curing times is not considerable. When the cement content increased from 10% to 20% in the 150 mm cube, the source signal was detected by sensors in the order of increasing distance between the source and receivers given in Table 1 complying with the straight raypath assumption (Figure 4b). This means with increasing cement content in backfill, the signal travel time to sensors has become steadier in the 150 mm block. In the cases of 300 mm blocks with 10% (Figure 4c) and 20% (Figure 4d) cemented backfills, no influence of backfill maturity can be observed in the signal travel times to receivers. However, in the former case, the signal travel time to sensor 7 is the highest, while in the latter situation of 20% cemented backfill, the detection behavior of sensor 7 is inconsistent at various backfill ages. This abnormal signal triggering behavior of the sensor 7 at various curing intervals can be explained by its close location to the backfilled hole (see Figure 1a). The AE signal to sensor 7 would have reached through the reflected off paths from the backfilled hole boundary according to Snell's law. Figure 4e shows the 450 mm block case with 10% cemented backfill, where signal travel times to sensors 5 and 6 was the same and to sensors 4 and 7 was similar with insignificant difference under various backfill ages. Although the signal travel time to sensors 2 and 3 located across the hole is similar when the 10% cemented backfill cured 8 hours and 1 day, at subsequent curing times of 7 days, 14 days, and 28 days, the signal travel time to these sensors increased exponentially (Figure 4e). This contradicts the hypothesis of the reduced travel time with the backfill age. The detection behavior of sensor 8 also does not comply with this hypothesis showing a variable travel time at increasing backfill curing times. In contrast, similar signal travel time to all sensors except to sensor 8 can be observed from Figure 4f when the 450 mm block hole was filled with the 20% cemented sand fill. Variable signal detection behavior of the sensor 8 can be explained by its location on top of the 450 mm concrete block close to the backfilled void.

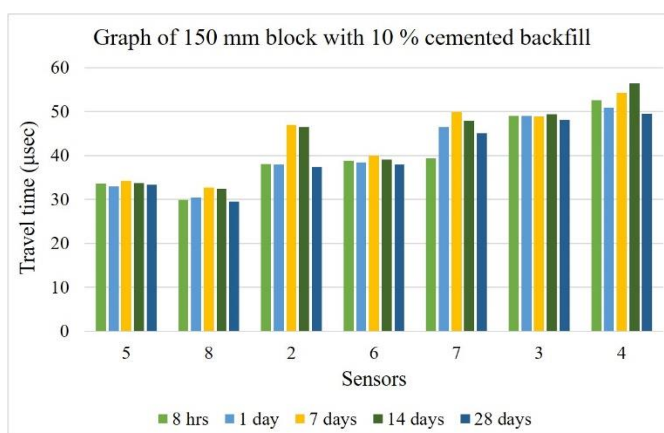

a) 150 mm block with 10% cemented backfill

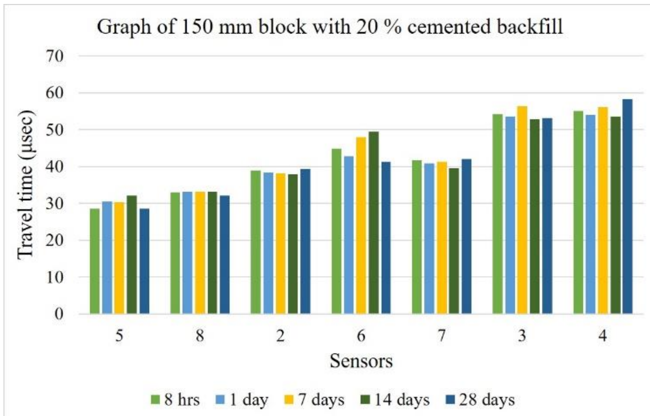

b) 150 mm block with 20% cemented backfill

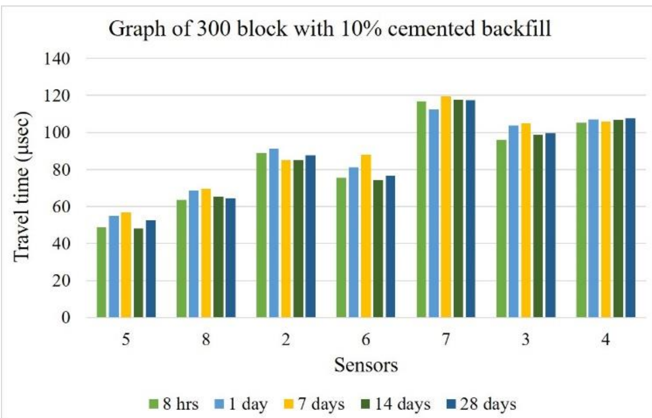

c) 300 mm block with 10% cemented backfill

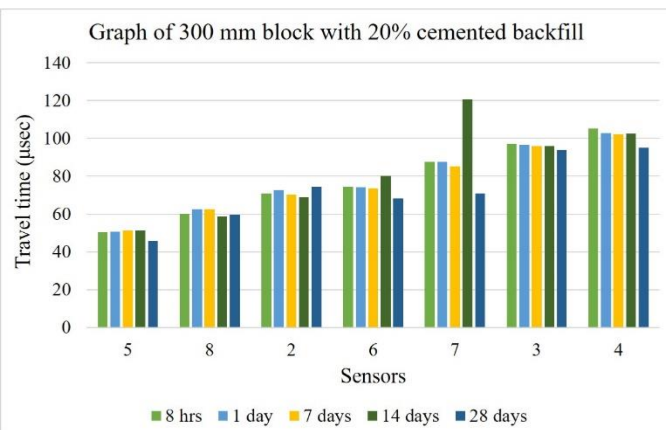

d) 300 mm block with 20% cemented backfill

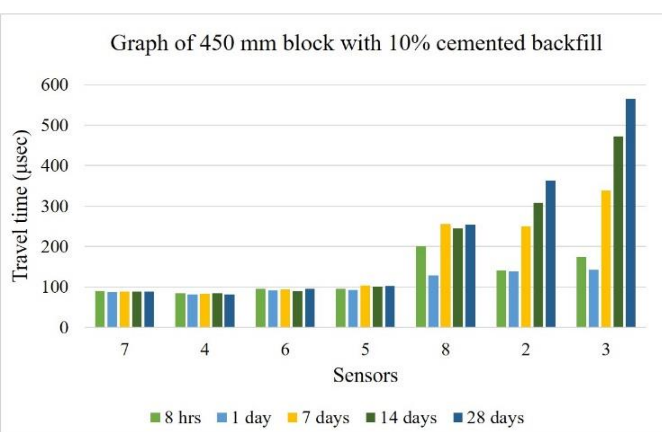

e) 450 mm block with 10% cemented backfill

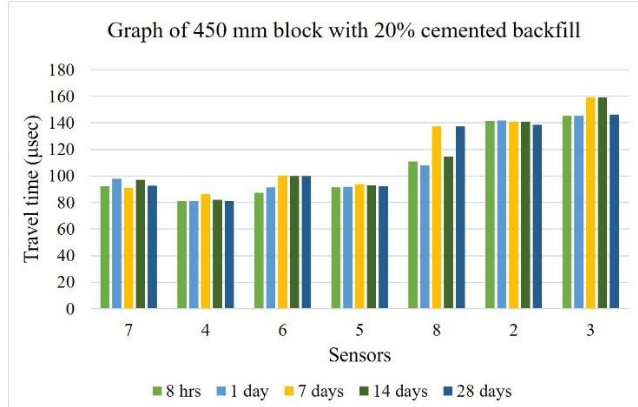

f) 450 mm block with cemented backfill

Figure 4. The graphs of the source signal travel time to sensors when the holes were filled with the 10% and 20% cemented backfills.

In general, similar to the AE measurement outcome for the saturated sand case, the AE signal travel time has not been affected by the curing time of the backfills in the majority of measurements taken in the 150 mm, 300 mm, and 450 mm blocks. Furthermore, the straight raypath assumption associated with the signal detection by sensors in the incremental distance order is not exactly complied with according to Figure 4. Particularly, sensors 7 and 8 located on top of the concrete blocks and close to the block holes indicate a higher signal detection time compared to the remaining sensors. As discussed before, AE signals would have reached the sensors following the longest path defined by the series of reflected paths. Thus, the increased signal travel time might be associated with the long traveling distance than the varying wave velocity.

3.4. *AE signal propagation to sensors across the block hole*

The AE signal travel to sensors located across the hole requires close attention to understand the AE wave propagation characteristics. For this purpose, Figures 5 and 6 show the AE signal travel times to sensors 3 and 4 in the 300 mm block and to sensors 2 and 3 in the 450 mm block, respectively, under various sample conditions. Due to the geometrical location of the sensors placed across the hole from the source, it is expected that the AE wave propagates through the hole to these sensors from the perspective of the straight raypath assumption. Surprisingly, both figures demonstrate that AE signal wave propagation time to sensors located across the hole is quite similar at all sample testing conditions except the saturated sand fill and 10% cemented. This implies that in the presence of a medium with different characteristics than the host environment, the AE wave follows the path of least resistance, which is described by Fermat's principle (Robinson and Clark, 1987). Fermat's principle states that the seismic wave travels from source to receiver following the path of minimum travel time among all possible paths connecting source and receiver. An efficient approach to determining the minimum travel time and ray trajectory from source to receivers is the theory of graphs, which is based on the network of ray paths (Cervený, 2001; Amman et al., 2020). The ray tracing solutions based on this theory are also known as the shortest path method and network ray tracing. A detailed discussion of the network ray tracing can be found in Moser (1992), while its recent application based on the Dijkstra algorithm to locate mining-induced seismicity was implemented by Peng et al. (2020).

The AE measurement results indicate that with increasing block size, the effect of the empty voids and backfill becomes considerable. However, although the empty void and different backfill types affect the AE wave propagation, the AE signal ray path to sensors across and next to holes does not cross these media. In the presence of the empty void and backfill with some cement content, AE signals to sensors across the hole bypass the hole and follow the path of least resistance or the minimum travel time path defined by Fermat's principle. According to Fermat's principle, the minimum travel time path, also termed the shortest path, can be described as a curved raypath opposite to the straight raypath assumption. Considering these characteristics of AE signal travel, using the uniform VM in a homogeneous medium and layered VM in an inhomogeneous medium may be feasible for seismic source location in the presence of the voids and cemented backfill. Dry sand fill strongly attenuates the AE wave propagation and cause late arrival times to sensors across and near the hole. When establishing the sensor array network in underground mines under porous and wet medium conditions, the effect of these conditions on the signal arrival time delay should be considered. A remarkable result of the study is that the wave to sensors located on top of the blocks close to the holes did not follow the straight raypath concept, although the wave raypath geometry theoretically does not cross the hole. This implies that the traditional velocity models, which assume a straight raypath assumption are not valid for the signal-sensor geometry in the vicinity of the backfilled hole. Rather, this case is governed by Snell's law according to which the source signal reaches the receivers through the reflected off paths from the block-backfill boundary.

The observations of the AE wave propagation characteristics lead to the inference that the optimal and promising solution for the accurate seismic source location should consider the integration of both Fermat's principle and Snell's law. Thus, research attention in seismic source location studies should be shifted to the ray tracing approach rather than the modification of the traditional velocity models.

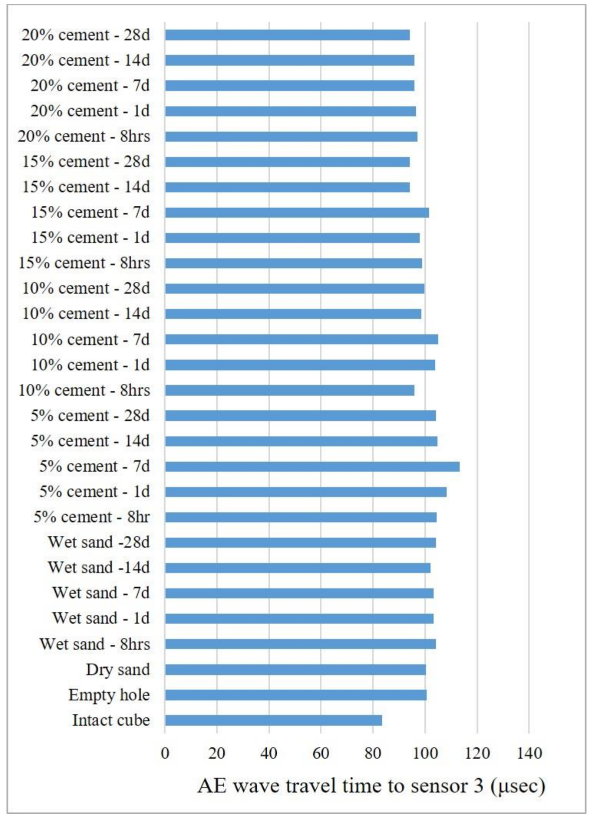

a)

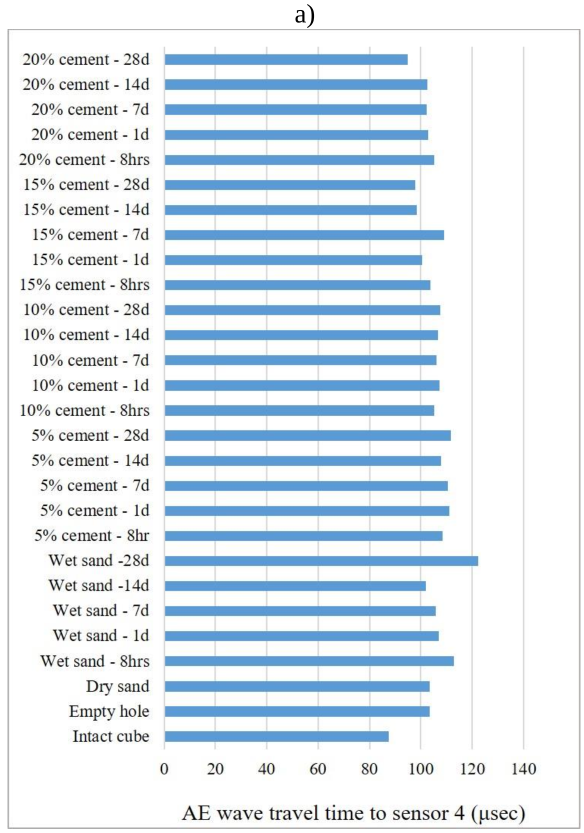

b)

Figure 5. AE signal travel time to a) sensor 3 and b) sensor 4 in 300 mm concrete block. AE signal wave propagation time to sensors 3 and 4 is relatively similar at all testing conditions.

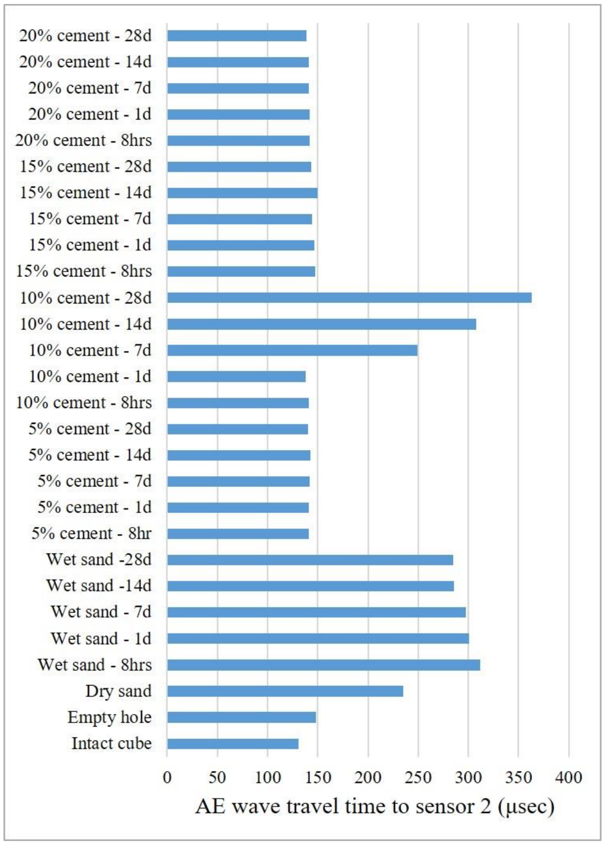

a)

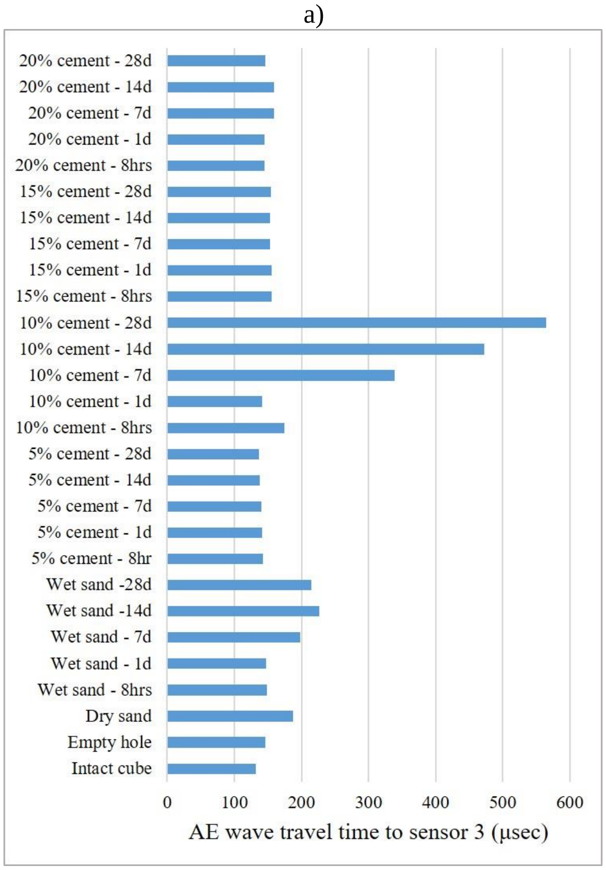

b)

Figure 6. AE signal travel time to a) sensor 2 and b) sensor 3 in 450 mm concrete block. AE signal travel time to sensors located across the hole is similar at all testing conditions except dry sand and saturated sand fill cases.

4. CONCLUSION

The accurate location of aseismic event source in underground mining plays a critical role in mitigating damage from rockburst and microseismic events, particularly, when the ground conditions and mine geometry are continuously changing due to mining activities. Although it is known that existing voids, fractures, and backfills affect the seismic wave velocity, the microseismic monitoring system relies on the constant wave VM, in which these adverse effects are not reflected. This study was conducted to investigate the AE signal propagation characteristics towards signal receivers under these adverse conditions taking advantage of the laboratory physical blocks, which were designed to mimic the complex mining environment. The following conclusions are derived from the AE measurements taken for various concrete block conditions: 1) in isotropic homogeneous (intact) blocks, the straight raypath assumption is valid, and constant and layered VMs can be safely used in the presence of voids and cemented backfills; 2) void and backfill effect on AE signal travel time is negligible in small 150 mm blocks. However, with increasing block size and void diameter and with backfill in the voids, the signal travel time to sensors increase; 3) in the presence of the void and backfill with various cement to sand ratios, AE signal follows the minimum travel time path towards sensors across the hole. Hence, ray tracing theory based on the shortest path and Fermat's principle is an efficient approach to locating the seismic sources; 4) In the 450 mm block case, dry sand fill presenting the porous medium attenuates the signal and causes longer signal travel times; 5) the signal triggering behavior of the sensors in the proximity of the block voids is governed by Snell's law. This study concludes that the combination of the network ray tracing method with Snell's law would be an ideal and efficient solution to accurately locate the seismic sources.

ACKNOWLEDGEMENTS

This study is supported by Nazarbayev University Collaborative Research Program (CRP) under Grant Number OPCRP20200114. The authors also wish to gratefully acknowledge the support of the Los Alamos National Laboratory's Laboratory Directed Research and Development – Exploratory Research program (LDRD-ER-20220175ER).

REFERENCES

1. Ammon, C. J., Velasco, A. A., Lay, T., & Wallace, T. C. (2020). *Foundations of modern global seismology*. Academic Press.
2. Brantut, N. (2018). Time-resolved tomography using acoustic emissions in the laboratory, and application to sandstone compaction. *Geophysical Journal International*, *213*(3), 2177-2192.

3. Cervený, V. (2001). *Seismic ray theory* (Vol. 110). Cambridge: Cambridge university press.
4. Collins, D. S., Pinnock, I., Toya, Y., Shumila, V., & Trifu, C. I. (2014a, August). Seismic event location and source mechanism accounting for complex block geology and voids. In *48th US Rock Mechanics/Geomechanics Symposium*. American Rock Mechanics Association.
5. Collins, D. S., Toya, Y., Pinnock, I., Shumila, V., & Hosseini, Z. (2014b, September). 3D velocity model with complex geology and voids for microseismic location and mechanism. In *Proceedings of the Seventh International Conference on Deep and High Stress Mining* (pp. 681-688). Australian Centre for Geomechanics.
6. Ge, M. (2003). Analysis of source location algorithms: Part II. Iterative methods. *Journal of Acoustic Emission*, *21*(1), 29-51.
7. Hedley, D. G. (1992). *Rockburst handbook for Ontario hardrock mines* (Vol. 92, No. 1). Canmet.
8. Horie, A., & Aki, K. (1982). Three-dimensional velocity structure beneath the Kanto district, Japan. *Journal of Physics of the Earth*, *30*(3), 255-281.
9. Husen, S., and J.L. Hardebeck. (2010). Earthquake location accuracy, Community Online Resource for Statistical Seismicity Analysis, doi:10.5078/corssa-55815573. Available at http://www.corssa.org.
10. Jackson, D. D., & Anderson, D. L. (1970). Physical mechanisms of seismic-wave attenuation. *Reviews of Geophysics*, *8*(1), 1-63.
11. King, A. (2012). Velocity model determination for accurate location of mining-induced seismic events. *ASEG Extended Abstracts*, *2012*(1), 1-4.
12. Mukhamedyarova, Z., Suorineni, F., Aldubay, T., & Sapinov, G. (2022). Impact of voids and backfill on seismic wave velocity-preliminary results. *Journal of Sustainable Mining*, *21*(4), 319-333.
13. Müller, T. M., Gurevich, B., & Lebedev, M. (2010). Seismic wave attenuation and dispersion resulting from wave-induced flow in porous rocks—A review. *Geophysics*, *75*(5), 75A147-75A164.
14. Peng, P., Jiang, Y., Wang, L., He, Z., & Tu, S. (2020). A Fast ray-tracing method for locating mining-induced seismicity by considering underground voids. *Applied Sciences*, *10*(19), 6763.
15. Reyes-Montes, J. M., Sainsbury, B. L., Andrews, J. R., & Young, R. P. (2012). Application of cave-scale rock degradation models in the imaging of the seismogenic zone. In *Proceedings sixth international, conference and exhibition on mass mining, Massmin* (pp. 10-14).
16. Riefenberg, J. S. (1989). *A simplex-method-based algorithm for determining the source location of microseismic events* (Vol. 9287). US Department of the Interior, Bureau of Mines.
17. Robinson, E., & Clark, D. (1987). Fermat and the principle of least time. *The Leading Edge*, *6*(2), 34-37.
18. Spencer, J. W., & Shine, J. (2016). Seismic wave attenuation and modulus dispersion in sandstonesSeismic wave attenuation in sandstones. *Geophysics*, *81*(3), D211-D231.

ARMA 23–346

Effects of fractures on seismic wave propagation path: laboratory studies

Madenova, Y.[1,2]
[1]*Nazarbayev University, Astana, Kazakhstan*
[2]*Current affiliation: Los Alamos National Laboratory, Los Alamos, NM, USA*
Suorineni, F.T.[1] and Mukhamedyarova, Z.[1]
[1]*Nazarbayev University, Astana, Kazakhstan*

This paper was prepared for presentation at the 57th US Rock Mechanics/Geomechanics Symposium held in Atlanta, Georgia, USA, 25-28 June 2023. This paper was selected for presentation at the symposium by an ARMA Technical Program Committee based on a technical and critical review of the paper by a minimum of two technical reviewers. The material, as presented, does not necessarily reflect any position of ARMA, its officers, or members.

ABSTRACT: In this study, discrete physical models using different blocks and hole sizes, and backfill characteristics are used to simulate changing underground mine conditions due to mining activities. In addition to voids and various backfills, this study includes fractures to investigate their effect on seismic wave propagation. The fracture systems in concrete blocks with sizes of 150 mm, 225 mm, 300 mm, 375 mm, and 450 mm were created by filling holes of various diameters in the concrete cubes with a static cracking agent (SCA). This process mimicked blast and stress-induced fracturing in the underground mine environment. AE measurements indicate that AE signal attenuation from fractures is more severe than due to backfill and in presence of fractures, backfill did not create a favorable environment for AE wave propagation toward receivers. AE signal arrival time to receivers mainly depends on the direction of AE wave propagation rather than the geometrical arrangement of the sensors in the presence of the voids, backfills, and fractures. AE signal arrivals to receivers are governed by the subsurface variability, Snell's law, and AE wave propagation direction. These factors should be considered to enhance the current source location approaches in microseismic monitoring systems.

1. INTRODUCTION

A major concern in deep underground mines is seismicity and rockburst of which frequency increases with mining depth. These phenomena significantly influence mine safety, productivity, and operating costs. Considering the undesirable impacts and consequences of seismic activities and rockbursts, their forecasting and control play a critical role in deep underground mines. Seismically active mines rely on microseismic monitoring systems to predict microseismic events and to minimize the exposure of personnel and equipment to seismic hazards. The microseismic monitoring system is able to identify, locate and quantify the mine seismicity enabling a better understanding of the rockburst mechanism.

The working principle of microseismic monitoring systems is related to the traveling velocity of the radiated waves from the seismic event source through the rockmass. Thus, accurate and reliable seismic source location depends on the input velocity model (VM) integrated into the microseismic monitoring system source location algorithm. Large source misplacement errors in seismic source locations using the constant VM were evidenced in studies by Collins et al. (2014a) and Peng et al. (2020). Thus, conventionally used single static VM and layered VM assuming homogeneous rockmass are unsatisfactory and inappropriate for underground mine environments because of the constant changes of the rockmass qualities and void conditions.

The traditional VMs and source location algorithms assume that the seismic wave propagates to receivers through a straight path (Riefenberg, 1989; Hedley, 1992; Ge, 2003). Although this assumption of the straight raypath can be valid in isotropic homogeneous media, it is not applicable in anisotropic heterogeneous rockmass characteristic of the Earth's subsurface. Seismic wave propagation is affected by various factors underground. While seismic wave velocity is highly reduced when transitioning from the rockmass layer to the underground void, and existing fractures attenuate the seismic wave energy. However, seismic events detected by the microseismic monitoring system might follow different propagation paths around the possible obstacles such as voids, discontinuities, and backfill. Given that several possible paths of seismic wave rays arrivals are possible for a pair of source-receiver (Ammon et al., 2020), investigation of the seismic wave propagation under various conditions may have important implications for the improvement of the seismic source location approaches under the continuously changing ground conditions in underground mines. This study presents acoustic emission (AE) wave propagation characteristics under designed and controlled laboratory experiments, which mimicked a complex underground mining environment. Particularly, the effects of voids, backfills, and fractures on the seismic wave propagation were analyzed using AE measurements.

2. MATERIALS AND METHODS

Discrete physical block models using different blocks and hole sizes, induced fractures, and backfill characteristics are used to simulate the changing underground mine conditions in the laboratory. The concrete blocks (cubes) of sizes 150 mm, 225 mm, 300 mm, 375 mm, and 450 mm were cast following the procedure in the ASTM C109-C standard (ASTM, 1966) to mimic the homogeneous rockmass. The underground void is simulated by placing pipes of diameters of 50 mm, 75 mm, 100 mm, 125 mm, and 150 mm in the center of the casting cube molds in order of the increasing cube sizes. Dry sand, saturated sand, and backfills with cement to sand ratios of 5%, 10%, 15%, and 20% are filling types used in the block holes for designed backfill void conditions. In addition to voids and various backfills, this study includes fractures to investigate their effect on seismic wave propagation. The fracture systems in concrete blocks were created by filling holes of various diameters in the concrete cubes with a static cracking agent (SCA). The swelling pressure of SCA due to hydration causes the concrete blocks to fracture.

The effect of fractures combined with the empty and backfilled block holes on the signal wave propagation was analyzed using the AE system. AE measurements were taken by assembling the fractured parts of the blocks and conducting AE measurements with 8 sensors mounted around the cube at known locations based on grids marked on the cube faces. One of the 8 sensors was used as a pulser to represent the seismic source while the other seven sensors served as receivers. AE sensor arrangements around 150 mm and 300 mm blocks were similar, while 225 mm, 375 mm, and 450 mm blocks also had similar sensor arrangements but different from those on the 150 mm and 300 mm blocks. The sensor positions on the XY block plane (plan view) with the Z position given in brackets are shown in Figure 1 for 300 mm and 450 mm concrete blocks representing the two different sensor arrangements on the blocks. It should be noted that a similar AE sensor configuration in concrete blocks is maintained in both the fractured and unfractured block testing conditions.

AE wave propagation in the fractured block conditions is examined using the signal travel time rather than traveling velocity. This is because the wave velocity is reduced or increased depending on the properties of various propagation mediums (i.e., fractures, backfill, void, and varying concrete block conditions). On the other hand, AE signal travel time, defined by the difference between AE signal arrival time to receivers and source origin time, implicitly measures all known and unknown factors in the way of AE signal propagation.

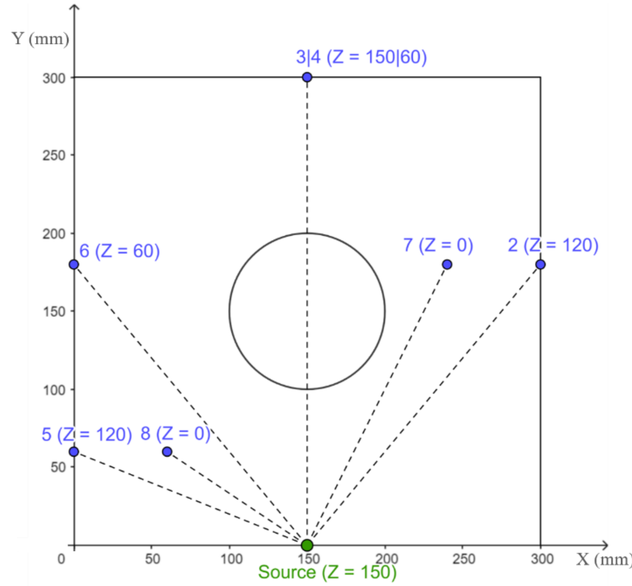

a)

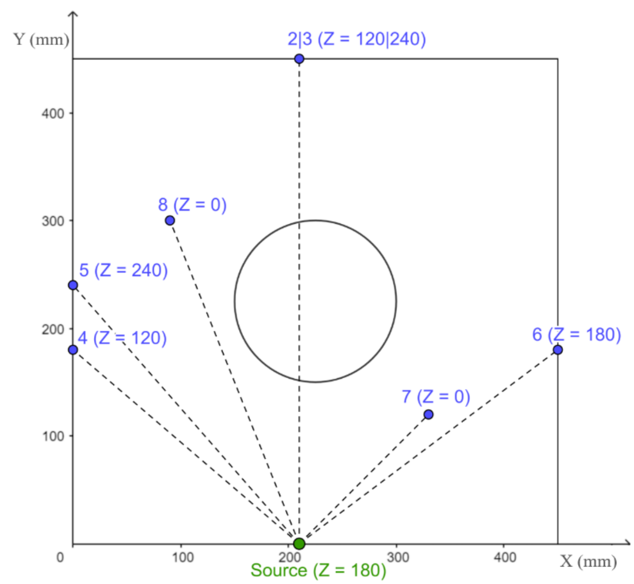

b)

Figure 1. The source-receiver arrangements with the projected straight ray paths on the XY plane for a) 300 mm block; and b) 450 mm block. Sensors 7 and 8 on top of the 300 mm and 450 mm blocks, respectively, are the closest to block holes, while sensors a) 3 & 4 and b) 2 & 3 are located across the hole of the 300 mm and 450 mm blocks, respectively.

According to the straight raypath concept, in the 150 mm and 300 mm concrete blocks, the AE signal first reaches sensors 5, 8, 2, 6, and 7, and then sensors 3 and 4, which are located across the hole. In cases of the 225 mm, 375 mm, and 450 mm concrete blocks, the AE signal detection by sensors is accomplished in the sensor order of 7, 4, 6, 5, 8, 2, and 3. These sensor detection arrangements are taken as a reference to analyze the AE wave propagation under various block conditions in this study.

3. RESULTS AND OBSERVATIONS

The SCA fractured all concrete blocks into 2 and 3 parts. Examples of SCA-fractured blocks are shown in Figures 2a and b. It is difficult to observe the fractures in the 225 mm fractured block in Figure 2a since it is well tightened when assembled. In contrast, a distinct 375 mm fractured block can be seen in Figure 2b. From both unfractured and fractured block testing conditions, it was observed that the effects of voids, backfills, and fractures on AE wave propagation are more distinct in larger concrete blocks than in smaller ones. Hence this study focuses on AE measurements taken on 300 mm, 375 mm, and 450 mm concrete blocks. In addition, only 10% and 20% cemented backfill cases are presented for brevity. The remaining data can be provided upon a reasonable request.

a)

b)

Figure 2. SCA fractured a) 225 mm and b) 375 mm blocks. The 225 mm fractured block is well tightened while assembled, while a loose form of the 375 mm block shows the fractures distinctly.

3.1. *Results for blocks with an empty hole, holes filled with dry sand and saturated sand*

The fracturing pattern was the same when the block holes were empty, filled with dry sand, and saturated sand in each block case. Figures 3, 4a and 4b illustrate the plan view of fracture propagation patterns relative to sensor positions in the 300 mm, 375 mm, and 450 mm concrete blocks, respectively. In all these cases, SCA disintegrated blocks into two parts. The AE measurements taken in both unfractured and fractured blocks are provided in Tables 1-3.

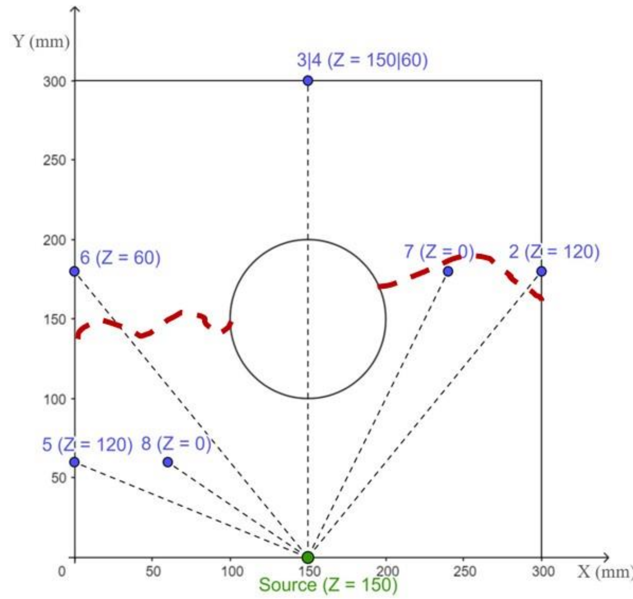

Figure 3. Plan view of the 300 mm fractured cube for the cases of an empty hole, hole filled with dry sand, and wet sand. Sensors 5, 7, and 8 located prior to hole and fractures were able to detect the AE signal.

Table 1. The signal travel time (μsec) to sensors in the 300 mm blocks with the empty hole, the hole filled with dry and wet sands

300 mm cube with 2 fractures					
Backfill	Age	Sensors			
		TT4	TT5	TT7	TT8
No	0	0	58.4	76.2	160.1
Dry sand	0	0	56.3	275.4	65.7
Wet sand	8 hours	0	56.5	300.8	67.0
Wet sand	1 day	0	52.8	80.5	59.9
Wet sand	7 days	0	64.6	227.1	62.0
Wet sand	14 days	0	58.9	167.9	69.9
Wet sand	28 days	0	60.3	168.7	71.5
300 mm cube with no fractures					
No	0	103.6	53.0	77.3	55.3
Dry sand	0	103.4	52.9	77.2	55.2
Wet sand	8 hours	112.8	47.5	148.4	61.1
Wet sand	1 day	107.1	45.7	153.8	59.1
Wet sand	7 days	105.9	46.3	152.2	60.7
Wet sand	14 days	101.9	46.8	144.6	60.1
Wet sand	28 days	122.5	46.0	155.4	59.6

In the 300 mm fractured block, sensors 2, 3, 4, and 6 located across the hole and fractures (Figure 3) were not able to detect the AE signal from the source. The signal energy towards these sensors is fully dissipated in fractures and holes when the latter were empty, filled with dry sand and saturated sand. Sensors 5, 7, and 8 located before the holes and fractures on the same side with the source detected the AE signal in all cases as expected. However, AE signal travel time to sensor 8 is three times greater in the 300 mm fractured block with an empty hole than in its unfractured counterpart as can be noted from Table 1. The analogous situation of abnormally high signal travel time to sensor 7 can be noted in the case of the fractured cubes with dry and wet sand filling. The signal travel times to sensors 5 and 8 in Table 1 indicate that the detection behavior of sensors in fractured cube with wet sand backfill is consistent and comparable with the unfractured cases. However, the signal travel time to sensor 7 in both fractured and unfractured 300 mm blocks is scattered. This might be explained by the close location of sensor 7 to the block hole, which causes the signal reflections from the hole boundary

375 mm and 450 mm blocks had the similar SCA induced fracturing as shown in Figures 4a and 4b, respectively, for the cases of the empty hole, holes filled with dry sand and wet sand. According to AE measurements in Tables 2 and 3, in both fractured blocks, sensors 4 through 7 located prior to the block holes and fractures detected the signal. AE signal travel time to these sensors is more consistent and comparable in the fractured and unfractured 375 mm blocks than 450 mm blocks. When holes were empty and filled with dry sand in the fractured 375 mm blocks, AE signal arrived late to sensors 6 and 7, which are located on the right side and top of the concrete cube, respectively (See Figure 4a and Table 2).

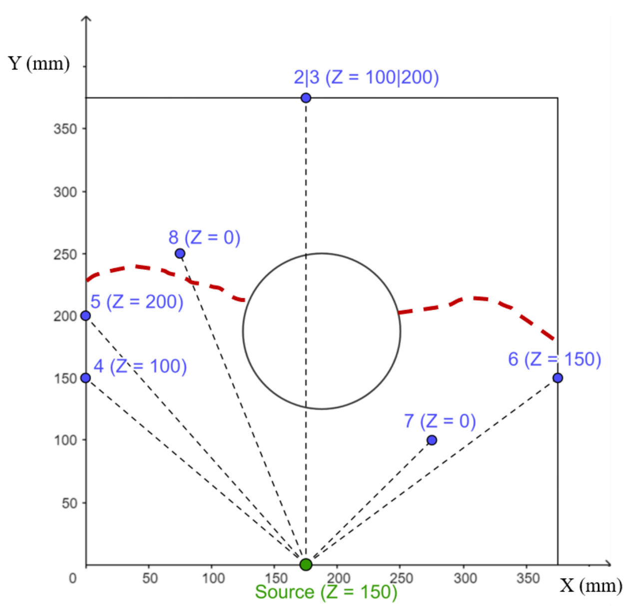

a)

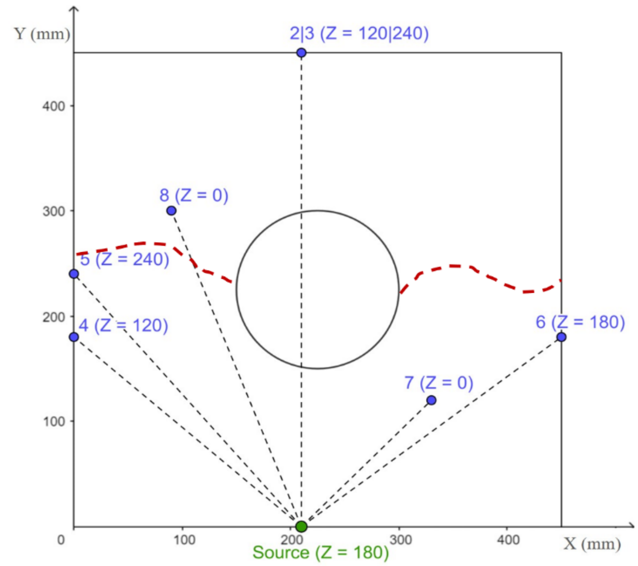

b)

Figure 4. Plan views of the a) 375 mm and b) 450 mm fractured blocks for the cases of an empty hole, the hole filled with dry sand and wet sand. AE signal arrived at sensors 4 through 7 located prior to holes and fractures in both 375 mm and 450 mm fractured blocks.

The analogous late signal arrivals to these sensors can be observed in the case of 450 mm fractured block with empty hole. It can be noted from Table 3 that when a 450 mm fractured block hole was filled with dry sand, AE signal travel time to sensors 4 through 7 is considerably higher compared to the unfractured counterpart despite the fact that the AE wave raypath does not cross both backfilled hole and fractures. AE signal arrival at sensors 4 and 5 is also significantly late in the 450 mm fractured block with saturated sand fill compared to the 450 mm unfractured block with saturated sand fill. In addition, AE signal arrival time to sensors 4, 5, 6, and 7 is irregular under various backfill ages of the saturated sand in the 450 mm fractured block according to Table 3.

Table 2. The signal travel time (μsec) to sensors in the 375 mm blocks with the empty hole, the hole filled with dry and wet sands

375 mm cube with 2 fractures					
Backfill	Age	Sensors			
		TT4	TT5	TT6	TT7
No	0	88.4	85.0	203.8	145.2
Dry sand	0	88.2	85.4	203.8	145.3
Wet sand	8 hours	76.7	79.9	79.6	64.9
Wet sand	1 day	76.3	79.5	78.4	62.1
Wet sand	7 days	77.0	79.9	83.9	67.1
Wet sand	14 days	77.1	80.2	84.6	67.0
Wet sand	28 days	79.9	82.6	92.9	73.4
375 mm cube with no fractures					
No	0	65.8	77.4	66.4	61.4
Dry sand	0	83.0	74.1	79.1	77.1
Wet sand	8 hours	80.8	85.1	86.1	76.1
Wet sand	1 day	83.6	80.3	91.5	73.1

Wet sand	7 days	89.6	83.5	85.5	69.5
Wet sand	14 days	78.4	84.7	77.3	70.7
Wet sand	28 days	80.0	70.2	77.8	83.8

Table 3. The signal travel time (μsec) to sensors in cases of the empty hole, hole filled with dry and wet sands in 450 mm cube

450 mm cube with 2 fractures					
Backfill	Age	Sensors			
		TT4	TT5	TT6	TT7
No	0	78.8	91.1	165.7	267.5
Dry sand	0	134.6	142.0	137.2	117.3
Wet sand	8 hours	235.8	262.4	97.1	95.9
Wet sand	1 day	235.5	272.6	95.8	94.8
Wet sand	7 days	286.3	200.5	100.1	82.8
Wet sand	14 days	286.4	290.5	111.3	105.7
Wet sand	28 days	228.5	266.4	108.7	137.7
450 mm cube with no fractures					
No	0	79.6	89.5	95.5	84.5
Dry sand	0	81.4	95.2	94.1	86.4
Wet sand	8 hours	81.5	95.7	94.3	95.9
Wet sand	1 day	81.9	101.0	95.6	85.6
Wet sand	7 days	80.6	95.1	93.7	84.9
Wet sand	14 days	79.9	95.3	99.1	87.7
Wet sand	28 days	81.3	97.0	92.6	89.8

3.2. *Results for blocks with holes filled with 10% and 20% cemented sand fills*

Two or three fractures were characteristic of the 300 mm, 375 mm, and 450 mm blocks with 10% and 20% cemented backfills. 300 mm blocks with 10% and 20% cemented backfills fractured into two and three parts with SCA as shown in Figure 5a and 5b, respectively.

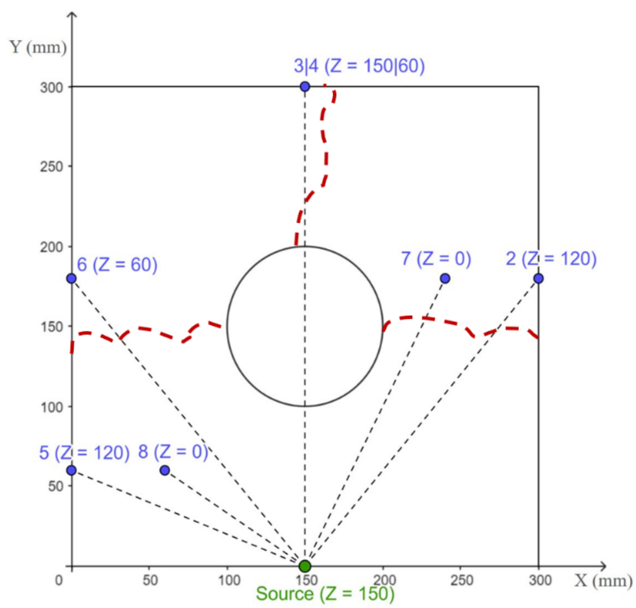

a)

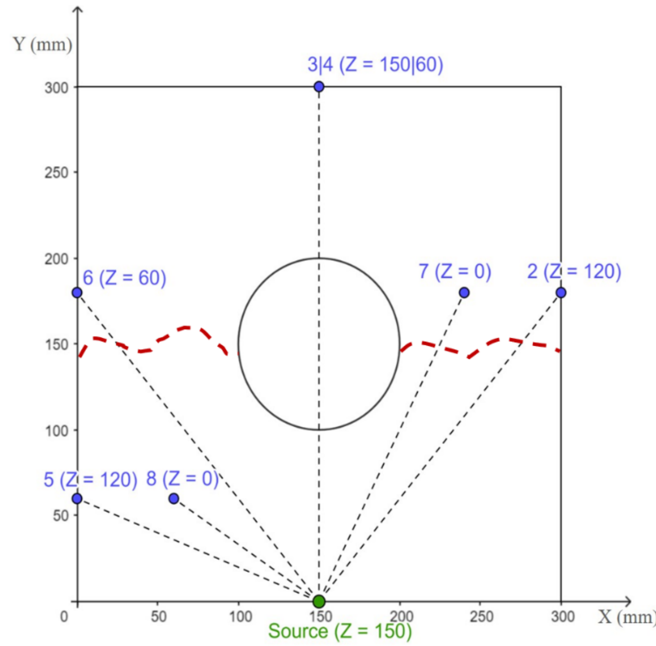

b)

Figure 5. Plan view of the fracture propagation pattern in the 300 blocks with holes with a) 10% and b) 20% cemented sand fills. Only sensors 5 and 8 were able to detect the AE signal in both cases.

It can be seen from these figures that despite varying fracture characteristics, only sensors 5 and 8 were able to detect the AE signal in both 300 mm fractured blocks with 10% and 20% cemented backfills. The AE signal energy to the remaining sensors is likely fully dissipated in the fractures. Despite the cemented backfills, which create a favorable medium for AE wave propagation, the fracture effect on the AE signal dominates. Probably, the fracture aperture was wide enough to fully attenuate the AE signal. According to Tables 4.1 and 4.2, AE signal travel times to sensors 5 and 8 in the fractured and unfractured block conditions are comparable under various backfill ages.

Table 4.1. The signal travel time (μsec) to sensors in the 300 mm cube with 10% cemented backfill

300 mm cube with 3 fractures		
Age	Sensors	
	TT5	TT8
8 hours	48.0	49.6
1 day	60.7	54.0
7 days	63.0	46.8
14 days	59.5	52.9
28 days	55.2	51.8
300 mm cube with no fractures		
8 hours	48.6	63.6
1 day	55.0	68.7
7 days	56.7	69.7
14 days	48.2	65.4
28 days	52.6	64.6

Table 4.2. The signal travel time (μsec) to sensors in the 300 mm cube with 20% cement backfill

300 mm cube with 2 fractures		
Age	Sensors	
	TT5	TT8
8 hours	44.7	58.7
1 day	44.5	57.7
7 days	46.3	68.3
14 days	50.8	63.5
28 days	53.2	68.0
300 mm cube with no fractures		
8 hours	50.4	60.3
1 day	50.7	62.6
7 days	51.3	62.6
14 days	51.1	58.5
28 days	46.0	59.6

Both 375 mm blocks with 10% and 20% cemented backfills had 2 fractures with different propagation directions along the hole as demonstrated in Figures 6a and 6b. In the case of fractured blocks with 10% cement backfill, the detection behavior of the sensors depending on their positions relative to fractures is consistent. As expected, the AE signal, whose straight path to sensors is hindered by fractures, was not reached to those sensors across the fractures, while sensors 2, 3, 4, 5, and 8 located on the left side of the fractured cube were able to detect the signal (Figure 6a). No significant influence of the backfill curing time on the signal arrivals at sensors can be seen from Table 5.1. The analogous sensor detection behavior can be observed in the 375 mm fractured blocks with 20% cemented backfill. All sensors except sensors 2, 3, and 8 located across the holes and fractures detected the AE signal, which is reasonable according to Figure 6b. No considerable difference in AE signal travel times to sensors between fractured and unfractured block cases can be noted from Table 5.2. Exception is the AE signal late arrivals at sensors 6 and 7 in the 375 mm fractured block at backfill age of 28 days.

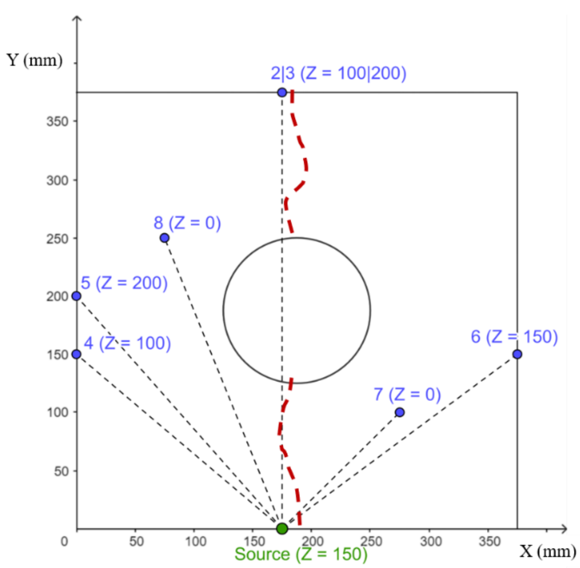

a)

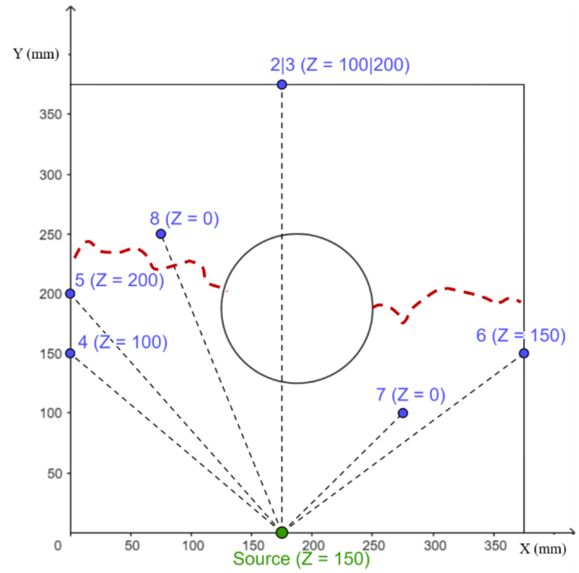

b)

Figure 6. Plan view of the fracture propagation pattern in the 375 blocks with holes filled with a) 10% and b) 20% cemented sand fills. AE signal arrived at sensors 2 through 5 and at sensor 8 when the hole of the 375 mm fractured block contained 10% cemented backfill. In the case of 20% cemented backfilling, sensors 4 through 7 were able to detect the AE signal.

Table 5.1. The signal travel time (μsec) to sensors in the 375 mm cube filled with 10% cement backfill.

375 mm cube with 2 fractures					
Age	Sensors				
	TT2	TT3	TT4	TT5	TT8
8 hours	109.7	125.2	66.3	77.3	96.3
1 day	110.2	123.7	65.7	76.5	94.7
7 days	108.9	116.7	65.6	76.6	94.2
14 days	107.9	112.5	66.8	75.7	93.1
28 days	109.8	119.6	69.2	79.1	112.5
375 mm cube with no fractures					
8 hours	114.2	113.3	63.6	73.3	100.0
1 day	113.4	112.3	63.7	73.2	99.7
7 days	113.3	111.1	64.3	73.5	103.8
14 days	113.0	113.0	66.6	73.8	98.8
28 days	117.0	110.4	67.0	74.0	99.5

Table 5.2. The signal travel time (μsec) to sensors in the 375 mm cube filled with 20% cement backfill.

375 mm cube with 2 fractures				
Age	Sensors			
	TT4	TT5	TT6	TT7
8 hours	66.7	70.1	77.9	76.8
1 day	68.3	71.5	75.9	72.9
7 days	69.1	70.1	84.9	91.7
14 days	68.8	71.2	80.8	105.9
28 days	71.4	74.3	166.2	123.7
375 mm cube with no fractures				
8 hours	69.9	79.6	71.8	122.6
1 day	68.5	77.8	73.1	135.7
7 days	67.8	78.2	72.3	71.9
14 days	68.6	81.3	75.1	113.3
28 days	67.8	84.4	75.6	75.8

Figures 7a and 7b illustrate the fracture propagation patterns in 450 mm blocks with 10% and 20% cemented backfills, respectively. The signal travel times to sensors in the fractured and unfractured block conditions are provided in Tables 6.1 and 6.2.

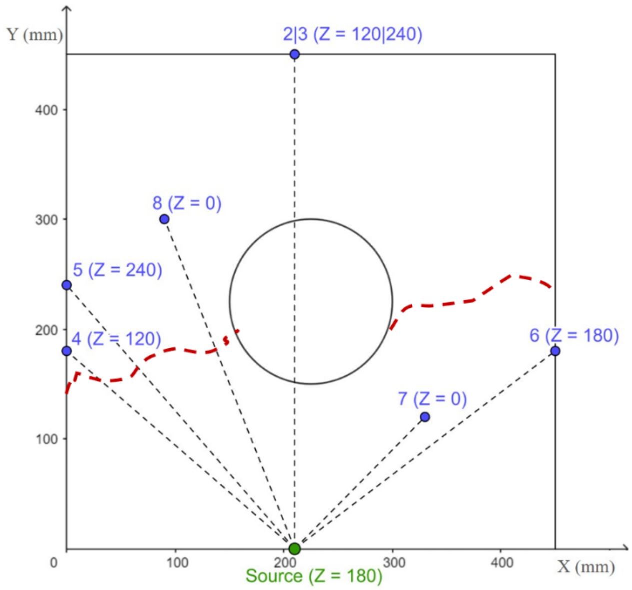

a)

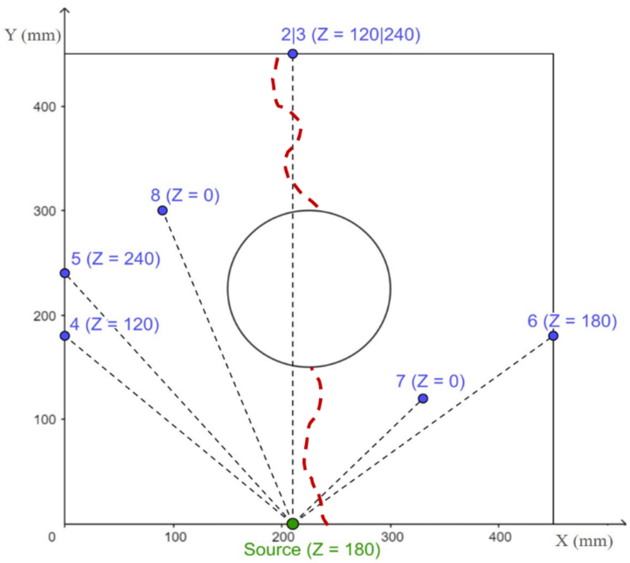

b)

Figure 7. Plan view of the fracture propagation pattern in the 450 blocks with holes filled with a) 10% and b) 20% cemented sand fills. Only sensors 6 and 7 located prior to 10% cemented backfill and fractures were able to detect the AE signal. In the case of 20% cemented backfill, AE signal arrived at sensors 4, 5, and 8.

According to these figures, all sensors located prior to fractures and holes were able to detect the AE signal, while those across the holes and fractures did not sense the signals. However, in the case of the fractured block with 10% cemented backfill, the AE signal arrived at sensors 6 and 7, located on the right side and top of the concrete block (Figure 7a), notably later compared to the AE measurements taken in the unfractured block case (Table 6.1). The analogous situation of late signal arrival to sensor 8 located on top of the concrete block and close to the block hole (Figure 7b) can be noted in the case of the fractured block with 20% cemented backfill (Table 6.2). AE signal travel time to sensors 4, 5, and 8 is abnormal at backfill age of 14 days in 450 mm fractured block with 20% cemented backfill. Despite the presence of the backfilled void, which is a potential medium for AE wave propagation, the AE signal was not sensed by sensors across the backfilled hole in the 450 mm fractured blocks with cemented backfills.

Table 6.1. The signal travel time (μsec) to sensors in the 450 mm cube with 10% cemented backfill.

450 mm cube with 2 fractures		
Age	Sensors	
	TT6	TT7
8 hours	148.9	205.6
1 day	150.2	192.9
7 days	146.7	179.1
14 days	153.7	169.7
28 days	126.0	199.2
450 mm cube with no fractures		
8 hours	95.0	90.3
1 day	91.4	86.70
7 days	94.6	89.1
14 days	90.2	89.4
28 days	95.2	88.5

Table 6.2. The signal travel time (μsec) to sensors in the 450 mm cube with 20% cement backfill.

450 mm cube with 2 fractures			
Age	Sensors		
	TT4	TT5	TT8
8 hours	83.8	94.7	190.1
1 day	83.9	93.6	197.9
7 days	85.0	94.6	216.8
14 days	199.3	170.6	324.8
28 days	83.8	102.9	197.1
450 mm cube with no fractures			
8 hours	81.3	91.5	110.7
1 day	81.3	91.8	108.0
7 days	86.5	93.8	137.3
14 days	81.9	93.0	114.5
28 days	81.2	92.2	137.2

4. DISCUSSION

The fractures strongly affected the AE signal propagation causing partial or full wave attenuation under various concrete block testing conditions. Several scenarios indicate that an unfavorable environment created by dry sand, saturated sand, and cemented backfills in block holes was supplemented by the fractures to impede the AE wave propagation toward receivers. This might be explained by the fact that the backfill did not infiltrate the fractures as infilling. In contrast, in the case of fractures hindering the wave propagation, backfill did not effectively serve as the medium for the AE waves to avoid the fractures and propagate through it and reach the signal receivers. The backfill might cause damping of the signal wave due to the inelastic material characteristics by its presence in the voids of the blocks. It was also observed that when the sample broken parts were well fitted when assembled, the sensors located across the cracks were able to detect the AE signal. This could also happen if backfill infiltrated the fractures to serve as infilling. Thus, the signal attenuation in fractures is highly dependent on fracture aperture size and content. It is concluded that AE signal attenuation from fractures is more severe than due to backfill. Rather, the AE signal reaches sensors through reflected paths if the signal is not fully attenuated on its way. The full or partial attenuation of the AE wave is governed by the fracture aperture size. Increasing fracture aperture leads to higher attenuation of the signal, more so without infilling. These observations are in agreement with the studies by Müller et al. (2010), Ekanem et al. (2014), Lissa et al. (2019), and Sawayama et al. (2022). Due to the attenuation effect of fractures and backfill, the signal travel time to some sensors was considerably higher in fractured concrete samples compared to unfractured ones despite the fact that those sensors located prior to holes and fractures. The increased travel time in fractured concrete blocks can also be explained by Snell's law (Robinson and Clark, 1987) according to which the raypath of the AE wave consists of several reflected and refracted paths. These paths increase the overall route length to the sensors and consequently, increase the signal travel time to the sensors. The considerably higher AE signal travel time was noted towards the sensors located on top of the concrete blocks. Since the AE pulse was generated from the side of the block, the AE wavefront can be considered expanding laterally rather than vertically (Cervený, 2001; Chapman, 2004). Late signal arrival times to top sensors despite their closest position to the AE source implies that the direction of the AE wave propagation is an important factor affecting the signal arrivals. Thus, AE signal arrival time to receivers mainly depends on the direction of AE wave propagation rather than the geometrical arrangement of the sensors in presence of the voids, backfills, and fractures. The dependence of the AE signal arrival time on subsurface variability, Snell's law, and AE wave propagation direction makes the straight raypath assumption in source location algorithms used in microseismic monitoring systems invalid.

The intention of using SCA in this study was to create fractures that would mimic the blasting and stress-induced fractures in concrete blocks. However, observed results of the AE wave propagation under fractured block conditions indicate that SCA-created fractures seem to model large discontinuities rather than blast or stress-induced fractures. This is because, in most cases, all sensors located across the fractures were not able to detect the AE pulse wave, which can be explained by the full attenuation of the signal wave in the fractures. While blast or stress-induced fractures may attenuate the AE signal, late signal arrival time rather than full signal damping would be more pertaining due to these fractures. In fact, SCA disintegrated concrete blocks into 2 and 3 parts, which might be insufficient to associate these fractures with the blast and stress-induced fracturing environment when blocks are assembled.

5. CONCLUSION

Velocity models and source location algorithms in microseismic monitoring systems assume uniform velocity and straight source wave raypath in the location of the microseismic events in underground mines. These assumptions are inappropriate in continuously changing ground conditions, where the seismic wave velocity and raypath may vary depending on the properties of the subsurface rockmass, geological features, and underground disturbances. Using the physical models and taking advantage of the controlled laboratory environment, this study attempted to explore the AE wave propagation in the presence of voids, various backfill types, and fractures. AE measurements taken revealed the following:

- The fractures adversely affect the AE signal propagation and cause partial or full wave attenuation.
- In the presence of fractures, backfill did not create a favorable environment for AE wave propagation to avoid the fractures and reach the signal receivers. It is concluded that the attenuation effect of fractures on AE signal is more severe than that of backfill.
- The signal arrival time to receivers increased considerably in fractured block conditions compared to unfractured ones. This is caused by the attenuation of the signal in fractures, voids, backfills, and increased signal travel path consisting of a series of the reflected paths that can be described by Snell's law.
- The direction of the AE wave propagation is an important factor affecting the signal arrivals to receivers. Geometrical positioning of the AE sensors relative to the source may not always state the signal arrival sequence to receivers in presence of the voids, backfills, and fractures.

These findings present significant implications to consider in the improvements of the seismic source location approaches.

ACKNOWLEDGEMENTS

This study is supported by Nazarbayev University Collaborative Research Program (CRP) under Grant Number OPCRP20200114. The authors also wish to gratefully acknowledge the support of the Los Alamos National Laboratory's Laboratory Directed Research and Development – Exploratory Research program (LDRD-ER-20220175ER).

REFERENCES

1. American Society for Testing and Materials. (1966). ASTM metric practice guide. Philadelphia.
2. Ammon, C. J., Velasco, A. A., Lay, T., & Wallace, T. C. (2020). *Foundations of modern global seismology*. Academic Press.
3. Cervený, V. (2001). *Seismic ray theory* (Vol. 110). Cambridge: Cambridge university press.
4. Chapman, C. (2004). *Fundamentals of seismic wave propagation*. Cambridge university press.
5. Collins, D. S., Pinnock, I., Toya, Y., Shumila, V., & Trifu, C. I. (2014a, August). Seismic event location and source mechanism accounting for complex block geology and voids. In the *48th US Rock Mechanics/Geomechanics Symposium*. American Rock Mechanics Association.
6. Ekanem, A. M., Li, X. Y., Chapman, M., Ian, M., & Wei, J. (2014). Effect of fracture aperture on P-wave attenuation: a seismic physical modelling study. *International Scholarly Research Notices*, *2014*.
7. Ge, M. (2003). Analysis of source location algorithms: Part II. Iterative methods. *Journal of Acoustic Emission*, *21*(1), 29-51.
8. Hedley, D. G. (1992). *Rockburst handbook for Ontario hardrock mines* (Vol. 92, No. 1). Canmet.
9. Lissa, S., Barbosa, N. D., Rubino, J., & Quintal, B. (2019). Seismic attenuation and dispersion in poroelastic media with fractures of variable aperture distributions. *Solid Earth*, *10*(4), 1321-1336.
10. Müller, T. M., Gurevich, B., & Lebedev, M. (2010). Seismic wave attenuation and dispersion resulting from wave-induced flow in porous rocks—A review. *Geophysics*, *75*(5), 75A147-75A164.
11. Peng, P., Jiang, Y., Wang, L., & He, Z. (2020). Microseismic event location by considering the influence of the empty area in an excavated tunnel. *Sensors*, *20*(2), 574.
12. Riefenberg, J. S. (1989). *A simplex-method-based algorithm for determining the source location of microseismic events* (Vol. 9287). US Department of the Interior, Bureau of Mines.
13. Robinson, E., & Clark, D. (1987). Fermat and the principle of least time. *The Leading Edge*, *6*(2), 34-37.
14. Sawayama, K., Ikeda, T., Tsuji, T., Jiang, F., Nishizawa, O., & Fujimitsu, Y. (2022). Elastic wave velocity changes due to the fracture aperture and density, and direct correlation with permeability: an energetic approach to mated rock fractures. *Journal of Geophysical Research: Solid Earth*, *127*(2), e2021JB022639.

ARMA 23–0482

Real-time Seismic Wave Velocity Prediction for Accurate Source Location in Underground Mines Based on Machine Learning

Mukhamedyarova Z., Suorineni F.

Mining Engineering, School of Mining and Geosciences, Nazarbayev University, Nur-Sultan, Kazakhstan

Maksut Z., Meiramov R., Yazici A.

Computer Science Department, School of Engineering and Digital Sciences, Nazarbayev University, Nur-Sultan, Kazakhstan

ABSTRACT:
The objective of this study is to develop machine learning techniques to forecast seismic wave velocities in real-time amidst the constantly changing conditions of underground mining. As human-induced seismicity in underground mining can negatively impact productivity, safety, and operating costs, it is crucial to have an accurate predictor for the source of microseismic events. To simulate the dynamic conditions of underground mining, laboratory experiments using AE systems and concrete blocks mimicking homogeneous rocks were conducted. The concrete blocks were of various sizes with different hole diameters and lengths representing variations in extraction ratio with mine maturity. Stress-induced fractures were produced using a static cracking agent. The blocks were tested with the voids empty and filled with various cement to sand ratios representing backfill in mining. The data collected from AE measurements, such as seismic wave velocity, arrival time, AE hits, and energy, were utilized to train different machine learning models, including linear regression, neural networks, Random Forest Decision Tree, and Gradient Boosted Decision Tree. The Gradient Boosted Decision Tree model demonstrated the highest accuracy with a mean absolute error of 7.15 m/s. The capability to predict seismic wave velocity in real-time would lead to better identification of the location of seismic events, ultimately improving the safety and efficiency of underground mining operations.

1. INTRODUCTION

This study specifically examines seismicity caused by underground mining operations. A seismic event refers to the sudden release of energy from the Earth crust, which leads to the propagation of seismic waves. In the mining industry, this release of energy can result in damage to equipment, injury, or even fatalities, in which case it is referred to as a rockburst (Feng et al., 2019). The impact of rockbursts and seismicity on mine safety, productivity, and costs is substantial. Despite this, predicting rockbursts remains a challenging task due to limitations in current knowledge and technology (Trifu and Suorineni, 2009). To address this issue, the implementation of microseismic monitoring systems in deep underground mines has become vital in managing mining-induced seismicity. These systems are critical in the management of seismic hazards, thus enhancing worker safety and mining productivity.

The accuracy of seismic monitoring systems, however, is contingent upon the velocity model used in the source calculation algorithm. The use of a single static input velocity or a layered model that assumes homogeneity in the rock mass and that the rock mass does not change in structure and composition is not realistic and often results in significant errors in the source location calculations. However, the process of rockmass response to mining that causes seismic energy release and potential damage to the excavations is complex and still not thoroughly understood.

According to Reyes-Montes et al. (2016), one major factor affecting the accuracy of source location is the velocity model used in the source location algorithm. Establishing a reliable velocity model in mining is challenging because multiple rock types are present, and the rock mass conditions are constantly changing due to the creation of voids and stress changes that cause continuous fracturing of the rock mass. This results in a continuously changing velocity model, which is different from the assumption of a single homogeneous rock mass or layered rocks with constant velocity used in current seismic monitoring systems for source location calculations. This research aims at developing a new method for tracking velocity changes in real time in the constantly changing underground mining environment, to

improve the accuracy of source location calculations in seismic monitoring systems.
Machine Learning was used to interpret the data and develop a smart algorithm for use in microseismic monitoring systems to determine real-time seismic wave velocities for source location calculations.

Rockbursts and seismicity are major concerns in deep mining and remain a significant engineering challenge (Wagner, 2019). Accurate source location calculations can improve the safety of workers in rockburst-prone areas, particularly as mines become deeper in the future. The research outcome will also enhance mine productivity by reducing downtime and assist in prioritizing the location of expensive rockburst-resistant support systems, ultimately improving mine profits. Improved source location will also enhance the reliabity of cave tracking when microseismic monitoring systems are used thereby mitigating potential airblast hazards.

2. METHODOLOGY

The study involves increasing the diameter of holes in rock blocks to simulate the increasing extraction ratio in mines with increasing mine maturity over time. The voids in the blocks were filled with various cement-ratios to represent different backfill types. The blocks used in the study were cast from sand and cement (synthetic rocks) and granite. were used to cover the desired range of hole diameters. The blocks were cubic and vary in size from 150 mm to 450 mm. the hole diameters in the blocks increased from 50 mm in the 150 mm cubes to 150 mm in the 450 mm cube considering boundary effect.

For each cube size some of the blocks were cast without holes to serve as controls and to repsent ground conditions prior to mining (undisturbed ground conditions). The blocks were tested with no holes, with holes empty, and later filled with different cement-sand ratios to represent mines with different backfill types.

The impact of different cement-sand ratios on seismic wave velocity was evaluated with time by curing each backfill for, 8 hours, 1 day, 7 days, 14 days, and 28 days. Dry and wet sand with zero percent cement were also tested to determine the effect of uncemented backfill on the seismic wave velocity. The cement ratio of backfills used in the tests ranged from 0% (dry and wet sand) to 20%, reflecting the cemented sand backfill commonly used in the mining industry, and included ratios of 5%, 10%, 15%, and 20% cement. Figure 1 depicts the sample geometry and hole diameters.

In each of the above discussed condition, a single sensor was employed as a pulse generator to simulate seismicity and act as a source. Seven additional sensors were utilized as receivers and located at pre-determined coordinates. The position of the pulse sensor was also determined. Thus knowing the source and receiver locations enabled the calculation of distances between the source and the receiving sensors.

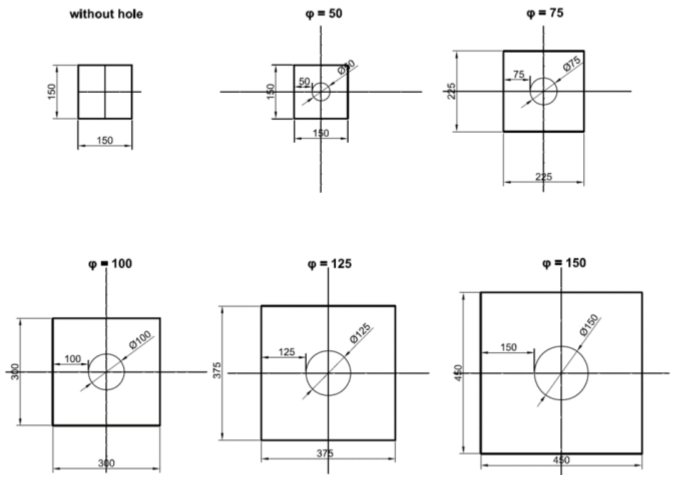

Fig. 1. Rock sample geometries, where ϕ is a hole diameter in mm.

2.1. Concrete and granite samples

Laboratory experiments were conducted on granite and concrete. Each block surfaces were polished to a tolerance of 1 mm, with each opposite face parallel to each other. Due to the high price of granite samples, only 300 mm granite cubes were sourced from local stone vendors.

The concrete cubes of each size were molded in the laboratory from a mixture of sand and cement to imitate rock. The sand to cement ratio and the water to cement ratio were established based on the ASTM C-109 C standard with a sand to cement ratio of 2.75 and a water to cement ratio of 0.485 (C109/109M-16a, 2016). The cubes were left to cure for 28 days before use. The mixture was vibrated for 4 minutes to compact it and remove excess air. To control the strength, 37mm diameter and 74mm height samples were taken from the same mixtures for UCS tests as a quality control measure to ensure the molded blocks had similar properties

2.1. Laboratory tests with AE system

Acoustic Emission Technique (AET) is a non-invasive testing method for materials. The laboratory testing of concrete through AE can simulate the field-scale seismic monitoring systems employed in the mining industry. This is achieved by translating mine scale coordinates to laboratory scale samples, with geometric similarity being the key factor (Ma & Du, 2020). Acoustic emissions (AE) and microseismicity in material failure processes share similarities, with the release of energy from a strained substance characterizing AE. The detection of these emissions is accomplished through sensors on the material's surface, leading to similarities between seismological approaches and AET as they are based on the same principles. In the AE identification system, the transformation of dynamic movements at the material's surface into electric impulses and detection of AE waves are performed by the AE sensors. The amplification of weak AE pulses was increased by over 1000 times using external preamplifiers and the internal AE system amplifier.

The propagation of the source within the material generates elastic waves which are recorded by AE sensors (Grosse, Ohtsu Masayasu, Aggelis, & Shiotani, 2022). The AE sensors were attached to the block surface using hot glue, as shown in Figure 2.

The laboratory tests employed the SAEU3H AE system, consisting of AE data acquisition modules, a frame with front and back panels, a disposable network connection module, a laptop, 8 sensors, preamplifiers, and cables (Figure 3). The SR150M High-frequency broadband AE sensor was used for testing 150 mm, 225 mm, and 300 mm rock samples, with a frequency band of 60-400 kHz and peak sensitivity greater than 75dB. For larger rock samples with dimensions 375 mm and 450 mm, the SRI150 sensor was employed, featuring an embedded pre-amplifier with a frequency band of 60 kHz-400 kHz and sensitivity of 40 dB.

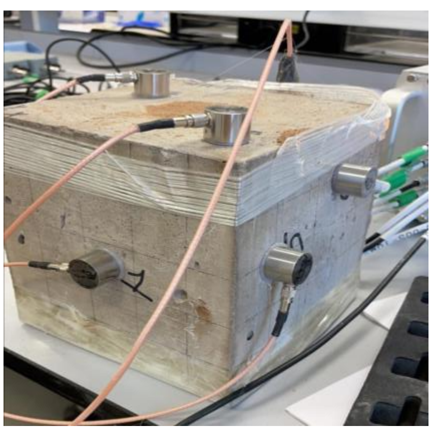

Fig. 2. Eight AE sensors attached to a concrete cube with backfill in the hole (see top of cube)

Fig. 4. AE system used in the study

2.3. Dataset

The data collected from the experiments consisted of three parts: base (839 readings), G80 Narrow-Band sensors cracked (269 readings), and fractured Cubes SR150M sensors (674 readings) obtained from 8 different sensors, where sensor 1 was the source. In total, there were 1782 readings available. Each reading provided information on the location coordinates (x, y, z), the distance from the source in millimeters, velocity, and arrival time in milliseconds. The source location coordinates were the only parameters provided for the source.

The dataset provided the coordinates of the source and receiving sensors, the arrival time of the wave at each sensor, and the quality parameters of the backfill, which affected the wave's velocity. Additionally, the quality of the fractured and unfractured cubes were assessed using the Rock Mass Rating (RMR) (Bieniawski 1989) system, and their corresponding wave velocities were measured.

To prepare the dataset for input into the neural networks, several methods were employed to improve the accuracy of the model. These techniques ensured that the data was pre-processed correctly and free of any errors or inconsistencies, which was crucial in achieving the desired results and the project's success. Specifically, these methods included one-hot encoding, handling missing values, and addressing recurring parameters.

Following the dataset cleaning process, the dataset for each sensor channel, excluding the source sensor, contained 23 different parameters. For the source sensor, 17 different parameters were generated, resulting in a total of 8 documents for each sensor. After the data cleaning process was completed, the number of readings across all sensors was reduced to 1365 readings.

2.4. Machine Learning Models

This study builds upon previous research by Maksut et al. (2022) on velocity prediction by utilizing several machine learning techniques, including Linear Regression, Neural Networks, and Decision Trees. In addition, the study introduces innovative neural network models and a novel Decision Tree methodology, and assesses the precision and reliability of the velocity predictions separately for seven different sensors.

Our study utilized Linear Regression to predict velocity by employing a linear model that forecasts the dependent variable using independent features. The primary aim of this method is to minimize the difference between the predicted and actual values.

Linear Regression is straightforward to implement, comprehend, and can be scaled to handle extensive datasets. Specifically, we applied Linear Regression to forecast velocity in our research, utilizing 22 concrete blocks and wave arrival parameters from seven distinct sensors.

Artificial Neural Networks (ANN), also known as Neural Networks, are a type of computing system that mimic the way human neurons function by transmitting signals through weighted connections. These networks are frequently utilized in deep learning, which is a method of machine learning that can identify complex relationships and patterns within features.

For our research, we designed and created several neural networks with varying numbers of hidden layers and neurons per layer. We utilized the rectified linear unit (ReLU) function as the activation function for all our networks. To test the effectiveness of the neural networks, we experimented with twelve distinct configurations, each with a different number of hidden layers and neurons per layer. By exploring different configurations, we aimed to find the optimal neural network architecture for our specific task. Through our experiments, we analyzed the accuracy and efficiency of each network configuration in order to identify the best one for our research. This approach allowed us to evaluate the performance of different neural network architectures and select the one that was most suitable for our study.

To achieve accurate and efficient predictions in our research, we employed alternative approach named Decision Trees (DTs), which encompass both Random Forest and Gradient Boosted DT. Although DTs can replicate the decision-making process, they are susceptible to overfitting. While Random Forest merges multiple decision trees to offer collective intelligence, this can compromise the balance between interpretability and speed. Alternatively, Gradient Boosted DT constructs trees sequentially to address limitations and minimize loss.

Decision trees and neural networks are both popular algorithms for regression problems. Decision trees are easy to understand and interpret, making them a good choice for exploratory data analysis. They can handle missing values and capture nonlinear relationships between variables. Neural networks, on the other hand, are capable of learning complex relationships in large and complex datasets. They can uncover hidden relationships and can be trained with a variety of optimization algorithms. Considering each approach’s exceptional prediction abilities and efficiency, we chose them for our study.

3. RESULTS AND DISCUSSION

3.1. Data Analysis

Material condition parameters and velocity have a non-linear dependence, as indicated by their joint distributions. Nonetheless, some parameters display a linear correlation, such as block size and hole diameter. The range of values for each function is diverse, leading to instability in training machine learning models. To address this, we utilized normalization techniques.

Table 1 includes a list of variables used for training the models. It is important to note that sensor coordinates, distance to source, and arrival time parameters differ among the sensors, resulting in seven distinct datasets for each sensor labeled #2 through #8. Channel #1 is the source channel, but the remaining parameters remain consistent across all datasets.

Table 1: Machine Learning Features

Feature	Description
Sample	The experimental cube's composition, whether it is made of concrete or granite.
Cement content, %	The proportion or amount of cement mixture within the hole, expressed as a percentage.
Curing time, days	The duration since the hole was filled.
RMR	The rating of the rock mass and the quality of fractured blocks.
Arrival time, ms	The time of wave arrival at the sensor.

Hole	A binary value indicating whether a hole is present in the cube or not.
Hole diameter, mm	The measurement of the diameter of the cylindrical hole in the cube.
Backfill Strength, MPa	The quality of the material used to fill the hole after it was created.
Block size, mm	The length of one side of the cube.
Sensor coordinates, (m, m, m)	The coordinates of the sensor location in a three-dimensional space.
Source coordinates, (m, m, m)	The coordinates of the source location in a three-dimensional space.
Distance to source, m	The distance between the sensor and the source of the wave.

3.2. Results

By utilizing new neural network models and the Decision Tree approach, we expanded upon the previous research conducted by Maksut et al. (2022) in our study. Our goal was to predict velocity for each sensor individually, enabling us to identify unreliable sensors and improve accuracy. We evaluated the accuracy of our models using the Mean Absolute Error (MAE) metric and selected the best model from each algorithm. MAE measures the average magnitude of errors between the predicted and actual values. A lower MAE value indicates a better accuracy, as it means the model is making fewer errors. Our study outperformed the previous research by achieving an accuracy of 7.146 m/s for sensor #2, compared to the best accuracy of 34.770 m/s in the previous study. The models' accuracy was considered high, as the error was significantly different from the mean velocity of all records, which was 1615.386 m/s.

$$\mathrm{MAE} = \frac{\sum_{i=1}^{D}|x_i - y_i|}{n} \quad (1)$$

The effectiveness of the models was assessed by comparing the predicted and actual values of the new records in Fig. 5. The ideal outcome is for the points to align with the line depicted in the graph. The closeness of the points to the line serves as a measure of the model's accuracy on fresh data. Table 2 corroborates the results in Figure 1, indicating that the Gradient Boosted Decision Tree outperforms all other models.

Table 2: Testing accuracy of the ML models.

Model	Accuracy, m/s
Linear Regression	478.43
DNN with 6 layers and 128 nodes at each layer	20.47
Gradient Boosted Decision Tree	7.15

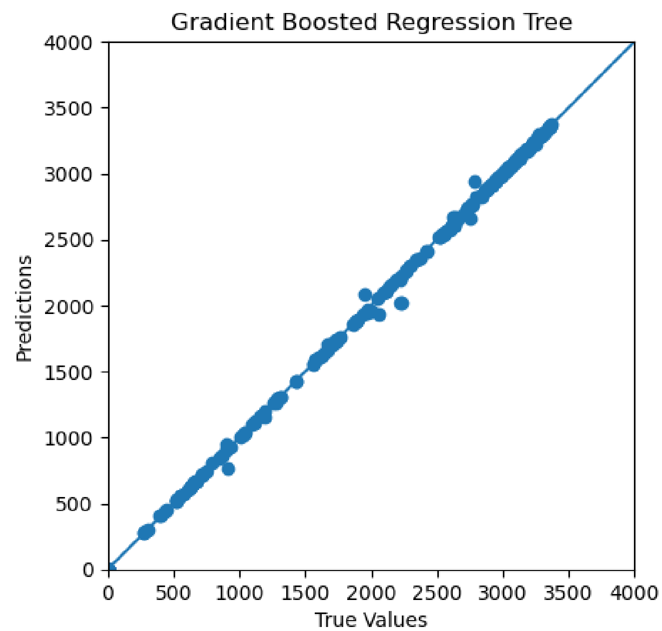

Fig. 5. Testing accuracy map for the GBDT model.

4. CONCLUSION

This study aimed to predict dynamic wave velocity in a constantly changing mining environment using laboratory experimental data. We explored various machine learning models, including deep learning, and found that the Gradient Boosted Decision Tree had the smallest error of 7.15 m/s, which represents a significant improvement over our previous best model, DNN_3_64, with an accuracy of 34.77 m/s. Accurate prediction of dynamic wave velocity is crucial for locating the source of seismic events in mining environments, which can significantly impact safety and productivity. In summary, this study highlights the potential of machine learning-based approaches for predicting dynamic wave velocity in a changing environment.

5. ACKNOWLEDMENTS

The authors acknowledge Nazarbayev University for support through the Collaborative Research Program Grant # OPCRP2020014

6. REFERENCES

1. Bieniawski, Z.T. (1989). Engineering rock mass classifications. New York: Wiley.
2. C109/109M-16a, A. (2016). Standard test method for compressive strength of hydraulic cement mortars (Using 2-in. or cube specimens). *Annual Book of ASTM Standards*, 1–10. https://doi.org/10.1520/C0109
3. Feng, X., Xiao, Y., Feng, G., Yao, Z., Chen, B., Yang, C., & Su, G. (2019). Study on the development process of rockbursts. *Yanshilixue Yu Gongcheng Xuebao/Chinese Journal of Rock Mechanics and Engineering*, *38*(4), 649–673. https://doi.org/10.13722/j.cnki.jrme.2019.0103
4. Grosse, C. U., Ohtsu Masayasu, Aggelis, D. G., & Shiotani, T. (2022). *Acoustic Emission Testing Basics for Research – Applications in Engineering* (second). Springer. Retrieved from http://www.springer.com/series/15088
5. Ma, G., & Du, Q. (2020). Structural health evaluation of the prestressed concrete using advanced acoustic emission (AE) parameters. *Construction and Building Materials*, *250*, 118860. https://doi.org/10.1016/j.conbuildmat.2020.118860
6. Maksut, Z., Meiramov, R., Yazici, A., and F. Suorineni. "A Machine Learning-Based Microseismic Event Location and Wave Velocity Prediction." Paper presented at the 56th U.S. Rock Mechanics/Geomechanics Symposium, Santa Fe, New Mexico, USA, June 2022. doi: https://doi.org/10.56952/ARMA-2022-0166
7. Reyes-Montes, J. M., Sainsbury, B. L., Andrews, J. R., & Young, R. P. (2016). Application of cave-scale rock degradation models in the imaging of the seismogenic zone. *CIM Journal*, *7*(2), 87–92. https://doi.org/10.15834/cimj.2016.9
8. Wagner, H. (2019). Deep Mining: A Rock Engineering Challenge. *Rock Mechanics and Rock Engineering*, *52*(5), 1417–1446. https://doi.org/10.1007/s00603-019-01799-4